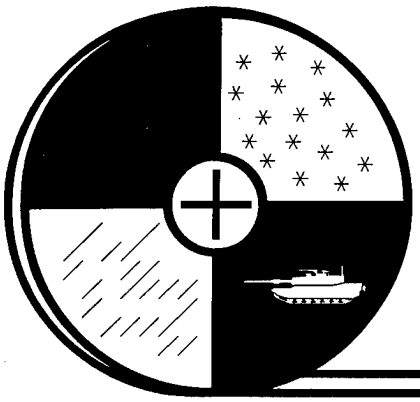
PROCEEDINGS
of the



1994 *Battlefield Atmospherics Conference*

Las Cruces, New Mexico

29 November - 1 December 1994

BATTLEFIELD ENVIRONMENT DIRECTORATE

U.S. Army Research Laboratory

White Sands Missile Range

New Mexico

APPROVED FOR PUBLIC RELEASE; DISTRIBUTION IS UNLIMITED.

DTIC QUALITY INSPECTED 1

19971215 104

NOTICES

Disclaimers

The findings in this report are not to be construed as an official Department of the Army position, unless so designated by other authorized documents.

The citation of trade names and names of manufacturers in this report is not to be construed as official Government indorsement or approval of commercial products or services referenced herein.

Destruction Notice

When this document is no longer needed, destroy it by any method that will prevent disclosure of its contents or reconstruction of the document.

Proceedings
of the
1994 Battlefield Atmospherics Conference

29 November - 2 December 1994

Sponsor

Battlefield Environment Directorate
U.S. Army Research Laboratory
White Sands Missile Range, New Mexico

Conference Chairmen

Mr. Edward D. Creegan
Mr. John R. Elrick

U.S. Army Research Laboratory

DTIC QUALITY INSPECTED 5

PROGRAM COMMITTEE

Battlefield Environment Directorate
White Sands Missile Range, New Mexico

Conference Manager
Mr. Edward D. Creegan (505) 678-4684

Conference Chairman
Mr. John R. Elrick (505) 678-3691

Conference Advisor
Dr. Richard C. Shirkey

Conference Support
Protocol/Public Affairs Office
Ann Berry
Elizabeth Moyers

Conference Technical Support
Technical Publication Branch
Maria J. Campolla

CONTENTS

Preface xi

SESSION I: SIMULATION/ANALYSIS

Visualization of Obscuration and Contrast Effects Using the Beams Models 3
Donald W. Hoock and *Patsy S. Hansen*, U.S. Army Research Laboratory; *John C. Giever* and *Sean G. O'Brien*, New Mexico State University

A Portable System for Data Assimilation in a Limited Area Model 15
Keith D. Sashegyi and *Rangarao V. Madala*, Naval Research Laboratory; *Frank H. Ruggiero*, Phillips Laboratory; *Sethu Raman*, North Carolina State University

Effect of High Resolution Atmospheric Models on Wargame Simulations 25
Scarlett D. Ayres, U.S. Army Research Laboratory

An Assessment of the Potential of the Meteorological Office Mesoscale Model for Predicting Artillery Ballistic Messages 37
Jonathan D. Turton and *Peter F. Davies*, Defence Services Division, Meteorological Office, United Kingdom; *Maj Tim G. Wilson*, Projects Wings, Royal School of Artillery, United Kingdom

Results of the Long-Range Overwater Diffusion (LROD) Experiment 47
James F. Bowers; U.S. Army Dugway Proving Ground; *Roger G. Carter* and *Thomas B. Watson*, NOAA Air Resources Laboratory

Modeled Ceiling and Visibility 57
Capt Robert J. Falvey, U.S. Air Force Environmental Technical Applications Center

A New PCFLOS Tool 65
K. E. Eis, Science and Technology Corporation

The Influence of Scattering Volume on Acoustic Scattering by Atmospheric Turbulence 75
Harry J. Auvermann, U.S. Army Research Laboratory; *George H. Goedecke* and *Michael DeAntonio*, New Mexico State University

Relationship Between Aerosol Characteristics and Meteorology of the Western Mojave 85
L. A. Mathews, and *J. Finlinson*, Naval Air Warfare Center; *P. L. Walker*, Naval Postgraduate School

SESSION II: OPERATIONAL WEATHER

Evaluation of the Navy's Electro-Optical Tactical Decision Aid (EOTDA) 97
S. B. Dreksler, *S. Brand*, and *A. Goroch*, Naval Research Laboratory

U.S. Army Battlescale Forecast Model 107
Martin E. Lee, **James E. Harris**, *Robert W. Endlich, Teizi Henmi*, and *Robert E. Dumais*, U.S. Army Research Laboratory; *Maj David I. Knapp*, Operating Location N, Air Weather Service; *Danforth C. Weems*, Physical Science Laboratory

Development and Verification of a Low-Level Aircraft Turbulence Index Derived from Battlescale Forecast Model Data 117
Maj David I. Knapp and *MSgt Timothy J. Smith*, Operating Location N, Air Weather Service; Robert Dumais, U.S. Army Research Laboratory

Current and Future Design of U.S. Navy Mesoscale Models for Operational Use 125
R. M. Hodur, Naval Research Laboratory

Combat Weather System Concept 133
James L. Humphrey, Maj George A. Whicker, Capt Robert E. Hardwick, *2nd Lt Jahna L. Wollard*, and *SMSgt Gary J. Carter*, Air Weather Service

Small Tactical Terminal Concept and Capabilities 141
2nd Lt Stephen T. Barish, *George N. Coleman III*, and Maj Tod M. Kunschke, Air Weather Service

Operational Use of Gridded Data Visualizations at The Air Force Global Weather Central 151
Kim J. Runk and *John V. Zapotocny*, Air Force Global Weather Central

Theater Forecast Model Selection 155
R. M. Cox, Defense Nuclear Agency; *J. M. Lanicci*, Air Force Global Weather Central; *H. L. Massie, Jr.*, Air Weather Service

Air Weather Service: Evolving to Meet Tomorrow's Challenges 161
Col William S. Weaving, *Maj Dewey E. Harms*, *Capt Donald H. Berchoff*, and *Capt Timothy D. Hutchison*, Air Weather Service

Air Force Weather Modernization Planning 171
Lt Col Alfonse J. Mazurowski, Air Weather Service

Uses of Narrative Climatologies and Summarized Airfield Observations for Contingency Support 181
Kenneth R. Walters, Sr. and *Capt Christopher A. Donahue*, U.S. Air Force Environmental Technical Applications Center

USAFTAC Dial-in Access 185
Capt Kevin L. Stone and *Robert G. Pena*, U.S. Air Force Environmental Technical Applications Center

Astronomical Models Accuracy Study 191
Capt Chan W. Keith and *Capt Thomas J. Smith*, U.S. Air Force Environmental Technical Applications Center

Atmospheric Transmissivity in the 1-12 Micron Wavelength Band for Southwest Asia 201
Capt Chan W. Keith, *Rich Woodford*, U.S. Air Force Environmental Technical Applications Center

SESSION III: BATTLE WEATHER

Owning the Weather: It Isn't just for Wartime Operations 211
R. J. Szymber, *M. A. Seagraves, James L. Cogan*, and *O. M. Johnson*, U.S. Army Research Laboratory

The Real Thing: Field Tests and Demonstrations of a Technical Demonstration Mobile Profiler System 221
J. Cogan, *E. Measure, E. Creegan, D. Littell*, and *J. Yarbrough*, U.S. Army Research Laboratory; *B. Weber, M. Simon, A. Simon, D. Wolfe, D. Merritt, D. Weurtz*, and *D. Welsh*, Environmental Technology Laboratory, NOAA

Characterizing the Measured Performance of CAAM 231
Abel J. Blanco, U.S. Army Research Laboratory

Evaluation of the Battlescale Forecast Model (BFM) 245
T. Henmi and *M. E. Lee*, U.S. Army Research Laboratory; *MSgt T. J. Smith*, Air Weather Service

Verification and Validation of the Night Vision Goggle Tactical Decision Aid 255
John R. Elrick, U.S. Army Research Laboratory

SESSION IV: BOUNDARY LAYER

Clutter Characterization Using Fourier and Wavelet Techniques 263
J. Michael Rollins, Science and Technology Corporation; *William Peterson*, U.S. Army Research Laboratory

Validation Tools for SWOE Scene Generation Process 273
Max P. Bleiweiss, U.S. Army Research Laboratory; **J. Michael Rollins**, Science and Technology Corporation

The Vehicle Smoke Protection Model Development Program 281
David J. Johnston, OptiMetrics, Inc.; *William G. Rouse*, Edgewood Research, Development and Engineering Center

Development of a Smoke Cloud Evaluation Plan 291
M. R. Perry, Batelle; *W. G. Rouse* and *M. T. Causey*, Edgewood Research, Development and Engineering Center

Analysis of Water Mist/Fog Oil Mixtures 301
William M. Gutman and *Troy D. Gammill*, Physical Science Laboratory; *Frank T. Kantrowitz*, U.S. Army Research Laboratory

New Millimeter Wave Transmissometer System 309
Robert W. Smith, U.S. Army Test and Evaluation Command; *William W. Carrow*, EOIR Measurements, Inc.

SESSION V: ATMOSPHERIC PHYSICS

Wind Field Measurement with an Airborne cw-CO_2-Doppler-Lidar (ADOLAR) 323
S. Rahm and *Ch. Werner*, German Aerospace Establishment DLR

Behavior of Wind Fields through Tree Stand Edges 331
Ronald M. Cionco, U.S. Army Research Laboratory; *David R. Miller*, The University of Connecticut

Transilient Turbulence, Radiative Transfer, and Owning the Weather 345
R. A. Sutherland, *Y. P. Yee, and R. J. Szymber*, U.S. Army Research Laboratory

Forecasting/Modeling the Atmospheric Optical Neutral Events Over a Desert Environment 355
G. T. Vaucher, Science and Technology Corporation; *R. W. Endlich*, U.S. Army Research Laboratory

SESSION I POSTERS : SIMULATION AND ANALYSIS

Combined Obscuration Model for Battlefield Induced Contaminants - Polarimetric Millimeter Wave Version (COMBIC-PMW) 367
S. D. Ayres, *B. Millard*, and *R. Sutherland*, U.S. Army Research Laboratory

A Multistream Simulation of Multiple Scattering of Polarized Radiation by Ensembles of Non-Spherical Particles 381
Sean G. O'Brien, Physical Science Laboratory

Combined Obscuration Model for Battlefield Induced Contaminants-Radiative Transfer Version (COMBIC-RT) 391
Scarlett D. Ayres, Doug Sheets, and *Robert Sutherland*, U.S. Army Research Laboratory

Emissive Smoke Modeling for Imaging-Infrared Seeker/Tracker Simulation 401
Joseph L. Manning, *Charles S. Hall, and Sheri M. Siniard*, Computer Science Corporation

SESSION II POSTERS: OPERATIONAL WEATHER

Performance of the U.S. Army Battlefield Forecast Model Performance During Operation Desert Capture II 413
R. E. Dumais, Jr., U.S. Army Research Laboratory

A Weather Hazards Program Used for Army Operations on IMETS 423
Jeffrey E. Passner, U.S. Army Research Laboratory

SESSION III POSTERS: BATTLE WEATHER

Comparison of Radiometer and Radiosonde Derived Temperature Profiles Measured at Wallops Island, VA 433
Edward M. Measure, U.S. Army Research Laboratory; *Dick R. Larson*, Physical Science Laboratory; *Francis Schmidlin* and *Sean McCarthy*, NASA Goddard Space Flight Center Facility, Wallops Island, VA

The Integrated Weather Effects Decision Aid Threat Module 443
David P. Sauter, U.S. Army Research Laboratory; *Carl H. Chesley* and *Andrew R. Spillane*, Science and Technology Corporation

Owning the Weather Battlefield Observations Framework 449
Richard J. Szymber and *James L. Cogan*, U.S. Army Research Laboratory

Electro-Optical Climatology Microcomputer Version 2.2 Demonstration (EOCLIMO) . . 461
Capt Matthew R. Williams, U.S. Air Force Environmental Technical Applications Center

SESSION IV POSTERS: BOUNDARY LAYER

Technical Exchange with Australia 467
James Gillespie and **Patti Gillespie**, U.S. Army Research Laboratory

Improvements to Modeling of Polarimetric Scattering 475
Michael DeAntonio, National Research Council Post Doc, U.S. Army Research Laboratory

Atmospheric Acoustic Characterization in Support of BAT-Vehicle Field Testing 487
John R. Fox, U.S. Army Research Laboratory; *Prasan Chintawongvanich*, Physical Science Laboratory

ARL Remote Sensing Rover as a Ground Truth Monitor at the XM-21 Challenge System Field Test 495
Frank T. Kantrowitz and *Dale U. Foreman*, U.S. Army Research Laboratory; *William M. Gutman*, Physical Science Laboratory

Lidar Observations During Smoke Week XIV 501
M. P. Bleiweiss and *R. A. Howerton*, U.S. Army Research Laboratory

Enhanced Photon Absorption in Multi-Component Aerosol Clouds 511
Young P. Yee and *Robert A. Sutherland*, U.S. Army Research Laboratory

Visualization of the MADONA Data Base and Use of Selected Sequences in a Wind Flow and Diffusion Simulation System 519
Harald Weber and **Welfhart aufm Kampe**, German Military Geophysics Office

SESSION V POSTERS: ATMOSPHERIC PHYSICS

Temperature Profile of the Nocturnal Stable Boundary Layer over Homogeneous Desert Using LA-Teams 529
R. Todd Lines, New Mexico State University; and **Young P. Yee**, U.S. Army Research Laboratory

Comparison of Boundary-Layer Wind and Temperature Measurements with Model Estimations 535
R. J. Okrasinski, Physical Science Laboratory; *A. Tunick*, U.S. Army Research Laboratory

Optical Turbulence Measurements at Apache Point Observatory 545
Frank D. Eaton, *John R. Hines*, and *William H. Hatch*, U.S. Army Research Laboratory; *James J. Drexler* and *James Northrup*, Lockheed Engineering and Sciences Company

The APRF SODAR: Bridging the Lower Boundary Layer 553
John Hines, *Frank Eaton*, *Scott McLaughlin*, and *William Hatch*, U.S. Army Research Laboratory; *G. Hoidale, W. Flowers* and *L. Parker-Sedillo*, Science and Technology Corporation

A Look at Thermal Turbulence Induced Radar Echoes in or Near Rain Clouds at the Atmospheric Profiler Research Facility 563
William H. Hatch, U.S. Army Research Laboratory

Border Area Air Quality Study 569
B. W. Kennedy, *J. M. Serna, J. R. Pridgen, D. Kessler, J. G. Moran, G. P. Steele*, and *R. Okrasinski*, Physical Science Laboratory; *J. R. Fox, R. Savage*, and *D. M. Garvey*, U.S. Army Research Laboratory

APPENDICES

Appendix A: Agenda 579

Appendix B: List of Attendees 587

Author Index 607

PREFACE

The 1994 Battlefield Atmospheric Conference was held 29 November through 1 December 1994 at White Sands Missile Range, New Mexico, under the sponsorship of the U.S. Army Research Laboratory, Battlefield Environment Directorate, White Sands Missile Range, New Mexico. The conference included oral presentations, posters, and demonstration sessions on five topics: Simulation and Analysis, Operational Weather, Battle Weather, Boundary Layer, and Atmospheric Physics. The conference had 219 attendees, including representatives from Denmark, France, Germany, Israel, The Netherlands, and the United Kingdom.

The genesis of the Battlefield Atmospherics Conference was the Electro-Optical Systems Atmospheric Effects Library (EOSAEL) and Tactical Weather Intelligence (TWI) Conference set up to analyze the 1993 Israeli War and the effective use of smoke by the Israeli forces to defeat electro-optical systems.

In 1991, in an effort to encompass additional aspects of battlefield atmospheric effects such as acoustic transmission, the conference became known as the Battlefield Atmospherics Conference.

The reader will find the items related to the conference itself (the agenda and the list of attendees) in the appendices. An author index is included after the appendices.

Session I

SIMULATION/ANALYSIS

VISUALIZATION OF OBSCURATION AND CONTRAST EFFECTS USING THE BEAMS MODELS

Donald W. Hoock
Patsy S. Hansen
Battlefield Environment Directorate
U.S. Army Research Laboratory
White Sands Missile Range, NM 88002-5501

John C. Giever
Sean G. O'Brien
Physical Science Laboratory
New Mexico State University
Las Cruces, NM 88003-0002

ABSTRACT

Interest in using highly interactive, real-time computer simulations as development, analysis, planning and training tools continues to expand within DoD and industry. Interactive simulations range from graphical manipulations of 3-D scientific data to realistic 3-D virtual and "fly-through" environments in real-time. Improvement in both real-time graphics hardware and wider access to off-the-shelf visualization software has particularly stimulated a user demand for better, "physically correct" models of processes, effects and appearances. One such improved, physics-based model for support of battlefield environment simulations is the U. S. Army Research Laboratory, Battlefield Environment Directorate, Battlefield Emission and Multiple Scattering Model (BEAMS). BEAMS computes both radiance (color values) and partial obscuration (opacity) of inhomogeneous battlefield clouds of obscurants, smoke, dust, haze and fog layers. In achieving a stable, accurate solution, BEAMS' long calculations are far from real-time. A full BEAMS 3-D radiative transfer calculation produces diffuse radiance outputs in 26 directions for each volume element of its non-uniform cloud concentration distribution. Thus, for real-time use in representing the "color" and "opacity" of battlefield clouds in simulators, it is necessary to develop simpler, parametric representations of BEAMS outputs. These outputs are now being analyzed to produce one of a number of "environmental representation" products to support real-time visualization of the battlefield environment. This paper addresses relative errors between: using a simple mean radiance profile derived from many sets of BEAMS calculations; using actual transmittance distributions through a given cloud along with the scaled (limiting) path radiance averaged from many BEAMS calculations; and performing a full BEAMS calculation for the entire cloud at each point in time. BEAMS outputs for these approaches to cloud visualizations are compared.

1. INTRODUCTION

Given a concentration distribution and a wavelength-dependent mass extinction for the aerosol, one can easily compute transmittance to an observer's position for every line of sight through an obscurant cloud. In visualization, one applies cloud transmittance as a 2-D map or array of the fractions of background radiance that will show through a cloud. However, transmittance is always less than one, so radiance can only be reduced (never increased) by just transmittance. Visualized only by using transmittance, every cloud appears dark against its background.

While this is appropriate for highly absorbing (black) obscurants, one usually also requires an array of the cloud diffuse scattered and emitted radiance that gives the cloud its own appearance (color value) or wavelength-dependent signature. This is called the "path radiance" of the cloud. It depends on external illumination, the cloud concentration and extinction per unit concentration, the relative amount of scattering versus absorption from individual particles, and the wavelength-dependent scattering pattern with angle (the phase function) for the type of obscurant particles in the cloud. Except for optically "thin" clouds, the path radiance is also dependent on the many possible paths over which the radiant power can be multiply-scattered before emerging.

The Battlefield Emission and Multiple Scattering Model (BEAMS) (Hoock et al. 1993; O'Brien 1993) is an approach to computing the steady state diffuse path radiance for finite clouds of non-uniform concentration. Typical run times for the BEAMS model to compute a 3-D cloud path radiance distribution can be tens of minutes to hours. It gives the path radiance in 26 solid angles at 3-D elements inside and on the surface of the cloud. A two-dimensional version (BEAMS-2D) also exists (Hoock and Giever 1993; 1994) for haze and fog in vertically stratified layers. BEAMS-2D requires a few seconds to minutes to compute the multiply-scattered path radiance distributions in and among the layers in 34 directions (17 upward and 17 downward solid angles).

Real-time and even near real-time interactive scene visualizations obviously cannot embed the BEAMS codes directly into the scene generation process. However, to represent clouds of obscurants, smoke, dust, haze and fog with physical accuracy one must give them both a correct transparency (transmittance) and color value (path radiance). Thus, the current approach to putting environments into interactive simulations is to pre-compute databases or scenario-dependent data sets (called environmental representations), such as scene illumination, visibility and obscurant cloud radiance. It is these tables or simple parametric curve fits that are then used to drive image generators and non-imaging combat simulations. Thus, it is first necessary to determine if BEAMS model outputs are general enough to apply to a sufficiently large range of cloud and illumination scenarios in battlefield environment simulations.

This paper addresses the extent to which BEAMS outputs can be reduced to useful data to support real-time battlefield scene simulation. The relevant parameters are described in section 2. The BEAMS methodology is briefly reviewed in section 3, and scenario-dependent inputs are given in section 4. Sections 5 and 6 are a case study of the analysis of BEAMS outputs. In particular, the question is to what accuracy can the consolidated outputs of many BEAMS runs be used to represent the path radiance (color values) of real-time simulated battlefield obscurant clouds. Section 7 gives conclusions.

2. CLOUD TRANSMITTANCE AND RADIANCE

Assume that the obscurant cloud dimensions and mass concentration C(x,y,z) distribution throughout the cloud are known. These can be from a dynamic model of transport and diffusion. Or, they can be provided by a mean obscurant concentration model such as the Combined Obscuration Model for Battlefield Contaminants (COMBIC) (Ayres and DeSutter 1994) and the 2-D or 3-D concentration fluctuations provided by the Statistical Texturing Applied To Battlefield-Induced Contaminants (STATBIC) model (Hoock 1991). We also assume that the wavelength-dependent mass extinction coefficient $\alpha(\lambda)$ is known. It can be obtained from the Electro-Optical Systems Atmospheric Effects Library (EOSAEL) phase function database (PFNDAT) (Davis et al. 1994) or computed from particle size distribution and wavelength-dependent refractive index via a shape-dependent particle scattering model, such as the AGAUS Mie code for spherical particles from EOSAEL (Miller,1983). Transmittance T at wavelength λ over a path from 0 to L through concentration C(s) = C(Ω•S) in direction Ω has concentration length CL and optical depth τ:

$$T(\lambda;\tau) = e^{-\tau(\lambda)} = e^{-\alpha(\lambda) CL} = e^{-\alpha(\lambda) \int_0^L C(s)\, ds} \qquad (1)$$

The change in radiance L(Ω•S) along the path in direction Ω is given in terms of all incoming radiances $L_{in}(\Omega';s)$, the obscurant and wavelength-dependent single scattering albedo ω (ratio of scattering to extinction), and a scattering phase function $P(\Omega',\Omega)$, by the radiative transfer equation

$$\frac{d}{ds} L(\Omega \bullet S) = -\alpha(\lambda)\, C(s) \left[L(\Omega \bullet S) - \omega \int L_{in}(\Omega'; s)\, P(\Omega; \Omega')\, d\Omega' \right] \qquad (2)$$

If the incoming illuminating radiance has the same relative directional dependence over a finite path of length Δs, so that an average incoming illumination can be defined over that path, then one can define a "limiting path radiance" $L_s(\Omega)$ as:

$$L_s(\Omega) = \omega \int L_{in}(\Omega'; \text{averaged over } \Delta s)\, P(\Omega; \Omega')\, d\Omega' \qquad (3)$$

The result, in terms of optical depth τ, transmittance T and path radiance $L_p(\Omega;s)$ is:

$$\begin{aligned} L(\Omega; s) &= e^{-\tau} L(\Omega; 0) + [1 - e^{-\tau}] L_s(\Omega) = e^{-\tau} L(\Omega; 0) + L_p(\Omega; s) \\ &= T(s)\, L(\Omega; 0) + [1 - T(s)]\, L_s(\Omega) \end{aligned} \qquad (4)$$

3. THE BEAMS MODEL

Equations 1 through 4 have direct implications to rendering propagation effects of haze, fog and obscurant clouds. If $L(\Omega;0)$ is the scene background and $L(\Omega;s)$ is the perceived radiance at the observer position s after passing through the cloud, then the first term is the transmitted background radiance through the cloud, and $L_p(\Omega;s)$ is the radiance (color value) observed from

the cloud itself. Furthermore, $L_s(\Omega)$ is the maximum (limiting) radiance from the cloud as the transmittance goes to zero over the path. It can be used with graphics hardware that allows a current (background) pixel color value to be blended toward a limiting value (thick cloud L_s) linearly with an opacity factor [1-T(s)]. While L_s is implicitly dependent on optical depth and position in the cloud (since these affect the incoming illumination L_{in}), L_s has far less dependence on local variations in τ than does $L_p(\Omega;s)$. We will exploit this in the following sections.

To compute $L_p(\Omega;s)$ and $L_s(\Omega)$ we use the BEAMS model. In the 3-D version of this model the cloud is gridded into cubical elements, each with its own concentration and scattering properties. The radiance is broken into 26 solid angles connecting each element with its nearest neighbors. The phase function $P(\Omega',\Omega)$ is integrated over the incoming solid angle and averaged over the outgoing solid angle to produce a 26x26 transfer matrix of incoming and outgoing radiance which can be used in place of the integral in the radiative transfer equation. The incident illuminations, both direct and diffuse, on the outside of the cloud are held constant as boundary conditions.

The internal cloud elements are repeatedly swept over from different directions, redirecting scattered or emitted radiance out of each element. When internal radiance fields settle down to "final" values, then the outgoing radiance at the cloud boundaries are the $L_p(\Omega,s)$ radiance of the cloud. The average $L_s(\Omega)$ is then computed through the cloud to each boundary point. Because of the many angular averages involved in integrating L_{in} in each element, specific contributions of external scene elements to the incoming radiance are not as important as the average diffuse scene illumination. Strong direct (for example solar) radiation incident on the cloud is used to determine the direct-to-diffuse radiance source terms in the cloud elements. Thus, the resulting diffuse radiance from the cloud can usually be determined from basic scene illumination inputs. The BEAMS-2D version for stratified layers is similar, although standard "doubling techniques" are used instead of iterations to determine the solutions (Hoock and Giever 1994).

4. SCENARIO-DEPENDENT VARIABLES

Scenario inputs can thus be identified as three types:

- Scene illumination in the form of: Sun Angle (θ,ϕ) or similar direct beam source; ratio of direct to diffuse incident irradiance; incident relative diffuse radiance on each element of the cloud boundary; reflectance or albedo A_g of the boundary below the cloud (if any).

- Cloud inputs in the form of: Number of cloud elements (Nx,Ny,Nz); length of the side of each element; concentration array C(i,j,k) for each element.

- Optical inputs in the form of: Obscurant type; phase function P; single scattering albedo ω; mass extinction coefficient α; steady-state emission source term for each element.

Outputs, as previously described, are $L_p(\Omega_m,s_{ijk})$ and $L_s(\Omega_m,s_{ijk})$ for m=1 to 26 directional solid angles, and ijk = coordinates of elements on the surface or interior of the cloud. The optical depths $\tau(i,j,k)$ of each element are computed simply by multiplying the concentration, mass extinction and element size. They are summed along lines of sight for total optical path τ's.

5. CASE STUDY - RADIANCE FROM SMOOTH VERSUS STRUCTURED CLOUDS

Assuming incident scene illumination and obscurant optical properties are fixed or vary slowly, one would still like to account for radiance changes due to cloud shape and concentration changes as it evolves and moves downwind. It would be particularly nice, for purposes of cloud rendering and real-time simulation, if one could reuse pre-computed tables or curves of cloud radiance for a variety of cloud configurations. Since L_s mainly averages over incoming illumination in all directions, one would hope that the L_s computed for smooth clouds and average concentrations (and optical depths) is still approximately valid for structured clouds and fluctuations in cloud concentration about the mean. Actual cloud output radiance L_p, however, is expected to vary greatly about the mean, correlating closely to the structure observed in cloud appearance.

To test these assumptions, a series of cases have been run. The obscurant used is white phosphorus smoke at a visual (0.55 μm) wavelength. The mass extinction for phosphorus smoke in the visual is 4.3 m^2/g, the single scattering albedo is 0.9912, and the phase function is from the PFNDAT database. A terrain surface albedo A_g of 0.3 is assumed. Solar zenith angles of 0, 30, 60 and 90 degrees were run at a fixed azimuth placing it over the positive y-axis (y-z plane). The ratio of direct sunlight irradiance (normal to propagation) to diffuse irradiance (on to a horizontal surface) was taken as 10, representing a clear day. The cloud was given a variety of simple rectangular shapes with coordinates x downwind, y crosswind and z vertical. Cloud dimensions, as simple ratios of X:Y:Z lengths per side, were assigned as: 1:1:1, 2:1:1, 4:1:1, 2:2:1, 4:2:1 and 4:4:1. The number of blocks used (8 to 64) and optical depths were varied in runs ranging from 0.25 to 64 across the total Y-dimension of the cloud (crosswind width).

Limiting path radiances for uniform concentration clouds were first computed. Several of the outputs are shown in figs. 1 through 4. In each case the sun is at an azimuth of 90 deg and a zenith angle of 60 deg. Figure 1 shows L_s computed for rays emerging at normal angles from the centers of each cloud face. Note the large value when the optical depth is low and the cloud is between the observer and sun. Figures 2 and 3 are other cases for radiance emerging at various directions from the cloud. Figure 4 plots the output L_s emerging across the face of the cloud, with sun at the right.

For optical depths below about 10 the variation is small. Above $\tau = 10$ distinct darkening or shadowing appears. This behavior has been found to be parameterized by the simple relation

$$L_s(\mathit{corrected}) \approx L_s(\mathit{uncorrected})\, e^{-\left(\frac{\mathit{perimeter}}{\mathit{area}}\right) s} \qquad (5)$$

which represents the "escape" of solar radiance through the sides of an optically thick cloud as the product of the physical (not τ) distance s from the major radiance source (sun) into the cloud, divided by the ratio of the cross sectional area of the cloud perpendicular to s to the perimeter of this area. (Effectively the exponent is thus the area to volume ratio of the cloud up to the distance s into the cloud.) These curves were then used to approximate the limiting path radiance L_s for non-uniform clouds of the same average optical depth across the cloud. STATBIC was used to generate these 3-D cloud concentrations, simulating the statistical properties of

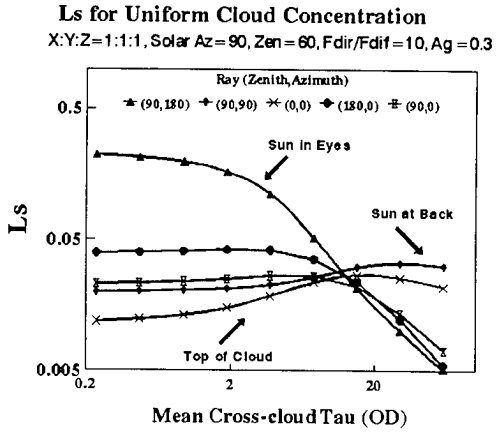


Figure 1. Limiting Path Radiance from Center of 6 Cloud Faces, Normal Angles, Showing Solar Angles.

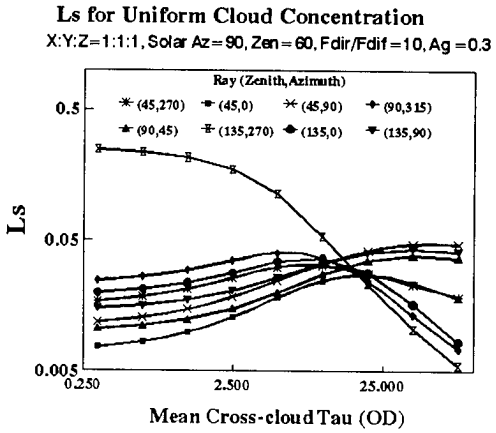


Figure 2. Ls Limiting Path Radiance as in Figure 1, but for Outgoing Angles at 45 degrees.

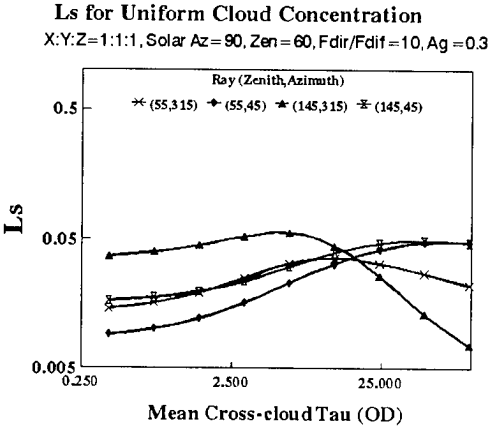


Figure 3. Ls Limiting Path Radiance as in Figs. 1, and 2, But for Upward and Downward Look Angles.

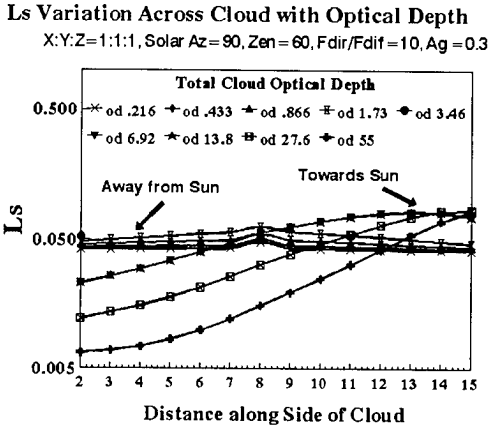


Figure 4. Variation in Output Radiance Across a 16 m Cloud with Darkening Shadows at $\tau > 10$.

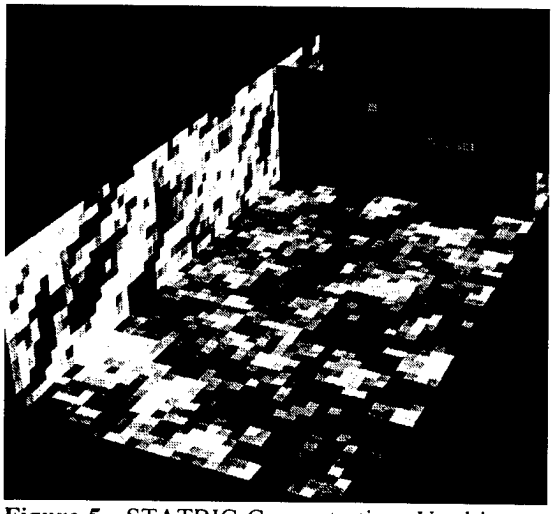


Figure 5. STATBIC Concentrations Used in Simulations. Cuts are through the x-y-z Planes.

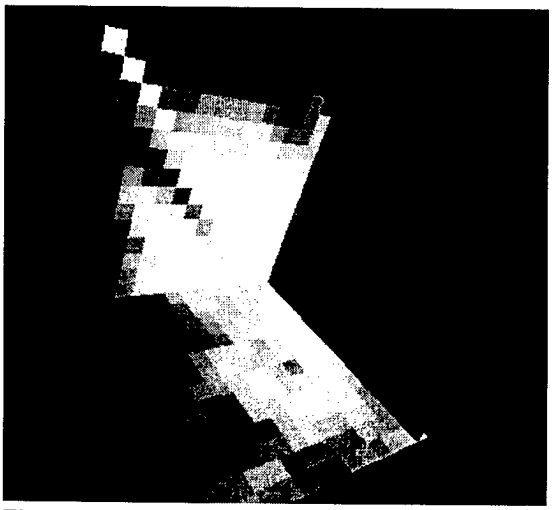


Figure 6. Radiance example Output from BEAMS run Using STATBIC Inputs.

concentration fluctuations in homogeneous, Kolmogorov turbulence. Figure 5 shows single x-y-z plane cross-sections through one of the STATBIC-generated input arrays of 3-D concentration fluctuations. Brighter regions represent greater concentrations.

As baseline cases, the non-uniform concentrations were run directly in BEAMS to obtain their resulting radiances. Then, for comparison, the same non-uniform concentrations were used, but with L_s values for Ω and the mean $\tau_\perp$ across the cloud. Concentration fluctuations lead to optical depth fluctuations τ'. So the proposed rapid (but approximate) cloud radiance calculation is just:

$$L_{cloud}(\Omega) = L_p(\Omega; \tau_\perp + \tau') \approx [1 - T(\Omega; \tau_\perp + \tau')] L_s(\Omega; \tau_\perp) \quad (6)$$
$$= [1 - e^{-\tau_\perp - \tau'}] L_s(\Omega; \tau_\perp) \quad (T \text{ fluctuating but } L_s \text{ mean})$$

Figures 6 and 7 compare the outputs of the full calculation for radiance L_p (fig. 6) and limiting path radiance L_s (fig. 7). Note that the resulting limiting radiance L_s is quite smooth even with the cloud fluctuations present. This supports the idea that most (but not all) of the fluctuation is in the transmittance, not L_s. Table 1 quantitatively compares the absolute and mean squared error between method #1 (complete BEAMS calculation for each fractal cloud realization) and method #2 (the rapid calculation using L_s for a uniform cloud superimposed on transmission fluctuations) for representative sets of runs. The most relevant values are those for error in L_s. The fluctuations in L_p from both fill calculation and from the approximate result from Eq. 6 are proportional to the input fluctuations in transmission, as one would expect.

TABLE 1. Error Analysis of BEAMS Output Diffuse Radiance Comparing Face-Averaged Differences in Full Calculation for Non-Uniform Cloud and Using Ls from Full Calculation for Uniform Cloud and Fluctuating Transmittance

Radiance Case	Ls(Exact Fluct.)-Ls(Fast Param.)		Lp(Exact Fluct)-Lp(Uniform)	Lp(Exact Fluct.)-Lp(from Ls Table)
Solar(Az 90, Zen 60); Fdir/Fdif = 10; Ag=0.3	% Absolute Error	% RMS Error	% Absolute Error	% Absolute Error
τ = 0.14 - 0.16, various rays	0.3-0.9%	0.2-0.7%	9-16%	4-6 %
τ = 0.234, Az 180, Zen 90	0.86%	0.77%	5%	1.8%
τ = 0.56 - 0.66, various rays	1.1-2.9%	0.9-1.9%	8-14%	4-8%
τ = 0.995, (180, 90) best case	0.83%	0.79%	1.3%	4%
τ = 2.2 - 2.6, various rays	4.0-5.8%	3.8-4.5%	6-12%	4-8%
τ = 3.75, (180, 90) best case	1.06%	0.91%	1.0%	2%
τ = 8.9 - 10.6, various rays	3-10%	2.5-7%	4-10%	5-8%
τ = 15., (180, 90) best case	4.0%	2.9%	4.0%	5%
τ = 36 - 43, various rays	4-8%	3-8%	4-8%	6-10%

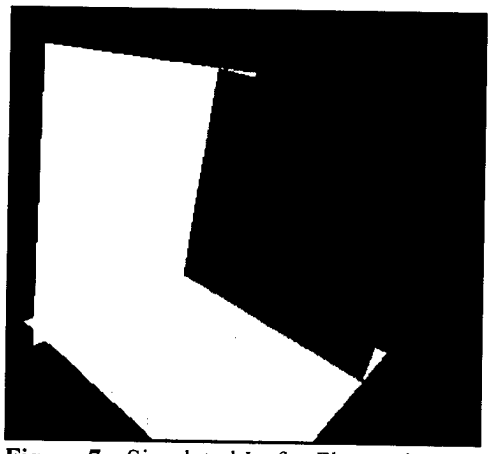


Figure 7. Simulated L_s for Fluctuating τ Input Case, Showing Smoothing Effects.

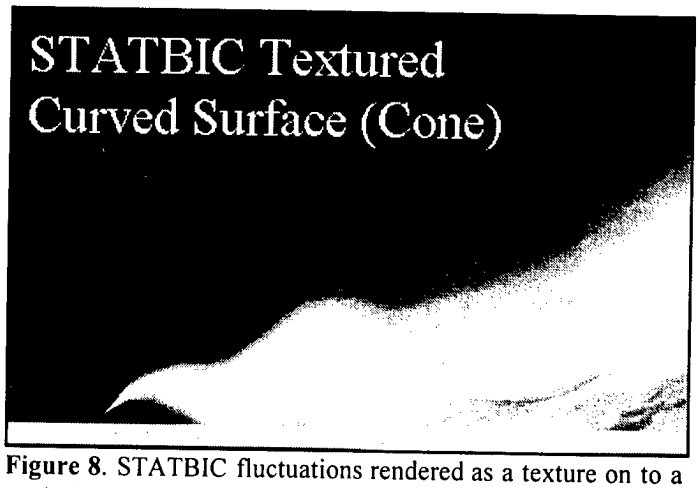


Figure 8. STATBIC fluctuations rendered as a texture on to a conical surface.

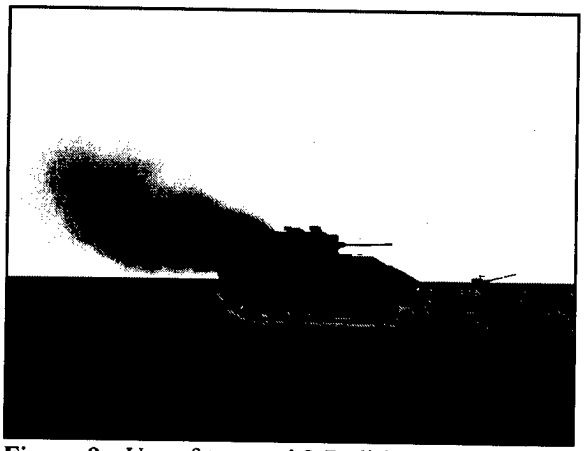


Figure 9. Use of textured 2-D disks for plumes in real-time scene simulation.

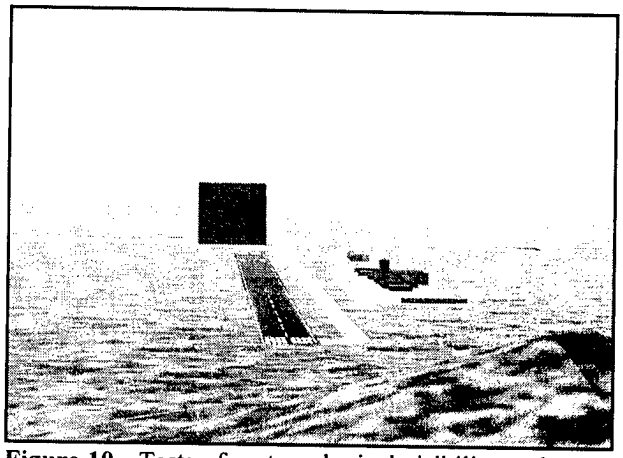


Figure 10. Tests of meteorological visibility and haze/fog in Real-Time Simulation (SGI Performer).

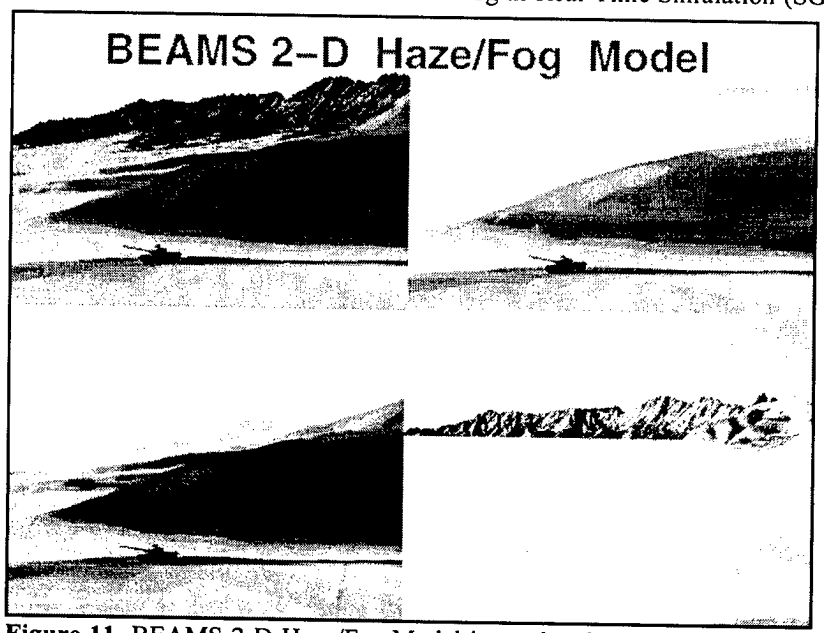


Figure 11. BEAMS 2-D Haze/Fog Model in rendered 3-D scenes of the Organ Mountains at White Sands Missile Range.

6. USE OF PARAMETRIC RADIANCE VALUES

Scene visualization of obscurant clouds, haze and fog requires both transparency (transmittance) and color value (path radiance) from realistic, three-dimensional, non-uniform distributions of aerosol concentrations. In actual simulators the cloud is rendered into a 2-D screen image by a variety of techniques. A common approach in real-time simulations is to use a two-dimensional "billboard" picture of a cloud as it would be seen from the current (and perhaps several) observer positions. This picture-icon is placed as a small, simple scene object which is kept turned toward the observer and blended to the background by being totally transparent at its edges. BEAMS can provide color values and opacity through the entire cloud for this approach, although values should be changed as the "billboard" is turned. A more ambitious approach to giving the cloud a 3-D presence, as in fig. 8, uses a semi-transparent cloud image wrapped over a 3-D object cloud "surface" as a semi-transparent texture. A third method uses many small, flat semi-transparent disks or planes that represent component, textured "puffs" in the cloud. These are distributed throughout the 3-D volume of the cloud region and turned to face the observer. They usually overlap so that one perceives the combined color and attenuation of nearer elements in front of farther ones. This is shown in fig. 9 for a real-time 3-D fly-through simulation of smoke from an M2 Bradley. Finally, given enough time, one can fully render the most accurate propagation representation of the cloud as a complete ensemble of semi-transparent volume elements (voxels) of different optical depths and color values in a 3-D cloud volume.

Whichever approach is used requires two arrays (over a 2-D surface or in a 3-D volume) of computer graphics parameters. The first is opacity of the cloud (usually rendered in the cpu or automatically in the graphics hardware as a random dithered matrix of clear pixels or sub-pixel points mixed in appropriate ratios with opaque colored points). Physically, the graphics opacity has a complementary relation (opacity = 1 - transparency) to the physical transmittance (transparency) of the cloud at the given wavelength. The second array is the color value (typically RGB) of the cloud itself (L_p) or a limiting blending color (L_s). The latter uses opacity as a linear interpolator between the unobscured background and the totally opaque cloud. In this case L_s is the color of the cloud when totally opaque. Opacity and L_s are direct inputs to the Silicon Graphics "fog function", for example, which renders visibility effects using its internally computed ranges (z-buffer) from the observer to each scene pixel (Hoock and Giever, 1994).

Figure 10 is from a real-time 3-D simulator of an airfield over Ft. Hunter-Liggett terrain. Haze effects make a similar use of τ (determined from visibility and the Koschmieder relation) with a solar-angle dependent L_s. The "monolith" at the end of the runway is a black cube, 100 m on a side. It has been placed into this 3-D simulation to measure the accuracy of SGI Performer real-time software to achieve the objective definition of meteorological visibility when given physically-correct Computer Image Generator (CIG) inputs. This scene is completely analogous to the test procedures done on the basic SGI GL language "fog function" presented by us at last years' BAC conference (Hoock and Giever, 1993). Figure 11 shows various simulations of reduced visibility due to haze, solar illumination and fog that can be generated using τ and L_s from the BEAMS-2D program. The scene is from a near real-time virtual 3-D representation of White Sands Missile Range (USGS terrain) and a rendered tank in the foreground.

7. CONCLUSIONS

Rapid progress is taking place in the incorporation of physics-based environmental effects in interactive, real-time scene simulations of the battlefield environment. One aspect, dealing with the visualization of obscurants, smoke, dust, haze and fog, is to properly simulate the obscuration and radiance effects of these clouds on propagation. These effects impact target acquisition, weapon engagement, identification friend or foe, concealment, deception, visual cues, mobility and the general "realism" of scenes. The non-real-time BEAMS model is thus being used to generate propagation data that can be used as data sets to support real-time 3-D synthetic environment simulations. We have found that it is feasible to combine tabulated (or parametric) mean values of limiting path radiance L_s (dependent on cloud type, mean transmittance and sun angle) with simulated fluctuations in transmittance about the mean. In the limited case study done here, the relative error in using this approach over the full (and very time consuming) multiple scattering calculations for each cloud realization is overall typically under 14%.

ACKNOWLEDGEMENTS

ARL/BED particularly acknowledges support from the Joint Project Office for Smoke/Obscurants and Special Countermeasures for the development of the BEAMS models. And, under support from the Defense Modeling and Simulation Office project Environmental Effects for Distributed Interactive Simulation (E2DIS), the BEAMS model outputs are being analyzed as one of the environmental representation products that can support real-time and near real-time 3-D scene visualization of the battlefield environment. The authors thank Mr. Mario Torres of Science and Technology Corp. and Mr. Steven McGee of Physical Science Laboratory, NMSU for their help in generating scenes for figures for this paper.

REFERENCES

Ayres, S. and S. DeSutter, 1993. *EOSAEL 92: Vol4. Combined Obscuration Model for Battlefield Induced Contaminants (COMBIC)*. In press, U.S. Army Research Laboratory, Battlefield Environment Directorate, White Sands Missile Range, NM 88002-5501.

Davis, B., A. Wetmore, D. Tofsted, R. Shirkey, R. Sutherland and M. Seagraves, 1994. *EOSAEL 92: Vol 19. Aerosol Phase Function Database PFNDAT.* In press, U.S. Army Research Laboratory, Battlefield Environment Directorate, White Sands Missile Range, NM 88002.

Hoock, D., 1991. "Modeling Time Dependent Obscuration for Simulated Imaging of Dust and Smoke Clouds." In *Proceedings of the SPIE*, SPIE Conference Vol 1486, pp. 164-175.

Hoock D. and J. Giever, 1993. "Methods for Representing the Atmosphere in Interactive Scene Visualizations." In *Proceedings of the 1993 Battlefield Atmospherics Conference*, U.S. Army Research Laboratory, Battlefield Environment Directorate, White Sands Missile Range, NM 88002-5501, pp 405-419.

Hoock, D., J. Giever and S. O'Brien, 1993. "Battlefield Emission and Multiple Scattering (BEAMS), a 3-D Inhomogeneous Radiative Transfer Model." In *Proceedings of the SPIE*, SPIE Conference Vol 1967, pp 268-277.

Hoock, D. and J. Giever, 1994. "Modeling Effects of Terrain and Illumination on Visibility and the Visualization of Haze and Aerosols." In *Proceedings of the SPIE*, SPIE Conference Vol 2223, pp 450-461.

Miller, A., 1983. *Mie Code AGAUS 82*, ASL-CR-83-0100-3, U.S. Army Atmospheric Sciences Laboratory, White Sands Missile Range, NM 88002-5501. (Now in reprints as *EOSAEL 92: Vol 1. Mie Code AGAUS*).

O'Brien, S., 1993. "Comparison of the BEAMS 2.2 Radiative Transfer Algorithm with other Radiative Transfer Methods." In *Proceedings of the 1993 Battlefield Atmospherics Conference*, U.S. Army Research Laboratory, Battlefield Environment Directorate, White Sands Missile Range, NM 88002-5501, pp 421-435.

A PORTABLE SYSTEM FOR DATA ASSIMILATION IN A LIMITED AREA MODEL

Keith D. Sashegyi and Rangarao V. Madala
Naval Research Laboratory
Washington, DC 20375, U.S.A.

Frank H. Ruggiero
Phillips Laboratory
Hanscom AFB, MA 01731, U.S.A.

Sethu Raman
North Carolina State University
Raleigh, NC 27695, U.S.A.

ABSTRACT

A numerical weather prediction system has been developed for assimilating regional and mesoscale data in a high resolution limited area model. The system, which can be run on both high performance workstations and super computers, has been used to study the assimilation of upper air soundings, surface observations, and precipitation estimates derived from satellite. The model's grid system is nested in horizontal with a fine resolution nest covering the area of interest surrounded by two coarser resolution nests. An efficient iterative analysis scheme is used for interpolating atmospheric sounding data and surface observations to the model grid. A sequential coupling of the mass and wind analyses is used for the upper air data outside of the tropical regions. Surface observations of wind, relative humidity and potential temperature are analyzed on the lowest model vertical level. An iterative adjustment of the surface fluxes, and the winds, temperature and humidity in the planetary boundary layer then follows. A normal mode initialization with the diabatic heating derived from observed precipitation is used to balance the initial mass and wind fields. During the first three hours of a subsequent forecast, the observed diabatic heating is merged with the model generated diabatic heating. The major impact of the assimilation scheme is in the enhancement of the mesoscale circulations and precipitation in the first twelve hours of model forecast. On the workstation, a twelve hour period of assimilation followed by a 24 hour forecast can be produced within two hours of clock time when two grids are used.

1. INTRODUCTION

High resolution regional weather prediction models have been successfully used in the past to study many mesoscale weather systems (Anthes 1990) and recently to provide operational forecasts (Benjamin et al. 1991). Now with the introduction of new high temporal and spatial resolution observing systems such as the Doppler Radar network, automatic surface observing stations and the GOES I satellite, there will be a dramatic increase in the amount of data available for the running of high resolution limited area models. The large volume of data produced by these

new remote sensing systems will limit the amount of data that can be included in the operational weather prediction systems at central weather forecasting centers. A high resolution weather prediction model run at a local center would be better able to utilize the data from such a local observing system for producing short range weather forecasts in the local region. Further with the increasing computational power and memory now available in desktop workstations, it has become possible to run a quite sophisticated weather prediction system on a workstation. Recently, Cotton et al. (1994) have demonstrated the running of the Regional Atmospheric Modeling System (RAMS) on a RISC workstation at Colorado State University. While the detailed cloud microphysics used in the model improved the forecasts, this was at an increased cost in CPU time required to run the model. In the very near future with further increases of computational power in these workstations, it should be possible to run a high resolution weather prediction system on a workstation at a local site, utilizing the available high resolution data to produce accurate short range weather forecasts for the local region.

At the Department of Defense there is a great need for accurate short range regional and mesoscale weather forecasts in support of military operations which can be used in different regions around the globe. It is envisioned that a portable weather prediction system that can run on a workstation will be able to produce high resolution short range 3-12 hour forecasts for this purpose. The short range forecasts of high resolution would compliment the larger scale forecasts which would available from a central site such as the from the Navy's Operational Global and Regional Atmospheric Prediction Systems (NOGAPS, NORAPS). These central site data sets, with high resolution surface conditions (elevation, sea surface temperature, albedo, etc.) and available observations could be transmitted by satellite from the central site to the local site, such as a Navy

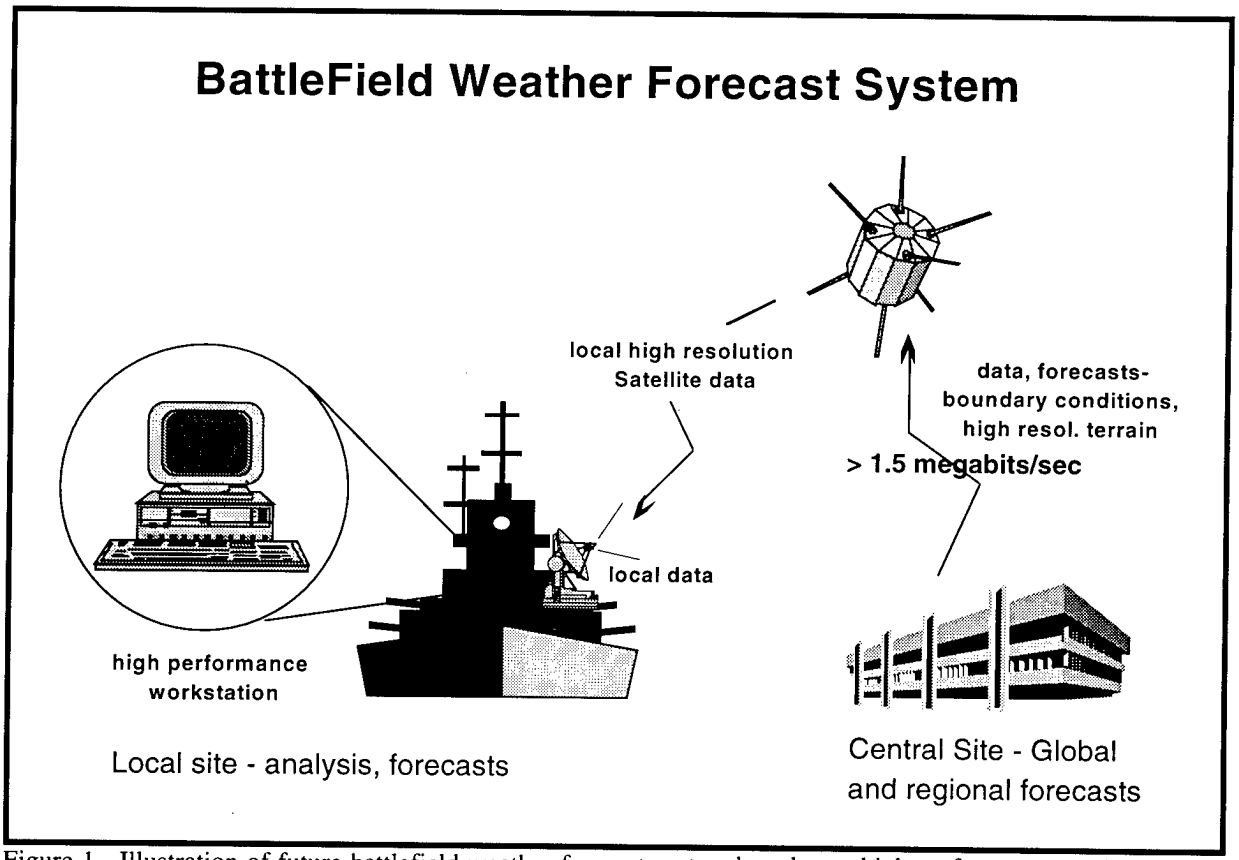


Figure 1. Illustration of future battlefield weather forecast system based on a high performance workstation on a Naval ship with high speed satellite communications link to on-shore weather forecasting center.

ship (Fig. 1). Then utilizing any local observations and high resolution satellite observations, very high resolution analyses and forecasts could be run on the local high performance workstation to support the military operations. Such a system will depend on the availability of high speed satellite communications between the local military operation and the central weather forecasting site. Several recent trials have demonstrated that transmission speeds of up to 1.5 megabits/sec can be achieved between a Navy ship and a shore site (Masud 1994*). With these speeds, the data needed for the initial conditions and boundary values could easily be rapidly transmitted to the ship within 10 minutes for use on the workstation system.

At the Naval Research Laboratory we have ported a simplified version of our numerical weather prediction system to a high performance workstation. As a demonstration of the concept of a local analysis and forecasting system using current technology, the limited-area modeling system is run on the workstation using upper-air data collected during the Genesis of Atlantic Lows Experiment (GALE), which was conducted over the southeastern U.S. during the winter of 1986. A 12-hour period, prior to the start of the forecast run, is used to assimilate the observations into the model using an intermittent data assimilation method as in Harms et al. (1992). A 12 hour prediction with a 10-layer version of the numerical model utilizing a coarse mesh covering the continental U.S. and a fine mesh covering the eastern U.S. took 30 mins of CPU time on the workstation. The analysis component itself used 12 mins of CPU time to produce analyzes at 19 pressure levels with a hundred soundings.

2. THE ANALYSIS/FORECAST SYSTEM

The intermittent data-assimilation method is used as in Harms et al. (1992) to assimilate upper air observations during a 12-hour period prior to the start of the forecast. During the assimilation period, the numerical model forecast provides the first guess or background for the analysis of the new upper air data at 3-hourly intervals. A diabatic initialization procedure is used to balance the mass and wind fields. The assimilation is first started from an operational analysis which is interpolated to the model grids and initialized. After the assimilation, short range predictions of 12-24 hours are produced.

2.1 Forecast Model

The forecast model used was developed at the Naval Research Laboratory and is described in detail in the reports by Madala et al. (1987) and Harms et al. (1992). This is a hydrostatic primitive equations model in terrain-following sigma coordinates with a triple nested grid network in the horizontal. Spherical coordinates are used in the horizontal, with the mass and momentum variables staggered on a C grid. The model uses the split-explicit method of time integration (Madala 1981). The finite-difference scheme in flux form is second-order accurate, and in the absence of sources and sinks, conserves total mass, energy and momentum. The model uses horizontal diffusion of second order and includes large-scale precipitation, dry convective adjustment and a modified Kuo cumulus parameterization scheme. A multi-level planetary boundary layer utilizes similarity theory in the surface layer and vertical turbulent mixing above (Gerber et al. 1989; Holt et al. 1990). The mixing is modeled using a turbulent kinetic energy equation (Detering and Etling 1985). The lateral boundary values for the coarse grid are derived from 12 hourly operational analyses and forecasts by linearly interpolating in time. Boundary values for an inner grid are provided by the integrations on the coarser grid. The model variables at each grid boundary are updated each time step, using the relaxation scheme of Davies (1976).

In the version of the model used on the workstation, 10 equally spaced vertical layers are used and the boundary layer is parameterized using a single layer with the fluxes computed from a

---

* *Government Computer News, July 11, 1994, pp 45,47.*

generalized similarity theory as in Chang (1981). For the demonstration on the workstation two nested grids are used, where the model's coarse grid covers the continental U.S. from 40° to 140°W and 10° to 70°N with a resolution of 2.0° latitude and 1.5° longitude. The fine grid covers the eastern U.S. from 58° to 102°W and 23.5° to 56.5°N with a grid spacing a third less than the coarse grid (of approx. 50 km). For comparison, the full version of the model with the multi-layer PBL is run on the Cray super computer with 16 layers in the vertical and a third fine mesh. The third grid run on the Cray covers the south-eastern U.S. from 90°W to 70°W and 29.5°N to 40.5°N with a resolution of 2/9 degree in longitude and 1/6 degree in latitude (about 20 km).

2.2 Analysis Method

Our analysis method uses the successive corrections scheme of Bratseth (1986), which converges to the same solution as that obtained by optimum interpolation. Such iterative analysis schemes are generally more efficient than the optimum interpolation method, which requires solving a large linear system of equations (Sashegyi and Madala 1994). The Bratseth scheme, in which the weights are also based on the statistical correlations of the forecast error, is therefore a very attractive method for use in a portable system to be run on a workstation. This method has been successfully applied operationally in the multivariate analysis scheme in Norway by Grønås and Midtbø (1987). In our application of the scheme (Sashegyi et al. 1993), univariate analyses of the mass and wind fields are initially produced. To provide a coupling of the mass and wind fields, the mass analysis is enhanced using gradient information derived from estimates of the geostrophic wind. The wind analysis is used to provide the initial estimate of the geostrophic wind. The wind analysis is then also updated to reflect the new geostrophic wind. The components of the analysis method are
(a) data preparation and quality control,
(b) univariate analyses of the mass and wind field,
(c) enhancement of the geopotential gradient, and
(d) enhancement of the wind field.
The analysis scheme is described in more detail in Sashegyi et al. (1993) and Harms et al. (1992). We now briefly describe each of these components in turn.

2.2.1 ***Data preparation and quality control.*** Sounding data are smoothed in the vertical and retained at 50 mb levels. The soundings are sorted into 5° latitude-longitude boxes for each pressure level from 1000 mb to 100 mb. We perform a "gross" check and a simplified "buddy" check in which observations with large deviations from the first-guess or from neighboring observations are removed. Observations in close proximity of each other are averaged to generate "super" observations and any remaining isolated observations are eliminated. If an operational analysis is available at the time, bogus data derived from the operational analysis can be used in regions where we have no soundings.

2.2.2 ***Univariate analyses of the mass and wind field.*** Univariate analyses of sea-level pressure, geopotential the u- and v- wind components and the relative humidity are conducted on 19 pressure levels at 50 mb steps from 100 mb to 1000 mb, using a 1.5° latitude/longitude grid. In the successive corrections method of Bratseth (1986), the analysis weights are derived from the forecast error covariance, and include a "local data density", which reduces the weights in regions of higher data density and prevents extrapolation into data void regions (Bratseth 1986). In the method, the background field is updated by the latest analysis after each iteration or pass, where the interpolated value at an analysis grid point after n such iterations is given by

$$\phi_{a,x}(n+1) = \phi_{a,x}(n) + \sum_{j=1}^{J} w_{x,j}\left[\phi_{o,j} - \phi_{a,j}(n)\right] \qquad (1)$$

where $\phi_{o,j}$ is one observation at location r_j (of a total of J such observations), $w_{x,j}$ is the weight for that observation and $\phi_{a,x}$ is the analyzed value at a grid point r_x. In the previous successive corrections schemes, the updated analyzed values $\phi_{a,x}$ were then interpolated to the observation locations using a polynomial interpolation method, in order to compute the observation corrections for the next iteration. Here, an "observation estimate" $\phi_{a,i}$ is computed instead by using the same interpolating equation as was used for the analyzed values in *eq.* (1),

$$\phi_{a,i}(n+1) = \phi_{a,i}(n) + \sum_{j=1}^{J} w_{i,j}\left[\phi_{o,j} - \phi_{a,j}(n)\right] \tag{2}$$

A starting guess for the analysis $\phi_{a,x}(1)$ and observation estimate $\phi_{a,j}(1)$ are derived from the background forecast ϕ_b by a cubic polynomial interpolation. Instead of using empirical weights as in earlier schemes, the weights in each equation are defined in terms of the covariance of the corrections to the background forecast, which are then reduced by dividing by a local data density

$$w_{x,j} = \frac{\overline{[\phi_t(r_x) - \phi_b(r_x)][\phi_o(r_j) - \phi_b(r_j)]}}{M_j} = \frac{\rho_{x,j}}{m_j} \tag{3}$$

$$w_{i,j} = \frac{\overline{[\phi_o(r_i) - \phi_b(r_i)][\phi_o(r_j) - \phi_b(r_j)]}}{M_j} = \frac{\rho_{i,j} + \varepsilon^2\delta_{ij}}{m_j} \tag{4}$$

where the local data density is defined by

$$M_i = \sum_{j=1}^{J} \overline{[\phi_o(r_i) - \phi_b(r_i)][\phi_o(r_j) - \phi_b(r_j)]} \tag{5}$$

$$m_i = \frac{M_i}{\sigma^2} = \sum_{j=1}^{J}\left[\rho_{i,j} + \varepsilon^2\,\delta_{ij}\right] \tag{6}$$

The $\rho_{x,j}$ and $\rho_{i,j}$ are the values for the correlation function for the true background forecast errors $[\phi_t - \phi_b]$ between values at an observation location r_j and at a grid point r_x, and between the values at observation locations r_i and r_j, respectively. Here we have assumed that the observation errors are not correlated with the forecast errors. The variance of the background forecast errors is σ^2, ε^2 is the ratio of the observation error variance σ_ε^2 to the background forecast error variance σ^2 and δ_{ij} is the Kronecker delta function (one for i=j, zero otherwise). The error correlation function $\rho(r)$ for the mass and humidity is modeled by a Gaussian function,

$$\rho(r) = e^{-r^2/d^2} \tag{7}$$

which is a function of the distance r and the length scale d is 600 km. For the components of the wind field the correlation functions are reduced across the direction of the flow using

$$\rho_u = \left[1 - \frac{(y - y_j)^2}{d_u^2}\right]\rho(r) \tag{8}$$

$$\rho_v = \left[1 - \frac{(x - x_j)^2}{d_u^2}\right] \rho(r) \qquad (9)$$

where d_u is 700 km and (x,y) and (x_i,y_j) are the positions of the analysis grid point and the observation, respectively. After the first three or four iterations the length scales d, d_u are reduced to 330 km and 380 km, respectively, for one additional iteration, to speed convergence of the scheme (see also Grønås and Midtbø 1987).

2.2.3 ***Enhancement of the geopotential gradient.*** We use the analyzed wind as an initial estimate of the geostrophic wind, which is then used to extrapolate the geopotential to the grid point locations for a further iteration of the geopotential analysis, in a fashion similar to Cressman (1959). That is,

$$\phi^*_{o,i}(r_x) = \phi_{o,i} + (r_x - r_i) \bullet \nabla\phi_{o,i} \qquad (10)$$

where $\nabla\phi_{o,i}$ is the gradient derived from the horizontal wind at the observation location using the geostrophic relation. A fixed correlation length scale of 600 km is used for the re-analysis. An updated geostrophic wind estimate is then defined by the new geopotential gradient. Three further iterations of the geopotential are used for the geostrophic wind estimate to converge.

2.2.4 ***Enhancement of the wind gradient.*** The geostrophic wind changes produced by the geopotential enhancement are then used to update the univariate wind analysis as in Kistler and McPherson (1975), where the updated wind is given by

$$v^* = v + \Delta v_g \qquad (11)$$

for geostrophic wind changes Δv_g. Four additional passes of the wind univariate analysis are then used to enhance the ageostrophic components of the wind.

The final analyzed corrections on pressure surfaces are interpolated to the horizontal model grids using a cubic polynomial interpolation. Both the background forecast fields and the new analyzed fields on pressure surfaces are interpolated to the sigma levels of the model. Analysis corrections are then recomputed on the sigma levels to update the model forecast fields.

2.3 Surface Analysis and Boundary Layer Adjustment

To utilize the large volume of surface observations which are available, analyses of potential temperature, relative humidity and wind are carried out on the model's lowest sigma layer with a horizontal grid of 0.5° resolution that covers the domain of the middle grid. For surface pressure, the observed and model forecast surface pressures are reduced to sea level following a procedure similar to Benjamin and Miller (1990). In our case we use a lapse rate computed from the virtual temperature at 255 and 105 mb above the surface, extrapolating the virtual temperature to the surface to define an effective mean surface temperature. Univariate analyses are then produced for the lowest model layer as in the upper air analysis described in section 2.2.2. For the analysis of sea level pressure, the Gaussian correlation function in *eq.* (7) is used with a correlation length scale d of 300 km, as in Miller and Benjamin (1992). For potential temperature, humidity and the u and v components of the wind, the Gaussian correlation functions are similarly modified as in Miller and Benjamin. The potential temperature and wind in the planetary boundary layer are then adjusted by a forward integration of the vertical diffusion equation for a number of time steps.

2.4 Diabatic Normal Mode Initialization

In this forecasting system, the updated forecast fields are initialized on the coarse and fine grids for the first three vertical modes of the numerical model as described in Sashegyi and Madala (1993) using the vertical mode scheme of Bourke and McGregor (1983). For each vertical mode of the forecast model, the equations for the vorticity ζ, divergence D and a generalized geopotential Φ are

$$\frac{\partial \zeta}{\partial t} + f D = A_{\zeta} \tag{12}$$

$$\frac{\partial D}{\partial t} + \nabla^2 \Phi - f \zeta = A_D \tag{13}$$

$$\frac{\partial \Phi}{\partial t} + g h_k D = A_{\Phi} \tag{14}$$

where h_k is the equivalent depth for the kth vertical mode, f is the Coriolis parameter, g is the acceleration due to gravity and the terms on the right hand sides of the equations include the non-linear advection, friction and cumulus heating. The generalized geopotential is defined by $\Phi = p_s[\phi - \phi_s + R\,T^* - \phi^*]$, where p_s is the surface pressure, ϕ the geopotential, ϕ_s the surface geopotential, T^* and ϕ^* a mean temperature and geopotential profile. The filtering conditions used to remove the fast inertia-gravity waves are

$$\frac{\partial D}{\partial t} = \frac{\partial \left(f \zeta - \nabla^2 \Phi \right)}{\partial t} = 0 \tag{15}$$

with the further condition that the linearized potential vorticity $\zeta - f\,\Phi/(gh_k)$ is unchanged by the procedure. The amplitude of the inertia-gravity modes depends only on the divergence D and the ageostrophic "vorticity" $f\zeta - \nabla^2\Phi$, and setting their tendencies zero initially, effectively removes the inertia-gravity waves. In applying these conditions for the first three vertical modes, the scheme is solved iteratively. This and other methods which can be used to apply normal mode initialization to a limited area model are further discussed in Sashegyi and Madala (1994).

For the initialization on the fine grid, boundary values for the mass field and the tangential wind are updated using the results of the initialization on the coarse grid. As in Harms et al. (1992; 1993) diabatic forcing is included as a fixed forcing function in the initialization, where the diabatic heating rates are computed from a merged field of observed and model- produced rainfall. A reverse Kuo cumulus parameterization scheme is used to convert these prescribed rain rates into vertical heating profiles in regions where the lower atmosphere is convectively unstable. During the first three hours of a subsequent forecast, the prescribed heating rates (used in the initialization) are linearly combined with the model generated heating rates. The weighting factor for the prescribed heating rate is one initially and decreases as a sine function to zero after three hours of integration (Harms et al. 1993).

3. DISCUSSION

As an example, three hourly upper air soundings, which were collected during the second Intensive Observing Period (IOP) of GALE, were used to generate analyses and forecasts with our analysis/forecast system on the workstation. The 1000 mb analysis for 1200 UTC 25 January 1986 is shown in Fig. 2. The cold air damming and the strong temperature gradient along the East Coast, which were generated by the first guess forecast, are retained in the analysis of the upper air

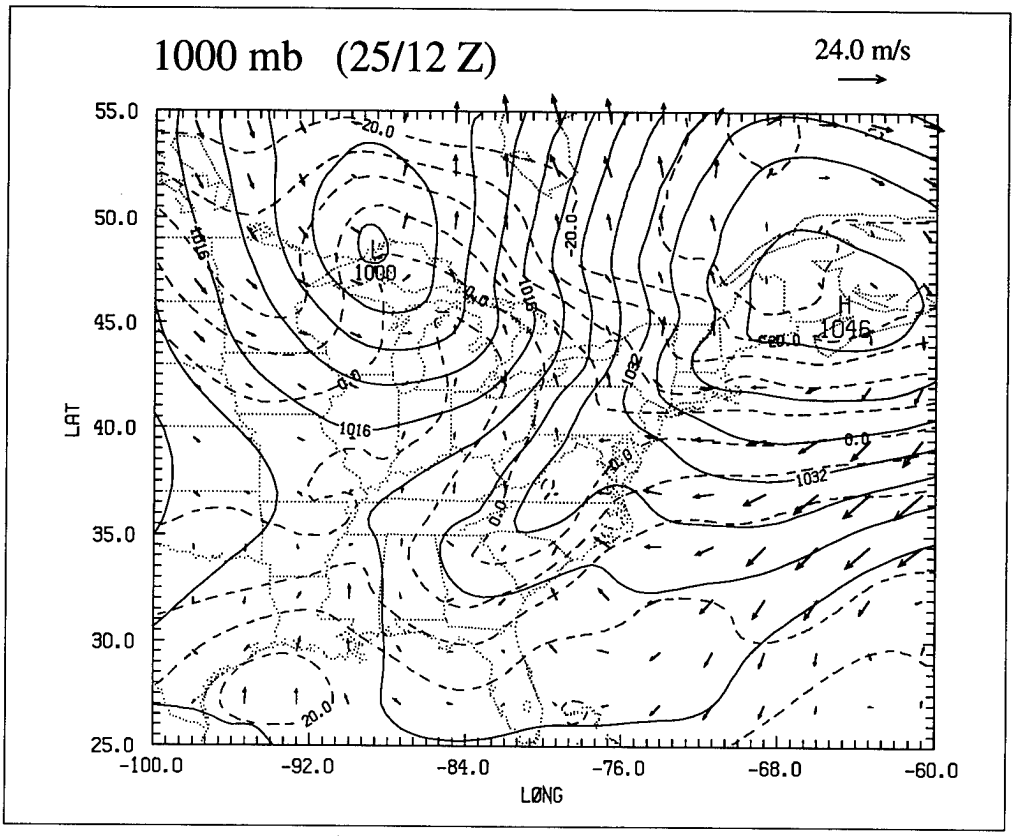


Figure 2. The analyzed 1000 mb temperature, winds and sea-level pressure for 12 UTC 25 January 1986. The solid contours of sea level pressure are every 4 mb, dashed contours of temperature every 5°C, and vectors indicate the direction and magnitude of the winds.

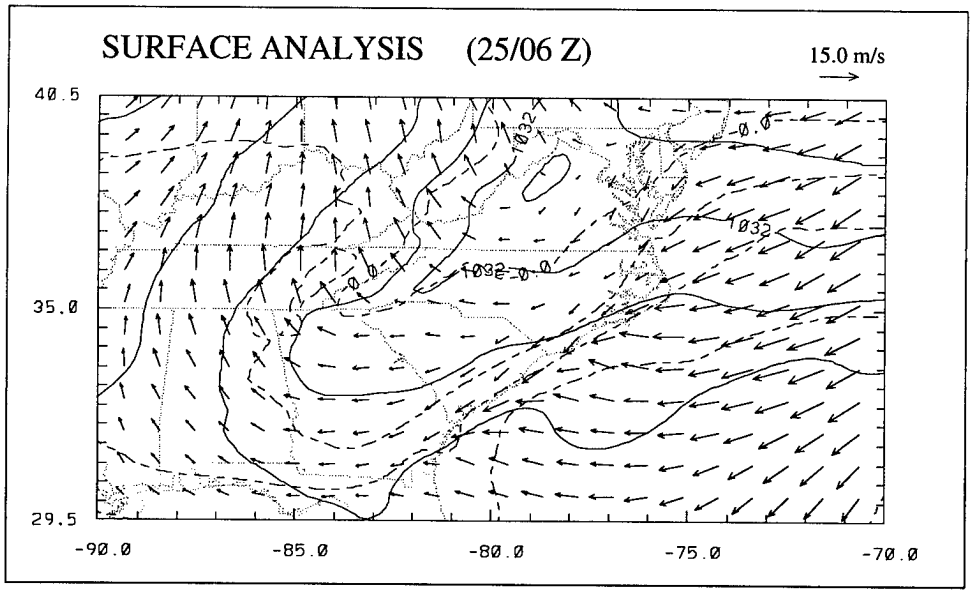


Figure 3. The analyzed sea level pressure, temperature and winds at the lowest model level for 6 UTC 25 January. Contours as in Fig. 2.

soundings. The low over the Great Lakes, which was too weak in the first guess (Sashegyi et al. 1993), was corrected by the analysis. The surface analysis produced by the 16 layer Cray version of the model is shown in Fig. 3 for 0600 UTC 25 January as the strong temperature gradient was developing across the coastline. On this higher resolution grid, the confluence of the flow and the temperature gradient along the coastline are stronger, but the general features were similar to that produced on the coarser grid on the workstation. The prediction of rainfall during the first 12-hours of integration is much improved by using the 12-hour period of assimilation prior to running the forecast (Harms et al. 1992). In Fig. 4, the rainfall seen over the Carolinas and across the Florida panhandle in the first six hours of the forecast was produced as a result of the assimilation on the workstation.

4. CONCLUSIONS

An analysis/forecasting system with a 12-hour period of assimilation prior to the running of a forecast was run on a high performance workstation. The intermittent scheme with 3 hour updates successfully assimilates upper air observations, maintaining the ageostrophic circulations generated by the forecast model. A higher resolution planetary boundary layer, a third horizontal grid of finer resolution and a surface analysis in the full model were run on the Cray super computer for comparison. With 10 layers used in the vertical and quite a coarse operational analysis used as the starting point for the assimilation, good results were achieved in a reasonable CPU time of two hours on the workstation when compared with the full run on the Cray.

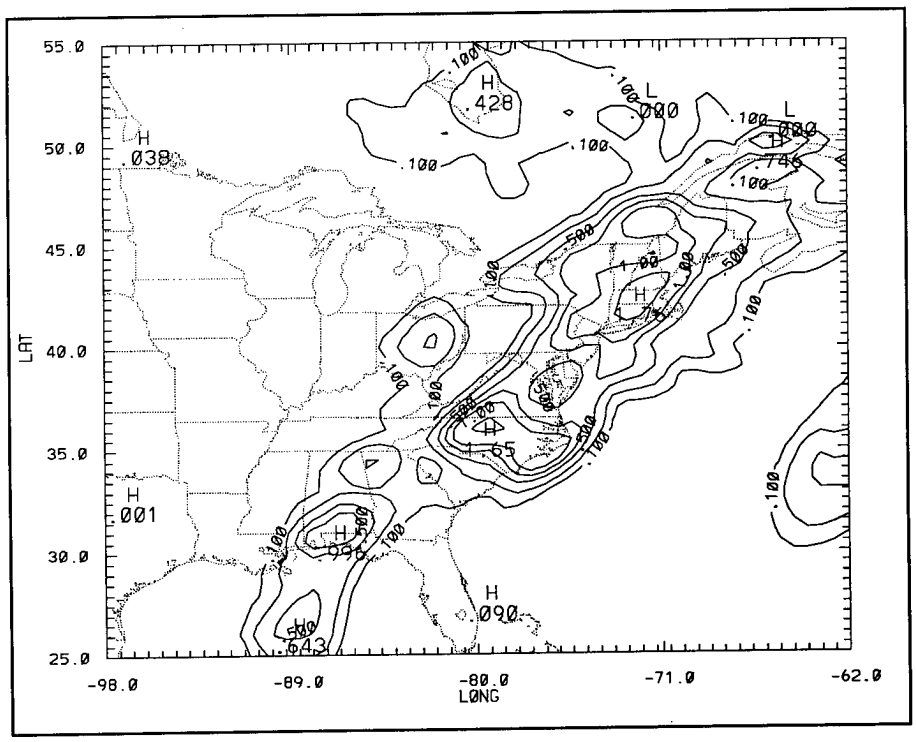


Figure 4. Six hour forecast of accumulated precipitation in cm valid at 6 UTC 26 January 1986. Contours 0.1 cm, every 0.25 cm up to 1.0 cm and then every 0.5 cm.

ACKNOWLEDGMENTS

Support for this research was provided by SPAWAR of the U.S. Navy and by basic research programs at the Naval Research Laboratory. The computing was supported in part by a grant of HPC time from the DOD HPC Shared Resource Center for use on the Cray YMP-EL at NRL.

REFERENCES

Anthes, R.A., 1990: "Recent applications of the Penn State/NCAR mesoscale model to synoptic, mesoscale and climate studies." *Bull. Amer. Meteor.* Soc., ***71***, 1610-1629.

Benjamin, S.G., K.A. Brewster, R. Brummer, B.F. Jewett, T.W. Schlatter, T.L. Smith and P.A. Stamus, 1991: "An isentropic three-hourly data assimilation system using ACARS aircraft observations." *Mon. Wea. Rev.*, ***119***, 888-906.

Benjamin, S.G. and P.A. Miller, 1990: "An alternative sea level pressure reduction and a statistical comparison of geostrophic wind estimates with observed surface winds." *Mon. Wea. Rev.*, ***188***, 2099-2116.

Bourke, W., and J.L. McGregor, 1983: "A nonlinear vertical mode initialization scheme for a limited area prediction model." *Mon. Wea. Rev.*, ***111***, 2285-2297.

Bratseth, A.M., 1986: "Statistical interpolation by means of successive corrections." *Tellus*, ***38A***, 439-447.

Chang, S.W., 1981: "Test of a planetary boundary-layer parameterization based on a generalized similarity theory in tropical cyclone models." *Mon. Wea. Rev.*, ***109***, 843-853.

Cotton, W.R., G. Thompson and P.W. Mielke Jr., 1994: "Real-Time mesoscale prediction on workstations." *Bull. Amer. Meteor. Soc.*, ***75***, 349-363.

Cressman, G. 1959: "An operational objective analysis system." *Mon. Wea. Rev.*, ***87***, 367-374.

Davies, H.C.., 1976: "A lateral boundary formulation for multi-level prediction models." *Quart. J. Roy. Meteor. Soc.*, ***102***, 405-418.

Detering, H.W. and D. Etling, 1985: "Application of the E-eps turbulence model to the atmospheric boundary layer." *Bound.-Layer Meteorol.*, ***33***, 113-133.

Gerber, H.S., S.W. Chang and T.R. Holt, 1989: "Evolution of a marine boundary layer jet." *J. Atmos. Sci.*, ***46***, 1312-1326.

Grønås, S. and K.H. Midtbø, 1987: "Operational multivariate analyses by successive corrections." Collection of papers presented at WMO/IUGG numerical weather prediction symposium, Tokyo, 4-8 August 1986, *J. Meteor. Soc. Japan*, 61-74.

Harms, D.E., K.D. Sashegyi, R.V. Madala, and S. Raman, 1992: *Four-dimensional data assimilation of GALE data using a multivariate analysis scheme and a mesoscale model with diabatic initialization.* NRL Memo. Rep. No. 7147, Naval Research Laboratory, Washington, D.C., 219pp. [NTIS A256063].

Harms, D.E., R.V. Madala, S. Raman and K.D. Sashegyi, 1993: "Diabatic initialization tests using the Naval Research Laboratory limited area numerical weather prediction model." *Mon. Wea. Rev.*, ***121***, 3184-3190.

Holt, T.R., S.W. Chang and S. Raman, 1990: "A numerical study of the coastal cyclogenesis in GALE IOP 2: Sensitivity to PBL parameterization." *Mon. Wea. Rev.*, ***118***, 234-257.

Kistler, R.E., and R.D McPherson, 1975: "On the use of a local wind correction technique in four-dimensional data assimilation." *Mon. Wea. Rev.*, ***103***, 445-449.

Madala, R.V., 1981: "Efficient time integration schemes for atmosphere and ocean models." *Finite Difference Techniques for Vectorized Fluid Dynamic Calculations*, Chpt. 4, Springer Verlag, pp 56-74.

Miller, P.A. and S.G. Benjamin, 1992: "A system for the hourly assimilation of surface observations in mountainous and flat terrain." *Mon. Wea. Rev.*, ***120***, 2342-2359.

Sashegyi, K.D, D.E. Harms, R.V. Madala, and S. Raman, 1993: "Application of the Bratseth scheme for the analysis of GALE data using a mesoscale model." *Mon. Wea. Rev.*, ***121***, 2331-2350.

Sashegyi, K.D. and R.V. Madala, 1994: "Initial Conditions and Boundary Conditions." *Mesoscale Modeling of the Atmosphere,* Meteorological Monographs, Vol. 25, No. 47, Chpt. 1, Amer. Meteor. Soc., pp 1-12.

Sashegyi, K.D. and R.V. Madala, 1993: "Application of vertical-mode initialization to a limited-area model in flux form." *Mon. Wea. Rev.*, ***121***, 207-220.

EFFECT OF HIGH-RESOLUTION ATMOSPHERIC MODELS ON WARGAME SIMULATIONS

Scarlett D. Ayres
Battlefield Environment Directorate
U.S. Army Research Laboratory
White Sands Missile Range, New Mexico 88002-5501

ABSTRACT

Battlefield weather conditions have affected, sometimes determined, the outcome of military conflicts and the resultant global order for generations. An area of continuing concern for military strategists, the operations research community, and soldiers throughout history has been atmospheric variability and its impact on the battlefield. The Combat-Induced Atmospheric Obscurants (CIAO) system is a prototype computer-based atmosphere modeling and simulation system designed to demonstrate the impact of the effects of advanced high-resolution atmospheric models on force-on-force wargame simulations, such as the Combined Arms and Support Task Force Evaluation Model; thus, impacting tactics and doctrine derived from the simulations. Wargames use low-resolution atmospheric models that tend to ignore some of the more realistic effects of the battlefield environment and weather that could prove highly significant on the wargame outcome. In the past, this limitation was necessary because of computer restrictions and the unavailability of appropriate atmospheric models. The goal of the research behind the CIAO system is to determine the impact of advanced high-fidelity, high-resolution obscuration models on simulated battles. A poster/paper was presented at the 1994 Battlefield Atmospherics Conference detailing the purpose of the models included in CIAO. This paper illustrates the expected effect of these models on the wargame.

1. INTRODUCTION

The Combined Arms and Support Task Force Evaluation Model (CASTFOREM) deals with a plane-parallel atmosphere with wind varying neither with direction nor speed in the horizontal direction. Terrain can cause a nonlinear inertial character of the flow interacting with the terrain surface. Terrain sheltering and channeling, wakes, and flow separation are features of wind fields in rugged terrain. CASTFOREM uses a fairly detailed smoke model (Combined Obscuration Model for Battlefield Induced Contaminants (COMBIC) (Ayres, DeSutter 1993)) to determine the degradation of transmission caused by smoke. However, COMBIC uses a simple atmospheric boundary layer model. The wind field direction and horizontal windspeed profile in COMBIC are uniform and static everywhere in the scenario. Wind fields and diffusion rates are determined by the effects of complex terrain and surface properties in the real world. COMBIC is a flat-terrain model. It allows only a uniform boundary layer wind field that is assumed to apply over the entire geographic region. COMBIC smoke flows through hills instead of over and around them. The CIAO system adds high-resolution atmospheric and modified smoke models to the

CASTFOREM wargames to more realistically simulate the battlefield atmosphere. The models discussed are SANDIA, High-Resolution Wind (HRW), Onion Skin, and Radiative Energy Balance Redistribution (REBAR), and the radiative transfer (RT) and polarimetric millimeter (PMW) version of COMBIC.

2. CASTFOREM

CASTFOREM is a high-resolution, two-sided, force-on-force, stochastic, event-sequenced, systemic simulation of a combined arms conflict (Mackey et al. 1992). CASTFOREM represents tactics through the use of decision tables, and it embeds an expert system for battlefield control. Battle orchestration up to the battalion level is accomplished strictly through the use of decision tables. CASTFOREM provides extensive line-of-sight (LOS) calculations along various observer-to-target directions, accounting for terrain, elevation, and vegetation. CASTFOREM also accounts for intervening atmospheric conditions that can include effects of combat induced obscurants through the use of the COMBIC model. Digitized terrain is included but is not, at present, coupled with the meteorological conditions. The original CASTFOREM assumes homogeneous weather, considered constant in time and space.

3. IMPROVEMENTS

3.1 Effects of HRW

Modifying COMBIC for complex terrain would greatly increase the run time, a fact that could adversely affect CASTFOREM users. Instead of using a simple wind model with a complex smoke model, it was decided to use a complex wind model with a simplified smoke model. The HRW model developed at the Army Research Laboratory can be used to determine wind fields and, in conjunction with rudimentary smoke clouds produced by the SANDIA and Onion Skin models, examines the effects that terrain-induced wind fields can have on the modern battlefield. The HRW model is a high-resolution micro-alpha scale, two-dimensional, surface layer wind and temperature model (Cionco 1985; Cionco, Byers 1993). The model supplies high-resolution calculations of surface layer wind, temperature, and turbulence parameters at selected grid points over a limited area, considering both the terrain topography and thermal structure. SANDIA and Onion Skin are highly parameterized smoke obscuration models. SANDIA treats smoke as binary entities in either of two electro-optical (EO) bandpasses (visible and infrared) (Sutherland, Banks 1986). Onion Skin models smoke as if it were layered like an onion. SANDIA and Onion Skin are easily modified to have the smoke clouds follow the wind streamlines, as determined by HRW, for a particular terrain. The affect on wargaming can be seen in figure 1. Figure 1a represents the prevalent smoke representation in CASTFOREM. The smoke blows in a constant direction, unmodified by the existing terrain. Figure 1b illustrates the affect on wargaming when SANDIA, combined with HRW, produces smoke clouds that follow the complex wind field. The LOS is obscured by smoke; whereas, it is not obscured in figure 1a. The smoke follows the complex wind field when HRW is included; thus, changing position changes the effectiveness of the smoke screen.

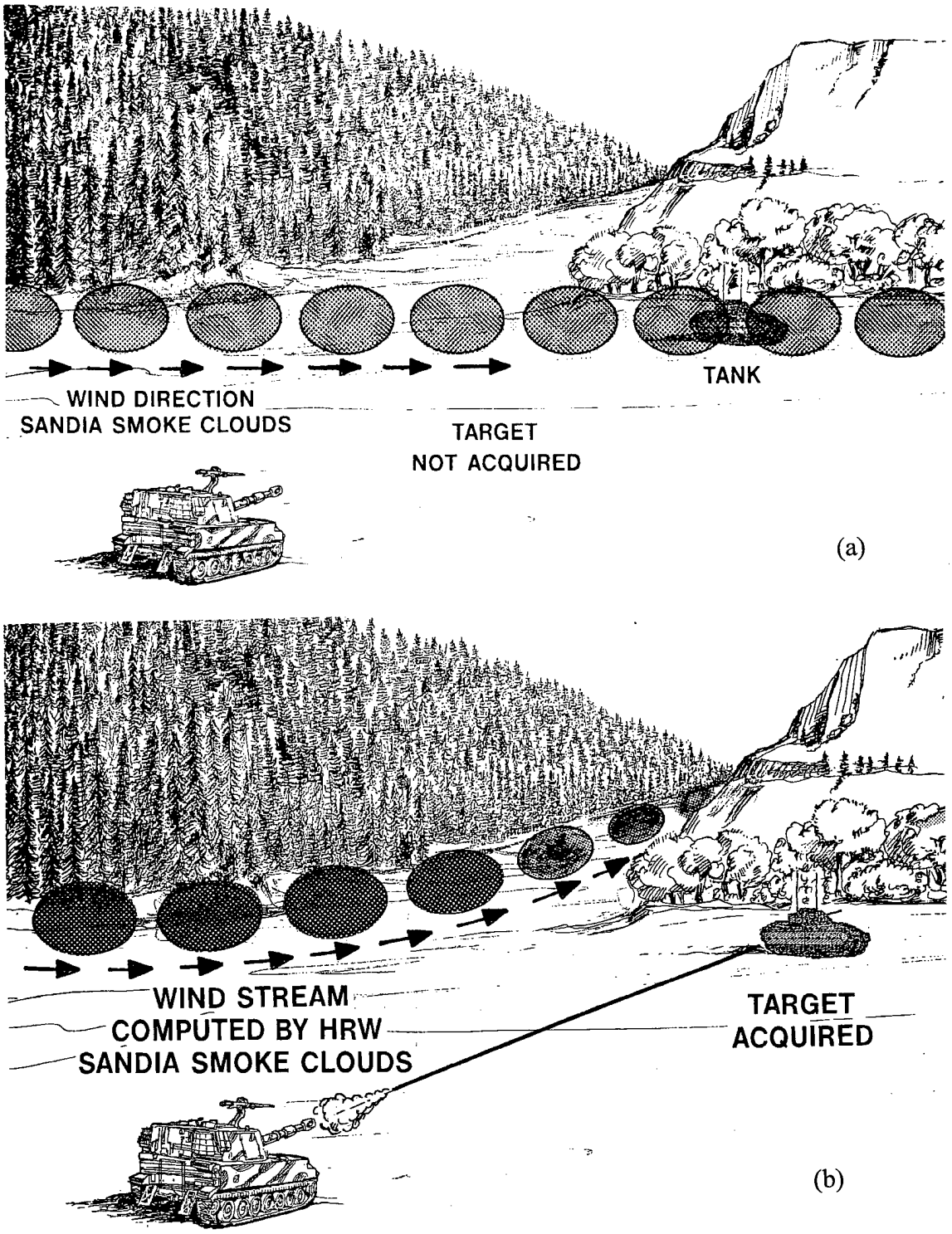


Figure 1. The simplified smoke model (a) allows smoke to blow in one direction. An advanced atmospheric model like HRW (b) allows smoke to flow with the complex wind field generated from the complex terrain data.

SANDIA was modified to compute the location of the clouds by utilizing the complex wind fields generated by HRW. The wind fields are computed for a height of 10 m from the terrain surface. The standard windspeed profile was used to allow the windspeed to vary with height. The profile is defined as follows:

$$\frac{\mu(z)}{\mu(z_{ref})} = \left(\frac{z}{z_{ref}}\right)^{P} \tag{1}$$

where

z = height above terrain
z_{ref} = 10 m
μ = windspeed at height z and at 10 m.

P depends on surface roughness and stability.

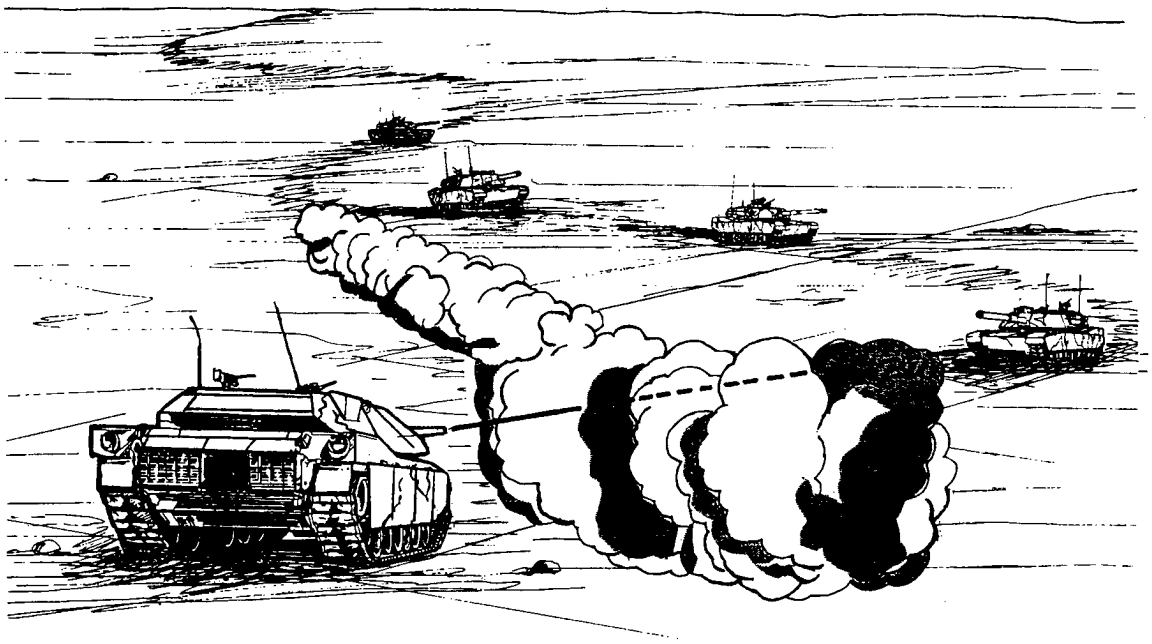
CASTFOREM passes the initial position of the smoke cloud, the LOS information, and the time into SANDIA. SANDIA determines the size and new position of the cloud using HRW complex wind fields. For a given threshold, SANDIA determines if the LOS intersects a cloud and is defeated. HRW can be run off line to generate the wind field output used to compute the updated cloud location and size. The updates are used to determine if the LOSs are affected by the clouds, which saves computer time, an important consideration to CASTFOREM users. SANDIA was ascertained to be twice as fast as COMBIC. The addition of the algorithm to compute complex wind driven smoke clouds should not slow CASTFOREM.

3.2 Effects of Adding Elevation Data to Smoke Models

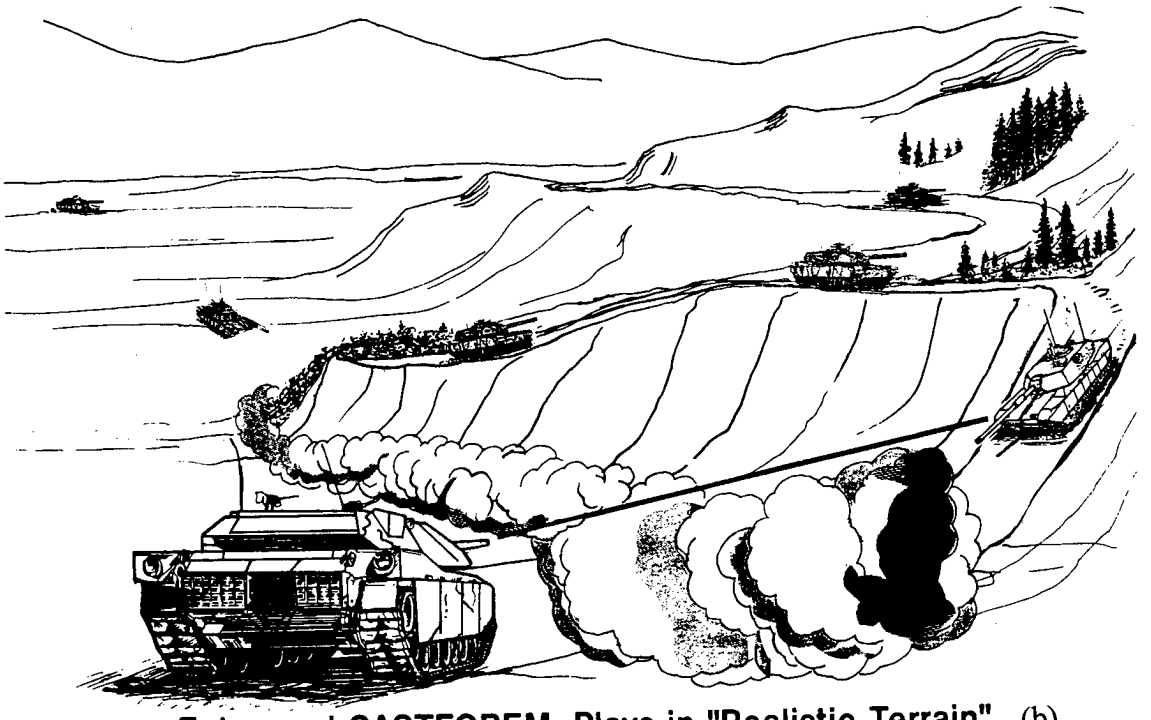
CASTFOREM uses an algorithm that determines if the LOS can acquire the target through the complex terrain; if so, the LOS is passed into the COMBIC or SANDIA smoke model to determine if the LOS is obscured. The smoke models are utilized as if all the smoke, observers, and targets are on the same level. The height of the LOS is the height of the sensor above the ground. However, the observer might be on one hill, the target on another, and the smoke in a valley between them in a complex terrain scenario. Figure 2 illustrates the effect of complex terrain on an obscured scenario. Figure 2a presents the normal way of modeling an obscured battlefield scenario. Figure 2b presents the new methodology for taking terrain elevation into account. Figure 2b shows that the tank acquires the target because the LOS passes above the smoke to reach the targets on the hill.

3.3 Effects of Onion Skin-HRW (OS-HRW)

The Onion Skin model is an extension of the SANDIA model previously described; however, the smoke clouds are not modeled as binary entities, but are resolved into layers representing various thresholds of optical thickness. Thus, clouds can be played at a higher resolution without much loss in computational speed. Another advantage is that the cumulative effects of multiple clouds can be treated with OS-HRW; whereas, only the binary option for a single cloud can be used with SANDIA. As with SANDIA, the OS-HRW approach can be made much more compatible with complex wind models such as HRW. Figure 3 illustrates the Onion Skin concept. Figure 3a



Current methodology in CASTFOREM plays smoke on "flat terrain" (a)



Enhanced CASTFOREM Plays in "Realistic Terrain" (b)

Figure 2. The prevalent methodology in modeling smoke is to pretend the terrain has no elevation (a). CIAO includes an enhancement that allows elevation to be included in modeling smoke by COMBIC and SANDIA (b).

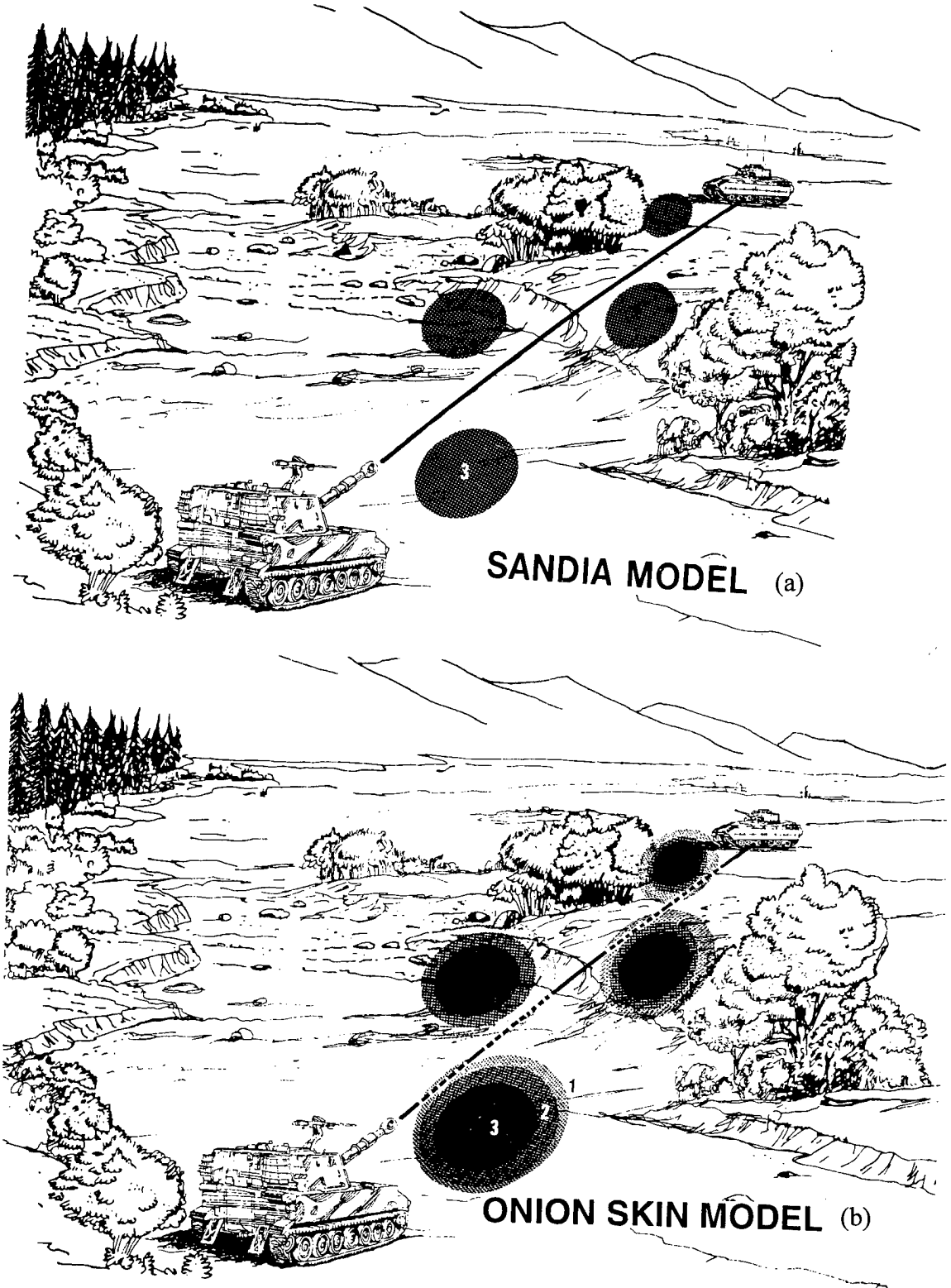


Figure 3. The LOS does not encounter the SANDIA produced clouds (ellipses) (a) so it is not defeated. The LOS goes through enough outer edges of the Onion Skin produced clouds (b) so it is defeated.

shows SANDIA produced clouds specified by an optical depth of three. Optical depth is the product of the mass extinction coefficient and concentration length (CL). The LOS from the observer to the target is not defeated because it does not go through any part of the cloud (represented by the ellipses). However, figure 3b shows that the LOS goes through enough outer layers of the onion-like cloud to build up an optical depth of three to be defeated. The OS-HRW model increases the number of LOSs obscured in wargames, as compared to the SANDIA model, which means increased survivability for the targets.

3.4 Effects of REBAR

A large area smoke screen (LASS) that endures a long time can significantly depress the surface irradiance and drive the local atmosphere toward more stable conditions (Yee, Sutherland 1993). Smoke operations can be affected because the rise and diffusion of smoke is critically dependent upon the stability class. Figure 4 shows how critical the Pasquill Category (PC) is in determining the height and width of the cloud. The stability of the atmosphere is related to PC as follows: PC = A, extremely unstable; PC = B, moderately unstable; PC = C slightly unstable; PC = D, neutral; PC = E, slightly stable; PC = F, moderately stable; and PC = G, extremely stable. Note how width and height increase with increasing instability. The overall concentration decreases as the cloud increases with size. Thus, any factor influencing the stability should be modeled in the wargames.

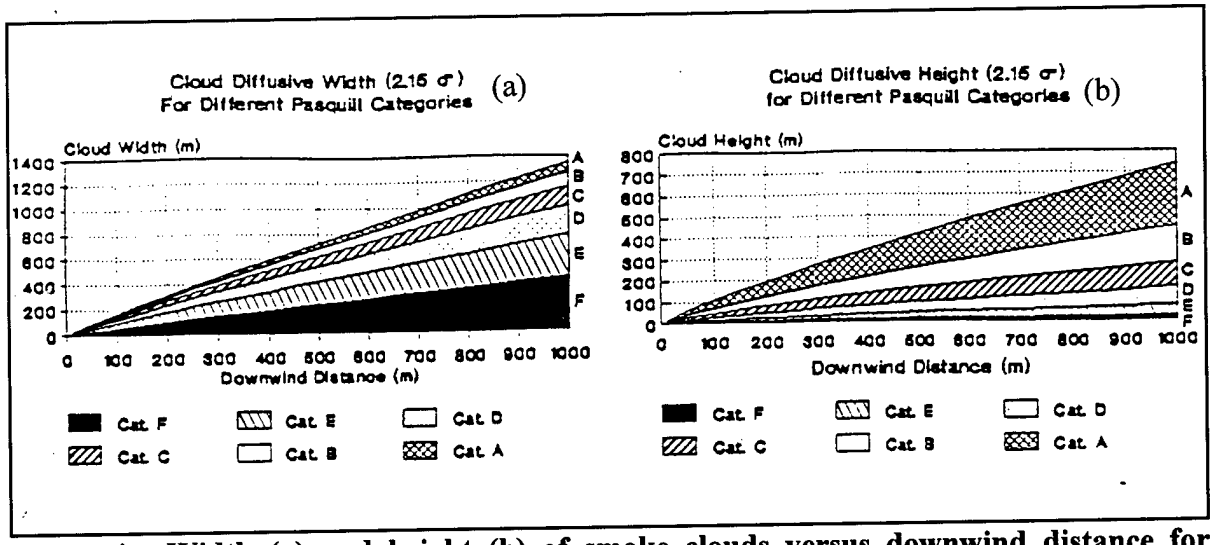


Figure 4. Width (a) and height (b) of smoke clouds versus downwind distance for different Pasquill Stabilities.

Figure 5 illustrates the effect of aerosol-induced radiative damping on turbulence and Pasquill Stability for different optical depths (τ). Figure 5a shows that thicker smoke clouds tend to prevent the atmosphere from becoming more turbulent. Similarly, figure 5b shows the effect of smoke clouds in increasing the stability of the atmosphere as modeled using the REBAR model. Notice that at noon (solar elevation = 90) an unsmoked atmosphere would be extremely unstable (PC = 1). However, the atmosphere becomes only slightly unstable when a dense LASS is present. The REBAR model is the first attempt to model this important aspect of LASSs. The

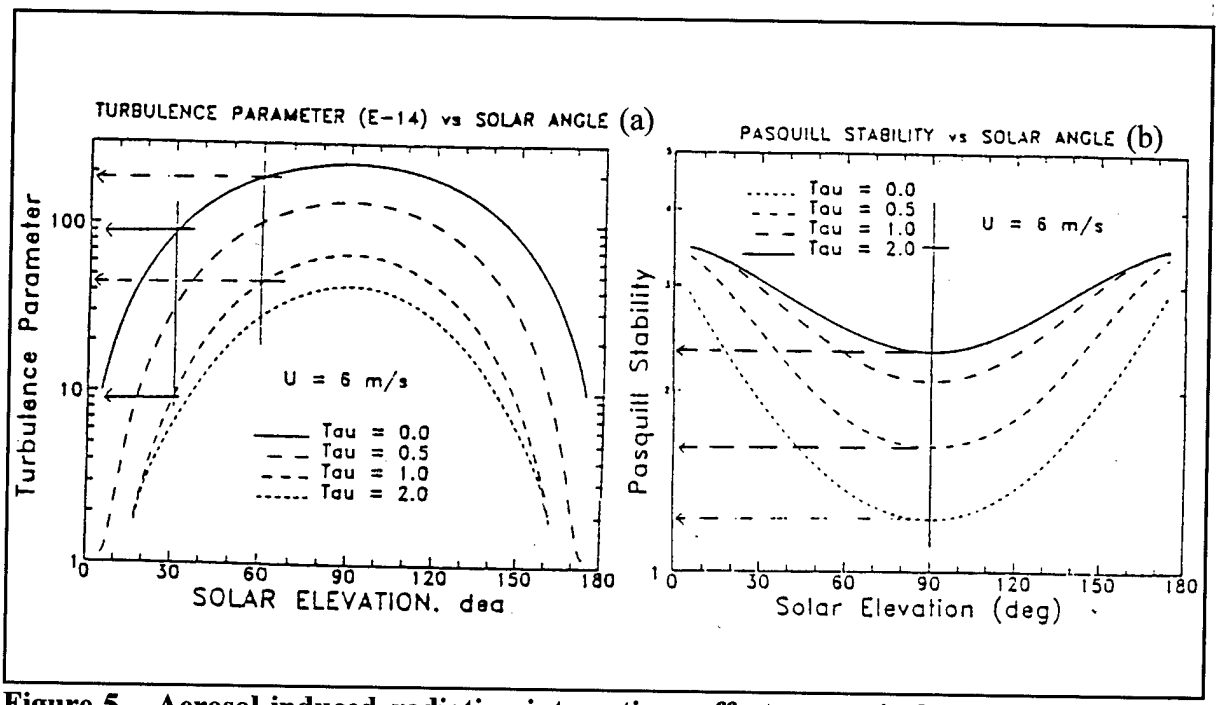


Figure 5. Aerosol-induced radiative interactions effect on optical turbulence (a) and Pasquill Stability (b).

CIAO system will use REBAR to determine the impact of radiative damping on the battlefield. Significant reductions in the amount of smoke are expected to occur if the wargame developers are aware of the depressed conditions caused by the LASS because neutral conditions are often ideal for smoke deployment and a desired smoke screen can be maintained with less smoke. If the wargame developers are not aware that less smoke is necessary, the battlefield might be over smoked, inhibiting target acquisition on both sides. Inhibition of target acquisition might be advantageous to the side modeled with the best ability to observe through an obscured environment. A smart commander might create a LASS in the early morning to inhibit the development of turbulence.

3.5 Effects of COMBIC-RT

Models like CASTFOREM directly relate transmission to EO system performance and smoke effectiveness by considering only the directly transmitted signal. However, EO systems respond not only to directly transmitted radiation but also to contrast. The contribution caused by path radiance, which may be caused by scattering of ambient radiation (sun, sky) into the path of propagation, emission along the path, or both, must be determined to determine contrast. Path radiance has a directional nature causing asymmetries to exist between target and observer. The target or observer has an optical advantage not present when only the direct transmission component is modeled. The LASS model was developed to model the effects. The radiative transfer algorithms were integrated with COMBIC-RT to enable COMBIC to compute path radiance.

Most target acquisition models work by determining the number of resolvable cycles across the target, which directly relates to the target contrast at the aperture of the nonthermal sensor. It is possible to determine the probability of acquisition of a given target through a LASS cloud at any given point in space and time using COMBIC-RT and a target acquisition model like the one in CASTFOREM (Ayres, Sutherland 1994), providing a direct measure of the effectiveness of smoke. Figure 6 shows the effect of sun angle on detection probabilities for different optical depths (τ). The probability of detection for τ of 1 varies from 34 percent for the sun in front of the observer to 63 percent for the sun behind the observer, as expected. A force with the sun behind it has a tactical advantage.

Figure 7 shows the affect that the observer azimuth angle (defined clockwise with respect to North) can have on contrast transmission. Contrast transmission is shown for five CL values. The scenario is for early morning and the zenith angle of the observer is 10°. Notice that low contrast transmission occurs when the observer is looking into the sun (0°) and high contrast transmission occurs with the sun to the back (180°) of the observer. Further, note that the curve flattens as the CL increases. The degree to which a force with the sun in their opponent's eyes, has a tactical advantage, can depend upon the density of the LASS. However, it must be noted that very thick clouds can reflect all light and cause inverse situations.

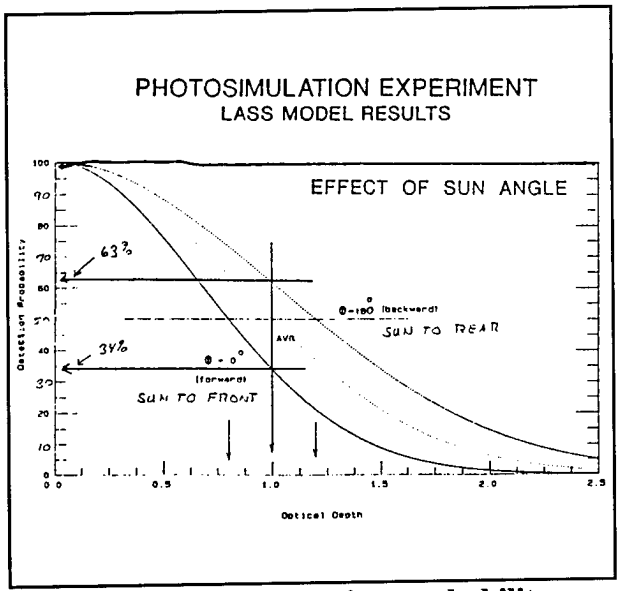


Figure 6. Plot of detection probability as a function of optical depth for various solar azimuth angles.

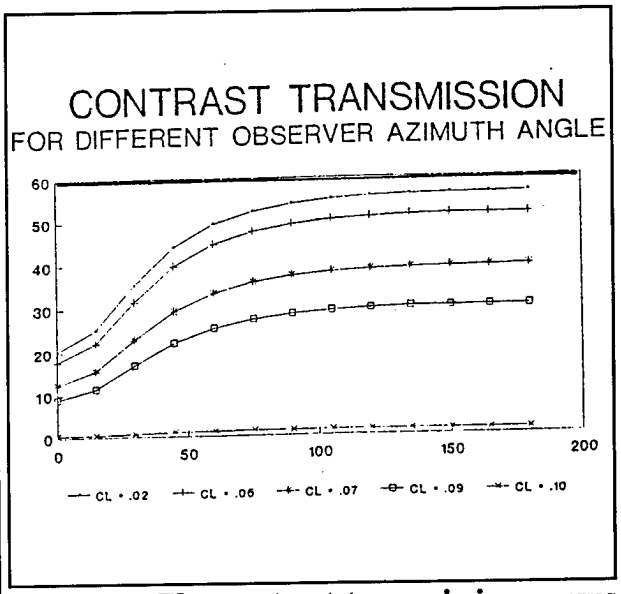


Figure 7. Plot contrast transmission versus observer azimuth angles.

3.6 Effects of COMBIC-PMW

Perhaps the greatest single parameter describing the effectiveness of an obscurant is the mass extinction coefficient. The mass extinction coefficient is used in Beer's law, along with the path integrated concentration, to determine the obscurant optical depth and, hence, transmission for a specified wavelength. The mass extinction coefficient lumps together electromagnetic (EM) radiation scattering out of the LOS and EM absorption radiation along the LOS. The mass extinction coefficient is used by smoke models, such as COMBIC, to determine degradation of

the atmosphere caused by battlefield obscurants. The COMBIC model was originally developed for Electro-Optical Systems of Atmospheric Effects Library (EOSAEL) to model aerosols for which spherical symmetry can be assumed to describe the physical and optical properties of the aerosols. Whereas this is a reasonable assumption when considering the older, conventional obscurants such as fog oil and white phosphorus, the approximation breaks down for newer developmental obscurants designed to be effective at longer wavelengths. Many of the new millimeter wave (MMW) and radar obscurants are highly nonspherical. The propagation of EM radiation in any medium containing particles is governed by the combination of absorption, emission, and scattering, making the particles a subject of great importance in determining effects of obscurants on EM radiation. Scattering and absorption by particles depend upon the size, shape, refractive index, and concentration of the particles. Mathematically determining the radiation field scattered by particles of arbitrary shape at any point in space can be quite difficult. Exact analytical solutions are only available for the sphere and infinite cylinder. However, the scattering properties of simple geometries have been well studied (Bowman et al. 1987). Numerical techniques and approximate analytical methods are used to analyze the properties, usually, over a limited range of conditions. New techniques are required to model the obscurants. The authors have created COMBIC-PMW (Ayres et al. 1994), which is a merger between COMBIC and the techniques that account for the optical and mechanical behavior of finite cylinders. The techniques determine EM properties, such as the ensemble orientation averaged extinction, absorption, and scattering, as well as mechanical properties, such as fall velocity and angular orientation of the obscurant particles when released into the turbulent atmospheric boundary layer.

Extinction for MMW obscurants can widely vary depending upon the fiber properties. Such intrinsic particle properties like shape and bulk density, and bulk EM properties (complex indices of refraction) must be determined for accurate extinction determination. Furthermore, ensemble characteristics such as orientation distribution of the obscurant cloud and incident beam properties like direction, wavelength, and polarization must also be included. Orientation distribution is needed because particle scattering phase functions and attenuation can depend strongly on the orientation of the particle relative to the polarization of the illuminating radiation. Also, the direction of the LOS can be of significance in determining obscurant effectiveness, although current wargames use one value for obscurant extinction per scenario. For example, there can be differences in extinction for horizontal and vertical LOSs when particles are preferentially oriented. The vertical LOS is exposed to this preferred orientation, while the horizontal LOS is exposed to a randomly oriented ensemble if the particles are released in a stable atmosphere and oriented with their long axis horizontal. All the characteristics affect the computation of extinction for cylindrical obscurants, which can affect the loss-exchange-ratios used to describe the results of the wargame.

4. SUMMARY

Battlefield weather conditions have affected, sometimes determined, the outcome of military conflicts and the resultant global order for generations. Accounting for atmospheric variability has been an area of continuing concern for military strategists, planners, and soldiers throughout history. With the emphasis on restructuring the Armed Forces into a streamlined fighting force equipped with advanced technology weapon systems, it is necessary to develop tactics, doctrine, and weapon systems to minimize friendly and collateral casualties while destroying the enemy's capability to fight. Obscurants can be a very important tool on the battlefield. Obscurants are

often described as low technological countermeasures to the high technological weapons of today. It is imperative that the technological tools can realistically depict the battlefield with accurate physics and engineering algorithms. This paper shows that the effectiveness of obscurants is influenced in many ways by the atmosphere; therefore, better atmospheric algorithms must be included in the wargames that define so much of the tactics and doctrine. The CIAO system is an important part of the effort to produce a better atmospheric algorithm. In particular, the improved algorithm includes: (a) terrain effects on smoke transport, (b) contrast effects caused by multiple scattering, and (c) polarimetric effects of nonspherical particles.

ACKNOWLEDGMENTS

The author would like to thank Robert Sutherland and Doug Sheets of the Battlefield Environment Directorate, Army Research Laboratory and Steve LaMotte of the Physical Sciences Laboratory, NM for their advice and assistance in developing the CIAO model.

REFERENCES

Ayres, S. D., and S. DeSutter, 1993. *Combined Obscuration Model for Battlefield Induced Contaminants (COMBIC) Users Guide*. In Press, Department of the Army, U.S. Army Research Laboratory, Battlefield Environment Directorate, White Sands Missile Range.

Ayres, S. D., and R. A. Sutherland, 1994. "Combined Obscuration Model for Battlefield Induced Contaminants-Radiative Transfer Version (COMBIC-RT)." In *1994 Battlefield Atmospherics Conference*, In Press, Department of the Army, U.S. Army Research Laboratory, Battlefield Environment Directorate, White Sands Missile Range, NM 88002-5501.

Ayres, S. D., R. A. Sutherland, and J. B. Millard, 1994. "Combined Obscuration Model for Battlefield Induced Contaminants-Polarimetric Millimeter Wave Version (COMBIC-PMW)." In *1994 Battlefield Atmospherics Conference*, In Press, Department of the Army, U.S. Army Research Laboratory, Battlefield Environment Directorate, White Sands Missile Range, NM 88002-5501.

Bowman, J. J., T. B. A. Senior, and P. L. E. Uslenghi, 1987. *Electromagnetic and Acoustic Scattering by Simple Shapes*. Hemisphere Publishing Corporation, ISBN 0-89116-885-0.

Cionco, R. M., 1985. *Modeling Windfields and Surface Layer Wind Profiles Over Complex Terrain and Within Vegetative Canopies. The Forest-Atmosphere Interaction.* Editors: Hutchison and Hicks. D. Reidel Publishing Co., Holland.

Cionco, R. M., and J. H. Byers, 1993. "A Method for Visualizing the Effects of Terrain and Wind Upon Battlefield Operations." In *Proceedings of 1993 Battlefield Atmospherics Conference.* U.S. Army Research Laboratory, Battlefield Environment Directorate, White Sands Missile Range, NM 88002-5501.

Mackey, D. C., Dixon, D. S., Jensen, K. G., Loncarich, and J. T. Swaim, 1992. *CASTFOREM (Combined Arms and Support Task Force Evaluation Model) Update: Methodologies.* U.S. Army TRADOC Technical Report TRAC-WSMR-TD-92-011.

Sutherland, R. A., and D. E. Banks, 1986. "Smoke Modeling in the Trasana Wargames-The Comprehensive Smoke Study." In *Smoke Symposium X*, Volume 1, pp. 259-268, Aberdeen Proving Ground, MD.

Yee, Y. P, and R. A. Sutherland, 1993. "The Radiative Energy Balance and Redistribution Model, REBAR." In *Proceedings of the 1993 Battlefield Atmospherics Conference*. U.S. Army Research Laboratory, Battlefield Environment Directorate, White Sands Missile Range, NM 88002-5501.

AN ASSESSMENT OF THE POTENTIAL OF THE METEOROLOGICAL OFFICE MESOSCALE MODEL FOR PREDICTING ARTILLERY BALLISTIC MESSAGES

Jonathan D Turton, Peter F Davies
Defence Services Division, Meteorological Office
Bracknell, Berkshire, RG12 2SZ, UK
and
Maj. Tim G Wilson
Developments Division, HQ Director Royal Artillery, Larkhill, Salisbury, Wilts, SP4 8QT, UK

ABSTRACT

An assessment of the potential of using data from the Met Office Mesoscale Unified Model (MM) for producing artillery ballistic messages was made by the Royal Artillery and the Meteorological Office, Defence Services during Summer 1994. This paper reports the results of this assessment.

MM forecasts of vertical profiles for Larkhill were compared with routine radiosonde ascents made at Larkhill. Specifically, wind and temperature data were compared over the various height zones used in artillery ballistics. In addition, both the MM data and the measurements were applied in a ballistic model to evaluate the likely impact on gunnery accuracy that would be achieved using MM data for meteorological corrections.

The implications of the results of this assessment are discussed in terms of the potential use of the MM for making routine ballistic forecasts for (i) artillery training ranges in the UK and (ii) incorporating model predictions into future Royal Artillery battlefield meteorological systems.

1. INTRODUCTION

The motivation for this work is two-fold. Firstly, Larkhill met office is responsible for providing ballistic meteorology for a number of Army training ranges around the UK. Many of these ranges are distant from Larkhill and artillery meteorological (artymet) soundings are seldom made. The only available upper air data comes from those trials ranges with an on-site met office and the UK Met Office upper air network. Thus there is often no measured upper air data for the training ranges, from which to determine ballistic messages (SBMM, SCMM). However, the Larkhill met office, through their meteorological information system, the Outstation Display System (ODS), do have access to all the observational data that is available together with forecast upper air winds and temperatures at WMO standard levels from the "limited area" version of the Met Office Unified Model (Cullen, 1993). Consequently, the accuracy of these ballistic messages is very dependent upon the skill of the Larkhill forecasters and their ability to interpret the available data. It is postulated that the provision of site-specific mesoscale model profiles for the UK training areas could provide valuable information to assist in this task.

Secondly, there is the potential application of mesoscale models to enhance the accuracy of in-theatre meteorological information obtained using the Royal Artillery BMETS (Battlefield METeorological System), or to improve the quality of ballistic information when there are insufficient BMETS deployed. Typically, atmospheric conditions account for some 30% - 70% (depending upon range) of the total error budget for the accuracy of artillery fire and, as longer range artillery pieces come into service, the requirement for better meteorological data becomes more critical. In the future it is anticipated that mesoscale models, or rather battlefield-scale models, will be used to provide optimum battlefield meteorology for artillery purposes. The use of such models is already being investigated by the US Army as part of the CAAM (Computer Assisted Artillery Meteorology) program (Grunwald, 1993; Spalding et al, 1993). A possible future concept for UK artymet, CMETS (Computerised METeorological System), may well embrace this approach and so this work is a useful precursor to any CMETS studies.

2. RADIOSONDE DATA

The radiosonde equipment currently used at all UK upper air sounding stations and ranges is the Vaisala PC-Cora system. The PC-Cora system has been described by Nash (1991) and uses the standard Vaisala RS80 sonde for temperature and humidity measurements. At Larkhill the winds are determined by tracking a radar target using a Cossor 353C wind-finding radar. Soundings are usually made several times a day (typically in summer around 06Z and 10Z), with additional ascents being made as required. The RS80 temperature and humidity sensors have an accuracy of ± 0.2 °C and $\pm 2\%$ and give measurements every 2 s ($\approx$10 m) from launch. Winds at Larkhill are computed from 30 s of radar tracking data, with reported values updated at 2 s intervals during flight. Previous studies (Edge et al., 1986) of the reproducibility of Cossor radar winds have found that the rms vector errors attributable to the radar are about 0.4 m/s at 20 km range increasing to about 1.3 m/s at 80 km range. Thus the wind errors are typically 0.4 m/s up to 9000 m height, increasing to 0.8 m/s at 20000 m height.

In this study, archived 2 s data were used to compute winds and temperatures for the ballistic zones. These zones are given in Table 1. Winds were computed as mean winds through the zones whilst the pressures and virtual temperatures were for the zone mid points. The PC-Cora systems at the range stations have additional software to produce specialised artillery ballistic data, i.e. Standard Ballistic Met Messages (SBMM) and Standard Artillery Computer Met Messages (SCMM).

3. THE MET OFFICE MESOSCALE MODEL

The Met Office Mesoscale Unified Model (MM) is integrated within the operational Unified Model (UM) suite which is run routinely at the Met Office, Bracknell. The suite, which is described by Cullen (1993), consists of global, "limited area" and mesoscale versions of the Unified Model. The global version has 19 vertical levels up to 4.6 mb (typically 35-40 km) with a horizontal resolution of 0.83° in latitude and 1.25° in longitude (giving a typical grid spacing of about 90 km). The "limited area" model covers an area extending from North America in the west to Russia in the east, covering Greenland to the north and North Africa to the south, and has the same vertical structure as the global model but with a horizontal grid length of 0.44° (about 50 km).

The mesoscale version of the model has a grid length of 0.15° (about 17 km) on a 92×92 grid covering an area of about 1500 km×1500 km and has 31 levels up to 4.6 mb, with an increased number of levels in the troposphere. These levels are shown in Table 2, the heights are approximate since the levels are defined

using a hybrid sigma/pressure co-ordinate system. There are 28 levels up to 20000 m as normally required for artillery ballistics. The MM can be run for a number of relocateable areas, with a standard version being run for the UK region, together with two "crisis area" windows covering the Gulf and the region around the former Yugoslavia. However, this paper will concentrate on the UK version of the MM which is run four times each day to produce forecasts out to t+24 (hrs).

Zone No.	Zone range (m)	mid point (m)
00	surface	0
01	0 - 200	100
02	200 - 500	350
03	500 - 1000	750
04	1000 - 1500	1250
05	1500 - 2000	1750
06	2000 - 2500	2250
07	2500 - 3000	2750
08	3000 - 3500	3250
09	3500 - 4000	3750
10	4000 - 4500	4250
11	4500 - 5000	4750
12	5000 - 6000	5500
13	6000 - 7000	6500
14	7000 - 8000	7500
15	8000 - 9000	8500
16	9000 - 10000	9500
17	10000 - 11000	10500
18	11000 - 12000	11500
19	12000 - 13000	12500
20	13000 - 14000	13500
21	14000 - 15000	14500
22	15000 - 16000	15500
23	16000 - 17000	16500
24	17000 - 18000	17500
25	18000 - 19000	18500
26	19000 - 20000	19500

Zone No.	Zone range (m)	mid point (m)
00	surface	0
01	0 - 200	100
02	200 - 500	350
03	500 - 1000	750
04	1000 - 1500	1250
05	1500 - 2000	1750
06	2000-3000	2500
07	3000-4000	3500
08	4000-5000	4500
09	5000-6000	5500
10	6000-8000	7000
11	8000-10000	9000
12	10000-12000	11000
13	12000-14000	13000
14	14000-16000	15000
15	16000-18000	17000

Table 1. Heights of (left) Standard Artillery Computer Meteorological Message (SCMM) zones and (right) Standard Ballistic Meteorological Message (SBMM) zones.

Level	Height (m)	Level	Height (m)	Level	Height (m)
1	10	11	1365	21	6800
2	40	12	1600	22	7900
3	100	13	1870	23	9040
4	190	14	2200	24	10260
5	300	15	2600	25	11750
6	435	16	3080	26	13700
7	595	17	3640	27	16200
8	770	18	4300	28	19700
9	955	19	5050	29	23850
10	1155	20	5870	30	29000

Table 2. Approximate heights of levels in the Met Office MM.

In this study site-specific profiles for Larkhill (51.2°N, 1.8°W) were interpolated from the four surrounding MM grid points and model data were extracted at each grid level. The heights (above 10 m) were then recomputed using the hydrostatic relationship. (Typically at low levels, at 1000 m, the recomputed heights differed from the nominal heights by ≈10 m, whilst higher up, at 2000 m, the difference increased to ≈100 m.) The data were extracted from the midnight run of the model, for 06Z (t+6) and 10Z (t+10) to coincide with the Larkhill radiosonde ascents. The MM data were then interpolated to the mid points of the standard levels (Table 1) and used to produce SCMM data (winds and virtual temperatures for the 26 zones up to 20000 m) and SBMM data (ballistic winds and temperatures for the 15 zones up to 18000 m). Both the MM and radiosonde data were archived over a two month period July/August 1994. Radiosonde ascents were only made at Larkhill on weekdays giving 59 ascents for comparison purposes.

4. COMPARISON OF MODEL PROFILES WITH ACTUAL DATA

4.1 Wind Profiles

For artillery ballistics the quality of the wind data is the most critical factor and this is generally quantified in terms of the vector wind error. Fig. 1 shows the rms vector wind errors (MM - radiosonde) against height (for the SCMM zone mid points). Up to 5500 m (zone 12) the errors are similar for both the t+6 and t+10 predictions, being typically 2.5-3 m/s. The errors increase from 6500 m to 12500 m (zones 13 to 19) and here the t+10 winds have larger errors. This region is associated with the jet stream, near the tropopause, where there are strong winds and shears. Above 13500 m (zone 20) the errors reduce to about 2-3 m/s. Over all 26 zones the average rms errors were 3.1 m/s (t+6) and 3.3 m/s (t+10)

In an earlier study examining the potential capability of Met Office models to provide ballistic data (Whitelaw, 1989) the average model rms error, from the Met Office "fine-mesh" model, up to 20000 m was 3.0 m/s for the analysis (t+0) and 4.7 m/s for a t+3 forecast. The "fine-mesh" model has now been replaced by the "limited area" model and the mesoscale model has since been integrated into the UM suite. The accuracy of the available model winds has clearly improved.

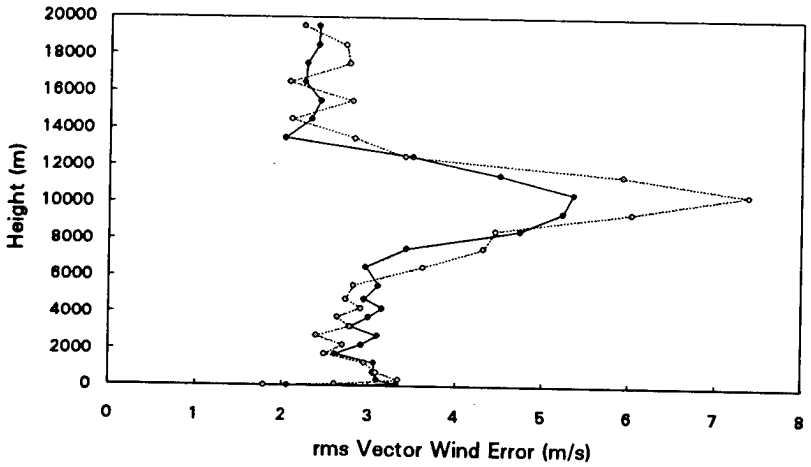


Figure 1. Mesoscale Model rms vector wind errors (m/s) against height. The solid line shows the predictions for t+6, the dashed line for t+10.

Wenckebach (1991) looked at SBMM and SCMM data derived from operational models run by the German Military Geophysical Office, these were a Boundary Layer Model (BLM) for the near surface region (zones 0 to 2) and a 9-level baroclinic model for zones 3 to 18. The results showed that for zones 3

to 18 the rms vector error was in the range 3 to 5 m/s, and tended to increase with height. The errors for the lower winds, zones 0 to 2, were typically 2 m/s (zone 0) and 3.5 m/s (zones 1 and 2). At these lower levels the t+6 forecast winds were better than those for t+12, however at the higher levels there was no significant difference between the t+6 and the t+12 winds.

4.2 Temperature Profiles

Fig. 2 shows the rms errors (MM - radiosonde) for the temperature data. At levels below 10000 m the rms errors are generally < 1°C, the t+6 predictions being slightly better than those for t+10, particularly nearer the surface. At higher levels the rms errors increased up to a maximum of 2.3°C.

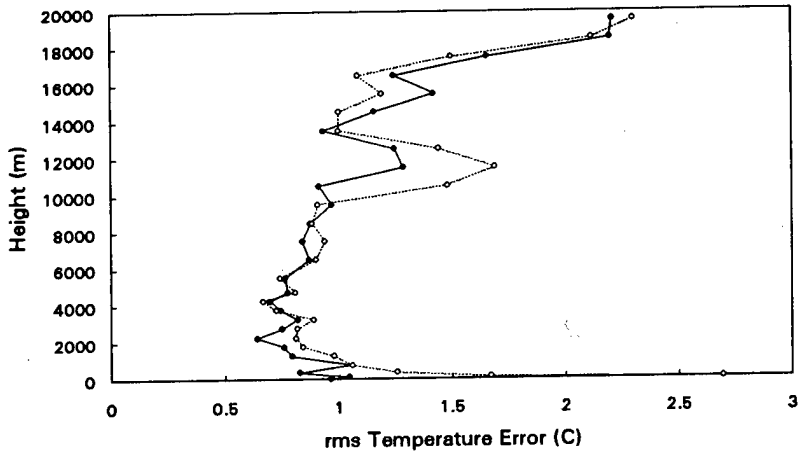


Figure 2. Mesoscale Model rms temperature errors (°C) against height. The solid line shows the predictions for t+6, the dashed line for t+10.

4.3 Ballistic Winds

The ballistic wind is that wind, constant in speed and direction up to a specified zone, which would produce the same displacement of a shell as the actual wind profile, and can be computed from the actual winds by applying standard weighting factors to the winds within the various SBMM zones. For each radiosonde and model profile a ballistic wind profile was computed and the vector differences (MM - radiosonde) were calculated. Fig. 3 shows the profile of the rms ballistic vector wind errors.

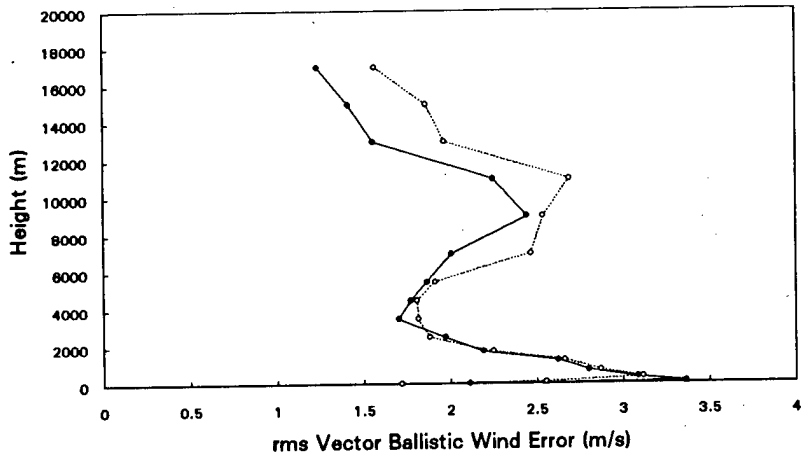


Figure 3. Mesoscale Model rms ballistic wind errors (m/s) against height. The solid line shows the predictions for t+6, the dashed line for t+10.

This also exhibits a region with larger errors which is associated with the jet stream. However, the errors in the ballistic winds are generally less than those for the actual winds.

One of the ways of quantifying the representativeness of meteorological data for ballistic predictions is to describe it in terms of its equivalent "staleness". Blanco (1988) gives some simple algebraic formulae which relate the meteorological variability in terms of a time staleness, this is given in Eq. (1) for the ballistic wind.

$$\sigma_{bw} = 0.061\ (1 + 0.03455\ v_{bw} - 0.05846\ z_b)^2\ t_{st}, \qquad (1)$$

where σ_{bw} is the variance in the ballistic wind (kts^2), v_{bw} is the ballistic wind speed (kts), z_b is the top of the ballistic zone for which the ballistic wind is evaluated (km) and t_{st} is the staleness (min). The staleness can also be equated to a spatial separation through the generally accepted relationship that, over fairly level terrain, a time staleness of 1 hour is equivalent to a spatial displacement of 30 km. Fig. 4 shows an illustration of the equivalent time staleness for a ballistic wind up to 8 km (line 10), in which a ballistic wind speed of 30 kts was specified. In this illustration a ballistic wind error $(\sigma_{bw})^{1/2}$ of 3 kts (1.5 m/s) is equivalent to a staleness of 1 hour and an error of 6 kts (3 m/s) is equivalent to a staleness of 4 hours.

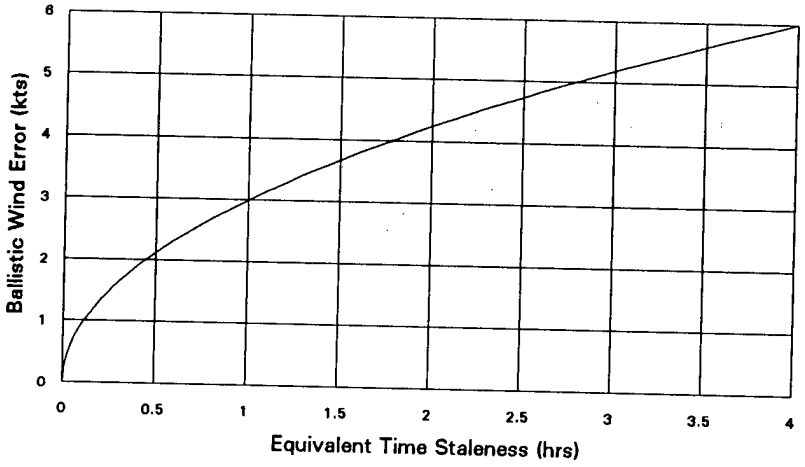


Figure 4. Illustrating the equivalent time staleness of the ballistic wind, up to 8000 m (line 10), in terms of the rms error in the ballistic wind.

It should be noted that Eq. (1) gives the staleness based on a statistical analysis of upper air measurements, but that the staleness for any particular situation will depend upon the homogeneity of the atmosphere (i.e. the synoptic situation). Given the errors in the ballistic winds, as shown in Fig. 3, it is possible to use Eq. (1) to estimate the typical equivalent time staleness. In doing this the square of the rms vector ballistic wind error was applied in Eq. (1). Figure 5 shows the estimated equivalent staleness for the MM ballistic winds relative to the on-site radiosonde winds. At the lowest levels (zones 1 to 3) the model data has an equivalent staleness of 4 hours or more, this reflects the fact that site-specific low level winds are particularly difficult to predict as they are influenced by the local topography (which is not resolved in the MM) and stability, and so tend to vary more than those winds aloft. Away from the ground the equivalent time staleness varies between 1½ to 3 hours for the t+6 forecast and between 1¾ to 4 hours for the t+10 forecast. These figures are similar to the results of Wenckebach (1991), who concluded that model derived messages (above zone 2) were preferable to stale measured ones when the staleness exceeded 3 hours.

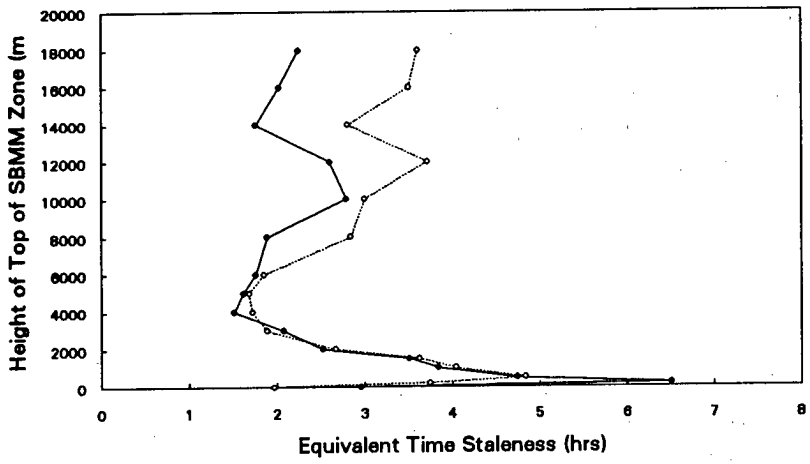


Figure 5. Equivalent time staleness of the mesoscale model winds, the solid line shows the staleness for the winds from the t+6 forecast, the dashed line for the t+10 forecast.

5. BALLISTIC PREDICTIONS

Whilst the above gives an indication of the accuracy of the forecast winds and temperatures from the MM, it does not provide any specific information on the likely impact of using model winds for artillery ballistics. To do this the data were applied in a fire control computer to determine the expected targeting errors, which were quantified in terms of the range (distance) and line (deflection) corrections. These computations were done for a typical Royal School of Artillery training scenario, for an FH70 gun, firing charge 8. Other factors specified were a charge temperature of 21°C and a muzzle velocity of 820 m/s. The specified target was 23 km due north of the gun. Figure 6 shows the computed range and line corrections using the on-site radiosonde ascents. These corrections correspond to the miss distances that would be expected if meteorology was ignored (i.e. assuming a standard ballistic atmosphere) and assuming that the radiosonde data accurately characterised the meteorological conditions.

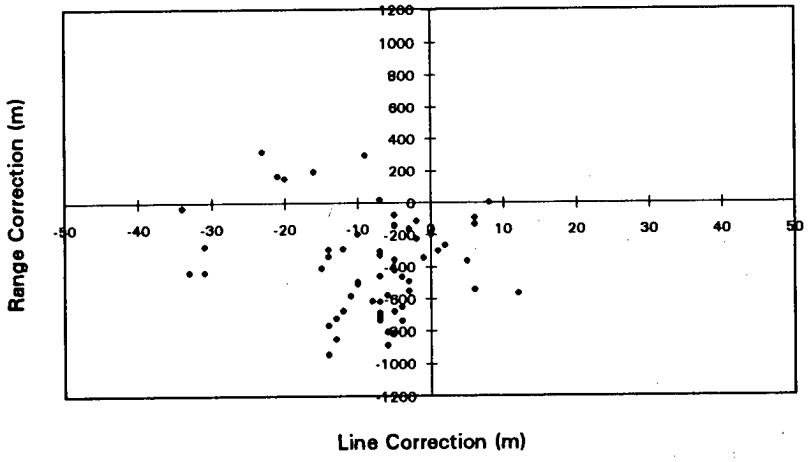


Figure 6. Showing the computed gun corrections based on the measured meteorological conditions.

Figure 6 shows that most of the points fall in the quadrant for which a negative (reduced) range correction is needed together with a negative (westerly) line correction. This is because the predominant wind was from the south-west, with a tendency to carry a shell further towards the north-east. The results give rms corrections of 12 m (line) and 484 m (range). Similar calculations were also made using the MM data. An

assessment of the accuracy of the ballistic forecasts using the MM data can then be made by comparing the computed corrections against those made using the radiosonde data. Assuming that all other factors which contribute to the artillery error budget are constant, then the differences in range and line corrections (MM-sonde) give an indication of the targeting error introduced by using MM data rather than real-time on-site radiosonde measurements. The differences are shown in Figure 7, where the rms errors are 7 m in line and 228 m in range. Thus for a typical training scenario, use of the MM data could reduce the meteorological error by over 50% .

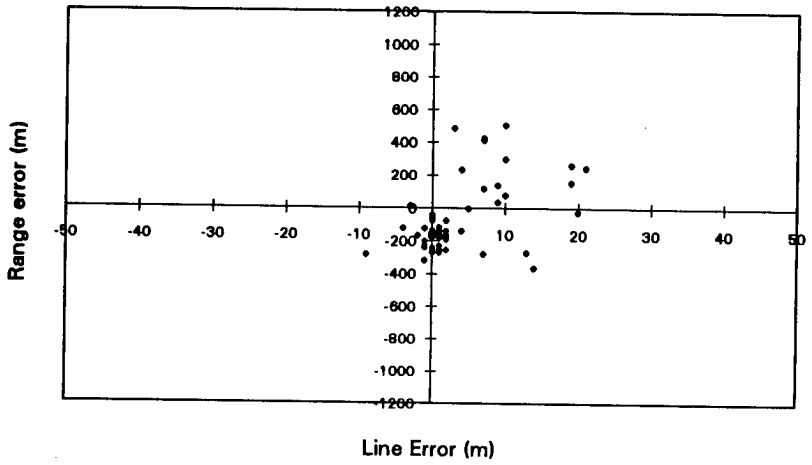


Figure 7. Targeting errors resulting from using MM data instead of radiosonde measurements.

6. DISCUSSION AND CONCLUSIONS

The above results give an indication of the expected accuracy of ballistic met messages derived from MM data. The accuracy of these messages is dominated by the quality of the wind data. The results show that the MM derived winds are least reliable near to the surface (i.e. in the lowest 1000 m up to zone 3). For ballistic messages, above zone 3, the model winds are equivalent to measured winds with a staleness of 1½ to 4 hours, this equates to a spatial displacement of 45 to 120 km.

The training ranges are all more than 130 km away from the nearest station making radiosonde ascents (and at weekends when the range stations are closed may be much further from the nearest ascent). Even if the radiosonde data were available for the time of interest (which is rarely the case), the forecaster would still have to to interpolate between ascents. It is concluded that, there would be a clear benefit in making site-specific MM data for the training ranges available to forecasters, as it will give them much more representative meteorological profile information to work with. Plans are now in hand to allow forecasters to access these data, to provide them with software to view and edit the data, and to automatically produce SBMM and SCMM. It is considered preferable to allow the forecasters to edit/quality control the data, rather than provide a totally automated hands-off facility, as there will be occasions when the model information provides poor guidance (e.g. in mobile synoptic situations when timing errors occur). This facility will also allow them to modify the low level winds on the basis of local surface wind information.

6.1 BMETS

BMETS (Battlefield METeorological System) is expected to enter service with the Royal Artillery in 1995 and will replace the current, but dated, AMETS (Artillery METeorological System). BMETS will employ a modern, ground passive RDF radiosonde tracking system to obtain meteorological data. Each BMETS detachment will consist of 2 light wheeled vehicles with trailers carrying a total detachment of 4 men. One system will be deployed with each field artillery and MLRS (Multiple Launch Rocket System) regiment. BMETS will provide the capability of generating hourly ballistic meteorological messages, Basic Wind Reports and WMO TEMP messages. Typically 6 BMETS would deploy with a Division and operate about 20 km apart. BMETS will have an automated interface to BATES (the Battlefield Artillery Target Engagement System) which will allow messages to be passed between units.

BMETS will provide much more timely and more densely spaced ballistic meteorological data on the battlefield. This will lead to significant improvements in the efficiency of artillery fire, both operationally and during training. However, as artillery ranges increase, the met induced error increases accordingly and becomes particularly significant when considering deep operations where instrumental measurement is particularly difficult. In order to provide more representative meteorological data to support deep and depth operations, it will be necessary to use meteorological models.

6.2 Future Concepts - CMETS

There is currently a project underway at the Met Office to develop a portable workstation-based high resolution crisis area model which can be run in a secure environment (e.g. at the Principal Forecast Office, HQSTC). This will include a full dynamic data assimilation scheme which will allow it to assimilate all the available in-theatre data, e.g. from BMETS and other military sources (which for security reasons cannot be used in NWP schemes run at Bracknell) and so should be capable of providing the best quality theatre NWP. This capability is expected to become operational in a few years time and it will then become the primary source for short-period meteorological forecasts for crisis areas. However, it is envisaged that it will be a theatre-scale model, with a resolution $\approx$15 km, rather than a battlefield-scale capability. The results presented here suggest that the present MM is capable of giving the most representative meteorological information when the radiosonde measurements are between 1½ and 3 hours old (or 45 to 120 km distant), although these figures should be reduced for forecasts up to t+6. (It is worth noting that no upper air data from Larkhill was assimilated into the MM for the forecasts assessed here, such that these figures are representative of its accuracy away from sources of upper air data.) Thus, away from the BMETS network, e.g. in the target area, it would be expected that the model would be the best source of meteorological information.

The CMETS (Computerised METeorological System) concept is to provide "now-casts" (i.e. for 0 to 3 hrs ahead) of ballistic messages based on meteorological profiles at the point of the vertex of a shells trajectory, or even along a shell or rocket trajectory. This will necessitate information on battlefield locations and demands that any processing/modelling is done at a lower echelon. An idea, currently being considered, is to use a PC/workstation-based battlefield-scale model. This would cover, say, a 200 km× 200 km area, with a horizontal resolution of 5 km or better, containing orographic information. This model would receive background fields derived from the portable theatre-scale models run at a higher echelon and assimilate the BMETS data (and any other available target area data) in order to provide an optimum 3-dimensional analysis of the meteorological conditions. Additional detail in the boundary layer wind field could be diagnosed using a complex terrain model (e.g. based on mass continuity or linear inviscid flow) which should improve the low level winds (which is where the current MM winds are poorest). Thus the

aim is to provide a mobile computer work-station with the communications facilities to update the meteorological field both from strategic background information from a higher echelon and from tactical data available in-theatre. Using this information, it is hoped to provide mission specific ballistic data to artillery users.

REFERENCES

Blanco A J, 1988: Methodology for Estimating Wind Variability, ASL-TR-0225, US Army Atmospheric Sciences Laboratory, White Sands Missile Range, NM, US.

Cullen M J P, 1993: The Unified Forecast/Climate Model, Meteorol Mag, 122, 81-94.

Edge P, Kitchen M, Harding J and Stancombe J, 1986: The Reproducibility of RS3 Radiosonde and Cossor WF MkIV Radar Measurements. Observational Services Memorandum OSM No. 35, Meteorological Office, Bracknell, UK.

Grunwald Maj A A, 1993: Computer Assisted Artillery Meteorology (CAAM). Briefing to the NAAG ISWG.3 at Army Research Laboratory, Battlefield Environment Directorate on 10 March 1993.

Nash J, 1991: Implementation of the Vaisala PC-Cora upper air sounding system at operational radiosonde stations and test ranges in the United Kingdom. In Proceedings of the 7th Symposium on Meteorological Observations and Instrumentation, New Orleans, LA, US. pp 270-275.

Spalding J B, Kellner N G and Bonner R S, 1993: Computer-Assisted Artillery Meteorological System Design. In Proceedings of the 1993 Battlefield Atmospherics Conference, Las Cruces, NM, USA. pp 45-54.

Wenckebach K, 1991: On the accuracy of meteorological messages computed from numerical forecasts. German Military Geophysical Office. Presentation given at the NATO Panel IV SP2/ISWG.3 Joint Symposium on Ballistic Meteorology, May 1991, NATO HQ, Brussels, Belgium.

Whitelaw A, 1989: Study of Future Artillery Meteorological Techniques. Technical Note 3. Short Term Forecasting. Logica Report 242.20103.003.

RESULTS OF THE LONG-RANGE OVERWATER DIFFUSION (LROD) EXPERIMENT

James F. Bowers
West Desert Test Center
Dugway, Utah 84022-5000

Roger G. Carter and Thomas B. Watson
NOAA Air Resources Laboratory
Idaho Falls, Idaho 83402

ABSTRACT

The Long-Range Overwater Diffusion (LROD) Experiment was a Joint Services, multi-agency project to help fill the data gap on the alongwind diffusion (especially at intermediate to long range) of a vapor or aerosol cloud instantaneously released to the atmosphere. LROD was conducted northwest of the island of Kauai, Hawaii in July 1993. As described in detail in a 1993 Battlefield Atmospherics Conference paper, the experiment consisted of a series of crosswind line source releases of sulfur hexafluoride (SF_6) from a C-130 transport. The tracer cloud was tracked to 100 km using an aircraft-mounted continuous SF_6 analyzer. The SF_6 cloud was also sampled by continuous analyzers on boats at downwind distances of up to 100 km. This paper summarizes the LROD results and provides an overview of the data that will be available to researchers and model developers.

1. BACKGROUND

Current atmospheric transport and diffusion models commonly assume that the alongwind and crosswind diffusion rates are the same because little is known about alongwind diffusion. However, both short-range diffusion experiments (Nickola, 1971) and theoretical analyses (Wilson, 1981) indicate that this is a poor assumption. Little data exist to characterize alongwind diffusion, especially at distances of more than a few kilometers, because: (1) alongwind diffusion usually is not an issue when modeling continuous sources of air pollution, (2) total dosages traditionally have been assumed to be more important for hazard assessments than concentration exposure histories, and (3) samplers capable of making time-resolved concentration measurements have not been readily available until recently.

The data gap on alongwind diffusion affects the accuracy of model predictions of the transport and diffusion of any material from a short-term atmospheric release. These

releases often present an immediate threat to life and property when they involve the accidental release of a toxic substance from a failed containment vessel (for example, rupture of a chlorine tank car). If diffusion models are used in these cases to make decisions about evacuation routes and priorities, erroneous model assumptions about alongwind diffusion could have disastrous consequences.

The Long-Range Overwater Diffusion (LROD) Experiment was conducted near Kauai, Hawaii in July 1993 to help fill the data gap on alongwind diffusion, especially at intermediate to long range. The experiment was conducted over water rather than land primarily because it was desired that meteorological conditions be essentially constant over distances of 100 km or more for days at a time. (Steady-state mesoscale meteorological conditions were desired to facilitate both experiment conduct and the interpretation of experiment results.) Because the experiment was conducted over water, a secondary objective was to acquire data that will contribute to meteorologists' understanding of atmospheric transport and diffusion processes over oceans. The design of the LROD experiment is discussed in a paper presented at the 1993 Battlefield Atmospheric Conference (Bowers, 1993). This paper briefly summarizes the results of the experiment.

2. EXPERIMENTAL DESIGN AND CONDUCT

The design and conduct of the LROD experiment are discussed in detail by Bowers et al. (1994) and summarized in a paper presented at the 1993 Battlefield Atmospheric Conference (Bowers, 1993). Briefly, LROD consisted of 13 crosswind releases of inert, nontoxic sulfur hexafluoride (SF_6) from a C-130 transport flying 90 m above the ocean's surface. The tracer cloud, which formed a 100-km crosswind line source, was tracked to 100 km downwind using a continuous SF_6 analyzer mounted in a twin-engine aircraft. The sampling aircraft repeatedly measured the alongwind concentration profile 150 m above the ocean as it flew through the cloud in a series of downwind and upwind passes. The SF_6 cloud was also sampled by continuous analyzers on five boats at downwind distances of up to 100 km. Because all aircraft- and boat-based SF_6 concentration measurements were made near the midpoint of the 100-km line source, the measured concentrations should be unaffected by diffusion from either end of the cloud, even at 100 km downwind. Meteorological measurements were made from one of the boats and a specially instrumented single-engine aircraft.

The unseasonably high seas experienced in Hawaiian waters during LROD often prevented the small sampling boats from going out into open ocean. Even when the boats were able to leave port, the scientists on the boats were generally incapacitated by seasickness. Consequently, the boat-based SF_6 measurements were quite limited (six trials with one or more sampling boats). However, the aircraft-based SF_6 measurements were highly successful, yielding over 230 measurements of the alongwind cloud concentration profile. The only significant problems with the aircraft sampling system were a data logger problem during Trial 1 and a Global Positioning System (GPS) failure during

Trial 12, which resulted in termination of aircraft sampling at 47 km. Because of the data logger problem during Trial 1, aircraft sampling data are not available for this trial.

3. LROD EXPERIMENT RESULTS

3.1 SF_6 Dissemination

The SF_6 tracer was released from the C-130 in liquid form. Because SF_6 has a boiling point of -63.9 °C, the liquid SF_6 vaporized almost instantaneously and was quickly mixed with ambient air by the aircraft's wake turbulence. The dissemination rate was measured by a flow meter, and the SF_6 cylinders were weighed before and after use. The average SF_6 dissemination rate was 12 g/m for Trial 1 and 5 g/m for the remaining trials. Because the concentrations measured during Trial 1 were much higher than anticipated, the dissemination rate was reduced after the first trial by decreasing the flow rate and increasing the speed of the C-130. The dissemination rate standard deviations average less than 5 percent of the corresponding mean dissemination rates, which indicates that the dissemination rate was fairly uniform.

3.2 SF_6 Sampling

The aircraft SF_6 concentration measurements were paired with GPS position and time information during data acquisition. During post-experiment data processing, the SF_6 concentrations were converted from millivolts to parts per trillion (ppt) by volume using the calibrations made during each trial. The positions were also adjusted to account for the measured 9-s delay between the time when air entered the sampling inlet on the aircraft's exterior and the time when it reached the continuous analyzer. For convenience in data analysis, the positions were converted from longitude and latitude to a Cartesian coordinate system of the type used in Gaussian diffusion models. For each trial, the origin of the coordinate system was placed at the midpoint of the dissemination line, the positive x axis extended in the downwind direction, and the y axis was positive to the right when looking downwind. Because of the easterly trade winds during the experiment, the x axis pointed approximately to the west and the y axis pointed approximately to the north. Time was converted to seconds after the C-130 was at the midpoint of the dissemination line.

If the SF_6 cloud had been stationary, the aircraft measurements could be used to estimate the alongwind cloud width under the assumption that cloud expansion was negligible for a single pass. However, the cloud transport speed was 10 to 20 percent of the aircraft's ground speed. Consequently, it was necessary to correct the downgrid coordinates of the aircraft concentration measurements to remove the effects of the cloud's motion. Assuming that the cloud's alongwind expansion was negligible during each pass and that neither the cloud transport speed nor the aircraft ground speed varied during the pass, the corrected downgrid coordinate of a concentration measured at time t is

$$x' = x + \bar{u}(t_o - t) \quad (1)$$

where x is the uncorrected coordinate, ū is the cloud transport speed, and t_o is the time when the aircraft passed through the cloud's center of mass. The cloud transport speed was determined from the motion of the cloud's center of mass as determined from the aircraft measurements. Equation (1) was used to construct the alongwind SF_6 concentration profile at time t_o for each pass through the cloud.

Figure 1 shows examples of upwind and downwind aircraft SF_6 cloud concentration profiles both before and after the correction for cloud motion. Because the concentration profiles in the figure are from a trial that had one of the highest cloud transport speeds, the correction for cloud motion is more evident than for most of the other trials. As shown by the figure, the corrected profile is narrower than the original profile for the downwind traverse and broader for the upwind traverse.

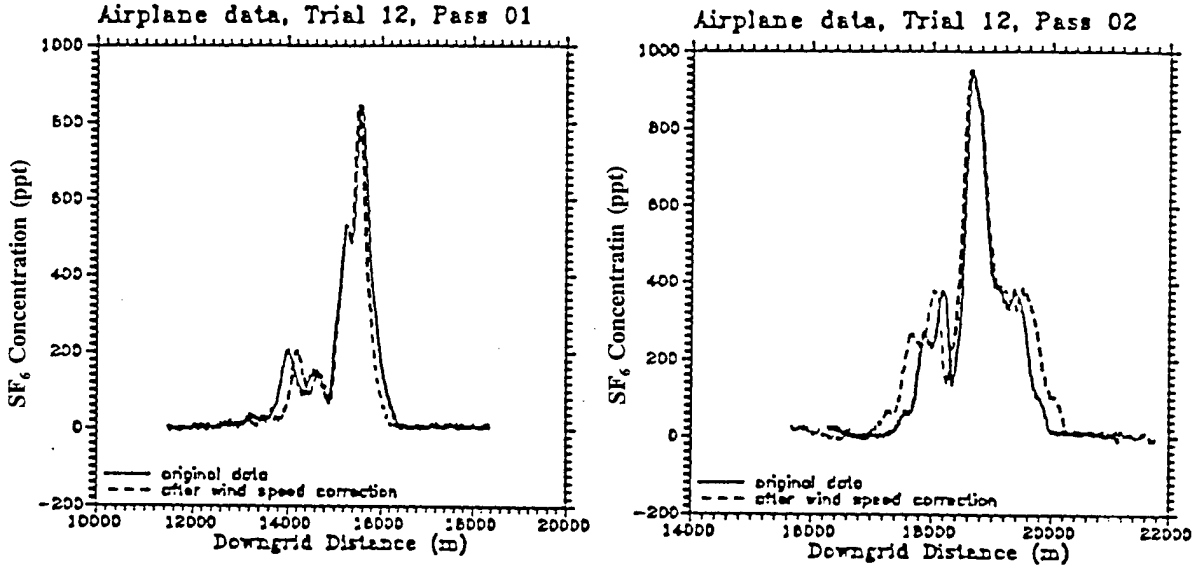


Figure 1. Corrected (dashed line) and original (solid line) SF_6 cloud concentration profiles for aircraft Pass 1 (downwind) and Pass 2 (upwind) through the cloud during Trial 12.

The LROD data can be used to test or develop a number of types of diffusion models, but the type of model most frequently used for operational applications is the Gaussian puff or plume model. As suggested by Figure 1, the individual cloud concentration profiles usually were not Gaussian in appearance. Nevertheless, most of the profiles could be described reasonably well by a Gaussian distribution. The LROD report contains best-fit Gaussian cloud parameters for three different fitting methods, but the method that appeared to give the best overall representation of the actual profiles was the

peak/area match method. In this method, the fitted peak concentration χ_o was set equal to the measured peak concentration and the Gaussian alongwind dispersion coefficient σ_x was computed from

$$\sigma_x = \frac{CL}{\sqrt{2\pi}\ \chi_o} \tag{2}$$

where CL is the alongwind-integrated concentration. Note that this fitting method ensures that the fitted and actual profiles account for the same total mass. Figure 2 shows the peak/area Gaussian fits to the corrected cloud concentration profiles from Figure 1.

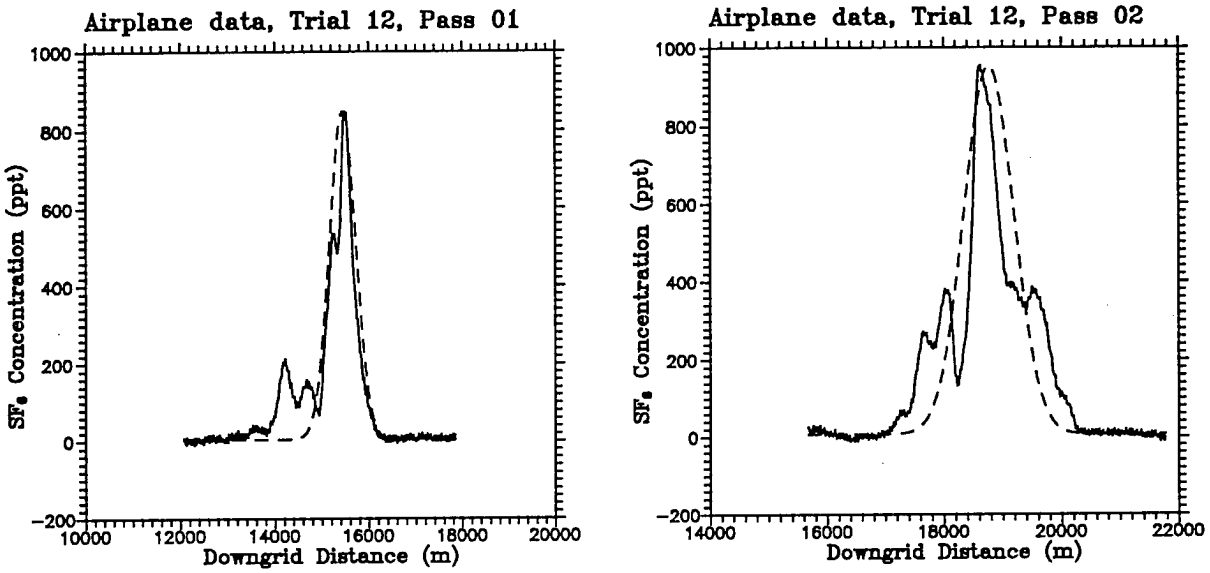


Figure 2. Measured (solid line) and fitted (dashed line) SF_6 cloud concentration profiles for aircraft Passes 1 and 2 of Trial 12. Measured profiles have been corrected for cloud motion.

The boat continuous analyzer measurements were processed in the same manner as the aircraft measurements, including conversion to trial grid coordinates and correction for cloud motion. Each boat continuous analyzer SF_6 concentration profile was compared with the aircraft profiles for the two passes made nearest to the boat during that trial. Figure 3 shows an example of two aircraft profiles superimposed on a boat profile. In this case, the differences between the two consecutive aircraft profiles are greater than the differences between the boat profile and the first aircraft profile. A statistical comparison of the Gaussian model cloud parameters σ_x and χ_o estimated from the boat and aircraft measurements showed that the differences are not significant at the 95 percent confidence level. Thus, the aircraft σ_x and χ_o should be representative of σ_x and χ_o near the surface, at least at the downwind distances of the available boat measurements (60 and 100 km).

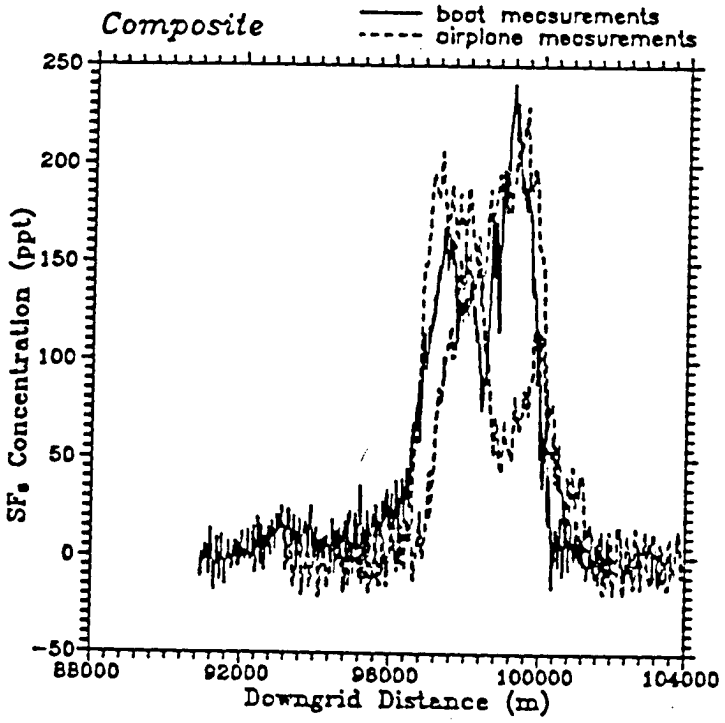


Figure 3. Comparison of aircraft and boat continuous SF_6 analyzer measurements for Trial 5, Boat 5 (100 km).

3.3 Meteorological Measurements

Standard surface and upper-air (radiosonde) measurements were made from Boat 1 approximately 10 km downwind from the dissemination line during the first three trials. Because of high seas, it was not possible to keep Boat 1 in the experiment area for days at a time during the remaining trials. Beginning with Trial 6, Boat 1 was sent each day to a position 15-20 km south of Kauai, outside of the island's wake. The observations should therefore be representative of conditions in open ocean, but not necessarily of conditions in the experiment area 200 km to the northwest. Wind, temperature, and humidity measurements were made at nominal height of 10 m on the boat's main mast and sea surface temperature was obtained from a thermometer mounted on the hull. The wind observations were corrected for pitch, roll, and boat heading. In addition to the Boat 1 radiosonde soundings, standard synoptic radiosonde soundings are available from the Lihue Airport on the east shore of Kauai.

The meteorological research aircraft, a specially instrumented Rutan Long-EZ, entered the experiment area after the C-130 had completed SF_6 dissemination. Flying a track approximately parallel to and 45 km south of the sampling line, the Long-EZ began each trial by measuring the vertical profiles of wind, temperature, and humidity as it slowly descended from 2500 m above mean sea level (MSL) to about 25 m MSL. The long-EZ then flew to the dissemination line and back while it measured the vertical fluxes of

sensible and latent heat, momentum, and carbon dioxide (CO_2). After completing the flux runs, the Long-EZ again measured meteorological profiles as it slowly ascended from 25 to 2500 m MSL during its return flight to the dissemination line. The only aircraft meteorological measurements included in the LROD final report (Bowers et al., 1994) are the vertical profiles of temperature and dewpoint and two derived parameters: potential temperature and equivalent potential temperature. The wind, turbulence, and flux measurements will be provided in a supplemental report.

Table 1 summarizes the meteorological conditions at the start of each LROD trial. The 10-m wind speeds and atmospheric stabilities are based on the Boat 1 surface observations. Both the Naval Postgraduate School overwater stability classification scheme (Schacher et al., 1982) and the widely used Turner (1964) scheme give the Pasquill stability category as the neutral D category. The inverse Obukhov lengths were calculated from Boat 1 observations using the bulk methods of Wu (1986). The cloud transport speeds were determined from the aircraft measurements of the motion of the SF_6 cloud's center of mass and the mixing depths were calculated from the SF_6 mass balance at long downwind distances.

Table 1. Summary of LROD Trial Meteorological Conditions[a]

Trial	u_{10m} (m/s)	$\bar{u}$ (m/s)	Stab.	1/L (m^{-1})	H_m (m)
2	8.2	10.5	D	-0.001	810
3	9.8	10.1	D	-0.001	1155
4	--	11.1	--	--	815
5	--	11.5	--	--	1495
6	7.7	10.7	D	-0.003	735
7	9.3	12.0	D	-0.001	1110
8	10.3	12.7	D	0.003	1005
9	10.3	10.1	D	0.000	665
10	5.1	9.9	D	0.002	435
11	10.3	10.3	D	0.000	635
12	11.3	13.5	D	0.002	715
13	11.3	15.6	D	0.002	765

[a] u_{10m} = 10-m wind speed, $\bar{u}$ = cloud transport speed, Stab = Pasquill stability category, 1/L = inverse Obukhov length, H_m = mixing depth

4. DISCUSSION OF RESULTS

Figure 4 shows all of the LROD aircraft σ_x measurements plotted as a function of downwind distance. Figure 4 also shows the Pasquill-Gifford σ_y (lateral dispersion coefficient) curves for the D (neutral), E (stable), and F (very stable) Pasquill stability categories (Turner, 1970) because many current diffusion models for instantaneous releases assume that σ_x can be approximated by σ_y. The measured σ_x values range from near the Pasquill-Gifford σ_y curve for D stability to well below the σ_y curve for F stability. Thus, although meteorological conditions were similar during all trials, there were significant trial-to-trial variations in σ_x. It therefore appears that the LROD data set is suitable for use in investigating the quantitative relationship between alongwind puff growth and meteorological conditions. If this relationship can be established, σ_x can be predicted for other meteorological conditions and other settings, including over land.

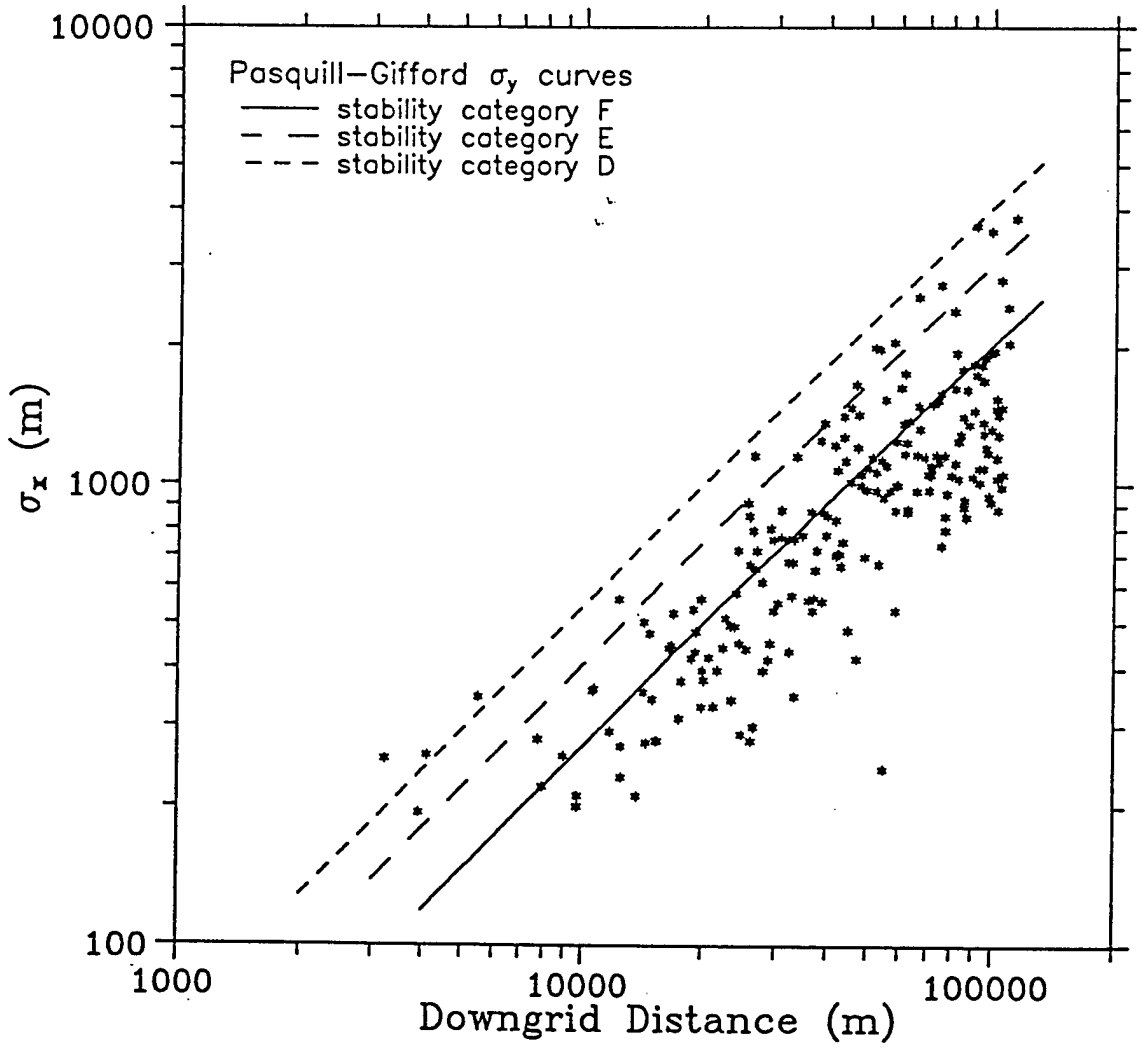


Figure 4. Alongwind dispersion coefficient σ_x versus downgrid distance for all LROD trials.

5. SUMMARY

The LROD experiment yielded a unique data set that should contribute to an improved understanding of both the physics of alongwind diffusion and atmospheric transport and diffusion processes over oceans. The data presented in the LROD final report will likely meet the needs of most model developers and researchers. For those who require more detailed information, the 4-Hz (aircraft) and 1-Hz (boat) continuous analyzer SF_6 concentration measurements are available from the Meteorology Division, West Desert Test Center (formerly the Materiel Test Directorate, U.S. Army Dugway Proving Ground).

ACKNOWLEDGMENTS

The sponsors of the LROD experiment were the Joint Contact Point Directorate (Project DO49), U.S. Army Dugway Proving Ground, Dugway, Utah; Chemical and Biological Defense Division, Brooks Air Force Base, Texas; and Naval Surface Warfare Center, Dahlgren, Virginia.

REFERENCES

Bowers, J. F., 1993: "Overview of the Long-Range Overwater Diffusion (LROD) Experiment." In Proceedings of the 1993 Battlefield Atmospherics Conference, U.S. Army Research Laboratory, White Sands Missile Range, NM 88002-5501, pp 157-170.

Bowers, J. F., G. E. Start, R. G. Carter, T. B. Watson, K. L. Clawson, and T. L. Crawford, 1994: "Experimental Design and Results for the Long-Range Overwater Diffusion (LROD) Experiment." Report No. DPG/JCP-94/012, U.S. Army Dugway Proving Ground, Dugway, UT 84022-5000.

Nickola, P. W., 1971: "Measurements of the Movement, Concentration, and Dimensons of Clouds Resulting from Instantaneous Point Sources." J. Appl. Meteor., 8: 962-973.

Schacher, G. E., D. E. Speil, K. L. Davidson, and C. W. Fairall, 1982: "Comparison of Overwater Stability Classification Schemes with Measured Wind Direction Variability." Naval Postgraduate School Report No. NPS-61-82-0062 prepared for Bureau of Land Management, Los Angeles, CA.

Turner, D. B., 1964: "A Diffusion Model for an Urban Area." J. Appl. Meteor., 3: 83-91.

Wilson, D. J., 1982: "Along-wind Diffusion of Source Transients." Atmos. Env., 15: 489-495.

Wu, J., 1986: "Stability Parameters and Wind-Stress Coefficients Under Various Atmospheric Conditions." J. Atmos. and Ocean. Tech., 3: 333-339.

MODELED CEILING AND VISIBILITY

Robert J. Falvey
United States Air Force
Environmental Technical Applications Center
Simulation and Techniques Branch
859 Buchanan Street
Scott AFB, IL 62225-5116

ABSTRACT

Modeling distributions of climatological data using mathematical equations is an effective data compression technique. Since ceiling and visibility data are not normally distributed, modeling their distributions is accomplished using the Weibull family of curves. Cumulative frequency distributions using 20 years of ceiling and visibility data are analyzed and Weibull curves are fit to the data. The Weibull coefficients are calculated and stored for use with the microcomputer based MODCV software. The software uses these coefficients, along with current conditions and serial correlations in a first-order Markov process, to produce conditional and unconditional probability forecasts of ceiling and visibility and joint ceiling and visibility probabilities. The MODCV software uses the standard Microsoft Windows interface which allows the user to quickly select conditional and unconditional probabilities. The output consists of bar graphs and tables of ceiling and visibility probabilities for ten wind stratifications and eight user-selected forecast times up to 72 hours in the future.

1. INTRODUCTION

In the past, climatological requirements of the typical weather station have been satisfied by bulky paper copies of the Revised Uniform Standard Surface Weather Observations (RUSSWO), Wind Stratified Conditional Climatology (WSCC) tables, and Air Weather Service (AWS) Climatic Briefs. As microcomputers have become integrated into weather station operations, the opportunity to complement and/or replace these printed summaries with electronic climatological databases is possible. The MODeled Ceiling and Visibility (MODCV) software was originally designed to replace the WSCC tables. However, in the original version of the program, the data was not wind stratified. Since winds play a vital role in both ceiling and visibility, this lack of wind stratification made the software fall short of the end-user's needs. The methodology described below is the same as in the original version and is taken directly from Kroll and Elkins (1989). The results of the wind stratified modeling are described in section 3.

2. METHODOLOGY

MODCV was developed to provide rapid transportable access to unconditional and conditional probability forecasts of ceiling and visibility based on climatological data.

2.1 Unconditional Probability

Unconditional climatology data, which is simply the relative frequency of occurrence that a certain condition was observed, is easily tabulated at any location that has a representative observational record. The unconditional probability that the visibility below 1 mile at 12 GMT is calculated by summing the number of times the visibility at 12 GMT was below 1 mile and dividing by the number of observations at 12 GMT. This is the method used to produce the RUSSWO summaries.

A very powerful alternative to tabulating each condition into frequency tables is to model the Cumulative Distribution Function (CDF). This process involves the use of mathematical equations to fit the cumulative frequency distribution. If the variable being modeled is continuous, the cumulative probability associated with any value of that variable can be calculated using the equation:

$$P = F(x) \qquad (1)$$

where F(x) is the function that models the distribution of the CDF. In MODCV, therefore, given any threshold value of x, this function is used to calculate the unconditional probability that x will be below that threshold value.

2.2 Conditional Probability

The basic component of the conditional ceiling and visibility is based on the Ornstein-Uhlenbeck (O-U) stochastic process, a first order Markov process for which each value of a random variable x_t is considered a particular value of a stationary stochastic process. The stochastic model relates a value of x at time t (x_t) to an earlier value of x at time zero (x_0). A frequent assumption in statistical application is that the variable is normally distributed. Unfortunately, many meteorological variables, such as ceiling and visibility, are not normally distributed. Non-normal variables can be transformed into normal distributions through a process called transnormalization. Transnormalization involves expressing the raw variables in terms of it's equivalent normal deviate (END). This process is discussed by Boehm (1976). Once the variable has been normalized, the joint density function associated with x_0 and x_t becomes:

$$f(x_0, x_t) = \frac{1}{2\pi\sigma^2\sqrt{(1-\rho^2)}} e^{\left[\frac{(x_0-\mu)^2-2\rho(x_0-\mu)(x_t-\mu)+(x_t-\mu)^2}{2\sigma^2(1-\rho^2)}\right]} \qquad (2)$$

where ρ is the serial correlation between successive values of x and where μ and σ are the

mean and standard deviation of x. Since we are interested in the probability of x_t given the initial value of x_0, a conditional distribution of x is required. If x can be approximated by a first-order Markov equation, then x_t is dependent only upon x_0. If successive observations of x have a bivariate normal distribution, the conditional distribution of x_t is normal with a mean of:

$$E[(x_t|x_0)] = \sigma+\rho(x_0-\mu) \quad (3)$$

and a variance of:

$$var[(x_t|x_0)] = \sigma^2(1-\rho^2) \quad (4)$$

Equations 3 and 4 are basic to the first-order Markov equation. A value of x_t can be calculated using:

$$x_t = \mu+\rho(x_0-\mu)+\sigma\sqrt{1-\rho^2}\eta_t \quad (5)$$

If the variable is distributed normally with a mean of zero and a variance of one, equation 5 reduces to:

$$x_t = \rho x_0+\sqrt{1-\rho^2}\eta_t \quad (6)$$

where ρ is the correlation coefficient between x_0 and x_t separated by time interval t, and η_t is a random normal number. The process is considered to be Markov if $\rho = \rho_0^t$, where ρ_0 is the hour-to-hour correlation associated with x. If ρ_0 is a constant, then this process is considered stationary and is known as the *Ornstein-Uhlenbeck* or O-U process.

Application of the O-U process to meteorological variables is well documented in Gringerton (1966), Sharon (1967), and Whiton and Berecek (1982). Its use with variables whose time series have a random component and adhere to the restrictions of the Markov is justifiable. Stationarity is a feature that is especially favorable for application to weather variables since predictions derived from stationary processes will converge toward the mean as time increases. Thus, the conditional probabilities will converge to unconditional probabilities as the forecast time period increases.

From equation 6, we can conclude that, for a specific value of x_0, the value of η_t will exceed a minimum value η_{min} as frequently as x_t exceeds a minimum value x_{min} given an initial value x_0. In terms of probability,

$$P(\eta_t>\eta_{min}) = P(x_t>x_{min}|x_0) \quad (7)$$

Now we replace the value of η_t as x(t|0), the normalized value corresponding to the conditional probability of x_t. Thus, equation 7 becomes:

$$P(x_t \mid x_0) = P(x_t > x_{min} \mid x_0) \quad (8)$$

where $P(x_t|x_0)$ is the conditional probability of x_t given the value of x_0, $P(x_t)$ is the unconditional probability of x at time t, and $P(x_0)$ is the unconditional probability of x at time zero. MODCV uses equation 8 to calculate conditional probabilities of ceiling and visibility.

2.3 Modeling Cumulative Distributions

Observations for a station's entire period of record (POR) are extracted from USAFETAC's database and binned by month, hour, and wind direction category (calm, 22.5° either side of N, NE, E, SE, S, SW, W, NW, and all). The Cumulative Distribution Function (CDF) is fit using the Weibull family of curves. Since ceiling and visibility distributions are not normal, fitting their CDF requires the Weibull's flexibility. The use of the Weibull curve for modeling ceiling and visibility is well documented (Somerville and Bean, 1979; Somerville and Bean , 1981; and Whiton and Berecek , 1982).

Using the transnormalization process, Equivalent Normal Deviates, or ENDs, are calculated for each month, hour, wind category. Once the variables are normalized, the Weibull and Reverse Weibull are used to fit the visibility and ceiling CDF, respectively. The equations are expressed as:

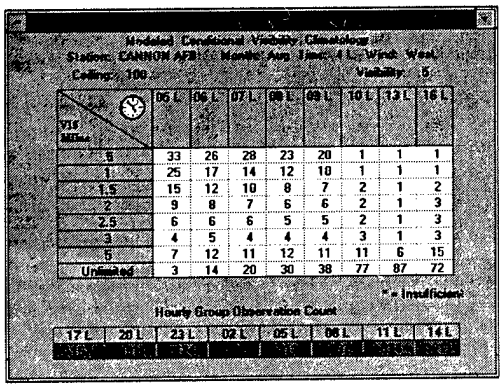
$$P = 1 - e^{(-\alpha X_t^{\beta})} \quad (9)$$

and

$$P = e^{(-\alpha X_t^{\beta})} \quad (10)$$

where α and β are the modeling coefficients, X_t is some threshold of ceiling or visibility, and P is the probability that an actual ceiling or visibility observation (X) will be less than X_t. The values of the empirical cumulative distribution are regressed on the Weibull and Reverse Weibull distribution function.

The modeling coefficients are used by the microcomputer program to calculate normalized probabilities which are inverse transnormalized to convert the END probability back to an actual probability. This process allows the user to generate conditional and unconditional climatological forecasts of ceiling, visibility, and joint ceiling and visibility. The user selects a wind direction category and in the case of conditional climatology, an initial value of ceiling and/or visibility. The program then displays the probability of ceiling and/or visibility at user specified thresholds and times out to 72 hours in either tabular or bar graph form, as shown in Figures 1 and 2.



Vis \ Ceil	05 L	06 L	07 L	08 L	09 L	10 L	13 L	16 L
1/2	33	26	28	23	20	1	1	1
1	25	17	14	12	10	1	1	1
1.5	15	12	10	8	7	2	1	2
2	9	8	7	6	6	2	1	3
2.5	6	6	6	5	5	2	1	3
3	4	5	4	4	4	3	1	3
5	7	12	11	12	11	11	6	15
Unlimited	3	14	20	30	38	77	87	72

Hourly Group Observation Count

17 L	20 L	23 L	02 L	05 L	08 L	11 L	14 L

Figure 1. MODCV tabular output

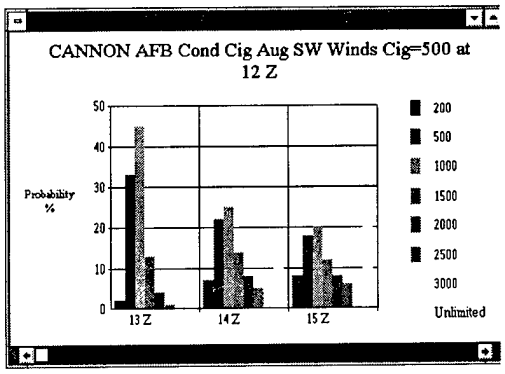


Figure 2. MODCV graphical output

3. MODEL VERIFICATION

Verification of MODCV was conducted for eight locations around the world in order to test the model under different climatological regimes. MODCV was tested against Wind Stratified Conditional Climatology (WSCC) tables which are produced by USAFETAC OL-A located in Ashville, NC. The goal was to provide a compact computer based product that was at least as good as the bulky WSCC tables.

3.1 Brier Skill (P) Score

The Brier Skill or "P" score (Brier, 1950) is a statisitcal technique used to measure the amount of skill in the probability forecast. The P-score equation is:

$$P = \frac{1}{2N}\left[\sum_{j=1}^{r}\sum_{i=1}^{r}(f_{ij} - E_{ij})\right] \qquad (11)$$

where r is the number of forecast categories, N is the number of days, f is the probability forecast of the event occurring in the category, and E takes the value of one or zero according to whether the ceiling or visibility occurs in that category. P ranges from zero for a perfect forecast to two for no skill. The number of forecast categories was determined from the WSCC tables for each of the eight stations.

Verification data was collected during the months of April and November of 1988. Because of the sheer bulk of the data, only the 3-hour and 24-hour forecasts were verified. For each day in April and November, MODCV and WSCC forecasts were compared to observed conditions and a P-score was calculated for each. The MODCV P-scores averaged over the month were consistently lower than the WSCC P-scores at both the 3-hour and 24-hour forecast times for both ceiling and visibility. Figures 1-3 show the average P-scores of all

nine stations combined for the months of April, November and for both months combined, respectively. Note that the scores are consistently lower (better) for the MODCV forecasts, especially at the 3 hour point. Table 1 lists the numeric P-scores for each of the nine stations averaged over the 30 days of April and November. Also included are the averages for all stations for April, November, and for both months combined.

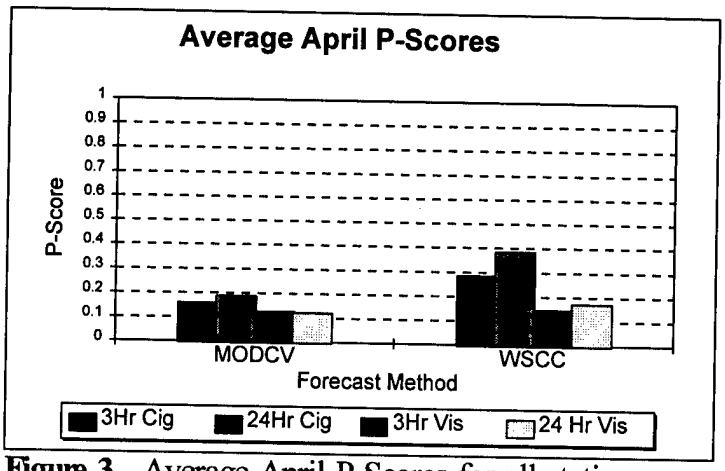


Figure 3. Average April P-Scores for all stations

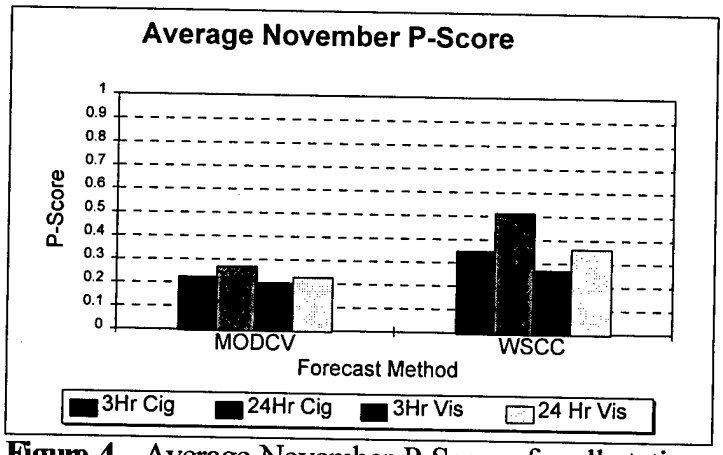


Figure 4. Average November P-Scores for all stations

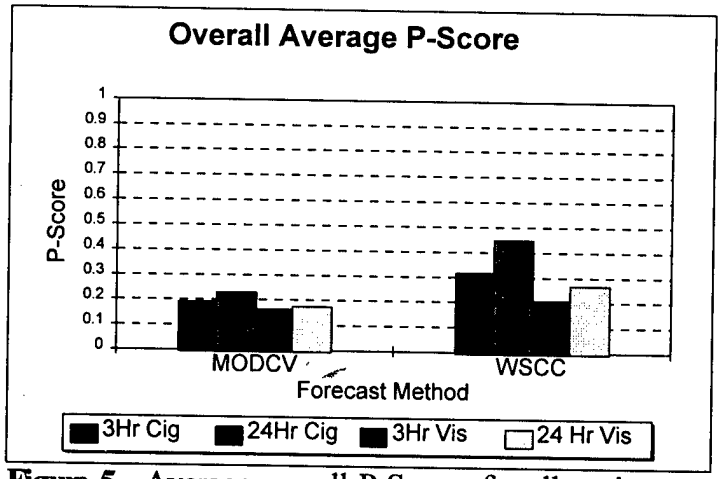


Figure 5. Average overall P-Scores for all stations

Table 1. P-Scores for 9 stations for April and November for MODCV and WSCC.

Base-Apr Base- Nov	MODCV Ceiling		MODCV Visibility		WSCC Ceiling		WSCC Visibility	
	3 Hr	24 Hr	3 Hr	24 Hr	3 Hr	24 Hr	3 Hr	24 Hr
Cannon	0.131	0.151	0.084	0.078	0.226	0.296	0.124	0.152
Cannon	0.379	0.331	0.267	0.25	0.403	0.608	0.34	0.515
Eglin	0.167	0.175	0.147	0.144	0.246	0.327	0.173	0.191
Eglin	0.156	0.19	0.148	0.163	0.24	0.348	0.127	0.177
Lajes	0.059	0.077	0.08	0.059	0.101	0.138	0.039	0.044
Lajes	0.233	0.308	0.238	0.278	0.372	0.585	0.379	0.459
McChord	0.135	0.173	0.065	0.072	0.315	0.469	0.106	0.126
McChord	0.183	0.253	0.129	0.153	0.401	0.608	0.274	0.312
Minot	0.234	0.246	0.165	0.168	0.41	0.448	0.139	0.146
Minot	0.197	0.261	0.205	0.261	0.328	0.484	0.23	0.357
Mildenhall	0.232	0.284	0.154	0.156	0.544	0.712	0.237	0.294
Mildenhall	0.314	0.409	0.32	0.375	0.583	0.796	0.51	0.68
Ramstein	0.206	0.297	0.187	0.187	0.269	0.555	0.293	0.379
Ramstein	0.198	0.279	0.259	0.304	0.227	0.484	0.251	0.37
Scott	0.02	0.034	0.049	0.044	0.015	0.024	0.022	0.022
Scott	0.146	0.209	0.183	0.257	0.24	0.402	0.368	0.553
Shaw	0.241	0.252	0.185	0.18	0.446	0.48	0.183	0.188
Shaw	0.183	0.193	0.095	0.083	0.273	0.324	0.033	0.03
Apr Ave	0.158	0.188	0.124	0.121	0.286	0.383	0.146	0.171
Nov Ave	0.221	0.27	0.205	0.236	0.341	0.515	0.279	0.384
Overall Ave	0.19	0.229	0.164	0.178	0.313	0.449	0.213	0.278

4. SUMMARY

MODCV was originally created to give forecasters an easy-to-use microcomputer program to make climatological data easier to use. Unfortunately, the fielded program lacked the wind stratification needed to provide useful probabilistic guidance. Wind stratification has been added and the results indicate that MODCV provides more accurate climatological forecasts than the WSCC tables. Also, the P-Scores calculated using the new version are smaller than those calculated using the original version (not shown). Since the conclusion at that time was that MODCV was practical for operational use, it can be concluded that the new version can be used operationally.

5. REFERENCES

Boehm, A. R., 1976, *Transnormalized Regression Probability*", AWS-TR-75-259, Air Weather Service, Scott AFB, IL

Brier, G. W., 1950, "Verification of Forecasts Expressed in Terms of Probability", *Mon Wea Rev*, 78: 1-3.

Gringerton, I. I., 1966: *A Stochasitc Model of the Frequency and Duration of Weather Events*, United States Air Force Cambridge Research Laboratories, Bedford, MA

Kroll, J. T., and H. A. Elkins, 1989, *The Modeled Ceiling and Visibility (MODCV) Program*, USAFETAC/TN-89/001, United States Air Force Environmental Technical Applications Center, Scott AFB IL 62225-5116.

Somerville, S. J. and P. N. Bean, 1979, *Stochastic Modeling of Climatic Probabilities*, AFGL-TR-79-0222, United States Air Force Geophysics Laboratory, Bedford, MA

Somerville, S. J. and P. N. Bean, 1981, *Some Models for Visibility for German Stations*, AFGL-TR-81-0144, United States Air Force Geophysics Laboratory, Bedford, MA

Whiton, R. C. and E. M. Berecek, 1982, *Basic Techniques in Environmental Simulation*, USAFETAC TN-82-004, Air Weather Service, Scott AFB, IL

A NEW PCFLOS TOOL

K.E. Eis
STC-METSAT
Fort Collins, CO 80521, U.S.A.

ABSTRACT

Probability of Cloud-Free-Line-of-Sight (PCFLOS) is a powerful tool used by all components of the DoD in weapons and sensor development. *STC*-METSAT has just completed the development of a medium-resolution (12 to 15 km) 3-dimensional satellite-derived database under DOE sponsorship that provides PCFLOS interrogation of unprecedented resolution in the Korean and Iraq areas of interest. The database and PCFLOS extraction software includes the 13 month period of record from April 1990 through April 1991. This package allows user-defined target and sensor altitudes and unlike any other PCFLOS analysis package, can provide azimuthally dependent results. Analysis of PCFLOS using this package helped confirm earlier investigations into the behavior of PCFLOS and its dependence not only on mean cloud cover, but also on cloud structure in the area of investigation. The study includes both temporal and spatial variance analysis of the new, satellite-based PCFLOS.

1. INTRODUCTION

Airborne sensors such as RAPTOR are effected by both cloud obscuration and clear-air IR wavelength attenuation. Previous methods of quantifying these degradations have used statistically-based Probability of Cloud-Free-Line-of-Sight (PCFLOS) algorithms that use little, or no, satellite data and are dominated by low-resolution surface databases. This DOE-sponsored study provides a 13-month database over the Iraqi and Korean areas and the appropriate extraction software to compute PCFLOS directly from satellite data for the period April 1990 to the end of April 1991. Temporal, spatial, and frequency analyses were generated from this database.

This 15-km resolution 3-hourly database can be improved to a 5-km resolution, 1-hour global analysis using the STC developed Climatological and Historical ANalysis of Clouds for Environmental Simulations (CHANCES) database (Reinke et al. 1993). This paper will

describe the elements of the tool and outline some of the results obtained from the analysis in regard to temporal and spatial variations, cloud structure, and azimuthal behavior of PCFLOS.

2. BACKGROUND

The method used to create a 3-dimensional cloud field was fully developed in a Phase I study (Eis 1993). A geosynchronous IR image is first interrogated for clouds. The IR radiance is then converted to a blackbody temperature, which is then converted to cloud top height by using an interpolated rawinsonde value computed using local rawinsonde stations analyzed with a Barnes algorithm.

The cloud/no cloud algorithm is a modification of the International Satellite Cloud Climatology Project (ISCCP) and High Resolution Satellite Cloud Climatologies (HRSCC) cloud detection algorithms. Only IR images were used for cloud detection. Infrared satellite imagery from GMS (Korea) and METEOSAT 3 and 4 (Iraq) was used for the time period from April 1990 through April 1991. The details of the cloud/no cloud algorithm are beyond the scope of this paper but are fully developed in the Raptor II report (Eis 1994). Figures 1 and 2 show the locations of the rawinsonde data used in the estimation of the vertical cloud portion of the data base.

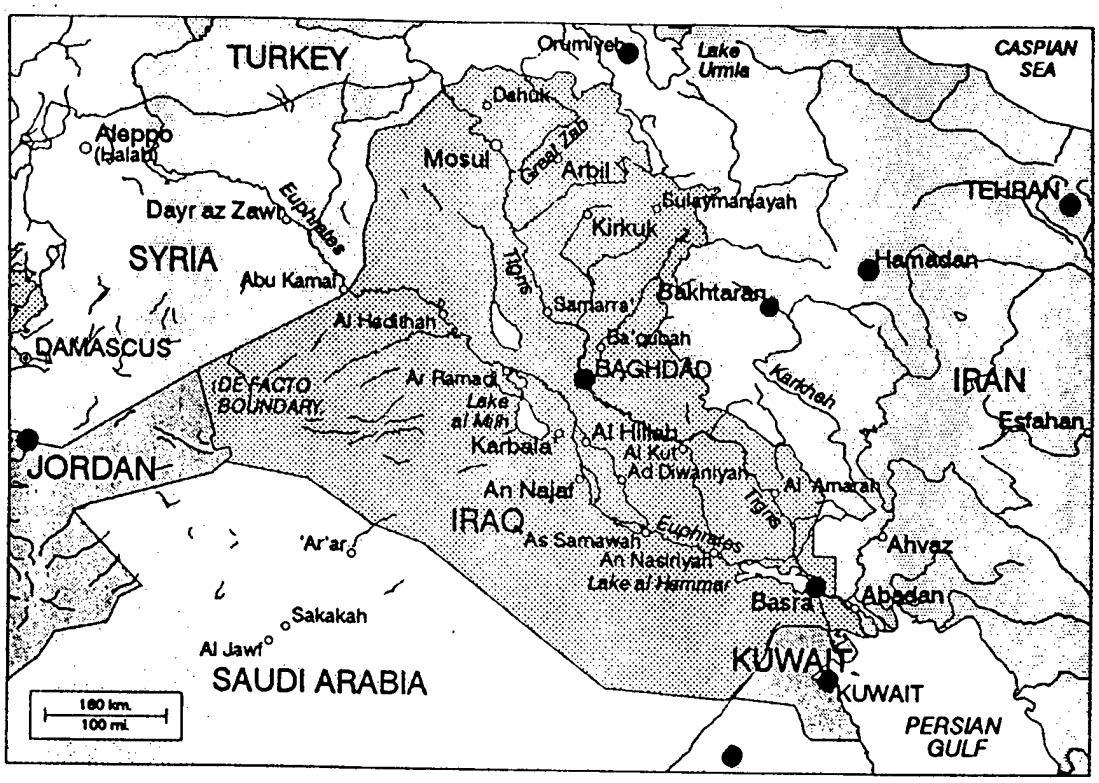


Figure 1. Iraq area of interest. Dots indicate upper air data locations.

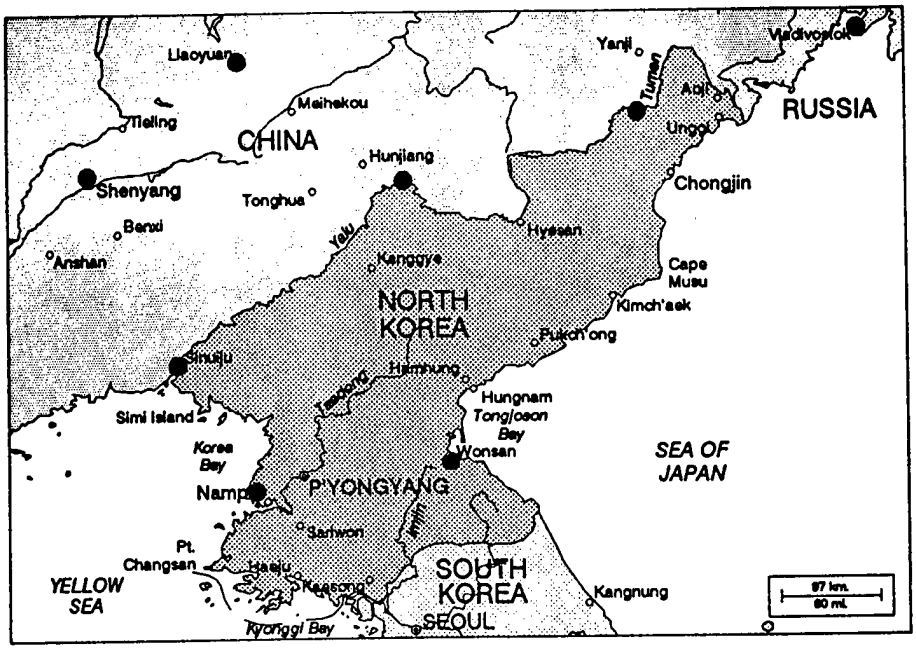


Figure 2a. Korean (North) area of interest. Dots indicate upper air data locations.

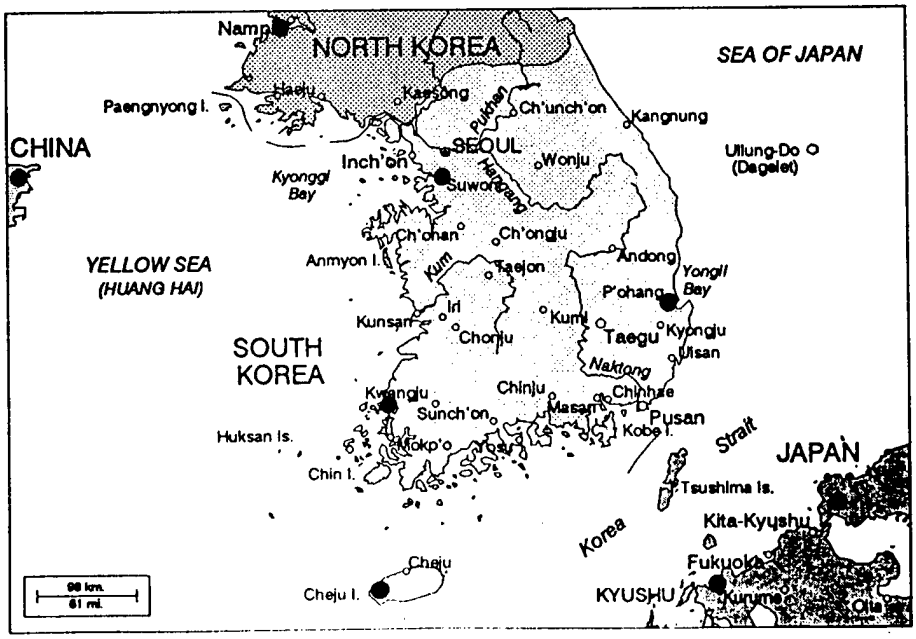


Figure 2b. Korean (South) area of interest. Dots indicate upper air data locations.

The analyzed height and temperature fields at the mandatory levels were merged with the temperature of the cloudy pixels to determine the cloud-top height. A linear interpolation between levels, or an extrapolation if the cloud was above the uppermost level, was used to find the height of the cloud top. Again, the details of the cloud top and base algorithms can be found in Eis (1994).

To determine the cloud base, a check was first made to see if the temperature minus the dew point at 850 and 700 mb was less than a specified threshold, in this case, 5 K was used for both Iraq and Korea. If the lower levels of the atmosphere were determined to be moist, the cloud base was placed at the LCL, on the assumption that the clouds were caused from moisture near the surface (e.g. a thunderstorm). If the cloud top was less than the LCL, the base was assigned a value of the top height minus 250 m. This condition could be brought about by a poor objective analysis, very low clouds with emittance of less than one, or a partly cloudy field of view of the satellite. The cloud base was never allowed to go below the LCL.

3. ERROR CONSIDERATIONS

There are several sources of error associated with the creation of the 3-dimensional database. The cloud detection algorithm was developed to match IR images with the eye's response, consequently, subvisual cirrus will not be detected. The cloud detection algorithm was tuned for each day. Cloud detection over cold land was manually edited for 146 of the 1259 images used in this study (106 for the Korean sector and 40 for Iraqi sector).

Cloud height values are the database parameter with the largest possible error. In both the Korean and Iraqi cases the distances between sampling points is well over 500 km. The result is that there is significant temporal and spatial spreading of the data to each grid point. If an air mass discontinuity between two adjacent stations is sensed, we have no way of determining where along the station-to-station line the front lies.

The cloud base and top values were analyzed statistically for the Iraq data to show some of the bulk behavior of the cloud/no cloud and top and bottom assignment algorithms. Figure 3 shows the normalized histogram of cloud top temperatures, as measured with the METEOSAT 3 and 4 satellites for the Iraq area of interest for all 13 months of 0000 UTC interrogated pixels.

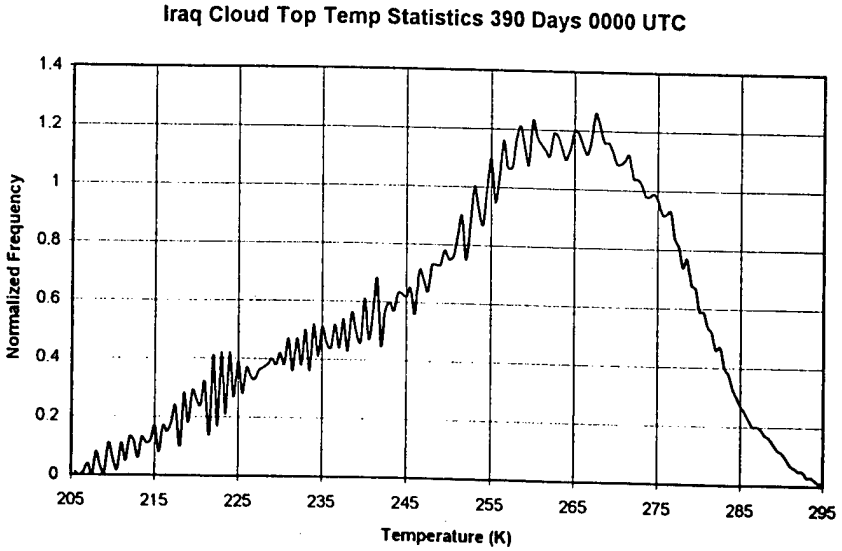


Figure 3. Normalized histogram of cloud top temperatures for Iraq at 0000 UTC.

Note the assigned temperatures behave quite well and appear to fall into a Chi-squared distribution. This is logical since most continuous-bounded meteorological parameters (i.e., humidity and winds are bounded by zero and cloud heights by the earth's surface) exhibit this type of statistical behavior. The "noise" in the trace was expected. It represents local effects caused by terrain, water bodies, etc. Figure 4 shows the normalized distribution of computed cloud top heights (in meters) for the same Iraq sector data set. You would expect these distributions (temperature and height) to be very similar since height is directly derived from temperature. The only departure from the Chi-squared distribution are the spikes at 100, 2800, 3250, 6000, 7700, 9800, and 16400 meters, due to the dominance of mandatory levels in the rawinsonde data.

Figure 5 is the distribution of cloud base assignments. Again, the spikes show how the rawinsonde's mandatory levels effect the cloud base values. Cloud base height clustering is seen in ceiling statistics, but there is clearly more error associated with base height assignment than any other part of this analysis.

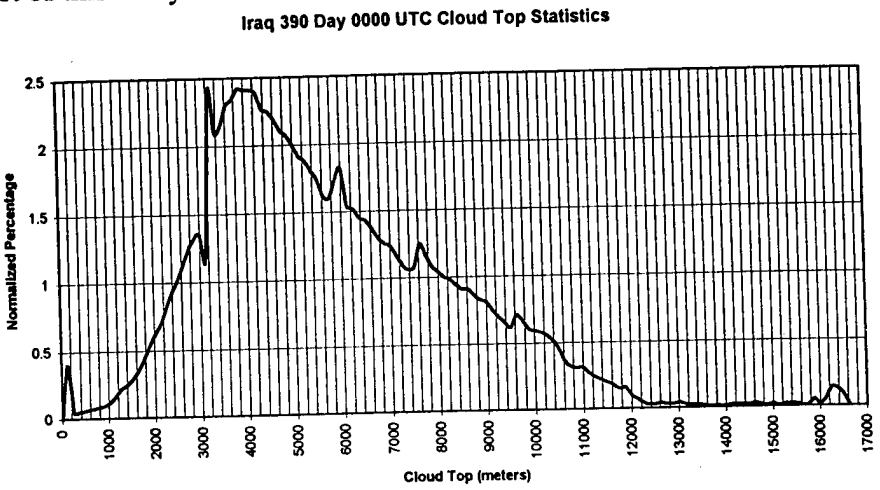


Figure 4. Normalized distribution of computed cloud top heights in meters at 0000 UTC.

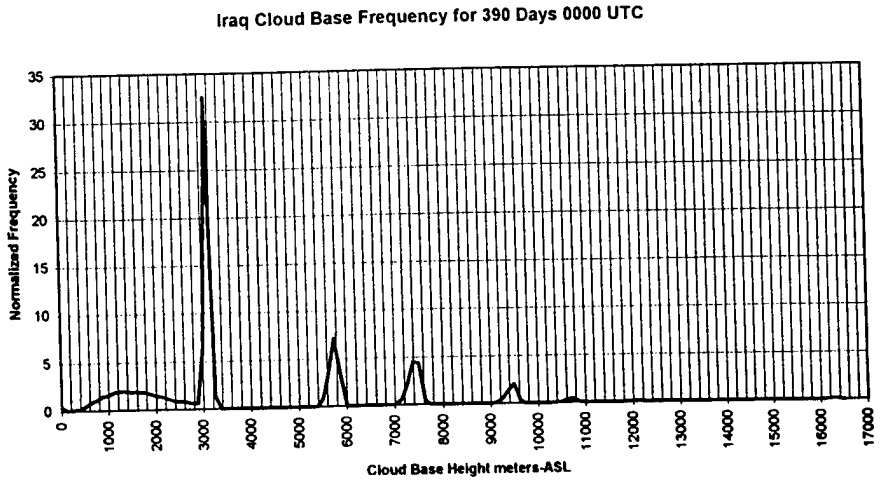


Figure 5. Distribution of cloud base assignments.

4. PCFLOS TOOL DESCRIPTION

Eis (1994) describes the input variables and output format in detail. Basically, the user is allowed to specify the location and elevation of both the target and sensor. Other specifications allow the user to integrate over azimuth, time, or date. Range is typically the independent variable. The algorithm interrogates each path length for a clear/obscured path and averages over the user defined parameters range to produce a PCFLOS value. In addition to PCFLOS, the algorithm also computes the mean cloud cover in the circle whose radius is defined by the maximum range set by the user.

5. ANALYSIS

Several analyses were performed using the new PCFLOS tool. These included: High resolution composite climatologies (not discussed in this paper, see Reinke (1993)), temporal correlation analysis, cloud structure effects, spatial analysis, and azimuthal variance.

5.1 Temporal Correlation Analysis

A 3-hourly database (0000, 0300, 0600, 0900, 1200, 1500, 1800, and 2100 UTC) was created using the November 1990 imagery for both Iraq and Korea. In order to show the temporal behavior we ran each hour available for a selected day in November 1990 for four points in the Iraqi and Korean areas. In all cases we used the following parameters: Sensor height = 18 km, azimuth values used the full 360 degrees, and target altitudes were 0, 2.5, 5, 7.5, 10, 12.5, and 15 km for the low resolution cases and 0, .5, 1, 1.5, 2, 2.5, and 3 km for the high resolution cases. The purpose of this analysis was to explore what changes occur in PCFLOS over short (3 hour) time spans. The following example was for western Iraq where many of the SCUD TELs were located during Desert Storm. As you will see, there were major differences at the 3-hourly intervals.

PCFLOS went from a cloud-free unobstructed view at 100 km to 20 percent PCFLOS at 25 km just 3 hours later (midnight to 0300 UTC). The rapid variation in PCFLOS and mean cloud cover indicate a smoothed temporal climatology will contain large errors. Most examples studied with the limited data set confirm that PCFLOS values vary rapidly and, in fact, vary faster than the temporal variance in mean cloud cover.

5.2 Cloud Structures Interrogated Over Korea

We interrogated a flight path (sensor at 18 km) over Korea along the 38th parallel. The mean cloud cover for the January days (sensor at 18 km, target at the surface) is depicted in Figure 6. Again, the rapid variation between 0 and 100 values indicates frontal-produced clouds. The spatial variance of the PCFLOS is plotted on Figure 7. Note that for a full 360 degree azimuthal integration and with a target-sensor separation of 100 km, the variance of the daily PCFLOS is less than the mean cloud cover. This is in contrast to the temporal variance study (Figure 8).

Lastly, Figure 9 depicts the mean cloud cover probability versus PCFLOS scatter diagram. It shows a markedly larger scatter on the clear cloud end of the scatter diagram than does the Iraq case. This is evidence of cloud structure impacting PCFLOS more than the variation in mean cloud cover.

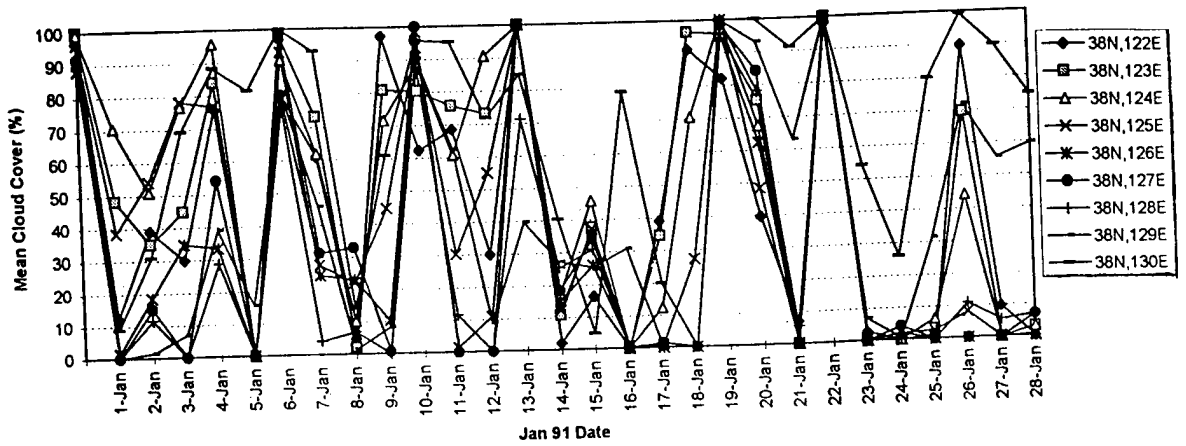


Figure 6. Mean Cloud Cover over Korea, January 1991.

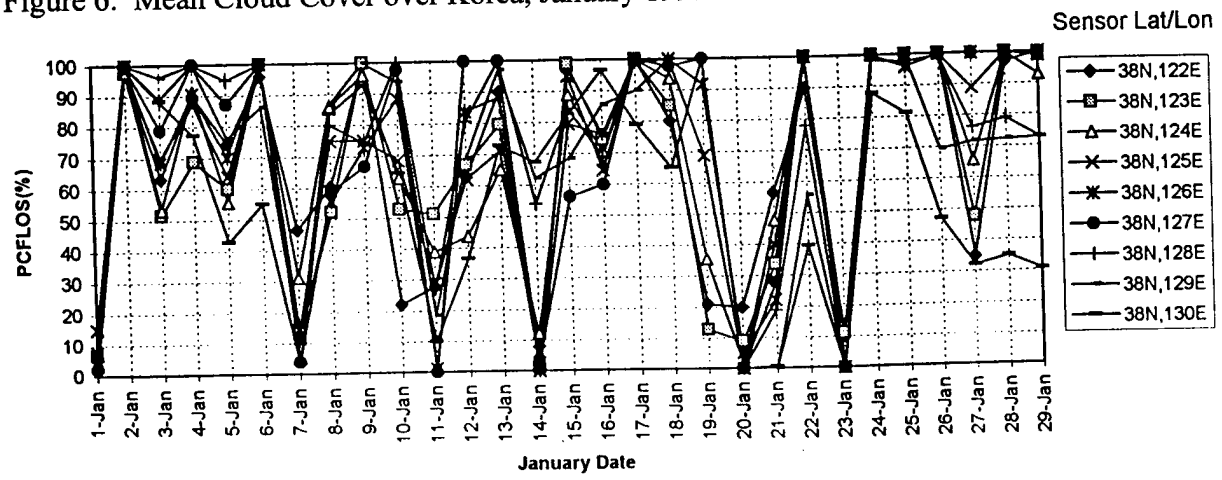


Figure 7. Korea Spatial Variance, January 1991.

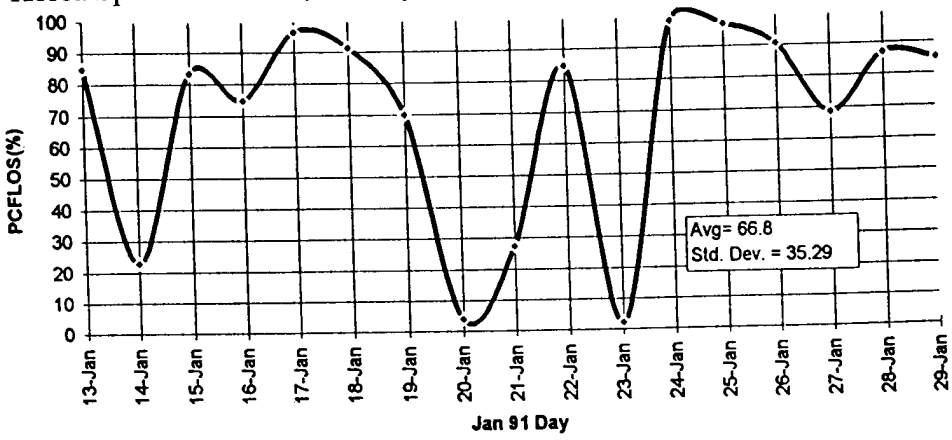


Figure 8. Korea Temporal Variance (Daily).

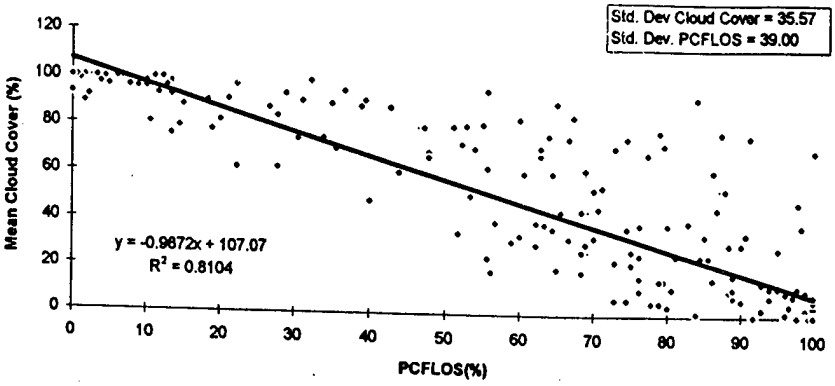


Figure 9. Korea PCFLOS versus Mean Cloud Freeness.

5.3 Azimuthally Dependent Analysis

Up to now, all of the analyses have used an azimuthally independent method where all PCFLOS values are derived using target and sensor range and heights. The delivered database can also be set for an analysis of azimuths integrated over sectors of less than 360°.

In Figure 10, the 0 to 25 km range shows several periods of totally clear cloud cover where all four quadrants show 100 percent PCFLOS conditions (3-8, 10-12, 15, 16, 19, 20, 22, 23, and 28) for January. On the 2, 3, 9, 18, 24, and 25 of January, the conditions were overcast in all directions causing CFLOS values to be 0. All the other dates show wide variances in CFLOS. For instance, if Baghdad were to be attacked on January 1, and if the pilot were to approach from the northwest, a ground target would be totally clear at 25 km, from the southeast the CFLOS shows a totally obscured condition.

Figure 11 shows similar behavior. A clearing trend is evident from January 24-28. Note that on January 1, a northwest approach would still have a CFLOS value of over 90 percent.

6. SUMMARY

The new PCFLOS tool gives an unprecedented window into the behavior of clouds, PCFLOS, and cloud structure as they relate to military operations. In the age of stealth aircraft and smart munitions, knowledge of the detailed behavior of clouds at a specific target (azimuthally variable) could be used to mask the delivery system's IR signature. A mission planner could select an attack profile using day, time, and direction information derived from an advanced version of this tool. The database and extraction software are on 8mm media and are written in UNIX based ANSI standard C.

The utility of this tool is even higher in regions of the world with strong terrain-anchored clouds such as coast lines (navy and amphibious operations) and mountains. The fact that there was such a strong azimuthal dependence in western Iraq indicates the utility extends to non-mountainous areas also.

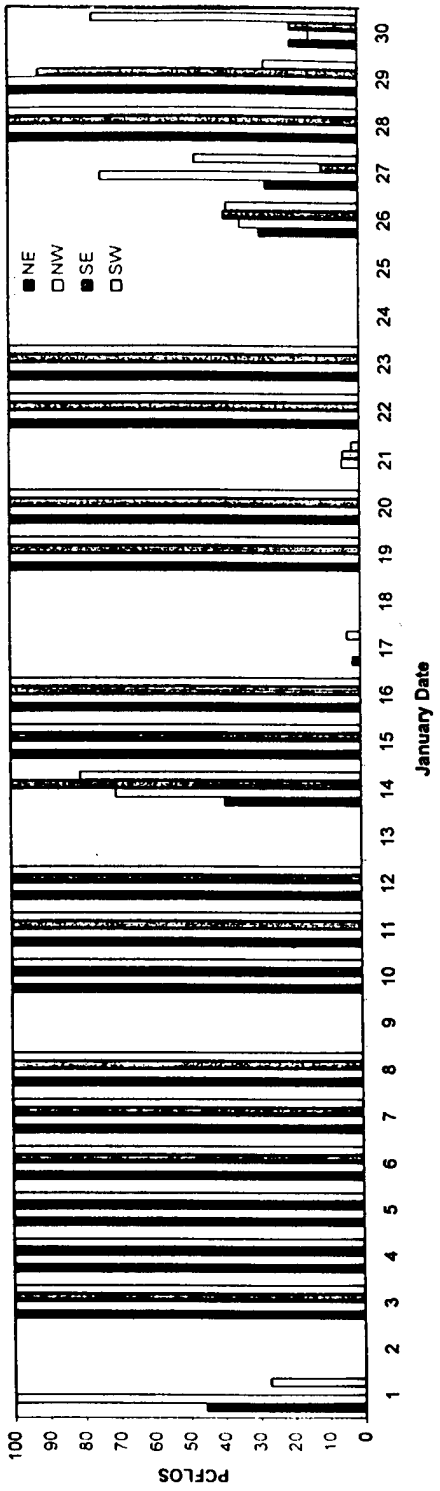


Figure 10. 25 km PCFLOS Baghdad, Iraq, January 1991, 0000UTC

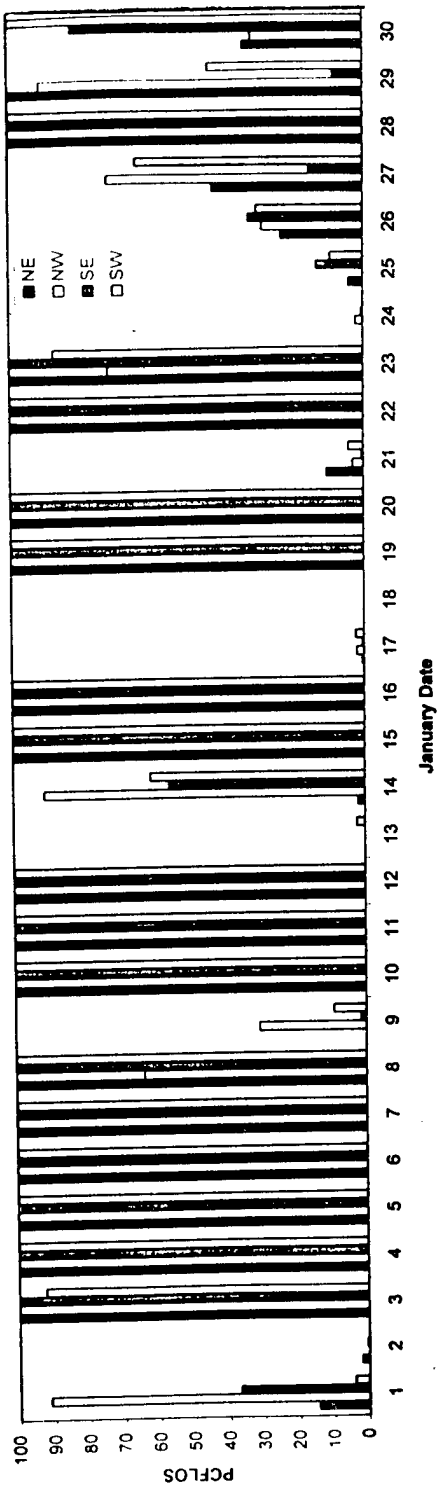


Figure 11. 50 km PCFLOS Baghdad, Iraq, January 1991, 0000UTC

ACKNOWLEDGMENTS

This paper summarizes the work performed under University of California, Lawrence Livermore National Laboratory Subcontract No. B218795. The author wishes to thank Dr. Thomas H. Vonder Haar and Mr. Donald. L. Reinke of *STC*-METSAT for their scientific expertise and assistance in analyzing the data. The valuable support and cooperation provided by Mr. Dennis Hakala, Technical Monitor, Lawrence Livermore National Laboratory, during the period of this task are gratefully acknowledged. The authors would also like to thank John M. Forsythe for developing the database and Mr. Mark Ringerud for developing the PCFLOS algorithm and extraction code. If the reader would like interaction about the database and extraction code, please contact the author with a copy of your request to Mr. Dennis Hakala, University of California, Lawrence Livermore National Laboratory, P.O. Box 808, Livermore, CA 94551.

REFERENCES

Eis, K.E., T.H. Vonder Haar, J.M. Forsythe and D.L. Reinke, 1993: "Cloud Free Line of Sight Model Differences". *Proceedings of the 1993 Battlefield Atmospherics Conference*, U.S. Army Research Lab, White Sands Missile Range, New Mexico 88002-5501, pp. 863-870.

Raptor II - Climatology Studies in Relation to Cloud Type Occurrences, Final Report to the University of California, Lawrence Livermore National Laboratory, P.O. Box 808, Livermore, CA 94551, by K.E. Eis, March 1994.

Reinke, D.L., T.H. Vonder Haar, K.E. Eis, J.M. Forsythe, and D.N. Allen, 1993: "Climatological and Historical ANalysis of Clouds for Environmental Simulations (CHANCES)". *Proceedings of the 1993 Battlefield Atmospherics Conference*, U.S. Army Research Lab, White Sands Missile Range, New Mexico 88002-5501, pp. 863-870.

THE INFLUENCE OF SCATTERING VOLUME ON ACOUSTIC SCATTERING BY ATMOSPHERIC TURBULENCE

Harry J. Auvermann
Army Research Laboratory, Battlefield Environment Directorate
White Sands Missile Range, New Mexico

George H. Goedecke and Michael DeAntonio
Dept. of Physics, New Mexico State University
Las Cruces, New Mexico

ABSTRACT

From a complete set of fluid equations, a complete set of coupled linear differential equations for the acoustic pressure, temperature, mass density, and velocity in the presence of stationary turbulence may be derived. To first order in the turbulent temperature variation and flow velocity, these coupled acoustic equations yield an acoustic wave equation given in the literature. Further reduction of this wave equation results in a second equation given in the literature which is good for turbulent length scales a much greater than the acoustic wavelength λ. The length scale a_s of the scattering volume is found to be just as important as a and λ in predicting the general behavior of acoustic scattering by turbulence. In particular, if $a << a_s$, then the first Born temperature and velocity scattering amplitudes for any ratio a/λ are the usual ones predicted by the first equation, and both the forward and backward velocity scattering are essentially zero for solenoidal turbulent flow velocity. The latter is not true if $a > a_s$. If $a \geq a_s >> \lambda$, then the first Born scattering amplitudes are those predicted by the second equation. If $\lambda \geq a \geq a_s$, other forms result for the scattering amplitudes. Implications of these findings for predicting results of acoustical scattering experiments where the scattering volume is often ill defined are discussed.

1. INTRODUCTION

This is the third paper given at Battlefield Atmospherics Conferences that deals with acoustic scattering by atmospheric turbulence. In the first paper (Auvermann, Goedecke, DeAntonio 1992), experimental evidence was presented showing that atmospheric turbulence near the ground was neither homogeneous nor isotropic, two conditions

required for the usual statistical model of turbulence to be valid. An alternate model consisting of a collection of isolated vortices of different sizes was proposed. This model was termed a structural model previously. The more descriptive name of Turbule Ensemble Model (TEM) will now be adopted. A turbule is an isolated inhomogeneity of either fluid temperature or fluid velocity. The first paper (Auvermann, Goedecke, DeAntonio 1992) presented a general formulation of the method by which acoustic signal levels in shadow zones may be estimated using TEM. The second paper (Auvermann, Goedecke, DeAntonio 1993) showed how TEM may be used to explain theoretically the extreme variability of acoustic shadow zone signals that has been documented experimentally. In TEM, the scattering pattern of the various individual turbules is assumed known. The analysis proceeds by assuming a distribution function for the sizes, and then locating the turbules of each size randomly within the atmospheric region of interest. The shadow zone signal is then the summation of the contributions from each turbule. To carry out the summation in the first paper (Auvermann, Goedecke, DeAntonio 1992), a uniform concentration of turbules (number of turbules per unit volume) was assumed accompanied by a reasonable estimation of the volume from which the detector could receive signals. The summation in the second paper (Auvermann, Goedecke, DeAntonio 1993) was carried out directly because a relatively small number of turbules was postulated, the position and size of each being chosen randomly within appropriate limits.

In this paper, the problem of determining the volume from which significant scattering can occur is addressed in a more rigorous manner. Acoustical signals of interest to the Army are in general low frequency. The import of this is that the wavelengths of interest are large compared to the dimensions of either source or detector. Therefore, both source and detector are nearly omni-directional and thus cannot serve to define a scattering volume. This is a complication not usually experienced in optical scattering scenarios. For example, optical scattering by atmospheric aerosol is usually modeled with a narrow beam from a laser source and a narrow field-of-view detector system, the overlap or union of the two defining a small scattering volume. This geometric construction is the usual way scattering volume is defined. In this paper (except in section 4), scattering volume will denote the volume from which significant scattering can occur. An additional simplification that can be taken advantage of in aerosol scattering is the fact that the largest aerosol particle dimension is small compared to the dimension of the scattering volume. Even though acoustic wavelengths are large, turbule sizes can be larger, and may approach the scattering volume dimension. In section 2, the scattering pattern of individual turbules is used to define a scattering volume as a function of turbule size. Then, in section 3, scattering cross-section modified by number concentration is used to determine the relative contributions from the various size classes. Section 4 contains general results that may be applied to determine if surface integrals from scattering theory may be ignored, as is usually done in optics. Conclusions that may be drawn from this work are discussed in section 5.

The symbols for the some of the variables, parameters and mathematical operations are summarized in the following list. Others are defined in the text. Bold quantities in the

list (for example **r**) are three-vectors.

NOTATION

a	= turbule characteristic size, m
c_∞	= asymptotic acoustic wave speed = 344 $m \cdot s^{-1}$
∂_i	$\equiv \partial/\partial x_i$; $x_1 = x$; $x_2 = y$; $x_3 = z$
$\exp(-j\omega t)$	= time dependence of acoustic wave
f	= acoustic wave frequency = 500 hz
$\mathbf{k}$	= propagation vector, m^{-1}
k	= magnitude of $\mathbf{k} = \omega/c_\infty$
λ	= wavelength, m
$\mathbf{r}$	= position vector, m
r	= magnitude of $\mathbf{r}$
$\mathbf{r}_1$	= integration variable position vector
t	= time variable, s
$\tau(\mathbf{r})$	= turbulence field temperature difference ratio
$\mathbf{v}_0(\mathbf{r})$	= turbulent flow velocity in the absence of the acoustic wave
v_{0i}	= i-th component of $\mathbf{v}_0$
ζ	= scattering volume limit angle for velocity turbule ensemble
ξ	= velocity turbule ensemble relative scattering cross-section
χ	= size parameter = ka
ψ	= scattering angle between $\mathbf{k}$ and $\mathbf{r}$
ω	= wave angular frequency = $2\pi f$

2. SCATTERING PATTERN INFLUENCE ON SCATTERING VOLUME

The theory of acoustical scattering from turbules is too lengthy to be covered in this paper. It is covered elsewhere (Goedecke, DeAntonio, Auvermann 1994a). The following is a brief synopsis of how scattering patterns are determined theoretically. Beginning with a complete set of fluid equations in density, pressure, temperature, and velocity, each variable is assumed to be made up of a time independent part representing the inhomogeneous medium plus a small time dependent part representing the acoustic wave. Expressions representing the above are substituted in the fluid equations and terms second order or higher in the ratios (v_0/c_∞, τ) are discarded. Assuming harmonic time dependence, the resulting wave equation is

$$(\nabla^2 + k^2)\eta(\vec{r}) = \partial_i \tau \partial_i \eta(\vec{r}) + 2j\omega^{-1}\partial_i(v_{0l}\partial_l\partial_i)\eta(\vec{r}) = -4\pi S(\vec{r})\eta(\vec{r}) \tag{1}$$

where the summation convention is used for repeated subscripts and

$$S(\vec{r}) = S_T(\vec{r}) + S_v(\vec{r}) = -(4\pi)^{-1}\partial_i(\tau\partial_i) - (j/2\pi\omega)\partial_i(v_{0l}\partial_l\partial_i). \tag{2}$$

$[S_T(\vec{r}), S_v(\vec{r})]$ define the scattering operators for (temperature, velocity) inhomogeneities respectively. $\eta(\mathbf{r})$ is the acoustic wave field quantity, the ratio of the acoustic pressure to the total fluid pressure.

The Green's function solution for an incident plane wave is written down, and a Born approximation is made in the scattering integral. The Born approximation involves replacing the field in the scattering integral by the incident field. The result is where

$$f_B(\hat{f}) = \int d^3r_1 \exp(-jk\hat{f}\cdot\vec{r}_1) S(\vec{r}_1) \exp(j\vec{k}\cdot\vec{r}_1) \tag{3}$$

f_B is called the scattering amplitude. Equation (3) has been used (Goedecke, DeAntonio, Auvermann 1994a) to derive the scattering cross-section for temperature and velocity turbules. The scattering cross-section is equal to the scattering amplitude multiplied by its complex conjugate, and has units of length squared. Only velocity turbules will be considered further in this paper.

It has been shown (Goedecke, DeAntonio, Auvermann 1994b) that an isotropic ensemble of turbules having a given scale length a but arbitrary velocity morphology except for $\nabla\cdot\vec{v}_0 = 0$ can be replaced by an ensemble with velocity $\vec{v}_0$ given by $\vec{v}_0 = \vec{\Omega}\times\vec{r}\,f(r)$, where f(r) is a function of the distance r from turbule "center", and $\vec{\Omega}$ is a randomly oriented angular velocity. A Gaussian form of f(r) has proved convenient (Goedecke 1992), so that

$$\vec{v}_0(\vec{r}) = \vec{\Omega}\times\vec{r}\exp(-r^2/a^2) \tag{4}$$

The scattering cross-section obtained from the theory outlined above was given in the report (Goedecke 1992). To simplify the presentation in this paper, the cross-section averaged over orientation angles will be used. This cross-section is (Goedecke 1992)

$$\sigma_v(\vec{k},\hat{r}) = \left(\frac{\pi}{3}\right)\left(\frac{\Omega a\chi^4}{4kc_\infty}\right)^2 [\sin(\psi)\cos(\psi)]^2\exp\{-\chi^2[1-\cos(\psi)]\} \tag{5}$$

Two normalized expressions are defined in eq. (6) below for the purpose of illustration of

$$\begin{aligned}\sigma_{vN} &= 4[\sin(\psi)\cos(\psi)]^2\exp\{-\chi^2[1-\cos(\psi)]\}\\ \sigma'_{vN} &= 4\left(\frac{\chi^4}{8^4}\right)^2[\sin(\psi)\cos(\psi)]^2\exp\{-\chi^2[1-\cos(\psi)]\}\end{aligned} \tag{6}$$

the behavior of eq. (5). The first contains all of the angular dependence and the second includes the multiplicative size parameter dependence. These two functions are plotted in

the next figures to show the nature of the velocity cross section in the (χ, ψ) domain. Figure 1 shows the angle dependent part, the axis label "Sigma" being σ_{vN}. Hereafter, the axis label "Chi" is ξ and the axis label "Psi" is ψ. Figure 2 shows the influence of the size parameter on the cross-section, the axis label "Sigma" being σ'_{vN}.

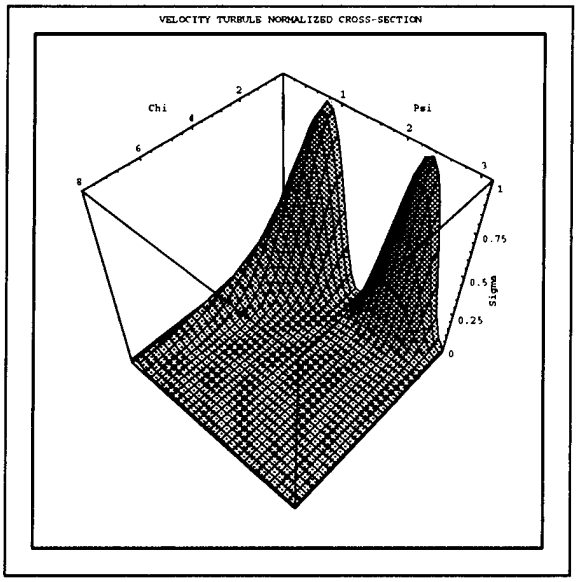


Figure 1. Normalized velocity turbule cross-section (angle part only)

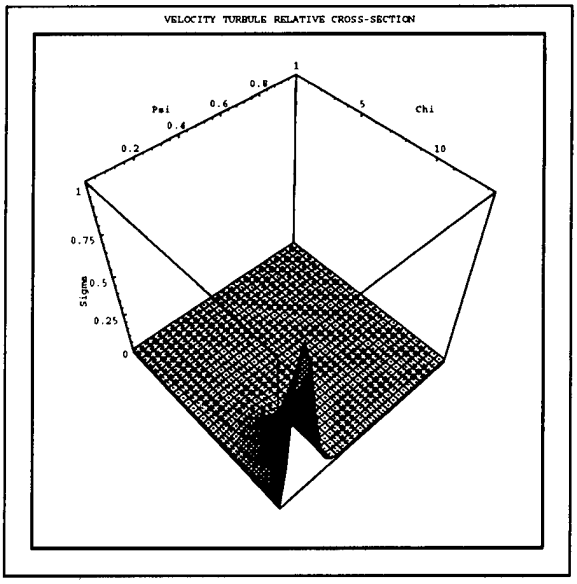


Figure 2. Velocity turbule scattering cross-section

The range of the independent variables χ and ψ were chosen in figure 2 to illustrate interesting features of the function σ'_{vN}. When χ is 13.4 and ψ is 0.1, σ'_{vN} peaks at very nearly unity. For ψ not near zero, the exponential drives σ'_{vN} to zero. As χ increases beyond the values in the figure, the peak of σ'_{vN} continues to increase. However, the width of the peak decreases and the value of ψ at the peak decreases. These curves for the cross-section are not the entire story because other factors influence the scattered signal at a detector. Consideration of these other factors is undertaken in the next section.

3. NUMBER CONCENTRATION INFLUENCE ON SCATTERING VOLUME

In the previous section, the dependence of the cross-section upon size parameter was shown to emphasize the importance of large turbules which have narrow scattering patterns. To do an incoherent summation for the signal scattered from an ensemble of turbules, the first expedient to employ is to simply add the effects of the many by multiplying by a number concentration. Since the scattering volume as a function of turbule size is the desired quantity in this paper, the number concentration as a function of size is necessary. An estimate of this has been made (Goedecke, DeAntonio, Auvermann 1994c). Furthermore, an estimate of the characteristic velocities of the turbules is necessary. The following power law scaling functions are first assumed:

$$\frac{N_\alpha}{N_1} = \left(\frac{a_\alpha}{a_1}\right)^{-\beta}, \qquad \frac{v_\alpha}{v_1} = \left(\frac{a_\alpha}{a_1}\right)^{\nu} \qquad v_\alpha = \Omega_\alpha a_\alpha \tag{7}$$

The meaning of eq. (7) is as follows. The largest turbules are identified by the subscript 1. The largest turbules have the concentration N_1. Their characteristic size is a_1. The largest velocity turbules have characteristic velocities v_1. Other sized turbules are identified by the index α. The exponents (β, ν) are chosen so that a homogeneous isotropic ensemble of turbules matches the Kolmogorov spectrum. The results are (Goedecke, DeAntonio, Auvermann 1994c) $\beta = 3$, $\nu = 1/3$. An interesting feature of this result is the concentration exponent being 3. This means that the packing fraction is the same for all size classes. The velocity scaling exponent is 1/3 as may be derived from a simple energy cascade calculation.

It is now possible to write the size parameter dependence of the cross-section for each size of turbules. Multiplying eq. (5) by N_α and using eq. (7) yields for the cross-section per unit volume for turbule size a_α and size parameter χ_α

$$\sigma_v(\vec{k},\hat{r}) = \pi a_1^2 \left(\frac{v_1^2 N_1}{48 c_\infty^2}\right) (k a_1)^{1/3} \chi_\alpha{}^{17/3} [\sin(\psi)\cos(\psi)]^2 \exp\{-\chi_\alpha{}^2[1 - \cos(\psi)]\} \tag{8}$$

The size parameter subscript will be dropped hereafter. The largest turbule size has been assumed to be 10 m, which is appropriate for a velocity turbule centered ten meters above the ground. The size parameter for this size turbule is 91.325. A velocity turbule is produced by wind shear with the wind velocity zero at ground level. Further assuming that the velocity ratio (v_1/c_∞) is 0.01, this size turbule would have a characteristic velocity of 3.44 $m \cdot s^{-1}$. This velocity would be produced by a wind gradient with this velocity at turbule center at 10 m height and twice this velocity at turbule upper edge at 20 m height. The scenario including the ground is more complex than is possible to treat in this paper. Rather, the assumption will be made that both source and detector are in free space and that the atmospheric turbulence is homogeneous and isotropic with characteristics of that at 10 m height. Considering the line joining source and detector a reference line from which to measure scattering angles and that the source is a long distance away, the scattering angle is the offset angle from the detector to a differential scattering volume. The total signal received by the detector will be a volume integral of the differential scattering volume times the expression in eq. (8). A further simplification will be taken in that no further specification of scenario parameters will be given. Thus, no range dependent effects will be considered. The volume integration will be confined to a shell around the detector of radius R_s and thickness ΔR_s. Figure 3 depicts this geometry on a plane section through the scattering volume under consideration. The scattering angle is ψ and the view angle is ψ'. These two angles are equal for this choice of source wave incident direction. The differential scattering volume will then be the ring around the axis

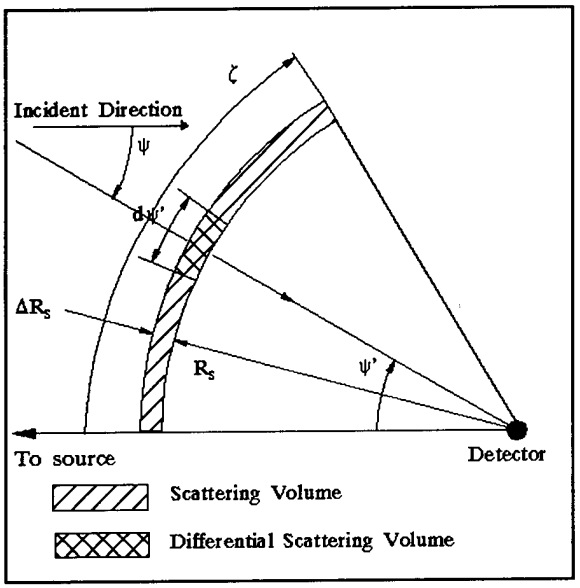


Figure 3. Scattering volume geometry

whose cross-section is shown in the figure and is $[2\pi\ R_s^2\ \Delta R_s\ \sin(\psi')\ d\psi']$. Equation (9) below derived from eq. (8) gives the specific mathematical form for the velocity turbule ensemble scattering cross-section.

$$\xi_v(\chi,\zeta) = \left(\frac{\pi^2 a_1^2 v_1^2 (k a_1)^{1/3} R_s^2 \Delta R_s N_1}{24 c_\infty^2} \right) \chi^{17/3} \int_0^\zeta d\psi' \sin^3(\psi') \cos^2(\psi') \exp\{-\chi^2[1 - \cos(\psi')]\} \quad (9)$$

The expression involving the size parameter χ and the scattering volume limit angle ζ in eq. (8) will be plotted in figure 4 for the case of $\zeta = \pi$. This is the case in which the cross-section for an entire spherical shell has been determined and which contains the maximum of the expression. The maximum occurs at $\chi = 91.325$ and is 3701.82. That which has been plotted in figure 4 is the ratio of the scattering cross-section to this value, so the maximum in figure 4 is unity. The curves for which the relative scattering cross-section is 0.01 and 0.95 are plotted in figure 5. A few of the calculated points are listed below:

$\xi_{v;rel}(88.5592,\pi)$	$= 0.95$	$\xi_{v;rel}(91.3250,0.033716)$	$= 0.95$
$\xi_{v;rel}(60.2799,\pi)$	$= 0.50$	$\xi_{v;rel}(91.3250,0.020059)$	$= 0.50$
$\xi_{v;rel}(6.2246,\pi)$	$= 0.01$	$\xi_{v;rel}(91.3250,0.005969)$	$= 0.01$

These curves are interpreted as an aid to forming a turbule distribution as follows. As an example limit angle, take 0.05 radian on figure 5 at the largest size parameter. This is larger than the size for the 0.95 contour. Extend a cone of this central angle out to 200 m and it will contain an entire 10 m radius turbule. Even if turbules were placed in a hexagonal close-pack configuration, the six turbules in the next circle can at most contribute 0.05 to the total scattering. Thus, our distribution need contain only one turbule of the largest size, or at the most seven. Assume that the shell thickness ΔR_s is 20.0 m, large enough to accommodate a collection of the largest turbules. At the other end of the distribution, consider those whose size parameter is 6.2246. The radius of these would be 0.682 m. Some 5,047,000 of these could be packed into the entire spherical shell at a range of 200 m. However, this entire ensemble would scatter no more than 0.01 times that scattered by the single tubule of the largest size. Consider now turbules with size parameter 88.5592 or radius 9.697 m. The complete shell would need to be filled with turbules of this size to scatter 0.95 times the scatter of the largest turbule. The number of these would be in the neighborhood of 1,755. For turbules of size

parameter 60.2799 or radius 6.600 m, the number in the shell would be 5,566. These

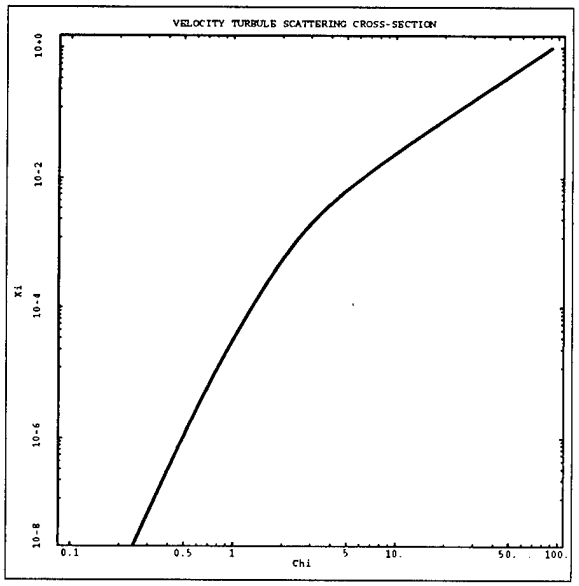


Figure 4. Relative velocity scattering cross-section

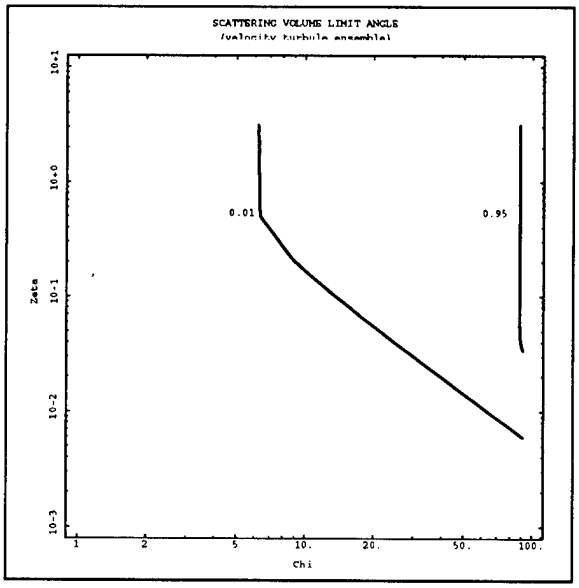


Figure 5. Scattering volume limit angles for velocity

would contribute only 0.50 times the scatter of the largest turbule. Although integration with respect to size parameter has not been attempted, and therefore it cannot be said definitely, it does seem likely that the scatter from turbules less than 0.682 m radius will total a great deal less than 0.01 times the scatter from those of larger radius. This means that an upper bound has been established above on the number of turbules that need to be placed in a representative distribution for the scenario considered. It is clear that the larger turbules dominate the scattering to be considered.

4. APPLICABILITY OF STANDARD SCATTERING THEORY

Standard scattering theory for scattering from a single localized scatterer involves a plane wave incident on the scatterer and a Green's function solution of the wave equation. The quantities obtained are the scattering amplitude and the scattering cross-section in the far field of the scatterer. In the analysis of the previous section, standard theory results were used for the scattering from individual turbules, in the Born approximation. The summation of cross-sections for the collection of turbules in each size range neglects the coherence properties of the scattered signals which is appropriate for the ensemble average scattering by a collection of scatterers having random locations except in the near forward direction (Goedecke, DeAntonio, Auvermann 1994c). Standard scattering theory for an ensemble of scatterers is usually applied when the detector is in the far field of the scattering volume occupied by the ensemble. For the scenario used in this paper, the detector is assumed to be in the "near field" of the scattering volume, but the far field of each turbule. This will not actually be true for the larger turbules in a more realistic scenario. Also, in many scenarios, the incident wave is not plane. The importance of

deviations from standard far field scattering geometry has not been determined.

Some general conclusions may be drawn from the standard scattering theory, general in the sense that they do not depend on the form of the temperature and velocity distributions considered (Goedecke, DeAntonio, Auvermann 1994a). Using the formal result of eq. (3), it is recognized that the volume integral need only extend over a finite scattering volume. In this section, the expression scattering volume is thought of as the intersection of the illuminated region and the detector field-of-regard, perhaps made of limited extent by the use of a parabolic reflector. Although this volume may have a complicated shape, a single scale length a_s is ascribed to it for convenience. The effect of turbulence outside the scattering volume rapidly goes to zero. Integration of eq. (3) by parts yields two terms, the first being essentially the Fourier transform of the turbulence distribution (either temperature or velocity) and the other a surface integral over the scattering volume surface. In the commonly treated case where $a << a_s$, there are many turbules in the scattering volume and the surface integral will be negligibly small. The result is the standard theory that has been used in the first parts of this paper. If, however, the turbule scale a is greater than a_s, the surface integral is not negligible. The result is the same as our result above except the cosine factor, which makes scattering at right angles to the incident wave zero, is not present. In the third case, where the wavelength is greater than the turbule size which is in turn greater than a_s, the surface integral is again not negligible. The scattering pattern can deviate appreciably from the standard results.

5. CONCLUSIONS

Battlefield scenarios in which acoustic propagation can have significant importance will often be such that standard scattering theory will not fully apply. This may occur when the wavelength, the length scale of the turbulence, and the length scales of some of the turbulent eddies, and the length scale of the scattering volume are of the same order, or when the detector is not in the far field of the scattering volume and/or the individual turbules. Thus, definition of the scattering volume is an important element in calculating turbulence scattering.

Using specific examples of turbule morphologies and a particular simplified scenario, it was shown that large scale turbulence dominates scattering and that the scattering pattern of these large scale entities tends to limit the effective scattering volume. The scenario involved a 4π detector assumed to be in the far field of each turbule in an ensemble of randomly located turbules of different sizes.

Future work will need to deal with more complex scenarios. However, considerable information may be derived with the use of standard scattering theory, such information giving an initial approximation to the true result. Also, to be included are the effects of ground reflections, shadow zones, and the $1/r^2$ effects of source and scattered fields. All of these effects may further limit effective scattering volumes and/or modify the current results.

Concerning the enormous fluctuations of scattered signals measured in shadow zones (Auvermann, Goedecke, DeAntonio 1993), these must occur because of relative motion among a moderate number of large entities. This situation requires consideration of scattering amplitudes rather than cross-sections. Even if the signal from all turbules at 6.22 size parameter were in phase and the signal from all turbules at 91.325 size parameter were in phase separately, the former could produce only a plus or minus 20% variation in the overall summed signal. The experiment showed the variation was 100%, indicating that the relative amplitudes of the different significant contributors are nearly equal.

REFERENCES

Auvermann, H. J., and G. H. Goedecke, 1992, "Acoustical Scattering from Atmospheric Turbulence," Proceedings of the 1992 Battlefield Atmospherics Conference, 1 - 3 Dec., 1992, Ft. Bliss, Texas.

Auvermann, H. J., G. H. Goedecke and M. D. DeAntonio, 1993, "Fluctuations of Acoustic Signals Scattered by an Ensemble of Turbules," Proceedings of the 1993 Battlefield Atmospherics Conference, 30 Nov. - 2 Dec., 1993, Las Cruces, New Mexico.

Goedecke, G. H., 1992, "SCATTERING OF ACOUSTICAL WAVES BY A SPINNING ATMOSPHERIC TURBULE," Contractor Report CR-92-0001-2, U. S. Army Atmospheric Sciences Laboratory, White Sands Missile Range, NM 88002.

Goedecke, G. H., M. DeAntonio and H. J. Auvermann, 1994a, "First-order acoustic wave equations and scattering by atmospheric turbulence," (submitted for publication in the Journal of the Acoustical Society of America).

Goedecke, G. H., M. DeAntonio and H. J. Auvermann, 1994b, "Acoustic scattering by atmospheric turbulence I: Individual and randomly oriented turbules," (submitted for publication in the Journal of the Acoustical Society of America).

Goedecke, G. H., M. DeAntonio and H. J. Auvermann, 1994c, "Acoustic scattering by atmospheric turbulence II: Homogeneous isotropic ensembles," (submitted for publication in the Journal of the Acoustical Society of America).

RELATIONSHIP BETWEEN AEROSOL CHARACTERISTICS AND METEOROLOGY OF THE WESTERN MOJAVE

L.A. Mathews and J. Finlinson
Naval Air Warfare Center
China Lake, CA 93555, USA

P.L. Walker
Naval Postgraduate School
Monterey, CA 93943, USA

ABSTRACT

The Visibility Impact Study was an intense, comprehensive project intended to measure aerosol size, chemical composition and optical properties. Sites at Tehachapi Pass, Antelope Valley and China Lake were instrumented with nephelometers, aerosol filter samplers, meteorological instruments and in the case of the Antelope Valley and Tehachapi Pass with aerosol sizing instruments operated continuously from mid-July through mid-September 1990. Most data collected were for ambient conditions. Also, data were collected for intensive smog conditions in the Tehachapi Pass and for windy conditions on the high desert. Four six hour filter samples were collected daily in the Tehachapi Pass. The purpose of this report is to present some results of analysis of the aerosol data and to relate the observed aerosol characteristics with meteorological conditions. Usually, polluted air is transported into the western Mojave from Los Angeles through the Soledad and Cajon Passes and from the San Joaquin Valley through the Tehachapi Pass primarily during thermal lows in the San Joaquin Valley and high desert which occur most frequently in the summer. Polluted air at China Lake originates in the San Joaquin Valley. Fine particle (0-2.5μ) concentrations by mass are 35-40% organic carbon and 30% sulfates, nitrates and elemental carbon. The remainder is dust. The organic carbon component of the Tehachapi aerosols increased dramatically during some intensive periods. Also, large amounts of sulfur were observed for some of these periods. Wind and dust conditions occur during Rocky Mountain highs causing flows from the northeast. Dust mass and composition dependence on wind speed were determined at each of the sites from filter data. The dust mode aerosols are made of clays and those clays have been identified. Their composition is wind speed independent for speeds up to 10 m/s, i.e. there is no silicate mode. Dust mass is wind speed independent up to 6 m/s. Beyond that dust mass is exponentially related to wind speed by $m = 0.55\exp(0.59u)$. Dust mass computed from size distributions also exhibits the 6 m/s threshold.

1. INTRODUCTION

Objectives of the present work are to characterize aerosols of the Mojave Desert and to relate those characteristics to meteorological conditions. Simultaneous visibility, meteorological and aerosol data were taken at four wide-spread locations in the western Mojave Desert of California starting the first week in July and running through the second week in September 1990. Locations of the sampling sites are shown in the first figure. Size distribution data were taken at Tehachapi Pass and on Edwards Air Force Base in the Antelope Valley 2 miles south-east of Rogers dry lake. Filter sampling was performed daily on the China Lake dry lake in the Indian Wells Valley, Edwards and Tehachapi.

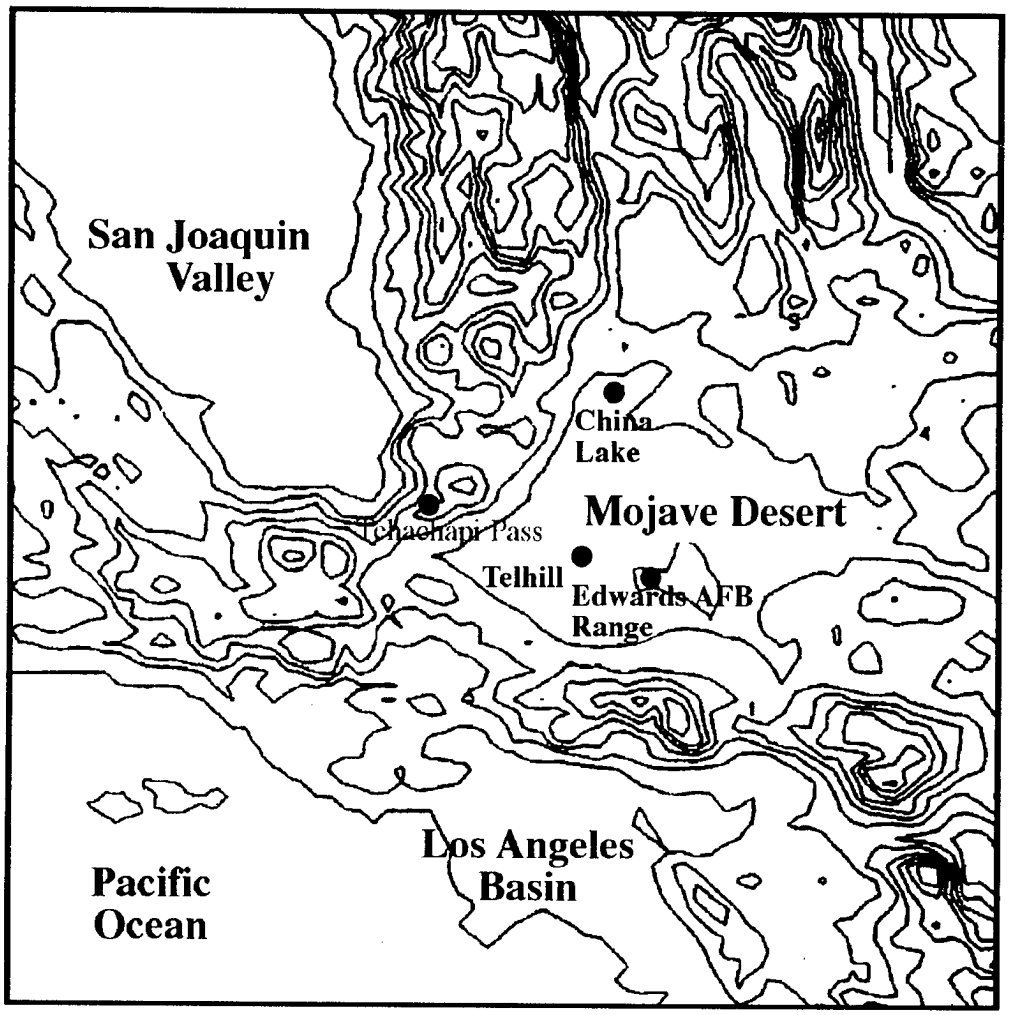


Figure 1. Topographical Map of the Mojave Desert, San Joaquin Valley, and Los Angeles Basin Marked with the Measurement Sites at Tehachapi, Edwards Air Force Base and China Lake. Air pollution is transported from the San Joaquin Valley to China Lake and Antelope Valley through the Tehachapi Pass and from the Los Angeles Basin into the Antelope Valley through Soledad and Cajon Passes.

The Antelope Valley is part of the southwestern Mojave Desert beginning fifty miles north of Los Angeles International Airport. The Mojave Desert is in the rain shadow of the Sierra Nevada and Tehachapi Mountains to the west and the San Gabriel Mountains to the south leaving the desert relatively dry and cloud free. The Antelope Valley is separated from the Los Angeles and San Fernando Valley air basins by the San Gabriel Mountains. The Tehachapi Mountains, to the west, separate the Antelope Valley from the San Joaquin Valley. The Indian Wells Valley lies in the north-western Mojave Desert 200 km northeast of Los Angeles at the southern entrance to the Owens Valley. It is bounded by the Sierra Nevada Mountains to the west and the Panamint range to the northeast.

Combustion aerosols are transported into the Mojave from the San Joaquin Valley through the Tehachapi Pass and through the Soledad and Cajun passes from the Los Angeles air basin.[1] Thus the valley's atmosphere contains a spatially and temporally complex mixture of aerosols of urban,

industrial and desert origin. Combustion aerosols at China Lake originate in the San Joaquin Valley.

The prevailing air flow tends to be from the west or northwest most of the year, with a shift to southwesterly flows in the summer. The actual flow patterns and wind directions in the lower levels of the atmosphere are controlled by the locations of high and low pressure systems. In the summer months solar heating in the desert creates a thermal low pressure area which tends to persist through the night, generating flow into the desert for most of the day. Winds speeds are typically highest in the afternoon and lowest in the morning.

The prevailing mesoscale flow patterns tend to be dominated in the lower levels by topography and thermal effects. Without convective mixing associated with wind, the air in the Mojave tends to be stable, with mixing depths comparable to, but somewhat higher (in the afternoon) than the heights of the mountain ranges which separate the desert from the coastal valleys. Thus, the prevailing westerly flows tend to be channeled into the desert through passes in the mountain ranges most of the day. Flow into the Indian Wells Valley is from the San Joaquin Valley through the Tehachapi Pass. This flow bypasses the Indian Wells Valley in the morning, but flows through it in the afternoon.

2. EXPERIMENTAL PROCEDURE

2.1 Meteorological Data

Radiosonde data were taken daily at 0230 PST at Edwards and at 0530 at China Lake at 1000 foot intervals from surface to 100,000 feet. Wind speed and direction were obtained at China Lake and Edwards with Handar Wind Speed and Direction Sensors while temperature and dew point were obtained with a Handar Temp/RH Probe. Climtronics instruments were used to take similar data at Telhill and Tehachapi. The meteorological instruments were placed ten meters above the ground and recorded data 24 hours a day.

2.2 Aerosol Filter Samplers

Continuous, twenty-four hour samples were taken with Wedding 2X4 Filter Samplers. These samplers acquired one coarse and three fine aerosol samples daily. The coarse filter sample and two of the fine filter samples were collected on Teflon filters for mass, absorption, and elemental composition. The second fine Teflon filter serves as a data quality check. The third fine particle filter was quartz fiber and was used for elemental and organic carbon capture.

Two five hour samples were taken daily from 0700 to 1200 and from 1200 to 1700 PDT at Edwards, Tehachapi and China Lake using NEA Sequential Filter Samplers (SFS). The PM10 size fraction was transmitted through Sierra-Andersen 254I size-selective inlet into a plenum. At Edwards and China Lake the PM2.5 fraction was obtained using a Bendix 240 Cyclone PM2.5 Inlet. At Tehachapi the PM2.5 fraction was obtained using a Desert Research Institute (DRI) MEDVOL Model 3030F with Bendix 240 Cyclone PM2.5 Inlet. Two sets of filters were used simultaneously in both PM10 and PM2.5 SFS. One set consisted of a Teflon-membrane filter which collected particles for gravimetric and x-ray fluorescence (XRF) analyses. The other fine filter holder contained a quartz-fiber filter. Deposits on this filter are submitted to ion and carbon analyses.

Nitrate, sulfate, ammonium, chlorine and potassium masses were determined gravimetrically as each was chemically extracted from the Teflon filter. XRF analysis was performed on Teflon-membrane filters. Analyses were performed using a Kevex Corporation Model 700/8000 energy dispersive x-ray (EDX) fluorescence analyzer. The analyses were controlled, spectra acquired, and elemental concentrations calculated by software implemented on an LIS 11/23 microcomputer interfaced to the analyzer.

2.3 Particle Sizers

Particle sizers were located at Edwards and Tehachapi for the 1990 experiment. The sizers were mounted four meters above the ground and took 20 minute data twenty-four hours a day. At Edwards aerosol size distributions were obtained with a TSI Differential Mobility Particle Sizer (DMPS) for particles with diameters in the range 0.01 to 0.8μ and with an APS-33 Aerosol Particle Sizer for particle diameters ranging from 0.5 to 30μ. Aerosol size distribution measurements were also taken at Tehachapi with a TSI Electrical Aerosol Analyzer (EAA) for particles in the size range 0.01 to 0.6μ and a Laser Aerosol Spectrometer (LAS-X model) Optical Particle Counter for particles in the size range 0.09 to 3 μ.

3.0 AEROSOLS DURING AMBIENT METEOROLOGICAL CONDITIONS

3.1 Composition

The average composition of the aerosols captured on the NEA SFS five-hour samplers at Tehachapi, Edwards and China Lake is tabulated in Tables 1, 2 and 4. The anomalously high organic content of accumulation mode aerosols in the western Mojave (Table 1) has been observed several times before and there has been some concern that this is due to contamination. Therefore, blank quartz-fibers were randomly examined for organic carbon contamination before use in the field. They were heated for at least three hours at 900 °C before use and kept refrigerated prior to heating.

TABLE 1. PM2.5 Composition (in μg/m^3) Averaged Over the Period of the Project.

	Edwards		China Lake		Tehachapi		Tehachapi Intensive	
Ion	Mass	%	Mass	%	Mass	%	Mass	%
Chloride	0.04		0.033		0.037	0.4	.08	.94
Nitrate	0.5		0.34		0.96	9.8	.15	1.76
Sulfate	1.76		1.37		1.61	16.4	2.37	27.8
Ammonium					0.66	6.7	.93	10.9
Organic	4.46		4.57		4.87	49.5	3.13	36.7
Soot	0.78		0.7		1.7	17.3	1.86	21.8
Total Mass					9.84		8.52	

Table 1 is a tabulation of PM2.5 aerosol composition captured on glass fiber filters. (PM2.5 aerosols are actually a mix of accumulation and dust mode aerosols.) The optical properties of sulfate and nitrate aerosols depend upon whether they are present as acids or ammonium compounds. The acids are clear liquids; whereas, the ammonia compounds are white, hygroscopic solids. Unfortunately, ammonium ion mass was only recorded for Tehachapi. For both normal and intensive smog periods there is just enough ammonia present in Table 1 to neutralize the sulfuric and nitric acids. Thus, the sulfates and nitrates appear as ammonium sulfate and ammonium nitrate. The source of the organic carbon is yet to be determined. It may reside in the atmosphere in vapor form which has subsequently condensed on the filters or in aerosol form or some combination thereof.

Table 2 is a tabulation of the elemental composition of PM10 aerosol at Edwards and China Lake. Table 3 is a tabulation by per cent of the elemental composition of the most common clays. Comparison of Tables 2 and 3 show that the best match, except for excess sulfur and calcium, is with illite clay, which is common to deserts.[2] (The compositions of the listed clays are averages obtained from an extensive review of the literature[3]; thus, compositional agreement cannot be expected to be exact.) It remains to be determined whether the excess sulfur and calcium are associated with the clay. Calcium and silicon masses strongly correlate for both Edwards and China Lake; so, calcium is a clay component. On the other hand, silicon and sulfur masses are not at all correlated for Edwards and are only weakly correlated for China Lake. Thus, sulfur is not a dust mode component at Edwards. Gypsum ($CaSO_4$) could be present at China Lake. However, sulfur and calcium masses do not correlate at China Lake. Other possible sources of dust mode sulfur are sodium and potassium sulfates. Unfortunately, there was no check for sodium. Sulfur and potassium are weakly correlated at China Lake in the same way as are sulfur and silicon. The most

TABLE 2. Averaged Mass and Relative Composition of PM10 Aerosols Caught on Teflon Filters.

	Edwards		China Lake	
Element	Mass	%	Mass	%
Al	2.5	20.7	1.62	19.6
Si	5.87	48.5	4	48.46
P	0.004	0.03	0.0053	0.06
S	0.69	5.7	0.63	7.6
Cl	0.0076		0.068	
K	0.87	7.2	0.55	6.6
Ca	0.78	6.4	0.68	8.3
Ti	0.11	0.9	0.06	0.7
Mn	0.025		0.015	
Fe	1.28	10.6	0.71	8.6
Ba	0.039		0.0004	
La	0.018		0.013	
Total Clay	12.1		8.26	

likely source of the PM10 sulfur is accumulation mode sulfates. PM2.5 sulfur masses from sulfates at both Edwards and China Lake are only slightly less than the PM10 masses. Thus, at Edwards sulfur and dust have totally independent origins; whereas, some of the sulfur is associated with clay

at China Lake.

TABLE 3. Composition of Clays Averaged from Data Taken from All Over the World (Reference 5).

	Illite	Glauconite	Montmorillonite	Chlorite	Illite_ montmorillonite	Chlorite_ montmorillonite	Palygorskite	Sepiolite	Kaolinite	Allophanes
Al	24	9.15	21.93	33.52	28.5	12.1	6.82	0.6	35.18	44.95
Si	51.7	49.22	59.49	39.85	51.5	41.2	61.6	52.5	48.8	26.68
P										10.57
S										0.22
K	5.59	6.88	0.34	1.61	9.07	0.22			0.4	
Ca	0.97	0.64	1.18	0.15	0.05	1.4	0.67	0.47	0.22	2.37
Ti	0.68		0.25	1.03	0.77	0.04			0.61	
Fe	4.57	21.38	3.97	4.56	1.52	2.13	0.87	3.6	1.24	0.12

PM10 samples were not taken at Tehachapi Pass. Nevertheless, the composition of dust mode aerosols needs to be known for this location. Because the China Lake site is located on a dry lake bed, its dust composition may not be typical of deserts at all. The Edwards and Tehachapi sites are not on a dry lake bed. The composition of aerosols captured on PM2.5 Teflon filters is tabulated in Table 4.

TABLE 4. Reconstruction of Composition of Dust Mode Aerosol Captured on PM2.5 Teflon Filter.

	Edwards AFB			China Lake			Tehachapi		
	Mass	%	Corrected	Mass	%	Corrected	Mass	%	Corrected
Al	0.43	13.8	17.1	0.264	12.7	15.7	0.238	10.2	14
Si	1.118	35.9	44.5	0.722	34.7	43	0.723	31.2	42.5
P	0.00047	0.015	0.019	0.0041	0.2	0.2	0.0022	0.09	0.13
S	0.737	23.7		0.526	25.3		0.732	31.6	
Corrected	0.143		5.7	0.1277		7.6	0.1138		6.7
Cl	0.00096			0.00626			0.0012		
K	0.249	8.01	9.9	0.161	7.7	9.6	0.189	8.1	11.1
Ca	0.199	6.4	7.9	0.169	8.1	10	0.162	7	9.5
Ti	0.028	0.9	1.1	0.0138	0.7	0.8	0.0154	0.7	0.9
Mn	0.0094			0.00536			0.005		
Fe	0.377	12.1	15	0.216	10.4	12.9	0.261	11.2	15.4
Ba	0.0204			0.01976			0.0343		
La	0.0116			0.1126			0.0115		
Clay Mass	3.11			2.08			2.32		
Corrected Clay Mass	2.5			1.68			1.7		

Sulfur mass is in agreement with that captured on the PM10 Teflon filters, which is to be expected if most of the sulfur is in the accumulation mode. The clay components are under represented relative to sulfur since PM2.5 filters capture only part of the dust mode particles. If the sulfur fraction is adjusted to match that of PM10, then the distribution of the other elements on the PM2.5

filters falls in line with that of the PM10 except for a greater abundance of clay trace elements. Perhaps these elements reside on the surface of alumino-silicate particles so that they represent a greater fraction of the volume of the smallest dust particles. In conclusion, the dust mode composition at Tehachapi Pass is also illite clay.

4. METEOROLOGICAL EFFECTS ON AEROSOL CHARACTERISTICS

4.1 Wind Speed Dependence of Aerosol Mass

Wind Speed dependence of the mass (in $\mu g/m^3$) of PM10 aerosols in Figure 2 was obtained by plotting the five-hour integrated mass captured on the NEA Sequential Filter Sampler at Edwards against wind speeds averaged over the same period. The NEA samplers were operated from 0700 to 1200 and again, with new filters, from 1200 to 1700 PDT. The U-shaped dashed line in the figure is a least-squares fit to the data. A more sensible fit would be no Wind Speed dependence below 6 m/sec and an exponential fit that approximates the least-squares curve for greater wind speeds. This fit is indicated by the solid lines in the figure. Thus, the wind speed dependence of dust mode mass at Edwards is given by Equation 1.

$$\begin{aligned} m &= 7\ \mu g/m^3 && \text{for } u < 6 \text{ m/sec} \\ m &= 0.13\exp(0.66u)\ \mu g/m^3 && \text{for } u > 6 \text{ m/sec} \end{aligned} \qquad (1)$$

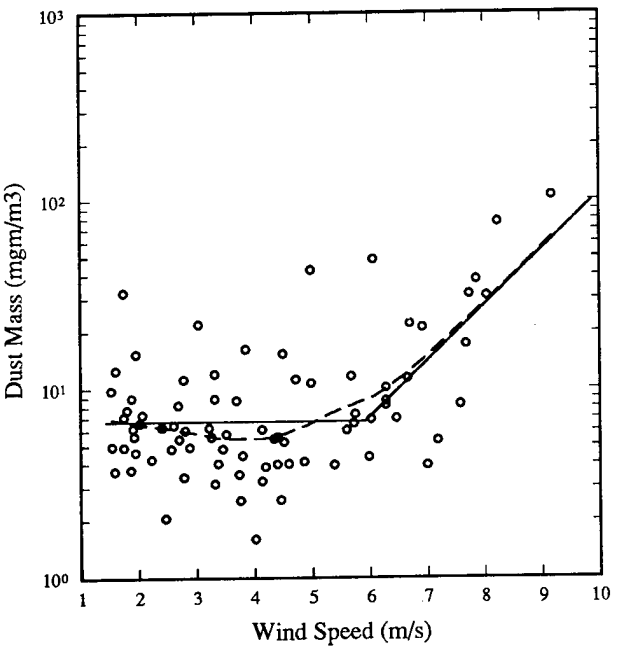


Figure 2. Wind Speed Dependence of Dust Mass at Edwards Air Force Base.

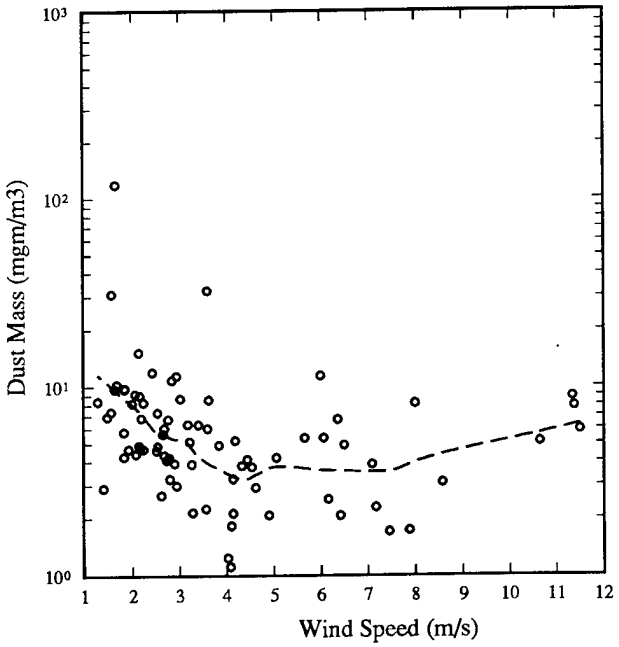


Figure 3. Wind Speed Dependence of Dust Mass at China Lake.

Wind speed dependence of dust mass at China Lake is plotted in Figure 3. There is no wind speed dependence for wind speeds up to 12 m/sec according to the filter measurements. This outcome is consistent with anecdotal information.

It was hypothesized in the last section that gypsum is a major dust component. The wind speed dependence of sulfur and calcium for Edwards AFB are plotted in Figure 4. The wind speed dependence of calcium mass is similar to that of dust as a whole. On the other hand sulfur has no wind speed dependence. Calcium is probably a dust component; whereas, sulfur has some other origin. The most likely source of the sulfur is ammonium sulfate and nitrate.

Edwards aerosol mass in the size range .06 to 1 μ diameter is dominated by accumulation mode particles typically made of the substances listed in Table 1. Aerosols in the size range 1 to 10 μ are typically clays. There is supposed to be yet another size distribution mode, due to blowing sand, made of quartz. Therefore, the composition of the PM10 captured particles might also be wind speed dependent. Figure 5 is a plot of the ratio of PM10 silicon to aluminum versus the short-term averaged wind speed. Clearly, not even a part of a silicon dominated sand mode is being captured even at wind speeds of 9 m/sec.

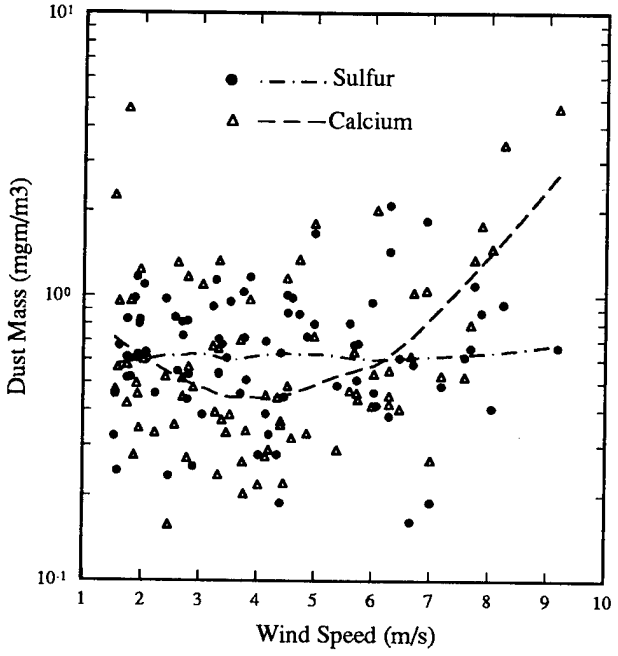


Figure 4. Different Wind Speed Dependence of Calcium and Sulfur at Edwards Implies Different Origins.

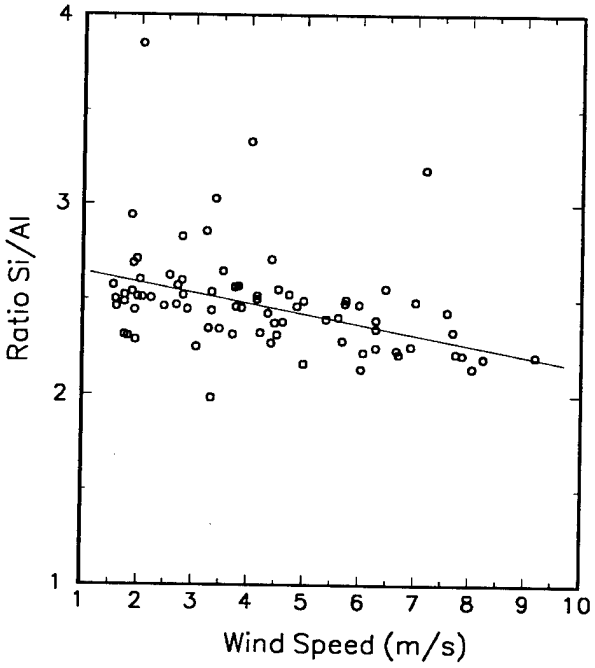


Figure 5. Mass Ratio of Silicon to Aluminum at Edwards Does not Change with Wind Speed Indicating the Absence of the Blowing Sand Mode.

4.2 Size Distribution

The size distributions of Figures 6 and 7 are for pre-storm winds at 0200, maximum aerosol loading at 1600 with wind speed at 8.9 m/sec, and post-storm at 2400. These size distributions were calculated from aerodynamic particle data assuming particle specific gravity of 2.7. The pre-storm aerosol environment was dominated by accumulation mode particles with light dust loading. The post-storm atmosphere is dominated by residual dust with no apparent accumulation mode particles. Maximum particulate loading at wind speeds near 10 m/sec is dominated by dust mode clay particles with the possible presence of a larger mode with mode diameter of about seven microns.

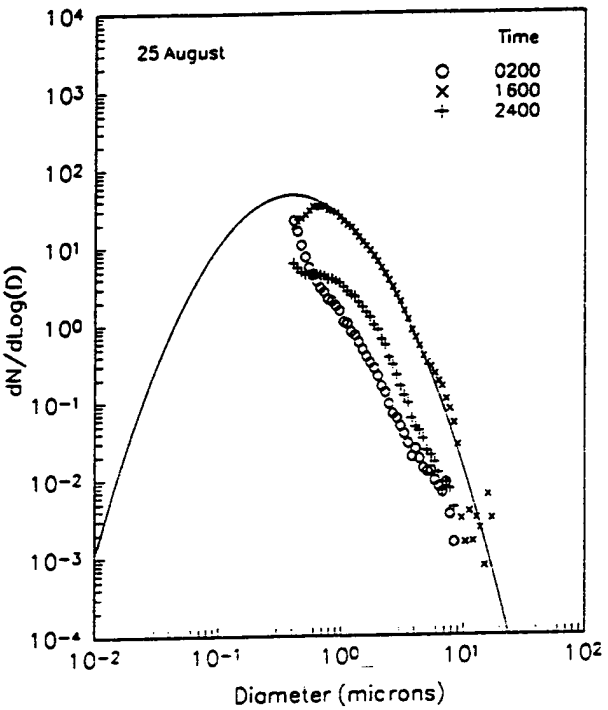


Figure 6. Aerosol Number Distribution Before, During and After Wind Storm of of August 25, 1990.

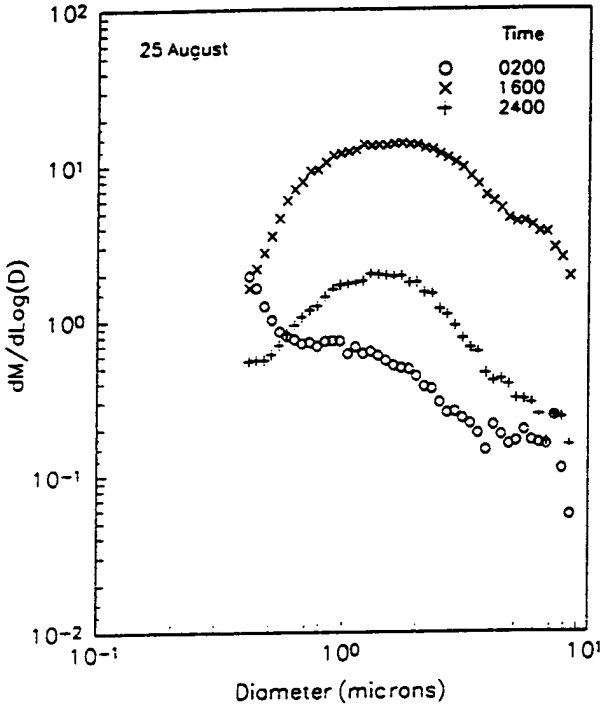


Figure 7. Mass Distribution, Before, During and After Wind Storm at Edwards.

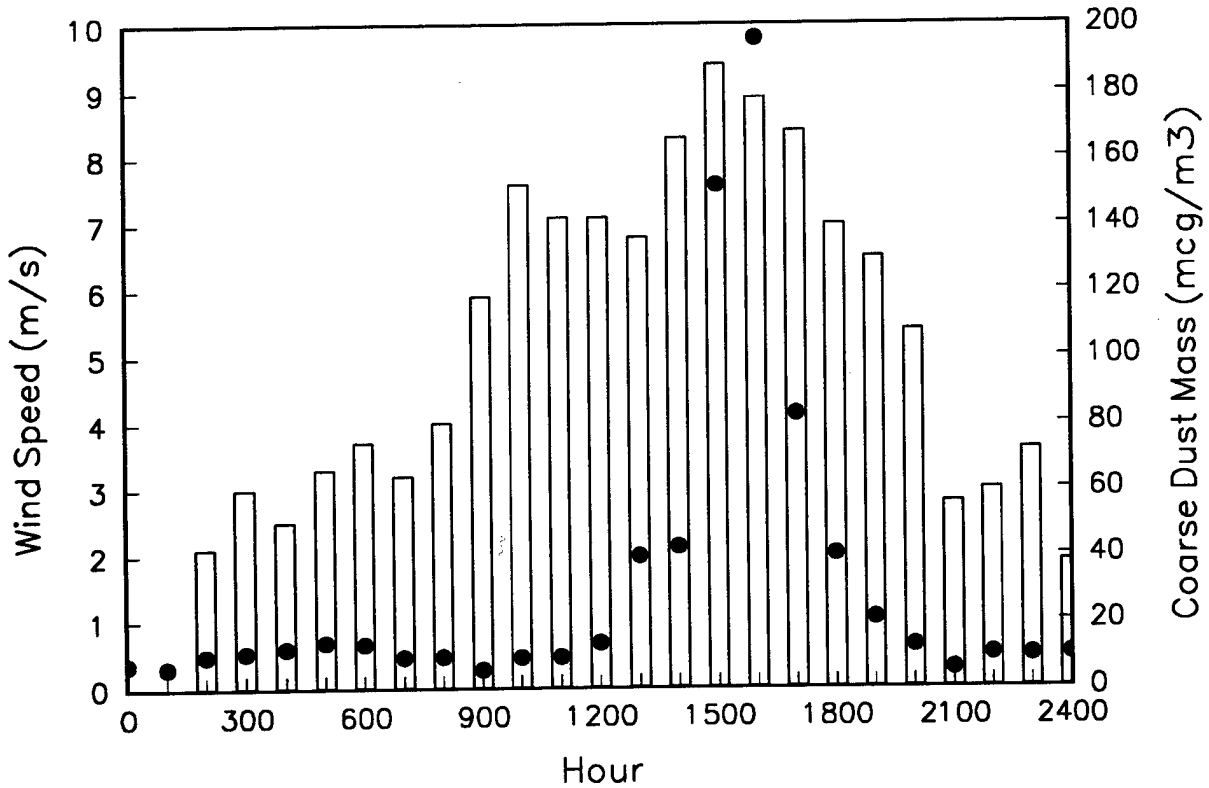


Figure 8. Wind Speed and Dust Loading Calculated from Size Distribution Data Taken at Edwards.

5. DISCUSSION

Results from the present study differ in several significant ways from that of Longtin, et al[4], whose model is incorporated in LOWTRAN 7[5]. First, the accumulation (or water soluble) mode is predominantly organic carbon instead of being composed of sulfates. That may be due to the proximity to large urban, industrial and oil producing and refining regions. Secondly, the Longtin model does not even include the dust mode, which is the predominant continental large aerosol mode. It may be that the Sahara Desert from which part of their model is extracted[6] has been depleted of small particle clays. Last, there is a hint in the current study of the presence of the so-called blowing sand mode which is supposed to appear when wind speeds exceed 10 m/sec. However, the composition of this mode is that of clay, not sand.

6. REFERENCES

1. Trijonis, J. et al., "RESOLVE Project Final Report", Naval Weapons Center, China Lake, Calif., December 1987. 179 pp. NWC TP 6869.
2. Pye, K., Aeolian Dust and Dust Deposits, Academic Press, New York, 1987.
3. Weaver, C.E. and Pollard, L.D., The Chemistry of Clay Minerals, Elsevier, New York, 1973.
4. Longtin, D.L., Shettle, E.P., Hummel, J.R., and Pryce, J.D., "A Desert Aerosol Model for Radiative Transfer Studies", in Aerosols and Climate, Hobbs, P.V. and McCormick, M.P., eds., Deepak Publishing. 1988.
5. F.X. Kneizys, E.P. Shettle, W.O. Gallery, J.H.V Chetwynd, Jr., L.W. Abreu, J.E.A. Selby, S.A. Clough, and G.P. Anderson, "Atmospheric Transmittance/Radiance: Computer Code LOWTRAN 7", Air Force Geophysics Laboratory, Hanscom AFB, Mass. 01731, August 1988. 146 pp. AFGL-TR-88-0177.
6. d'Almeida, G.A., "On the variability of desert aerosol radiative characteristics", J. Geophys. Res. 92 D33017 (March 20, 1987).

Session II

OPERATION WEATHER

EVALUATION OF THE NAVY'S ELECTRO-OPTICAL TACTICAL DECISION AID (EOTDA)

S. B. Dreksler
Computer Sciences Corporation
Monterey, CA 9393-5502

S. Brand and A. Goroch
Naval Research Laboratory Monterey
Monterey, CA 93943-5502

ABSTRACT

The Naval Research Laboratory EOTDA evaluation program evaluates the accuracy and utility of the EOTDA in forecasting forward looking infrared (FLIR) system performances. The program has focused on the collection of performance data for three specific FLIR systems in use by Naval training squadrons. Both the model and analysis methods have been refined since the earlier work described by Scasny and Sierchio at the 1992 Battlefield Atmospherics Conference. The EOTDA model now uses physical background models rather than empirical backgrounds. Analysis procedures include a variation of target/background pairs to allow for typical uncertainties. The results of the analysis are discussed, and future direction will be described.

1. INTRODUCTION

The strike warfare community requires accurate meteorological analyses and forecasts to properly plan and effectively execute tactical operations. While meteorological information itself is very important, it is generally of more value to the tactical decision-maker if it is presented in a tactically relevant form. An example of such an environmental tool is the Electro-Optical Tactical Decision Aid (EOTDA), under development at the Naval Research Laboratory, Monterey. This product was derived from the Mark III EOTDA, which was originally developed by the USAF Phillips Laboratory (Freni, et al., 1993)

EOTDAs are models that predict the performance of electro-optical weapon systems and night vision goggles, based on environmental and tactical information. Performance is expressed in terms of maximum detection and lock-on ranges or designator and receiver ranges. The

EOTDAs consist of three microcomputer based programs supporting infrared (IR) (8-12 μm), visible (0.4-0.9 μm), and laser (1.06 μm) systems. Each program is comprised of three sub-models: an atmospheric transmission model, a target contrast model, and a sensor performance model.

As part of any development process, it is important to have a good understanding of the environmental sensitivity of any meteorological decision aid. It is also equally important to thoroughly evaluate these applications under various environmental conditions to establish their strengths and weaknesses. This documentation of strengths and weaknesses can assist operational users and can help direct research and development efforts.

Since the initial phase of this evaluation, the EOTDA has been upgraded to version 3.0 from version 2.0 and 2.2[1]. The primary modifications in the EOTDA included different methods of entering target, background and weather data. Additional generic targets were added so the user could specify particular parameters for dams, bridges, buildings, bunkers, Petroleum/Oil/Liquification (POL) tanks, power plants, and runway targets. The number of backgrounds were reduced from over 150 empirical backgrounds to 6 first principles of physics generic backgrounds: Vegetation, Soil, Snow, Water, Concrete, and Asphalt. The user can adjust several parameters for each background. The method for entering meteorology data was simplified and data are now entered using the standardized Terminal Aerodrome Forecast (TAF).

2. METHODOLOGY

The Navy's EOTDA evaluation consists of the comparison between calculated and observed sensor performance. Actual sensor performance data were collected in conjunction with normal training missions, Navy and DoD test programs, ship deployments, reserve cruises, naval exercises, and Naval Postgraduate School experiments. This paper focuses on forward looking infrared (FLIR) data because much FLIR data had been collected to date. Also, our experience indicates that the IR EOTDA is the most used EOTDA module; therefore, it is the most important to evaluate.

To collect both operational and meteorology data, a two-sided "knee-board" information card was distributed to the participants. Scasny and Sierchio (1992) provide a more detailed description. Side one of the data cards was used by the weapon system operators (WSO)[2] for recording FLIR detection ranges, sensor, target and background information. The WSOs were asked to choose detection targets that were closest in description to those targets in the EOTDA Target List or those that could be reproduced using the generic models option. To obtain the operational sensor detection data, FLIR operators were asked to begin approach of the target from beyond maximum detection range and to maintain a constant altitude and airspeed. As the aircraft neared the target, the operator logged the appropriate data. If possible,

[1]Version 2.2 was an update to version 2.0 and was specifically used during DESERT SHIELD/STORM operations.

[2]The Weapon System Operator (WSO) is the person who records the sensor range and other tactical data. In different scenarios, the weapon system operator can be the Pilot, the Bombardier/Navigator, an Electronic Warfare Officer or any other member of the air crew.

multiple passes over the target at different altitudes and approach angles were accomplished. After the flight was completed, the data card was given to weather personnel for completion of weather data on the reverse side of the card. In addition to the card, the weather personnel were requested to provide copies of their observation sheets for the day preceding and the day of the data collection. This provided approximately 12 to 24 hours of background information for input into the EOTDA. The meteorology information required is wind, temperature, humidity, and cloud cover.

The completed data sets were entered into the Mark III EOTDA. The EOTDA was run for each completed data set and the calculated output was then compared to the observed values of detection range. Due to the importance of choosing the correct target/background pair, and the fact that we did not always have exact knowledge of the precise target and background, we ran the model with different backgrounds and sometimes different targets. For example, if the target was a POL tank, the model was run with the POL tank as full, empty and half empty. If the background was described as grass, the model was run with several different vegetation and soil types.

Data previously run using EOTDA versions 2.0 or 2.2 were rerun using version 3.0. The resultant data between the two versions were compared. Data collected since the EOTDA was upgraded to version 3.0 were not run using previous versions.

3. ASSUMPTIONS AND LIMITATIONS

Our data collections were done without actually interacting with the WSOs prior to or after the mission. Because of this lack of interaction, we would expect the EOTDAs, in many cases, to predict longer ranges than seen by the WSO, since the WSO may not have reported the target at the maximum detection range. Additionally, we do not know exactly what targets or background parameters the WSO saw at detection range, resulting in an uncertainty in selecting the target-background pair. The interactions and feedback in an operational environment have been shown to improve the skill of the EOTDAs (Kelly and Goforth, 1994).

Weather biases are always present. In many cases, the weather used by the model was taken at the nearest reporting station and not at the target site. However, we were able to develop a fairly accurate 12-24 hour weather history. This weather history is necessary to initialize the thermal contrast model. In many real-time operations, weather data could be less accurate, since forecast data instead of archived data would be used as the input to initialize the EOTDA model.

No temperature or moisture measurements of the targets or backgrounds were available. In an operational setting, model output, observations and feedback would provide some insight as to the nature of these variables.

Statistical tests for each sensor were limited because the independence of the data collected could not be established at this time. This is not a simple task, since independence is a function of differences in dates/times of data collected as well as differences in target/background pairs, approach angle, flight altitude of aircraft, time of day, etc.

3.1 EOTDA Limitations

In addition to the data collection limitations, several assumptions were made during the development of the EOTDA (Dunham and Schemine, 1993). The major model assumptions are: 1) the target is in the sensor's field of view, and time in view is not an issue, 2) targets are all ground-based, and operating vehicular targets have been operating long enough to reach thermal equilibrium, 3) the immediate background around the target is homogeneous, 4) high-value-targets detection criteria are similar to those used for vehicular targets, 5) the atmosphere is horizontally homogeneous with only two vertical layers, 6) cloud cover is continuous (scattered or broken coverages are not modeled), and 7) there exists a cloud free-line of sight between the sensor and the target.

4. RESULTS AND DISCUSSION

Sensor data from three FLIR sensors have been obtained and preliminary analysis has begun. The present analysis examines the data collected to date. The following paragraphs discuss the comparison of the observed versus predicted detection ranges. Due to the classification of sensor data when associated with sensor nomenclature, the sensors will be identified in this paper solely as sensor 1, sensor 2, and sensor 3. For a complete discussion of the sensor results, refer to Dreksler et.al., 1994.

4.1 Best Choice

As mentioned earlier, for every observed detection range, we ran many input combinations of the EOTDA varying the backgrounds and the complexity of the scene. In some cases the target was also varied. Backgrounds were reported by the WSO; however, these were usually brief comments, such as grass field. Several similar backgrounds were evaluated. For the grass field example, background selections were made from the following categories: growing states (intermediate, dormant or growing), coverages (dense, medium or sparse), and soil moisture (dry, wet, or intermediate).

To help us build the backgrounds, we examined the season and the previous rainfall data. Then we selected background parameters such as dormant, sparse, dry for California summer or growing, dense, or wet for New England spring. In many cases we selected three or four different realistic vegetation backgrounds, varying the soil moisture from wet to intermediate or varying the coverage from dense to medium. We then made separate EOTDA model runs for each background. We believe this is a good method to provide a basis for analysis because an experienced EO forecaster will make many EOTDA runs per mission, and then will decide on an EOTDA forecast based on his knowledge of what the target-background pair will look like to the WSO.

A measure of model success that was examined was the best case (where the background was chosen to provide a range closest to that observed - see Figure 1). We refer to this as "best choice" and use it extensively during the analyses.

4.2 Background Analysis

Since one of the major upgrades between versions 2.0 and 3.0 was the change in backgrounds from empirical (version 2.0) to first principles (version 3.0), we were interested to see how well

Case	Obs	Pred 2.0	Pred 3.0	obs-pred total Error 2.0	obs-pred total Error 3.0	err/obs*100 percent error 2.0	err/obs*100 percent error 3.0	Complex	Method	Target	Bkgnd	snr dir	snsHt(ft)	tgt dir	tgt ht	month	time
K8D	30.4	130.0	34.0	99.6	3.6	327.6	11.8	0	N-R	missile site	foliage-dmt	90	1500	0	522	dec	930
K8D	30.4	2.0	2.0	28.4	28.4	93.4	93.4	0	N-R	missile site	rock	90	1500	0	522	dec	930
K8D	30.4	88.0	43.0	57.6	12.6	189.5	41.4	0	N-R	missile site	fol-d,s	90	1500	0	522	dec	930
K8D	30.4	125.0	34.0	94.6	3.6	311.2	11.8	1	N-R	missile site	foliage-dmt	90	1500	0	522	dec	930
K8D	30.4	2.0	2.0	28.4	28.4	93.4	93.4	1	N-R	missile site	rock	90	1500	0	522	dec	930
K8D	30.4	84.0	42.0	53.6	11.6	176.3	38.2	1	N-R	missile site	fol-d,s	90	1500	0	522	dec	930
K8D	30.4	120.0	34.0	89.6	3.6	294.7	11.8	2	N-R	missile site	foliage-dmt	90	1500	0	522	dec	930
K8D	30.4	2.0	2.0	28.4	28.4	93.4	93.4	2	N-R	missile site	rock	90	1500	0	522	dec	930
K8D	30.4	80.0	42.0	49.6	11.6	163.2	38.2	2	N-R	missile site	fol-d,s	90	1500	0	522	dec	930
K8D	30.4	88.0	6.0	57.6	24.4	189.5	80.3	0	W-R	missile site	foliage-dmt	90	1500	0	522	dec	930
K8D	30.4	55.0	7.0	24.6	23.4	80.9	77.0	0	W-R	missile site	fol-d,s	90	1500	0	522	dec	930
K8D	30.4	49.0	5.0	18.6	25.4	61.2	83.6	1	W-R	missile site	foliage-dmt	90	1500	0	522	dec	930
K8D	30.4	35.0	7.0	4.6	23.4	15.1	77.0	1	W-R	missile site	fol-d,s	90	1500	0	522	dec	930
K8D	30.4	49.0	5.0	18.6	25.4	61.2	83.6	2	W-R	missile site	foliage-dmt	90	1500	0	522	dec	930
K8D	30.4	31.0	7.0	0.6	23.4	2.0	77.0	2	W-R	missile site	fol-d,s	90	1500	0	522	dec	930

best choice 2.0

best choice 3.0

Figure 1. Example of all EOTDA runs for one mission. The best choice is determined by selecting the case with the smallest error. A best choice case for each EOTDA version (2.0 and 3.0) is selected as annotated.

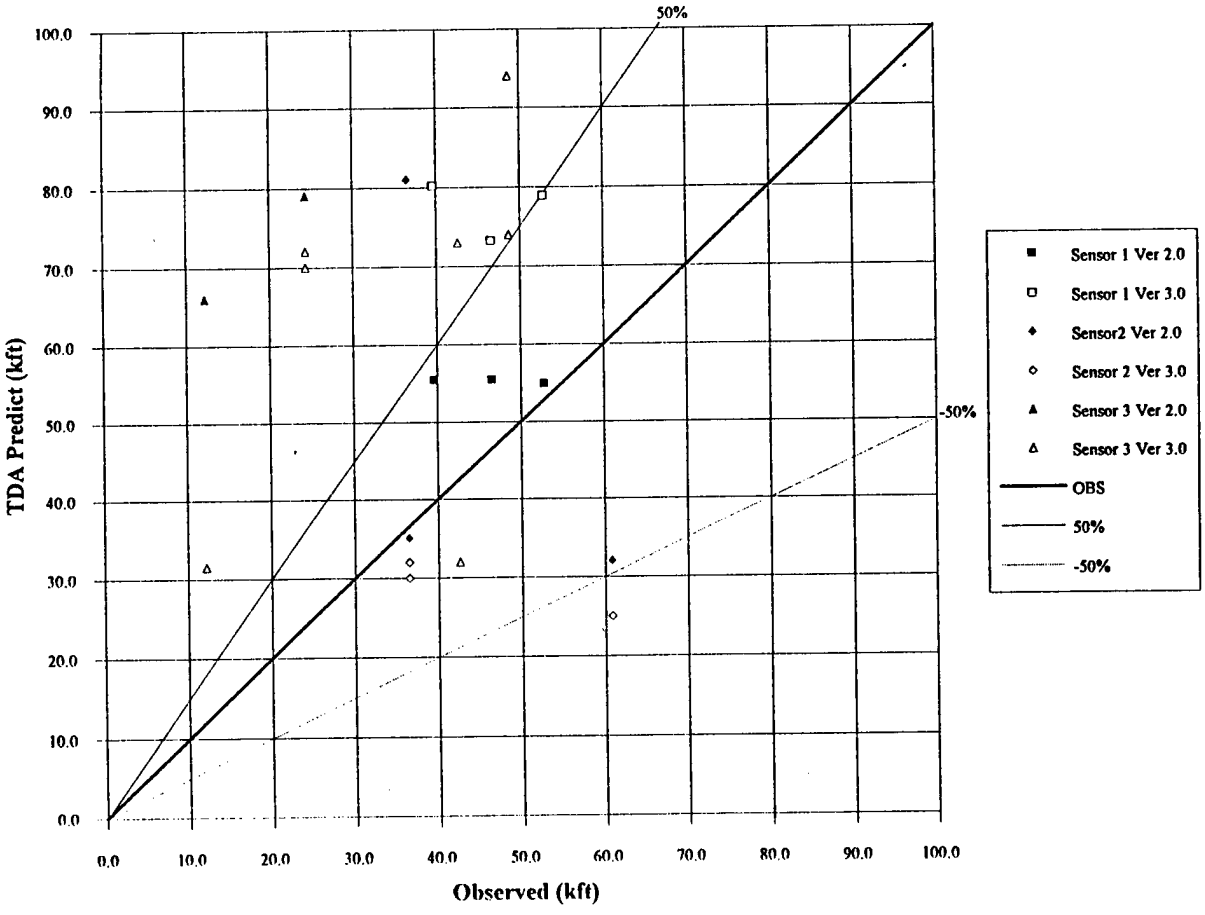


Figure 2. Comparison of EOTDA versions 2.0 and 3.0 best choice selections for the water background.

each background performed. We divided all the best choice runs from all three sensors by background type. We then compared version 2.0 and version 3.0 backgrounds.

4.2.1. Water Background

Figure 2 shows the results of using the water background for each of the three sensors. For EOTDA version 2.0, sensors 1 and 2, 50% (3 of 6) of the best choice runs were within 20% of the observed value and 83% (5 of 6) of the best choice runs were within 50% of the observed value. By comparison, for EOTDA version 3.0, sensors 1 and 2, 33% (2 of 6) of the best choice runs were within 20% of the observed value and 50% (3 of 6) of the best choice runs were within 50% of the observed value. However, for sensor 3, EOTDA version 2.0, all 5 cases had errors in excess of 225% and an average error of 355%. For version 3.0 , the same 5 cases had errors in excess of 159% and an average error of 172%. For sensor 3, the EOTDA version 3.0 average of the 10 cases was 120%.

Version 3.0 had percent errors 42% lower and root mean square (RMS) errors 25% lower than version 2.0 for the same 11 cases. But overall, the error using the water background was over 90% for version 3.0. The empirical water background did a better job of representing the actual background for those cases using sensors 1 and 2. However, when the empirical background was off, it was far off. The first principles water background appears to be more consistent, but still produced large errors. The following describes how well the water background compared with the other backgrounds.

4.2.2. Other Backgrounds

Figures 3 and 4 compare the backgrounds regardless of sensor type. The Y-axis is in percent for the percent error analyses and in thousands of feet (kft) for the RMS analyses. Comparing the same 33 cases (Figure 3) for the other backgrounds, version 2.0 was slightly better for soil and asphalt, while version 3.0 was slightly better for vegetation and water. There was only one case where concrete was the background and there were no cases that used a snow background. The soil background (7 cases) gave the best results for each version, 26% error for version 2.0 and 33% error for version 3.0. Asphalt was the next most accurate background (3 cases), 79% error for version 2.0 and 94% error for version 3.0. However, the RMS error from version 3.0 was considerably lower than the version 2.0 error: 39,000 feet versus 61,000 feet. For the water and vegetation backgrounds, version 3.0 had lower percent errors and lower RMS errors. However, version 3.0 still had over a 100 percent errors for these backgrounds.

These results are supported by the Schemine and Dunham (1993) assessment of the first principles background signature predictions in the Target Contrast Model. Schemine and Dunham (1993) showed the soil model provided excellent signature predictions, while the foliage (vegetation) model produced fairly good predictions and the water and concrete models were highly inaccurate. The greatest inaccuracies were found in the water background model, due primarily to two factors. First, the bi-directional effects from the reflection of the sky temperature are not included in the water background model. Second, during model initialization, the water background model sets the water's initial core temperature equal to the air temperature at the initial input time. Both problems need to be addressed.

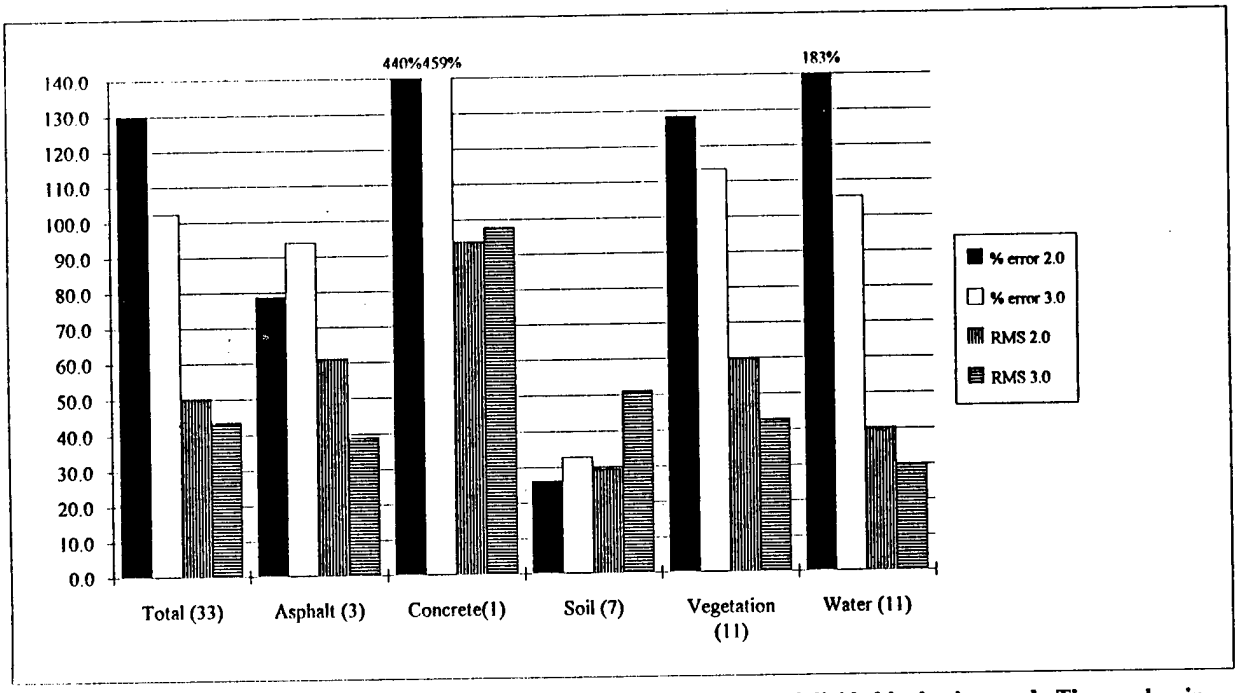


Figure 3. Comparison of EOTDA versions 2.0 and 3.0 best choice selections subdivided by background. The number in parenthesis is the number of cases for that background. The Y-axis is in percent for the percent error analyses and in thousands of feet (kft) for the RMS analyses.

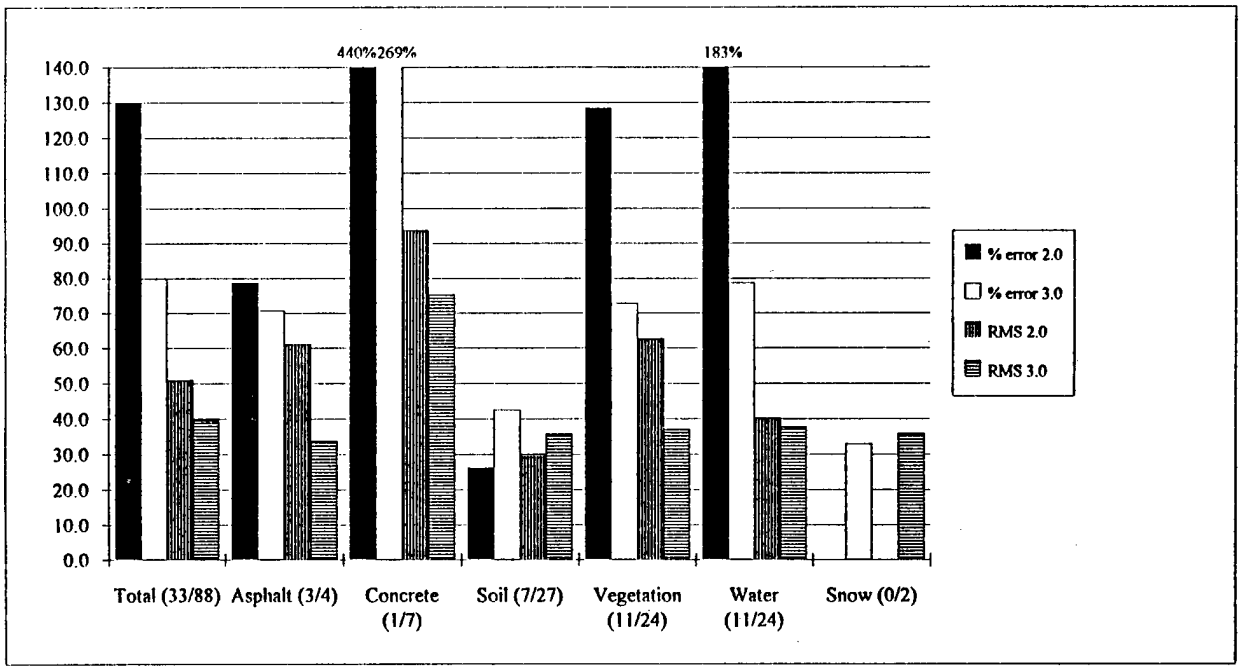


Figure 4. Comparison of all best choice selections subdivided by background. The numbers in parenthesis are the number of cases for that background from EOTDA versions 2.0 and 3.0 respectively. The Y-axis is in percent for the percent error analyses and in thousands of feet (kft) for the RMS analyses.

5. SECOND PHASE

The second phase of the EOTDA evaluation is designed for controlled operational validation of the EOTDA. In this phase, each range data point used in the analysis is supervised by the analyst in cooperation with the WSO and the local weather detachment. The WSO is provided with a detailed briefing of sensor and weather information and data requirements by the analyst. After the mission, the WSO is debriefed by the analyst about activity during the mission.

The purpose of this detailed analysis is to determine the detailed chronology of each event, including detection, classification and identification ranges. These data will identify the detailed operational and environmental characteristics controlling the utility of the EOTDA. It has been found in previous analyses that when information gathering duties are added to the already full workload of air crews and met personnel, data quality suffers substantially.

There are two types of analyses being conducted, aboard ship and at an air station. The procedure at the Naval Air Station involves the analyst obtaining environmental information from the weather detachment prior to mission pre-brief. At the pre-brief, the analyst provides support to the weather briefer in identifying conditions expected over the target. The analyst also obtains details on the mission profile, including aircraft operations plan, target definition, and the sensor utilization plan. During the mission the analyst remains with flight control noting location of the aircraft and communications between the aircraft and flight control. It is anticipated that some of the sensor ranges will be noted by the WSO, and this should be duly recorded to the nearest second by the analyst. After the mission, the analyst debriefs the WSO, answering any questions which arise from the mission communications or in the review of data taken by the WSO. If video records are available of the mission, these are to be reviewed by the analyst with the WSO.

The aboard ship evaluation will be conducted with the LAMPS SH-60B helicopter as primary airborne sensor platform, and the Navy Mast Mounted Sight (NMMS) as the ship borne platform. The helicopter procedures are similar to the procedures at the air station. It is expected that the weather team deployed aboard the ship will provide similar air-WSO briefings supported by the analyst. During the mission, the analyst maintains station at Combat Information Center (CIC) to monitor communications and helicopter location using standard ship resources. The analyst will debrief the sensor operator to obtain complete information about each contact. The NMMS is used for surface-surface classification and identification. The modus operandi includes obtaining a target range and bearing from another source (radar, sonar, or pilot report), and then searching the expected target region. The control is usually mounted on the bridge with video supplied to CIC. With this arrangement the analyst can maintain a watch over the NMMS, although communication with the NMMS operator may be limited. An important element of this data set is to recognize when the operator is cued to a target, and when the operator actually detects the target.

6. CONCLUSIONS AND RECOMMENDATIONS

This paper has described the evaluation of the sensor performance model portions of the EOTDA for Navy and Marine Corps EO sensors. As previously mentioned, data are limited and many more data points must be collected under various environmental and operational conditions to show a statistically sound representation for each sensor's performance. Efforts to

collect additional data for these sensors and others are ongoing and will provide the needed information to produce a useful evaluation of the EOTDA's prediction performance for the full range of Navy and Marine Corps electro-optical sensors.

We are continually looking for ways to collect more controlled data for more sensors under different scenarios. Most data were collected from just a few sources with few scientific controls. No thermal or moisture measurements of the targets or backgrounds were taken. These data collection efforts require interactions with participants before the data collection mission, as well as briefings following the missions. We need to measure the weather at the target and to determine the background parameters at detection, and we need to get all targeting information. We also need to explore the impact of using atmospheric numerical output as input to the EOTDAs.

Based on previous sensitivity studies (Keegan, 1990), one of the most important parameters is the target-background pair. The first principles of physics backgrounds were more consistent, while the empirical backgrounds were as likely to over-predict or under-predict.

The first principles of physics water background appeared to be more consistent than the empirical water background, but it still produced large errors. A more detailed examination of the physics of the water background is needed. As a start, the ability to set the initial sea surface temperature is needed and also to include the bi-directional effects from the reflection of the sky temperature. The utility of a nonhomogeneous water background could be studied for applicability to account for moving targets and target heading changes.

To overcome model limitations cited earlier, the transmissivity model could be examined, and we could study the effects of improving the vertical resolution and of including near surface aerosols. Human factors studies could also be examined. As mentioned earlier, the EOTDA is not concerned with the target search process. It assumes that the target is in the sensor's field of view. This assumption could lead to over predictions of target detection.

The efforts to collect the data discussed above proved to be an enlightening experience. Detailed information was obtained about the varying methods used in the different types of tactical aviation missions. As scientific researchers, one can get lost in the realm of the "way things should be done" without the legitimate knowledge of the "way things <u>are</u> done" in the operator's or user's world. Discussions with sensor operators provided insight into the "way things <u>are</u> done" and as is always the case in research, the test plan was adjusted. Continuing discussions with the aviation community and sensor operators on their tactics will provide the required information to collect useful sensor detection data.

Strong interaction with the WSOs also provides insights into the way the environmentalist needs to interact with the tactical users. For example, Air Force weather forecasters at Cannon AFB NM, working closely with tactical pilots, were able to achieve remarkable success; that is over 82% of the time, the **forecasters** predicted detection and lock-on ranges within 10% of what was observed (Kelly and Goforth, 1994). We need to learn to understand the limits of these tools as well as the extent of tactical/environmental interactions while using them.

In summary, the EOTDA evaluation program has observed the following: 1) results differed for each sensor; 2) predicted versus observed errors were particularly large for over water

targeting; 3) soil backgrounds gave excellent results; 4) some biases became evident for selected sensors; 5) more controlled experiments/evaluations are needed to determine causes of error; and 6) some errors in data sets were induced by mission tactics and not algorithm errors. The present or second phase of the EOTDA evaluation will attempt to remedy some of the "lessons learned" during the first phase by including direct interaction with the WSOs prior to and after the missions. This should provide a firmer basis for assisting operational users as well as help redirect research and development efforts.

ACKNOWLEDGMENT

The Navy effort in the tri-service development of the Electro-Optical Tactical Decision Aid is sponsored by the Oceanographer of the Navy (OP-096) through the Space and Naval Warfare Systems Command Program Office, Washington D.C., program element 0603207N.

REFERENCES

Dreksler, S. B., S. Brand, J. M. Sierchio, and K. L. Scasny, 1994: Electro-Optical Tactical Decision Aid Sensor Performance Model Evaluation. NRL/MR/7543--94-7216, Naval Research Laboratory, Monterey, CA 93943-5502. (In Final Review)

Dunham, B. M. and K. L. Schemine, 1993: Intermediate Grade Infrared TDA Analyst's Manual. Battelle Report for Period March 1993 through September 1993. WL-TR-94-1084, Wright Laboratory, Wright-Patterson AFB, OH 45433-7409.

Freni, J. M. L., M. J. Gouveia, D. A. DeBenedictis, I. M Halberstam, D.J. Hamann, P. F. Hilton, D. B. Hodges, D. M. Hoppes, M. J. Oberlatz, M. S. Odle, C. N. Touart, and S-L Tung, 1993: Electro-Optical Tactical Decision Aid (EOTDA) Users Manual Version 3. Hughes-STX Scientific Report No. 48. PL-TR-93-2002, Phillips Laboratory, Hanscom AFB, MA 02731-5000.

Keegan, T. P., 1990: EOTDA Sensitivity Analysis. STX Scientific Report No. 44(II). GL-TR-90-0251 (II), Phillips Laboratory, Hanscom AFB, MA 02731-5000.

Kelly, J. L., and B. K. Goforth, 1994: ACC Cannon AFB User EOTDA Experience. Proceedings of the Weather Impact Decision Aids (WIDA) Conference, Las Vegas, NV, 22-23 March 1994.

Scasny, K. L., and J. M. Sierchio, 1992: Mark III Electro-Optical Tactical Decision Aid Sensor Performance Model Evaluation. Proceedings of Battlefield Atmospheric Conference, Fort Bliss, Texas, 1-3 December 1992.

Schemine, K. L., and B. M. Dunham, 1993: Infrared Tactical Decision Aid Background Signature Model Assessment. Battelle Report for Period March 1993 through August 1993. WL-TR-94-1064, Wright Laboratory, Wright-Patterson AFB, OH 45433-7409.

U.S. ARMY BATTLESCALE FORECAST MODEL

Martin E. Lee, James E. Harris, Robert W. Endlich,
Teizi Henmi, and Robert E. Dumais
U.S. Army Research Laboratory
White Sands Missile Range, NM 88002, USA

Major David I. Knapp
Operating Location N, Headquarters Air Weather Service
White Sands Missile Range, NM 88002, USA

Danforth C. Weems
Physical Science Laboratory, New Mexico State University
Las Cruces, NM 88003, USA

ABSTRACT

The U.S. Army Research Laboratory (ARL), Battlefield Environment Directorate (BED) is conducting research and development to satisfy Army Science and Technology Master Plan, Science and Technology Objectives (STOs) which call for target area meteorology and automated decision aid capabilities by FY95. This STO technology will be provided to the battlefield soldier through the Integrated Meteorological System (IMETS) and the Army Battle Command System. ARL/BED is working to provide the IMETS Block II an operational Battlescale Forecast Model (BFM) by FY95 that will accurately forecast target area weather and provide input weather data to automated weather effects decision aids. This paper describes how ARL/BED envisions the BFM and subsequent models will be used operationally on the tactical battlefield, both from a general and technical perspective, and discusses future improvements that are planned.

1. INTRODUCTION

The U.S. Army Research Laboratory (ARL), Battlefield Environment Directorate (BED) is conducting research and development (R&D) to satisfy Army Science and Technology Master Plan, Science and Technology Objectives (STOs) IV.K.1 and IV.K.3. STO IV.K.1 calls for a 12 hour target area weather forecasting capability by FY95, and 24 hours by FY97. STO IV.K.3 requires development of automated weather decision aids by FY95 and FY97 that use

artificial intelligence techniques to provide the Army Battle Command System (ABCS) the capability to assess and exploit battlefield environmental effects for tactical advantage. This STO technology will be provided to the battlefield soldier through the Integrated Meteorological System (IMETS) and the ABCS. Thus ARL/BED is working to provide the IMETS Block II with an operational mesoscale meteorological model by FY95 that will provide it the capability to forecast target area weather and provide input weather data to automated weather effects decision aids.

In meteorology, the mesoscale domain can range from 2,000 km (often referred to as the regional or theater scale) to 2 km, which is near the microscale. Of primary interest to the Army is an intermediate mesoscale domain of approximately 500 km which ARL/BED refers to as the battlescale. ARL/BED's focus therefore is to develop a battlescale model capable of forecasting battlefield and target area meteorology at the accuracies sufficient to support Army operations and automated decision aids. A model capable of these accuracies will significantly improve the intelligence preparation of the battlefield process and specifically the planning and execution of deep strike fire support missions, increase the first round hit probability of artillery ballistic systems, and prevent using high cost "smart" munitions and "precision strike" assets in atmospheric conditions that would render them ineffective.

To achieve the milestones above and build a strategy for future development, ARL/BED has elected to rely on the Navy and Air Force to perform the basic research of mesoscale model development, freeing ARL/BED to concentrate its resources on adapting and applying this research to specific Army applications. This strategy is consistent with the Joint Directors of Laboratories Project Reliance, whereby, the Navy was assigned the lead in mesoscale modeling research within the DOD R&D laboratory community, with the Army and Air Force R&D laboratories agreeing to adapt the Navy's model for service specific applications. The Air Force is also pursuing an independent initiative outside the DOD R&D laboratory environment to evaluate mesoscale modeling technology to insure that the most suitable technology, federal or nonfederal, is adopted for Air Force and Army battlefield weather support.

2. CURRENT SITUATION

Currently neither the Navy Operational Regional Atmospheric Prediction System (NORAPS) — which is currently being tested for operational cases using 45 km single mesh grids (Liou et al., 1994) — or the Air Force's Relocatable Window Model are well suited for forecasting small scale weather features within complex terrain domains $\lesssim 500 \times 500$ km^2, important to Army battlefield operations. However, as mentioned above, both the Air Force and Navy have either in-house research efforts underway or they are supporting research through contractual mechanisms to develop a model that will support the smaller domain at the accuracies that the Army requires. Until this technology matures to the point that it can be used operationally, and to satisfy STO and IMETS milestones, ARL/BED has adapted a hydrostatic model HOTMAC (Higher Order Turbulence Model for Atmospheric Circulation) which was initially developed by Dr. Yamada while at Los Alamos National Labs (Yamada and Bunker, 1989). ARL/BED

scientists have subsequently, with Dr. Yamada's assistance, improved and tailored HOTMAC for Army applications. This Army version of HOTMAC is called the Battlescale Forecast Model (BFM). The BFM uses the hydrostatic approximation, is relatively fast, numerically stable, easy to use, and has detailed boundary layer physics, a most important feature for Army operations.

ARL/BED will continue to work jointly with the Navy and Air Force to identify, develop, and evaluate an objective model capable of the accuracies required by the Army. ARL/BED will contribute its expertise in boundary layer physics and complex terrain interactions as this development process evolves. However, until the objective model is considered mature enough for operational use, ARL/BED will use the Army BFM to satisfy its near term STO and IMETS milestone requirements. Once the objective model is judged ready for operational use, then ARL/BED will replace the BFM with the objective model and adapt it for Army applications. The purpose of this paper is to describe how ARL/BED envisions the BFM and subsequent models will be used operationally in the field, both from a general and technical perspective, and to discuss future improvements that are planned.

3. GENERAL CONCEPT OF OPERATIONS

The BFM takes into account local effects on weather patterns which may take an experienced forecaster years to learn for a particular area. Running a mesoscale model on a workstation computer offers the SWO the opportunity to produce a fine-tuned local forecast for unfamiliar areas with accuracy far superior to the large-scale products currently available in the battlefield. The BFM automatically incorporates knowledge of local terrain, important battlefield weather observations, and centrally-produced boundary conditions close to the Area of Operations (AO) to produce its mesoscale forecast gridded fields (see section 4.3.b). The BFM predicts battle scale weather features causing localized effects often missed by the coarse-grid resolution output from global and regional models. These large-scale models do not incorporate high resolution terrain and timely local observations; the BFM does, and thus is able to more accurately characterize battlefield weather both spatially and temporally.

The BFM will essentially serve as the automated forecast portion of the Local Analysis and Forecast Program (LAFP). In a battlefield scenario, the BFM will automatically determine the influence of terrain and local features on atmospheric conditions which the forecaster has heretofore been determining manually and subjectively in the LAFP process. The BFM calculates intercepted solar radiant energy that is converted to budgeted atmospheric and terrestrial thermal energy over complex gridded terrain — which is translated into pressure gradient driven, mesoscale wind production (e.g., predicted daytime heating of mountains and high terrain reverses nocturnally forced localized downslope drainage flows into upslope flows and vice versa).

BFM initialization will include all observations from the AO such as data from nearby airfield/brigade weather teams, soundings from the division or corps Artillery Met teams, other

deployed military units' weather observation data, and any indigenous observations being transmitted. Data from global or theater scale models are also used in this process, and this is discussed later. Observations from Automated Meteorological Surface Sensors, Unmanned Aerial Vehicles meteorological sensors, and meteorological satellites will also be included in the initialization process as they become available in the future. Initialization can also consist of only the observation taken from the Tactical Operations Center. In the event that no observations are available from the AO, the BFM will be initialized using only the gridded analysis and/or forecast data from global or theater scale models.

Boundary meteorological conditions are automatically input for the region surrounding the mesoscale AO. Typically, these data would be derived from grid point data closest to the AO taken from global or regional model output valid at analysis and forecast times of interest. The BFM forecast is executed using these boundary conditions and AO raw data as initialization guidance and solves towards the forecast solution dictated by the global/theater scale forecast boundary condition gridded data. Thus, large-scale flow patterns produced by the BFM will automatically solve towards the global/theater model's forecast solution.

Looking ahead, we envision the use of mesoscale forecast models as part of the LAFP at most fixed airfields, for test range and shuttle operations, and in more civilian applications such as air pollution episodes, natural disasters and emergencies, etc. In the immediate future, the BFM offers the SWO deployed to an unfamiliar AO the opportunity to accurately predict the weather on the battlescale in real time at resolutions never before possible.

4. BFM IMPLEMENTATION PLAN

4.1 Technical Characteristics

The BFM selected for inclusion in the IMETS Block II software deliverable was developed to provide operational short-range ($\leq$ 12 hour) forecasts. The BFM is suitable for use within battlescale areas ($\leq$ 500 km $\times$ 500 km). The basic equations for the BFM are the conservation relationships for mass, momentum, potential temperature, water vapor mixing ratio, and mean turbulent kinetic energy. The composite influence of diurnally forced solar, atmospheric, and terrestrial radiation effects on evolving Planetary Boundary Layers (PBLs) over complex terrain is accurately simulated by the BFM.

Second-moment[1] mean turbulence equations in the BFM are solved by assuming certain relationships between unknown higher-order turbulence moments and known lower-order moments. Presently, the BFM assumes hydrostatic equilibrium and uses the Boussinesq approximation. The Boussinesq approximation is the assumption that the modeled fluid is

[1] *A second statistical moment is the double correlation, or normalized covariance, of two turbulent quantities (Stull, 1988).*

incompressible to the extent that thermal expansion produces a buoyancy (Huschke, 1959; and Houghton, 1985). Buoyancy forces are retained in a hydrostatic basic state with respect to pressure and density [p_o, ρ_o] via the inclusion of small pressure and density deviations [p', ρ']. This assumption holds as long as the $(\rho_o+\rho')/\rho_o$ term in the vertical equation of motion is close to unity (i.e., density variations are only considered when they are closely coupled to gravity).

4.2 BFM Initialization Interface

The BFM X-window interactive initialization interface, summarized in fig. 1, will provide users with the following flexibility when initializing all model executions:

a. Users will specify the center of the BFM forecast domain via: i) an input longitude and latitude; or ii) a user specified Military Grid Reference System (MGRS) input - consisting of a UTM zone, **x**, and **y** coordinate; or iii) if a map display is active, by using a mouse to graphically point and click at the desired center point on the map background.

b. Table 1 depicts all possible combinations of grid spacing and grid point array configurations to produce the BFM's horizontal dimensions. These options will be specified by users to structure model domains that can range from 40×40 km^2 to 500×500 km^2. An estimate of the model run-time for the specified number of grid points and grid spacing will be displayed on the screen with a display of the selected grid extent before the user executes the BFM program.

c. The BFM is initialized with user selected data inputs. All available and current data will be listed for the automatically defaulted model initialization time. The default initialization times may commence at any hourly interval from 00:00 UTC (i.e. 00, 01, 02, ... 23 Z), which ever is the most relevant to the local IMETS hardware system time and which can also be supported with currently available data; this time will be posted on the interface screen. The primary Boundary Condition (BC) initialization data, as a function of pressure, consists of alternating, 3-dimensional coarse grid (381 km × 381 km grid spacing) sets of 12, 24, and 36 hour forecasts of wind, temperature, water vapor, and geopotential height.

Currently boundary condition data are obtained from the Global Spectral Model (GSM), which is regularly transmitted by the U.S. Air Force (USAF) Global Weather Central via the Automated Weather Distribution System (AWDS). This GSM data has alternating valid times of 00:00 and 12:00 UTC for: i) analyses; and ii) 12, 24, 36, and 48 hour forecast fields. Future plans call for obtaining boundary conditions from the Navy Operational Global Atmospheric Prediction System (NOGAPS) if it replaces the GSM as the AWDS' global model, and finally a higher resolution theater level model, such as NORAPS, when one becomes operational on AWDS.

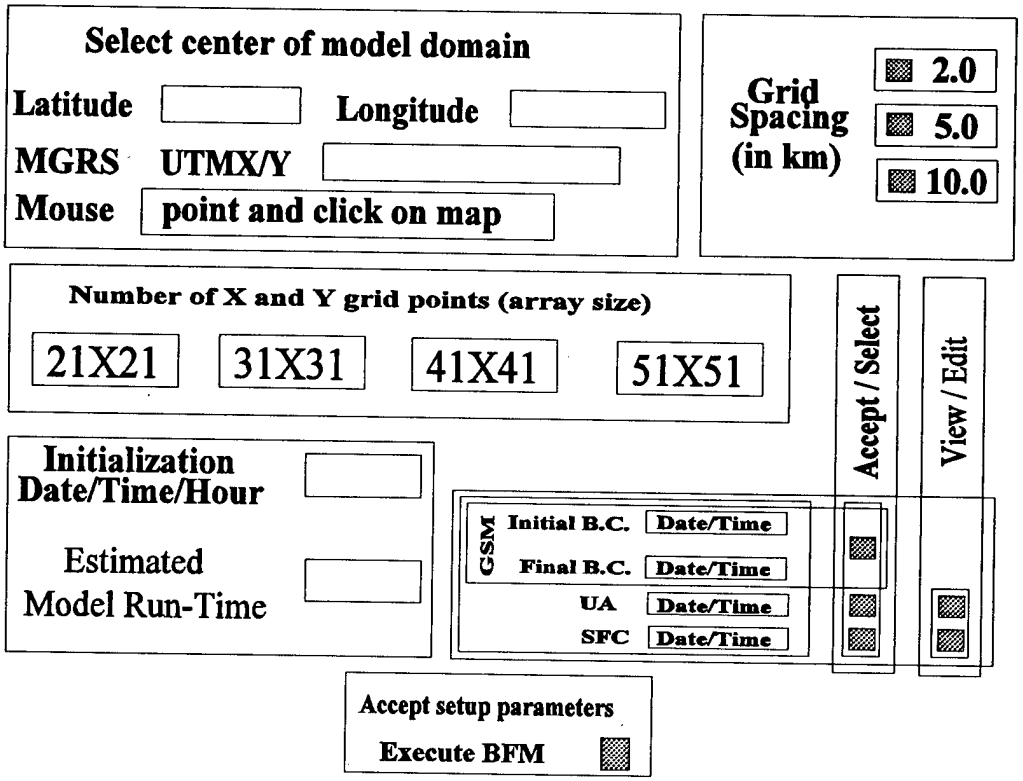


Figure 1. BFM initialization user interface concept.

Table 1. BFM domains in km^2 as a function of user-specified BFM grid spacing.

BFM Parameters	Array Number of BFM Grid Points ↓			
Grid Spacing ↓	21×21	31×31	41×41	51×51
2 km	40×40 km^2	60×60 km^2	80×80 km^2	100×100 km^2
5 km	100×100 km^2	150×150 km^2	200×200 km^2	250×250 km^2
10 km	200×200 km^2	300×300 km^2	400×400 km^2	500×500 km^2

Typically, the set of GSM data necessary to produce a 12 hour BFM prediction will consist of 12, 24, and 36 hour GSM forecasts. This is due to the receipt time-lag of GSM data in the field being typically ≥ 4 hours. For example, a user may desire to run the BFM for a twelve hour period commencing at 07:00 UTC and ending at 19:00 UTC on January 28th. To produce hourly boundary conditions for this forecast, three GSM forecasts will be required (i.e., the 12, 24, and 36 hour GSM forecasts): between 07:00 UTC and 12:00 UTC January 28th hourly boundary conditions will be produced via interpolation between the GSM 12 hour forecast valid at 00:00 UTC January 28th, and

the 24 hour GSM forecast valid at 12:00 UTC January 28th; and finally, for the period between 12:00 to 19:00 UTC on January 28th, BFM hourly boundary conditions will be produced by interpolating between the GSM 24 hour forecast valid at 12:00 UTC January 28th and the 36 hour GSM forecast, valid at 00:00 UTC on January 29th.

During BFM execution, GSM data sets ($\Delta t \geq 12$ hours) are linearly interpolated in time and 3-dimensional space to produce hourly forecast boundary condition data that coincide with the selected BFM time and space domain. The date/time group (or non-availability) of GSM, and/or radiosonde upper-air, and/or surface data, applicable to the selected model domain, will be listed on the user's display. If GSM data are not available, radiosonde data with or without surface data can be used as initialization fields to produce short term forecasts of up to six hours. The user has interactive window mouse/switch control (e.g., ☐ = unselected, or ☒ = an activated option) over the selection of the possible initialization observations, GSM analyses, and forecast data stream to the BFM in this mode. The capability to review and manually edit radiosonde and surface BFM input observation data will also exist.

After all initialization inputs satisfy the user's specifications for the model forecast run, the user starts execution of the BFM via a window interface switch. Actual model execution begins only after an automated initialization data program transforms GSM, surface and upper air data into a BFM compatible format. Upon selecting this switch, if the model domain has been altered from the previous BFM forecast run, the user will be prompted to load the terrain data from a Defense Mapping Agency compact disk applicable to the model domain selected. After this operation is completed, model execution commences.

4.3 BFM Output Interface

Upon completion of the model forecast run a BFM X-window interactive output interface, summarized in figure 2, will provide users with the following BFM forecast data output review capabilities:

a. The principle BFM calculations consist of forecasted 3-dimensional: 1) **u** and **v** horizontal wind vector components; 2) potential temperature; and 3) liquid water potential - which is the combination, within each grid volume, of all predicted: i)liquid water; and ii) water vapor converted to liquid water. These 3-dimensional forecast fields will be saved at 3 hour intervals over a 12 hour forecast period commencing at the user-specified initialization time.

b. In the field data output mode, users will be able to graphically analyze BFM wind speed and direction, ambient temperature, and/or the relative humidity via line and/or shaded contours (including velocity vectors and/or streamlines for wind fields) at 7 different levels: i) 10 m above ground level (AGL); ii) 250 m AGL; iii)

500 m AGL; iv) 1,000 m AGL; v) 1,500 m AGL; vi) at the 700 mb constant pressure surface; and vii) at the 500 mb constant pressure level.[2]

c. Users will also be able to graphically review vertical profiles of wind speed and direction, temperature, and/or relative humidity (in percent) at user specified points within the model domain. These profiles are constructed by vertically interpolating results between the model domain terrain ground level and the highest model level, using a linear interpolation scheme. Users will be able to select any point within the model domain, to obtain vertical profile outputs, using a mouse to point-and-click on the map background, and/or from manual keyboard entry of point location data. And relevant radiosonde and/or surface observation sites within selected BFM model domains will be graphically identified on the map background display along with the location of domain bounded GSM grid data points.

d. As indicated in the **Parameter Selection** decision frame (fig. 2), the option to select two-dimensional horizontal field predictions of the occurrence of fog and/or stratus are also planned for inclusion in the IMETS Block II BFM. These outputs will be presented in planar Cartesian coordinates above sea level - unlike the remaining parameters, which are in either terrain following Sigma coordinates (10 m → 1,500 m, AGL) or pressure coordinates (700 mb and 500 mb surfaces). Planar Cartesian coordinates are more correlated to the horizontal stratification of fog and/or stratus along geopotential surfaces than terrain following Sigma or pressure surfaces.

5.0 FUTURE PLANS

ARL/BED plans to provide beta releases of the BFM to the Tactical Fusion Systems Branch, Software Engineering Directorate (SED), Communication and Electronics Command Research and Development Engineering Center (CERDEC), Fort Huachuca, Arizona during 1-3QFY95 for testing and evaluation. The final version of the BFM for the IMETS Block II will be delivered to SED/CERDEC 4QFY95 with supporting software documentation to include software design specifications, software test procedures, software user's guide, and verification and validation statistics/reports. SED/CERDEC will then integrate the BFM software into the IMETS Block II and, in partnership with Air Force weather personnel, accredit it for operational use.

---

[2] *Mesoscale atmospheric models are typically designed to focus attention primarily on internal PBL dynamics and interactions near the earth's surface. As a result, global or synoptic scale models are more suitable in making high altitude (e.g., ≤ 500 mb) transport and diffusion predictions, which do not fluctuate significantly compared to the same predictions in the PBL.*

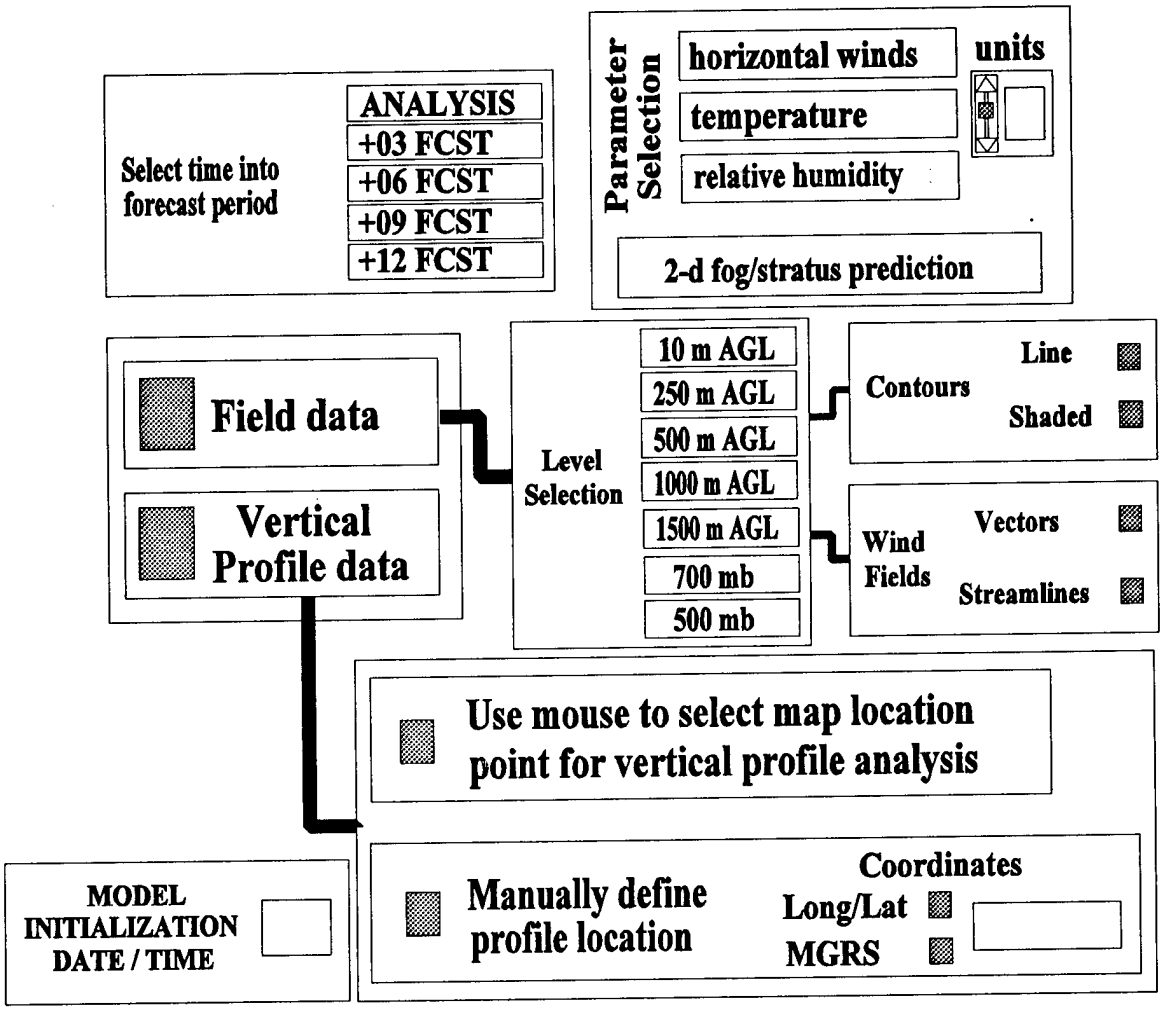


Figure 2. BFM output user interface concept.

Since the objective mesoscale model referred to in paragraph 2.0 will probably not be available until FY97 or later, ARL/BED plans to improve the BFM for the IMETS Block II and III, with improvements delivered to SED/CERDEC in FY96 and FY97 as they become available. Planned improvements include extending the BFM maximum forecast limit of 12 hours to 24 hours in the IMETS Block III delivery, better quality control and editing of input data, and increased output parameters to include turbulence and icing index, temperature and moisture advection, vorticity, visibility, precipitation, improved cloud predictions, and meteorological satellite data assimilation. Other I/O interface refinements, resulting from a maturing "user feedback-product improvement cycle" anticipated to occur, will also be implemented. Once the objective model matures then it will replace the BFM, provided its performance in comparison to the BFM justifies replacement.

REFERENCES

Houghton, D.D. (Editor), 1985: **Handbook of Applied Meteorology**, John Wiley & Sons, 1461 pp.

Huschke, R.E. (Editor), 1959: **Glossary of Meteorology**, American Meteorological Society, 638 pp.

Liou, Chi-Saan, Hodur, R., and Langland, R., 1994: "NORAPS: A Triple Nest Mesoscale Model," *Proceedings of the Tenth American Meteorological Society Conference on Numerical Weather Prediction*, Portland, Oregon.

Stull, R.B., 1988: **An Introduction to Boundary Layer Meteorology**, Kluwer Academic Publishers, 666 pp.

T. Yamada and S. Bunker, 1989: A Numerical Model Study of Nocturnal Drainage Flows with Strong Wind and Temperature Gradients, Journal of Applied Meteorology, Volume 28, 545-554.

DEVELOPMENT AND VERIFICATION OF A LOW-LEVEL AIRCRAFT TURBULENCE INDEX DERIVED FROM BATTLESCALE FORECAST MODEL DATA

Major David I. Knapp and MSgt Timothy J. Smith
Operating Location N, Headquarters Air Weather Service
White Sands Missile Range, NM

Robert Dumais
U.S. Army Research Laboratory
White Sands Missile Range, NM

ABSTRACT

Improving the accuracy of low-level aircraft turbulence forecasts is addressed using high resolution gridded data and terrain fields to derive localized horizontal and vertical wind flow patterns. Two objective upper-level aircraft turbulence indices are tested at lower levels using mesoscale model data in an effort to calculate "first guess" estimates of potential low-level turbulence areas. The Turbulence Index (TI) is the product of two independent terms, vertical wind shear and the sum of the horizontal deformation and convergence. The Panofsky Index (PI) is a function of horizontal wind speed and the Richardson Number. The TI, its independent terms, and the PI are calculated, stratified and evaluated using multivariate linear regression for specific low-level layers across three CONUS mesoscale regions for 20 cases from January to April 1993. Using results from the regression analyses, new low-level turbulence forecast equations are proposed for future refinement and verification.

1. INTRODUCTION

Staff Weather Officers and forecasters supporting U.S. Army aviation operations provide low-level turbulence analyses and forecasts for fixed and rotary wing aviation missions. New advancements in the use of "smart" munitions and unmanned aerial vehicles sensitive to turbulence make these forecasts even more important to mission accomplishment. Forecasters generally rely on empirical low-level turbulence forecast rules that have been used for years, resulting in the habit of consistently underforecasting or overforecasting suspected turbulence areas.

Upper-level instabilities believed to cause turbulence have been approximated using the components of Petterssen's (1956) frontogenesis equation. Mancuso and Endlich (1966) found that the deformation and vertical wind shear components of this equation were independently correlated with the frequency of moderate or severe turbulence. Ellrod and Knapp (1992) went further by deriving a turbulence index (TI) based on certain assumptions to Petterssen's equation. Assuming that frontogenesis results in an increase in vertical wind shear (VWS), horizontal deformation (DEF), and horizontal convergence (CVG), a similar increase in turbulence occurrence should also be expected. For a given layer, the index is stated as:

$$TI = VWS \times (DEF+CVG), \qquad (1)$$

The range of TI values associated with turbulence occurrence were found to be model-dependent based on grid resolution and other physical and dynamic parameter calculations unique to every model. Typical TI values ranged from 1.0 to 12.0 ($x10^{-7}s^{-2}$), with highest values correlated with moderate and greater turbulence intensities.

At levels below upper-level jet stream maxima, Ellrod and Knapp found the TI's performance to be unreliable. This was attributed to coarse synoptic scale model grid-point resolution that missed the more subtle features in low-level wind fields contributing to turbulence occurrence. The resolution problem is solved by deriving the TI from mesoscale model grid data. The purpose of this study is to evaluate the TI and its individual component indices at lower levels. This is part of a project to find or develop an accurate objective low-level turbulence forecast technique for future use by Air Force Staff Weather Officers supporting the U.S. Army.

2. MODEL AND TURBULENCE TECHNIQUE DESCRIPTIONS:

The Higher Order Turbulence Model for Atmospheric Circulations (HOTMAC) was used to provide a mesoscale nowcast analysis of meteorological variables using observed upper-air and surface data reported at rawinsonde locations. This analysis is produced by horizontally interpolating observed rawinsonde wind data onto the mesoscale grid with a resolution of 20 km. In the vertical, wind observations are interpolated to predefined levels. Utilizing a transformation to a terrain-following vertical coordinate system, 22 staggered levels are retained to allow for high resolution (Yamada and Bunker, 1989), with eight levels within the first 1000 feet AGL, five levels from 1,000-5,000 feet AGL, and eight levels from 5,000-16,000 feet AGL. (NOTE:

Hereafter, levels AGL will be in hundreds of feet, i.e., 010-050, 050-160, etc.) Rawinsonde data reported from 00 UTC provide the raw input to the mesoscale objective analysis for this study. The TI is calculated from HOTMAC's u and v wind components at each grid point in the horizontal and vertical. Layer average values of VWS, DEF, and CVG are used for the final TI calculation at every grid point for each prescribed layer.

3. TECHNIQUE VERIFICATION

The TI has been tested using data in the Huntsville, Chicago, and Denver mesoscale regions (Fig 1) for twenty 00 UTC cases during February, March, and April 1993. Point verification was used to verify the TI's effectiveness using pilot reports (PIREPs) from 2130 UTC to 0230 UTC for each case studied. PIREP data included reports of turbulence level(s) and intensity, as well as reports of no turbulence for each case. If a PIREP did not contain any turbulence remarks, it was not counted as a valid report. A program was written to extract values for the TI and its components at the grid point closest to each verifying report. Turbulence reports in the vicinity of thunderstorms were not included in the verification process. Data from the National Lightning Detection Network were used to filter out these reports in or near active cloud-to-ground lightning strikes during the times studied. Reports from heavier aircraft (i.e., civilian airliners and military transports) were also eliminated from the database to keep findings specific to the lighter-weight aircraft used by the Army. The majority of the reports in the database were from these lighter aircraft, resulting in only 5% of the reports being filtered out.

Turbulence reports were assigned numerical values based on intensity to establish correlation coefficients when compared to grid point output from each of the techniques. Intensities, abbreviations, and corresponding numerical values are listed in Table 1. Correlation coefficients (r) for the TI at different turbulence intensities in all three regions studied for the 010-040 and 040-070 levels are shown in Tables 2 and 3, respectively. The TI is shown to be a poor indicator of NEG and LGT intensities. However, for reports of LGT-MDT or greater turbulence, r-values centered around .80 show a good relationship between calculated TI values and intensities for both layers below 070.

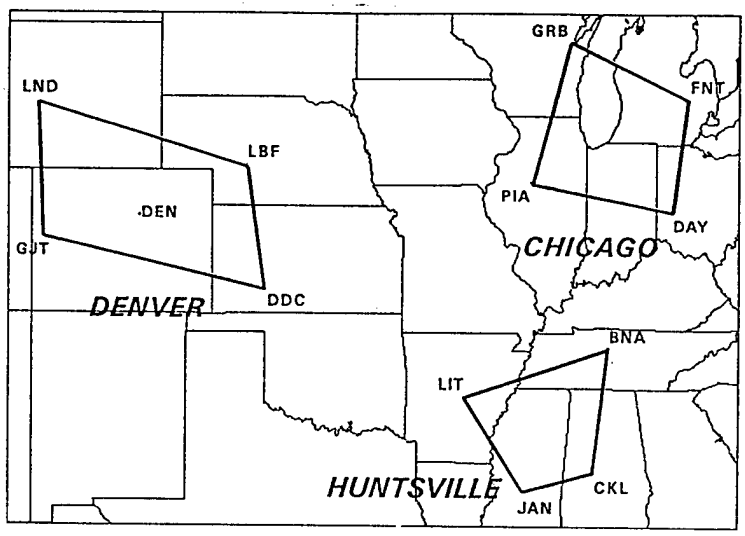


Figure 1. Mesoscale regions used for turbulence study. RAOB locations indicated with 3-letter identifiers.

Table 1. Turbulence intensities and abbreviations with associated numerical values.

PILOT REPORT		NUMERICAL VALUE
No Turbulence	NEG or NIL	0
Light	LGT	1
Light-Moderate	LGT-MDT	2
Moderate	MDT	3
Moderate-Severe	MDT-SVR	4
Severe	SVR	5
Severe-Extreme	SVR-XTR	6
Extreme	XTR	7

Table 2. Correlation coefficients (r) relating turbulence parameters to turbulence intensities from 010-040 in the three mesoscale regions studied for 20 cases from February-April 1993. INTENSITY values taken from Table 1. # is the number of pilot reports in the sample.

INTENSITY	#	TI	VWS	[DEF + CVG]	VWS AND [DEF + CVG]
ALL	54	.58	.21	.51	.51
0-1	37	.22	.07	.21	.21
>1	17	.80	.49	.80	.81
>2	9	.80	.32	.81	.86

Table 3. Same as Table 2, for the 040-070 layer.

INTENSITY	#	TI	VWS	[DEF + CVG]	VWS AND [DEF + CVG]
ALL	66	.58	.24	.58	.59
0-1	48	.10	.04	.07	.08
>1	18	.79	.49	.77	.78
>2	11	.84	.64	.76	.80

4. TOWARD AN IMPROVED TURBULENCE INDEX

In a case study of moderate and greater turbulence reports occurring across the Huntsville region (Knapp, et. al., 1993), turbulence reports occurred in regions of varied VWS and DEF+CVG. A report of extreme turbulence was reported near the center of an area of maximum DEF+CVG with a minimum of VWS. Reports of moderate and moderate-severe turbulence occurred in local maxima of VWS with only moderate values of

DEF+CVG. No distinctive pattern from either term could be seen as dominating the other. Based on this case, and on the 19 other cases examined for each mesoscale region, r-values were also calculated independently for each of the TI's terms (VWS and DEF+CVG). These are also summarized in Tables 2 and 3. As for the TI, VWS and DEF+CVG performed poorly as turbulence indicators for the NEG and LGT intensities, while statistics dramatically improve for greater intensities. In both layers, DEF+CVG correlated better with turbulence intensity than did VWS, implying the importance of horizontal wind flow changes in low-level turbulence generation. Notice also that VWS r-values increased significantly in the higher layer (Table 3). DEF+CVG compared favorably to the TI as an independent low-level LGT-MDT and greater turbulence indicator. Treating the TI's two independent terms together in a multi-variate analysis shows this new combination slightly outperforming the TI from 010-040 (Table 2) with the reverse occurring from 040-070 (Table 3).

Another index considered was the Panofsky Index (PI), which has been used by the Navy to forecast low-level turbulence up to 850mb (Boyle, 1990). The formula for this index is

$$PI=(\text{windspeed})^2 x[1.0-Ri/Ri_{crit}] \qquad (2)$$

where windspeed is the average speed in the prescribed layer in ms^{-1}, Ri is the Richardson Number, and Ri_{crit} is a critical Richardson Number. This value should theoretically be .25 for very fine scale data, but in this study (using 3000 foot layers) as well as for the Navy's purposes (1000mb-850mb layer), the best empirically derived value is 10.0. The PI takes into account vertical wind shear as well as the vertical lapse rate by virtue of the Richardson Number. Studies for the Huntsville region included the PI as an additional turbulence index. As an independent term considered by itself, r-values for the PI were insignificant for all layers. However, when treating it as an independent term in a multivariate analysis with DEF+CVG, r-values exceed all others at both low levels studied (Tables 4 and 5).

Table 4. Same as Table 2, for the 010-040 layer in the Huntsville Region.

INTENSITY	#	TI	VWS AND [DEF + CVG]	PI AND [DEF + CVG]
ALL	26	.68	.65	.63
0-1	17	.12	.25	.39
>1	9	.81	.87	.87
>2	6	.82	.96	.97

Table 5. Same as Table 4, for the 040-070 layer.

INTENSITY	#	TI	VWS AND [DEF + CVG]	PI AND [DEF + CVG]
ALL	23	.66	.63	.64
0-1	16	.31	.08	.58
>1	7	.80	.82	.81
>2	5	.87	.90	.91

Based on the high correlation coefficients shown in Tables 2 through 5, new indices for predicting low-level turbulence intensities are derived as linear regression equations. Using data for the 010-040 layer which produced the r-values depicted in Tables 2 and 4 for all turbulence intensities, the following equations can be derived as a starting point for future refinements and verification:

$$Y=.0065(TI)+1.0888 \quad (3)$$

$$Y=.0078(DEF+CVG)-.0003(VWS)+1.074 \quad (4)$$

$$Y=.0089(DEF+CVG)+.0006(PI)+1.1751 \quad (5)$$

where Y is turbulence intensity as defined in Table 1; TI, VWS, and DEF+CVG are in units as depicted in Figs 3, 4, and 5, respectively; and the PI is not scaled.

5. CONCLUSIONS

A previously validated upper-level aircraft turbulence index (TI) was studied using mesoscale model gridded analysis data in an effort to develop a useful objective low-level index for use by military forecasters. The TI output were shown to be strongly correlated with LGT-MDT or greater intensity for light-weight aircraft. A TI case study

examining the specific contributions of each term of the TI was accomplished. This led to further correlating turbulence occurrence and intensity for each pilot report independently with each term of the TI. DEF+CVG proved to be comparable to the TI as a turbulence indicator. Combining DEF+CVG with VWS as two independent variables in a regression improved performance as correlation coefficients exceeded those of the TI from 010-040. Another tool, the Panofsky Index (PI), was combined as an independent term with DEF+CVG to produce correlation coefficients which exceed all others.

New turbulence potential tools derived as multivariate linear regression equations were proposed for further study. These equations will be refined by increasing the database from which they were derived with additional data from the winter 1994 season. Final equations will then be verified for both intensity and horizontal extent of turbulence forecast areas using an independent data set from 1992.

REFERENCES

Boyle, J.S., 1990: *Turbulence Indices Derived From FNOC Fields and TOVS Retrievals*, NOARL Technical Note 47, Naval Oceanographic and Atmospheric Research Laboratory, Stennis Space Center, MS 39529-5004.

Ellrod, G.P., and D.I. Knapp, 1992: "An Objective Clear-Air Turbulence Forecasting Technique: Verification and Operational Use." *Wea. Forecasting*, **7**: 150-165.

Knapp, D.I., T.J. Smith, and R. Dumais, 1993: "Evaluation of Low-Level Turbulence Indices on a Mesoscale Grid." In *Proceedings of the 1993 Battlefield Atmospherics Conference*, U.S. Army Research Laboratory, White Sands Missile Range, NM 88002-5501, pp 501-514.

Mancuso, R.L., and R.M. Endlich, 1966: "Clear Air Turbulence Frequencies as a Function of Wind Shear and Deformation." *Mon. Wea. Rev.*, **94**: 581-585.

Petterssen, S., 1956: *Weather Analysis and Forecasting, Vol 1*. McGraw-Hill Book Co., 428 pp.

Yamada, T., and S. Bunker, 1989: "A Numerical Model Study of Nocturnal Drainage Flows With Strong Wind and Temperature Gradients." *J. Appl. Meteor.*, **28**: 545-553.

CURRENT AND FUTURE DESIGN OF U. S. NAVY MESOSCALE MODELS FOR OPERATIONAL USE

1994 BATTLEFIELD ATMOSPHERICS CONFERENCE

R. M. Hodur
Naval Research Laboratory
Monterey, CA 93940-5502

ABSTRACT

The Naval Research Laboratory (NRL), which has developed, implemented, and improved Navy operational mesoscale models for over 10 years, plans a series of further significant improvements. The current operational system, the Navy Operational Regional Atmospheric Prediction System (NORAPS), has produced over 35,000 operational forecasts over the past 12 years. This has been possible through the computer support and cooperation with personnel at the Fleet Numerical Meteorology and Oceanography Center (FNMOC), co-located with NRL in Monterey. NORAPS is a complete data assimilation system that contains 4 major components: 1) quality control to maintain consistency and integrity of the incoming data, 2) multivariate optimum interpolation analysis, 3) nonlinear vertical mode initialization, and 4) a hydrostatic forecast model with physical parameterizations for cumulus, radiation, and the planetary boundary layer. Three major design changes are being developed and tested. The first is the incorporation of horizontally nested grids, which will allow for high-resolution (10 km or less) over limited domains. The second is the development of a nonhydrostatic atmospheric model which will replace the hydrostatic model in NORAPS within the next two years. The third project is a redesign of the operational mesoscale system so that it can be ported to other mainframes and/or workstations with little or no modifications. This will allow for use of the prediction system by other labs, universities, regional forecast centers, and aboard Navy ships. These design changes will ensure that the U. S. Navy maintains state of the art mesoscale forecasting capabilities, particularly in littoral regions, for the years to come.

1. INTRODUCTION

The U. S. Navy is poised to move into a new era of operational numerical weather prediction (NWP). The first era began over 20 years ago when FNMOC implemented, and began running on a twice-daily basis, a hemispheric model based on the primitive equations using a grid spacing of 381 km and 5 levels (Kesel and Winninghoff 1972). The focus of this model was to provide 3 day forecasts of systems of synoptic-scale and larger. The next era in U. S.

Navy NWP began about a decade later with the introduction of the Navy Operational Global Atmospheric Prediction System (NOGAPS, Rosmond 1981), the Navy Operational Regional Atmospheric Prediction System (NORAPS, Hodur 1982), and the arrival of high-speed vector processors. The purpose of NOGAPS was to provide 3-5 day global forecasts for systems of synoptic-scale and larger. NORAPS, on the other hand, using a horizontal grid-spacing approximately one-third that of NOGAPS, was implemented to produce 24-48 h forecasts over given regions of the world. The NORAPS forecasts were used as an "early-look" when run before NOGAPS, and to provide mesoscale forecast information due to its higher resolution. Over the past decade, both NOGAPS and NORAPS have improved due to increased computer speed and memory, and also due to improvements in the prediction systems themselves. Now, with the arrival of another generation of supercomputers featuring vector and parallel processing, the Navy is preparing for another era of improved NWP products. The improvements to NOGAPS and computer technology have already been such that NOGAPS is now capable of mesoscale forecasts previously performed by NORAPS. This implies that we must push mesoscale modeling to higher resolutions, which calls for a redesign of the model equations and parameterizations. It is expected that these improvements to our mesoscale effort will lead to NWP forecasts that can directly support future battlescale missions.

The purpose of this paper is to describe the current and future design of Navy mesoscale NWP. A description of the currently used mesoscale model, NORAPS, is given in Section 2. A description of the system that will replace NORAPS, the Coupled Ocean/Atmosphere Mesoscale Prediction System (COAMPS), is given in Section 3. Section 4 presents the work being conducted to allow for the use of NORAPS and/or COAMPS on a workstation. A summary is presented in Section 5.

2. NORAPS

The structure of NORAPS is basically unchanged from that described by Hodur (1987), that is, NORAPS is a mesoscale data assimilation system with four major components: quality control, analysis, initialization, and forecast model. The system is designed so that it can be run over any region of the world using any of the following map projections: Mercator, Lambert Conformal, polar stereographic, or spherical. The grid spacings and grid dimensions can be set to any value within the speed and memory limitations of the computer system. Global databases of terrain, surface roughness, albedo, and ground wetness are bilinearly interpolated to the model grid for each forecast application.

The NORAPS analysis is now based on the multivariate optimum interpolation (OI) technique using the volume method similar to that described by Lorenc (1986). The D-values and u- and v-components are analyzed at 10, 20, 30, 50, 70, 100,150, 200, 250, 300, 400, 500, 700, 850, 925, and 1000 mb. Wind observations are used from radiosondes, pibals, aircraft reports including ACARS data, SSM/I, surface reports over the water, and cloud track winds. D-values and/or thicknesses are obtained from radiosondes, and DMSP and NOAA satellites. All data is subject to the complete quality control (QC) system which includes the National

Meteorological Center's (NMC) complex QC of radiosondes (Collins and Gandin 1990) as well as the more traditional QC techniques described in Baker (1992) and Norris (1990).

The NORAPS hydrostatic forecast model is based on the primitive equations using the sigma-p vertical coordinate system. The horizontal grid is the Arakawa and Lamb (1977) staggered "C" grid. The nonlinear vertical mode initialization described by Bourke and McGregor (1983) has been incorporated as an integral part of the forecast model. Recent improvements of the physical parameterizations include the use of the Louis (1982) surface layer parameterization, the Detering and Etling (1985) turbulence parameterization and the Harshvardhan et. al. (1987) radiation scheme, which includes cloud interactions.

Several improvements of NORAPS are currently being worked on. The first is horizontally nested grids, which will allow for high resolution (10 km or less) over given areas of interest. Another advantage of the nested grid structure is to move the boundary zone where NORAPS and NOGAPS fields are blended together as far away from the area of interest as possible. The second improvement is the ability to predict aerosols. Currently, we allow for generation of sea-salt aerosols over water, specifying a point source of aerosols at any point in the grid, advection, diffusion, fallout, and rainfall scavenging. The third improvement is in the PBL parameterization in which we are examining methods to introduce counter-gradient flux terms into the model, thereby giving us more realistic temperature and moisture profiles.

3. COAMPS

The use of a hydrostatic mesoscale model, such as NORAPS, with resolutions finer than about 10 km, can pose problems in certain situations. These occur when the hydrostatic assumption is violated, i.e., when vertical accelerations become significant. Events such as convection, sea breezes, and topographic flows often exhibit strong nonhydrostatic effects and these need to be included for proper simulation. To account for these effects, NRL is developing a new mesoscale model using the fully compressible form of the primitive equations following Klemp and Wilhelmson (1978). This model is the atmospheric component of the Coupled Ocean/Atmosphere Mesoscale Prediction System (COAMPS). The other component of COAMPS is a hydrostatic ocean model (Chang 1985). The two models can be used separately or in a fully coupled mode. Although the ocean model plays a vital role in the basic research we conduct with COAMPS, the remainder of this section will focus on the details and plans for the nonhydrostatic atmospheric model only.

COAMPS has been designed to make the transition from a hydrostatic model within NORAPS to a nonhydrostatic model as easy as possible. This has been done by incorporating many of the details already in NORAPS into COAMPS. This includes the data QC and multivariate OI analysis. COAMPS also has the same global relocatability features found in NORAPS, and the user can set the type of grid projection, the number of nested grids (a maximum of 3 is allowed), as well as the grid dimensions and resolutions of each mesh.

The COAMPS atmospheric model is based on the sigma-z vertical coordinate. The prognostic

variables are the u-, v-, and w-components of the wind, perturbation exner function (related to perturbation pressure), potential temperature, water vapor, cloud droplets, raindrops, ice crystals, snowflakes, and turbulent kinetic energy (tke). The choice of five moisture variables allows for the explicit prediction of clouds, rain, and snow, using the Rutledge and Hobbs (1983) explicit moist physics scheme. For resolutions coarser than 5-10 km, such as for the coarser meshes of a nested grid simulation, cumulus parameterization must still be used. For this, we have included a scheme developed for mesoscale convective events (Kain and Fritsch 1990, Kain 1993). The 1-1/2 order tke prediction scheme presented by Deardorff (1980) is used. The Harshvardhan et. al. (1987) radiation scheme, used in NORAPS, is also included in COAMPS.

4. PORTABILITY

Until very recently, the computational power needed to execute numerical models such as NORAPS or COAMPS existed only on large mainframes. However, workstation technology has now improved to the point where these models can be tested on them, although the best performance is still on vectorized, multi-processor machines. Given the pace of workstation technology, it is expected that over the next few years, realistic, operationally useful forecasts will be produced on workstations.

To take advantage of this emerging technology, NRL is leading a program, the purpose of which is to make the mesoscale prediction systems, NORAPS and COAMPS, easy to port to other systems. The benchmark operational systems will still reside at NRL/FNMOC in Monterey, but execution of a single program can build a file containing all the source code and the surface parameters databases that are required to run and install either system. This file can then be sent, via tape, internet, etc., to another machine in which the install program is used to install the system. At this point, the remote site must have the ability to get fields for the first guess and boundary conditions, as well as observational data.

Of course, there are certain constraints on the portability of these systems. First, the source code is written in the FORTRAN language. Currently, we adhere to FORTRAN 77 standards, but will be transitioning to FORTRAN 90 standards over the next year or so. Second, the prediction systems require the use of dynamic memory allocation. While this is a standard feature in FORTRAN 90, it only exists as extensions on some FORTRAN 77 compilers. Third, it is required that the operating system be UNIX, or a compatible version, such as UNICOS, on Cray machines. Generalized scripts to execute, build, and install NORAPS and COAMPS are written for the UNIX operating system. In addition, the generalized database that we use in these systems is based on the existence of a UNIX environment.

The portability of NORAPS and COAMPS is rapidly becoming a reality. Recently,we have ported each prediction system to other Cray systems and have been able to perform data assimilation experiments the same day. Porting to smaller workstations is still under development. The long term goal is to be able to use NORAPS or COAMPS for data assimilation at a regional center or onboard a Navy ship. The first step toward accomplishing

this goal will be taken in the SHAREM 110 exercise in the Gulf of Oman during February 1995. During this time, NORAPS will be run at FNMOC for the Gulf of Oman area and the forecast fields will be sent to a remote station near the Gulf of Oman. There will be a workstation at this location on which the NORAPS multivariate OI analysis is installed. Analyses will be generated at this site using the NORAPS forecast fields for the first guess and all on-scene observations. This will serve as a test for the communication, personnel, hardware, training, and timing necessary to extend this to a full on-scene predictive capability.

5. SUMMARY

The U. S. Navy is committed to improving its mesoscale NWP capabilities. The major focus is on improving its efforts in the numerical prediction of mesoscale events in littoral regions. Recent improvements to our current operational mesoscale model, NORAPS, such as improved boundary layer and radiation parameterizations and horizontally nested grids make it a practical choice for now. We are also developing a new mesoscale forecast system, COAMPS, which will use all the functionality already found in NORAPS, but which is also better suited to mesoscale prediction since it uses a nonhydrostatic formulation and can perform explicit prediction of precipitation processes. The operational switch from NORAPS to COAMPS is expected to occur within the next 2 years. Finally, both NORAPS and COAMPS have been designed so as to be used on systems other than mainframe supercomputers. This feature makes these systems attractive for porting to other mainframes for research or to workstations at other labs, regional centers, or onboard Navy ships.

ACKNOWLEDGMENTS

The support of the sponsors, Office of Naval Research under program element 0602435N, and Space and Naval Warfare Systems Command under program element 0603207N, is gratefully acknowledged.

REFERENCES

Arakawa, A., and V. R. Lamb, 1977: "Computational design of the UCLA general circulation model." *Methods in Computational Physics*, Vol. 17, Academic Press, pp 173-265.

Baker, N. L., 1992: "Quality control for the Navy operational atmospheric database." *Wea. Forecasting, 7:*250-261.

Bourke, W. and J. L. McGregor: "A nonlinear vertical mode initialization scheme for a limited area prediction model." *Mon. Wea. Rev., 111:*2285-2297.

Chang, S. W., 1985: "Deep ocean response to hurricanes as revealed by an ocean model with free surface. Part I: Axisymmetric case." *J. Phys. Oceanogr., 15:*1847-1858.

Collins , W. G., and L. S. Gandin, 1990: "Comprehensive hydrostatic quality control at the National Meteorological Center." *Mon. Wea. Rev., 118:*2752-2767.

Deardorff, J. W., 1980: "Stratocumulus-capped mixed layers derived from a three-dimensional model." *Bound.-Layer Meteor., 18:*495-527.

Detering, H. W., and D. Etling, 1985: "Application of the E-ϵ turbulence model to the atmospheric boundary layer." *Bound.-Layer Meteorol., 33:*113-133.

Harshvardhan, R. Davies, D. Randall. and T. Corsetti, 1987: "A fast radiation parameterization for atmospheric circulation models. *J. Geophys. Res., 92:*1009-1016.

Hodur, R. M., 1982: "Description and evaluation of NORAPS: The Navy operational regional atmospheric prediction system." *Mon. Wea. Rev., 110:*1591-1602.

Hodur, R. M., 1987: "Evaluation of a regional model with an update cycle." *Mon. Wea. Rev., 115:*2707-2718.

Kain, J. S., and J. M. Fritsch, 1990: "A one-dimensional entraining/detraining plume model and its application in convective parameterization." *J. Atmos. Sci., 47:*2784-2802.

Kain, J. S., 1993: "Convective parameterization for mesoscale models: The Kain-Fritsch scheme." *The representation of cumulus convection in numerical models. Meteor. Monogr. No. 24*, Amer. Meteor. Soc., pp 165-170.

Kesel, P. G., and F. J. Winninghoff, 1972: "The Fleet Numerical Weather Central operational primitive-equation model." *Mon. Wea. Rev., 100:*360-373.

Klemp, J., and R. Wilhelmson, 1978: "The simulation of three-dimensional convective storm dynamics." *J. Atmos. Sci., 35:*1070-1096.

Lorenc, A. C., 1986: "Analysis methods for numerical weather prediction." *Quart. J. Roy. Meteor. Soc., 112:*1177-1194.

Louis, J. F., M. Tiedtke and J. F. Geleyn, 1982: "A short history of the operational PBL-parameterization at ECMWF. *Workshop on Planetary Boundary Parameterization*, ECMWF, Reading, pp 59-79. [Available from The European Centre for Medium-Range Weather Forecasts, Shinfield Park, Reading RG2 9Ax, U. K.]

Norris, B., 1990: "Preprocessing and general data checking and validation." *Meteorological Bulletin of the ECMWF.* M1.4-3., European Centre for Medium-Range Weather Forecasts, Reading, U. K.

Rosmond, T. E., 1981: "NOGAPS: Navy operational global atmospheric prediction system." *Preprints Fifth Conf. Numerical Weather Prediction*, Monterey, CA, pp 74-79.

Rutledge, S. A., and P. V. Hobbs, 1983: "The mesoscale and microscale structure of organization of clouds and precipitation in midlatitude cyclones. VIII: A model for the "seeder-feeder" process in warm-frontal rainbands." *J. Atmos. Sci., 40:*1185-1206.

COMBAT WEATHER SYSTEM CONCEPT

Mr James L. Humphrey
Science Applications International Corporation
Headquarters Air Weather Service
Scott Air Force Base, Illinois 62225-5206

Maj George A. Whicker, Capt Robert E. Hardwick,
2nd Lt Jahna L. Wollard, SMSgt Gary J. Carter
Headquarters Air Weather Service
Scott Air Force Base, Illinois 62225-5206

ABSTRACT

Current weather information is critical in a deployed environment, however, in a combat environment it can mean the difference in mission success or failure. Air Force units supporting Joint Forces Commander, Air Force, and Army combat operations require the means to produce and apply environmental information to support the employment of military power. The Combat Weather System (CWS) will enable users to provide combat and support forces the required timely and accurate global, theater, and local weather information for effective planning, deployment, employment, and redeployment in response to worldwide crises. The CWS will integrate highly capable automated weather observing and forecasting systems into a light-weight easily transportable system capable of meeting the CWS critical mission, which is, to support launch and recovery of aircraft. Headquarters Air Weather Service, Directorate of Program Management and Integration is the CWS Standard Systems Manager and is the interface with the Implementing Agency, Electronic Systems Center, Weather Systems Division. There will be two major components of CWS: observing and forecasting. The observing components will provide accurate observations of more weather elements and distribute these data more quickly than current systems to the weather forecast system. The forecasting portion provides a platform on which forecasters can integrate observations and generate tailored forecast information quicker and make it readily available for operational customers through the automated Theater Battle Management Command, Control, Communications, Computer and Intelligence systems. The mission areas supported by CWS will be Air Force: Counter Air, Strategic Attack, Interdiction, Close Air Support, Strategic Airlift, Aerial Refueling, Aeromedical Evacuation, Operation Support, Airlift, Electronic Combat, Surveillance and Reconnaissance, Special Operations, Base Operability and Defense, and Logistics; and Army: Aviation, Air Defense, Close Combat (Heavy/Light), Land Combat Engineering Support, Special Operations, Fire Support, Biological, and Chemical operations. The CWS is being acquired to provide the warfighter, planner, and commander the current, timely, and accurate weather information.

1. INTRODUCTION

Air Force, Army, Joint and Combined warfighters require detailed weather observations and forecasts across the depth and breadth of the combat zone to refine mission tactics and to manage combat resources. The system to meet these needs must be a small, lightweight, modular system for maximum functionality. It must be durable, quickly activated, packaged for rapid deployment, and field maintainable. The systems' modular design must allow for an initial deployment capability that can be expanded, as required, to a more capable system.

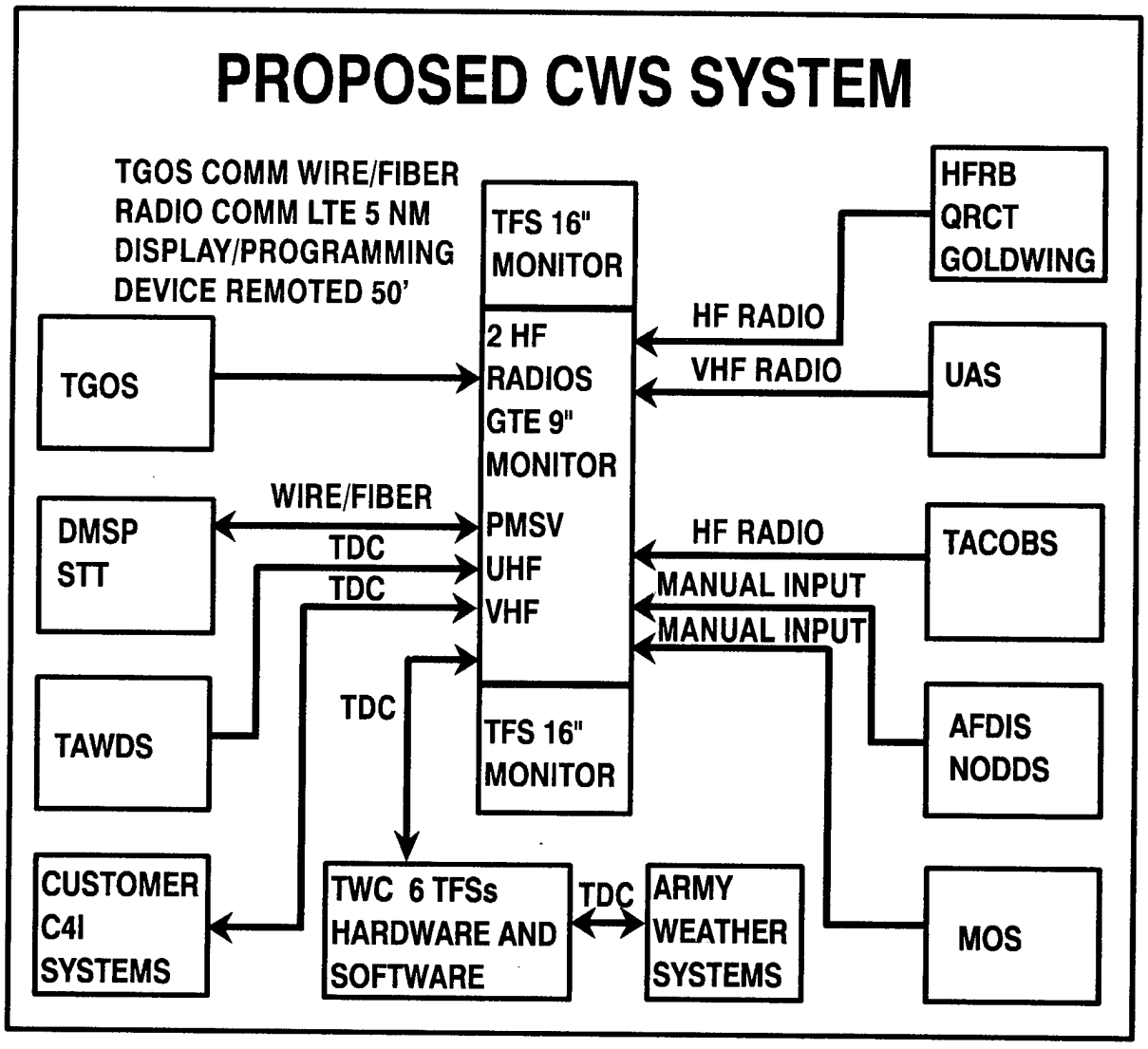


Figure 2.1 Proposed CWS System

The system must also provide responsive, reliable, accurate weather information in near real time directly to the warfighter/decisionmakers. Combat Weather System (CWS) was proposed and developed to meet these needs. The CWS was to have two components, Tactical Forecast System (TFS) and Tactical Weather Observing System (TWOS). Recent funding cuts have canceled all funding for CWS beyond FY95. As a result, CWS, as originally planned, has been canceled. The system was to be fielded in FY96 to FY99. While Air Weather Service (AWS) is no longer able to field a deployed weather system as defined by the operational users in the CWS Opperational Requirements Document (ORD) 211-89-I/III, there still remains valid mission needs. USAF Statement of Operational Need (SON) 211-89, Tactical Weather Observing Systems (TWOS), 5 Mar 90, and USAF SON 212-89, Tactical Forecast System (TFS), 3 Aug 90, define the needs. AWS has developed a plan to acquire and field a TFS and TWOS capability that will satisfy the stated needs for initial combat operations.

2. REQUIREMENTS

The primary objective is to integrate highly capable forecasting and automated weather observing systems with combat planning and execution systems (Figure 2.1). The TFS and TWOS will enhance the effectiveness of combat operations by improving the capability of deployed weather forces to produce comprehensive and timely weather decision products for combat zone commanders, planners, and aircrews. The critical and most basic mission for the TFS and TWOS is to support launch and recovery of aircraft by: providing tailored weather support, which includes receipt of data, ingesting, displaying, processing, and disseminating data and products (excluding administrative functions); and observing weather elements (cloud height, cloud amount, surface wind speed and direction, surface visibility, surface free air temperature, and surface pressure). This primary objective and critical mission must be met while meeting the users stated set-up/tear-down times, weight and size requirements. The set-up/tear-down requirement is for two people in full chemical protective clothing to be able to complete either function in 6 or less hours. The size requirement is for the system to fit within the 2/5 standard 463L airlift pallet. The TWOS will provide accurate observations of weather elements and distribute these data more quickly than current systems permit to the weather forecast system and operational customers. In turn, the TFS will integrate these observations and generate tailored forecast information quicker and distribute it faster to operational customers through the automated Theater Battle Management (TBM) Command, Control, Communication, Computer, and Intelligence (C4I) systems. The weather operator will use the TFS to build weather products to meet the needs of the Air Force's C4I systems. The main weather data source will be Air Force Global Weather Central (AFGWC) via long haul communications reach back capability. TFS will be interoperable (be able to exchange data) with other services; e.g., Navy, environmental support systems at the AF Component Theater Weather Center (TWC), and at lower levels as appropriate. Additionally, TFS must respond to single points of failure both within and outside the theater and degrade gracefully to a point where it will function with whatever data is available (e.g., complete data set, set of theater observations only, or single-station). The TFS must produce the most accurate analysis and

forecast fields current state-of-the-art technology and science provides to meet operational customer requirements.

3. OPERATIONAL CONCEPT

TFS will provide a first-in and eventually a sustainment capability for the conduct of weather operations and will be interoperable with automated C4I systems such as the Contingency Theater Automated Planning System (CTAPS), Wing Command and Control System (WCCS), and Command and Control Information Processing System (C2IPS) (Figure 3.1).

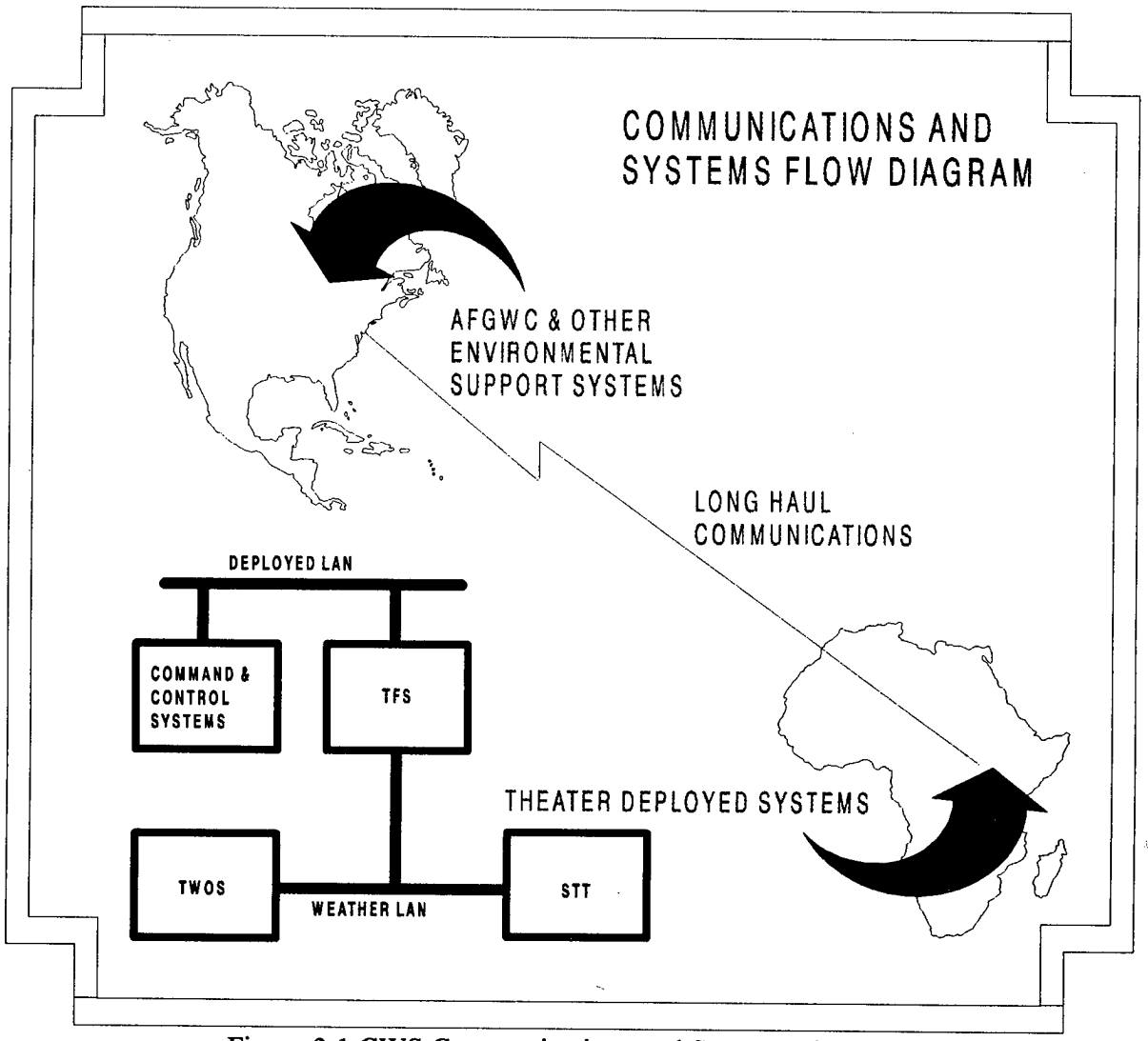


Figure 3.1 CWS Communications and Systems Flow Chart

Figures 3.2 and 3.3 show examples of TFS display screens.

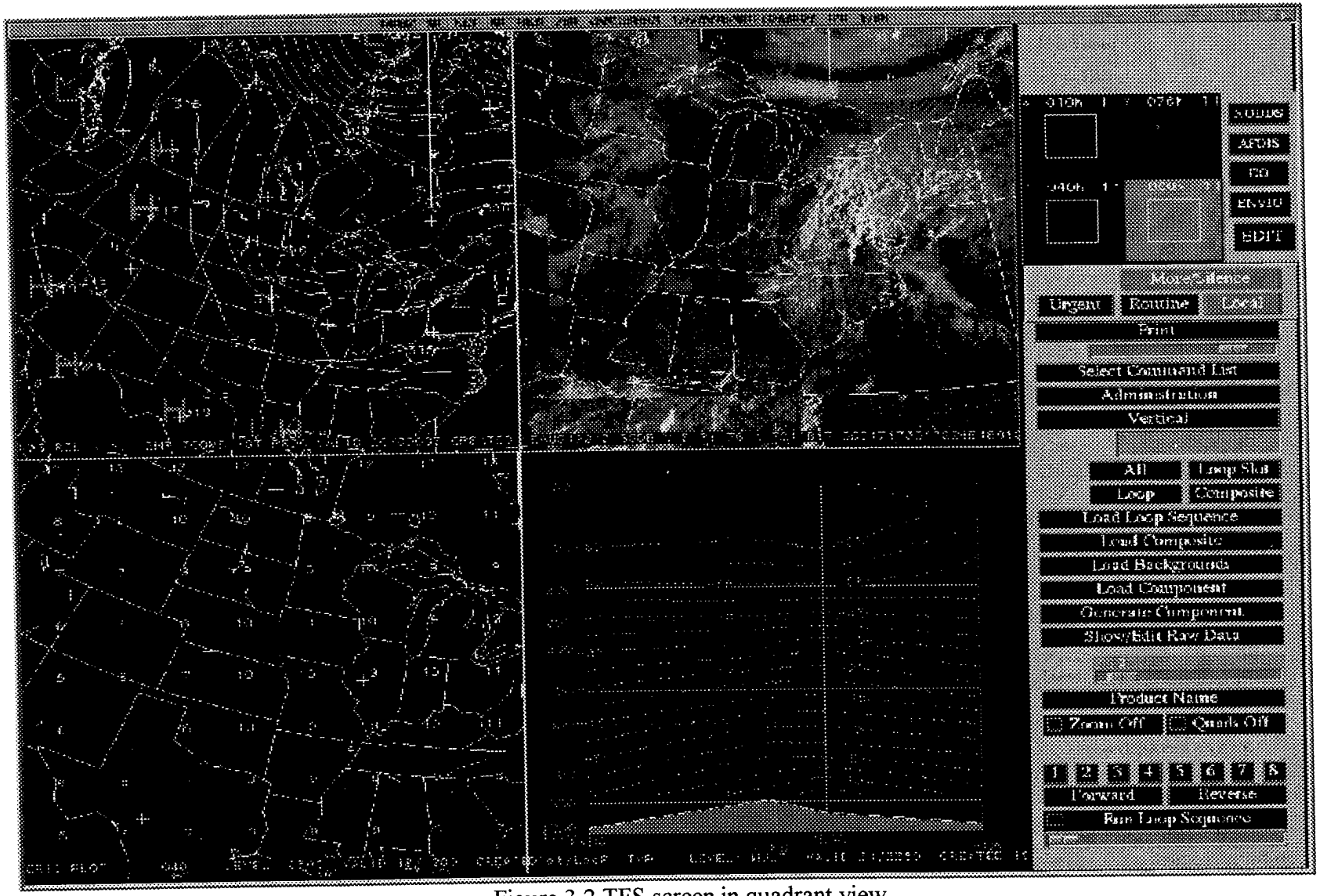


Figure 3.2 TFS screen in quadrant view

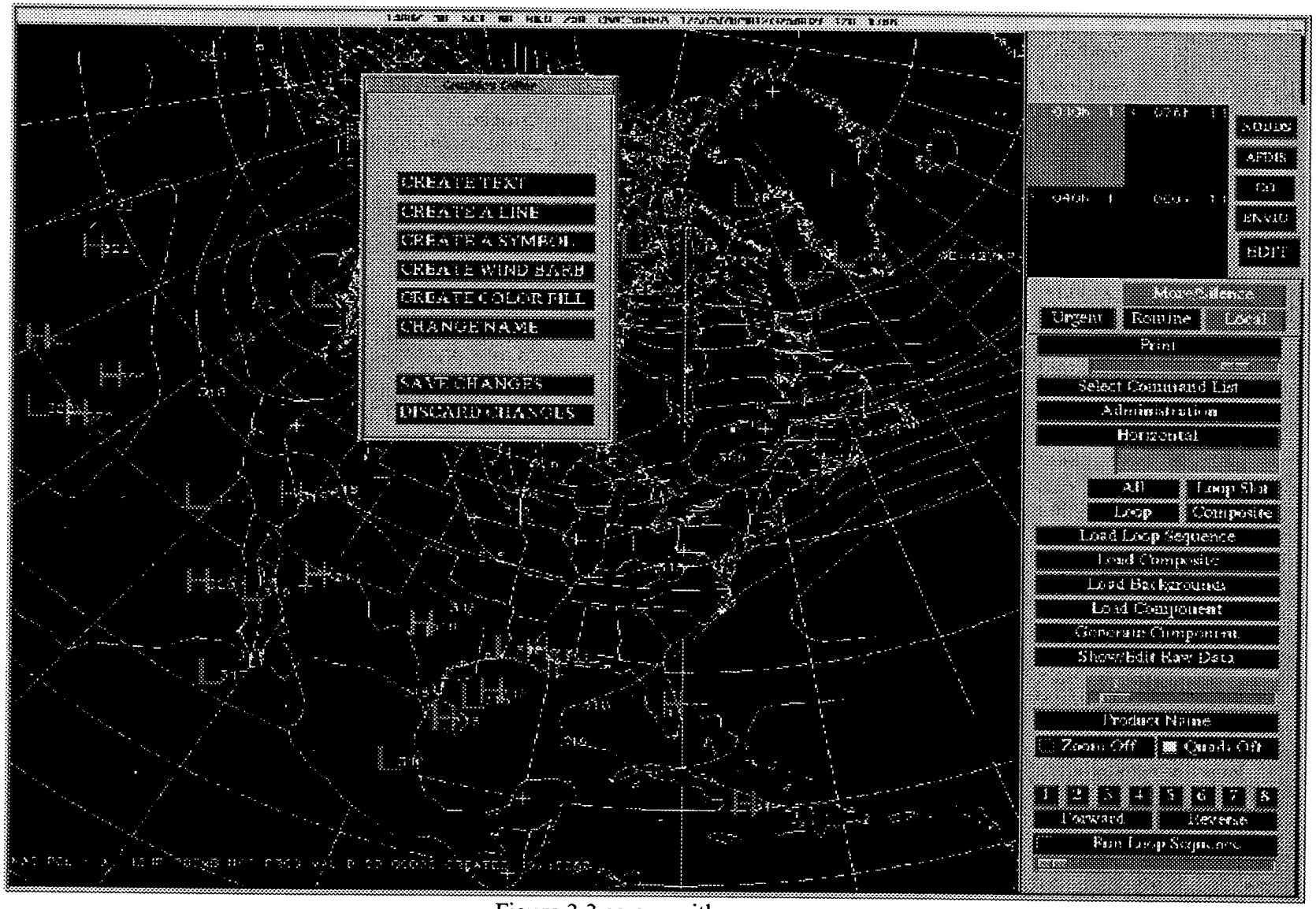


Figure 3.3 screen with pop-up menu

Weather data in the C4I weather data base will be in a standard relational data base format that will enable personnel on C4I user positions to overlay weather products on products from any other functional area. C4I customers can use their systems to access weather information (observations, forecasts, warnings, and advisories, etc.) and locally generated mission forecast products. In addition, weather operators using the TFS will make available gridded weather data fields on the C4I data base for use by automated mission planning and intelligence applications. The TFS will also allow weather operators to access and display information from the C4I data base to generate mission-specific forecasts; e.g., display flying operations data from the Air Tasking Order (ATO) and target information from the Intelligence Summaries to tailor and provide departure, enroute, and recovery flight weather briefings. TFS fielding will allow a shift in weather operator duties; a decrease in face-to-face support and an increase in weather data base interpretation, manipulation, and systems management duties. However, weather operators will still be required to augment automated weather observations and provide direct support to customers upon their request. Exact configuration of the TFS and TWOS deployed/employed will vary depending on the mission and customer supported.

4. PROGRAM EXECUTION

Under the revised phased program (Figure 4.1), the software developed under the original CWS program, exploiting existing Automated Weather Distribution System (AWDS) and Combat Air Forces Weather Software Package (CAFWSP) software, would become the TFS software baseline. AWS would then purchase the CAF standard hardware on which the TFS software would be hosted. Under this plan, the total number of TFSs would be reduced to 44 systems.

	PROGRAM SCHEDULE						
EVENT	1995	1996	1997	1998	1999	2000	2001
TFS SOFTWARE BASELINE	⇧						
TFS HARDWARE 44 SYSTEMS	⇧						
MOD TFS SOFTWARE			⇧				
ADDITIONAL TFS HARDWARE			⇧				
MOD EXISTING TACMET				⇧			⇧

Figure 4.1 Program Schedule

These systems will be single user positions verses the three-position systems in the original program. This represents a great reduction in total numbers, however, operational users would have a standard deployable state-of-the-art system by late 1995. This would insure compatibility

between MAJCOMs in the deployed environment. In 1997 the plan is to acquire the remaining TFSs to meet the users requirements. Additionally, AWS would seek to modify the TFS Software Baseline in the FY98-01 time frame to incorporate changes to the AWDS software and to integrate a tactical automated observing capability. This tactical automated observing capability would be achieved via modification programs to replace and upgrade existing Tactical Meteorological systems (TACMET), i.e., Transportable Cloud Height Detector (GMQ-33), Tactical Meteorological Observing System (TMQ-34), and Tactical Wind Measuring Set (TMQ-36). These modified systems may be modular enough to meet most of the original TWOS requirements.

5. CONCLUSION

In today's environment of shrinking budgets, new and innovative approaches to meeting operational requirements will have to be considered and employed. As a representative of the user, AWS is deeply committed to meeting the users operational requirements. With the planned phased approach a modicum of success can be salvaged from a program broken by fiscal constraints and a redirection of national priorities.

6. REFERENCES

Air Force PMD 2326(3)/PE0604707F/0305111F/0305117F/0305123F, Program Management Directive for the Weather System (WXSYS) - IWSM 20 Jun 94.

USAF Statement of Operational Need (SON211-89), Tactical Weather Observing Systems (TWOS), 5 Mar 90.

USAF SON 212-89, Tactical Forecast System (TFS), 3 Aug 90.

CWS Operational Requirements Document I (ORD I), 26 Mar 93.

Air Force Systems Command /Military Airlift Command Mission Area Analysis, Weather 2000, 20 Sep 84.

Air Force System Command Electronic Systems Division Technical Alternatives Analysis 30 Sep 91.

Concept Paper for Weather Support to Air Force Theater Operations 1995-2005, 5 May 92.

SMALL TACTICAL TERMINAL (STT) CONCEPTS AND CAPABILITIES

2Lt Stephen T. Barish
Mr. George N. Coleman III, Maj Tod M Kunschke
Directorate of Systems and Communications
Headquarters Air Weather Service
Scott Air Force Base, Illinois 62225-5206

ABSTRACT

Real-time satellite imagery is vital to first-in deployed troops and aircraft; it can enhance the mission's effectiveness and ensure a maximum safety margin for deployed personnel. It is often the only source of meteorological data available upon deployment. As such, Air Force weather teams require the capability to receive, process, and display real-time satellite imagery in order to support Army, Air Force, and Joint Force combat operations world-wide. The Small Tactical Terminal (STT) will provide users with a stand-alone platform to receive and process real-time polar orbiting meteorological satellite data from the Defense Meteorological Satellite Program (DMSP) and National Oceanographic and Atmospheric Administration (NOAA) satellites. It will receive near real-time geostationary weather facsimile (WEFAX) data from both foreign and domestic satellites. There are three configurations of the STT, each designed for use during specific phases of any conflict. The Basic STT is a first-in asset intended for rapid deployment to the theater and receives low-resolution imagery. The Enhanced STT consists of a modular kit added to the Basic STT and will be used in the sustainment phase of the operation. It adds the capability to receive high resolution data from DMSP and NOAA satellites. The Joint Task Force Satellite Terminal (JTFST) consists of a modular kit added to the Enhanced STT and is a sustainment phase asset intended to provide weather support to the theater commander. It adds the capability to receive high resolution data from geostationary satellites. All STT configurations will interface with the following weather forecasting systems: Tactical Forecast System (TFS), Transportable Automated Weather Distribution System (TAWDS), and Integrated Meteorological System (IMETS). They will provide the warfighter, mission planner, and commander real-time satellite imagery for use in operations from the first-in through sustainment phases of a conflict. Headquarters Air Weather Service, Directorate of Systems and Communications is the STT User Representative and interface to the Implementing Agency, Space and Missile Center, Defense Meteorological Satellite Program.

1. INTRODUCTION

The United States Air Force and Army provide forces for the world-wide conduct of combat operations. Military personnel operate in both peace-time and war-time scenarios. Past experience has shown a direct correlation between mission effectiveness and accurate,

dependable knowledge of present and future weather conditions. In a war-time scenario, the ability to observe and forecast weather conditions in both the local area of operations, as well as over hostile territory, vastly enhances the ability of Army and Air Force pilots to successfully complete their missions and return home safely. In peace-time, accurate weather observations give pilots critical information needed to fly sorties safely, while ground forces' mobility can be enhanced significantly..

One of the most effective sources of real-time weather data, and the sole-source over enemy-held territory, is meteorological satellite data. The Air Force has long recognized the need of its combat planners, commanders, and pilots to have recent, accurate, and dependable weather observations in order to accomplish its mission. However, the Air Force has a capability shortfall in meeting its combat weather operations commitments.

The lessons learned from Operation DESERT SHIELD/DESERT STORM showed current tactical direct satellite readout terminals do not meet the full needs of deployed forces. Current systems do not provide a fast enough data refresh rate, often have limited data reception, and are too large to be easily transported. Additionally, current systems require too many personnel to operate. While interim systems were procured to fill the gap in the short run, a long-term solution was needed. Thus, Headquarters USAF directed Air Weather Service (AWS) and Space and Missile Center (SMC) to acquire a small, light-weight, tactical, semi-automated, two-person transportable tactical satellite imagery receiver, the Small Tactical Terminal (STT).

2. OPERATIONAL CONCEPT

In today's global society, threats to the United State's National Security and foreign interests can crop up virtually anywhere with very little notice. The way the Air Force mobilizes has changed to reflect this. Combat forces must now deploy with little to no notice to any location world-wide, taking with them their support organizations and services. Weather operations are no exception.

Weather teams in the deployed environment will retrieve their equipment from the airlift or other mode of transportation used to transport them in-theater. In general, there will not be an established source of meteorological data. This is particularly true for those Air Force weather personnel dedicated to supporting Army units. Once deployed to a secure area, a weather team will set up for operations. The STT will be one of the first weather systems deployed. It will provide real-time satellite imagery, and enable weather teams to begin performing their duties within an hour of arrival. It will operate 24 hours per day, for a minimum duration of 30 days without re-supply, with no dependence on outside communications. It is light-weight, highly reliable, and easily maintainable, all of which enhance its capability as a combat system.

The STT will operate in three configurations, each with its own concept of operations. The Basic STT (BSTT) (Fig 2.1), weighing 470 pounds, is the bare-base system. It is deployed with the initial cadre of weather forecasters and observers to deployed units in-theater. The BSTT gives weather teams low resolution satellite data from a variety of sources, both foreign

and domestic. It allows weather teams to give mission planners, commanders, and pilots up to the minute satellite imagery over the theater.

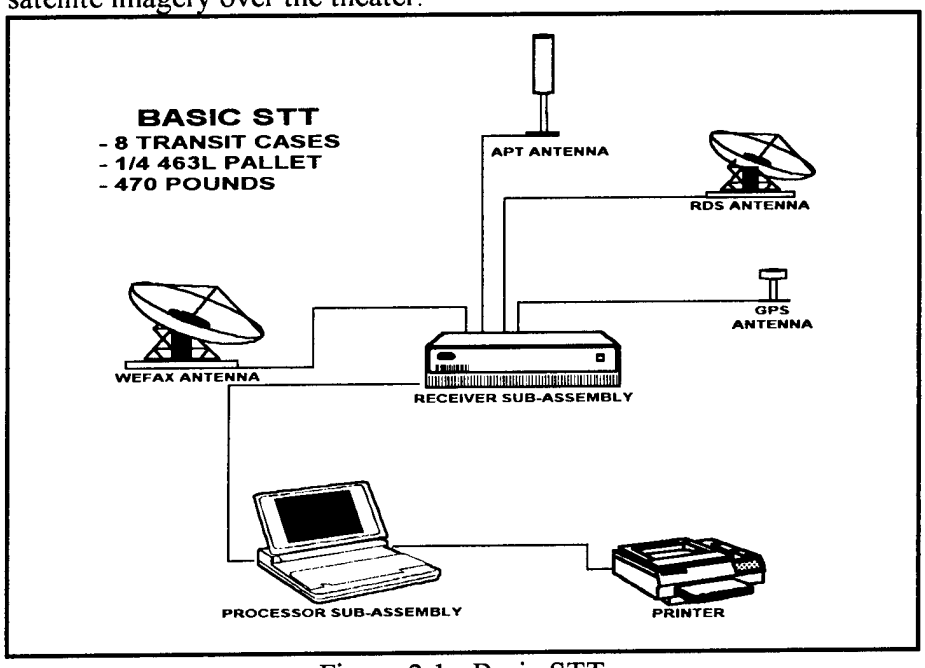


Figure 2.1: Basic STT

The Enhanced STT (ESTT) configuration is composed of the BSTT and an Enhancement Kit. The ESTT receives high-resolution imagery from polar orbiting satellites in addition to the low resolution data available on the BSTT. The enhancement kit will typically follow the BSTT to the theater within the first 30 days of deployment, although it can be deployed at any time. The ESTT weighs 790 pounds and is intended to operate as a sustainment asset.

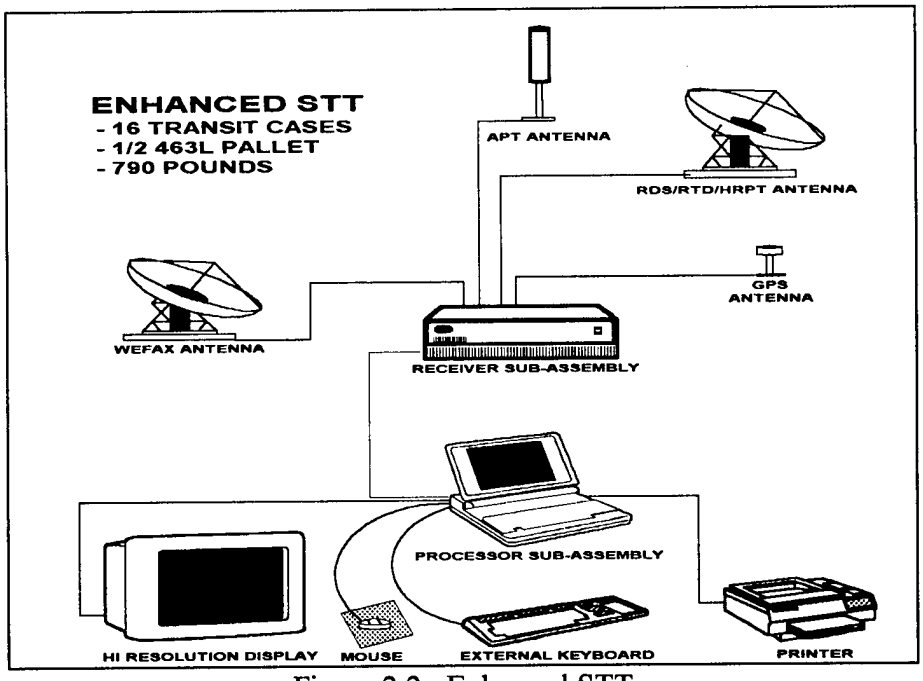


Figure 2.2: Enhanced STT

The final configuration, the Joint Task Force Satellite Terminal (JTFST), is a modular addition to the ESTT. The JTFST receives high-resolution data from geostationary satellites. The JTFST kit will deploy during the first 30 days, and will be used at theater weather centers, and Joint Task Force command/control centers. This configuration is still in its design phase, but certain key physical parameters are known. The completed JTFST will weigh less than 3000 lbs. It will receive high-resolution geostationary data. It will allow operators to send satellite products to remote customers via a facsimile network, or via the Air Force weather link into the command, control, communications, computers, intelligence (C4I) network.

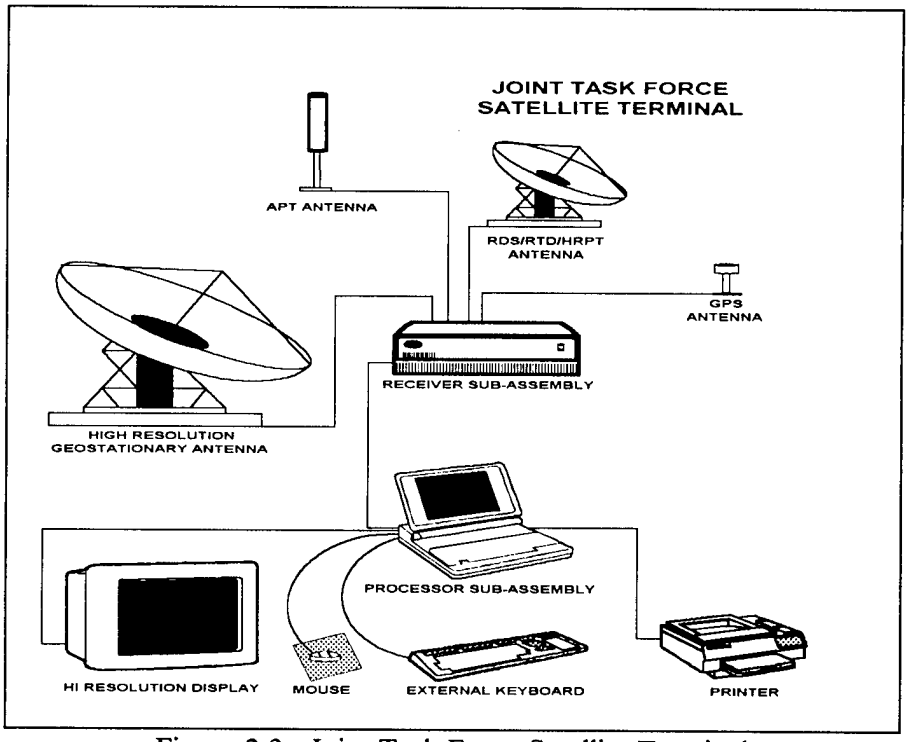


Figure 2.3: Joint Task Force Satellite Terminal

3. MAINTENANCE CONCEPT

The STT was designed to be a highly reliable system. However, it also had to be capable of being maintained by weather personnel rather than dedicated technicians. This concept of Operator Maintenance allows the fielding of a new system without additional maintenance personnel. This approach provides unique challenges to the program. First, there is a design issue: weather personnel are not trained as technicians, and the equipment and any maintenance actions are designed with this in mind. Second, there is a training issue: weather personnel have never performed Operator Maintenance before, and the learning curve will be steep initially. Third, there is a maintenance issue: preventative maintenance is essential to keep any equipment operating correctly. The STT is designed to simplify preventative maintenance.

The solutions to these problems are found in the maintenance concept and in the system design. In the field, weather teams will remove and replace large components of the system

called Line Replaceable Units (LRUs). The STT LRUs will be large items, such as a receiver sub-assembly or the computer. Removal and replacement of LRUs will not require weather teams to open any chassis, or replace any electrical circuit cards or components. All LRUs can be removed without the use of hand tools. This minimizes the level of technical expertise necessary to maintain the system.

When a system fails in the field, the operator will initiate a Built In Test (BIT) routine, and identify the problem. The BIT will isolate the problem, and direct the operator to a set of actions to correct the malfunction. The operator will remove the faulty LRU, replace it with a spare, and return the faulty LRU to the supply office at his/her location.

The faulty item will then be shipped back the maintenance depot at Sacramento Air Logistics Center (SM-ALC), McClellan AFB, CA. The depot will repair the faulty LRU in-house or send it to the manufacture for repair.

Additionally, when the faulty item is shipped back to depot, a replacement spare will be shipped back to the deployed weather team. As no single removal/replacement action will take greater than 30 minutes, the down time of the system will be minimal. In the event an LRU fails and there is no spare on site, the system is designed to be redundant. If any single source of data becomes unavailable, the remaining data sources will still be available. This redundancy assures the operator mission capability in virtually all failure modes.

These maintenance procedures will be extensively addressed during initial skills training, as well as through an aggressive recurring training program. Additionally, the system's software has a built in help program designed to provide quick access to these procedures. The training effort will be minimized as the maintenance actions will be virtually identical with the set up and tear down actions.

The only other maintenance actions are preventative maintenance instructions. These are limited to the cleaning and changing of filters, and occasional loading or cleaning of the printer. Otherwise, the STT requires no preventative maintenance. This addresses the third issue, since there will be no calibration of the equipment necessary to keep it working properly.

4. THEORY OF OPERATION

The STT system is designed as a direct satellite read out terminal. The system's antennas receive telemetry and data from polar orbiting and geostationary meteorological satellites. The receivers then synchronize (bit synch) the data stream and pass the data along to the COMSEC equipment for decryption (if necessary). Once the data is decrypted, the receiver then sends it to the processing equipment for framing into an image. The data are processed into visible and infrared imagery, and assorted meteorological products. The processing equipment is also the operator's point of interaction. By using a graphical user interface (GUI) the operator can manipulate and enhance the data, resulting in better observations and forecasts.

The STT hardware is designed to be rugged and transportable. It is capable of operating in extremes from 0°C to 55°C (for the computer equipment -- antennas are operable down to - 45°C). All connectors are ruggedized, environmentally sealed, and require no tools to connect. In fact, all fasteners and connectors on the system are captive hardware and cannot be separated from the system. The entire system can be assembled without using any hand tools. Size and weight of the hardware were minimized wherever possible without reducing effectiveness.

Much of the hardware exploits state of the art technology. The computer that operates the STT software uses a Sun SPARC 10/41 microprocessor, one of the more powerful microprocessors currently available. This highly capable processor is packaged in a specially designed, ruggedized laptop, using an active-matrix color 10.2 inch LCD monitor. In the enhanced configuration, a 16 inch color monitor is added, along with an external keyboard and mouse to allow operators to interact with the machine more effectively. The receivers were designed specifically for this system. Each receiver is contained on a single PC board, all of which are contained in a single chassis. Also contained in the receiver sub-assembly are the Communications Security (COMSEC) devices, and a removable hard drive. The COMSEC devices were also specially engineered for this system (to minimize weight). Figure 4.1 shows a block diagram of the system's design.

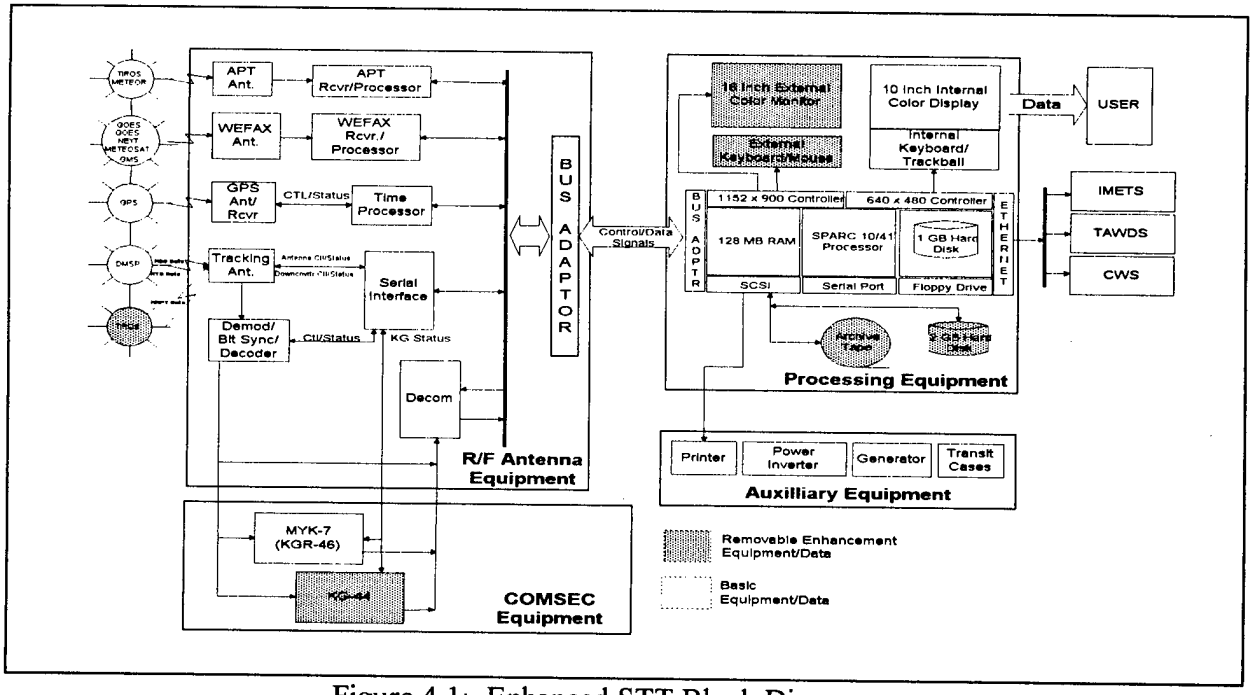


Figure 4.1: Enhanced STT Block Diagram

The robust hardware is complemented by a well-designed and stable software package. The STT software was designed in accordance with the Software Engineering Institute's principles, and in accordance with applicable sections of DOD-STD 2167A. This design approach yielded a mature software package capable of fully exploiting the unique advantages of the system's hardware.

The software operates in the Unix environment, is Unix/POSIX compliant, and uses an X-Windows/Motif interface. The Graphical User Interface (GUI) allows the operator to quickly and easily perform a wide variety of meteorological analyses on the data, with little wait time. The true benefit of the GUI is found in its simplicity. All functions of the software can be accessed quickly, and with a minimum of instructions. The GUI performs multiple tasks: it provides an interactive interface with the data, monitors equipment status, informs the operator of equipment failure, logs significant events occurring in both hardware and software (including both failure data and corrective maintenance data), and provides a computer based instruction (CBI) module that covers set up and tear down of the equipment, use of the COMSEC devices, and maintenance actions.

The software ingests data at the same time the operator is interactively analyzing previous passes, thus minimizing time delays. Typically, an operator will be able to analyze a pass within 2 minutes of the end of the pass. Any stored product will be available within 1 minute of request, and any printed hard copy will be available within 5 minutes of request. In short, the system provides products in a prompt fashion to allow the operator to brief customers with the latest data available.

5. IMAGERY AND PRODUCTS

The STT is designed to receive both polar orbiting and geostationary satellites. Table 5.1 shows the satellite data each configuration of the STT will receive.

Satellite	BSTT	ESTT	JTFST
DMSP RDS (Vis/IR)	X	X	X
DMSP RTD (Vis/IR)		X	X
DMSP Microwave Sensors	X	X	X
NOAA APT (Vis/IR)	X	X	X
NOAA HRPT		X	X
Geostationary (WEFAX)	X	X	X
Geostationary (High-Res)			X

Table 5-1: STT Data Reception

Polar orbiting satellites provide real-time coverage of an area of interest, at a horizontal resolution that is generally greater than that offered by geostationary satellites. There are two types of domestic polar satellites received by the STT: Defense Meteorological Satellite Program (DMSP) satellites, and National Oceanographic and Atmospheric Administration (NOAA) satellites. The STT also receives selected foreign polar orbiting satellites, including Russian METEOR and Chinese FENG-YUNG.

Geostationary satellites provide near real-time weather facsimile (WEFAX) data at a significantly lower resolution than that available on polar orbiting satellites. However, the geostationary imagery gives weather personnel the capability to give a quick, synoptic scale view of the weather in the area of interest. Combined with the ability to set up animation loops, this imagery gives operators a powerful tool to brief their customers. Selected units

receiving the Joint Task Force Satellite Terminal (JTFST) configuration will also have real-time access to high resolution data from geostationary satellites. The STT will receive GOES, GOES-NEXT, METEOSAT, and GMS satellites.

6. ANALYSIS TOOLS

The STT provides weather teams with satellite analysis tools never before available in the combat environment. Users will be able to enhance the data using a variety of tools including image filters and color enhancement. The STT allows the user to zoom into the image, in effect magnifying the image. Any given image can be displayed in the satellite (overhead) projection, mercator projection, or polar stereographic north/south projection. This allows the operator to select the best way to view the data for the given location. The STT also allows operators to annotate images with meteorological symbols and text, thereby adding to the information available to the customer. Additionally, unique tools allow the STT to position the cursor/mouse at specific points of latitude/longitude. This ability is enhanced by the use of the Global Positioning System (GPS), making the STT's latitude/longitude fixes extremely accurate.

The most innovative tool provided by the STT is its ability to generate Environmental Data Records (EDRs) from the Satellite Data Records (SDRs) generated by the microwave sensors on board the DMSP spacecraft. These EDRs give the operator detailed information about the environmental conditions of a region. These EDRs can be viewed as images, and enhanced as such, or they can be viewed as contours, and overlayed on top of DMSP imagery. Again, this capability can dramatically enhance the quality of forecasts and briefings given to customers.

7. EXTERNAL INTERFACES

All the data in the world is useless if it cannot be used to meet the customer's needs. In the world of combat weather operations, many of the customers are commanders and planners. Most of these customers work through the command, control, communications, and computer, and intelligence (C^4I) wide area network set up in theater. There are several combat weather systems which provide inputs to this network. The Transportable Automated Weather Distribution System (TAWDS), the Integrated Meteorological System (IMETS), and the Tactical Forecast System (TFS) are three which the STT interfaces with. These systems act as primary sources of meteorological satellite data for the entire deployed C^4I community.

TAWDS is a currently fielded system that will be modified in late FY95 to accept STT products. These products will be restricted to images, Satellite Data Records (SDRs -- the raw output of the microwave sensors), and EDRs. The images will be transmitted as rasters, the SDRs and EDRs as Uniform Gridded Data Fields (UGDFs). This will allow the TAWDS to overlay these UGDFs on the images and/or other products. IMETS is an Army communications system providing access to the C^4I network. It broadcasts meteorological data and forecasts to deployed users via a set of high frequency radios. Its software is similar to that resident on the TAWDS, and will receive the same products. TFS is the combat forecasting system of the future. It will send weather data from a wide variety of sources to the local C^4I network. The STT will act as a front end satellite data receiver/processor for this

system. It is important to note that while the STT will have a one way interface to TAWDS and IMETS, it will have a two way interface with the TFS, allowing the TFS to remotely log on and operate the STT. This automation allows fewer personnel to accomplish more work in the deployed environment. Raster images and UGDFs will be transmitted to the TFS.

8. CONCLUSION

Combat operations and weather go hand in hand. Accurate weather forecasts enable pilots to avoid dangerous weather conditions, while ground forces are prepared to find easier routes to travel, and positions more advantageous to their mission. Knowledge of future weather conditions is of critical importance when planning aviation missions. Fuel loads, flight safety, take-off and landing are all central elements of any aviation operation, and all are impacted by the weather. On the ground operations side, knowledge of the weather and surface conditions can allow armor divisions to move more rapidly, and prevent them from being bogged down in soft terrain. Troop safety is enhanced by warning of hazardous weather conditions, thus enabling commanders to take protective actions.

Many of today's modern weapon systems employ electro-optical guidance systems. Weather conditions can have significant impact on the effectiveness of these guidance systems. Even aircraft relying on free-fall gravity bombs, or Army troops moving through a battlefield are affected by weather conditions, such as visibility and precipitation. Without a dependable weather forecast, mission planners may not be able to identify achievable mission goals. Without accurate knowledge of current conditions, combat commanders may send their crews into hazardous situations where their mission goals cannot be achieved. In today's military where budget limitations force the services to operate more efficiently, these types of limitations are unacceptable.

Throughout the history of warfare, accurate and dependable knowledge of the weather has been critical to successful mission execution. When properly utilized, weather forecasts can act as a force multiplier, enhancing the combat effectiveness of our air and ground forces. Currently, weather personnel in the combat environment are dependent on sparse sources of data to support their customers. The field of combat weather operations has a critical deficiency in meeting the needs of combat planners, commanders, and pilots.

Air Weather Service and Space and Missile Center, is meeting the challenge. The delivery of the STT, beginning in July 1995, will substantially enhance the quality of today's combat weather operations by providing real-time imagery and products in-theater, and by doing so in a largely automated fashion. This will allow combat weather personnel to concentrate on using the data, rather than gathering it. The Small Tactical Terminal will become a mission critical piece of equipment, and in conjunction with expert Air Force weather personnel, will dramatically improve the safety and effectiveness of the combat operations of the United States Air Force and Army.

9. REFERENCES

General Operational Requirement For a Pre-Strike Surveillance/Recon System (PRESSURS), MAC 508-78, 28 Dec 78.

Air Force Space Command (AFSPC) Mission Need Statement (MNS) for Environmental Sensing (ES), AFSPC MNS 035-92, 6 Jan 93

Operational Requirement Document (ORD) for the Follow-On Defense Meteorological Satellite Program (DMSP), AFSPC ORD 035-92-1-A, 27 Dec 93

Program Management Directive (PMD) for Defense Meteorological Satellite Program (DMSP), PMD 3015(35)/PE030516F/PE0305162F, 3 Sep 93

Small Tactical Terminal (STT) System/Segment Specification, CDRL A024/DI-CMAN-80008A, Contract F040701-93-C-0007, 11 Apr 94

Air Force Systems Command /Military Airlift Command Mission Area Analysis, Weather 2000, 20 Sep 84.

Air Force System Command Electronic Systems Division Technical Alternatives Analysis, 30 Sep 91.

Concept Paper for Weather Operations to Air Force Theater Operations 1995-2005, 5 May 92.

OPERATIONAL USE OF GRIDDED DATA VISUALIZATIONS AT THE AIR FORCE GLOBAL WEATHER CENTRAL

Kim J. Runk and John V. Zapotocny
Headquarters, Air Force Global Weather Central
Offutt AFB, Nebraska, 68113

ABSTRACT

In modern weather support operations, the forecaster is forced to process and assimilate tremendous volumes of data in a short period of time. Thus, it is becoming increasingly important to provide forecasters with tools which enable them to use that information more effectively to quickly and accurately assess the state of the atmosphere and evaluate the meteorological processes affecting the forecast. The Air Force Global Weather Central (AFGWC) has experimented with several such tools which convert gridded data sets into image visualizations and animations for use in the operational forecast routine. These visualization tools have proven to be useful aids for enhancing a forecaster's ability to assimilate the data, providing a greater sense of weather system temporal evolution and numerical model continuity. This paper will discuss and illustrate some of the data visualization methods which have been developed at AFGWC. Particular attention will be given to imagery products created from gridded data unique to AFGWC, such as the RWM (Relocatable Window Model), the HALT (high altitude turbulence) model, and SSM/I (Special Sensor Microwave Imager) mosaic grids.

1. INTRODUCTION

A large assortment of gridded data sets are produced to support operations at AFGWC. Those which are built for use on the Satellite Data Handling System (SDHS), which is the primary delivery system for weather analysis data at AFGWC, are generally formatted into either polar stereographic projection grids, tropical mercator grids, or cross-sectional grids. Spatial resolution of these grids ranges from 48km to 381km, depending on the application. A discussion of the operational grid-to-imagery generation process on the SDHS can be found in Zapotocny (1993).

There are also a number of gridded data sets which are created on Unix-based workstations for the purpose of providing supplemental data visualizations to AFGWC forecasters. Since these tools are delivered as prototypes, forecasters can provide critical feedback to programmers, thereby participating in the definition and refinement of the final software configuration.

2. VISUALIZING OBSERVATIONAL DATA AND NUMERICAL MODEL OUTPUT

The ability to highlight, or even isolate key meteorological features through color imaging is generally superior to the cluttered appearance presented by overlaying several contoured fields. This is particularly true when images are animated in time series. During critical decision periods, when time is short and events are unfolding rapidly, the task of evaluating whether a given region is becoming more favorably disposed toward a specific weather condition can be made more manageable through creative use of model derived imagery products.

A number of operational and prototype data analysis techniques developed by Sterling Software and the Product Improvement Branch at AFGWC provide the forecaster with the flexibility to interactively define the image display structure. This has been well received by forecasters since the suite of tools favored by one is not necessarily the same as that which is preferred by another. One popular technique involves the analyst selecting specific fields, assigning minimum (or maximum) threshold values, then masking out values which do not fall within the assigned range. That data set is then colored using values defined by another field. As an example, hourly grids of surface divergence with an absolute value greater than $2x10^5$ sec^{-1} could be colored with a palette defined by all values of moisture convergence or by the surface-based lifted index from the same array. By employing this form of colorized displays in animation, the forecaster can fashion a more ordered and focused portrayal of the parameters of interest.

Several visualization tools have been designed specifically for viewing or evaluating in-house model output. A variety of display formats, including user-defined plan views, cross-sections, and animations of both observed and derived fields are being developed for operational use.

Four general types of displays are notable for the unique value they add to the forecast process:

(1) *Color-enhanced images overlaid with contours.* This format enables the user to distinguish features in animation more easily; patterns and trends often become more distinctive.

(2) *Time-height cross-sections of individual RWM fields.* These perspectives are often more revealing than viewing a single level in an instant of time.

(3) *Along-track displays of aviation hazards tools.* This technique facilitates tailoring briefings to specific mission requirements utilizing either Global Spectral Model(GSM), RWM or HALT model grids.

(4) *Model error field diagnostics.* These displays provide a quick, objective evaluation of recent model performance, assisting the forecaster in determining the need for, and scope of necessary adjustments to current model guidance.

AFGWC has also begun to explore some new techniques which are very useful for initializing numerical guidance, and for nowcasting convective development. Superimposing tropopause level isentropic potential vorticity and low level equivalent potential temperature on water vapor imagery is one such example. Juxtaposition of these two fields with a well-defined dry prod shows strong correlation with cyclogenesis. Building composites of hourly changes in various surface-based indices of static stability, lid strength, and other convective predictors overlaid on visual satellite imagery is another example.

3. VISUALIZATIONS UTILIZING DMSP IMAGERY

Because AFGWC supports operations and contingencies worldwide, the organization is often called upon to provide weather forecasts in regions for which data availability is extremely limited. In such cases, pass-by-pass animations of polar orbiter imagery are valuable aids for identifying synoptic trends. Animation frames are created by mapping routines which convert images with different local swath orientation to a common map projection. This permits a stable image looping capability over a fixed region in areas with limited or non-existent geosynchronous coverage.

For some limited applications, AFGWC has begun to utilize three dimensional data visualizations in analyzing satellite imagery. The three dimensional view is produced using a combination of surfacing routines and image mapping. The infrared component is used to produce a wire-mesh surface whose height values correspond to brightness temperatures. The visual component is then mapped onto that surface, yielding a three dimensional visualization of the original image. For extended animation sequences, the IR is generally mapped onto itself since continuity of visual data is lost at night.

Several analysis techniques exploiting the capabilities of SSM/I data (NRL Cal/Val, 1991) have been integrated into operations at AFGWC. When blended with corresponding conventional observations, these data can provide significant insight into the character of the synoptic setting.

(1) *Intercomparison of horizontally and vertically polarized 85GHz with IR imagery.*
These perspectives have proven to be useful for detecting thunderstorms concealed beneath large cirrus canopies. This technique is extremely valuable for positioning tropical cyclone circulations.

(2) *Analysis of multichannel algorithms used to estimate maritime surface windspeeds.*
Estimating tropical cyclone gale wind radii or evaluating extent and intensity of wind fields surrounding large polar storms are primary applications of this technique.

(3) *Bichannel differential between 37GHz and 19GHz.* Imagery derived from this data permits qualitative evaluation of surface moisture conditions.

4. FUTURE DIRECTION

At AFGWC, emphasis will continue to be placed on improving our capability to provide timely and accurate weather information to the warfighter. For example, several projects are in progress now to refine our aviation hazards algorithms, such as incorporating the Schultz-Politovich scheme (Schultz, Politovich, 1992) into our aircraft icing forecast algorithm, and upgrading the HALT model (based on Bacmeister et al, 1994) to include background shear.

AFGWC will soon implement an upgrade to faster, more powerful microcomputers for operational production. This robust workstation environment will make widespread application of the types of techniques discussed in this paper much more feasible. In addition, forecasters will have tools at their disposal which permit them to interact with the data themselves, to create their own visualizations and algorithms; in short, to employ new technologies and data sources more creatively and effectively.

While it is true that our applications development is generally oriented toward operations at a weather central, many of these display capabilities could be readily adapted to a tactical environment. In fact, a number of our products are already accessible to deployed troops via the Air Force Dial-In System (AFDIS). Details regarding the AFDIS are outlined in a companion paper in these proceedings (Engel, 1994).

REFERENCES

Bacmeister, J.T., P.A. Newman, B.L. Gary, and K.R. Chan, 1994: "An Algorithm for Forecasting Mountain Wave Related Turbulence in the Stratosphere." ***Wea. and Fcstg.***, **9**: 241-253.

Engel, Gregory T., 1994: "Operational Applications of the Air Force Dial-In System." Proceedings, ***1994 Battlefield Atmos. Conf.***, (in press).

Naval Research Laboratory DMSP SSM/I Calibration/Validation Report, Vol 2. Coordinated by J.P. Hollinger, 1991: NRL, Washington, D.C., 257 pp.

Schultz, P., and M.K. Politovich, 1992: "Toward the Improvement of Aircraft Icing Forecasting for the Continental United States." ***Wea. and Fcstg.,*** **7**: 491-500.

Zapotocny, J.V., 1993: "Meteorological Applications Tools for Generating Images from Gridded Data on the Satellite Data Handling System at AFGWC." Preprints, ***10th Intl. Conf. on Interactive Info. and Proc. Sys. for Meteo., Oceano., and Hydro.,*** Nashville, TN, Amer. Meteor. Soc., 37-38.

THEATER FORECAST MODEL SELECTION

R. M. Cox
Defense Nuclear Agency
Alexandria, VA 22310

J. M. Lanicci
Air Force Global Weather Central
Offutt AFB, NE 68113

H. L. Massie, Jr.
Air Weather Service
Scott AFB, IL 62225

ABSTRACT

Recent contingencies including Operation DESERT STORM have shown a need for a finer-resolution weather forecast capability to aid decision making in theater-level combat air and land operations. To address this need, Air Force Weather (AFW) and the Defense Nuclear Agency (DNA) have begun a joint effort to create a Theater Forecast Model (TFM) architecture from government and commercial off-the-shelf hardware and software.

The concept calls for global model data (temperature, pressure, geopotential, winds, and humidity) of approximately 100 km x 100 km horizontal resolution to provide boundary and initial conditions. The TFM will have a horizontal domain of approximately 2400 km x 2400 km and a horizontal grid mesh resolution of at least 40 km with a goal of becoming approximately 10 km. It will run a 36-hour forecast within 1-hour after data assimilation. The TFM will use in-theater observations as it generates 0 to 36 hour forecast data for theater applications (clouds, visibility, present weather, aviation hazards, etc.).

AFW and DNA are comparing four mesoscale models to the current Air Force Global Weather Central Relocatable Window Model to determine which is best suited for theater operations. The models include the Colorado State Regional Atmospheric Modeling System, the National Center for Atmospheric Research (NCAR)/Pennsylvania State Mesoscale Model, the Navy Operational Regional Analysis and Prediction System, and the DNA Operational Multiscale Environment model with Grid Adaptivity. Comparisons include model numerics, physics, fidelity, accuracy, sustainability, maintainability, flexibility, and extensibility.

Global model data from NCAR and AFW will provide boundary and initial conditions for test cases over five topographically and seasonally complex regions. Accuracy measurements will include interpolated grid point to rawinsonde paired difference root mean square error, mean absolute error, relative error, bias, and evaluations of standard map sets.

This paper will outline AFW and DNA activities to ensure selection of a model best suited to joint needs. A brief overview of numerical weather prediction limitations, the TFM approach, theater requirements, and selection requirements will be presented.

1. INTRODUCTION

Recent contingencies including DESERT STORM have shown a need for finer-resolution weather forecast capabilities to aid decision making for a myriad of theater-level combat air and land operations. Centralized facilities like Air Force Global Weather Central (AFGWC) generate much of the theater weather information for these contingencies. However, the centralized, reach-back approach takes more time to transmit weather information into and out of the theater.

The use of timely in-theater observations can greatly increase Theater Forecast Model (TFM) accuracy and value to the decision maker. Because observations are perishable, from a modeling perspective, most theater observations do not arrive in time to be used in the centrally run models.

To address the need for timely and accurate theater weather forecasts, including the benefits from in-theater observations, the Air Force Chief of Staff has approved Air Force Weather (AFW) Mission Need Statements (MNS) for the Combat Weather System (CWS) and the Global Theater Weather Analysis and Prediction System (GTWAPS). These programs require a TFM to supply theater warfighters with theater-optimized weather information.

The Air Weather Service (AWS) pre-screened numerous mesoscale models before finally settling upon four primary candidates for the TFM. The candidate models for this study include the Colorado State University (CSU) Regional Atmospheric Modeling System (RAMS), the National Center for Atmospheric Research (NCAR)/Pennsylvania State University Mesoscale Model (MM 5), the Navy Operational Regional Analysis and Prediction System (NORAPS 6), and the Defense Nuclear Agency's (DNA) Operational Multiscale Environment model with Grid Adaptivity (OMEGA). After detailed comparison tests, one of the four models will be selected for adaptation and transition to a Department of Defense (DoD) standard, theater weather architecture.

2. NUMERICAL WEATHER PREDICTION LIMITATIONS

Despite improvement over the past two decades, Numerical Weather Prediction (NWP) still has limitations. We will first review some basic NWP limitations before providing a general discussion on our approach for the TFM selection.

There has always been a trade-off in NWP between resolution and computer power. Whenever the horizontal grid resolution is increased by a factor of two, the resultant computer time required to produce a forecast increases by a factor of eight. This happens because there is change in the x and y direction along with the change in time step. Also, this limitation is magnified by the necessity to resolve geographically induced meteorological features. As it is well known, weather patterns are often result from a given terrain feature. Whether it is a coastal pattern (land/sea breeze) or mountain flows (lee-side cyclogenesis), to forecast meteorological phenomena in an accurate and timely fashion, the model must be able to resolve these terrain induced features. However, that resolution requires a fine-scale numerical grid, which stated earlier requires more computational power. The new generation

of computer workstations may well put this limitation behind us in the not to distant future.

Model spin-up time presents another challenge. When gridded data fields are used for the model's initial conditions, a 0 - 12 hour period is needed for the model to adjust to numerical artifacts created by the differences between the initial fields and the model equations. This time can be remedied by using a data assimilation procedure. Although data assimilation procedures such as nudging may reduce spin-up time, there is no real "best" technique.

Many physical processes are simulated in mesoscale models. This simulation or parameterization is a very challenging task. If the parameterization is in error, then the resultant atmospheric simulation will be suspect. Several areas which are parameterized in NWP models include radiation, soil moisture, evapotranspiration, cloud energetics, surface fluxes, etc. These parameterizations are of significance because often in meteorology we have unobserved or inadequately observed parameters. Also, the process may exist on a scale not resolved by the observational network. Most NWP models have the above mentioned parameterizations; however, the values used for the variable may be in error because it has not been studied fully to provide a sound basis for the value.

3. APPROACH FOR THEATER FORECAST MODEL SELECTION

These limitations and others can and will have significant impact on the results produced by a NWP model. To compound that impact, this efforts seeks to port a model that generally operates on a supercomputer to a workstation. The model must produce a 36-hour forecast one hour after data assimilation. To accomplish this task, the model must be effectively downsized. One can develop an engineering version of the model that will operate quicker than its first principles version. This will require the model will be downsized, allowing for tradeoffs between run time and accuracy.

Under the auspices of the DNA and AFW, a modeling team is porting and downsizing candidate models first on a supercomputer and then to a workstation class machine. This approach will provide insight into what can be optimized within the model to meet the TFM run times and still achieve acceptable forecast accuracies.

All the models have a four dimensional data assimilation scheme to help model stability and reduce model spin-up time. The models also have a flexible domain, which is important when relocating the model operational forecast region.

These models will predict most but not all required theater weather elements out to 36- hours. Other needed weather elements will require the development of applications models, which will get their basic input from gridded TFM data (pressure, temperature, winds, and humidity).

4. THEATER FORECAST MODEL REQUIREMENTS

The AFW Functional Area Plan (FAP) includes joint operational requirements for the TFM. These requirements call for a basic capability to have a fine-resolution weather analysis and forecast capability to support theater combat and non-combat operations.

The TFM will ingest Gridded Data Fields (GDFs) along with additional observational and model data to calculate "derived" parameters such as present weather, visibility, and clouds. The TFM will also provide higher resolution GDFs for use in other applications as directed by theater operations.

The AFGWC will receive GDFs of basic parameters like temperature, pressure, winds, and dew point from the Navy at approximately 1 degree x 1 degree horizontal resolution. The relocatable TFM will use these GDFs for its lateral boundary conditions and initial conditions. Next, the AFGWC will provide additional meteorological information, e.g., theater observations, satellite imagery, cloud information, etc., for the TFM data assimilation.

The TFM is required to operate with a horizontal domain of 2400 X 2400 km. Its horizontal resolution is required to be 40 km with an objective resolution of 10 km. Theater operations dictate producing a 36-hour forecast within 1 hour run time after data ingest. Initial plans call for two cycles per day, eventually becoming eight cycles per day.

To identify and assemble government and commercial off-the-shelf technologies to meet these needs, AFW has developed a coordinated TFM strategy with the DNA, Argonne National Laboratory (ANL), and the Phillips Laboratory (PL) Geophysics Directorate. This strategy falls under the auspices of the Electronic Systems Center (ESC) and includes various proof-of-concept studies on the candidate TFM technologies. The ESC has outlined TFM requirements in their report number E-1243U, dated 15 December 1993.

5. THEATER FORECAST MODEL SELECTION CRITERIA

A team of scientist from AWS, AFGWC, ANL, PL, and DNA met at AFGWC and developed the criteria which will be used to ensure the model best suited for theater operations is chosen. It was the intent of these individuals to provide objective measures, which could be easily followed for model comparison and subsequent selection. The team considered model configuration, theaters of operation, and verification criteria.

Initially the team wanted to ensure the models had the necessary numerics, physics, and run options to fulfil the TFM requirements and that also allow for a graceful degradation in data denied scenarios. The horizontal grid spacing will be 40 km with a computational domain of 71 x 71, and a verification domain of 61 x 61. The model will have approximately 20 vertical levels. AFW and NCAR will provide observational and first guess data fields for initial conditions and lateral boundary conditions. Each model will be allowed to use whatever observations and variables it can incorporate in its analysis scheme. Models will be evaluated out to the 36-hour forecast period and compared at 3-hour intervals.

To ensure a relocatable, worldwide TFM capability, test cases will be run over five topographically and seasonally complex regions. The regions are Alaska, Central America, Middle East, Korea, and the United States. Data collection for each test case will cover a 72-hour period. Output from the TFM candidates will be compared against each other and the AFGWC Relocatable Window Model (RWM). To be a viable candidate, a model must outperform the RWM. The data will cover specific seasons in each of the theaters.

The verification criteria includes the analysis, 6, 12, 24, and 36 hour forecasts for the u-component and v-component of the wind, temperature, pressure, relative humidity, and specific humidity. These forecast periods and variables will be evaluated at the surface and mandatory upper-air levels. The evaluation will include a measurement of accuracy for each of the variables, forecast periods, and atmospheric levels. Measures of accuracy will include mean absolute error, relative error, bias, and root mean square error determined from the paired differences of interpolated model grid point data to rawinsondes. The accuracy comparisons will also include comparisons of standard map sets from each model for given time periods. After all the above measures have been complied for each of the models, AFW and DNA will decide which model best meets the TFM meteorological accuracy requirements.

The atmospheric accuracy of each model will be evaluated against the computational requirements and technology transition factors, including the model's sustainability, maintainability, flexibility, and extensibility. Each candidate model will have timing statistics gathered on its operation on a supercomputer and a workstation. The final selection of a model will depend on which one best satisfies timing, accuracy, and technology transition requirements.

6. CONCLUSION

Recent DoD contingencies have demonstrated the need for high quality and timely meteorological information at the theater level of operations. To address this need, the Air Force Chief of Staff approved a MNS for CWS and GTWAPS. AFW and DNA have undertaken a joint effort to ensure theater operators in future contingencies will receive value-added meteorological information when they require it.

The selection of the TFM will take place within the next 12 months after a series of tests are completed. These tests will compare four leading mesoscale numerical weather prediction models against each other. The tests will be conducted using data from five geographically, topographically, and seasonally complex regions. Accuracy comparisons will involve basic meteorological variables for forecast periods of 0 - 36 hours. The model best meeting the theater forecast requirements, including technology integration factors, will be selected.

AIR WEATHER SERVICE:

EVOLVING TO MEET TOMORROW'S CHALLENGES

Col William S. Weaving, Maj Dewey E. Harms, Capt Donald H. Berchoff, and
Capt Timothy D. Hutchison
Headquarters Air Weather Service
Scott AFB, Illinois, 62225-5206, USA

ABSTRACT

Air Weather Service (AWS) has undergone a notable evolution since activation on 1 July 1937. Through all the changes, the basic AWS mission remains the same; to assist the warfighter in any way possible to achieve victory on the battlefield. With the rapid advancement of technology, and the resulting increase in technical training requirements, AWS' role as the technical leader for Air Force and Army weather units is as vital as ever. To ensure military weather capability keeps pace with technology, a number of major programs and initiatives are underway within AWS to upgrade its two major production centers, Air Force Global Weather Central (AFGWC), and the USAF Environmental Technical Applications Center (USAFETAC). At the headquarters, AWS continues to evolve and adapt to improve technology transition, equipment acquisition, and training. Working closely with the Pentagon and other major commands, AWS continues to field a host of new standard weather systems. With the rapid integration and the limitless potential of these new weather systems, effective technology transition through innovative training methods is extremely critical. With this in mind, AWS is working not only to field these systems, but has also set in place a mechanism for assuring their maximum exploitation. This paper will concentrate on Air Weather Service's role in providing centralized products to the warfighter and in improving those forecaster skills necessary to optimize exploitation of new and existing technology.

1. INTRODUCTION

During most of our nation's military history, weather personnel have played a vital role in maximizing the effectiveness of the warfighter by accurately identifying windows of opportunity for aviators to seize.. Whether it be providing decision assistance in the Normandy invasion, the Berlin Airlift operation, or hunkering down with the United Nations coalition forces during Operation DESERT STORM, Air Weather Service has

always been ready to provide weather advice to military decision makers. In most instances, the advice is a key ingredient to mission success. According to the book, Air Weather Service: A Brief History 1937-1991, during the Berlin airlift, low clouds, fog, freezing rain, and turbulence frequently impacted airlift activities. The success of the airlift mission, and in turn, the future of the residents of Berlin depended on the ability of our aircrews to deliver ample supplies and break the Soviet stranglehold on the city. As history shows, despite the frequent occurrences of inclement weather, the Berlin airlift was a success. Precise forecasts played a major role then and still do today. Despite the development of "all weather" aircraft, low ceilings and visibility, and hazardous weather still impact mission effectiveness. Additionally, weather can impact the aircrew "rules of engagement". During DESERT STORM, pilots were required to visually acquire targets before firing. This requirement made accurate cloud forecasts an absolutely critical ingredient for mission success.

AWS has gone through many structural and organizational changes since activation on 1 July, 1937. For 54 years, AWS maintained command and control of all Air Force and Army weather units worldwide. This changed in 1991 as world events dictated major changes in the direction of national policies.

In August 1991, as part of the 25 percent Department of Defense (DoD) manpower reduction, a new era in AWS began when the Air Force directed the transfer of Air Force weather field units from Headquarters AWS (HQ AWS) to local operational commanders. The purpose was to substantially streamline middle management, and assign the weather field units directly to the local wing commander. This initiative meant the total deactivation of six AWS weather wings and associated subordinate weather squadrons. HQ AWS and its remaining subordinate agencies moved out from under Military Airlift Command and became a field operating agency reporting directly to the Pentagon. Today, the Directorate of Weather at the Pentagon assumes responsibility for Air Force atmospheric and space policies, plans, and resources while the focus of HQ AWS and its subordinate centers is on meeting the present and future operational needs of the Air Force, Army, and other military and government agencies.

Although AWS has undergone a notable evolution, the basic mission remains the same as it was over 57 years ago; to assist the warfighter in every way possible to achieve victory on the battlefield. The AWS role as the technical leader for Air Force and Army weather units is vital. Internally, AWS continues to evolve and adapt to increase the peacekeepers ability to use weather to gain all possible advantage. This paper will concentrate on Air Weather Service's role in providing centralized products to the warfighter and in improving those forecaster skills necessary to optimize exploitation of new and existing technology.

2. THE NEW STRUCTURE: CONCEPT OF OPERATIONS

AWS provides centralized weather products and technical assistance to the Air Force, Army, selected DoD agencies, and classified programs of the highest priority. Centralized weather information is critical to operational planners, weapon system designers, and field units who rely heavily upon centrally produced analyses and forecasts and climatological studies. Due to the large amount of data and complexity of global, regional, and mesoscale models, the atmospheric products and services to DoD warfighters are beyond the resources of the operational military commands. AWS provides these products and services during peace and war.

Figure 1 depicts the operational weather architecture as the Air Force moves into the 21st Century. Conceptually, observational data that is collected and used in global (hemispheric) analysis and forecast models will be sent to a centralized weather facility as input to theater-scale (mesoscale) forecast models. Here, "theater" refers to a domain approximately 2500 km by 2500 km centered over the area of interest where military operations are occurring. The theater model will use this data along with other observed and model output data to produce finer resolution mesoscale forecasts. The primary goals are to provide timely, accurate observations and forecasts to help ensure successful air, ground, and sea battlefield operations.

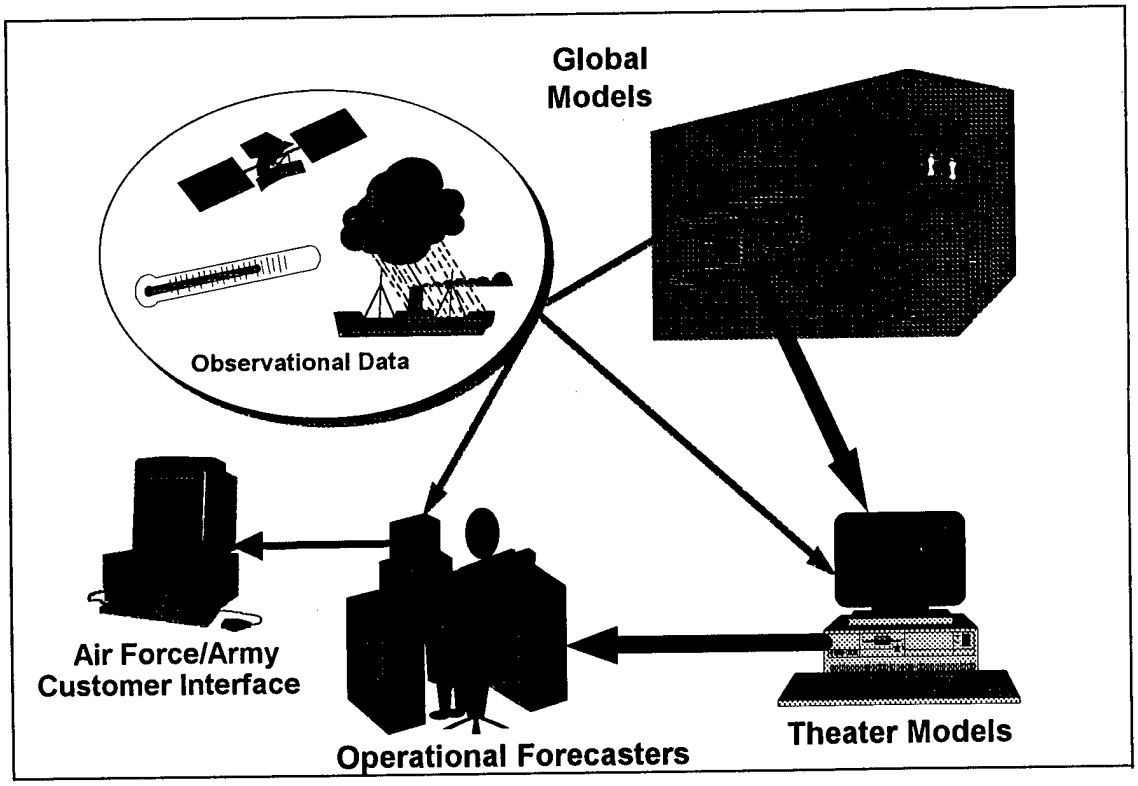


Figure 1. Weather Support Concept into the 21st Century

2.1 Headquarters Air Weather Service

HQ AWS, which is located about 15 miles east of St. Louis MO at Scott Air Force Base (AFB) IL, provides meteorological technical expertise to the Air Force and the Army, and directs the operations of its subordinate units. It provides oversight for the standardization and interoperability of Air Force and Army weather units worldwide, plans for and fields standard weather systems, transitions new technology to field units, develops standardized training programs, and assesses the quality and technical goodness of weather information, (AWS Mission Directive 49-1, 1993).

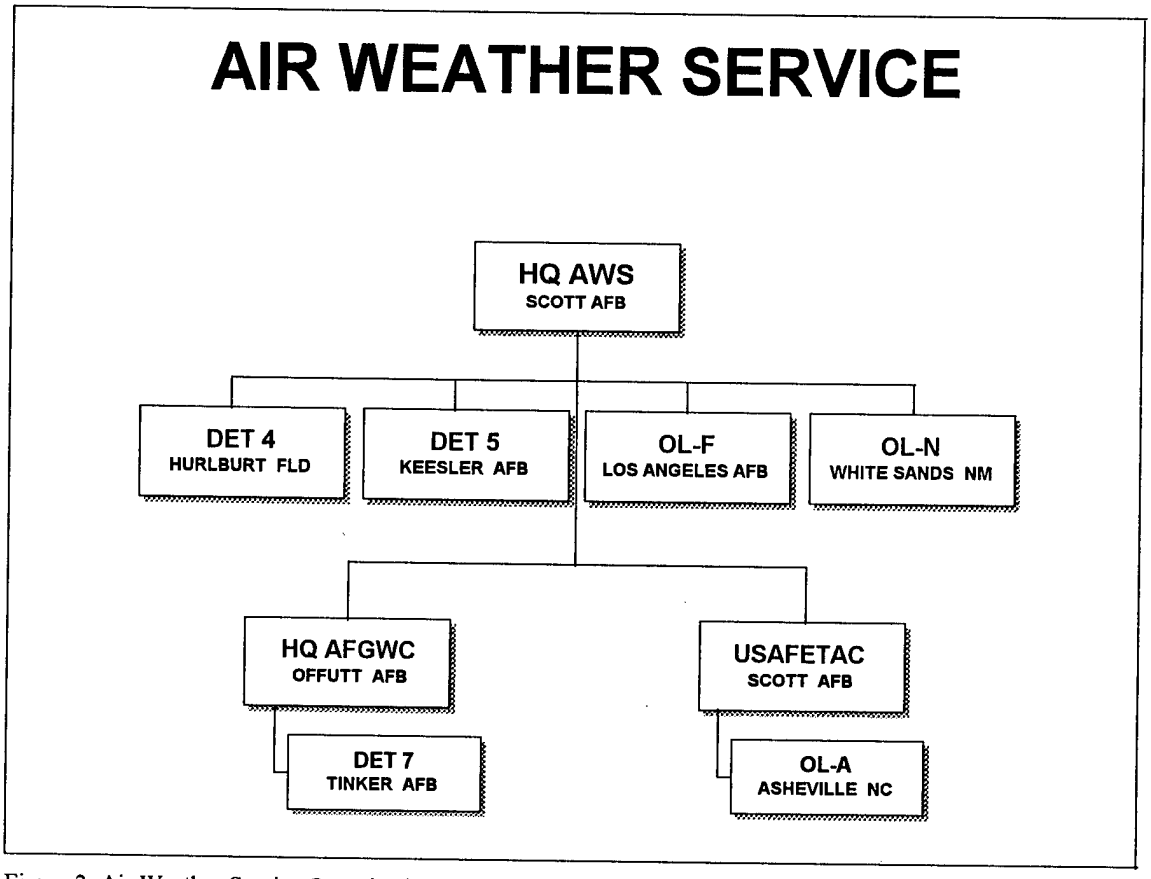


Figure 2. Air Weather Service Organizational Structure

2.2 Centralized Facilities

Essential components of the Air Force weather concept are centralized weather facilities capable of producing tailored global and theater weather products to enhance operations worldwide. The current Air Force centralized weather functional architecture is dedicated towards the synthesis of worldwide weather data, the ingest and manipulation of numerous meteorological satellite (METSAT) datasets, daily operational runs of global weather analysis and prediction models, storage of the data and imagery files within a

centralized database structure, and the generation of gridded data field, graphical, and alphanumeric forecast products for global and theater applications. Centralized products normally will be used to enhance command, control, communication, computers, and intelligence activities. Although these activities are frequently decentralized, they require consistent, automated weather information at multiple decision points.

2.2.1 Air Force Global Weather Central (AFGWC)

Centralized weather information is provided to military forces for planning, training, resource protection, and operational decision assistance. AFGWC (located at Offutt AFB, Omaha NE) primarily provides this information to fixed weather units located at Air Force bases, Army posts, and tactical units within a theater of operations.

AFGWC is designated as the DoD center for theater-scale weather analyses and forecasts, meteorological satellite (METSAT) data processing, and cloud analyses and forecasts. Before the turn of the century, AFGWC will run theater weather analysis and forecast models for not only the Air Force and the Army, but all warfighters conducting operations on land, sea, and in the air. The Navy's Fleet Numerical Meteorological and Oceanographic (METOC) Center (FNMOC) will provide global model gridded data as one source of input for the AFGWC theater-scale model.

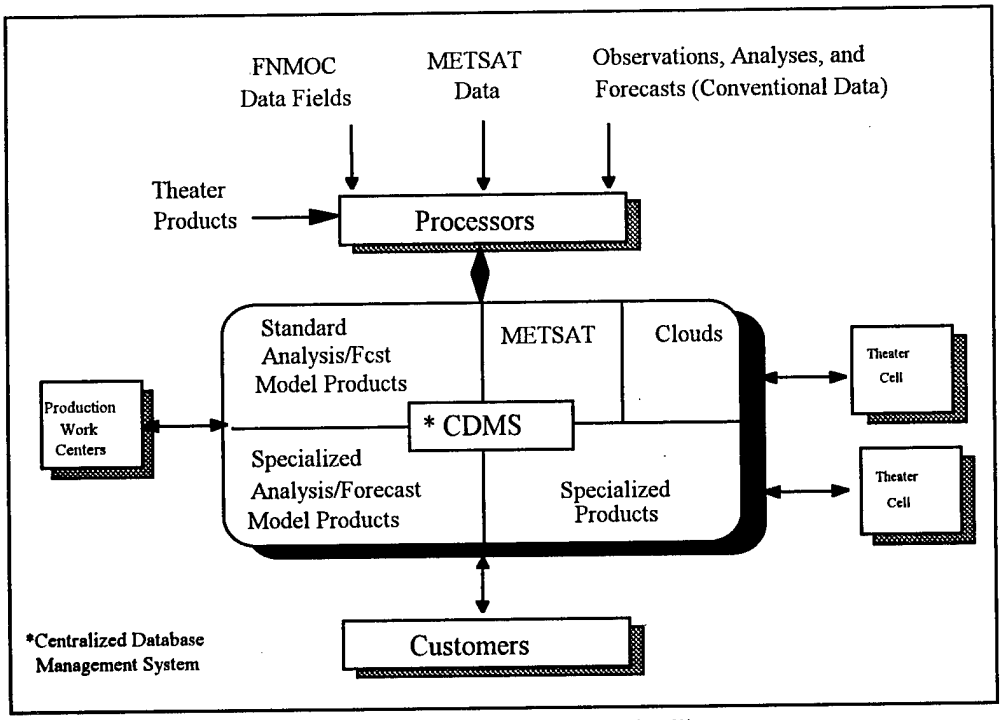


Figure 3. Future AFGWC Operational Weather Support Information Flow

Figure 3 depicts the flow of centralized operational weather information in the future. AFGWC will receive Gridded Data Fields (GDFs), and/or spectral coefficient datasets of "basic" meteorological parameters (e.g., temperature, pressure, winds, and dew-point) from the Navy. AFGWC theater and hemispheric models will use these datasets along with additional observational, satellite, hemispheric, and internal model data to calculate "derived" parameters (e.g., clouds, visibility, etc.) and provide theater and hemispheric uniform GDFs (UGDFs). UGDFs will be the field weather teams' primary source of centralized data.

AFGWC will ingest all available foreign and domestic observations from atmospheric and satellite data sources to build an accurate environmental database. In addition to currently available information, these data include automated surface and upper-air meteorological observations, automated tactical surface observations, wind and thermodynamic profiler information, and aircraft upper-air meteorological observations.

AFGWC will use regional data assimilation systems which feed atmospheric data into its theater analysis and forecast models. The atmospheric and satellite data collected will be processed and incorporated into the AFGWC environmental data base on a standardized grid. The observational data base will be automatically updated on a regular basis as newer data become available. Specialists will use weather workstations to tailor the output of the regional/theater models periodically (e.g., every 6 hours) and update the forecast portion of the data base. The workstations will allow specialists to generate four-dimensional visualization of the analysis and forecast fields (Air Force Weather Support System Concept Paper 2015, 1994).

AFGWC production work centers will consist of personnel trained to produce standard, routine meteorological products and mission-tailored products serving warfighters' needs worldwide. Also, AFGWC will operate theater cells as required, which will have the responsibility for operational execution of theater-scale models for a specified theater. Up to two cells will be required to cover two regional conflicts simultaneously. Each cell will manipulate data available from the Centralized Database Management System (CDMS) and run theater model(s). Each individual cell will tap into the centralized database, updating information for its respective area of interest. The CDMS itself is the central computer repository for weather information--analyses, forecasts, METSAT imagery, and cloud information. The CDMS will be capable of simultaneous communications with each theater cell, as well as any field request for information.

In addition to near real-time forecasting information, there must be a timely response to all climatological information requests to enhance theater operations and contingencies anywhere in the world. For instance, military planners needed climatological information on cloud cover, frequencies of precipitation, and diurnal ranges of temperature for Kuwait within hours of the initial Iraqi invasion.

2.2.2 USAF Environmental Technical Applications Center (USAFETAC)

USAFETAC (located at Scott AFB IL) collects, maintains, and applies climatological information to determine the environmental effects on military operations and systems and to meet requirements of the Air Force, Army, and other military and civilian agencies. USAFETAC's data processing and archival center at Asheville NC receives worldwide observations from AFGWC and combines this information with that received at the National Climatic Data Center from other sources to continually build and maintain a climatological archival database available for global and theater applications.

Dedicated USAFETAC personnel provide tailored climatological products for any DoD mission upon request. Some requests will be supported by products generated automatically by computer. The majority of requests received (dial-in or message) from DoD customers, however, will be evaluated and provided tailored support by trained specialists, particularly those requests requiring significant climatological expertise to solve. Climatological assistance ranges from preparation of historical area weather data for contingencies to providing data for combat simulation war games.

Environmental simulation data will provide combat simulation models the ability to present statistically representative weather in both time and space (ground/air/underwater) domains. These models will integrate weather information into combat (war gaming) and weapon simulators, taking advantage of fractals, data-compression techniques, and other advances in statistics, to provide more realistic training to the warfighter.

2.3 Technology Transition and Training

With the rapid integration of new technology and the limitless potential of new weather systems, effective technology transition through innovative training methods is as important as ever in assuring maximum exploitation of new systems. Throughout the operational weather community, the key to meeting the training challenges of tomorrow lies in keeping pace with technology. New systems such as the WSR-88D Doppler weather radar offer a wealth of information, and frequently, users don't have the time or knowledge to build up quick system expertise. These problems are further compounded within the military. Besides keeping pace with the rapid technological advances, the military also contends with shrinking weather unit staffs and a younger forecaster work force; both of which are at their lowest levels ever. Ironically, as the need for training is increasing due to new technology, the available manning resources dedicated to providing the training is decreasing. The challenge of the future is to develop training and technology transition programs that keep pace with technology and overcome acknowledged manpower constraints. AWS is working in this area, exploring innovative training approaches for new weather system acquisitions, and follow-on training, which are responsive and meet the unique requirements of today's Air Force.

AWS manages training requirements for all new standardized Air Force weather systems deployed to the field. Working closely with Headquarters, United States Air Force and the operating commands, AWS performs new system task analyses using the Air Force Instructional System Design (ISD) process. In the past, training on new systems was usually worked out late in the system acquisition phase. The ISD process places more focus on analyzing the training requirements early in the acquisition phase. Proper application of IDS principles enables the best mix and match of training for the operator in today's high tech environment. Recognizing requirements early in the acquisition process allows for smoother and more efficient implementation of new training concepts such as "on-line" training. "On-line" training enables the user to train on the same system used in day-to-day operations; as a result, it reduces the need for a human trainer, saves operator time, and provides user help on demand. On-line training will carry new systems acquisition training into the 21st century.

Besides seeking innovative training methods, AWS is attempting to make standardized training/transition programs more flexible. The complexity of new computer systems and their growing number of potential applications makes training/transition program flexibility critical.

Following the deployment of new weather systems and completion of initial system training, AWS becomes the focal point for technology transition and exploitation. AWS provides direct assistance to the field through various training methods by developing and transitioning new and/or existing meteorological techniques, and by exploiting technical capabilities of fixed based or tactical weather station equipment. It manages the transition of new forecast techniques to the field through a regional approach that encourages active field unit participation through regional working group meetings/conferences, and bulletin boards.

AWS manages the exchange of technical information between the field units and AWS through 11 regional managers. Regions are broken out based on geographic location and climatology with six regions in the CONUS, three in the Pacific and two in Europe. Regional managers seek to facilitate the exploitation of technology within a region by tailoring assistance to a sub-synoptic level and acting as the central focal point for technology transition and technique sharing within a region. Communication is achieved through regional bulletin boards, telephone, and annual regional conferences and working groups. Regional managers assure similar initiatives are not worked simultaneously in other regions. The crossfeed concept relieves unit workload by eliminating redundancy in initiatives and maximizes use of techniques already developed in the field. Additionally, rather than depending solely on the development initiatives from a centralized facility, the concept utilizes the intellect of forecasters in the field. Regional managers work closely with a group of functional experts who specialize in AWDS, WSR-88D, meteorological computer applications, and theater forecast techniques. These experts provide technical assistance to the regional managers and the field during technique development and assure technical goodness of the final product.

AWS also provides on-site technical assistance through Meteorological Enhancement Teams (METs). The MET is a team of functional and regional experts sent to the field to present one-day, multi-media presentations on various meteorological topics. AWS visits units by request only and tailors each MET presentation to meet the needs of the individual unit. The purpose of the MET is to introduce new or existing meteorological techniques and to show the forecaster how to exploit the new technology in applying these techniques. MET teams have already presented over 100 seminars on topics ranging from "Fog and Stratus Forecasting Problems" to "Severe Weather Forecasting."

AWS is also working to modernize the AFW follow-on training (FOT) program. The new program exploits the use of interactive courseware (instructional software and hardware) and Computer Aided Instruction (CAI) replacing the old slide projection technology. In 1991, AWS fielded the first of 253 Multimedia Training Systems (MTS) to weather units worldwide. The MTS provides interactive video, CD-ROM , and a VCR to run self-paced FOT courseware to enhance forecaster technical skills and supplement formal school and on-the-job training (OJT). Interactive courseware enhances retainability of information by engaging the learner's senses and involving the individual in the learning process by presenting the material through a variety of media such as videotape, compact disk, videodisk, graphic animation, and sound. Students proceed at their own pace and can exit and enter the course as required. This feature ensures maximum flexibility so the students can fit training into their busy schedule. The first videodisk modules fielded included, "Workshop on Doppler Radar Interpretation" and "Boundary Detection and Convective Initiation." Military forecasters successfully used both these modules to prepare for formal WSR-88D training courses.

Development of interactive software is a lengthy process, often taking 1 to 2 years per module. Occasionally, circumstances require the quick fielding of a training module to respond to a noted technical shortfall. In these instances, AWS exploits the capability of CAI. CAI is not as visually effective as interactive courseware, but because development time is less than a year, it provides an effective method of quickly addressing a critical technical deficiency. In 1992, a deficiency was noted in the forecasting of icing and turbulence. AWS quickly developed two CAIs on icing and turbulence forecasts using the WSR-88D. The WSR-88D Operational Support Facility at Norman Oklahoma also develops CAIs; they have already developed ten CAIs on WSR-88D algorithms. Both CAIs and interactive courseware are an integral part of the weather FOT training plan.

AWS is also an active participant with the National Weather Service (NWS) and the Naval Oceanography Command (NOC) in the Cooperative Program for Operational Meteorology, Education, and Training (COMET). COMET was originally developed by the NWS as part of their modernization program to place emphasis on improving the professional background and operational capabilities of meteorologists to use mesoscale data. Three COMET programs have been developed to meet the objectives of improving

mesoscale forecasting: a Distance Learning Program, an Outreach Program, and a Residence Program.

AWS, NWS, and NOC provide funds as sponsors in the Distance Learning Program. The objective of the program is to provide professional development education for operational weather forecasters, university facility, and other meteorologists who do not have the time or money to attend COMET resident courses. Training is mainly conducted via interactive courseware that is developed for in-station use. The two modules used to successfully prepare military forecasters for formal WSR-88D training, "Workshop on Doppler Radar Interpretation" and "Boundary Detection and Convective Initiation" were both the result of COMET initiatives.

Additionally, AWS provides funds for research under the Outreach Program and participates in the Resident Program. The Outreach Program creates partnerships between the academic research community and operational weather forecasters that focus on resolving forecast problems of utmost concern to the operational weather community. For example, under the Outreach Program, North Carolina State University was paired with AWS to work on nowcasting convective activity during space shuttle launches and landings. The Resident Program brings meteorologists together with nationally recognized experts for the purpose of improving their collective understanding of mesoscale meteorology. The program conducts courses, symposiums, and workshops that provide operational weather forecasters, hydrologists, and other atmospheric scientists with new skills and concepts in mesoscale meteorology. Through the years, AWS' association with COMET has been very productive, and prospects for the future are just as bright.

3. CONCLUSIONS

Over the last few years, AWS has experienced significant structural and organizational changes and technological advances. Even though AWS no longer has operational control of Air Force field weather units, its role in providing decision assistance to the warfighters has not diminished. AWS still provides centralized analysis and forecast information to operations worldwide and the technical weather expertise to the Air Force and the Army.

AIR FORCE WEATHER MODERNIZATION PLANNING

Alfonse J. Mazurowski
Headquarters Air Weather Service
Scott Air Force Base, Illinois, 62225-5206, USA

ABSTRACT

Air Force modernization planning results in the development of documents which evaluate all aspects of specific functions, pinpoint deficiencies, and demonstrate how the Air Force plans to affordably satisfy those deficiencies to achieve required capabilities. The Air Force Weather (AFW) Functional Area Plan (FAP) is a 25-year modernization planning document that details the programs and laboratory technologies required to enhance operational capabilities. Laboratory funding will be based, in part, on their role in satisfying Technology Needs documented in FAPs and Major Command Mission Area Plans (MAPs). A FAP Integrated Product Team (FAPIPT), consisting of weather representatives from Headquarters United States Air Force and Army, Army and Air Force major commands, product centers, and laboratories, was formed to construct the plan. A FAP Steering Group, made up of senior Air Force leaders in weather, provided oversight and guidance for the FAPIPT. The FAP addresses the two major segments of AFW: unit capabilities, which includes fixed-base weather station and tactical unit areas; and centralized facilities, which includes the Air Force Global Weather Central, United States Air Force Environmental Technical Applications Center, and the Air Force Space Forecast Center. The FAP was developed by compiling a comprehensive set of customer weather requirements, evaluating AFW's capability to provide those products, and satisfying any capability deficiencies through the development of a modernization roadmap. The modernization roadmap in the FAP contains planned acquisition programs for hardware and software in addition to descriptions of Critical Enabling Technologies that are the contribution of science and technology programs to correct deficiencies. The FAP is a living document that will be updated annually. Through successful execution of the modernization roadmap, Air Force Weather will be able to respond to the complex, evolving requirements of tomorrow's operational missions.

1. INTRODUCTION

During the 1992 Fall Corona, the Air Force Chief of Staff initiated the Air Force's Year of Equipping by charging the major commands (MAJCOMs) and Field Operating Agencies (FOAs) to build 25-year modernization plans. These plans are called Mission Area Plans (MAPs).

Functional areas such as weather, intelligence, communications, and security police were tasked to develop FAPs, since they are not specifically operational mission areas, but rather are backbone, cross-cutting functions which support all mission areas. The FAP follows the MAP format and methodology as documented in Air Force Policy Directive 10-14, Draft, and Air Force Instruction 10-1401, Draft.

The purpose of the completed MAP/FAP is to guide the development of the Program Objective Memorandum (POM) and to push technology development through Air Force Material Command's Technology Master Process.

2. MODERNIZATION PLANNING

MAPs/FAPs are developed through a modernization planning process which uses a mission area assessment (MAA), mission needs analysis (MNA), and an assessment of possible solutions. The MAA process evaluates force structure, the operational environment, and the threat we expect to encounter while conducting the assigned mission. The MAA process uses a strategy-to-task (STT) evaluation of operational/support mission tasks requiring certain capabilities (current and programmed). These tasks are derived from the National Military Strategy and identify what capabilities are needed to achieve military objectives. The STT is a framework used to better understand and communicate how Air Force Weather's activities support the nation's security needs.

During the MNA, operational tasks are analyzed to determine the factors which impact the current and programmed capability to accomplish identified operational objectives. The MNA ultimately identifies deficiencies in current and future capabilities to provide adequate weather products for operational missions.

After deficiencies are identified, an assessment of possible solutions is accomplished. Non-material solutions, such as doctrine, tactics, techniques, procedures, and training, are examined to determine if changes in these areas can solve the deficiencies. If not, new technologies needed to improve the warfighting capability in the field are identified and prioritized through interaction among AFW, the supported operational customers (the warfighters), and Air Force laboratories.

3. DEVELOPMENT OF THE AFW FAP

In August 1993, HQ USAF/XOW tasked Air Weather Service (AWS) to develop an AFW MAP (which subsequently became the AFW FAP). A FAPIPT, co-chaired by AWS (the user command) and Electronic Systems Center's system program director for weather programs (AFMC Product Center) and consisting of weather representatives from Headquarters United States Air Force and Army, Army and Air Force major commands, product centers, and laboratories, was charged to develop, document, and continually update the FAP. An AFW FAPIPT Steering Group, comprised of senior weather functional managers from the Air Force major commands, the FOA, and Headquarters Air Force and Army, was organized to provide direction for the FAP planning process.

In October 1993, the Steering Group directed the FAPIPT to limit the initial focus of the then MAP to evaluate the Air Force Global Weather Central's (AFGWC's) capability to provide Theater Battle Management (TBM)-required meteorological and oceanographic (METOC) products. The FAPIPT's evaluation of AFGWC's capabilities identified the hardware and software deficiencies in satisfying the centralized product requirement for wartime operations. The initial MAP was completed on 18 February 1994.

In March 1994, HQ USAF/XOW directed AWS to expand the scope of the AFW MAP to include all areas of AFW activities and redesignate it as a FAP. Now the FAP addresses the two major segments of AFW: centralized facilities and unit capabilities. The centralized area includes the three meteorological centers within AFW: AFGWC (operational weather products), USAF Environmental Technical Applications Center (USAFETAC) (climatological products), and Air Force Space Forecast Center (AFSFC) (space environmental products). The unit area concentrates on fixed base weather station (BWS) and tactical weather unit operations. In keeping with the concept of "train in peace as we fight in war," the far-term goal is to combine the software and hardware functionalities of the fixed BWS and tactical weather unit to the maximum extent possible.

4. DESCRIPTION OF THE AFW FAP

The AFW FAP is a weather modernization plan which will serve as a roadmap for weather operations through 2019. It highlights deficiencies that still need to be corrected to meet mission requirements into the 21st century. This plan is a living document which is updated at least annually to initiate and validate POM actions. It also provides the basis for technology programs to be developed which will chart AFMC's science and technology investment strategy.

4.1 Centralized Facilities

4.1.1 AFGWC is designated as the DoD center for theater-scale weather analysis and forecast models, meteorological satellite (METSAT) data processing, and cloud analyses and forecasts. The primary mission of AFGWC is to provide centralized weather products to US combat forces to include unified and specified commands and all Air Force and Army major commands. AFGWC uses super computers, large computer mainframes, minicomputers, and workstations to manage the enormous amount of incoming weather data and run complex weather analysis and forecast models to meet customer needs.

AFGWC was assessed on its capability to provide the required suite of 1340 METOC products in uniform gridded data field (UGDF) format as identified through the TBM program. As a result of this assessment, shortfalls in AFGWC's capability to satisfy stated product requirements were determined. Hardware shortfalls were primarily due to inadequate processing power, internal communications, and data storage. Software shortfalls included limited or no capability to provide certain METOC parameters.

Solutions to correct AFGWC hardware shortfalls are planned through a combination of upgrade and modernization programs:

Satellite Data Handling System (SDHS) is an interactive computer system within AFGWC for centralized weather forecast generation and dissemination. The SDHS ingests meteorological data, both conventional and satellite, for interactive display and manipulation at the forecaster consoles. It provides the user-interface and computational support for producing specific meteorological analysis and forecast products required to support AFGWC and its external customers. The SDHS Upgrade (SDHSU) program provides enhancements to the SDHS and bridges the gap until the scheduled SDHS replacement program (SDHS II) comes on-line. The enhancements include a logistical upgrade/replacement of the user-interfaces, further development of the Air Force Global Weather Central Dial-In System, storage expansion, upgrade of processors, and hardware/software modifications to receive new meteorological satellite data types/formats and foreign meteorological satellite data. In addition to these enhancements, three more user-interfaces will be included in SDHSU. The SDHSU enhancements will alleviate hardware saturation and will completely meet identified TBM METOC requirements. The SDHS II program will modernize the SDHS hardware architecture and will support data access and retrieval from a centralized weather data base to meet anticipated future operational requirements.

Cloud Depiction and Forecast System (CDFS) uses polar orbiting satellite imagery and continually builds and updates the Satellite Global Data Base (SGDB) upon receipt of the polar satellite imagery. Also, CDFS builds a global cloud analysis based upon satellite imagery and conventional meteorological data. CDFS provides all customers with global satellite imagery, cloud analyses, and forecasts products. CDFS II is an acquisition program that will replace satellite data processing hardware and will develop a new cloud analysis model, thereby improving cloud forecasts for TBM.

Global Theater Weather Analysis and Prediction System (GTWAPS) will replace the Automated Weather Analysis and Prediction System (AWAPS) with an open system architecture workstation environment which will host advanced, high-resolution theater weather analysis and forecast models to meet TBM resolution requirements for theater-scale operations. The CDFS II and GTWAPS programs, along with other software initiatives (e.g., laboratory technology efforts, utilization of Navy data, AFGWC software development), will meet TBM METOC product requirements.

Weather Information Processing System (WIPS) is made up of two areas: Weather Information Processing-Production (WIPP) and the Weather Information Processing-Development (WIPD). WIPP primarily receives and processes conventional weather data. Conventional weather data consists of surface and upper air data accumulated from weather stations around the world. WIPD serves as a development system and back-up to some of the hardware on WIPP. The WIPS Expansion (WIPS-E) Program and the WIPS processor modification program procure new processors that will alleviate current saturation and expand the capability of WIPS and CDFS to meet TBM product requirements. The WIPS-R program will replace the existing WIPS computer hardware and operating system to satisfy future operational requirements.

HYPERchannel (HYPER) is the means by which required information is transported from computer system to computer system within AFGWC and ultimately to the Communications Front-End Processor for transmission to the field. The HYPERchannel Replacement Program procures the hardware and software to replace the existing HYPER communication link which is not compliant with Air Force Open System Standards and does not have sufficient throughput capability to meet TBM METOC product requirements.

Software enhancements are planned to support modernization plans and future improvements in AFGWC's capability. Key technologies are needed to meet TBM METOC requirements for clouds, surface visibility, present weather conditions, snow depth, soil moisture, turbulence, icing, thunderstorms, volcanic ash, and layered visibility.

4.1.2 USAFETAC is the AFW center for global climatological products. Their mission is to archive worldwide atmospheric and space environmental data and to prepare analyses and studies from manual and computer manipulation of this data for DoD applications. Air Force and Army combat planning and employment decisions, development of weapon systems, and national programs are examples of their products. USAFETAC uses two large computer mainframes, minicomputers, workstations, and large amounts of mass storage to manage the tremendous amounts of climatological data required for product generation.

USAFETAC product evaluation used customer identified, coordinated climatological product requirements. The following assessed product categories attempt to cover all types of customer needs: climatic summaries, descriptive climatology, electromagnetic propagation, engineering climatologies, studies/product improvement, tailored operational support, forensic studies, and simulation/modeling. Hardware shortfalls included inadequate processing power and mass storage. Software shortfalls were primarily due to the lack of worldwide data availability and insufficient simulation models.

Hardware upgrades through the USAFETAC-Replacement (ETAC-R) program are planned to satisfy the above deficiencies. ETAC-R will replace/upgrade computer systems required at USAFETAC and AFGWC in order to provide climatological products to DoD customers worldwide. At USAFETAC, the program replaces its existing mainframe computer system and associated storage with a cluster of workstations and state-of-the-art storage devices. This equipment will provide necessary processing required to run high resolution mesoscale models, which may partially solve data availability, and storage for rapidly expanding databases. At AFGWC, ETAC-R upgrades the AFGWC Centralized Database (CDB) and allows the new ETAC systems access to the CDB.

Software solutions include: in-house training programs, increasing the availability of additional worldwide data, and development of advanced climatic models.

4.1.3 The AFSFC provides space environmental forecasts, warnings, and anomaly assessments to enhance the capability of DoD forces worldwide. As the basis for these products, the AFSFC collects data from a mix of global networks of DoD-unique, national, and international ground- and space-based instrumentation which monitors the solar and near-earth environment. This data

is processed into a wide range of products by various computer algorithms which model the space environment. Assistance includes alerts of solar and geomagnetic events and assessments of event impacts on satellite drag, satellite performance, radar correction, early warning radar and space surveillance performance, and communications effectiveness.

AFSFC uses three computer systems, large databases, and communications in both their hardware and software operational clusters. These systems run specific application programs for customer products while a separate computer cluster is used for unclassified software development. The assessment of hardware capabilities led to a determination of shortfalls in computer processing and storage capabilities. Software shortfalls include the inability to provide solar and geophysical alerts, analyses, and forecasts to the level of accuracy required by users.

The solution to the hardware and software limitations is the AFSFC Replacement(AFSFC-R) Program. The AFSFC-R program provides for replacement of AFSFC's four Digital VAX computer systems (clusters) and current database environment with a system of new computers (to include replacement of the Uninterruptable Power Supply). Additionally, the program includes upgraded external communication interface hardware and software for each of the operational clusters. The program also contains software transition and integration support for application software to be transitioned from the current AFSFC Digital VAX environment to the new vendor's hardware. The new hardware will include the capability to satisfy software solutions by processing new model software being developed under the Space Environmental Technology Transition (SETT) program. This program also includes development of the follow-on SETT models. The program will comprise an integrated effort beginning in the early 2000s to accomplish both the Operational Software Development (OSD) and the software maintenance for the Ionospheric Models, the Magnetospheric Model, the Neutral Atmospheric Models, the Integrated Space Environmental Models (ISEM), and for the coupling of these follow-on space models. These improved, follow-on space models will concentrate on the advanced development of algorithms that will use new space measurements to improve model accuracy.

4.2 Unit Areas

Unit Areas include both tactical and fixed BWSs. Functions of these units include weather warning, observing, forecasting, briefing, and resource protection. Weather personnel use a combination of visual observations and equipment-sensed measurements to observe, record, and report weather elements. Fixed BWSs take advantage of state-of-the-art computer hardware and software technology improvements to provide operational products at Army posts and Air Force bases worldwide. Tactical units currently rely on less sophisticated systems to provide decision assistance to deployed combat forces.

Assessments were made from a hardware and software viewpoint to determine the tactical and fixed BWSs capability to satisfy customer requirements for METOC products. In the near term there will be different solutions to achieve desired capability at tactical and fixed BWSs. However in the far term, the software and as much of the hardware solution as possible should be the same.

4.2.1 AF Systems' Enhancements

The following programs are planned to satisfy Unit Area shortfalls:

Tactical Forecasting System (TFS) is a hardware/software upgrade of AFW tactical forecasting capability. TFS must be a small, lightweight, modular system that is rapidly deployable, durable, quickly activated, and field maintainable. TFS' modular design must allow for an initial deployment capability that can be expanded, as required, to a more capable system. TFS will provide responsive, reliable, accurate weather information in near real time. In addition, the system's products will flow to other systems locations using the in-theater communication system. The system's modules at the in-theater forecast center must provide a theater-scale weather analysis and forecast model capability that will produce tailored, accurate, and reliable forecast products in a more responsive fashion than is currently possible.

Modifications to existing tactical observing systems, GMQ-33s, TMQ-34s, and TMQ-36s, are required to provide an automated capability to determine: cloud amount, cloud heights, visibility, surface pressure, surface wind speed and direction, surface temperature, surface dew point, and precipitation (amounts and type) and the capability to add additional sensors to determine lightning (direction and range), nighttime illumination, present weather, soil moisture and soil temperature, precipitation (fall rates), and cloud type. They must automatically collect and transmit data directly to the TFS. The TFS will then transmit the quality controlled data to the C4I systems making it available to operational customers.

Modifications to the current upper air observing system, MARWINs, must be a lightweight, deployable subsystem that determines vertical profiles of wind speed and direction, temperature, pressure, geopotential heights, and dew point. The base station will transmit this data to the TFS.

Modifications to the current manual surface observing system, Belt Weather Kits, must be single-person portable, consisting of components that can be hand held or ground mounted to manually determine cloud heights, visibility, surface pressure, surface wind speed and direction, surface temperature, surface dew point, precipitation amount, and infrared visibility.

The solution for remote, automated capability must be an expendable, lightweight, and small sensor system deployable to remote areas under friendly or enemy control. It must automatically determine cloud heights; visibility; surface pressure; surface wind speed and direction; cloud coverage; cloud type; infrared visibility; precipitation type, rate, and amount; surface temperature; and surface dew point. These determinations will be automatically transmitted to a designated TFS location.

Meteorological Operational Capability (MOC) develops and procures observing and data processing systems to meet Army and Air Force operational requirements in the fixed BWS environment. This program replaces and improves existing fixed meteorological observing and processing systems, improving support to the planning and execution of aerospace operations, while satisfying critical flight safety and resource protection requirements. The MOC will build

upon technological advances developed under the TFS and tactical observing programs. The transition of tactical systems technology back into the fixed base/post environment supports the "train in peace as you fight in war" concept, ensuring combat and peacetime support systems are as similar as possible; ultimately reducing unit wartime training requirements. The MOC must ingest all available sources of METOC information and, from a single user position, quality control, format, display, process, analyze, and archive all required observed and forecasted weather data and products. The MOC must disseminate this meteorological information to local C4I systems and worldwide weather communications systems. Improved weather observing capabilities must provide continuous and automatic sensing, collection, quality control, and display of local weather conditions. Also, new automated observing capabilities must provide lightning detection for ground refueling, munitions safety and support to base and post central computer facilities, measurement of wind and temperature vertical profiles for wind shear detection and warning, and measurement of slant range visibility to improve flight safety. Improved forecasting capabilities must include the integration of a local environmental forecast model (designed to improve short-range forecasting), replacement or upgrade of existing meteorological data manipulation and display systems, and an integrated platform dedicated to the timely collection, assimilation, processing, and dissemination of all required METOC information.

NEXRAD is a hardware/software development and upgrade to current weather radar systems. The NEXRAD will replace a majority of current fixed radars (FPS-77s and FPQ-21s) and improve weather forecasts. Doppler and computer technology will allow better storm detection and assessment of severity, improve warning accuracy, increase warning lead-times, and permit the automated exchange of digital radar data with civil agencies.

Automated Weather Distribution System Pre-Planned Product Improvement (AWDS P3I) program develops, procures, installs, and maintains evolutionary AWDS improvements. A timely processing improvement will increase the responsiveness and processing abilities of the original system to meet increasing system demand and operational requirements. Communications and computer systems interfaces between AWDS and customer C4I systems, weather satellite receiving systems, and other weather systems will allow timely forecasting and dissemination of critical weather information to customer decision makers. A Remote Briefing Capability (RBC) will allow AWDS to provide selected alphanumeric and graphic products to customer facilities both on and off base/post for briefings. Software improvements include severe weather algorithm calculations, solar and lunar data calculations, toxic corridor calculations, high resolution grid processing, improved archival abilities, and model climatology processing. AWDS P3I will support the migration of this software to an open systems environment.

4.2.2 Army Systems' Enhancements

The following Army programs are planned to satisfy tactical unit shortfalls:

The Integrated Meteorological System (IMETS), AN/TMQ-40 is predominately a non-developmental item that provides automation and communications support to Air Force Weather

Teams assigned to Army Intelligence (G2/S2) Sections at echelons from separate brigade through the echelon-above-corps level and Special Operations Forces. IMETS will receive, process, and collect weather forecasts, observations, and climatological data used to produce timely, accurate products tailored to meet supported commander's requirements for state-of-the-art weather support. IMETS produces, displays, and disseminates, over the Army Tactical Command and Control System (ATCCS), weather forecasts and decision aids that compare the impact of current, projected, or hypothesized weather conditions on both friendly and enemy capabilities.

The Meteorological Measuring System (MMS), AN/TMQ-41 is under development by the Army Research Laboratory (ARL), Battlefield Environment Directorate. The system will have the capability to provide meteorological support to Army artillery operations. The information provided will be the same that is provided by radiosonde-based systems through the use of profiling radars, ground based sensors, and meteorological satellites. This system will provide more frequent atmospheric profiles then are currently provided.

4.2.3 Science and Technology Programs

Key technologies are needed to support modernization plans and future improvements in capability for meeting shortfalls in wartime and peacetime requirements. Software development research for battlefield operations is needed for the following:

A Theater-Scale Analysis Procedure (TAP) capable of ingesting and fusing observations available in-theater, including ground, upper-air, and satellite data in a nearly continuous manner and of providing timely analyzed values of wind, temperature, moisture, and surface pressure.

Analytical, statistical, and artificial intelligence (AI) (e.g., Expert Systems and Neural Network) techniques and models to serve single station and regional data analysis and forecast scenario requirements, including battlefield models capable of predicting/inferring precipitation rates, soil moisture, vertical density variations (atmospheric refractive (atmospheric refractive index structures), ceiling, visibility (obscurants, e.g., dust and smoke), height of the low-level (atmospheric boundary layer) inversion, and severe and extreme low-level turbulence (e.g., due to downslope windstorms).

In addition, a theater-scale numerical weather prediction model will be selected, prototyped, evaluated, and validated. The model will have the capability of providing reliable, very high resolution forecasts of atmospheric elements, including wind, temperature, pressure, and moisture.

Research is also needed to develop improved battlefield atmospheric sensors. Sensors, algorithms, and strategies necessary to automate the detection of the elements of the surface observation will be developed.

R&D is needed to develop improved algorithms for the NEXRAD. The following research efforts are needed to meet customer requirements:

Severe Storms (automated mesocyclone identification and prediction of supercell tornadoes)
Aviation Hazards (icing and turbulence)
Storm Structure (automated wind analysis and non-severe weather)
Tropical Cyclone Analysis (storm strength and wind analysis)

5. FUTURE FAP PLANNING

Currently, several studies are underway that will determine future requirements and operational concepts of AFW. One example is a study scheduled for completion in December 1994 to provide options on the capability of a centralized weather unit on the battlefield. A second example is the AFW architecture study scheduled for completion in December 1995 to determine several functional and physical model options for future AFW development. A third effort is the study to determine joint-level communication connectivity needs. These studies will be used to update and modify the FAP's operational concept and adjust future modernization plans. These may form additional customer requirements and initiate the need to start acquisition and technology programs to solve the newly created deficiencies. The modernization planning process described is continually evolving to optimally meet the changing requirements of our nation's defense. As new technological improvements enhance and change the mission capabilities of AFW's customers, our challenge is to keep AFW at the forefront of technology and poised to provide the warfighter with the best possible decision assistance.

USE OF NARRATIVE CLIMATOLOGIES AND SUMMARIZED AIRFIELD OBSERVATIONS FOR CONTINGENCY SUPPORT

Kenneth R. Walters, Sr. and Christopher A. Donahue
U. S. Air Force Environmental Technical Applications Center
Scott Air Force Base, Illinois 62225-5116

ABSTRACT

A recurring problem for the United States military is supporting contingency operations worldwide. Integral to effective planning of such operations is detailed knowledge of regional climate and weather. USAF Environmental Technical Applications Center (USAFETAC) fills this void by providing tailored narrative studies and summarized airfield observational statistics. Planners use the narrative studies to ascertain weather associated-problems for the entire area in question. Summarized airfield observational statistics give detailed airfield information for both ground and air operational planning. Additional tailored specialized studies are provided as requested, packages are prepared and transmitted electronically to worldwide users within as little as eight hours of request receipt. Examples will be presented at the conference for various recent real world contingencies.

1. INTRODUCTION

The Readiness Support Branch of the United States Air Force Environmental Technical Applications Center (USAFETAC) serves as the focal point for climatological support to contingency operations levied on the USAF and USA. Products go through the Unified and Specified Commands to all subordinate United States military commands as determined by the tasking Unified Command senior meteorological/oceanographic (METOC) officer. Such tailored, point or area specific products are often the only climatological information available to planners who are responding on very short notice to unforeseen deployment of the United States military. Where possible, these products are operationally tailored.

2. SCOPE AND CONTENT OF SUPPORT

Two products form the core of such support: a narrative study and summarized airfield weather observations for airfields to be used either in the area of operations (AOR) or by forces enroute.

The focus of the narratives varies greatly from one study to the next, both spatially and temporally. These normally range from "point" studies, which cover the weather for a city-sized area, up to "small area" studies such as that done for the former

Yugoslavia. Such studies may concentrate on a specific time period or cover the complete annual cycle. The emphasis is placed on weather affecting the type of operations planned, which can cover the gamut of military operations.

Such studies begin by covering, in as much detail as possible, the terrain, vegetation and, if required the flora and fauna of the area of interest. Greatest detail is in the small point studies, such as the heights of nearby hills, ridges, and mountain ranges; a discussion of current speeds and flooding potential of local rivers and drainage systems; and a discussion of indigenous flora and fauna. This last item is not always possible.

Next a very brief discussion of the synoptic, mesoscale, and local meteorological factors which drive the local climate is provided. The discussion is aimed at the audience specified by the requestor. Normally, at least a limited meteorological background is assumed, but some have been tailored for non-meteorologists.

The core of the study is a description of the weather cycle for the requested time period. These are usually divided by local seasons--which are not necessarily the classical temperate zone ones. Conditions that impact military operations are highlighted. In some studies, only those factors (fog, low clouds, heavy rain, high winds, flood and so on) that have adverse affects are discussed. Included are discussions and frequencies of the "rare events"--severe thunderstorms, dense fog, heavy snows, and the like.

Finally, a subjective "confidence factor" is assigned. As most of these studies concern areas for which both studies and raw data are sparse, such confidence factors are necessary if the users are to fully integrate the information into contingency operations. This allows us to discuss our evaluation of the quantity and quality of the information used in preparing the study.

Source material encompasses the total USAFETAC information base. The primary source is the superb collections of USAFETAC's Air Weather Service Technical Library. Its over 500,000 documents make it arguably the largest dedicated atmospheric sciences library in the United States. Summarized numerical data is extracted from the Air Weather Service Climatic Database maintained by USAFETAC's Operating Location A (OL-A) at Asheville NC. Located in the Federal Climate Complex with the National Climatic Data Center and the Navy's Fleet Numerical Meteorology and Oceanography Detachment Asheville, OL-A has immediate access to the combined data bases. If we are lucky, the area of interest is within the area covered by one of our regional climatologies. Research is simplified greatly by such a coincidence.

These studies are normally transmitted via secure telecommunication links to the requestor(s); illustrations are necessarily kept to a minimum due to the very short amount of time

allowed to complete such studies. During "DESERT SHIELD", for example, such studies were routinely researched, prepared, and sent within 24 hours after receiving the request. Studies are under 10 pages.

The second product is one or more airfield climatological data summaries. Such summaries are highly desirable for those locations where flight operations are planned. These give not only standard mean and extreme monthly temperature and precipitation information, but also percent frequencies of occurrence of selected joint ceiling and visibility values by three hour blocks (00-02 local time, 03-05, etc), prevailing and extreme winds, mean number of days with fog, dust, and so on. Such a summary can be prepared, if sufficient data is available in the database, within 4 to 8 hours after request receipt. Observation availability is, of course, key in preparing such summaries. Data receipt from many Third World areas is somewhat limited. Observations may not be available for nighttime hours; often observations are transmitted only every three hours even during the day. Such constraints often mean that only a "limited hour summary" can be prepared. In the worst, and most frustrating, cases insufficient observations are available to prepare such a summary.

Other products may be provided as requested by the senior METOC officer. For example, climatological refractive index profiles can, under certain conditions, be extremely useful in determining radar performance. Electro optical climatologies are vital for determining just what sensors will work effectively under various weather conditions. Wet-bulb globe temperature climatologies are crucial in tropical regions in establishing deployed personnel work schedules. Conversely, climatological wind chill factors for certain seasons and areas of the world are equally vital. Engineers tasked to build everything from runways to ports in the AOR require specialized temperature and precipitation climatologies.

3. USES

Effective planning for any military operation require a thorough knowledge and integration of the effects of weather and/or climate into such plans. Papers in the *9th Applied Climatology Conference* discuss the uses of climatology in long term, or "deliberate" planning. Here we focus on the rapid, or "contingency," response to unforeseen, rapidly developing operations. Few military operations are not affected by weather.

The specialized climatological packages discussed in this paper allow planners to modify deploying equipment to effectively operate in the particular conditions of the small area of interest. Often all this requires is slight modification of already existing plans. On occasion, it may require more comprehensive changes. Such information becomes especially important now that most operations occur in Third World areas

where little current meteorological data is available. both the Somalia and the Rwanda Humanitarian Relief Operations are excellent examples.

Experience has shown the narrative studies are best for general discussions of area conditions and for ground operations. Summarized point data are best for air operations over a specific point, *if such observational data are available*. In some cases, such climatological contingency packages provide the major portion of the on-site weather information available to deploying, including weather support, forces. This is particularly true for Special Operations Forces. These packages not only provide the deploying weather personnel with badly needed background information on the area concerned, they also provide packages that, often with little modification, can be given to flying and ground operations personnel to acquaint them with expected general conditions. Such packages do not take the place of real-time weather support; they do provide invaluable information which allows effective planning for immediate operations.

Such packages mark a departure from standard climatological support as it has been provided for the past 20 years. The combination of computer sophistication and the availability of a large atmospheric sciences library allows preparations of such packages on very short notice and rapid dissemination to DoD units worldwide. Such centrally prepared and distributed climatological packages ensure that weather personnel and operations staff at all levels are provided with identical information. To quote General of the Air Force "Hap" Arnold, "Weather is the essence of successful air operations." Given its effect on present and future weapons systems, this is now true for all operations. Our climatological contingency packages are designed to help maximize weather support quality.

USAFETAC DIAL-IN ACCESS

Kevin L. Stone and Robert G. Pena
USAF Environmental Technical Applications Center
Scott AFB, Illinois 62225

ABSTRACT

Describes the USAF Environmental Technical Applications Center's (USAFETAC's) Online Climatology Dial-In Service (Dial-In). Dial-In allows Department of Defense (or any U.S. Government agency) users to gain direct access, using a PC and modem, to certain climatological applications available on USAFETAC's IBM 3090 mainframe computer. Dial-In uses a batch-type communication technique called "Advanced Program-to-Program Communication (APPC)." Dial-In works cooperatively with commercial APPC software to allow information exchange between a PC and the IBM mainframe. A menu system allows users to run pre-selected programs to receive standard output. Applications currently available are divided into three categories: Surface (12 applications), Upper-Air (2 applications), and Utilities (3 applications).

1. INTRODUCTION

The USAF Environmental Technical Applications Center's (USAFETAC's) Online Climatology Dial-In Service (Dial-In) allows Department of Defense or any U.S. Government agency users direct access, using a personal computer (PC) and modem, to certain climatological applications available on USAFETAC's IBM 3090 mainframe computer. Dial-In, which became operational in 1992, makes climatological data quickly and easily available to USAFETAC's customers.

A user can login to Dial-In by entering a valid user ID and password. The ™·ystem allows users to run pre-selected programs and receive standard output. The output can be downloaded to the remote PC. The program features "point and click" commands to control 3-D buttons that prompt the user with dialog windows for required input information.

Dial-In has a messaging capability that allows communication between remote users and USAFETAC. Seventeen applications are currently available and are divided into three categories: *surface* (twelve applications), *upper-air* (two applications), and *utility* (three applications).

2. HARDWARE/SOFTWARE CONFIGURATION

Dial-In uses a batch-type communication technique called "Advanced Program-to-Program Communication (APPC)." Dial-In works cooperatively with commercial APPC software to

allow information exchange between a PC and the IBM mainframe. To access Dial-In the end user needs an IBM or compatible 286 based PC with 640KB main memory, 1.5MB of available hard-disk space, MS DOS version 3.2 or better, EGA or better graphics display (256KB) memory, and Hayes compatible 2400 baud or better modem. The end user connects to a PC at USAFETAC which serves as an asynchronous controller. The controller contains a coprocessor board and control program allowing up to eight simultaneous users. The commercial APPC software communicates with the mainframe computer host through the asynchronous controller.

3. MAIN DISPLAY

The Dial-In main display screen (see Figure 1) consists of two sections: Control Buttons and the Log Area.

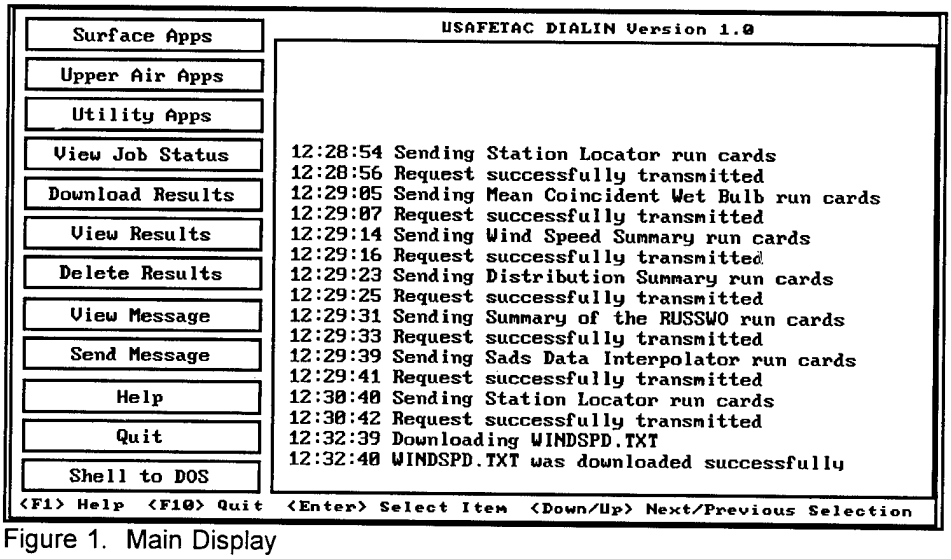


Figure 1. Main Display

3.1 Control Buttons

The Control Buttons line the left side of the main display. Activating the control buttons allows the user to enter into any of three types of applications (surface, upper air or utility), a job status viewer, a module to download the job results, other modules to view and delete results, and a message viewer allowing the user to read messages stored on the mainframe computer. The user can send a message to USAFETAC by activating the Send Message button.

3.2 The Log Area

The log area appears on the right two-thirds of the screen displaying a summary of transactions. The log is copied to a file and stored on the user's PC for a history of the Dial-In session.

4. APPLICATIONS

Surface applications run against the DATSAV2 surface data set. The data set consists of worldwide weather observations collected through the USAF Automated Weather Network (AWN); decoded at the Air Force Global Weather Central (AFGWC), Offutt AFB, Nebraska; and stored on magnetic tape at USAFETAC, Scott AFB, Illinois and at USAFETAC's Operating Location A (OL A), Asheville, North Carolina. The database contains synoptic, METAR, SMARS, AMOS, AERO, MARS, and airways observations.

Upper air applications run against the DATSAV Upper-Air data set which contains rawinsonde and pilot balloon observations derived from reports received at AFGWC over the AWN. These observations are quality checked before they are sent to USAFETAC.

Utility applications are general purpose utilities which help with locating Block Station information. These applications run against the Air Weather Service Master Station Catalog (AWSMSC) which is a comprehensive listing of environmental observing sites current to the last nine months. For each station, it lists the name, identifier, location, types of data reported, field elevation, pressure reporting locations, equipment types, etc.

4.1 Surface Applications

4.1.1 A Summary (Weather Conditions)

This program provides output that is equivalent to part A of the Surface Observation Climatic Summary (SOCS). The program provides for both a total occurrence count and a percent frequence of occurrence for a specified period of record (POR) for the following weather categories: thunderstorms, rain and/or drizzle, freezing rain and/or drizzle, snow and/or sleet, hail, fog, smoke and/or haze, blowing snow, dust and/or sand.

4.1.2 Conditional Weather Summary

This program provides the mean number of days a selected surface weather element (e.g., fog, rain, precipitation) or a combination of two elements occurred for each month of a specified POR. The data are arranged in hourly and 3-hourly groups in local time. A range of values may be used to further describe an element (e.g., visibility from 4800 to 8000 meters).

4.1.3 Distribution Summary

This program prints hourly, monthly, or annual cumulative frequency distributions for density altitude, pressure altitude, or dry bulb temperature for a specified POR.

4.1.4 Ceiling Durations

This program provides the duration each time the ceiling is below a specified level for a specified POR. The beginning and ending date and hour are provided for each duration.

4.1.5 Mean Coincident Temperature

This program gives the mean frequency of occurrence of a primary temperature with a mean coincident secondary temperature for each primary temperature range. It provides the number of occurrences within a range of a temperature type and the average corresponding value of another specified temperature type. This information may be used in temperature or design studies. The possible primary and secondary temperature types are dry bulb, wet bulb, and dew point.

4.1.6 Percent Cloud Free Line of Sight

The Percent Cloud Free Line of Sight program provides matrices of percent probability of cloud free line of sight above a selected location. The matrices give average percent values by month for three hourly periods. The angles above the location are computed every 10 degrees from 0 to 80 degrees. Surface-derived databases require a specified Block Station number. Satellite-derived databases can be run for any latitude and longitude point.

4.1.7 Phenomena Summary

This program supplies output that is equivalent to part A of the Surface Observation Climatic Summary (SOCS). The program accesses data already in the computer database; however, the period of record may not be as complete as what is available for the "A Summary" program which runs all available tape data. The program provides both a total occurrence count and a percent frequency of occurrence for a specified POR for the following weather categories: thunderstorms, rain and/or drizzle, freezing rain and/or drizzle, snow and/or sleet, hail, fog, smoke and/or haze, blowing snow, dust and/or sand.

4.1.8 Precipitation Summary

The Precipitation Summary presents precipitation, temperature, and sky cover data for a selected station and POR. The data is derived from the DATSAV database and can be obtained for any reporting station back through the year 1973. The program is relatively fast and produces a large amount of data but is limited to an 11 year POR per request due to size limitations in the program.

4.1.9 Surface Package

The Surface Package program produces a percent frequency of occurrence for specified elements and POR. A list of over 50 elements may be compared against each other for a specified block station. The program is designed for either a one element percent frequency of occurrence or a detailed comparison of many elements.

4.1.10 Temperature, Relative Humidity, and Wind Climo Summary

This program provides the following tables of climatological statistics using a specified POR not to exceed 30 years.

1) Monthly/annual temperature and relative humidity statistics.

2) Percent frequency of occurrence of wind direction and wind speed (knots) for both sustained winds and gusts.

3) Monthly/annual winds (knots).

4) Maximum wind occurrence - the five highest values per year.

4.1.11 Wind Chill

The Wind Chill program provides the percent frequency occurrence of equivalent chill temperature (wind chill). The frequency distributions are given for user specified temperature categories and POR.

4.1.12 Windspeed Analysis

The Windspeed Analysis program provides the five strongest wind speeds (sustained or gust) for each year and month of a specified POR.

4.2 Upper Air Applications

4.2.1 Probability of Icing

The Probability of Icing program computes icing information for a selected rawinsonde site and determines the probability of icing at the following levels: 1000, 850, 700, 500, and 400 mb. The probabilities are multiplied by a correction factor from AWSM 105-39 (AWS/TR-80/001) based on 20,000 aircraft flights in icing conditions to obtain the potential for icing.

4.2.2 Upper Air Reader

The Upper Air Reader program extracts RAOB data for a particular station from USAFETAC's climatic database. Pressure, temperature, moisture, and wind data are interpolated to either pressure or height. Pressure interpolation is from the surface to 100 mb in 100 mb intervals. Height interpolation is from the surface to 50,000 feet MSL in 1,000 foot intervals.

4.3 Utility Applications

4.3.1 Nearest 50 Stations

The Nearest 50 Stations program provides the 50 closest active weather stations to a given point. The program searches the Air Weather Service Master Station Catalog and helps locate stations which may be used for climatological studies.

4.3.2 Station Locator

Station locator helps find the best reporting station(s) for either surface or upper air data. The program selects and displays reporting stations in specified areas and provides the frequency of reports for surface or upper air data. Five degree squares or less are the optimum input, especially in data dense areas.

4.3.3 TAFVER II Statistics

The TAFVER II program is an automated tool designed to measure the quality of weather forecasting support provided by the Air Force weather community. The program verifies all Terminal Aerodrome Forecasts (TAFs) issued by Air Force weather forecasters, providing the corresponding observations are available.

5. SUMMARY

The Dial-In service was fielded to provide USAFETAC's customers with more responsive support. The system allows remotely located users to access USAFETAC's mainframe computer, which benefits USAFETAC and the customer. A menu system allows the user to run pre-selected programs to receive standard output. Programs construct commonly requested summarized profiles of meteorological variables. The output can then be downloaded to the end user's PC. The Dial-In service was implemented to augment the traditional system to help relieve backlogs and provide information quickly, not as a replacement to the traditional system.

REFERENCES

Pena, Robert G., 1994: USAFETAC Online Climatology Dial-In Service Users Manual, USAFETAC TN-94002, USAF Environmental Technical Applications Center, Scott Air Force Base, IL, 80 pp.

ASTRONOMICAL MODELS ACCURACY STUDY

Chan W. Keith and Thomas J. Smith
USAF Environmental Technical Applications Center
Scott AFB, Illinois 62225-5116

ABSTRACT

Several astronomical routines and their accuracy in calculating solar and lunar event times were compared. The Naval Observatory MICA (Multiyear Interactive Computer Almanac) model was used as ground truth and assumed to be correct. Programs compared to MICA were the USAFETAC Nitelite for Windows model; LightPC version 4.2, developed by Sgt Schweinfurth of Detachment 5, 5th Weather Squadron; the Illum routine used in the USAFETAC program INSOL; and the Army model, NVG versions 4.0 and 5.1. Model output for a series of latitudes between the equator and 80 degrees north were compared.

1. INTRODUCTION

The USAF Environmental Technical Applications Center (USAFETAC) performed a study to determine the accuracy of various astronomical event time calculation routines. Model accuracy was determined by using the models to calculate sunrise, sunset, moonrise, moonset, and various twilight times over a three year period, and comparing these values to an acceptable standard. The Naval Observatory's MICA (Multiyear Interactive Computer Almanac) model was used as ground truth in the study. Programs compared to MICA were (a) the USAFETAC Nitelite for Windows model, (b) LightPc version 4.2, developed by Sgt Schweinfurth of Det 5, 5th WS, (c) the Illum routine used in the USAFETAC program INSOL and the Electro-Optical Tactical Decision Aid (EOTDA) software, and (d) versions 4.0 and 5.1 of the Army model, NVG. Statistical parameters including average error, root mean square error, standard deviation, and total error were computed. Model output for a series of latitudes between the equator and 80 degrees north were compared. The Illum routine was the most accurate model compared to MICA. Accuracy degraded only slightly at the extreme northern latitudes. The next most accurate model was LightPC. Nitelite performance was nearly equivalent to LightPC at latitudes below 60 degrees north, but accuracy decreased rapidly at the higher latitudes. The latest version of NVG performed comparably with Nitelite in computing the sunrise, sunset and moonrise, but performance degraded somewhat for the other event times. The average errors for all of the models except NVG were less than 3 minutes for all of the latitudes and event times tested.

All of the models are capable of running on a desktop PC, although our version of ILLUM 92 was run on an IBM R/S 6000 workstation using IBM's XL FORTRAN compiler, which defaults to double precision for floating point calculations. Output from LIGHTPC version 3.2 and earlier is assumed to be identical to NITELITE, since they used the same algorithm for computing the sun and moon locations.

2. MODEL DESCRIPTIONS

2.1 NITELITE

NITELITE is the latest USAFETAC-developed program produced for calculating astronomical data. It is the only program tested that is available in a Windows version. It computes the beginning and ending of nautical twilight, sunrise and sunset, moonrise and moonset, and percent illumination information. The output is in an easy to read graphical format, but the program will not output the data to a file in a tabular format. As a result, a slight modification was made to the program to save the data to a file for comparison purposes.

The algorithm that calculates the solar and lunar data was originally developed by A. C. van Bochove (1982) in FORTRAN; the NITELITE version contains a few minor corrections. The algorithm was converted to visual BASIC and adapted for use within the Windows program on the desktop computer. The program is maintained by USAFETAC/SYS. NITELITE uses the same algorithm (ILLUM, 1987) as LIGHTPC version 3.2, an USAFETAC program, and we assume LIGHTPC v3.2 performance would be nearly identical to NITELITE.

2.2 LIGHTPC

This program is an updated version of the original LIGHT program developed by 1Lt's D. Payne and J. Morrison from USAFETAC. This version was produced by Sgt J. Schweinfurth, of Det 5, 5WS, and was developed specifically for determining solar and lunar event times, and for night vision goggle support. In addition to computing event times, it can compute percent illumination and nighttime darkness data. The program is user friendly and menu driven. Processing time, however, is somewhat slow for large amounts of data (i.e. more than several months).

LIGHTPC calculations are based primarily on the methods developed by A. C. van Bochove (1982), with a number of corrections and updates. The solar semidiameter was assumed to be a constant 16 minutes (') of arc. The lunar semidiameter and parallax were individually computed and included as correction terms in the calculations of event times. Upgrades to this program can not be readily obtained.

2.3 ILLUM 92

Capt M. Raffensberger, in USAFETAC/SYT, developed the INSOL program in 1994, primarily to compute the daily cumulative insolation at the surface and the top of the atmosphere as an aid for forecasting fog dissipation. The original program did not provide the solar and lunar information directly, but since it made the astronomical computations and used the data internally, the program was modified to output that information so that its accuracy could be determined.

The algorithm is based on the program developed by A. C. van Bochove and Erlich (1982) and was modified by Sidney Wood (1986), Paul Hilton (1987), Maria Gouveia (1989) and Dan

DeBenedictis (1992) of Hughes STX. The ILLUM subroutine within the INSOL program was originally used in the Electro-Optics Tactical Decision Aid (EOTDA) program by Hughes STX; it computed solar position at 15 minute intervals, but was modified to make the computations every 20 seconds to ensure the event times we obtained were to the nearest minute. Solar and lunar locations were adjusted to account for a standard refractive index produced by the atmosphere, which corresponded to 34' of the solar or lunar path arc length. The sun's semidiameter (16') and moon's semidiameter (16') were also included in the adjustment, since event times are based on the upper limb of the disk. A search was then conducted to find the positions and times corresponding most closely to the appropriate solar and lunar locations described within the definitions of the various twilights and rise and set times.

2.4 NVG

The Night Vision Goggles program (NVG) was developed and recently updated (version 5.1) by the Army Research Laboratory (ARL), primarily for computing nighttime natural illumination values. User inputs include observer location, date and time, and current meteorological information for specific parameters. The model is capable of calculating solar and lunar position, rise and set times, two forms of twilight times, and illumination information. The calculated sun and moon positions are based on the methods developed in 1982 by A. C. van Bochove.

The program is menu driven and some background knowledge of the program is helpful, since some of the input parameters require a specific format. Weaknesses of this software include: (1) calculations are limited to the area between 64° S and 64° N, and (2) the program will only send the output to the screen or printer, and not to an output file for further processing. (ARL provided a modified version of the program that did allow for data to be sent to an output file.) One year of data from v4.0 was also used in the study. This model includes horizontal refraction and disk semidiameter corrections (34' and 16', respectively) in the event time computations.

According to D. Sauter (personal communication), NVG searches for the beginning of nautical and civil twilight (BNT, BCT), sunrise and sunset (SR, SS), then uses the time differential between BNT and BCT from SR to get an approximated end of civil and nautical twilight (ECT, ENT). While this procedure is a useful time saving tool, it can cause a non-occurring event to be predicted at higher latitudes. This occurs when the sun goes above (below) 12° elevation angle and stays above (below) 12°, for example, for many weeks in the summer (winter).

2.5 MICA

This Naval Observatory program superseded their Floppy Almanac in 1992, and was created for astronomers, surveyors, meteorologists, and navigators to provide high precision astronomical data for a variety of astronomical objects, including all of the planets, the moon and many stars. Stated accuracy is less than 1 minute of time. A sample of the parameters that can be calculated are three forms of twilight times, rise and set times, positions of celestial bodies, and fraction illumination. The calculated celestial body positions, as described in the Mica Users' Manual, are based on methods presented by C. A. Smith et al., and ephemeris data provided by E. M.

Standish, Jr. The program is user friendly, fast, and menu driven. A constant solar semidiameter of 16' of arc and a constant horizontal refraction (34') are assumed. The program individually computes the lunar semidiameter and parallax and includes them in the event time computations.

3. METHODS

3.1 Scope

Each program's data, except that from NVG v4.0, was compared to output from MICA for the 3 year period of record from 1 Jan 94 through 31 Dec 96. Output from NVG v4.0 was limited to 1 Jan 94 through 31 Dec 94.

The locations for which event times were calculated for each model corresponded to a constant longitude of 90° W and the latitudes given by Table 1. The latitudes were limited to the northern hemisphere. It was assumed that the results obtained apply to the southern hemisphere as well, and that model errors did not vary for different longitudes. Latitudes above 80° N were not used in this study because MICA accuracy decreased within a few degrees of the poles. Event categories indicated in Table 2 are available from the models. The program times were compared with the MICA times, and the statistical analyses described below were performed.

Table 1. Latitudes for computing event times used within this study for each of the models.

LAT	NITE LITE	ILLUM	LIGHT PC	NVG
0	✓	✓	✓	✓
10	✓	✓	✓	✓
20	✓	✓	✓	✓
30	✓	✓	✓	✓
40	✓	✓	✓	✓
50	✓	✓	✓	✓
60	✓	✓	✓	✓
65	✓	✓	✓	**NA**
70	✓	✓	✓	**NA**
75	✓	✓	✓	**NA**
80	✓	✓	✓	**NA**

Table 2. Event times predicted by each model for purposes of this study.

	NITE LITE	ILLUM	LIGHT PC	NVG
BNT	✓	✓	✓	✓
BCT	**NA**	✓	✓	✓
SR	✓	✓	✓	✓
SS	✓	✓	✓	✓
ECT	**NA**	✓	✓	✓
ENT	✓	✓	✓	✓
MR	✓	✓	✓	✓
MS	✓	✓	✓	✓

3.2 Statistical Parameters

Several statistical parameters were computed for each latitude for the results generated by the models. The following statistical parameters were computed (Wilmott, 1982).

Total error - the total number of minutes of error over the period of record;

$$\sum_{i=1}^{N} (P_i - O_i), \tag{1}$$

where N is the total number of observations for the period of record, O_i is the MICA predicted event time, and P_i is the model predicted event time. The total error provides an indication of the model bias, whether the model consistently predicts events to occur either before or after the MICA model. To determine the bias of model results, it is necessary to consider the magnitude of the total error, in conjunction with the magnitude of the total absolute error, described below.

Total absolute error - the total number of minutes of the absolute value of the error over the period of record;

$$\sum_{i=1}^{N} |(P_i - O_i)|. \tag{2}$$

The total absolute error describes the overall magnitude of the error for each model. This statistic is not normalized by the number of events and will vary significantly with the number of events in the period of record.

Average error - the total number of minutes of the absolute value of the error over the period of record divided by the total number of observations;

$$\frac{\sum_{i=1}^{N} |(P_i - O_i)|}{N}. \tag{3}$$

This is referred to as mean absolute error by Wilmott (1982), and it weights all errors equally in its determination. This statistic is normalized by the number of observations, so it will not change if a larger period of record is used, as long as the sample size is representative.

Root Mean Square Error (RMSE) - the square root of the sum of the individual errors squared divided by the total number of observations;

$$\sqrt{\frac{\sum_{i=1}^{N} (P_i - O_i)^2}{N}}. \tag{4}$$

The RMSE weights larger individual errors more heavily than the smaller errors. The RMSE is also normalized by the total number of observations.

4. RESULTS

4.1 Solar Events

In general, the models predicted the solar event times much more accurately at the low latitudes than high latitudes, particularly above 60 ° N. All of the models exhibited some seasonal trend. The models tended to work best near the equinoxes (March and September) and worst near the solstices (June and December). Results from NVG v5.1 did exhibit a slight degradation of performance over time.

Figure 1 depicts the frequency, in percent, that each model predicted the sunrise time within 1 minute of MICA, as a function of latitude. Below 60 ° N, all of the models except NVG were within 1 minute at least 80 percent of the time. NVG v4.0 performed worse than version 5.1, and since the latest version is strictly an update of v4.0, only v5.1 results are shown. For all latitudes and events, ILLUM 92 predicted at least 90 percent of the events correctly. At 60 ° N and below, the number of correctly predicted events generally exceeded 95 percent for this model. LIGHTPC was the second best performing model, and predictions were within 1 minute over 90 percent of the time over the entire range of latitudes. There is a decreasing trend in the performance of NITELITE with increasing latitude. NITELITE correctly predicts as little as 30 percent of any specific event at 80 ° N. Predicted event times were within 1 minute of the MICA determined time at least 67 percent of the time and within 2 minutes at least 83 percent of the time for any given latitude. NVG sunrise times within 1 minute decreased to 53 percent for the higher latitudes, but the model was within 2 minutes at least 80 percent of the time. NVG predicted sunset more accurately than sunrise.

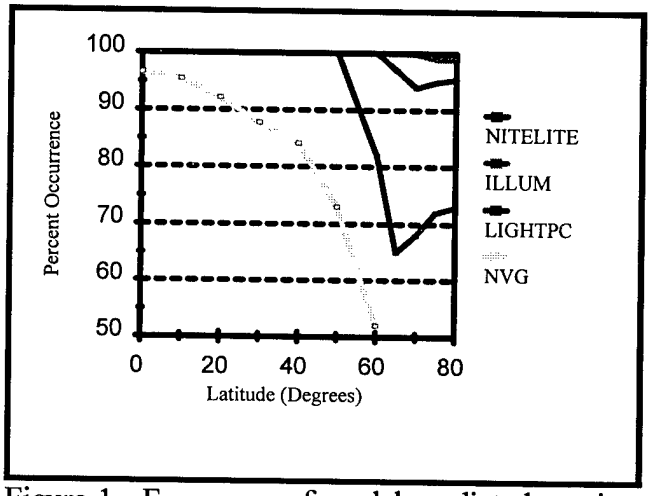


Figure 1. Frequency of model predicted sunrise times within 1 minute of MICA sunrise times.

Table 3 provides error statistics for a typical midlatitude. Statistical analyses from other latitudes showed similar results. The ILLUM 92 model performs the best of the group, compared to MICA. The maximum absolute error did not exceed 3 minutes for ILLUM 92, except for one occurrence of a 31 minute error at 65 ° N. Average errors were under 0.1 minute. The total error for the beginning event times are slightly negative, meaning the model forecasted the beginning times early more often than late overall. It also predicted the event ending times slightly early.

Error statistics for LIGHTPC show it to be the next best performing model. Total errors indicate a positive bias, meaning the model predicted event times were slightly later than MICA predicted event times. Average errors ranged from 0.02 minutes at the equator to 0.64 minutes at 50° N.

Table 3. Statistical analysis results for the model predicted solar event times for 40° N.

40 N	Tot No Obs	Tot Abs Err (min)	Tot Err (min)	Avg Err (min)	Max Abs Err (min)	RMSE (min)	Num Mssd Evnt	Num Non Occ
NITELITE BNT	1096	506	404	0.46	2	0.76	0	0
ILLUM 92 BNT	1096	15	-5	0.01	1	0.12	0	0
LIGHTPC BNT	1096	496	410	0.45	2	0.74	0	0
NVG BNT	1096	478	-370	0.44	2	0.66	0	0
ILLUM 92 BCT	1096	13	-9	0.01	1	0.11	0	0
LIGHTPC BCT	1096	324	138	0.30	1	0.54	0	0
NVG BCT	1096	423	-209	0.39	2	0.64	0	0
NITELITE SR	1096	422	120	0.39	1	0.62	0	0
ILLUM 92 SR	1096	23	5	0.02	1	0.14	0	0
LIGHTPC SR	1096	394	116	0.36	1	0.60	0	0
NVG SR	1096	1066	294	0.97	2	1.14	0	0
NITELITE SS	1096	436	12	0.40	1	0.63	0	0
ILLUM 92 SS	1096	33	7	0.03	1	0.17	0	0
LIGHTPC SS	1096	449	29	0.41	1	0.64	0	0
NVG SS	1096	705	283	0.64	2	0.83	0	0
ILLUM 92 ECT	1096	18	18	0.02	1	0.13	0	0
LIGHTPC ECT	1096	302	-16	0.28	1	0.52	0	0
NVG ECT	1096	2084	1482	1.90	4	2.19	0	0
NITELITE ENT	1096	478	-244	0.44	2	0.68	0	0
ILLUM 92 ENT	1096	27	27	0.02	1	0.16	0	0
LIGHTPC ENT	1096	490	-234	0.45	2	0.69	0	0
NVG ENT	1096	2183	1603	1.99	4	2.28	0	0

Event errors are distributed much more widely for NITELITE, and some of the events show a skewed distribution in the statistics. Below 60° N, the errors were approximately the same magnitude as those of LIGHTPC but at the higher latitudes, LIGHTPC performance was significantly better than NITELITE.

Error statistics for NVG v5.1 were the least accurate in the study, and they exhibited a definite

bias for several of the events. The model predicted the beginning of nautical and civil twilight early. Likewise, the model predicted the ending of civil and nautical twilight late, on average. Errors for sunrise were larger than those for sunset. NVG does not produce results poleward of 64°, so study results are limited to 0° N through 60° N latitude.

4.2 Lunar Events

Overall, the lunar event time predictions followed trends similar to those of the solar event times. All of the models exhibited a decrease in accuracy with increasing latitude. The results suggest a minor periodic trend for all of the models. None of the models exhibited a decrease in accuracy over time.

Except for NVG v5.1, there were fewer correctly predicted lunar event times than the solar event times, but as Figure 2 demonstrates, the number of moonrise times within 1 minute is nearly equivalent to those of sunrise times. NVG predicted moonrise much more accurately than sunrise. All of the models were within 1 minute at least 80 percent of the time for latitudes below 65° N. The ILLUM 92 predicted event times were within 1 minute of the actual event over 95 percent of the time for any latitude. LIGHTPC and NVG v5.1 performed as well as ILLUM 92 at the low and middle latitudes, but LIGHTPC degraded more quickly at the higher latitudes. NITELITE was within 1 minute over 90 percent of the time up to 60° N.

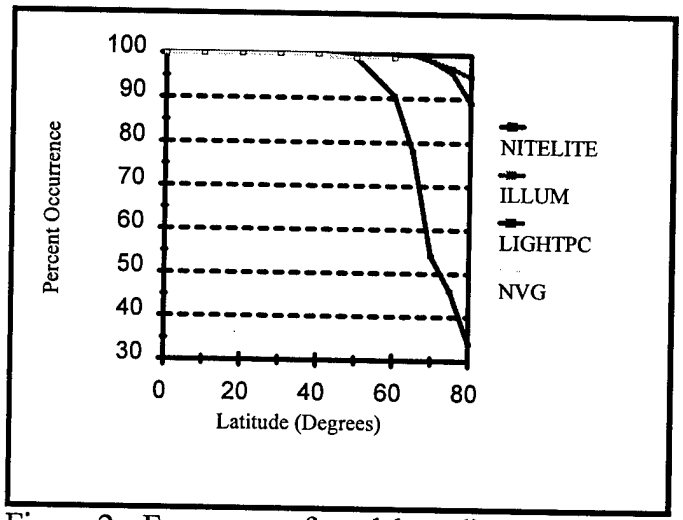


Figure 2. Frequency of model predicted moonrise times within 1 minute of MICA moonrise times.

The maximum absolute error for ILLUM 92 was only 12 minutes and this model performed best in predicting lunar events. Table 4 provides results for a typical midlatitude. The maximum absolute error for LIGHTPC was only one minute from the equator through 65° N, and there were no missed events for that range of latitudes. Prediction times rapidly deteriorated above that latitude and the maximum absolute error increased to as much as 26 minutes. The maximum absolute error for NITELITE was only 1 minute through 40° N, and 4 minutes through 65° N. NVG v5.1 moonrise errors were comparable with NITELITE, however, NVG performance degraded somewhat in predicting moonset.

5. CONCLUSIONS

Although the four models tested used variations of the same algorithm, updates and improvements in processing speed caused large variations in model performance results.

Table 4. Statistical analysis results for the model predicted lunar event times for 40° N.

40 N	Tot No Obs	Tot Abs Err (min)	Tot Err (min)	Avg Err (min)	Max Abs Err (min)	RMSE (min)	Num Mssd Evnt	Num Non Occ
NITELITE MR	1058	340	38	0.32	1	0.57	0	0
ILLUM 92 MR	1058	84	76	0.08	1	0.28	0	0
LIGHTPC MR	1058	86	58	0.08	1	0.29	0	0
NVG MR	1058	375	-279	0.36	2	0.60	0	0
NITELITE MS	1059	343	117	0.32	1	0.57	0	0
ILLUM 92 MS	1059	81	-17	0.08	1	0.28	0	0
LIGHTPC MS	1059	76	12	0.07	1	0.27	0	0
NVG MS	1059	861	-861	0.81	2	0.99	0	0

The most accurate model compared to the Naval Observatory's model, MICA, was the ILLUM 92 routine found in the USAFETAC-sponsored INSOL and Hughes STX provided EOTDA programs. This routine consistently produced the smallest average and root mean square errors. However, in its current state, the routine is not readily suitable for directly computing and displaying astronomical event times. The program needs to be capable of determining event times more efficiently. Some time saving methods could be incorporated into the routine to allow the model to determine event times more quickly. The program also needs to be converted into a user friendly format, such as making it Windows compatible.

LightPC version 4.2 is the next most accurate model. The high accuracy mode at the extremely high latitudes and the easy to use menus make this model a solid performer. A significant drawback to this program is the inaccessibility of the program code for maintenance and upgrade purposes, such as a full time high accuracy mode and changes to the output form.

Nitelite for Windows works fairly well at the low and middle latitudes but accuracy decreases rapidly above 60° N. The program is driven by friendly prompts and has the capability to display the data in an easy to read graphics format, but more options, such as the ability to save to a file and the computation of civil twilight, may be desirable. This program should be updated by the newer ILLUM 92 routine for improved accuracy if it continues to be used.

The Army model, NVG, had the largest errors for all latitudes when compared to MICA. Presumably, much of the error for several of the events can be eliminated by a simple correction factor within the program itself. The model uses prompts and Help Screens for input parameters that it requires. Although the documentation that comes with the program claims that the program is not for operational use, a few modifications to the program would make it slightly more accurate. An increase in accuracy for all of the event times and the capability to write to an output file are two changes that could be made.

All of the models assumed a constant correction for the effects of refraction (34') when computing event times. Variations in the refractive index occur due to natural atmospheric variations, such as inversions or stable layers, causing all of the models, including MICA, to produce erroneous results.

The magnitude of these errors are partially a function of the magnitude of the atmospheric variations in the index of refraction; in the tropics variations are relatively small; at the midlatitudes and higher, variations will be larger. A more important contributor to the magnitude of the errors is the sun's apparent path through the sky, or more precisely, the maximum zenith angle of the sun. This zenith angle decreases with increasing latitude. At the higher latitudes, the sun remains near the horizon for a longer period, so that variations in the refractive index will produce a larger error than the same refractive index variation at lower latitudes. Near the poles, this variation forces larger errors and may be sufficient to incorrectly predict the occurrence or nonoccurrence of an event.

This report was designed to provide accuracy information to users or potential users of the models studied to allow more informed decisions be made, based on model output. If the reader is looking for simple and accurate event times or fraction illumination information in tabular format, we suggest obtaining MICA from the address in the bibliography. If a graphical format is needed then NITELITE will be required. For specific support and output requirements needing a high degree of accuracy, such as support to night vision goggle users, additional programs or modifications to the existing programs will have to be sought.

BIBLIOGRAPHY

Duncan, Louis D., and David P. Sauter, *Natural Illumination under Realistic Weather Conditions*, Atmospheric Sciences Laboratory, ASL TR-0212, White Sands Missile Range, NM 88002, 1987.

Duncan, Louis D., and Gavino Zertuche, *Night Vision Goggles (NVG) Software User's Guide version 4.0,* U.S. Army Research Laboratory Battlefield Environment Directorate, White Sands Missile Range, NM 88002-5501.

MICA for DOS User's Guide, Astronomical Applications Department, U.S. Naval Observatory, Washington, DC 20392-5420.

van Bochove, A. C., *The Computer program "ILLUM": Calculation of the Positions of the Sun and Moon and the Natural Illumination,* Physics Laboratory TNO, National Defense Research Organization TNO, P.O. Box 96864, 2509 JG The Hague, The Netherlands, 1982.

Willmott, Cort J., Some Comments on the Evaluation of Model Performance, *Bulletin of the American Meteorological Society,* 63, 11, 1982, pp 1309-1313.

ATMOSPHERIC TRANSMISSIVITY IN THE 1 TO 12 MICRON WAVELENGTH BAND FOR SOUTHWEST ASIA

Richard A. Woodford and Chan W. Keith
USAF Environmental Technical Applications Center
Scott AFB, Illinois 62225-5116

ABSTRACT

The USAF Environmental Technical Applications Center (USAFETAC) performed a study to analyze the atmospheric transmittance for the path between a variety of target altitudes and a satellite based sensor over southwest Asia during Desert Storm, and to compare these results to transmittances computed for different climate regimes. The atmospheric transmittance computer model, LOWTRAN 7, was used to compute transmittances for specific atmospheric conditions. Model target height varied between the surface and 10 km above ground level. Actual sounding data from Baghdad, Iraq; Howard AFB, Panama; and Pyongyang, North Korea for the period from January 1973 through December 1988 was used in the model to provide a climatological reference for the analysis. Atmospheric slant path model (ASPAM) output for Iraq during January and February 1991 and climatologically averaged soundings from specific climate regions provided data sources for additional LOWTRAN 7 computations. Using the individual data sets, transmissivities were computed for the wavelength bands 1-2.5 μm, 3-4 μm, 1-4 μm, 1-8 μm, 8-12 μm and individual wavelengths between 8 and 12 μm. Results indicate that the ASPAM generated data set had considerably lower transmissivities than the climatological average over Baghdad, but were not as low as typical values computed for the tropical (Howard AFB) or midlatitude (Pyongyang) environments.

1. INTRODUCTION

This report is a synopsis of two separate studies evaluating atmospheric transmittance values at select locations in Southwest Asia. The objective of the first study was to derive atmospheric transmittance values for the 8 to 12 micron wavelength band, then determine if those values were lower than "normal" or expected values for the area. The second study extended the range to include the 1 to 8 micron wavelength band. The atmospheric transmittance model, LOWTRAN7, (Kneizys, et al, 1988) was used to generate both average and total transmittance values for the bandwidth in question.

LOWTRAN7 was run using two sensor/source geometries. The first series of model runs held the sensor directly above the source (i.e., at nadir). The second series increased the transmittance path length by moving the sensor to a 30 degree viewing angle (i.e., 30 degrees off-nadir). Source altitudes were varied incrementally from the surface to 10 km above the surface.

2. DATA SOURCES

The study was accomplished using three primary data sources. We will refer to the data throughout the rest of this report as datasets 1, 2 and 3. Dataset 1 included the January/February 1991 vertical temperature/moisture profiles for several select Southwest Asia locations. For this set, actual sounding data were not available at the locations requested by USAF Environmental Technical Applications Center's (USAFETAC's) customer for the study, so vertical temperature and moisture profiles were generated for those locations by the USAFETAC's Atmospheric Slant Path Analysis Model, ASPAM (Koermer,1984). Dataset 2 consisted of average climatological profiles of temperature and dewpoint; profiles not restricted to Southwest Asia, but representative of several different geographic regions. Dataset 3 was made up of actual sounding data covering a 15 year period of record (POR) from January 1973 through December 1988 for the following locations: Baghdad, Iraq; Howard AFB, Panama; and Pyongyang, North Korea. These sites were selected because USAFETAC believes they are representative of a desert, tropical, and continental-type climate, respectively.

3. BACKGROUND

The overall distribution of atmospheric gases and aerosols determine the spectral absorbency of the atmosphere. Any change in a beam of radiation passing through a layer of air is determined in part by the concentration and temperature of these resident constituents. Atmospheric transmittance throughout the 1 to 12 micron wavelength band is greatly affected by tri-atomic (H_2O, CO_2, O_3, etc.) molecular absorption. The absorption however, is not continuous across the band. There are regions where the atmosphere is nearly transparent to electromagnetic radiation, and absorption is at a minimum. These windows are located roughly between 1 to 2.5 microns, 3 to 4 microns, 8 to 9.5 microns, and 10 to 12 microns (Environmental Research Institute of Michigan, 1978).

USAFETAC's customer for this study originally supplied datasets 1 and 2, and requested an evaluation of atmospheric transmittance values based on those sets. We felt that because dataset 1 consisted of atmospheric profiles which might have been overly smoothed, dataset 1 might misrepresent actual conditions at the associated locations by, for example, eliminating temperature inversions. Dataset 2 was generated by compiling several hundred soundings averaged to produce one mean temperature, pressure, and moisture profile per geographic region noted. These soundings are mean values for the selected geographic regions, and also may not be representative of actual conditions. The temperature and moisture profiles have been smoothed considerably; subsequently, the resulting vertical profile may never actually occur. It is for this reason that USAFETAC suggested providing statistical distributions based upon atmospheric transmittance values generated by inputting actual soundings into LOWTRAN7.

The LOWTRAN7 computer code is capable of modeling many atmospheric parameters of transmittance and radiance over wavelengths from 0.2 microns to infinity (Kneizys, et. al., 1988); however, in this study, LOWTRAN7 was used to determine atmospheric transmittance only.

4. APPROACH

Datasets 1 and 2 were input directly into LOWTRAN7, and model runs made. Both total and average transmittance values for each location in each dataset were generated. Only the average transmittance values per bandwidth specified were used in the analysis. Dataset 3 consisted of USAFETAC's archived soundings for Baghdad, Howard AFB, and Pyongyang. USAFETAC soundings for those three stations covering a 15 year POR were input into LOWTRAN7 to produce both total and average transmittance values. The results of these model runs were then sorted by location, month, viewing angle, bandwidth, and source altitude. They were then processed through a statistical analysis package, SAS (SAS INSTITUTE, 1994), to create frequency distributions. Values derived from these distributions were then compared to the values computed for datasets 1 and 2.

5. ASSUMPTIONS / LIMITATIONS

A no cloud/no rain scenario was assumed for all datasets, however the presence of water vapor in the atmosphere was the primary source of atmospheric extinction. Adding both cloud cover and rain would significantly reduce transmissivity.

The LOWTRAN7 model assumed default atmospheric profiles for O_3, CH_4, N_2O, CO, CO_2, O_2, NO, SO_2, NO_2, NH_3, HNO_3, and for other background aerosols, such as dust and smoke. No effort was made to adjust the modeled extinction for higher or lower concentrations of these constituents.

Assumptions specific to datasets 1, 2 and 3 are as follows: (1) Station elevations were assumed to be 24 meters above mean sea level. NOTE: This input into LOWTRAN7 is used to modify aerosol profiles below 6 km. (2) Dataset 1 consisted of atmospheric profiles interpolated to needed levels by ASPAM. The boundary layer wind speed was extracted from the dataset-supplied surface wind speed. (3) Dataset 2 was generated by compiling several hundred soundings averaged to produce one mean temperature, pressure and moisture profile, per geographic region noted. (4) In dataset 3, a 6 meter per second surface wind speed was used to initialize the boundary layer aerosol model within LOWTRAN7 for Baghdad and Pyongyang. A 3 meter per second surface wind speed was assumed for Howard AFB.

6. RESULTS

Tables 1, 2 and 3 on the following pages compare dataset 1 average surface transmittances with those calculated for dataset 3. In the 1 to 8 micron band, water vapor is the dominant absorber with reduced transmittances indicated at approximately 2 and 3 microns. This held the average surface transmittance for dataset 1 to approximately 0.45. When compared to climatological records (dataset 3), 0.45 is expected to occur only 1% of the time at Baghdad. At Pyongyang, average transmittances could be expected to be less than 0.45 26% of the time, while at Howard, we would expect values to be at or below this average (0.45) 90% of the time. (All comparisons are being made to January dataset 3 data).

TABLE 1: 50th Percentile Values of Average Transmittance for Baghdad vs Average Transmittance Values for Dataset 1.

		MICRON BAND		
BAGHDAD	1- 8	1-2.5	3-4	1-4
JANUARY	0.54	0.65	0.62	0.58
FEBRUARY	0.53	0.63	0.60	0.56
BEST	0.54(JAN)	0.65(JAN)	0.62(JAN)	0.58(JAN)
WORST	0.50(MAY)	0.59(MAY)	0.54(SEP)	0.54(MAY)
ANNUAL	0.52	0.60	0.58	0.55
DATA SET 1	0.45	0.54	0.48	0.49
*FREQUENCY	1%	1%	3%	2%

*Percentile ranking of Average Transmittance Values for Dataset 1 vs Baghdad's January Cumulative Frequency of Occurrence.

TABLE 2: 50th Percentile Values of Average Transmittance for Pyongyang vs Average Transmittance Values for Dataset 1.

		MICRON BAND		
PYONGYANG	1- 8	1-2.5	3-4	1-4
JANUARY	0.48	0.54	0.65	0.51
FEBRUARY	0.47	0.53	0.64	0.50
BEST	0.47(JAN)	0.54(JAN)	0.65(JAN)	0.51(JAN)
WORST	0.35(JUL)	0.42(AUG)	0.40(JUL)	0.37(JUL)
ANNUAL	0.42	0.47	0.54	0.44
DATA SET 1	0.45	0.54	0.48	0.49
*FREQUENCY	26%	50%	1%	42%

*Percentile ranking of Average Transmittance Values for Dataset 1 vs Pyongyang's January Cumulative Frequency of Occurrence.

In the 1 to 2.5 micron band, water vapor is still the dominant absorber with reduced transmittance starting to show up at 2 microns. The effects are quite pronounced at 2.5 microns. The average surface transmittance for dataset 1 across this band was 0.54, 20% higher than the 0.45 average arrived at when considering the entire 1 to 8 micron band. Based upon dataset 3 runs, 0.54 is expected to occur only 1% of the time at Baghdad. At Pyongyang, average transmittances could be expected to be less than this value (0.54) 50% of the time, while at Howard, 94% of the time we would expect values to be at or below 0.54.

TABLE 3: 50th Percentile Values of Average Transmittance for Howard AFB vs Average Transmittance Values for Dataset 1.

		MICRON BAND		
HOWARD	1- 8	1-2.5	3-4	1-4
JANUARY	0.40	0.51	0.41	0.45
FEBRUARY	0.41	0.52	0.42	0.46
BEST	0.41(FEB)	0.52(FEB)	0.42(FEB)	0.46(FEB)
WORST	0.38(JUN)	0.45(JUN)	0.36(JUN)	0.40(JUN)
ANNUAL	0.39	0.47	0.38	0.42
DATA SET 1	0.45	0.54	0.48	0.49
*FREQUENCY	90%	94%	96%	95%

*Percentile ranking of Average Transmittance Values for Dataset 1 vs Howard AFB's January Cumulative Frequency of Occurrence.

Similar results were noted when evaluating the 3 to 4, 1 to 4, and 8 to 12 micron bandwidths. In general, the dataset 1 values would be expected to occur more often at Howard, rather than at Pyongyang or Baghdad. In the 8 to 12 micron wavelength band, there are two noticeable regions where the transmissivity values dropped considerably. They were at 9.5 and 12 microns. Ozone absorption was at a peak near 9.5 microns. The 12 micron wavelength was affected by absorption due to water vapor.

Atmospheric transmittance values are presented in tabular form for each location. Data from the months of January and February are evaluated, since this period corresponded with the dataset 1 time frame. Also presented are data for the month with the best transmissivity, the month with the worst transmissivity, and finally an average transmissivity for all months. The best month is defined as the month with the lowest cumulative percentage of occurrence of transmissivities equal to or less than 0.75. Based on this definition, the best month contained the fewest occurrences of transmissivity values at or below 0.75. Similarly, the worst month was defined as the month with the highest cumulative percentage of occurrence of transmissivity values at or below 0.75. Transmissivity in the 8 to 12 micron band at Baghdad is highest during the months of January and February. In general, over half of the transmissivities reported at all altitudes were greater than 0.80. The two poorest months were judged to be August and September, August being the worst. August surface transmissivity values were less than 0.75 more than 50% of the time, but 0.65 or less only 10 percent of the time. Transmissivity values rapidly improved with an increase in target altitude above the surface boundary layer. Transmissivities at 2 km and above were generally 0.70 or greater for any month.

Data from Howard AFB, was used to demonstrate transmissivity values from a tropical regime. The month of February was the month with the highest transmissivity values, and in general, over 50% of the time were greater than 0.50, for all altitude.

The two poorest months were June and July, July being the worst. A dramatic increase in low

level moisture gave July a transmissivity value of less than 0.40 at the surface more than 50% of the time. Transmissivity values rapidly improved above the surface boundary layer, and generally exceeded 0.65 at and above 2 km.

Data from Pyongyang demonstrated a much more seasonal bias in the transmissivity than did the other locations. January and February were the months with the highest reported transmissivity values, January being the best. In general, over 50% of the transmissivities reported at all altitudes were greater than 0.80. The poorest month was July, where a dramatic increase in low level moisture resulted in a transmissivity value of less than 0.45 at the surface more than 50% of the time. Transmissivity values again rapidly improved as altitudes above the surface boundary layer were evaluated, and nearly always exceeded 0.60 at source altitudes of 2 km or greater.

USAFETAC evaluated the 50th percentile frequency of occurrence to estimate the mean. In the 1 to 8 micron case, surface transmissivity is highest during the month of January at Baghdad (0.54). The poorest month was May (0.50). The annual average surface transmissivity was 0.52. Transmissivity values rapidly improved with altitude.

Data from Howard AFB, Panama showed February had the highest transmittance value of 0.41, while June was the poorest month at 0.38. The abundance of low level moisture keeps transmissivity values near the 0.40 value.

Pyongyang data demonstrated a much more seasonal bias in transmittance values. January had the highest transmittance of 0.48, while July was the poorest at 0.35. Annually, values were less than 0.42 at the surface 50% of the time.

Transmissivity values again rapidly improved as source altitudes above the boundary layer were evaluated. Similar results were found on the 3 to 4, 1 to 2.5, and 1 to 4 micron cases. Values of absolute humidity from dataset 1 were compared with the absolute humidity values from the Baghdad sounding, and are depicted in Table 4. The average surface absolute humidity for dataset 1 was 11.032 grams per cubic meter (g/m^3), and ranged from 6.121 g/m^3 to 13.89 g/m^3.

The surface absolute humidity from the Baghdad sounding averaged approximately 7.5 g/m^3, and humidities greater than 11 g/m^3 occurred 1.8% of the time. At approximately 2 km (data used was taken from 7000 feet), the absolute humidity from dataset 1 averaged 4.48 g/m^3, and ranged from 0.9232 g/m^3 to 7.021 g/m^3, compared to the average Baghdad humidity of 2.6 g/m^3. At this level, humidities greater than 4.0 g/m^3 occurred 11.8% of the time. This demonstrates that dataset 1 atmospheric profiles, at these 2 levels, do contain higher concentrations of water vapor than the average Baghdad 15 year POR sounding, but they do not exceed the extremes. Above 2 km, the humidities from dataset 1 continue to be slightly higher than the Baghdad soundings; as a result, transmissivities are slightly lower. However, the transmissivities from dataset 1 fall within the range of the expected transmissivity values for January.

TABLE 4. Absolute humidity for dataset 1, and for the archived data for Baghdad

DATA SET 1 LOCATION	SURFACE ABSOLUTE HUMIDITY (g/m^3)	UPPER LEVEL (7000 FT) ABSOLUTE HUMIDITY(g/m^3)
01A	9.064	3.836
02A	13.89	6.013
03A	6.121	3.396
04A	8.657	2.116
05A	8.261	3.574
06A	9.099	0.9232
07A	11.10	7.021
BAGHDAD	7.5	2.6

7. CONCLUSIONS

Review of preliminary results of combinations of transmissivity vs wavelength, altitude, and as a function of sensor view angles show no great surprises: (1) Dataset 1 atmospheric profiles do contain higher concentrations of water vapor than the average Baghdad 15 year POR sounding, but they do not exceed the extremes. Transmissivities fall within the range of expected transmittance values for January. (2) Transmissivity values increased as a function of source altitude. The decrease in water vapor with increasing distance from the surface contributed to the increase in transmissivity. (3) Transmissivity values for all cases were lower given an increased path length in the 30 degree off-nadir case. (4) The selection of the bandwidth interval affected the average transmittance values calculated. There are select regions in the 1 to 12 micron range band that are "opaque" to electromagnetic wave propagation. We ran LOWTRAN7 over the entire 1 to 12 micron bandwidth interval. Transmittance values calculated were substantially lower than values calculated in select subintervals of the 1 to 12 micron band. The reductions ranged anywhere from 7% to nearly 20%. This reduction was primarily due to inclusion of the "opaque" regions mentioned above. Also, when we used a large step size, on the order of 1 micron, for the calculations, the "opaque" regions were effectively masked in the model output. To help eliminate this bias, we calculated transmittances in selected spectral bands located within the atmospheric windows.

There were differences between the interpolated dataset 1 cases provided by USAFETAC's customer, and the desert source soundings selected by USAFETAC (Baghdad). January Baghdad surface transmissivities (8 to 12 micron band) were 50% of the time greater than 0.80. Transmissivities for dataset 1 averaged near 0.59 for sources at the surface. This value (0.59) has a very small probability of occurrence (1%) at Baghdad, but is more likely to occur (10%) at Howard AFB.

Dataset 1 showed lower surface transmissivities throughout the year when compared to a Baghdad 15 year POR, but did not approach the reduction experienced in a true tropical environment such as at Howard AFB. A tropical environment shows surface transmissivities on the order of 0.40, depending on the time of year.

It should be noted that dataset 1 was based upon ASPAM-derived data. Previous research at USAFETAC (O'Connor, 1994) has shown ASPAM-derived data to have a slight bias to report higher absolute humidity values than may actually be present.

The data extracted from the Pyongyang upper-air soundings show a definite seasonal bias, with lower transmissivities in the summer months, all tied to an increase in absolute humidity.

This study was an example of how climatological data might be used in determining expected atmospheric transmittance values. USAFETAC plans to apply this approach to geographic locations worldwide.

REFERENCES

Environmental Research Institute of Michigan for the Office of Naval Research, Department of the Navy, *The Infrared Handbook*, 1978.

Kneizys, F.X., et. al., AFGL-TR-88-0177, 1988, *Users Guide To Lowtran7*, Air Force Geophysics Laboratory, Hanscom AFB, MA.

Koermer, James P., and J.P. Tuell, *Improved Point Analysis Model (IPAM) Functional Description*, 1984, Internal Working Document, Air Force Global Weather Center, Offut AFB, NE.

O'Connor, Lauraleen, and Charles R. Coffin, *Atmospheric Slant Path Analysis Model Baseline Study*, 1994, USAFETAC/PR-94/001, Scott AFB, IL.

SAS Institute, Cary, NC, *SAS/STAT User's Guide, Version 6*, 1990, FOURTH EDITION

Session III

BATTLE WEATHER

OWNING THE WEATHER: IT ISN'T JUST FOR WARTIME OPERATIONS

R.J. Szymber, M.A. Seagraves, J.L. Cogan, and O.M. Johnson
U.S. Army Research Laboratory
White Sands Missile Range, NM 88002-5501

ABSTRACT

Owning the Weather (OTW) technologies that provide state-of-the-art weather support for Army tactical operations and battlefield simulations may also be used to support certain Army Operations Other Than War (OOTW), as well as civilian and commercial applications. Types of OTW technologies and products that may be used in applications other than tactical situations include remote sensing, atmospheric characterization, scene visualization, and atmospheric models. OTW products can be used in Army humanitarian assistance and disaster relief, peace enforcement, and peacekeeping operations, as well as in civilian applications such as air and noise pollution control, environmental cleanup, global climate change programs, transportation, forestry, and agriculture. Unique OTW meteorological testbeds are used in product development. Interactions and partnerships with other government agencies and private industry help to pave the way for technology transitions.

1. INTRODUCTION

In his essays on "The Art of War" written more than 2,000 years ago, Sun Tzu asserted, "Know the enemy, know yourself; your victory will never be endangered. Know the ground, know the weather; your victory will then be total." Historically, weather has decisively impacted battlefield success, and future warfighters prepared to exploit weather and terrain effects will also benefit in battle. Today's Army doctrine (Dept. of the Army, 1993) states, "The commander who can best measure and take advantage of weather conditions has a decided advantage over his opponents. By understanding the effects of weather, seeing the opportunities it offers, and anticipating when they will come into play, the commander can set the terms for battle to maximize his performance and take advantage of limits on enemy forces."

Owning the Weather (OTW) is the Army vision for improved battlefield weather support to Force XXI, the force projection Army of the 21st century. It is critical to out-thinking the enemy and winning the information war, and in executing precision strikes. OTW is defined as the use of advanced knowledge of the environment and its effects on friendly and enemy systems, operations, and tactics to gain a decisive advantage over opponents. The OTW strategy involves the observation, collection, processing, forecasting, and distribution of timely

battlefield environmental conditions. This information is transformed into weather intelligence and decision aids for final battlefield exploitation of the weather.

OTW will provide a digitized picture of battlefield weather and its effects for Intelligence Preparation of the Battlefield (IPB) to support mission planning, situation awareness, synchronized battle management, and advanced decision and execution support. The Integrated Meteorological System (IMETS) will collect data from various sources and distribute timely battlescale weather information to multiple command elements via the All Source Analysis System. This information will be used in tactical decision aids (TDA's) resident on computers in all battlefield functional areas to provide commanders and soldiers with real-time and predicted environmental effects on missions and systems.

OTW capabilities and products that provide state-of-the-art weather support for Army tactical operations and battlefield simulations are ideal for supporting Army force projection operations and joint military missions, including operations other than war (OOTW). OTW technologies also have important dual-use civilian and commercial environmental applications that can contribute to defense conversion and technology transfer.

1.1 OTW Battlefield Sensing

Weather conditions must be observed before they can be forecast and converted into weather intelligence. A suite of complementary and synergistic space-based, airborne, and ground-based sensing systems provides real-time observations at required accuracies, resolutions, and coverage. All available data are collected, validated, and assimilated to build a complete horizontal and vertical picture of the atmosphere over friendly and enemy controlled territory.

Battlefield sensing systems and technologies include:

- meteorological satellites;
- Automatic Meteorological Sensor System;
- Meteorological Measuring Set;
- Target Area Meteorological Sensors System (TAMSS), that is, the Mobile Profiler System (MPS), Unmanned Aerial Vehicles (UAV) with meteorological sensors and dropsonde payloads, and Computer Assisted Artillery Meteorology software; and
- remote sensing and data fusion techniques.

1.2 OTW Processing, Analysis, and Dissemination

The IMETS receives, processes, analyzes, and distributes mission-specific observations, forecasts, and weather intelligence. The IMETS is a mobile, tactical, automated weather data system designed to provide timely weather and environmental effects forecasts, observations, and decision aid information to appropriate command elements through the Army Battle Command System. It includes a battlescale (mesoscale) forecast model and satellite communications.

1.3 OTW Battle Decision Aids and Displays

TDA's permit commanders to rapidly war game courses of action; determine probable effects on friendly and enemy systems, tactics, and doctrine; and incorporate weather effects into tactical planning and operations. Decision aids not only provide information about weather effects, but also show the commander if and when weather conditions give a competitive edge over the enemy.

IPB, TDA's, and war gaming enable the commander to quickly and accurately analyze the effects of weather on impending operations. Examples of these types of products are:

- Integrated Weather Effects Decision Aid,
- IPB weather analysis overlays,
- mobile generator smoke screen TDA,
- night vision goggles TDA, and
- electro-optics TDA's.

1.4 OTW Technology Exploitation of Weather

Training, combat simulations, weapon development, and system testing and evaluation are all areas where the exploitation of weather-related technology results in having advantages over threats and in making adverse weather a force multiplier. Some examples of these exploitation technologies and products include:

- atmospheric scene visualization of battlefield obscurants (smoke, dust, haze, and fog),
- atmospheric transport and diffusion modeling over urban and complex terrain,
- target contrast change characterization, and
- simulation of optical turbulence effects.

2. OPERATIONS OTHER THAN WAR (OOTW)

The Army has evolved from the Cold War doctrine and structure to a new strategic era of force projection, and has consequently modified its weather support architecture to support new missions. War, that is, a major regional conflict, remains the baseline objective for OTW support to the Army. However, many new missions are now likely and a major regional conflict is only one of many contingencies for which the Army must provide weather support. These new missions require more flexible, mobile forces to respond to the wider range of unpredictable threats and situations. Tailored weather information is vital to the success of these noncombat operations. Planning now considers and integrates components of other service into joint task force meteorological and oceanographic support. Split-base operations provide support from the CONUS or theater to complement capabilities deployed with the joint task force.

OOTW are military activities during peacetime and conflict that do not necessarily involve armed clashes between two organized forces (Dept. of the Army, 1993). Today's Army conducts OOTW as part of a joint team and usually in conjunction with other government agencies. The Army has participated in OOTW supporting national interests throughout its

history. However, the pace, frequency, and types of OOTW have increased over the last 25 years. Furthermore, the future will likely see a growing percentage of the Army's activities committed to OOTW (Eden, 1994).

In general, OOTW have weather support requirements different from those for war. During war, the peacetime weather infrastructure is usually not available and all indigenous sources of local weather data in the war zone may be denied or lost. Therefore, the full range of OTW support capabilities is required in a war situation. In OOTW, availability of weather data from the existing peacetime indigenous sources will likely continue, allowing a much smaller weather support element to deploy to support missions with a greater reliance on indirect support from the CONUS or theater weather facilities. The exception to this is OOTW conducted in remote, under-developed areas where no weather infrastructure exists, such as in Rwanda. Generally, noncombat missions enable a small weather team deployed to the contingency area to incorporate all available indigenous weather information relayed to the center, integrate it with data from other sources, tailor and repackage it, and transmit it in minutes. Also, OOTW may occur in relatively benign environments where weather support concepts and procedures are much different from those in high- to mid-intensity conflicts.

2.1 Disaster Relief

Disaster relief operations occur when emergency humanitarian assistance is provided by DoD forces to prevent loss of life and destruction of property resulting from man-made or natural disasters. The diverse capabilities of the Army make it ideally suited for disaster relief missions. Assistance provided by U.S. forces is designed to supplement efforts by civilian agencies who have primary responsibility for such assistance.

OTW technologies are especially well-suited to provide support during severe weather and other weather-related disasters such as hurricanes, tornado outbreaks, flash flooding, windstorm fires, and toxic air pollution episodes. For example, weather support was critical during the disaster relief the Army provided during the landfall and aftermath of Hurricane Andrew in 1992 in southern Florida. In this type of operation, a detailed knowledge of predicted weather conditions and their effects on coastal zones, infrastructure, transportation, and public safety is important in quickly achieving stated objectives, while avoiding added injuries and destruction related to the weather.

2.2 Peace Enforcement and Peacekeeping Operations

Peace enforcement is military intervention designed to forcefully restore peace between belligerents engaged in combat. Peacekeeping operations use military forces to supervise a cease-fire and/or separate the parties at the request of the disputing groups. OTW support is required to initially project the force and for subsequent ground and aerial reconnaissance efforts to collect intelligence. During these operations Army combat power that benefits from the OTW capabilities may need to be applied.

2.3 Noncombat Evacuation Operations

Noncombat evacuation operations relocate threatened civilians from hazardous locations in foreign countries. These operations usually involve U.S. citizens whose lives are in danger. OTW support is critical to the success of these operations, as the failed Iranian hostage rescue mission demonstrated in 1980. The failure of this operation was directly attributed to the weather, specifically, the effects of unexpected dust and sand storms encountered along the helicopters' flight paths and at staging points.

OTW supports overall mission planning and execution, to include elements of concealment and surprise, by predicting weather conditions and their effects along planned flight paths and loading zones. During the successful 1983 Grenada action, for example, weather was an important factor in that overcast cloud conditions prevented Russian satellites from observing our aircraft and ships, adding to the element of surprise.

3. NONMILITARY/CIVILIAN APPLICATIONS

3.1 Air and Noise Pollution

Of the many civilian and commercial applications for OTW technologies, the problem of air pollution is one that impacts a great number of people. The air pollution problem has reached such a significance that urban areas that do not show positive efforts to meet Environmental Protection Agency standards will be penalized by reductions in federal funding. The pollution problem along segments of the U.S.-Mexico border has been noted as quite serious, particularly in the El Paso-Ciudad Juarez area. It often becomes evident at White Sands Missile Range (WSMR) when southerly wind flow carries the dark brown layer of contaminants northward into New Mexico. Concern for this regional situation has prompted state agencies of Texas and New Mexico, and city governments of El Paso and Ciudad Juarez to form the "Paso del Norte Task Force," dedicated to cooperation in attempting to correct the problem. The Task Force welcomed U.S. Army Research Laboratory (ARL) proposals to enter into Cooperative Research and Development Agreements (CRDA), which would benefit all partners by pooling resources and technologies in efforts to alleviate the mutual problem. The partnerships augment the civilian atmospheric monitoring capabilities with state-of-the-art direct and remote sensing instruments, which can continually monitor the state of the atmosphere. Some of the capabilities are fixed in place at WSMR, but many of the instruments can be transported to observation sites where needed. Major benefits to the Army include the testing and evaluation of transport and diffusion models in an urban and complex terrain environment, and the display of results on a computer-based geographic information system.

The Mobile Profiler System (MPS) proved its value as a primary source of atmospheric data during the Los Angeles Free Radical Experiment, a multi-agency and bi-national (U.S. and Canada) air pollution experiment in the Los Angeles basin during September 1993. The MPS consists of a radar wind profiler, a Radio Acoustic Sounding System, a ground-based microwave radiometer, and other instruments, as well as a meteorological satellite receiver. It provided vertical profiles of wind and temperature nearly non-stop throughout the four weeks

of the experiment, at an unprecedented level of detail in time and space as shown, for example, in figure 1. These profiles were averaged and displayed as often as every 3 minutes at vertical resolutions as fine as 100 m from the surface to 3-5 km (wind) and to 0.8-1.6 km (virtual temperature). Combining these profiles with those derived from satellite data extended the maximum height to over 14 km. The profiles from the MPS were used with measurements of concentrations of pollutant species (ozone, particulates, etc.) to describe the transport and diffusion of those pollutants within the local area.

Meteorological models of the type found in the IMETS use these MPS profiles to derive descriptions and forecasts of atmospheric conditions throughout a mesoscale region. These analyses and forecasts, in turn, provide essential input into regional transport and diffusion models also being developed as part of the OTW effort. More information on the experiment and the role of the MPS may be found in Wolfe et al. (1994), and Cogan et al. (1994).

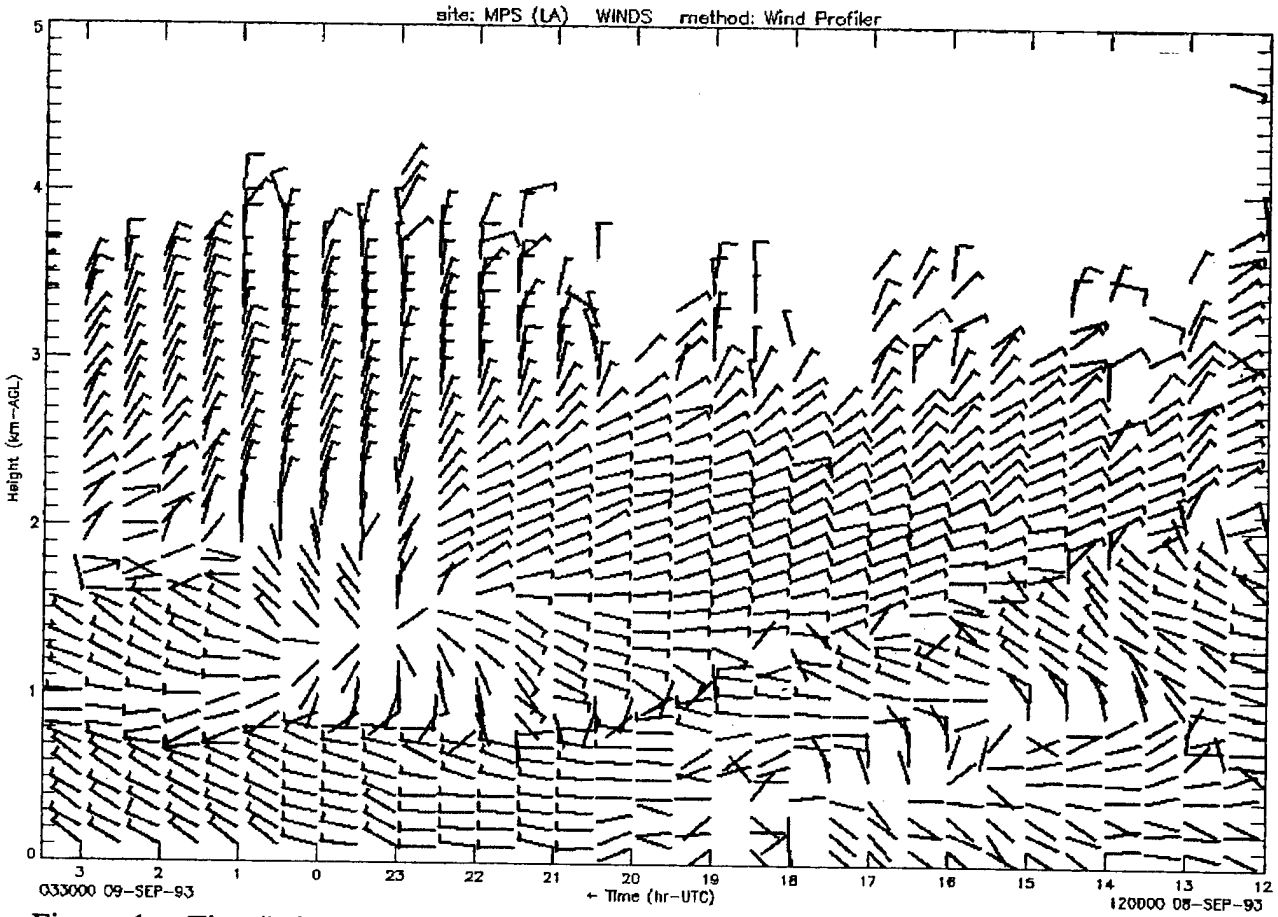


Figure 1. Time/height display of the MPS radar wind profiler data. Wind arrows have conventional meaning except a full barb represents 10 m/s and a half barb represents 5 m/s. Sounding derived from 15 min of data displayed every half hour.

Noise pollution is another area where OTW technologies can benefit the civilian community. An acoustic testbed is available to validate acoustic models that predict noise impacts of planned urban developments, such as airport placement, industrial development sites, and traffic routing. The testbed is located in an isolated area where an exceptionally wide range of frequencies may be produced without public disturbance. Scientists performing acoustic research have also provided assistance in dealing with the noise pollution associated with munitions testing in the Aberdeen Proving Ground area.

3.2 Environmental Cleanup

Environmental cleanup operations include the transportation and disposal of toxic/hazardous materials that have the potential for environmental disasters in the event of accidents. OTW technologies with potential in this area include the continuous remote monitoring of hazardous waste sites and the prediction of toxic corridors resulting from potential and actual chemical spills or nuclear radiation releases. The monitoring capability was recently demonstrated at WSMR when routine operation of the Remote Sensing Rover, a portable Fourier transform spectrometer, detected the presence of ammonia gas as a byproduct in the smoke from a forest fire at a distance of 8 km from the Rover. The gas was determined to have been produced from ammonia fertilizer compounds used in slurry for fighting the fire. While the concentration of the gas was not hazardous, its detection demonstrated one of the many areas for potential civilian applications.

3.3 Global Climate Change

Understanding climatic change and effects of human activities requires an intensive effort to monitor the atmosphere, generate essential input to environmental models, and provide data to update and check the quality of those models. OTW technology can assist in fulfilling those requirements. The MPS demonstrated the ability to continuously monitor the atmosphere over a period of nearly a month. The future MPS will have the ability to provide high-quality data for more extended periods. These data will feed mesoscale meteorological models in the IMETS, permitting high-resolution analysis and short-term forecasts over regional scales. Both the MPS and the IMETS can be deployed in remote areas not normally accessible by more conventional measurement and analysis systems. The mobility of these systems allows them to be placed in a variety of locations on short notice at a relatively low cost. At the same time, their durability and reliability result in lower costs of operation, repair, and maintenance.

The measurements provided by a network of MPS's may be supplemented by meteorological sensors and dropsondes carried by small manned or unmanned aircraft. The use of these instruments on, or deployed by, aircraft provides detailed, quantitative data over wide areas during experiments or unusual weather. The dropsondes can also become small meteorological ground (or sea-surface) stations when they reach the surface. Measurements from these sensors serve as input to analysis and forecast systems such as the IMETS, further increasing the ability of mesoscale models to accurately depict the atmosphere.

Global monitoring will be carried out by future space earth-observing systems that provide wide-area coverage. To obtain accurate and detailed measurements, satellite remote sensors require calibration both before and after launch, and periodically during their lifetimes. This calibration and validation (cal/val) process depends on having high quality "ground truth" measurements. The MPS and airborne sensors can provide these data with both high accuracy and wide coverage. The MPS can be moved to a large variety of locations around the globe, and the airborne sensors and processors may be fitted in light military and civil aircraft. These systems will allow, for the first time, cal/val over many different climatic regions at an affordable cost, as opposed to the common practice of taking data over a few limited areas and extrapolating those results for the entire earth. The unique earth-target provided by the White Sands National Monument, the world-class ARL Atmospheric Profiler Research Facility, and a vast array of other meteorological instrumentation make WSMR an ideal site for satellite sensor cal/val.

3.4 Transportation

OTW sensors can provide real-time data for aircraft safety and hazard avoidance. The MPS can generate wind profiles at airports that will enable rapid response warnings of hazardous conditions such as down-bursts and other sudden changes in wind speed or direction, including vertical motion. Current experimental sites at airports such as Denver, CO provide horizontal wind information as often as every 15 min. However, even this relatively rapid refresh rate may not be adequate for rapidly developing situations, for example, such as a gust front or sudden down-burst. The 3 min refresh time of the current MPS enables the detection of these events in time to provide adequate warning. Another useful MPS capability is the production of accurate wind data in the presence of overflying aircraft or birds, either of which produce erroneous results in current types of radar wind profiling systems. In the presence of strong, rapidly-changing convective conditions, radar profilers may not produce reliable winds. Nevertheless, the MPS will generate information that will indicate that the wind data are unreliable, and will provide estimates of probable errors that may be used as indicators of hazardous conditions. Unlike many lidars, the MPS will produce profiles through clouds and fog. It will be able to move to a location most suitable for the active runway and start operations in less than an hour. The MPS satellite receiver will help provide advance warning of potential severe weather that could affect airport operations. IMETS models may be used to extend the area of coverage to the mesoscale region around the airport, taking advantage of other sources of data, for example, from the National Weather Service. Civilian versions of decision aids will permit controllers and others to perform their functions more efficiently.

The models and decision aids of the IMETS will be able to provide short-term warning of hazardous conditions for ground transportation. Examples include ice on roadways, fog, high winds, and flooding. Data can be extracted from existing systems, such as rawinsondes and surface stations, and specifically deployed systems such as the MPS. Several MPS's, and perhaps light aircraft with meteorological sensors and dropsondes, would be sent to locations with a high potential for hazardous weather events. The mobility and consequent low cost of deploying OTW systems would allow the movement of these systems to locations of interest, even in remote areas.

ARL is in the process of making technologies available to civilian efforts in the development of the Intelligent Vehicle Highway System (IVHS). A low-visibility warning system being developed as part of the IVHS will provide early warning to transportation officials and traffic of rapidly deteriorating highway visibility due to the sudden onset of blowing dust, snow, smoke, fog, etc. To reduce development costs resulting from waiting for natural obscuring phenomena in which to validate the system, the developer plans to make use of some of ARL's technologies such as an artificial fog generator and remote measurement systems.

3.5 Forestry

Application of OTW systems to forestry is closely related to environmental monitoring and providing short-term warning of hazardous conditions. Of particular concern are the atmospheric conditions that affect the spread of forest and brush fires. During the unusually hot and dry period during the summer of 1994 at WSMR, NM a series of brush fires burned much of the vegetation covering the Organ and San Andreas mountains. Sudden and frequently unexpected changes in wind speed and direction caused the fire to spread rapidly, at one point threatening the WSMR main post area. Other recent examples include fires in the Los Angeles area in 1993, in Yellowstone National Park in 1988, and near Glenwood Springs, Colorado in 1994. The fact that sudden changes in atmospheric conditions cause fires to rapidly spread when they may have been thought to be under control is well known to many charged with fighting and controlling fires. The combination of high temperature ($>$ 40 °C), very low relative humidity (10-15%), and highly variable wind conditions led to a highly volatile "fire weather" situation that fed the fire at WSMR. In the Colorado fire, a sudden shift in wind direction over rugged terrain led to the death of 14 fire fighters.

The MPS and other OTW sensors can provide invaluable information for analysis and prediction of atmospheric conditions that affect forest fires. Especially valuable is the mobility of the MPS and its ability to reach remote areas accessible only by 4-wheel drive vehicles. The essential capability is the production of profiles of wind for the lowest few kilometers every 3 min, tracking sudden changes during highly variable conditions. The MPS also includes instruments that can provide equally frequent data for temperature and total moisture in the lowest kilometers. The satellite data acquired by the MPS will provide a general picture of the atmospheric situation over a large area around the location of the fire. The airborne instruments being developed may be carried or dropped by fire fighting or observation aircraft to provide required atmospheric data above the fire location. The very low weight, size, and power requirement of these instruments permit them to be added on a non-interference basis, such as in a removable pod.

The data gathered by these OTW sensors and more conventional instruments may be analyzed by software in the highly mobile IMETS to provide rapid analyses and predictions for the area of and nearby the fire. The predictions will enable fire fighters to place personnel and equipment in places where the fire is expected to spread ahead of time, and to avoid potential

high-risk areas. The overall result is the ability to control and extinguish fires quickly with less expenditure of resources, and with less danger to personnel.

3.6 Agriculture

Agriculture has always been extremely dependent upon weather conditions, especially floods, droughts, and freezes, but OTW technologies promise some applications that are not as readily evident as the daily weather reports and forecasts available through the news media. For example, ARL's FM-CW radar is used primarily to provide profiles of atmospheric turbulence, but is so sensitive that it can detect airborne insects. The atmospheric transport of adult moths is a critical concern in combating infestations of the Fall Army Worm, for example. This capability is advantageous for detecting and monitoring insect migration, thereby permitting more timely, effective, and efficient use of pesticides and minimizing contamination of the environment by chemicals.

4. CONCLUSIONS

State-of-the-art OTW technology that shows great promise in providing land warfare weather support has many applications outside of wartime operations. Knowledge of atmospheric conditions and their effects is essential to success in Army OOTW, such as disaster relief, peace enforcement, peacekeeping and noncombat evacuation operations. OTW is the next warfighting edge for enabling land force dominance by leveraging the power of information and technology to increase the lethality, survivability, and tempo of operations in war and OOTW. In addition, much of this technology will be extremely useful in a wide variety of civilian applications such as air and noise pollution control, environmental cleanup, global climate change analyses, transportation safety, forest fire control, and agriculture.

REFERENCES

Cogan, J. L., E. M. Measure, E. D. Creegan, D. Littell, and J. Yarbrough, 1994, "The Real Thing: Field Tests and Demonstrations of a Technical Demonstration Mobile Profiler System." In *Proceedings of the 1994 Battlefield Atmospherics Conference*, U.S. Army Research Laboratory, White Sands Missile Range, NM 88002-5501.

Dept. of the Army, 1993, Field Manual 100-5 Operations, U.S. Army Training and Doctrine Command, ATTN: ATDO-A, Fort Monroe, VA 23651-5000.

Eden, MAJ Steve, 1994, "Preserving the Force in the New World Order." *Military Review*, No. 6, pp 2-7.

Wolfe, D., B. Weber, D. Wuertz, D. Welsh, D. Merritt, S. King, R. Fritz, K. Moran, M. Simon, A. Simon, J. L. Cogan, D. Littell, and E. M. Measure, 1994, "An Overview of the Mobile Profiler System, Preliminary Results from Field Tests during the Los Angeles Free-Radical Study." Submitted to *Bull. Amer. Meteor. Soc.*

THE REAL THING: FIELD TESTS AND DEMONSTRATIONS OF A TECHNICAL DEMONSTRATION MOBILE PROFILER SYSTEM

J. Cogan, E. Measure, E. Creegan, D. Littell, and J. Yarbrough
U.S. Army Research Laboratory
Battlefield Environment Directorate
White Sands Missile Range, NM 88002-5501

and

B. Weber, M. Simon, A. Simon, D. Wolfe, D. Merritt,
D. Weurtz, and D. Welsh
Environmental Technology Laboratory
National Oceanographic and Atmospheric Administration
Boulder, CO 80303

ABSTRACT

A near real-time sounding of the atmosphere from the surface to ≥ 30 km over a battlefield may be obtained by combining atmospheric profiles from an array of ground-based remote sensors and meteorological satellites. This type of capability is essential for optimum use of Army assets such as artillery and defense against biological and chemical attack, as well as a variety of civilian applications. This paper briefly describes the technical demonstration (TD) Mobile Profiler System (MPS), and outlines the method for merging data from the satellite and ground-based systems. The processing software allows acquisition of valid ground-based data with a refresh time as short as 3 min and in the presence of overflying birds or aircraft. Results from field tests at sites in White Sands Missile Range, NM; near Los Angeles, CA; and at Ft. Sill, OK indicate the capability of the TD MPS to generate useful atmospheric soundings for the field artillery and a variety of other military and civilian users.

1. INTRODUCTION

The Mobile Profiler System (MPS) is being developed to provide military and civilian users with atmospheric soundings in close to real time. Applications include avoidance of hazardous wind conditions at airfields and training ranges, and obscurant and pollution monitoring. Szymber et al. (1994) discuss potential military applications in operations other than war and related civilian uses. The type of systems found in the Technical Demonstration (TD) MPS are described in Cogan and Izaguirre (1993), Miers et al. (1992), their references, Weber and Weurtz (1990), Hassel and Hudson (1989), and Strauch et al. (1987). This paper briefly describes the TD MPS, provides an outline of the combined sounding technique, and presents examples of actual data.

2. SYSTEM DESCRIPTION

The TD MPS consists of a 924-MHz radar profiler operating in a five-beam mode for winds, a Radio Acoustic Sounding System (RASS) for virtual temperature (T_v), a ground-based microwave radiometer for T_v and humidity, a small ground station for temperature, pressure, humidity, and wind velocity, and a small satellite receiving system for acquiring and processing satellite sounder data for temperature and humidity. Satellite sounding heights are computed for the standard pressure levels, and wind velocity is calculated using the geostrophic assumption. Temperature is converted to T_v as required. Pressure versus height is computed from the measured sounding data and, in the future, may be measured for the lower part of the sounding using the microwave radiometer. The main electronic components and some of the sensors of the TD MPS are housed in or on a 9-m trailer. The radar antenna, the four RASS sources, the satellite antenna, and the microwave radiometer are deployed around the trailer.

A single workstation controls the satellite terminal and processor, while a PC operates the radar and collects data from the remaining ground systems. A second workstation serves as the primary processor and data manager. Up to two balloon systems may be run from the trailer to obtain comparison data, as during the Los Angeles Free Radical Experiment (LAFRE) in the Los Angeles basin. Further tests have been held at White Sands Missile Range (WSMR), NM; near Boulder, CO; and at Ft. Sill, OK.

3. PROCESSING AND COMBINING METHOD

New algorithms help operate the ground-based sensors and considerably enhance the quality control of the output. Examples include updated software for the radar wind profiler and RASS. Entirely new routines eliminate most of the problems arising from birds or aircraft flying through the main radar beam or side lobes (Merritt 1994). In the few cases in which the atmospheric return cannot be separated out of contaminated data, the output for those particular times and altitudes can be flagged as unreliable. New techniques under development include neural-net-based methods for converting radiances from the ground-based microwave radiometer into T_v profiles and for converting satellite radiances into temperature and dewpoint profiles (e.g., Bustamante et al. 1994).

Merging algorithms are described in Cogan and Izaguirre (1993) and their references. Ground-based systems provide detailed soundings for the lower troposphere, while a satellite sounder covers the atmosphere from about 2 or 3 km up to $\geq$30 km. Profiles from ground-based systems are combined to form a single, multivariable sounding. The satellite sounding is weighted relative to the MPS location and time and merged with the ground-based sounding. Normally, satellite and ground-based profiles overlap; if not, satellite data for each variable are extrapolated down to the uppermost level of each ground-based profile. For each variable, routines within the merging program adjust the satellite profiles starting at the satellite sounding level immediately above the highest level of each ground-based profile. The merged profiles are entered in a single file to form a combined sounding.

4. DATA

This section presents samples of data acquired at WSMR, NM and Ft. Sill, OK. Figure 1 presents a plot from the Ft. Sill data of radar profiler winds in the form of standard wind barbs in which speeds are in meters per second instead of knots. The abscissa is time in hours UTC, from 1130 to 1330 on 15 September 1994. The included scale (original in color) at the bottom of the chart also gives an indication of wind speed. Radar wind profiles appear every 15 min, but satellite wind profiles generally are available every 2 to 6 h. For each satellite pass, the same satellite sounding is input into the processing program until the next satellite pass or until the current satellite sounding reaches a maximum time staleness (e.g., 6 h). Adjustments to the satellite winds are only slight as a consequence of the very light wind at uppermost radar heights (about 4 km in figure 1).

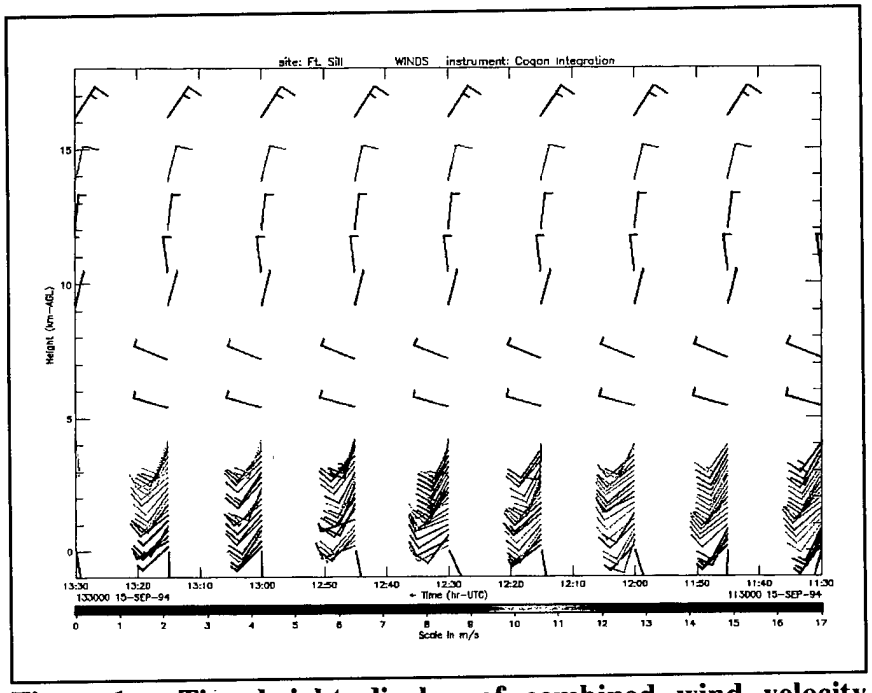


Figure 1. Time-height display of combined wind velocity profiles derived from radar profiler and satellite data.

The TD MPS can generate a variety of useful profiles. Figures 2 through 7 show profiles of wind (15 and 3 min) and temperature (15 and 3 min) as well as 3-min graphs of vertical velocity and an indicator of error (error estimate). Figure 2 presents 15-min wind profiles from the 924-MHz radar profiler from 1600 to 2000 UTC on 29 July 1994. The surface layer (up to 1 km) shows light and variable winds capped by a layer of westerly winds around 5 m/s that gradually veer with height reaching speeds near 10 m/s from the northeast at about 4 km. Toward the end of this period the wind becomes variable around 2 to 3 km. Figure 3 shows 3-min winds for part of the period of figure 2 (i.e., 1830 to 1930). The general pattern is roughly the same as for the 15-min winds for the same period even though more variability is

apparent (e.g., more variable wind direction and changes in maximum height). Particularly noticeable is the zone of missing data around 1920. It did not appear in figure 2 because the 15-min average displays a sounding if at least one 3-min profile occurs within the averaging period. This smoothing effect also is apparent in the T_v soundings from the RASS. The 15-min averages (figure 4) smoothed the 3-min values (figure 5), especially near the surface, eliminating some holes in the data created by removal of questionable values by the quality control algorithm. Figures 4 and 5 show useful RASS data to about 1.5 km. Under unfavorable conditions the maximum height may reach only up to 0.7 to 1.0 km.

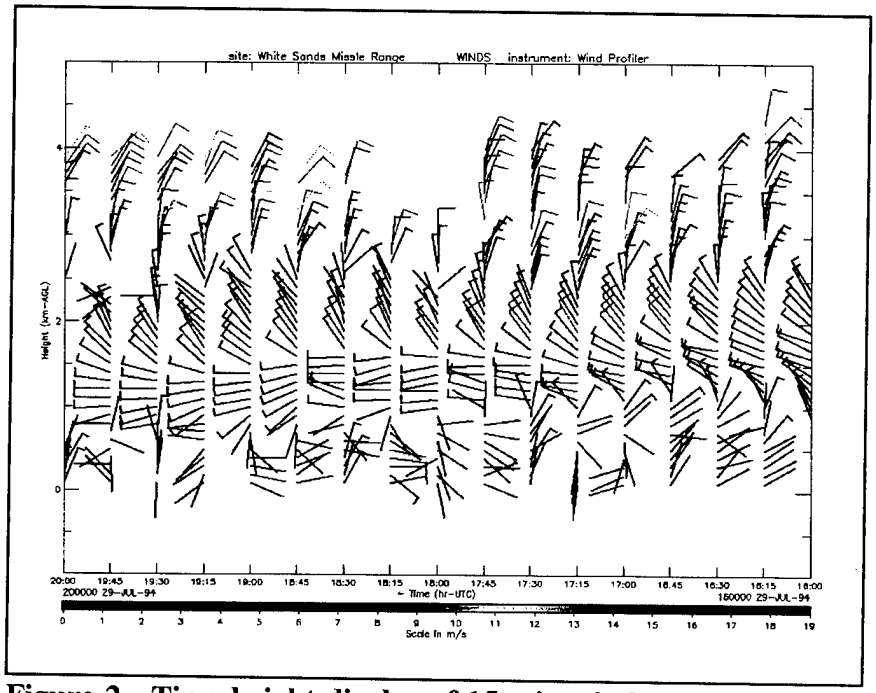


Figure 2. Time-height display of 15-min wind velocity profiles from the 924-MHz radar profiler.

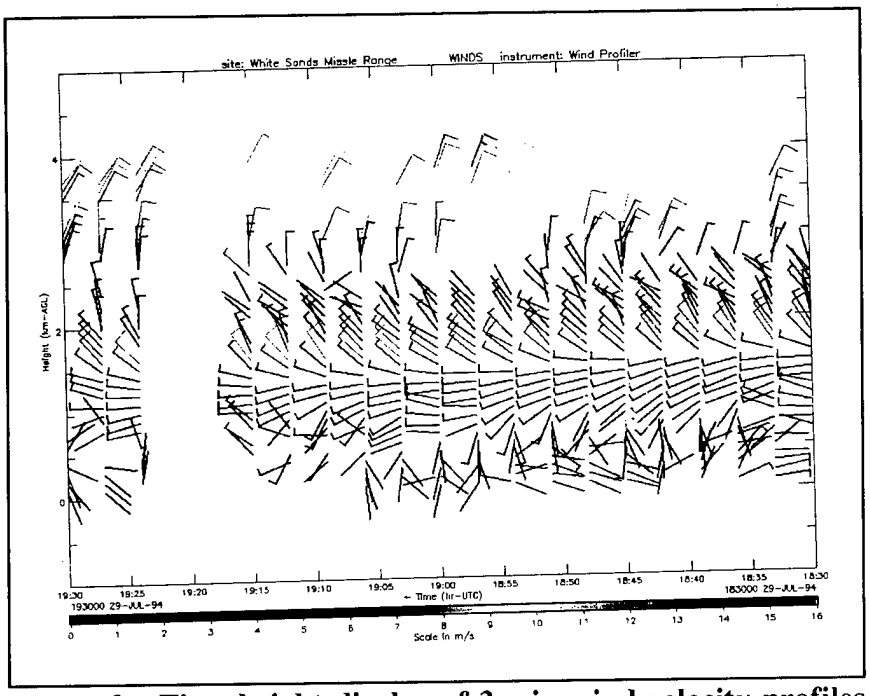


Figure 3. Time-height display of 3-min wind velocity profiles from the 924-MHz radar profiler.

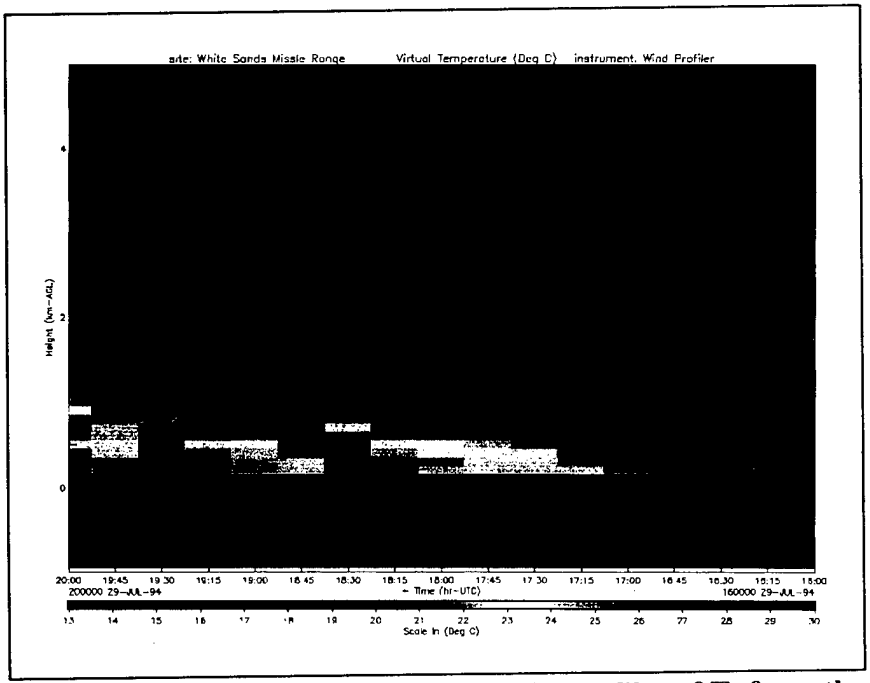


Figure 4. Time-height display of 15-min profiles of T_v from the RASS.

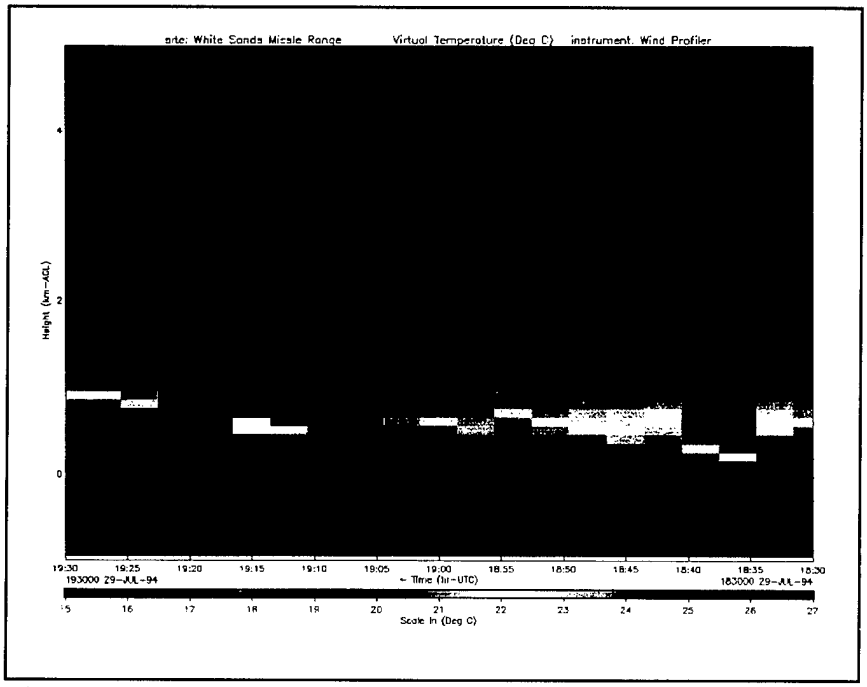


Figure 5. Time-height display of 3-min profiles of T_v profiles from the RASS.

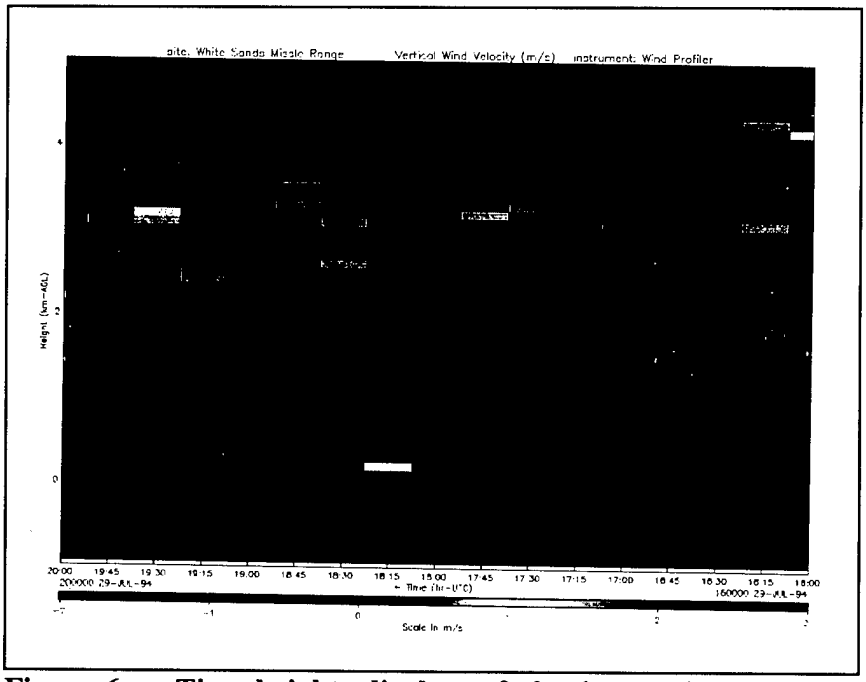


Figure 6. Time-height display of 3-min vertical velocity profiles.

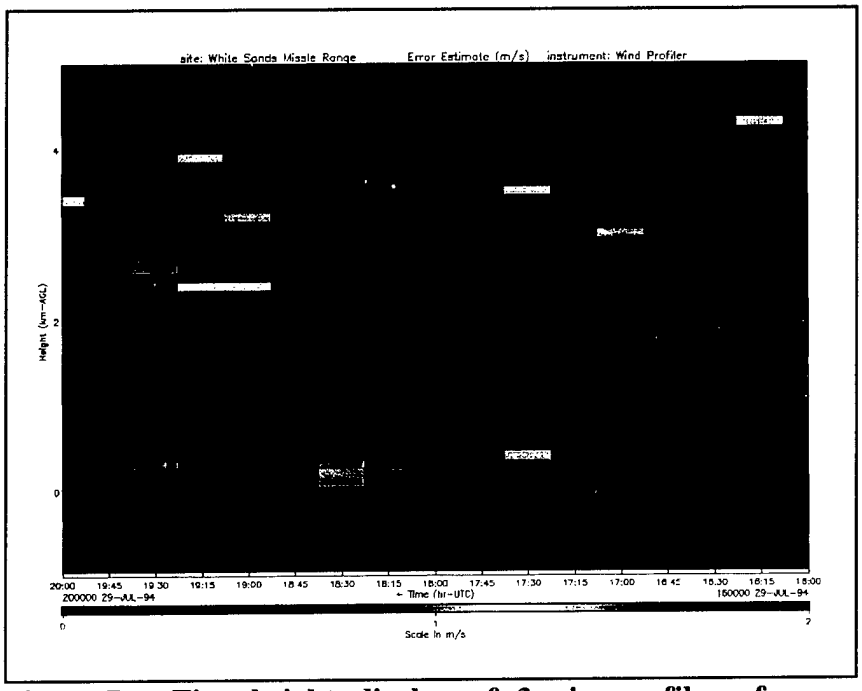


Figure 7. Time-height display of 3-min profiles of error estimate.

In the TD MPS the software computes and displays two other useful quantities, vertical velocity (figure 6) and error estimate (figure 7). Vertical velocity in this system is computed from the four oblique beams. The vertical velocity may be used in investigations of atmospheric dynamics, as well as providing a correction to the RASS measurements of T_v. More details on the algorithm may be found in Weurtz et al. (1988). Figure 7 presents a measure of the error in the computed horizontal wind in the form of error estimates (Weurtz et al. 1988). These estimates primarily indicate the nonuniformity of the wind at the specified height interval over the averaging period (e.g., 100 m and 3 min). For example, the radial wind velocity from the north beam should be of equal magnitude and opposite sign of that from the south beam for a uniform wind field in a particular layer. Normally, the assumption of uniformity is not exact, especially at higher altitudes, but in the absence of strong convection should be close enough to allow useful measurements. If the error estimate is high relative to the horizontal wind speed, the user at least knows that the measurement at that height and time is unreliable.

The profiles presented in figures 2 through 5 suggest that for many atmospheric situations 15 min averaged profiles may be sufficient for certain applications in which relatively small, very short term changes are not critical. An example would be routine analyses and forecasts for mesoscale areas. However, for applications such as detection of hazardous winds at airfields, defense against chemical attack, or fighting forest fires, 3-min profiles may be extremely important. Szymber et al. (1994) present some applications for operations other than war that require profiles with a very short refresh time.

5. COMPARISONS

T_v profiles from RASS, satellite, and combined RASS and satellite were compared with soundings from rawinsonde using the LAFRE data. A limited set of comparisons for 3 days indicated standard deviations of differences (sdd) between combined soundings and rawinsondes of around 1.5 to 2.8 K. The sdd for the combined sounding was lower for the satellite alone but usually higher for the RASS. The magnitudes of the mean differences (mmd) for combined soundings relative to rawinsondes were ≤ 0.7 K. The one case of large sdd (2.8 K) and mmd (0.7 K) may, in part, be a result of the large sdd and mmd of the satellite profile (2.4 and 2.8 K, respectively). The sdd and mmd for radar profiler wind speeds were in line with values reported in the literature (Miers et al. 1992), about 1.5 to 2.5 m/s and <1 m/s, respectively. Wind speeds derived from satellite data relative to those from rawinsonde varied widely depending on atmospheric conditions and time and distance from the ground-based sounding, ranging from about 3 to 4 m/s to over 15 m/s. Wind direction differences varied from around 10° to over 70°. These differences are in line with values found in Miers et al. (1992) and others. A possible method for reducing differences in wind speed and direction is the use of an analysis model to produce a satellite sounding at the location (and possibly time) of the ground-based profiles (e.g., Caracena, 1992).

To gain an idea of the quality of the rawinsonde data, wind soundings from two similar systems receiving data from one sonde were compared: (1) MARWIN and (2) Cross Chain Loran Atmospheric Sounding System (CLASS). Usually, wind speeds and directions tracked each another within 1 m/s and 10°. However, poor agreement occurred occasionally, with as much as 2 to 3 m/s and 70° for 100-m layers. A possible partial explanation is that the MARWIN software has more extensive built-in checks and somewhat smooths the data. Nevertheless, the user should make sure each sounding contains valid data and apply appropriate quality controls.

6. CONCLUSION

The TD MPS is a mobile system that combines the capabilities of an array of remote sensors to provide atmospheric soundings with a rapid refresh rate that can greatly reduce the error caused by time staleness. The MPS is a true dual-use system, capable of providing data that have a variety of applications. The rapid refresh capability is of great value for fire support, airfield operations, and chemical and biological defense. The ability to generate a picture of very short term flow and T_v patterns can lead to a better understanding of the atmosphere and to better modeling at smaller scales. As shown in the LAFRE, this system can be invaluable for pollution studies. Use of the MPS, especially if tied to prognostic models, could help reduce damage from forest fires, and lower the cost of fighting them in both lives and material.

7. REFERENCES

Bustamante, D., A. Dudenhoffer, and J. Cogan, 1994. "Neural Network Derived Thermal Profiles: Analysis and Comparison with Rawinsonde Data." In *Proceedings of the 1994 Battlefield Atmospherics Conference*, White Sands Missile Range, NM, (in press).

Caracena, F. 1992. "The Use of Analytic Approximations in Providing Meteorological Data for Artillery." In *Proceedings of the 1992 Battlefield Atmospherics Conference*, Ft. Bliss, TX, pp 189-198.

Cogan, J., and A. Izaguirre, 1993. *A Preliminary Method for Atmospheric Soundings in Near Real Time Using Satellite and Ground Based Remotely Sensed Data.* ARL-TR-240, U.S. Army Research Laboratory, White Sands Missile Range, NM.

Hassel, N., and E. Hudson, 1989. "The Wind Profiler for the NOAA Demonstration Network. Instruments and Observing Methods Rep. No. 35." At *Fourth WMO Technical Conference on Instruments and Methods of Observation.* (TE-CIMO-IV), Brussels, WMO/TD, pp 261-266.

Merritt, D.A., 1994. "A Statistical Averaging Method for Wind Profiler Doppler Spectra." *J. Atmos. Ocean. Tech.*, submitted.

Miers, B., J. Cogan, and R. Szymber, 1992. *A Review of Selected Remote Sensor Measurements of Temperature, Wind, and Moisture, and Comparison to Rawinsonde Measurements.* ASL-TR-0315, U.S. Army Atmospheric Sciences Laboratory, White Sands Missile Range, NM.

Strauch, R. G., B. L. Weber, A. S. Frisch, C. G. Little, D. A. Merritt, K. P. Moran, and D. C. Welsh, 1987. "The Precision and Relative Accuracy of Profiler Wind Measurements." *J. Atmos. Oceanic Technol.*, 4:563-571.

Szymber, R. J., M. A. Seagraves, J. L.Cogan, and O. M. Johnson, 1994. "Owning the Weather: It Isn't Just for Wartime Operations." In *Proceedings of the 1994 Battlefield Atmospherics Conference*, White Sands Missile Range, NM, (in press).

Weber, B. L., and D. B. Weurtz, 1990. "Comparisons of Rawinsonde and Wind Profiler Measurements." *J. Atmos. Oceanic Technol.*, 7:157-174.

Weurtz, D. B., B. L. Weber, R. G. Strauch, A. S. Frisch, C. G. Little, D. A. Merritt, K. P. Moran, and D. C. Welsh, 1988. "Effects of Precipitation on UHF Wind Profiler Measurements." *J. Atmos. Ocean. Tech.*, 5:450-465.

CHARACTERIZING THE MEASURED PERFORMANCE OF CAAM

Abel J. Blanco

Army Research Laboratory
Battlefield Environment Directorate
White Sands Missile Range, New Mexico 88002-5501, USA

ABSTRACT

The Computer Assisted Artillery Meteorology (CAAM) provides a proposed artillery meteorological (MET) message that can significantly improve predicted artillery fire. The CAAM design allows the artillery commander to use tailored MET messages computed by an advanced physics model using recent MET data input rather than his stale dedicated station message for adjusting a first-round-hit artillery fire mission. This paper presents two important kinds of estimates describing the performance of CAAM using data collected in the desert and mountains of southern New Mexico. These include the best single estimate and the confidence interval estimate derived from measured upper air data versus nowcasted and forecasted results. In complex terrain the confidence interval improves with the number of available initializing MET stations. Simulated cannon impact displacements effected by wind, virtual temperature, and pressure parameters are tabulated for the evaluation of an analytical objective analysis algorithm and a physical, time dependent, three-dimensional hydrodynamic forecasting model used in CAAM.

1. INTRODUCTION

The Computer Assisted Artillery Meteorology (CAAM) research was designed to include a two phase approach. The first phase included the solution for the immediate need of improving the accuracy of the current cannon/rocket systems and the developmental long range weapon systems. A short suspense for supporting the actual firings of an engineering development weapon system led to the design and implementation of the Time Space Weighted (TSW) CAAM. This proposal is described as a met message manager, "nowcasting" technique (Blanco, etc., 1993). Based on centralizing all available met data, this objective analysis algorithm automatically tailors a best met message for a particular user. Through a peer review including the Army designer, the weapon development contractors, and the Army Research Laboratory (ARL), the Project Office selected the TSW algorithm from available proposals. The selected technology was portable and required a PC environment. This

methodology derives the expected met variability due to time staleness and space separation of the collected data. It follows the same science applied by the U.S. Army Materiel System Analysis Activity (AMSAA) in their development of the Cannon Artillery Delivery Accuracy Model (CADAM) which is been used to defined met accuracy requirements in the development of the new weapon systems (Reichelderfer, etc. 1993). The TSW assigns weights to the available field data and takes advantage of applying functional relationships such that the time staleness follows more important role than the space separation in computing the best met to be disseminated.

The other phase, a longer term, proposal involves a time dependent, three dimensional Higher Order Turbulence Model for Atmospheric Circulations (HOTMAC) CAAM. Because of the complexity of this model the required platform consists of a HP 9000 Series 750 computer. The HOTMAC CAAM computer runs a complex suite of software that will manage all tactical communications and data sharing. HOTMAC is a computer code that forecasts wind, virtual temperature, and pressure over complex surface conditions. This model is based on a set of second-moment turbulence equations and can be used under quite general conditions of flow and thermal stratification. Effects of short and long wave solar radiation, tall tree canopies, and topography are included in the model. The surface temperatures are computed from a heat conduction equation for the soil and a heat energy balance equation at the surface. The model assumes hydrostatic equilibrium and uses the Boussinesq approximation. A terrain-following vertical coordinate system is used in order to increase the accuracy in the treatment of surface boundary conditions. Vegetation plays an active role in the apportionment of available heat energy between convective (sensible and latent) and conductive (into the soil) components.

Based on the U.S. Army Field Artillery School requirements and funding from the Project Manager, Electronic Warfare, Reconnaissance, Surveillance, Target Acquisition, ARL defined and monitored the development of two research proto-type systems that allow significant meteorological (met) accuracy improvements for the field artillery. These systems provide state-of-the-art software and hardware developments that allow automated field data integration, meteorological modeling, and dissemination techniques. The Fire Control Centers (FCC) are automatically refreshed with met data that can enhance the first round hit capability for predicted fire. No longer will the FCC be delayed in waiting for final met adjustments because CAAM will automatically refresh met messages for the particular user. The TSW CAAM was developed in-house (Vidal etc., 1994); and the HOTMAC CAAM was developed by the Physical Science Laboratory under contract with the ARL, Battlefield Environment Directorate (Spalding etc. 1993).

This report defines a methodology that demonstrates the worth of the proposed CAAM models. Available met data from White Sands Missile Range, New Mexico, has been utilized to test and evaluate CAAM performance. To qualitatively demonstrate the long term capability, data from the Target Area Meteorology Data Experiment (TAMDE) conducted during July - September 1992, is used to derive a spatial analysis for a 60 by 220 km area. The CAAM forecasting performance capability is also evaluated with this data set. The other set of data collected during the Proto-type Artillery Sub-System (PASS) Field Experiment conducted within the same area during November and December 1974 is used to quantitatively reveal the significant improvement over the current doctrinal method of adjusting artillery fire for met variations. Simulated 155mm rocket assisted round impact displacements are tabulated and

analyzed results are graphically presented to demonstrate the significant improvement afforded by each proposal. This improvement enhances the predicted fire accuracy such that the new capability approaches the accuracy afforded by registration/transfer fire techniques. Both proto-type systems are automatic and all modeling input and output are transparent to the operator except for met data editing and final recommendation to disseminate the best met messages. The systems were designed so that a high school graduate can effectively operate and efficiently interact with the FCC.

2. STATEMENT OF PROBLEM

All effective artillery fire includes meteorological (MET) aiming adjustments to compensate for the variations of atmospheric wind, temperature and density. Many times the current doctrine of utilizing data from a dedicated met station is not representative of the actual met effects experienced by unguided projectiles. This has become most noticeable for extended range artillery. The classical mechanics for predicting unguided projectile trajectories are well known and automated at artillery FCC. Under standard conditions, this simulation science is assumed to be exact. Since the atmospheric conditions are rarely standard, the U.S. Army Field Artillery deploys met teams to measure atmospheric conditions within the battle area. These teams are not co-located with the artillery fire systems, and the balloon-borne sensor may drift away or towards the point of application depending on the general wind flow within the battle area.

MET data time staleness must be significantly reduced if the artillery commander is to maintain effective predictive fire for future long-range targets. CAAM provides the field artillery with inexpensive techniques for automating representative met corrections by retrieving, analyzing, and disseminating best met data. All battlefield MET messages are received through existing tactical field equipment. These messages are cataloged with respect to time staleness and space separation from the point of application. The CAAM design allows the artillery commander to use tailored MET messages computed by an objective analysis or an advanced physics model using recent MET data input rather than the normally stale dedicated station message. This derived message enhances the first round hit probability for current and future artillery fire systems. Aiming adjustments will accurately deliver carrier projectiles and compensate for met effects on target area parachute delivered sub-munitions, scan and search patterns, chemical bursts, and wind gliding warheads. CAAM provides a proposed artillery MET message that can significantly improve predicted artillery fire. With the CAAM the field commander can review simulated results revealing his expected artillery accuracy before his mission engagement.

3. EVALUATION METHODOLOGY

The two data bases utilized in the comparison evaluation are the following: the 1992 TAMDE (Grace, 1993) and the 1974 PASS (Blanco etc., 1976). The tactical scenario addressed was a battle area covering 60 by 220 km. The emphasis was placed on a 60 by 40 km area corresponding to a more representative application of cannon/rocket artillery. Both data base experiments were conducted to help define meteorolgical effects on unguided

projectiles. Temporal and spatial variability of atmospheric conditions were the focus in these programs. The data bases may not be representative of other climates and regions, but their uniqueness is that the sets contain simultaneous upper air sounding from as much as nine stations with artillery computer messages simultaneously collected at 2 hours intervals, over a time of as much as ten hours, with the start and ending times varying with each day. The TAMDE data base is used to qualitatively demonstrate the analysis over a 60 by 220 km area that includes complex terrain. It is also used to demonstrate the forecasting capabilities.

Paired (measure/estimate) statistics is used in quantitatively comparing the accuracy and confidence limits in evaluating the worth of proposed CAAM solutions for improving the artillery accuracy. The emphasis is placed on the artillery miss instead of the actual met parameter. CAAM does not have to exactly predict the weather conditions, but it is designed to accurately predict artillery fire accuracy. The projectile's weight, velocity, and flight time determine the met effect it experiences along the trajectory. For example, the fine weather conditions that effect smoke particles have minor effects in aiming a 95 lbs artillery shell. But understand that the met is a major contributor in the total artillery error budget, and that the gross 0.2 - 2.0 km averages are used in adjusting artillery fire for met variability.

Since actual artillery firings have not been completed with the proposed CAAM solutions, expected accuracies are simulated using a demonstrator Battery Computer System (BCS) fire control. For example, a measured met message and a 27 km target range firing problem are inputed to the BCS, and the aiming solution is then assumed to represent the "truth" impact. Following a similar procedure using the derived aiming angles and the estimated met message, a new impact is computed. If the estimated and measured met messages are the same then the computed impacts should be identical. A bad estimated met message should then produce a large impact difference from the one derived by using the measured met message. The best solution is identified when the paired accuracy difference is equal to zero or the difference is well within the lethal radius of the delivered warhead. Note that the individual difference is derived from the comparison between the BCS computed impacts using the estimated (nowcasted TSW or the forecasted HOTMAC) and the measured met messages.

A day from each of the met data base experiments is selected to describe the worth of the proposed CAAM solutions. All data days will be analyzed and results will be documented in the final report. The purpose of this report is to present preliminary results and provide the status for the on-going applied research. The most variable weather day from each experiment was selected to reveal a maximum improvement. September 2, 1992 is selected to present the HOTMAC spatial analysis and forecasting capability over a 60 by 220 km, complex terrain, battlefield area. December 7, 1974 is used to present the expected improvement afforded by the HOTMAC and TSW CAAM solutions.

With this constraint the sample size is limited to analysis of computer met messages simultaneously collected at 2 hours intervals over a time of ten hours. Table 1 presents the met message pairing used in deriving time staleness results for the current doctrine of adjusting artillery fire to compensate for met variability. Table 2 presents the met message pairing used in deriving the TSW estimates. For example, if station 1 is considered the truth station, then the following staggered releases define the expected

time staleness: to estimate Stn 1 at 0715 use Stn 1 at 0515 and Stn 2 at 0715; and to estimate Stn 1 at 0915 use the above releases plus Stn 3 at 0915. TSW always uses a fresh message except for the case of simulating six hour staleness referenced to Stn 1. In reality at the sixth hour the commander using Stn 1 would have realtime data because the release cycle is repeated maintaining a new message every 2 hours among the three available stations. The same cycle is repeated to derive other replicates defining the sample size used in this preliminary analysis. One can start at 0715 and pair messages to increase the replicate size. All HOTMAC estimates are derived from the first, 0515, met message. The hourly forecasts are dependent on only one message. The same cycle is repeated to derive other replicates defining the sample size; for example use the 0715 to forecast, then use the 0915 to forecast, etc..

Table 1. Pairing met messages for deriving time staleness sample size.

Message	Staleness(h)			
Local time	2	4	6	
0515				
0715	1			
0915	1	1		
1115	1	1	1	
1315	1	1	1	
1515	1	1	1	
Total	5	4	3	Sample

Table 2. Pairing met messages for deriving TSW estimates.

Local time	Staggered Releases			Time Staleness			
Stn 1	Stn 1	Stn 2	Stn 3	2 h	4 h	6 h	
0515	X						
0715		X		1			
0915			X		1		
1115						1	
0715	X						
0915		X		1			
1115			X		1		
1315						1	
0915	X						
1115		X		1			
1315			X		1		
1515						1	
Total				3	3	3	Sample

4. PERFORMANCE CHARACTERISTICS

The first performance check is on HOTMAC CAAM's ability to provide a qualitative spatial analysis for an area 60 by 220 km using only one initializing met message. Frame 1 on figure 1 presents the contour map for the desert and mountainous region. The reporting stations are identified as circles within the simulated battle area. Notice that the open circle located at the lower left corner at about the (6,8) coordinates indicates the station used to start HOTMAC forecasting hourly computer met messages for the entire area. The darken circles represent the location of the other stations used to evaluate the accuracy of the computed estimates for each of the met parameters effecting the artillery accuracy. The index represents a normalized 4 km grided universal transverse mercator unit internal to CAAM. All terrain features are retrieved at this interval; however, CAAM is designed to compute the met message on an 8km grid. Each complete square in the map represents 40 by 40 km and the entire area contains more than the 60 by 220 km requirement. In this case the required area is oriented due north but CAAM has the capability to rotate the desired area in any direction.

Using the September 2, 1992 (fifth day - TAM5) data, frame 2 displays the wind vector plot for the terrain following 1227 m level. Note the speeding up of the wind at the location of the elevated terrain. The wind starts as westerly with changing direction as it travels through the mountain canyons. The current doctrine assumes that the met message collected at the open circle location is representative of the entire area. One can realize the CAAM improvement is already significant. Frame 3 reveals a more representative description because there are three open circles representing three met messages initializing the HOTMAC CAAM. In this case the two darkened circles represent available data for comparison with the generated estimates at the corresponding locations. Examining the station at about coordinate (14,32), one can see that the one station run over estimates the wind speed and predicts the wrong direction. The mountain provides a stronger sheltering than the model predicted. Frame 4 represents the most realistic description of the wind. Here all stations are used to initialize CAAM and simulate the effect of dropsondes in the target area. This case study reveals that space interpolation results contain the best confidence in the estimated results. An application for knowing the target area winds is the management of air delivery of supplies or personnel to a particular sector within the battle area.

The other qualitative performance check on CAAM is how well can it forecast. Figure 2 presents the terrain contour, 0600, and 0900 wind vector plots. Generally, CAAM estimates a persistence forecast and for this case the wind field was indeed following this same pattern. The pattern is much smoother at 0900 than at the initialization time at 0600. In the following section one can quantitatively see that the forecasting capability is significantly better than the current doctrine of using stale data that may be as much as 6 hours old.

5. EXPECTED ARTILLERY IMPROVEMENTS

Using the December 7, 1974 (julian day 341) data from the other met data base one can quantify the improvement afforded by the two proposed CAAM solutions. Figure 3 presents the station locations on a 20 km grid. Using

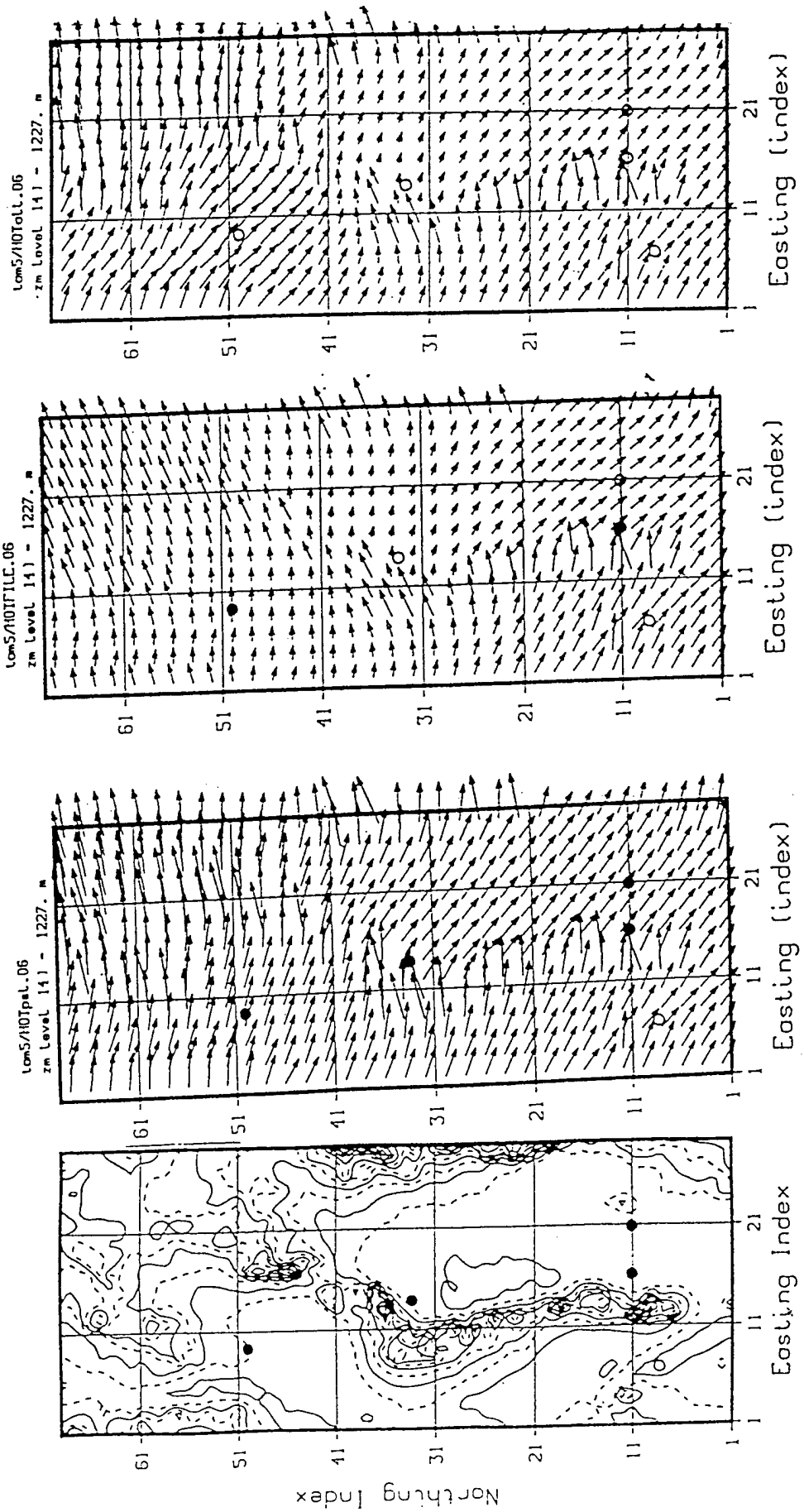


Figure 1. Terrain contour and wind vectors spacial analysis.

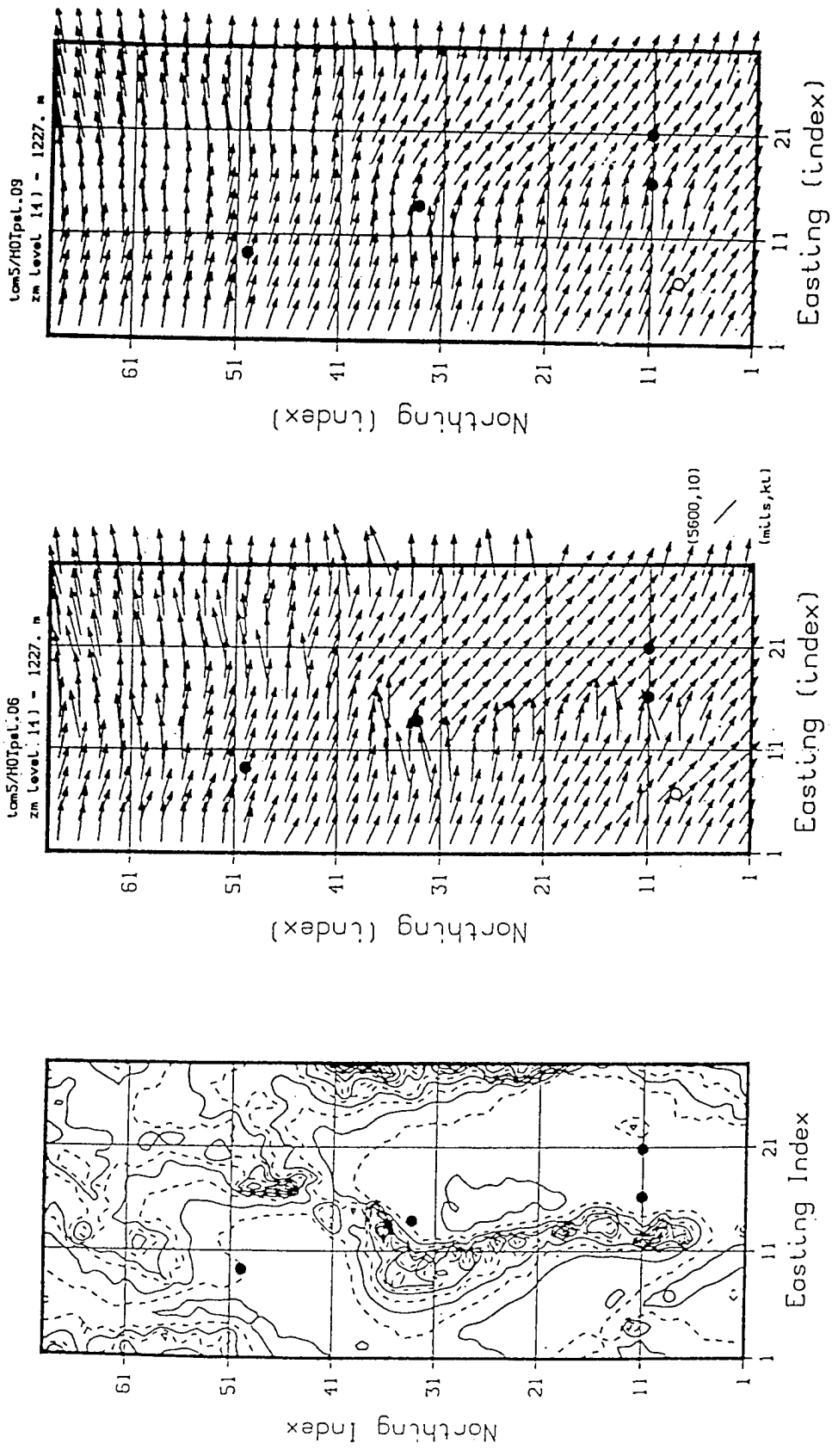


Figure 2. Terrain contour and wind vectors spacial and temporal analysis.

Figure 3. Terrain contour and station location on a 20 km grid.

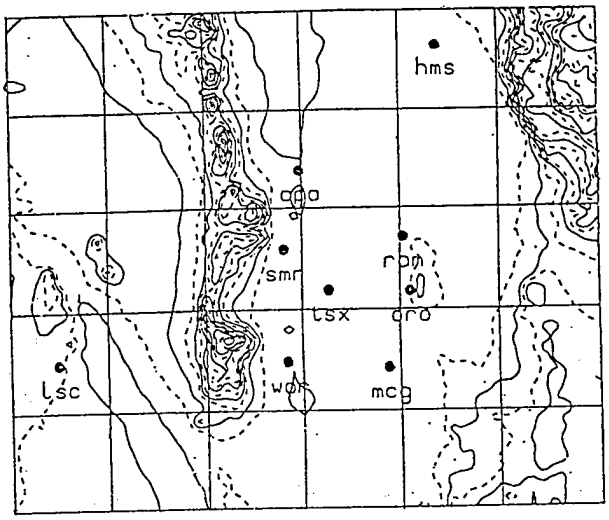


Figure 4. TSX statistical comparison (within 20 km).

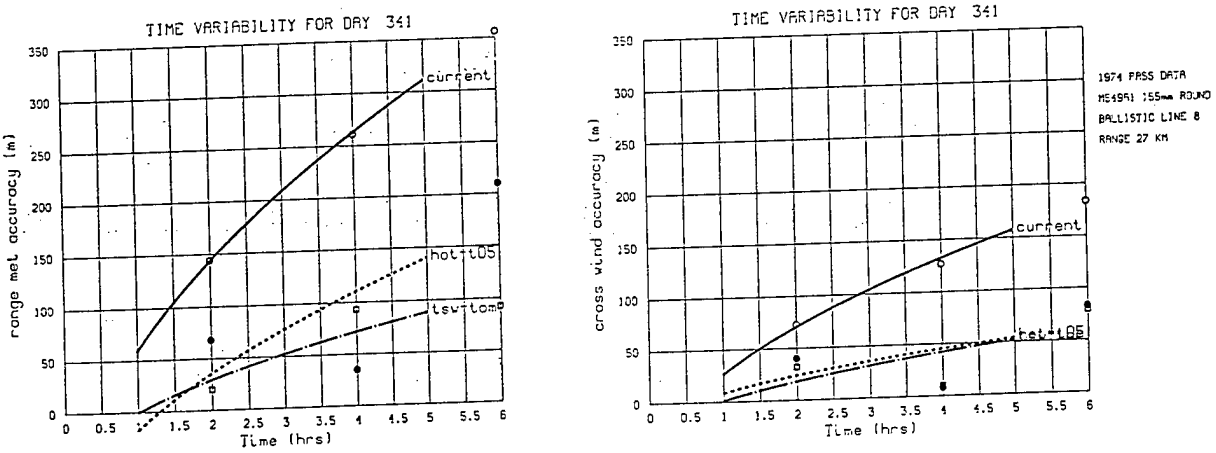
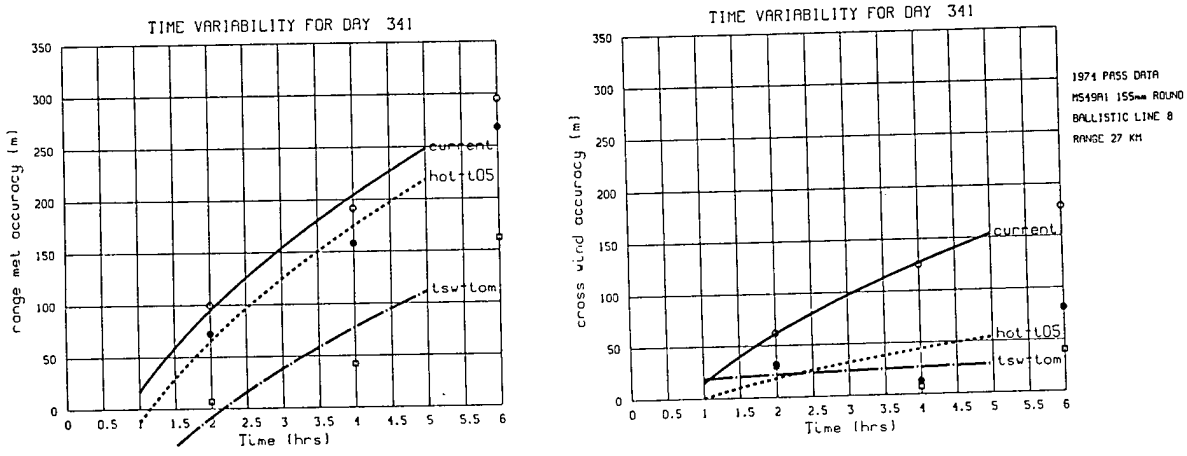


Figure 5. HMS statistical comparison (over 50 km).



the Table 1 scenario, the stations are identified as follows: Stn 1 is tsx; Stn 2 is oro; and Stn 3 is mcg. The Table 2 staggered releases are followed to predict the actual met messages measured at tsx. To compute the current met accuracy one pairs the appropriate met messages outlined in Table 1 and inputs into the BCS to compute a firing angle solution for a 155mm rocket assisted round fired at a 27 km range target. After completing the differences from the simulated impacts as described in the above section, Table 3 presents the comparison results.

Table 3. The tsx delta BCS output for jday 341.

stale(h)	pairs		Range(m)	Cross(m)	QE(mil)
		current doctrine tsx analysis			
2	0715	0515	116	62	547.2
4	0915	0515	51	15	"
6	1115	0515	228	112	"
2	0915	0715	-59	-44	541.9
4	1115	0715	111	50	"
6	1315	0715	333	133	"
2	1115	0915	174	97	544.7
4	1315	0915	397	181	"
6	1515	0915	452	254	"
2	1315	1115	220	81	537.0
4	1515	1115	274	150	"
2	1515	1315	55	65	527.6
		HOTMAC_tsx0515 forecasting tsx			
2	0715	0515	-68	-40	541.9
4	0915	0515	-35	8	544.7
6	1115	0515	-210	-83	537.0
		TSW_tom nowcasting tsx			
2	0715	0715	20	-32	541.9
4	0915	0915	93	10	544.7
6	1115	0915	-92	-79	537.0

Note that the deltas for the two hour staleness varies with the time of the day. For the range component the smallest variabilities are listed as occurring during the 0915-0715 and 1515-1315 periods. The -59m and the 55m represent the expected error for firing at 0915 and 1515 with met aiming adjustments from 0715 and 1315. Another observation is that the results for one case reveal the four hour stale data (0915-0515) providing more accurate results than the two hour stale data (0715-0515). This is the behavior of the weather; it is unpredictable and never standard. As we group the results

in a small sample and derive the mean and standard deviation, the results can be presented in another arrangement. The root-mean-square values are fitted to a function of the time staleness raised to the one-half power. Figure 4 presents the statistical results and demonstrates the accuracy of the fit with the data located on the derived curve. The solid line curve represents the accuracy of the current doctrine. If one aims with two hour stale data, one can expect about 150m miss in the range and about 75m miss in the cross. The other two curves represent the expected accuracy afforded by the two proposals: HOTMAC using one met message at the start of the day, and TSW using all messages available from the staggered balloon releases. The scenario presented in Table 2 is used in deriving the Figure 4 results. TSW is always using current data collected at the other stations except for the six hour staleness.

Table 4. The hms delta BCS output for jday 341.

			current doctrine hms analysis		
stale(h)	pairs		Range(m)	Cross(m)	QE(mil)
2	0745	0545	96	23	544.6
4	0945	0545	133	44	"
6	1145	0545	261	96	"
2	0945	0745	49	22	540.8
4	1145	0745	174	73	"
6	1345	0745	287	170	"
2	1145	0945	122	50	538.5
4	1345	0945	232	146	"
6	1545	0945	331	230	"
2	1345	1145	105	96	533.3
4	1545	1145	208	174	"
2	1545	1345	106	73	529.1
			HOTMAC_tsx0515 forecasting hms		
2	0745	0515	-88	30	540.8
4	0945	0515	-150	15	538.5
6	1145	0515	-269	-34	533.3
			TSW_tom nowcasting hms		
2	0745	0715	-7	30	540.8
4	0945	0915	-42	7	538.5
6	1145	0915	-162	-40	533.3

Table 4 present the results for estimating met data at the hms station from using data from the tsx, oro, and mcg stations. Again the HOTMAC using only one station and TSW using the staggered release schedule reveal a significant improvement over that expected from the current method of using a

dedicated met station that may provide 6 hour stale data. Figure 5 presents the graphical comparison that used historical met data to estimate the met at a 50 km location. Comparing figure 4 and 5 reveals that the range (wind, temperature, and pressure) variability at hms is lower than that at tsx. Note that the solid line curves are derived from actual measurements at each station as defined in Table 1. The other curves represent how well the estimates do in predicting the actual measurements. A general conclusion is that the two proposals do better when estimating closer to where the initializing data are collected. The cross component comparison in Figure 5 indicates that the HOTMAC temperature and pressure forecasts are not as accurate as those esimated by TSW using the 0715 and 0915 observations. Perhaps the single station HOTMAC can be improved by using surface observation in order to adjust for large changes in the pressure due to fronts moving in. TSW estimates at a distance greater than 50 km reveal a significant improvement over the current doctrine of using stale data from a dedicated station.

6. SUMMARY

The ARL, Battlefield Environment Directorate, has completed the development of two proto-type CAAM systems. The performance of the CAAM two phase approach has been qualitatively characterized for spatial analysis and forecasting. For a single, variable weather, day quantitative results have been tabulated. Graphical comparisons reveal impressive results. The TSW is already implemented in the software of an engineering development fire control weapon system. It is also under review and evaluation for inclusion in future FCC. This preliminary analysis presents results that quantify the improvement afforded by TSW under variable met conditions. The TSW improvement is significant and the algorithm is portable and requires no change to the actual tactical procedure in adjusting artillery fire for met variability. There are other days that reveal no significant improvement because of the homogeneity of the weather; the wind remains strong and persistent in its direction through the day. For very light wind days the expected improvement is also insignificant. For example under these conditions the time staleness takes a minor role because the four hour old message continues to be a good estimate of the present weather conditions. The final report will document all cases from available TAMDE and PASS data and present the general capability of TSW. Based on the on-going research ARL is already compiling a list of improvements for TSW.

The HOTMAC using a single met message has been demonstrated to significantly improve upon the current method of adjusting artillery fire. In the same variable met day that TSW was evaluated, HOTMAC revealed impressive results. The added advantage is that the staggard release met message schedule is not required in enhancing the first round hit capability. This means that the artillery commander can continue with his dedicated met station and update or forecast his met message until he receives fresh met data. However, this is not the case for the spatial analysis for the 60 by 220 km. One needs more initialization observations in order to obtain accurate results. If the application is over a time when no fronts are passing then the single message initialization may yield acceptable results. Many areas of improvement have been identified and the final report will

document the status and future plans for HOTMAC. This approach in the CAAM research has a longer implementation schedule.

Actual artillery firing using these two proposals are being planned. The quick implementation of TSW was accepted by the weapon system developer in order to show the required accuracy during the initial system technical demonstration. The on-going research findings can easily be incorporated by installing the new revision into the weapon's fire control subroutine. The CAAM specifications, requirements, and design were established to allow portable revision control. Because of the modular development, the HOTMAC can be the final revision of CAAM by replacing TSW, the intermediate CAAM solution.

REFERENCES

1. Blanco, Abel, Edward Vidal, and Sean D'Arcy, 1993: "Time and space weighted computer assisted artillery message", Proceeding of the 1993 Battlefield Atmospherics Conference, Army Research Lab, WSMR, NM.

2. Blanco, A. J. and L. E. Traylor, 1976: " Artillery meteorological analysis of project PASS," ECOM-5804, U.S. Army Atmospheric Sciences Laboratory, WSMR, NM

3. Grace, John, 1993: "TAMDE - The variability of weather over an army division size area," Proceeding of the 1993 Battlefield Atmospherics Conference, Army Research Lab, WSMR, NM.

4. Reichelderfer, Magan and Craig Barker, 1993: "155-mm howitzer accuracy and effectiveness analysis", Note DN-G-32, U.S. Army Materiel System Analysis Activity, Aberdeen Proving Ground, MD.

5. Spalding, John B., Natalie G. Kellner, and Robert S. Bonner, 1993: "Computer-assisted artillery meteorology system design", Proceeding of the 1993 Battlefield Atmospherics Conference, Army Research Lab, WSMR, NM.

6. Vidal, Edward, 1994: Personal communication, Army Research Laboratory, Battlefield Environment Directorate, WSMR, NM.

7. Yamada, T., and S. Bunker, 1989: "A numerical Model Study of Nocturnal Drainage Flows with Strong Wind and Temperature Gradients", J. Appl. Meteorol., 28:545-554.

EVALUATION OF THE BATTLESCALE FORECAST MODEL (BFM)

T. Henmi and M. E. Lee
U.S. Army Research Laboratory
White Sands Missile Range, NM 88002-5501, USA

T. J. Smith
Operating Location N, Air Weather Service
White Sands Missile Range, NM 88002-5501, USA

ABSTRACT

The performance of the Battlescale Forecast Model (BFM), developed at the U.S. Army Research Laboratory (ARL) to produce an operational short-range ($\leq$ 12 h) mesoscale forecast, is evaluated. The model test domain centers on the White Sands Missile Range (WSMR), NM where observation data from Surface Automated Meteorological System (SAMS) 10-m towers and Atmospheric Profiler Research Facility (APRF) profilers are available. Three different initialization approaches are examined to identify optimal model initialization methods. Statistical parameters such as mean residual and standard deviation of residual are calculated for hourly forecast fields of surface wind and temperature from comparisons of corresponding observations and twenty five 12-h forecast calculations. Results indicate that incorporation of surface wind observation data into the initial field is essential to produce good, short-range BFM forecasts.

1. INTRODUCTION

The Army Research Laboratory (ARL) developed the Battlescale Forecast Model (BFM) to produce an operational, short-range ($\leq$ 12 h) forecast over an area of $\leq$ 500 x 500 km. The BFM will become a major component of the Integrated Meteorological System (IMETS) Block 2 software. The BFM is composed of two major programs. A program called 3DOBJ creates initial and boundary values for the forecast model by processing selected U.S. Air Force Global Spectral Model (GSM) forecast field output data, and/or upper-air sounding and surface observation data, if available. The BFM was adapted from a mesoscale meteorological model called the Higher Order Turbulence Model for Atmospheric Circulation (HOTMAC) (Yamada, Bunker 1989). HOTMAC has been used extensively at ARL (Henmi et al. 1987; Henmi 1990; 1992) to simulate the evolution of locally forced circulations caused by surface heating and cooling over meso-β and γ scale areas. HOTMAC is numerically stable and easy to use, and thus suitable for operational use. Details of the BFM are described in Henmi et al. (1993; 1994).

In this study, the forecasting capability of the BFM is evaluated by comparing forecast results with surface and upper-air data observed by the White Sands Missile Range (WSMR) Surface Automated Meteorological System (SAMS) and Atmospheric Profiler Research Facility (APRF) profilers, respectively. To find an appropriate method to initialize the model, three initialization methods were selected, and 25 comparisons between 12-h forecasts and observations were made at hourly intervals. The purpose of this paper is to describe the three initialization methods and the method evaluation results.

2. MODEL DOMAIN AND OBSERVED DATA

The study area centered on WSMR, NM. Figure 1 shows the terrain elevation distribution of the selected BFM domain, covering a 250 x 250 km area. The latitude and longitude of the domain are 33.20° N and 106.41° W, respectively. Meteorological variables are calculated at 51 × 51 horizontal grid points × 16 vertical grid points with a unit horizontal grid distance of 5 km. The upper atmosphere model boundary is 7000 m above the highest surface terrain elevation in the domain. The locations of selected WSMR SAMS sites are marked by Arabic numbers in figure 1.

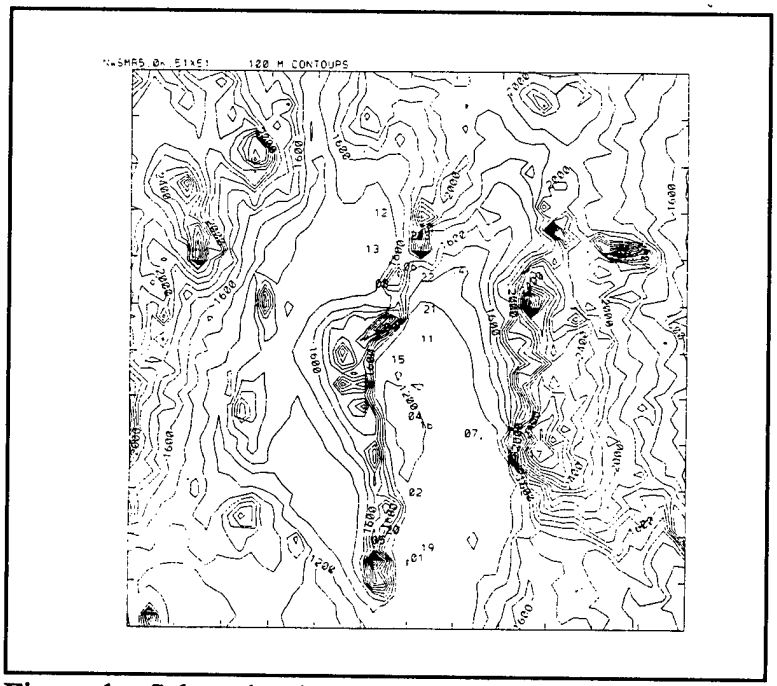


Figure 1. Selected WSMR BFM model domain (250 x 250 km). Contour lines are drawn every 200 m. The locations of SAMS sites are marked by Arabic numbers.

GSM output are reported on grid points spaced 381 km apart on mandatory pressure surfaces. A three-dimensional objective analysis of GSM data is made over an area covering 800 x 800 km centered on the BFM domain.

Twelve-hour forecast computations producing hourly outputs were made for 25 cases selected from the months of February and March 1994. Hourly averaged values of surface wind and temperature were used for comparison.

3. INITIALIZATION METHODS

Based on the case study reported in Henmi et al. (1994), the BFM was initialized by three different methods described in sections 3.1 through 3.3. Additionally, two computed data, mentioned in sections 3.4 and 3.5, are compared with observations.

3.1 Initialization Using GSM

GSM uses a normalized pressure $\sigma = p/p_s$ vertical coordinate. GSM analysis and 12-hour forecast values of horizontal wind components, temperature, dew-point depression, and geopotential height on mandatory pressure levels were used to produce three-dimensional fields for BFM initialization and time-dependent boundary values.

HOTMAC uses a z^* vertical coordinate, and is defined in the following manner:

$$z^* = \overline{H}\,\frac{z - z_g}{H - z_g} \tag{1}$$

where

- z^* = the transformed vertical coordinate
- z = the Cartesian vertical coordinate
- z_g = the ground elevation above mean sea level (MSL)
- $\overline{H}$ = the material surface top of the model
- H = the corresponding height in the Cartesian coordinates.

For simplicity, H is defined as

$$H = \overline{H} + z_{gmax} \tag{2}$$

where z_{gmax} is the maximum value of z_g.

Because different vertical coordinates are used in GSM and HOTMAC, the following two steps are needed:

(1) Horizontal interpolation of wind components (u,v), temperature, mixing ratio, and geopotential height from GSM grid points to BFM grid points on constant pressure surface. Barnes' method (1964) is used for horizontal interpolation.

(2) Vertical interpolation of the variables from BFM constant pressure surfaces to z^* surfaces at BFM grid points using a linear interpolation method.

GSM synoptic scale variations of meteorological variables are incorporated into the model equations by nudging (Hoke, Anthes 1976).

For 12-h forecasting, both the current analysis and the 12-h forecast fields from the GSM are analyzed using the above method, and hourly data are generated by a linear interpolation between the two time periods. The first hourly analysis field data are assimilated by using the nudging method for the hour preceding the initiation of forecast computation. The next hourly data are assimilated into the forecast 1 h into the forecast period; the process is repeated hourly over the 12-h forecast period.

Out of 16 vertical layers, nudging was applied only in the 9 upper layers (corresponding to z^* heights > than 151 m).

3.2 Initialization With GSM and Mean Surface Wind Direction and Speed

Wind directions reduced from GSM data in layers near the surface were frequently and significantly different from those observed. Thus, to improve the agreement between computed and observed wind vectors in short-range forecasts, mean surface wind data is incorporated into initial fields. From all the selected SAMS data obtained over WSMR, mean surface wind vector components were calculated at the initial time of forecast, and logarithmic wind profiles were assumed from the surface ($z^* = 10$ m) to the seventh layer ($z^* = 151$ m). Linear profiles were then interpolated between the 7th to the 10th model layers, above which only GSM data is used to initialize BFM grid points.

3.3 Nudging of Individual Surface Wind Data at Initial Time

In addition to the mean surface observation process described in section 3.2, individual SAMS site wind observation data obtained at initialization times are assimilated into model calculations at the grid points adjacent to the SAMS locations. The method of surface wind data assimilation is described in Henmi et al. (1994).

3.4 Surface Data Nudging Every Three Hours

In section 3.3, surface wind data is nudged only at the first hour of model computation. This method was extended in a way such that SAMS wind data are assimilated into model calculations every 3 h. For instance, the data observed at 5, 8, 11, 14, and 17 local standard time (LST) are nudged for 1 h starting at 4, 7, 10, 13, and 16 LST.

3.5 Linear Interpolation of GSM Data

For comparison purposes, the three-dimensional GSM data set, created by the method described in section 3.1 at two time periods, is linearly interpolated in time, and resulting data (at hourly intervals) is compared with observation.

4. STATISTICAL PARAMETERS

To examine the differences in the results using methods described in sections 3.1 through 3.5, the following statistical parameters are calculated hourly by using the data from the 25 different cases.

4.1 Mean Residual

The difference between observed and forecast values of a meteorological parameter can be written as

$$F_{res} = F_{obs} - F_{for} \tag{3}$$

where F represents a meteorological parameter and $_{res}$, $_{obs}$, and $_{for}$ represent residual, observation, and forecast, respectively.

A mean residual for 12 forecast hours is defined as

$$\overline{F_{res}}(t) = \frac{\sum_m \sum_n F_{res,m,n}(t)}{m \times n} \tag{4}$$

where m represents the number of forecast cases, and n represents the number of SAMS data at forecast time t.

4.2 Standard Deviation of Residual

The standard deviation of residual of a meteorological parameter is defined as

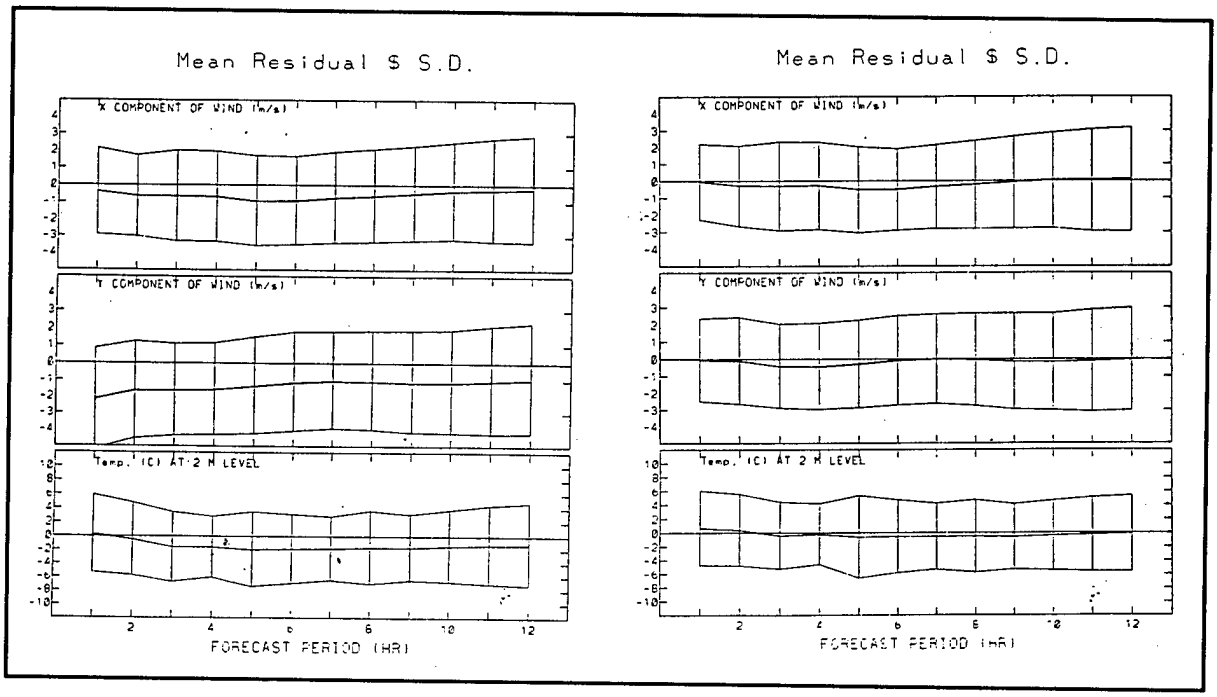
$$\sigma_{F_{res}}(t) = \pm \left(\frac{\sum_m \sum_n (F_{res,m,n}(t) - \overline{F_{res}}(t))^2}{m \times n} \right)^{\frac{1}{2}} \tag{5}$$

where $F_{res}(t)$ is the standard deviation of residual at forecast time t.

Improved forecast calculations result in mean residuals converging to zero in conjunction with smaller standard deviations of residual. Perfect agreement between observation and forecast results in zero values for both parameters.

5. RESULTS

In figures 2 through 4, the mean residuals (mean curves) and standard deviations (upper- and lower-bound curves) are plotted as a function of time.



(a) (b)

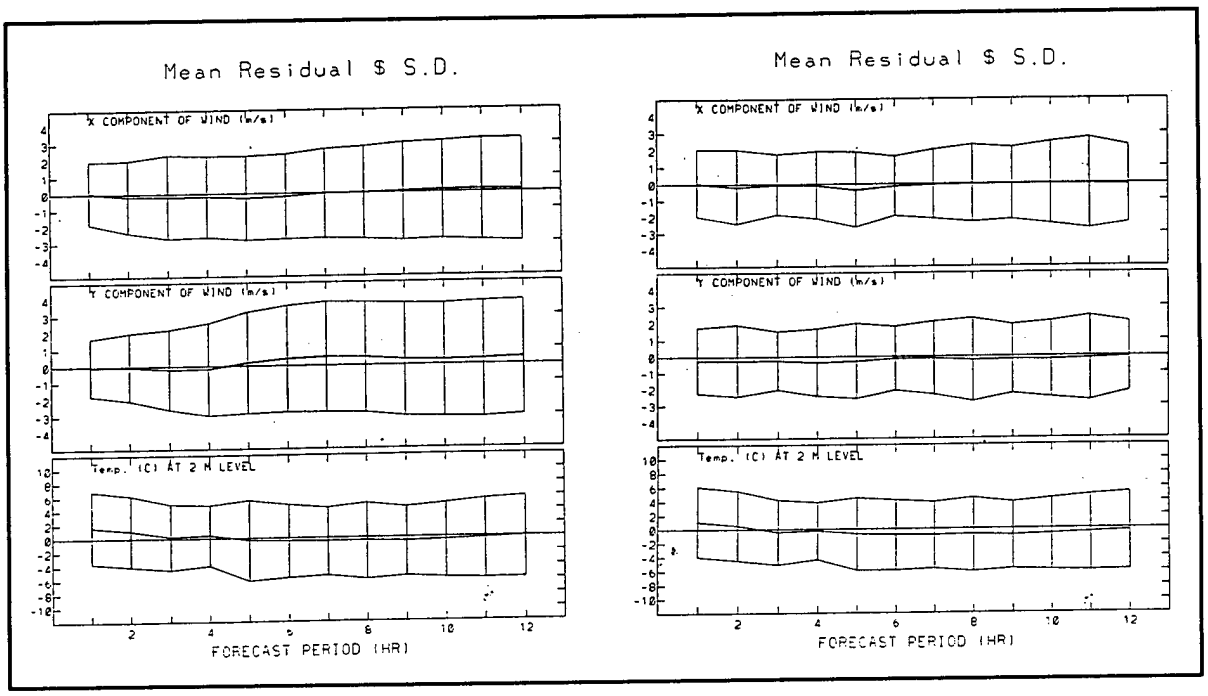
Figure 2. Temporal variations of mean residual (mean curves) and standard deviation (upper- and lower-bound curves) for methods in sections 3.1(a) and 3.2(b). Upper plots represent the surface x wind vector components, middle plots are the y wind vector components, and bottom plots are of surface temperature.

Comparisons of figures 2 through 4 reveal the following:

(1) Differences between figures 2(a) and 4 indicate that the BFM produced significantly improved forecast fields of wind and temperature (section 3.1) compared to the linear interpolation of GSM data (section 3.5). In general, the values of mean residuals and standard deviations are smaller in figure 2(a) than in figure 4. The physical scheme of the model produced better agreement with observation data than simple interpolation of GSM data in time and space.

(2) From figures 2(a) and (b), the initialization using the mean wind speed and direction (section 3.2) produced better forecast fields than the GSM data initialization (section 3.1). Substantial improvements in both x and y components of wind vectors were obtained. As can be seen in figure 2(a), the mean residual values of both wind vector components were negative. This means that BFM forecast calculations initialized with GSM data produced

larger wind vector components than observed. Conversely, the mean residual values in figure 2(b) are much closer to zero, indicating that on average the BFM, using mean wind speed and direction at model initialization times, produced surface wind vector component magnitudes similar to those actually observed. Even temperature mean residuals in figure 2(a) show larger negative values throughout the 12-h forecast calculation than in figure 2(b). Initial temperature fields in the methods in sections 3.1 and 3.2 are identical for all 25 simulations. The boundary layer scheme of the BFM produces improved temperature predictions using the method in section 3.2, compared to the method in section 3.1. Although it is not clearly understood, logarithmic profiles of wind components assumed in the method in section 3.2 may coincide to produce good surface temperature profile predictions in the boundary layer. Further studies are needed to understand this problem.



(a) (b)

Figure 3. Same as figures 2(a) and (b), except forecast calculation (a) is initialized by nudging surface wind data (section 3.3), and (b) is surface wind data nudged every 3 h of calculation (section 3.4).

(3) Comparison between figures 2(b) and 3(a) indicates that nudging the surface wind vector components at the forecast initial time (section 3.3) produced better forecast results in wind fields for a few hours during the early stage of calculation, but during the later stage of calculation the forecast method in section 3.2 produced superior agreement between predicted and observed parameters. This can be inferred from larger standard deviations in both x and y wind components in the last several hours of forecast calculation. Nudging of surface wind components that are not dynamically balanced with the numerical schemes of the model may be the reason for the results of the method in section 3.3. Temperature fields show little differences between the methods in sections 3.2 and 3.3.

(4) The method in section 3.4 produced the best agreement between predicted and observed parameters. In this method, observed wind vector components were assimilated into model calculations by nudging every 3 h. Figure 3(b) shows smaller standard deviations at 3, 6, 9, and 12 h when the data were nudged during the previous 1 h. It should be noted that, although the nudging of dynamically unbalanced wind vectors is done repeatedly, the numerical scheme of the model is stable enough to prevent numerical instability.

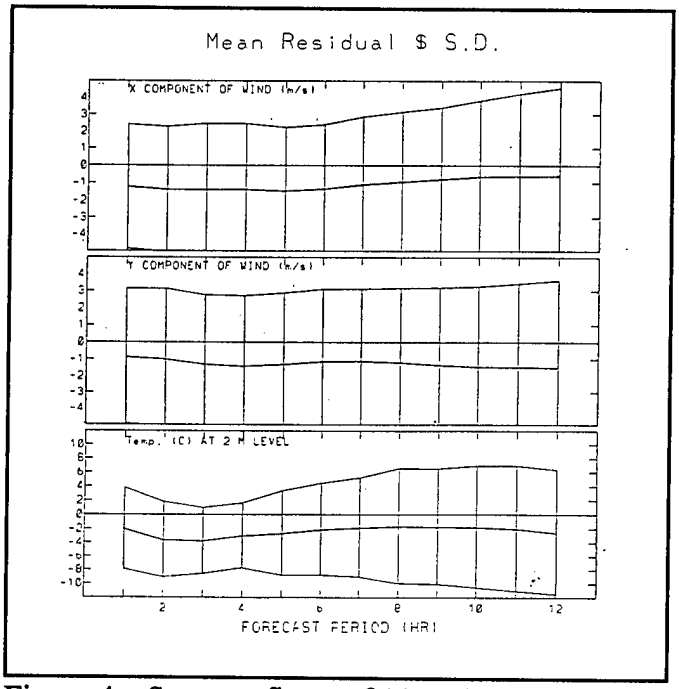


Figure 4. Same as figures 2(a) and (b), except for temporal and spatial interpolation of GSM data (section 3.5).

6. SUMMARY

Comparison of forecast results using the method in section 3.1, with space and time interpolation of GSM data, clearly shows that the BFM produced substantially improved forecast fields over methods using a simplistic interpolation of GSM data. Initialization by methods in sections 3.2 and 3.3 produced further improvement over the method in section 3.1, confirming that incorporation of observed data into initial fields is important.

In the present study, all the cases simulated were in February and March, 1994. Forecast fields of moisture were not compared with observation because observed data were not reliable. In a future study, cases will be simulated for the summer for which the data have been archived.

7. REFERENCES

Barnes, S. L., 1964. "A Technique for Maximizing Details in Numerical Weather Map Analysis." *J. App. Meteor.*, *3*:396-409.

Henmi, T., R. E. Dumais, Jr., and T. J. Smith, 1993. "Operational Short-range Forecast Model for Battlescale Area." In *Proceedings of 1993 Battlefield Atmospherics Conference*, BED, U.S. Army Research Laboratory, White Sands Missile Range, NM, pp 569-578.

Henmi,T., M. Lee, and T. J. Smith, 1994. *Evaluation Study of Battlescale Forecast Model (BFM) using WSMR Observation Data*, U.S. Army Research Laboratory, White Sands Missile Range, NM 88002-5501.

Hoke, J. E., and R. A. Anthes, 1976. "The Initialization of Numerical Models by a Dynamic-Initialization Technique." *Mon. Wea. Rev.*, *104*:1551-1556.

Yamada T., and S. Bunker, 1989. "A Numerical Study of Nocturnal Drainage Flows with Strong Wind and Temperature Gradients." *J. Appl. Meteor.*, *28*:545-554.

VERIFICATION AND VALIDATION

OF THE

NIGHT VISION GOGGLE TACTICAL DECISION AID

John R. Elrick
U.S. Army Research Laboratory
Battlefield Environment Directorate
White Sands Missile Range, New Mexico, 88002-5501, USA

ABSTRACT

The night vision goggle (NVG) tactical decision aid (TDA) is a computer software application used to determine the suitability of NVG use based on existing or forecast meteorological conditions. The TDA combines solar and lunar ephemeris data with the general effects of clouds and precipitation on illumination levels based on the weather data contained in standard weather observations. This TDA is one of a suite of TDAs that was delivered in the Block I, Integrated Meteorological System (IMETS) release to the Program Executive Office Command and Control Systems, Project Director, IMETS. Although the NVG TDA was acceptance tested before it was released, it was never formally verified and validated. The verification and validation (V&V) described here are results of Battlefield Environment Directorate efforts to include V&V as part of future software releases to U.S. Army weather support personnel. The accurate, early identification of software problems and their correction prior to operational applications are integral parts of providing physically and theoretically sound products to the end user. The methods that were used in the V&V of the NVG TDA are discussed and some of the pertinent findings are presented.

1. INTRODUCTION

The night vision goggle (NVG) tactical decision aid (TDA) is part of a suite of computer software applications that is designed to be included in the Integrated Meteorological System (IMETS). It is a product that will provide battlefield decision makers with detailed information about the solar and lunar illumination levels at user-specified locations, with general consideration for cloud cover and precipitation. It was one of the TDAs that was part of the block I IMETS release from the U.S. Army Research Laboratory's Battlefield

Environment (BE) Directorate to the Program Executive Office Command and Control Systems (PEO CCS) headquartered at Fort Monmouth, NJ. The block I release was delivered to the PEO CCS project director (PD) IMETS as the initial step in a three-block transition process to field an operational IMETS. The final version of the IMETS will be used by U.S. Air Force Staff Weather Officers (SWOs) to support future Army operations with modern hardware and software specifically tailored to the concept of a highly mobile fighting force capable of worldwide deployment. The IMETS will be used at the echelon-above-corps level down to the separate brigade and special operation force level where SWO support is necessary and defined by Army doctrine.

2. DEFINITIONS

The following definitions, taken from Army Regulation 5-11, "Army Model and Simulation Management Program" (1992), were used in the V&V of the NVG TDA (M&S in these definitions refers to model and simulation):

> "a. Verification.
>
> (1) Verification is the process of determining that M&S accurately represent the developer's conceptual description and specifications. Verification evaluates the extent to which the M&S has been developed using sound and established engineering techniques. The verification process involves identifying and examining the stated and pertinent unstated assumptions in the M&S, examining interfaces with input data-bases, ensuring that source code accurately performs all intended and required calculations, reviewing output records, performing structured walk-through techniques to determine if M&S logic correctly performs intended functions, and performing M&S sensitivity analyses. Unexpected sensitivity (or lack of sensitivity) to key inputs may highlight a need to review the M&S algorithm for omissions or errors.
>
> (2) Verification also includes appropriate data certification and M&S documentation (e.g., programmer's manual, user's guide, and analyst's manuals).
>
> (3) Verification should normally be performed by an independent V&V (IV&V) agent but remains the responsibility of the M&S proponent to ensure accomplishment.
>
> b. Validation. Validation is the process of determining the extent to which M&S accurately represent the real-world from the perspective of the intended use of the M&S. The validation process ranges from single modules to the entire system. Ultimately, the purpose is to validate the entire system of M&S data, and operator-analysts who will execute the

M&S. Validation methods will incorporate documentation of procedures and results of any validation effort."

The above document cites the types of validation that may be used in the process described here. "Face Validation" or the determination that an M&S, based on the software performance, seems reasonable to people knowledgeable about the system being modeled was used in this V&V effort in conjunction with "Peer Review" where people who are very familiar with the technical area being modeled evaluate its internal representativeness and the accuracy of the output of the M&S.

3. TECHNICAL DOCUMENT REVIEW

A comprehensive review of the technical references used in the NVG TDA research and development (R&D) effort was made along with a complete review of the technical documentation associated with the release of the NVG TDA to PD IMETS. This review was necessary for the validation of the physical principles used in the computer model. The validation described is of the "conceptual" variety described by Dale K. Pace in his article "Modeling and Simulation" (1993) because of the maturity level of the TDA. The following paragraphs present the findings of this review.

The first major document reviewed was the basis for the illumination calculations. The computer program ILLUM (van Brochove 1982) was the technical basis for all illumination values reported by the NVG TDA. This program was used for all solar and lunar ephemeris computations. A reasonable "constant" value for natural illumination without solar or lunar contribution is presented. There is a full explanation of the FORTRAN computer code used to develop the model. ILLUM calculates the illumination based on the geographical altitude and longitude of an earth-based observer (user) for clear skies. Infrequent solar and lunar phenomena, such as eclipses, are considered and the application warns of their occurrence. A natural illumination value of 1.1×10^{-3} lux (lumens(lm)m^{-2}) of natural illumination and the illumination value for the full moon of 0.267 are consistent with the RCA Electro-Optics Handbook (1978).

Another major contributor to this development was AFGL-TR-82-0039, Solar Radiance Flux Calculations from Standard Meteorological Observations (Shapiro 1982). Shapiro's work and associated computer models were used to include the effects that clouds have on the illumination reaching the ground. In its most complex form, the computer model described will calculate the solar radiation incident at or near the earth's surface through n-layers of the atmosphere through a system of $2n + 2$ linear equations. These equations comprise a closed set of equations that account for the physical processes of reflection, absorption, and transmission of the electromagnetic radiation along its path.

To be consistent with the standard methodology of reporting cloud cover, the n-layers are taken as three discrete cloud layers representing low, middle, and high clouds. Specific radiative transfer coefficients were developed that are dependent on cloud amount and

thickness for each layer. The effects of the earth's surface (albedo) are considered. Shapiro tested the model he described against independent data and found it to be accurate. The calculations presented in this work are based on simple scattering theory and Monte Carlo simulations. Nine cloud types were chosen to represent those clouds commonly observed. The World Meteorological Organization Synoptic Cloud Code recognizes other cloud types, but they are seldom observed.

The case where precipitation is occurring is the least reliable of the solar flux calculations used. Only a small number of precipitation events led to a small number of case studies. During precipitation, the cloud types present can be very complex and ground-based observers can see, and therefore report, cloud types and amounts up to and including the lowest overcast layer. Because of this, worst-case thick clouds are assumed at all levels when precipitation is occurring.

Neither Shapiro's work nor the NVG TDA computer model accounts for such radiative transfer processes as aerosol and molecular scattering and absorption. Ozone and water vapor absorption are treated only in the most rudimentary way. This seems a most reasonable approach in light of the other simplifying assumptions and the accuracy of the input observational data. Even with the simplified treatment presented by Shapiro, the process of radiative transfer is very complex and is handled in a physically realistic and rigorously complete way.

Finally, the Technology Exploitation Weather TestBed (TEWTB) User's Guide and Technical Reference for the Block I Integrated Meteorological System (IMETS) (Elrick et al. 1992) was reviewed for content and consistency. This document was prepared by scientists and engineers from the Physical Science Laboratory and the BE Directorate. It is intended as a reference manual for individuals who are unfamiliar with the IMETS but who possess some basic computer operating skills.

This document has some inconsistent references to "night vision devices" that could include such low-light-level equipment as starlight scopes and tank gunner's sights. The NVG TDA is geared toward aviation applications for nighttime flying operations.

Occasionally, computer jargon is used in the text. This could present a limitation to its use by operators who are not familiar with computer nomenclature. In other instances, incorrect reference is made to operations being "GO" or "NO GO" based on the existing or forecast weather. Conditions should be identified as being "FAVORABLE, MARGINAL, or UNFAVORABLE." TDAs are not intended to be directives; they are intended instead to be "intelligent" planning guides for battlefield decision makers based on existing doctrine and equipment limitations.

This document has a final weakness. It does not contain definitions for some of the terms used. Terms such as nautical and civil twilight need to be defined for operators who are not familiar with them. Inclusion of a complete set of definitions will make this document a valuable reference guide that will stand on its own merit.

4. SOFTWARE TESTING

During the period 1-18 November 1994, the NVG TDA computer software was exercised for a total of 11.5 hours in seven separate sessions. This testing was done on the system known locally as the ACCS4, which is a nonrugged commercial version of the Army common hardware system. The most current version of the block I IMETS baseline software resides on this computer and is identical to the baseline version on the Army Command and Control System. The purpose of this testing was to test for accuracy of the software application and its "user friendliness."

Several errors in the software were noted and documented according to the established configuration management practices employed in the BE Directorate. There are undoubtedly other errors that were not detected because of the inability to examine every possible scenario. The ephemeris data that are an output of the TDA were compared with data used at the official meteorological forecasting and observing station at White Sands. All ephemeris data were found to be within plus or minus 5 minutes of the data provided to the local station by the Nautical Almanac Office (1993). This is well within the acceptable operating envelope for most Army operations.

For this stage of the IMETS R&D effort, the software is acceptable. The minor errors found and documented during this test should be fixed before final fielding. Other errors that surface need to be documented and corrected before future baseline releases.

5. CONCLUSIONS AND RECOMMENDATIONS

The NVG TDA is complete and accurate based on its stage of development in the IMETS release cycle. It is based on sound physical principles, and it is certainly usable and trustworthy for limited operational considerations. Before the software can be fielded, it must be made absolutely "user-friendly" and any errors noted in this and future V&V efforts must be corrected. The TDA must be fully tested and independently evaluated in each baseline stage of its development before it is fielded as part of a fully operational IMETS. As in the past, software developers must periodically test changes and upgrades to verify the correctness of the computer code and its interaction with its associated computer hardware platform. IV&V must be thoroughly conducted, as part of sound configuration management practices, before the IMETS blocks II and III releases.

REFERENCES

Some references that are listed here were not referenced in this paper but were cited in the original V&V effort. They are included here for completeness.

Army Model and Simulation Management Program, Army Regulation 5-11, Headquarters, Department of the Army, Washington, D.C., 10 June 1992

Burks, J. D., 1993, Verification, Validation, and Assessment for the Technology Exploitation Weather TestBed (TEWTB), PSL-93/57, Physical Science Laboratory, Las Cruces, NM.

Electro-Optics Handbook, Technical Series EOH-11, RCA, Solid State Division, Electro-Optics Devices, Lancaster, PA, reprinted 5-78

Elrick, J. R., D. C. Shoop, P. V. Laybe, R. R. Lee, J. E. Passner, J. B. Spalding, J. D. Brandt, D. C. Weems, A. W. Dudenhoeffer, G. E. McCrary, and S. H. Cooper, 1992, Technology Exploitation Weather TestBed (TEWTB) User's Guide and Technical Reference for the Block I Integrated Meteorological System (IMETS), PSL-92/60, Physical Science Laboratory, Las Cruces, NM

Harris, J. E., 1992, "A Technology Exploitation Weather TestBed for Army Applications," Proceedings of the Eighth International Conference on Interactive Information and Processing Systems for Meteorology, Oceanography, and Hydrology, American Meteorological Society, 45 Beacon Street, Boston, MA 02108-3693, pp. 5-9

Lunar Ephemeris Tables for White Sands Missile Range, NM, for 1993, Nautical Almanac Office, U.S. Naval Observatory, Washington, D.C.

Pace, D. K., 1993, "Modeling and Simulation," Phalanx, The Bulletin of Military Operations Research, 26(3):27-29, ISSN 0195-1920

Shapiro, R., 1982, Solar Radiative Flux Calculations from Standard Surface Meteorological Observations, AFGL-TR-82-0039, Scientific Report No. 1, Systems and Applied Sciences Corporation, Air Force Geophysics Laboratory, Hanscom, MA.

van Brochove, Ir. A. C., 1982, The Computer Program ILLUM: Calculation of the Positions of Sun and Moon and Natural Illumination, PHL 1982-13, Physics Laboratory TNO, National Defence Research Organization TNO (the Netherlands)

Session IV

BOUNDARY LAYER

CLUTTER CHARACTERIZATION USING FOURIER AND WAVELET TECHNIQUES

J. Michael Rollins
Science and Technology Corporation
Las Cruces, New Mexico 88011, U.S.A.

William Peterson
U.S. Army Research Laboratory
Battlefield Environment Directorate
White Sands Missile Range, New Mexico 88002, U.S.A.

ABSTRACT

Clutter is a feature of scene content that can confuse an observer or automatic algorithm trying to locate and track a particular target object. It consists of variations in the radiance field that either camouflage an object or divert perceptual attention away from the object location. The ability to measure and quantify clutter is playing a growing role in reliably estimating target acquisition ranges.

Two methods for characterizing clutter are presented. They involve Fourier and wavelet analysis. Results of clutter analysis on terrain images are shown and the merits of the two characterization methods are discussed.

1. INTRODUCTION

An important aspect of scene characterization is measuring to what extent natural features of the terrain interfere with the ability to distinguish manmade objects. Scene characteristics that make such discernment difficult are qualitatively called "clutter." Various quantitative metrics for the assessment of clutter have been proposed, most of which are related in some way to the scene variance. Other types of analysis may provide metrics giving similar information, such as the fractal dimension and parameters derived from wavelet power distributions.

The presence of significant intensity variation in an image does not alone constitute clutter. The spatial extent of patches of intensities significantly different from the average intensity is also an important factor. If bright or dark patches are present that are of the same general spatial dimensions as an object of interest, the discernment of the object is the most challenging, especially if the patches are of the same brightness as the object of interest. If a measure can provide a reliable generalization about the rough dimensions of clutter, it is a useful tool in the validation of terrain simulators that might be used to predict detection and recognition ranges in the presence of clutter of varying spatial structure.

The simplest approach to clutter characterization is simply to analyze the scene in terms of pixel blocks of a certain size—most often, the size of a real or hypothetical object of interest. To further study scene features that constitute clutter of the same spatial dimension as a manmade object of interest, techniques that describe the spatial extent of scene information can be useful. Such techniques include Fourier analysis and wavelet analysis. The first is used to describe scene information in terms of a superposition of two-dimensional sinusoids and is most useful when the image pattern to be analyzed is distributed homogeneously across the entire image region of interest. The second describes scene information in terms of a superposition of very localized functions called wavelets, and is most useful in characterizing discrete features of limited spatial extent within the image region of interest.

Fourier techniques are attractive because they have been used, studied, and interpreted so thoroughly. Wavelet techniques are attractive because wavelet analysis appears to have similarities to the human visual decomposition process. The more closely an analysis procedure emulates biological vision, the more directly predictions can be made of visual performance under variable environmental conditions. Both Fourier and wavelet techniques have an advantage over the clutter metric in that each frequency or wavelet band contains completely unique and independent information about the size and relative weighting of scene features. The full set of Fourier and wavelet information gives a complete description of the image.

This paper presents the results of clutter analysis of two different types of terrain—forest and desert. The terrain images were obtained at two field tests sponsored by the Smart Weapons Operability Enhancement Joint Test and Evaluation (SWOE JT&E) program at Grayling, Michigan, and Yuma, Arizona. The analysis involves four metrics: direct measurement of clutter in terms of a hypothetical object five pixels wide and three pixels high, autocorrelation function (ACF) slope correlation length and fractal dimension, and the Haar wavelet horizontal centroid. The ACF and fractal dimension are derived from Fourier frequency analysis. The latter three metrics are not sought for replacing the first as contrast measures, but rather for providing information on the spatial extent of clutter. Special attention is given to the various measures in the case where the clutter metric is relatively high. Finally, problems specific to the type of wavelet analysis used are discussed.

2. SIMPLE CLUTTER METRIC

A simple, often-used metric for clutter is based on the horizontal and vertical dimensions of a target in the image field. This metric is given by Schmeider and Weathersby (1983) as

$$C = \sqrt{\frac{1}{M}\sum_{i-1}^{M} \sigma_i^2} \qquad (1)$$

where M is the number of image blocks obtained by partitioning the image into pixel blocks whose horizontal and vertical dimensions are twice those of the object and σ^2 is the variance

within each block. If no target is present in the image, a block size can be specified based on a hypothetical target at the center of the image. For instance, in this study, pixels in the center of the image represent a distance of approximately 0.5 m (horizontally) and a hypothetical object five pixels wide and three pixels high was used in the specification of the image block partitioning. This metric is easy to calculate and produces results that agree with visual assessment. Unfortunately, while the block size is related to the target size, the variances are calculated on a pixel basis and the relationship of this metric to image features of specific sizes is rather tenuous.

3. FOURIER ANALYSIS

A number of metrics based on the Fourier power spectrum can be used to describe scene data. One of the most popular is the correlation length, which is a measure of local uniformity. The correlation length can be determined in two ways—by integrating over the power spectrum and dividing by the variance or by modelling the ACF as a decaying exponential and determining the semilog slope of the decay. The latter method has been found more useful in this study.

The autocorrelation function in one dimension (τ) is given by

$$ACF(\tau) \propto e^{(-\alpha\tau)} \tag{2}$$

$$L_c = -\frac{1}{\alpha} \tag{3}$$

where α is a constant.

Figures 1 and 2 show typical radiance fields for the Grayling and Yuma sites respectively. For a small region of interest in the Yuma scene (figure 3) the two-dimensional autocorrelation is shown in figure 4. The ACF (0,0) in the upper left corner is the most intense pixel and the function decreases from this point monotonically in each direction. The decaying exponential model is well suited to this function.

A somewhat different measure is the fractal dimension, which is an indicator of the "roughness" of the image texture. The fractal dimension is based on the slope of the power spectrum (Peitgen and Saupe, 1988). More accurately, assume the power spectrum can be characterized such that

$$S(f) \propto \frac{1}{f^{\beta}} \tag{4}$$

where $f = \sqrt{k^2 + l^2}$ and β is some constant (k and l are the two-dimensional Fourier transform indices).



Figure 1. Far infrared scene from Grayling site.



Figure 2. Far infrared scene from Yuma site.

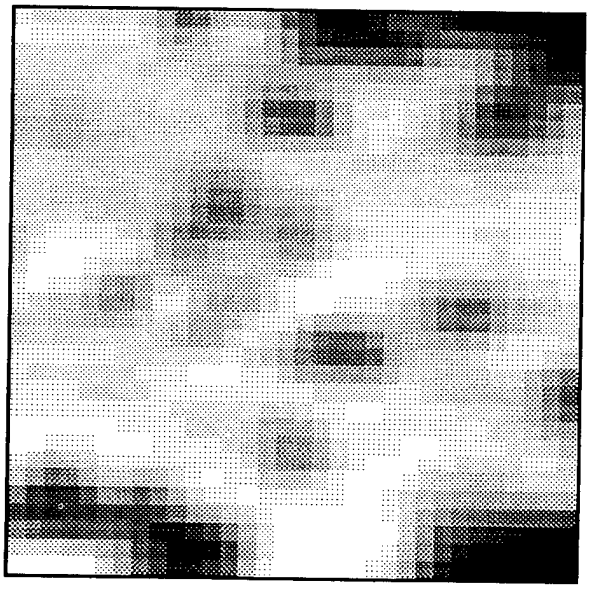


Figure 3. Region of interest from Yuma site with foliage causing scene clutter.

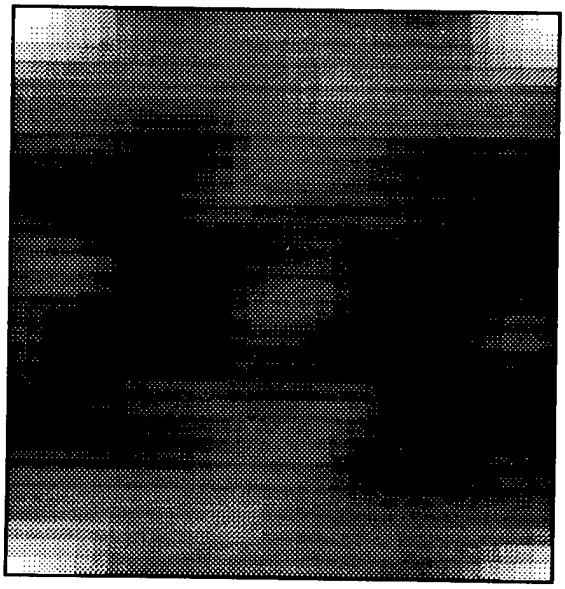


Figure 4. Corresponding ACF map of region of interest in Yuma site.

Taking the log of both sides and defining the fractal dimension as

$$D_f = \frac{7 - \beta}{2} \tag{5}$$

the result is

$$\log[S(f)] = (2D_f - 7)\log f \tag{6}$$

If the downward slope of the power spectrum is substantial, implying principally low-frequency components, the fractal dimension is low. Conversely, when the slope of the power spectrum is very shallow, approaching white noise, the fractal dimension is very high. Most natural terrain exhibits a β between 1 and 3. Since the fractal dimension is a measure of the "roughness" of a signal, it is a convenient measure for analyzing the clutter content of an image. A fractal dimension is a real-valued metric that has the clearest meaning when it happens to correspond to an integer value such as 1 or 2. A signal with a fractal dimension of 2 is represented by a simple two-dimensional topographical surface. As deviations from one pixel to the next increase in intensity, the roughness increases, as does the fractal dimension.

4. WAVELET PROCESSING

In addition to the one-dimensional power spectrum analysis, a study was made using wavelet analysis. Fourier analysis is concerned with the frequency (and phase) content of an image; wavelet analysis is concerned with its scale (and translation) content. Wavelet analysis recasts image content in terms of objects of various sizes (scales) and positions (translations). As this area of study is new, convenient metrics for encapsulating trends in the wavelet representation have not been developed and tested as thoroughly as has the fractal dimension in Fourier analysis.

In the previous section, a Fourier analysis of terrain images was described. The power spectra provide a catalogue of the frequency content of the images. The Fourier transform compares image patterns to sinusoidal basis functions differing in frequency and phase.

While there is a relationship between object sizes and frequency content, the Fourier-based methods applied to real scenes match periodic basis functions with nonperiodic data. The result is that objects of finite extent in space have a very widespread, nonlocalized signature in the frequency domain.

A logical response to this situation is to search for a basis of functions that are themselves at least somewhat local in space and then to catalog image content according to this basis. Since the basis functions are of finite extent, the word "scale" is more meaningful than "frequency" in indexing the functions. If an orthonormal basis of local functions is

available, a transform analogous to the Fourier transform can be developed. One such transform developed recently is the continuous wavelet transform, defined in one dimension as (Chui, 1992):

$$(W_\psi f)(b,a) = |a|^{-1/2} \int_{-\infty}^{\infty} f(t)\, \overline{\psi\left(\frac{t-b}{a}\right)}\, dt \tag{7}$$

where a is a scaling factor and b is a shift (translation) along the axis of support. The function ψ is a wavelet; $W_\psi f$ is the wavelet transform; overscore denotes the complex conjugate.

Most of the energy in the function ψ is concentrated in a small interval [c,d]; that is,

$$\int_{-\infty}^{\infty} |\psi(x)|^2\, dx \approx \int_{c}^{d} |\psi(x)|^2\, dx \tag{8}$$

For scale p and translation q, the Haar wavelet defined on the interval [0,1] is given by (Jain 1989)

$$h_k(x) = \frac{1}{\sqrt{N}} \begin{bmatrix} 2^{\left(\frac{p}{2}\right)}, & \frac{q-1}{2^p} \le x < \frac{q-1/2}{2^p} \\ -2^{\left(\frac{p}{2}\right)}, & \frac{q-1/2}{2^p} \le x < \frac{q}{2^p} \\ 0, & \textit{elsewhere} \end{bmatrix} \tag{9}$$

where

$$\begin{aligned} &0 \le p \le \log_2(N) - 1 \\ &q = 0,1 \textit{ for } p = 0 \\ &1 \le q \le 2^p \textit{ for } p \ne 0 \end{aligned} \tag{10}$$

The Haar coefficient index k is given by

$$k = 2^p + q - 1 \tag{11}$$

As with the Fourier analysis, it is instructive to use a metric that can represent the extensive information contained in the wavelet transform of an image. For this study, a metric was

used that roughly characterizes the mean horizontal scale of image features. This is the horizontal centroid given in equation 12 (Bleiweiss et al. 1994; Rollins et al., 1994).

$$Hor.\ cen. = \frac{\sum_{m=0}^{\log_2(N)} \sum_{n=0}^{\log_2(N)} \left(n \sum_{k=INT(2^{m-1})}^{2^m-1} \sum_{l=INT(2^{n-1})}^{2^n-1} W(k,l)^2 \right)}{\sum_{i=0}^{N-1} \sum_{j=0}^{N-1} W^2(i,j)} \qquad (12)$$

where $W(k, l)$ is the two-dimensional wavelet transform coefficient at indices k, l.

This equation partitions the wavelet transform domain into regions (bands, indexed by m and n) of the same wavelet scale and obtains the energy in each band. The horizontal centroid specifies the center of mass of energy location in terms of the horizontal band index. The value gives a rough indication of dominant horizontal feature sites in the logarithmic domain. No pair of indices should be simultaneously zero in this expression to avoid considering global brightness offsets (i.e., DC term). The centroid expression is only valid for the Haar wavelet, because it is the only wavelet for which the DC information is captured entirely within a single coefficient.

While the Haar wavelet and others commonly used are convenient for image analysis, they lack an important quality of Fourier power spectrum analysis—shift invariance. The Fourier power spectrum signature of an image feature does not change with small shifts. The wavelet transform and wavelet power spectrum of an image feature, however, can change with even a one-pixel shift.

5. RESULTS

In this study, terrain images were selected from Grayling, Michigan, and Yuma, Arizona, sites. In each scene, areas containing grass and/or bare soil were treated separately from regions containing thick foliage or trees, resulting in four regions of interest. In each region, the five metrics were calculated within a 32x32-pixel window advancing 1 pixel horizontally at a time. The following paragraphs discuss some salient results of the study.

5.1 Merit Criteria

In assessing the effectiveness of the metrics, several types of criteria were used. Visual assessment, level of sensitivity to scene changes, and correlation with the simple clutter metric can be used can all provide information about the metric's validity in representing the spatial extent of scene clutter.

For the metrics whose results can be cast conveniently in terms of size, such as correlation length and wavelet centroid, it is useful to compare the metric values with a visual assessment of scene feature sizes. The scenes were assessed with respect to 32x32-pixel

regions of interest, and objects smaller than about 3 pixels are difficult to discern visually in these images. Therefore, values for these metrics larger than 32 pixels or smaller than 5 pixels would obviously call the validity of the metric into question.

The regions examined in these studies were chosen to be visually homogeneous. If a metric displays a large standard deviation about its mean across a given region, that would suggest that the metric is too sensitive to very small changes in the scene.

The simple clutter metric varies in its accuracy with the size of the clutter being examined. As scene features approach sizes for which the clutter metric is increasingly responsive, it is desirable that the other metrics have a strong correlation with the clutter metric. Such correlation would show that the sizes each measures accurately reflect the same scene features.

5.2 Simple Clutter Metric

The clutter metric indicated negligible clutter for the Grayling images while showing considerable activity for the Yuma images, with a large number of discrete objects in the size order of the imaginary target. For the Yuma images, the clutter metric was of higher intensity than in the Grayling images, indicating that distinct background features here were more often of similar size to the imaginary target and had higher contrast than those in the Grayling scenes.

5.3 ACF Correlation Length

For the Grayling images, the average value for the correlation length was 15.56 pixels in the area with foliage and had a standard deviation of 0.58 pixels. For the bare/grassy area, the mean correlation length was 8.90 pixels and had a standard deviation of 0.87 pixels. The DC term was removed before the generation of the ACF, so that the discolorations within the bare areas are more important than the average intensity. Thus the correlation length demonstrated significant class separation between the thickly vegetated and bare/grassy areas.

For Yuma, the correlation lengths for vegetated areas and bare areas were very similar, (6.02 ± 0.76 and 6.38 ± 0.47 pixels, respectively) due to the small average size of the vegetation. With a high average intensity for the clutter metric, a correlation between the other metrics and the clutter metric indicated a strong relationship between the correlation length and the clutter metric ($|\rho| = 0.93$ for vegetation and $|\rho| = 0.80$ for bare soil). The sensitivity of the clutter metric and correlation length to each other demonstrated the useful auxiliary information that can be provided by the correlation length to further measure the clutter content in geometric extent when the clutter present is close to the size of the target. In essence, in conditions of significant clutter where the contrast is appreciable, the information the correlation length conveys is rather specifically about the clutter, whereas the other metrics are providing scene information somewhat less specific to the clutter. For the other metrics, $|\rho|$ was less than about 0.35 in every case.

5.4 Fractal Dimension

For the Grayling images, the fractal dimension had a mean of 1.81 in the vegetated area and 2.06 in the bare area with a standard deviation of 0.08 in each. The lower fractal dimension within the trees indicates the presence of larger, more distinct features than in the grassy regions.

For the Yuma images, the fractal dimension of the bare soil area had a mean of 2.00 and a standard deviation of 0.17, while the area with foliage had a mean of 1.89 and a standard deviation of 0.28. The fractal dimension was again slightly lower in the area of thick foliage. In general, the fractal dimension means did not differ appreciably between regions of apparently different clutter content.

5.5 Wavelet Metrics

In the Grayling region containing a fir tree, the horizontal centroid of the wavelet energy bands had a mean value of 0.74 with a standard deviation of 0.04. This value is between band 0 and band 1, closer to band 1. Band 0 represents the DC component (i.e., average intensity in the horizontal direction) whereas band 1 represents features of one half the breadth of the 32x32-pixel region of interest. A value of 0.74 for this centroid indicates the presence of a feature of width somewhat greater than 16 pixels, which is in fair agreement with visual assessment and in rough agreement with the correlation length. In the grassy area, the centroid mean increases to 1.25 with a standard deviation of 0.02, indicating the presence of clutter between 8 and 16 pixels in breadth. This result is in fairly strong agreement with the correlation length.

In the Yuma region with foliage, the horizontal centroid had a mean of 1.34 and a standard deviation of 0.09, indicating the presence of features between 8 and 16 pixels in breadth, somewhat larger than the 6.02 pixel correlation length. In the bare soil region, the centroid had a mean of 1.16 and a standard deviation of 0.10. There are no prominent discrete features here, however, and the result is somewhat ambiguous in descriptive meaning in terms of the presence of discrete clutter.

6. CONCLUSIONS

In conclusion, metrics derived from both Fourier and wavelet representations of the image provide concise and useful descriptions of clutter content in terms of clutter size. This study indicates that in the Fourier transform-based analysis, the correlation length is more reliable than the fractal dimension in ascribing a rough size to clutter content in a scene, at least in terms of separation of means between classes and in terms of agreement with visual assessment. The centroid obtained from the wavelet analysis also gives useful information regarding the horizontal size of discrete clutter, but has the disadvantage of correlating scene features with wavelet basis functions that are frozen in specific positions. This problem

may be somewhat alleviated by the use of complex-supported harmonic wavelets, which allow phase shifting of the basis functions and thus better congruence to scene features. An investigation into the use of harmonic wavelets in assessing clutter is ongoing.

Specification of a number such as the correlation length can provide an additional parameter in a scene generation process. For instance, a two-dimensional autocorrelation map can be generated corresponding to equation 2 in each direction. The map is then Fourier transformed and the square root of the resulting power spectrum is taken. This process produces a transfer function that can be used to filter another two-dimensional random map of white Gaussian noise, producing a synthetic "clutter" map with the desired correlation length. Such clutter maps can then be used to modify probability of detection and recognition of synthetic targets in the presence of clutter of various size distributions.

REFERENCES

Bleiweiss, M.P., J.M. Rollins, and C. Chaapel, 1994. "Analysis of Infrared Background Scenes from the Grayling I SWOE JT&E Field Test." In *Proceedings of the 1993 Battlefield Atmospherics Conference*, U.S. Army Research Laboratory, White Sands Missile Range, NM 88002, pp 281-295.

Chui, C.K., 1992. *An Introduction to Wavelets.* Vol. 1 of the series *Wavelet Analysis and its Applications*, Academic Press, San Diego, California.

Jain, A.K., 1989. *Fundamentals of Digital Image Processing*, Prentice-Hall, Englewood Cliffs, New Jersey.

Peitgen, H.-O., and D. Saupe, eds., 1988. *The Science of Fractal Images.* Springer-Verlag, New York.

Rollins, J.M., C. Chaapel, and M.P. Bleiweiss, 1994. "Spatial and Temporal Scene Analysis." *In Characterization and Propagation of Sources and Backgrounds*, SPIE Proceedings, International Society for Optical Engineering, Vol. 2223, W.R Watkins and D. Clement, eds, pp 521-532.

Schmeider, D.E., and M.R. Weathersby, 1983. "Detection Performance in Clutter with Variable Resolution." *IEEE Trans. Aerospace & Elect. Syst., 19(4):622-630.*

VALIDATION TOOLS FOR SWOE SCENE GENERATION PROCESS

Max P. Bleiweiss
U.S. Army Research Laboratory
Battlefield Environment Directorate
White Sands Missile Range, New Mexico 88002, U.S.A.

J. Michael Rollins
Science and Technology Corporation
Las Cruces, New Mexico 88011, U.S.A

ABSTRACT

The Smart Weapons Operability Enhancement (SWOE) scene generation process involves the simulation of infrared radiance fields produced by a variety of terrain and vegetation environments under diverse weather conditions. As part of the validation procedure, an ensemble of land-based and airborne terrain images were captured at two locations—Grayling, Michigan, and Yuma, Arizona. These mid and far infrared images were compared on a frame-by-frame basis to synthetic images of the same scenes generated by the SWOE process. Statistical procedures as well as metrics for feature segmentation were implemented in the comparison to assess the accuracy with which the SWOE process generates a facsimile of the real scene radiances. A description of the image registration process, the analytical tools used, and qualitative results for the SWOE process are presented.

1. INTRODUCTION

This paper describes some of the image analysis methodology used in the validation of the Smart Weapons Operability Enhancement (SWOE) Joint Test and Evaluation (JT&E) scene generation process. A diverse collection of measurement and analysis techniques was applied for the dual purpose of comparing real and synthetic images and of investigation methods for automatic segmentation of homogenous regions of interest within images of natural terrain.

The primary means of validation involves the comparison of real and synthetic image histograms using the chi square statistic. A secondary effort, reported here, seeks to develop a tool chest of various metrics that can be used to compare and contrast image features within real images and between real and synthetic images. Metrics that display invariance to temporal changes in environmental conditions are of special interest in this paper.

2. REAL IMAGE ACQUISITION

As described previously (Bleiweiss et al. 1994a), a large number of paired far and mid infrared images of natural terrain were acquired using an AGEMA BRUT 880 system. The imagery was acquired at sites near Grayling, Michigan, and Yuma, Arizona. The acquisition took place during periods of greatest seasonal change (near the spring and fall equinoxes) to capture as wide a range of variability in scene radiances as possible.

A subset of the images acquired was selected randomly and was used for comparison with corresponding synthetic images generated by the SWOE process. A typical real image is shown in figure 1, with its synthetic counterpart in figure 2. A comprehensive presentation and analysis of the results is given in a report that is being prepared by the SWOE JT&E office. Qualitative comparison results are discussed in this paper to highlight the utility of the various scene characterization metrics used in this image analysis.



Figure 1. Mid infrared image from Grayling site.



Figure 2. Synthetic counterpart of image in Figure 1.

3. IMAGE COMPARISON PROCESS

The metric comparison of real and synthetic images involved the following process:

1. Based on knowledge of the artificial scene generation process, designate appropriate image analysis tools as determined from experience and literature searches. These tools should be able to provide succinct, objective, and intuitively meaningful descriptions of image regions of interest for comparison between real and synthetic counterparts.

2. Align images through objective registration process so that comparisons will always involve exactly the same scene features. Without proper registration, objective comparison is impossible.

3. Apply each designated metric to the same regions of interest in each real and synthetic image.

4. Investigate the differences between the real and synthetic metrics for corresponding images and determine a useful measure of significance for the differences. If the metrics are for contrasting dissimilar types of terrain, measure the mean and standard deviation for each homogeneous type of terrain and establish whether or not the metrics demonstrate sufficient discrimination between classes. If the metrics or the histogram values are to be used to establish whether regions of interest are from the same population, use techniques to compare distributions such as chi-square techniques.

5. Based on the resulting agreement or disagreement from the comparisons, observe the performance of the scene generation process in terms of each metric and propose corrective modifications to the process as necessary.

4. IMAGE REGISTRATION

In order to make valid comparisons between real and synthetic images, it is necessary to register each image from a site to a given reference image. This process ensures that the regions of interest selected for analysis in each image correspond to the same area of terrain. Otherwise, the comparison becomes meaningless with offsets greater than 1 to 2 pixels. During the registration process, the initial misregistration was typically 5 to 7 pixels in both the horizontal and vertical directions. If the region of interest is within a tree, this amount of offset is enough to mistakenly include a large number of pixels from the background, which is of a considerably different statistical population in terms of radiance values and texture. Since different images of a scene may contain different features near the boundaries, only a subset of each image is common to all images. In this registration process, a 128x128-pixel region was cropped from the original larger image.

The method of registration ultimately employed in this effort involved the use of normalized cross correlation between a given image and the reference. In essence, the image is converted to its two-dimensional finite Fourier transform (FFT) and normalized at each coefficient to have a magnitude of 1. The same operation is performed on the reference image. The FFT arrays are multiplied at each coefficient, and the resulting array is inverse transformed.

The registration process was two tiered. The first tier consisted of the display of the reference image and the image to be registered superimposed over the same area of the screen. Arrow keys were assigned movements that allowed the registration image to be moved with respect to the reference image. In this way, a specific tree as seen in both

images, for instance, could be visually aligned. This process requires that the registration image have enough contrast to contribute useful feature information to the superposition. Even when contrast is comparatively high, the sharpness of the imagery is usually not sufficient for visual registration better than 2 or 3 pixels. Thus the visual registration process is followed by the slower but more accurate phase correlation process (Tian and Huhns 1986) in the second tier. The output array from the phase correlation process represents the normalized correlation between the two images. The position of maximum magnitude determines the amount of misregistration in each direction. The offsets required for registration can then be recast as phase shifts for each FFT coefficient for the image to be registered. Once the phase shifts are performed in the frequency domain, an inverse transform is implemented and the resulting image is registered correctly.

The frequency domain registration techniques can be used to implement registration accurate to the sub-pixel level. In the normalized phase correlation map, a sub-pixel location of the true maximum can be determined (accurate to about 0.1 pixel) by using two-dimensional quadratic interpolation over the pixel with the maximum amplitude and its eight nearest neighbors. In our procedure, we returned misregistration offsets with quarter-pixel accuracy to the frequency domain and implemented the corresponding phase shifts.

It is important to note that phase shifts corresponding to quarter-pixel translations require a four-fold lengthening of the signal vectors in the frequency domain. Suppose, for instance, that a given row in the frequency domain has N = 128 elements. The row must be lengthened to 512 elements, the first and last 64 being the same as before, but those in the center being assigned a value of zero. This represents the same information on a finer resolution grid. The center values' being set to zero correctly indicates that no information of frequencies higher than the 63rd harmonic are present. The phase shifting is implemented and the resulting data are inverse transformed, subsampled to the original resolution, and stored as the registered image.

Suppose a high-resolution grid had not been used in the frequency domain, but a quarter-pixel phase shift had been implemented. The resulting image upon inverse transforming would be complex, not real. This is due to the fact that phase shifts corresponding to sub-pixel amounts destroy the frequency domain arrangement in which the coefficients above N/2 are complex conjugates of those below N/2. This arrangement is required to represent real images.

The ability to use the frequency domain in shifting the images was also important in some cases where the images could not otherwise be registered because the real image scenery was a little too far to the left of the synthetic scenery to have a 128x128 pixel intersection. Using the cyclical representation of the image in the frequency domain, such images were scrolled slightly into an adjacent cycle so that as many features in the main image cycle could align with those in the reference image as possible.

Positions of certain features in the newly registered images were noted and compared to the positions of the same features in the reference images. It was found that the phase correlation

process worked very well in most cases. Conditions for which the visual registration overrode the phase correlation results were rare and occurred principally in the mid infrared images when the sun angle was low enough to cause bright outlines and shadows, changing the apparent structural content of the images. Occasionally, when the signal-to-noise level of an image was very low, the phase correlation method indicated a maximum at an obviously incorrect position. However, the phase correlation method in general was much more accurate in measuring the offset or indicating correct registration than the purely visual superposition method.

5. METRICS USED

In a previous paper (Bleiweiss et al. 1994a), several metrics for the characterization of histogram information, texture and structure of image features were demonstrated. These included the mean, median, maximum, minimum, variance, standard deviation, absolute deviation, skewness, kurtosis, autocorrelation integral correlation lengths, variance-based clutter, gray-level co-occurrence matrix (GLCM) statistics, and wavelet compaction. In addition to these, autocorrelation function (ACF) slope correlation lengths and fractal dimension are discussed here.

The correlation length determined from the slope of the autocorrelation function is based on the representation of the ACF as an exponential (Ben-Yosef et al. 1985):

$$ACF(r) \propto e^{(-\alpha * r)} \tag{1}$$

where r is the offset from ACF(0). The correlation length may thus be represented as

$$L = \frac{-1}{\alpha} \tag{2}$$

The slope α is determined numerically by calculating $ln[ACF(r)]$ close to $r = 0$ and performing a linear regression with respect to r. The fractal dimension is similarly based on the slope of the power spectrum, and is discussed further elsewhere (Rollins and Peterson *these Proceedings*).

First-order statistics are useful in assessing the macroscopic performance of the thermal radiance and diffusion model employed in the SWOE process. The emphasis here is on the accuracy of the temporal aspect of the model and its ability to predict thermal evolution as a function of time based on initial conditions. Second-order statistics such as the GLCM metrics and correlation lengths are useful in assessing reliable texture simulation and provide information on the accuracy of fine spatial detail simulated by the SWOE process. Second-order statistics are also used for their characterization of the structure present in a region of interest. Second-order statistics that demonstrate invariance to the diurnal cycle are desirable.

6. IMAGERY MEASUREMENTS AND COMPARISON RESULTS

6.1 Evaluation of Metrics

At this time, the analysis of real-to-synthetic measurement comparisons for significance is ongoing. The results will be given in the final SWOE report. The first-order comparison made between histograms of the real and synthetic images uses the chi-square statistic at 95% confidence to accept or reject the hypothesis that the samples come from the same distribution. A secondary effort is the evaluation of the metrics themselves as useful tools in the comparison of like regions or contrast of dissimilar ones. A complete set of images registered with sub-pixel accuracy has been produced and compared to their corresponding synthetic images. Based on initial correlation analysis, the first-order histogram measures correlate well between the real and synthetic images and better than the second-order measures. The second-order measures showing the highest correlation were the GLCM entropy and the ACF slope-based correlation length. The wavelet-based metrics showed poor agreement.

In some cases, it may be desirable for image metrics to exhibit invariance to environmental changes. For example, table 1 gives results for some of the metrics in regions containing foliage over the full testing period, during which seasonal and diurnal changes took place.

Table 1. Selected Metrics from Grayling and Yuma Sites

Metric	Grayling			Yuma		
	Mean	Std. Dev.	Ratio	Mean	Std. Dev.	Ratio
Clutter	0.07	0.09	0.778	0.37	0.33	1.121
Correlation Length	2.43	1.82	1.335	3.87	0.97	3.990
Fractal Dimension	1.72	0.59	2.915	1.80	0.32	5.625
Horizontal Centroid	1.12	0.33	3.394	1.30	0.26	5.000
GLCM Entropy	0.67	0.95	0.705	3.46	1.07	3.234
GLCM Contrast	0.19	0.18	1.05	2.91	3.43	0.848

The data in table 1 show that the fractal dimension and the horizontal centroid display more invariance to diurnal effects than the other measures, if the ratio of the mean to the standard deviation is used to indicate invariance.

It should be noted that even though the Grayling and Yuma regions of interest included foliage, the Grayling region was completely within a single coniferous tree, while the Yuma region contained as much foliage as possible but also contained bare soil, with a significantly different apparent radiance. Thus the Grayling region can be characterized as a radiance field with dull, amorphous structures, while the Yuma region is described by stark contrast between foliage and the background. As such contrast is necessary for visual identification

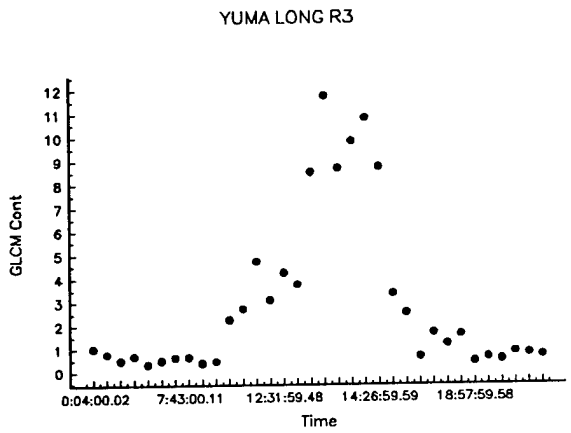


Figure 3. Plot of GLCM contrast with diurnal cycle from Yuma site region of interest.

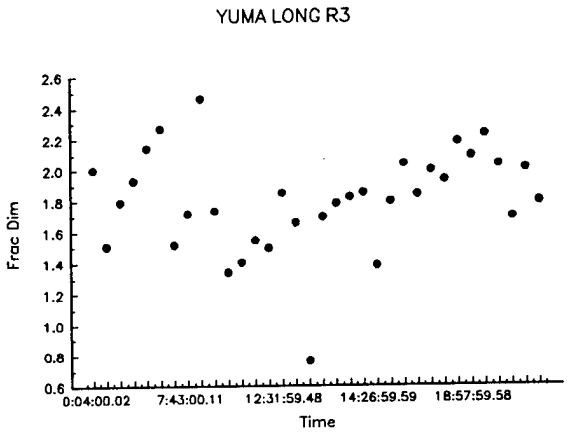


Figure 4. Plot of fractal dimension with diurnal cycle from Yuma site region of interest.

of discrete objects, examining regions with both foliage and background has its own importance in designing simulators to be used in predictions of recognition range. Such contrast for boundaries between different textures is also important to the reliability of the correlation length as an intuitive measure of structure extent in these images.

Plots of the GLCM contrast and fractal dimension for a Yuma region with thick foliage are given in figures 3 and 4, respectively. The sensitivity of the contrast to the diurnal cycle is clear, while the fractal dimension seems to indicate a greater invariance to diurnal changes.

7. CONCLUSIONS

In this paper, a description of some of the ongoing SWOE image analysis has been presented. The registration technique has been demonstrated to be both necessary and accurate. We have shown that the chosen image metrics are uniquely descriptive of scene content. Certain metrics have been found to show a degree of spatial invariance (Bleiweiss et al. 1994b) or temporal invariance, as seen above. For instance, this work has shown that the fractal dimension and the horizontal centroid retain much of the same information about the texture and structure in a scene from trial to trial, regardless of changes in thermal conditions.

REFERENCES

Ben-Yosef, N., K. Wilner, S. Simhony, and G. Feigin, 1985. "Measurement and Analysis of 2-D Infrared Natural Background." *Applied Optics*, 24(14):2109-2113.

Bleiweiss, M.P., M. Rollins, and C. Chaapel, 1994a. "Analysis of Infrared Background Scenes from the Grayling I SWOE JT&E Field Test." in *Proceedings of the 1993 Battlefield Atmospherics Conference,* U.S. Army Research Laboratory, White Sands Missile Range, New Mexico, pp 282-295.

Bleiweiss, M.P., M. Rollins, C. Chaapel, and R. Berger, 1994b. "Analysis of Real Infrared Scenes Acquired for SWOE JT&E." In *Proceedings of the 1994 International Geoscience and Remote Sensing Symposium*, in press.

Rollins, J.M., and W. Peterson, *these Proceedings*. "Clutter Characterization Using Fourier and Wavelet Techniques."

Tian, Q., and M.N. Huhns, 1986. "Algorithms for Subpixel Registration." *Computer Vision, Graphics, and Image Processing*, 35:220-23.

THE VEHICLE SMOKE PROTECTION MODEL DEVELOPMENT PROGRAM

David J. Johnston
OptiMetrics, Inc.
Bel Air, Maryland 21015-6181

William G. Rouse
U.S. Army Edgewood Research, Development, and Engineering Center
Aberdeen Proving Ground, Maryland 21010-5423

ABSTRACT

This paper reports on work in progress to adapt existing methodologies to develop a Vehicle Smoke Protection Model. The objective of this effort is to produce a data-rich model that will become the standard technique for simulating on-vehicle smoke protection systems. Other types of obscurants and dispensing mechanisms may also be included. Software will be designed and constructed using object-oriented techniques so that the simulation modules can be used in a stand-alone mode or adapted for use in other applications, including distributed interactive simulations.

1. INTRODUCTION

In 1993, the Defense Science Board convened a Task Force on Simulation, Readiness, and Prototyping to assess the impact of simulation technology on U.S. forces. In its findings, the task force enthusiastically embraced distributed interactive simulation (DIS) for training applications and strongly encouraged its continued use. In addition, it recognized that DIS could transform the acquisition process if it were used to support materiel development, combat development, training development, and operational testing. As a result, several advanced technology demonstrations (ATD) have been planned which will make extensive use of this simulation technology.

A major effort is now underway to enhance the DIS architecture so that it can be used in ATDs and similar applications. This is being accomplished through a rigorous standardization process with the voluntary cooperation of numerous organizations from government, industry, and academia. The architectural enhancements are required because DIS cannot currently simulate complex battlefield interactions in a physically realistic manner and it has insufficient resolution for detailed system studies. When DIS is finally ready to support dynamic effects, many operations will be added to the DIS environment that cannot currently be modeled with

acceptable fidelity. This includes the employment of smoke and obscurants on the virtual battlefield.

A number of techniques have been developed over the years to model the production, transport, diffusion, and effect of smoke and obscurants on the battlefield. Two of these, GRNADE and COMBIC, have gained considerable acceptance and are part of the Electro-Optical Systems Atmospheric Effects Library (EOSAEL). GRNADE simulates multiple-round salvos of tube-launched grenades (L8A1 and M76) and is used for self-screening analysis (Davis, Sutherland 1987). COMBIC is a more comprehensive model that simulates several obscurant sources, including: high explosive dust; vehicular dust; phosphorus and hexachloroethane munitions; diesel oil fires; generator-disseminated fog oil and diesel fuel; and, other screening aerosols (Hoock et al. 1987). It is used in numerous and diverse applications.

While GRNADE and COMBIC are accepted standards, they are somewhat dated and do not explicitly simulate many of these systems, sources, and materials currently in service or under consideration. In addition, a number of deficiencies have been noted which influence their fidelity. Given the expanded role of simulation technology in research, development, and acquisition, an immediate need exists for an updated standard. This is particularly true for on-vehicle smoke protection systems because they are most likely to be included in DIS simulations.

OptiMetrics, Inc. is addressing this need by developing a Vehicle Smoke Protection Model. This effort is being conducted under contract to the U.S. Army Tank-Automotive Research, Development, and Engineering Center (TARDEC) and in cooperation with the U.S. Army Edgewood Research, Development, and Engineering Center (ERDEC). This paper reports on that work in progress.

2. OBJECTIVES AND SCOPE

The objective of this program is to produce a data-rich model that will become the standard technique for simulating on-vehicle smoke protection systems. This will be achieved by building upon and enhancing the standard methods for simulating smoke and obscurant production (i.e. GRNADE and COMBIC) and related models. Self-screening systems will be emphasized, but other types of obscurants and dispensing mechanisms may also be included.

The goal is to increase the resolution of the simulation process, improve its overall fidelity, and package the product in a manner that will facilitate its use in a wide variety of applications, including DIS simulators. The program is focused on smoke production. Consequently, existing predictive techniques for transport, diffusion, radiative transfer, etc. will be used to the maximum extent possible and the Vehicle Smoke Protection Model will not deviate significantly from current procedures. Puffs and plumes will, for example, still be described by three-dimensional Gaussian distributions.

Rapid obscuration systems (ROS) will be addressed first, followed by obscuration reinforcing systems (ORS) and all other dispensers. Any vehicle, dispensing system, grenade, or obscurant

may be modeled from user-specified parameters, but a descriptive database will be constructed and it will include most fielded and developmental items. The vehicle database will, for example, include the : M1 family of main battle tanks; M2/3 family of fighting vehicles; M88A1E1 Improved Recovery Vehicle; CATTB/CCATTD; Breacher; Heavy Assault Bridge; Armored Gun System; and, M93 Reconnaissance Vehicle (FOX).

3. APPROACH

The Vehicle Smoke Protection Model development program is being conducted in three phases: analysis, design, and development. The program is currently in the analysis and design phases, which are being conducted concurrently.

In the analysis phase, GRNADE, COMBIC, and related models are being examined to identify the simulation techniques that are used for different sources and materials. The algorithms and parameters will be described in a set of flow charts with supporting documentation. They will also be evaluated using the Concentration and Path Length (CL) Product Visualization Utility (paragraph 4) to determine how well they simulate the smoke production process. If the algorithms produce satisfactory results, they will be included in the Vehicle Smoke Protection Model without modification. Otherwise, an alternative simulation technique will be sought.

In the second phase, the Vehicle Smoke Protection Model is being designed using object-oriented techniques (Coad, Yourdon 1991). A preliminary design is described in paragraph 5. The results of this phase will be documented in a report and submitted to ERDEC and the Army Research Laboratory - Battlefield Effects Directorate (ARL-BED) for evaluation.

The Vehicle Smoke Protection Model will be coded and implemented in the development phase using object-oriented programming techniques. The model will be completely self-contained and may be used in a stand-alone mode to support the analysis of smoke and obscurant effectiveness. In addition, its classes may be used independently to provide similar functionality in other applications. This will be particularly useful in the DIS arena.

4. CL-PRODUCT VISUALIZATION UTILITY

As described in paragraph 3, a CL-Product Visualization Utility has been developed to aid in the analysis of smoke production algorithms and investigate alternatives. This utility operates on IBM or compatible personal computers and runs under Microsoft Windows™. It was adapted from the CL computational routines in GRNADE (EOSAEL-1992 version).

The CL-Product Visualization Utility operates on a set of files that record puff and plume information in a specified format. These files can be produced by GRNADE and COMBIC (with proper modifications) or by any other application (e.g., a spreadsheet) that can describe puffs and/or plumes as a function of time. For a given puff or plume and for each sample (time increment) in the descriptive data, the utility computes a CL-product matrix for the front, side, and top views as depicted in Figure 1. The results are then displayed in accordance with a

mapping scheme that associates a range of CL-products with a specified color. This enables the user to visualize how the obscurant material is distributed in three-dimensional space and how that distribution changes with time.

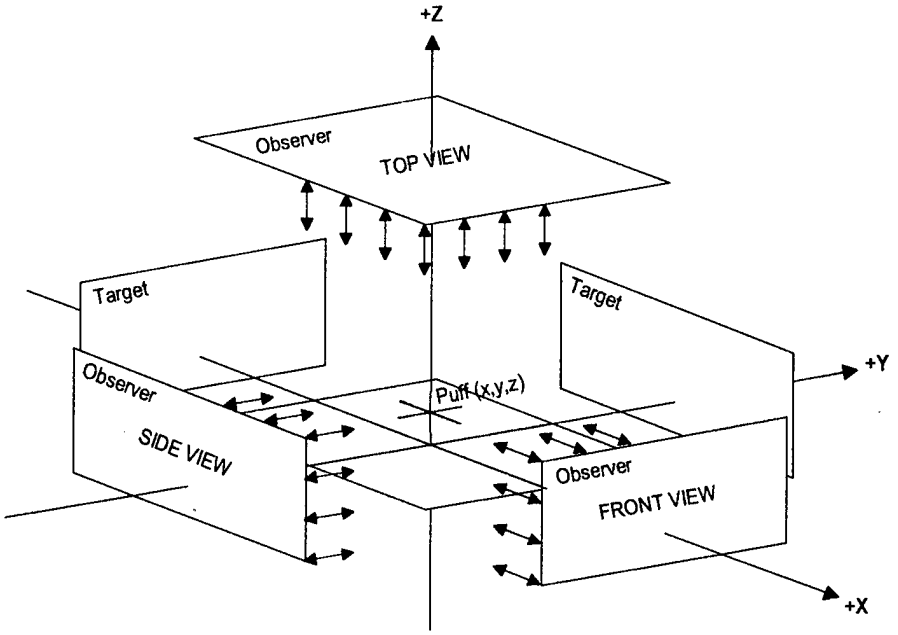


Figure 1. CL-Product Visualization Utility computational procedure.

To illustrate how this utility is being used in the analysis phase, consider the manner in which GRNADE simulates the M76 grenade. The model computes a detonation point that is thirty (30) meters from the launcher along a calculated azimuth and four (4) meters above the ground. The detonation occurs 0.75 seconds after launch and a simulated smoke cloud is formed. GRNADE models this cloud as a small spherical initial burst puff (Figure 2) that grows larger and moves downwind as a function of time. The CL-Product Visualization Utility displays these changes in a series of frames, such as those depicted in Figures 3 and 4.

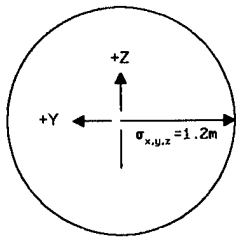


Figure 2. M76 Grenade modeled as a spherical puff.

It has been suggested that this simulation does not accurately model the manner in which the M76 grenade functions, particularly in the initial build-up phase. Field tests have demonstrated that the obscurant is released very rapidly after the grenade is detonated and a large smoke cloud is formed almost instantaneously. Furthermore, the cloud does not have a spherical shape; the

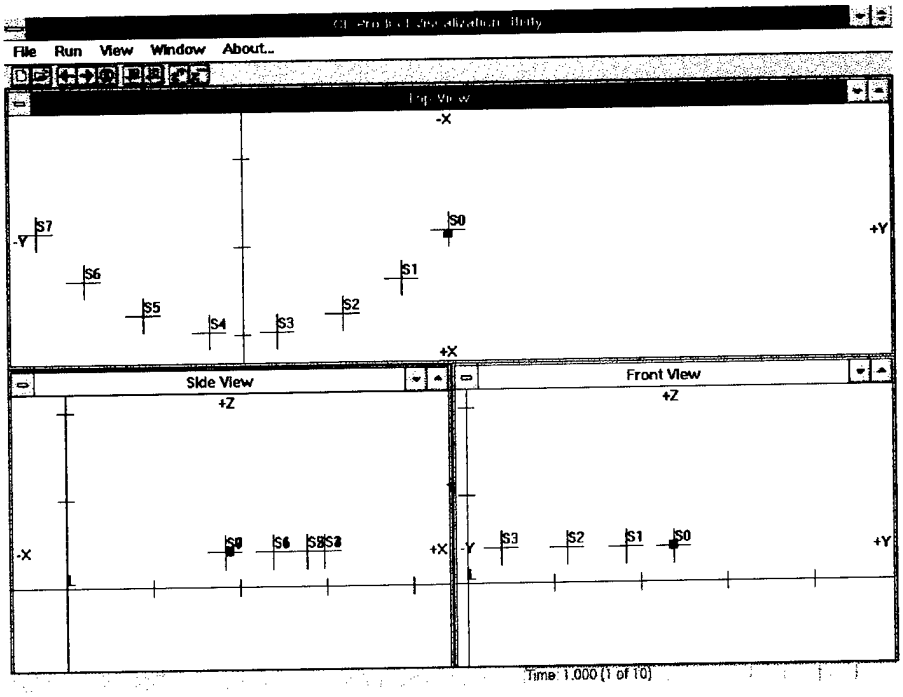


Figure 3. CL-Product Visualization Utility sample output (M76 Grenade modeled as a spherical puff one second after launch).

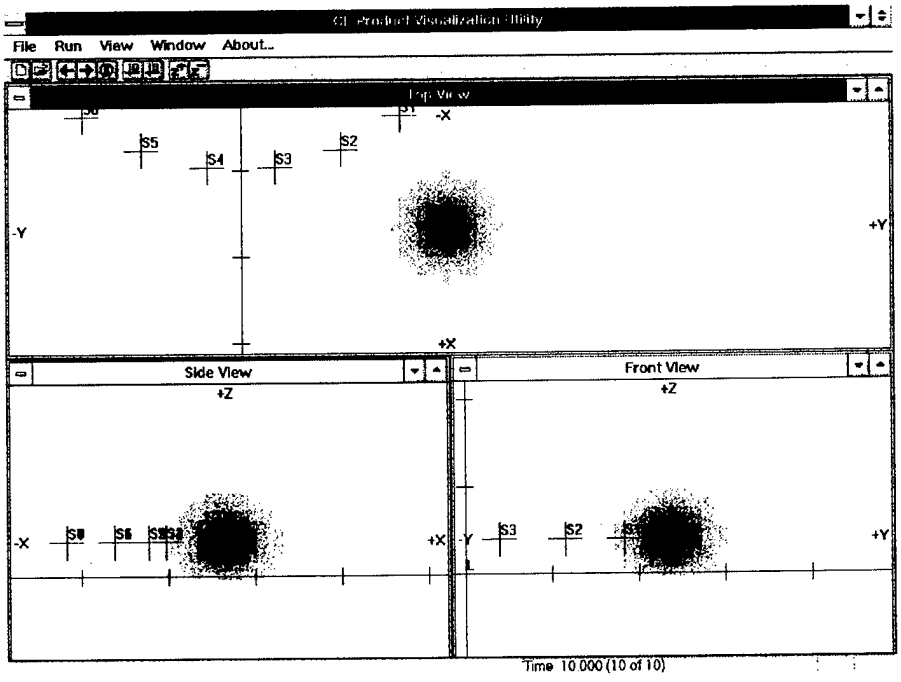


Figure 4. CL-Product Visualization Utility sample output (M76 Grenade modeled as a spherical puff ten seconds after launch).

obscurant material is generally distributed about the detonation point to form a toroidal puff. To experiment with alternatives, GRNADE was modified to model the resulting smoke cloud as a collection of six small spherical sub-puffs, which are distributed about the detonation point to form a torus (Figure 5). The CL-Product Visualization Utility was then used to examine this approach and determine if it improved the fidelity of the simulation process (Figures 6 and 7).

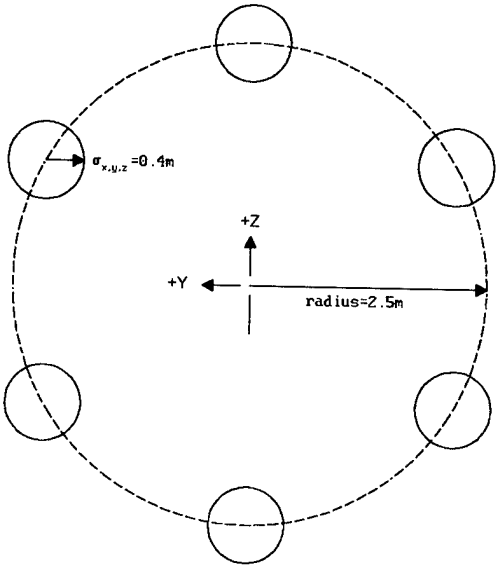


Figure 5. M76 Grenade modeled as a toroidal puff with six spherical sub-puffs.

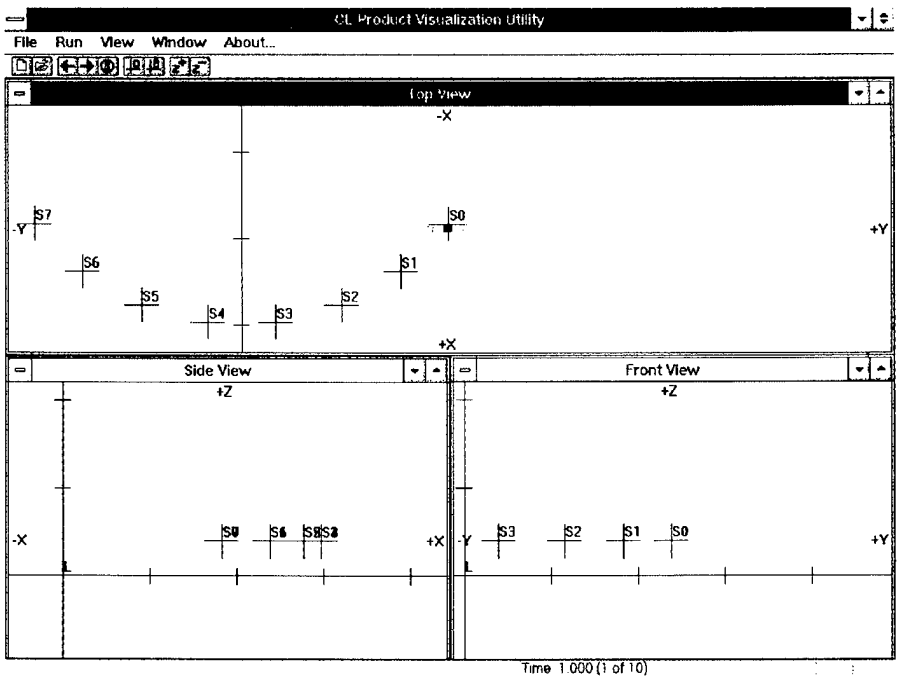


Figure 6. CL-Product Visualization Utility sample output (M76 Grenade modeled as a toroidal puff one second after launch).

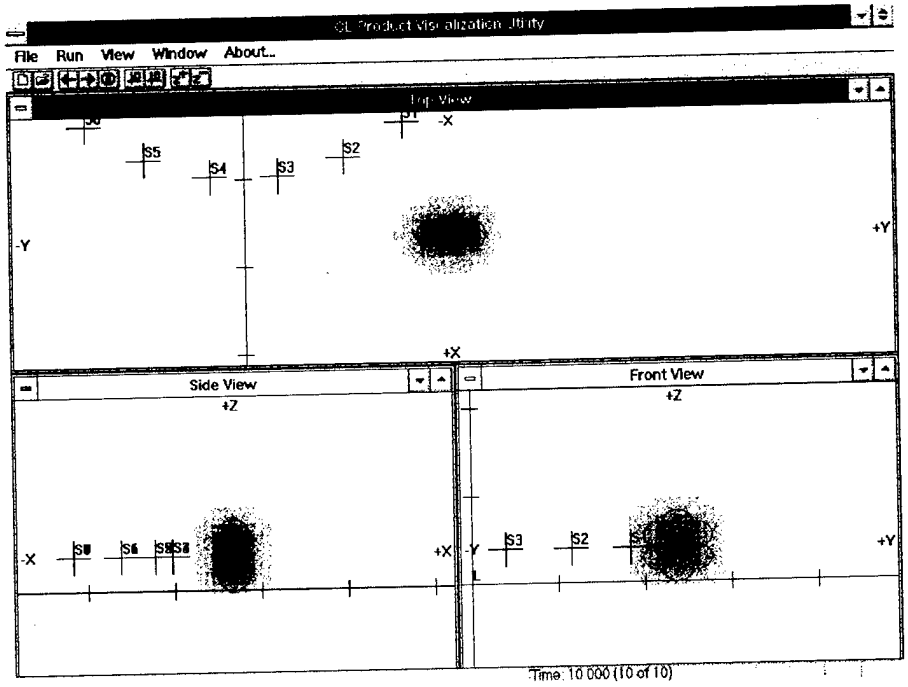


Figure 7. CL-Product Visualization Utility sample output (M76 Grenade modeled as a toroidal puff ten seconds after launch).

5. VEHICLE SMOKE PROTECTION MODEL PRELIMINARY DESIGN

A preliminary design has been developed for the Vehicle Smoke Protection Model and it will serve as the foundation for the evolving design. In its simplest form, the model consists of the six classes depicted in Figure 8.

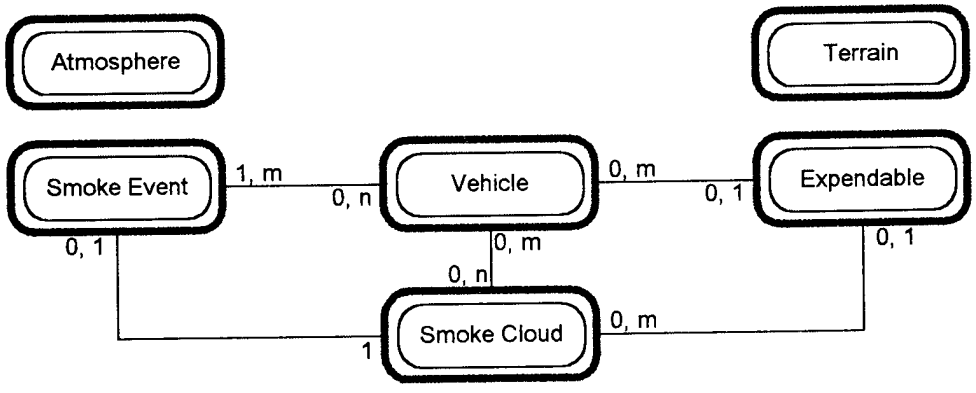


Figure 8. Vehicle Smoke Protection Model preliminary design.

In this design, vehicles are loaded with expendable material, such as smoke grenades and fog oil. The vehicles carry this material until an initiation event occurs, at which time the obscurant is

released and a smoke cloud is produced. The formation and fate of the cloud is influenced by the terrain and atmosphere. This simple representation has been expanded, as depicted in Figure 9, and additional details will be added as the design matures.

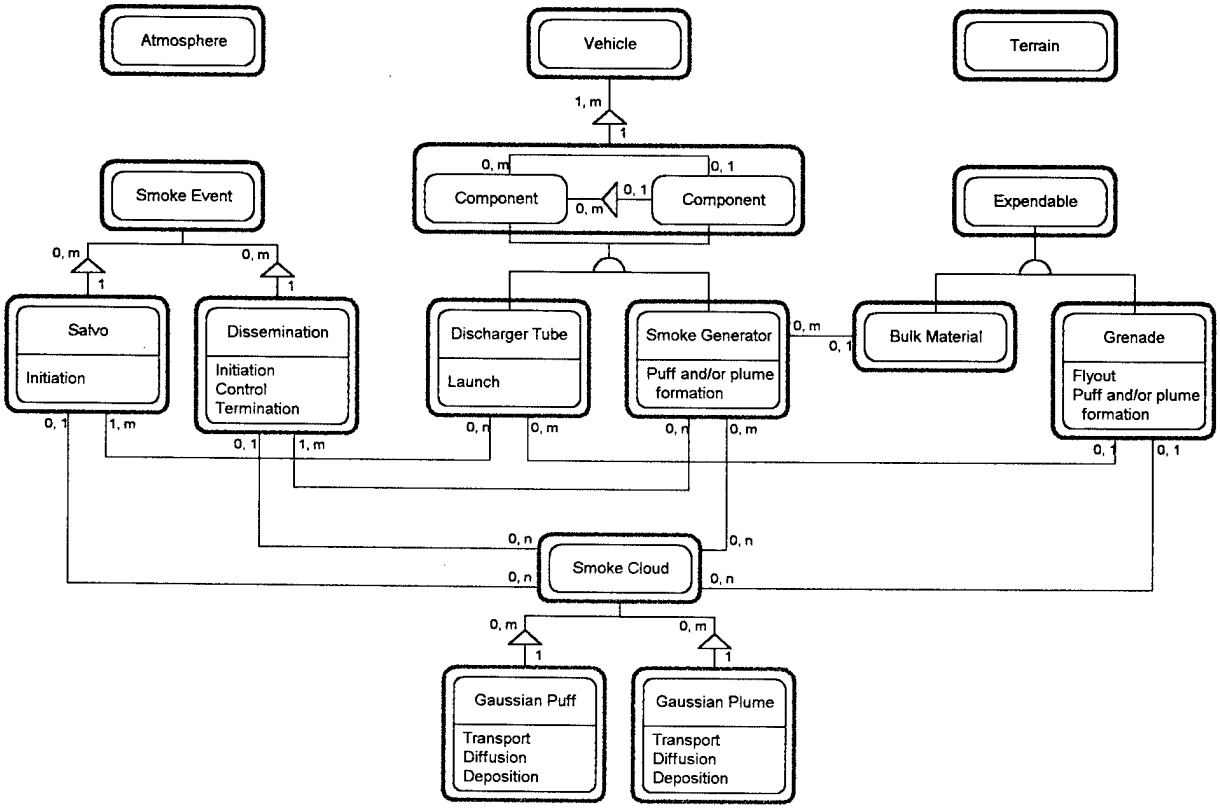


Figure 9. Vehicle Smoke Protection Model preliminary design (expanded).

6. SPATIAL CONSIDERATIONS

In the expanded design, the vehicle class comprises numerous components, which (for a given vehicle) might include grenade discharger tubes and/or smoke generators. The location and orientation of these components must be known when a grenade is launched or obscurant material is released because they determine where, in three-dimensional space, the smoke cloud is formed. This will be particularly important when the Vehicle Smoke Protection Model is included DIS applications where vehicle position and orientation cannot be known a priori. Similarly, the state of rotating and articulated components cannot be predicted in advance. Consequently, the Vehicle Smoke Protection Model must include a general method for computing component location and orientation given: a mounting hierarchy; vehicle location and orientation; and, the state of components in the mounting hierarchy. Note: the mounting hierarchy might be different from the parts breakdown structure. This methodology must be compatible with the DIS standard (Institute for Simulation and Training 1994).

This point is illustrated by the M1A1 tank in Table 1 and Figure 10. The vehicle has a number of components, each of which can be considered to have its own coordinate system. Components are mounted with an offset (three-dimensional translation) and orientation (three-dimensional rotation) in accordance with the vehicular design. However, some components are also free to move within specified constraints. The vehicle (i.e., its hull) is free to move about the terrain and assume any orientation that the topography permits. The turret is free to rotate in any direction about its axis.

Table 1. Example M1A1 parts breakdown structure and mounting hierarchy.

Whole	Parts	Mounted On	Translation (in)			Rotation (deg)		
			ΔX	ΔY	ΔZ	Yaw	Pitch	Roll
M1A1 Tank	Turret	M1A1 Tank	5	0	-30	0-360	0	0
	M250 launcher							
	VEESS	M1A1 Tank	-156	6	-26	180	-30	0
M250 Launcher	LH discharger							
	RH discharger	Turret	5	50	-24	0	25	-12.6
RH Discharger	RH tube #1	RH discharger	0	0	0	0	0	0
	RH tube #2	RH discharger	0	0	0	-10	0	0
	RH tube #3	RH discharger	0	0	0	-20	0	0
	RH tube #4	RH discharger	0	0	0	-30	0	0
	RH tube #5	RH discharger	0	0	0	-40	0	0
	RH tube #6	RH discharger	0	0	0	-50	0	0

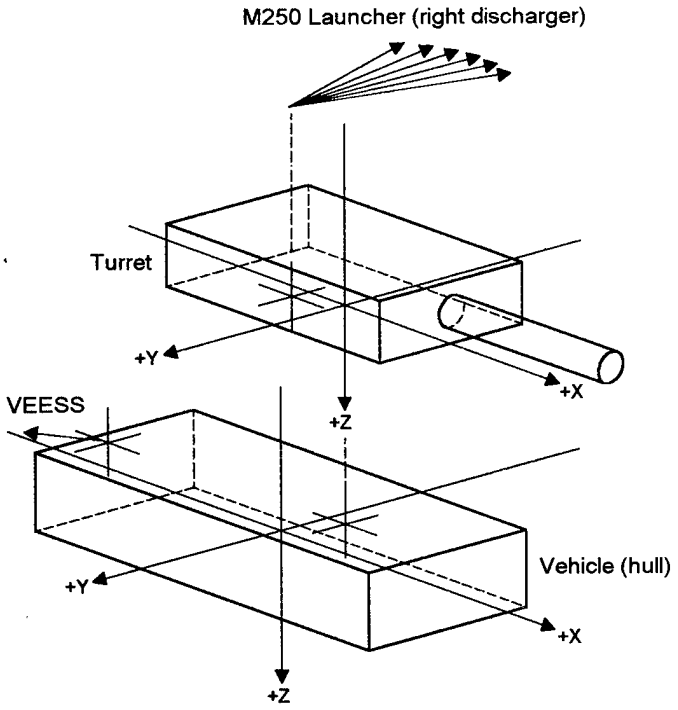


Figure 10. Example M1A1 mounting hierarchy.

Given this configuration, consider tube #3 on the right-hand discharger. Its location and orientation is dependent upon: (1) the location and orientation of the vehicle (hull) with respect to the terrain; (2) the offset and orientation of the turret with respect to the hull; (3) the offset and orientation of the right-hand discharger with respect to the turret; and, (4) the offset and orientation of the tube with respect to the right-hand discharger. The DIS standard specifies how this information will be expressed and reported to networked simulators through message protocols. The computational procedures for calculating component location and orientation are well established and widely used in such fields as robotic control (Paul 1981).

7. SUMMARY

Starting from vehicle position and attitude in variable-terrain scenarios, the Vehicle Smoke Protection Model will be able to provide the location, orientation, and initial cloud characteristics for diffusion and transport in any battlefield model. The resolution can be varied to support small-scale one-on-one simulations or large-scale organizational wargames. The software will be developed using object-oriented techniques so that it can be readily used in many applications.

REFERENCES

Coad, P. and E. Yourdon, 1991: *Object-Oriented Design*, Prentice-Hall, Inc., Englewood Cliffs, New Jersey.

Davis, R.E. and R.A. Sutherland, 1987: EOSAEL 87, Volume 14, Self-Screening Applications Module GRNADE. U.S. Army Laboratory Command, Atmospheric Sciences Laboratory Technical Report, TR-0221-14, White Sands Missile Range, New Mexico.

Hoock, D.W., R.A. Sutherland, and D. Clayton, 1987: EOSAEL 87, Volume 11, Combined Obscuration Model for Battlefield-Induced Contaminants (COMBIC). U.S. Army Laboratory Command, Atmospheric Sciences Laboratory Technical Report, TR-0221-11, White Sands Missile Range, New Mexico.

Institute for Simulation and Training, University of Central Florida, 1994: Proposed IEEE Standard Draft, Standard for Information Technology - Protocols for Distributed Interactive Simulation Applications, Version 2.0 (Fourth Draft), Orlando, Florida.

Paul, R.P. 1981: *Robot Manipulators: Mathematics, Programming, and Control. The Computer Control of Robot Manipulators*, The MIT Press, Cambridge, Massachusetts.

DEVELOPMENT OF A SMOKE CLOUD EVALUATION PLAN

M. R. Perry
Battelle
Columbus, Ohio, 43201, USA

W. G. Rouse and M. T. Causey
Edgewood Research, Development, and Engineering Center (ERDEC)
Aberdeen Proving Ground, Maryland, 21010, USA

ABSTRACT

This paper describes a methodology for field test design intended to achieve repeatability in smoke cloud evaluation. The objective is to establish standard test and data analysis procedures for the characterization of smoke clouds. Obscurant output rates, dissemination durations, and obscurant particle characteristics will be related to effective cloud size and duration for visible, infrared (IR) and millimeter (MM) frequency regions of the spectrum. If relationships can be established, they may be used later within a standardized Test Operations Procedure (TOP) for smoke generator cloud characterization. The Research and Technology Directorate, Armored Systems Modernization Team of ERDEC will be conducting a field test using visible, infrared, and millimeter wave smoke/obscuration generator systems at Dugway Proving Ground (DPG), UT, in September 1994. Three types of smoke generators will be used during the trials: XM56, MM Cutter, and MM Wafer Storage and Dispensing System (WSDS). The XM56 produces visible screening with a visible to near-IR (NIR) obscurant disseminated at two temperatures, IR screening with two types of visible to far-IR (FIR) obscurant, or a combination of both visible and IR. The Cutter and WSDS produce MM screening clouds by disseminating two types of MM obscurants of various lengths and diameters. More than 23 combinations of obscurant will be disseminated. There will be four main categories of equipment: cloud monitoring, aerosol sampling, obscurant consumption monitoring, and meteorological monitoring equipment. The test approach will focus on measurement of aerosol parameters near the point of generation only, and on measurement of the macroscopic obscurant cloud properties down range. This will lead to an ability to evaluate smoke generator performance without meteorological constraints on production testing.

1. INTRODUCTION

The goal of this task is to establish standard test designs and data analysis procedures for the characterization of smoke clouds. Obscurant output rates, dissemination durations, and obscurant particle characteristics will be related to effective cloud size and duration for visible, IR, and MM obscuring clouds. If relationships can be established, they will be used later within a Test Operations Procedure (TOP) for smoke generator cloud characterization.

1.1 Test Objectives

This paper will define repeatable methods for determining effective cloud size/duration, dissemination parameters and obscurant parameters that will be used to test the following hypotheses:

Effective cloud size = f_1(Generator parameters, Aerosol properties)

Effective cloud duration = f_2(Generator parameters, Aerosol properties)

The details of f_1 and f_2, and any other independent parameters influencing cloud effectiveness will be assessed once a relationship has been confirmed. The specific objectives that will test the above stated hypotheses are listed below:

a. Establish procedures for determining effective cloud size and effective cloud duration.

b. Establish procedures for determining smoke generator operation parameters (effective cloud formation time, delay time, generation time, dissemination duration, and feed rate).

c. Establish procedures for monitoring obscurant parameters (size distribution and condition).

d. Evaluate effective cloud size as a function of generator and obscurant parameters.

e. Evaluate effective cloud duration as a function of generator and obscurant parameters.

1.2 Approach

To meet the above objectives, the test approach focuses on measurement of aerosol parameters at the point of generation only, and on measurement of the macroscopic obscurant cloud properties down range. The expectation is that the resulting obscurant cloud can be predicted with substantial accuracy from the characterization of the generator output. This will enable developers to evaluate the performance of smoke generators free from the usual meteorological constraints.

1.3 Test Scope

This paper describes procedures for determining size and duration of smoke/obscurant clouds. Included are descriptions of the field test equipment needed to provide the required data from the field tests. In addition, this paper describes the method for analyzing the field test data. The procedures are appropriate for existing and developmental smoke/obscurant clouds that screen visible, near, mid, far infrared, and millimeter wavelengths.

2. Test Equipment and Material

2.1 Test Location and Grid Layout

The test will be conducted at the Romeo Grid at Dugway Proving Grounds, UT. The test grid layout, shown in Figure 1, illustrates the location of the monitoring equipment and the smoke generators within the test grid. The smoke generator(s) will operate from the north or south launch pads (LP2 and LP1, respectively) based on wind direction, to allow the smoke cloud to travel in front of the cloud monitoring equipment. All particle sampling equipment will be located within 5 meters of the launch pads.

2.2 Cloud Generating Equipment

Three types of smoke generators will be used during the trials; XM56, MM Cutter, and MM Wafer Storage and Dispensing System (WSDS). Table 1 summarizes the screening spectrum for each generator. The following sections describe each of the smoke generators.

Table 1. Summary of the intended screening spectrum of each of the smoke generators being used during the field test

Smoke Generator	Intended Screening Spectrum		
	Vis - NIR	Vis - FIR	MM
XM56	X	X	
Cutter			X
WSDS			X

2.3 Field Test Equipment

There are four main categories of field test equipment: cloud monitoring, aerosol sampling, obscurant consumption monitoring, and meteorological equipment. Tables 2-5 list all the field test equipment, the parameters monitored, the organization(s) that will support the equipment and the applicable spectrum(s).

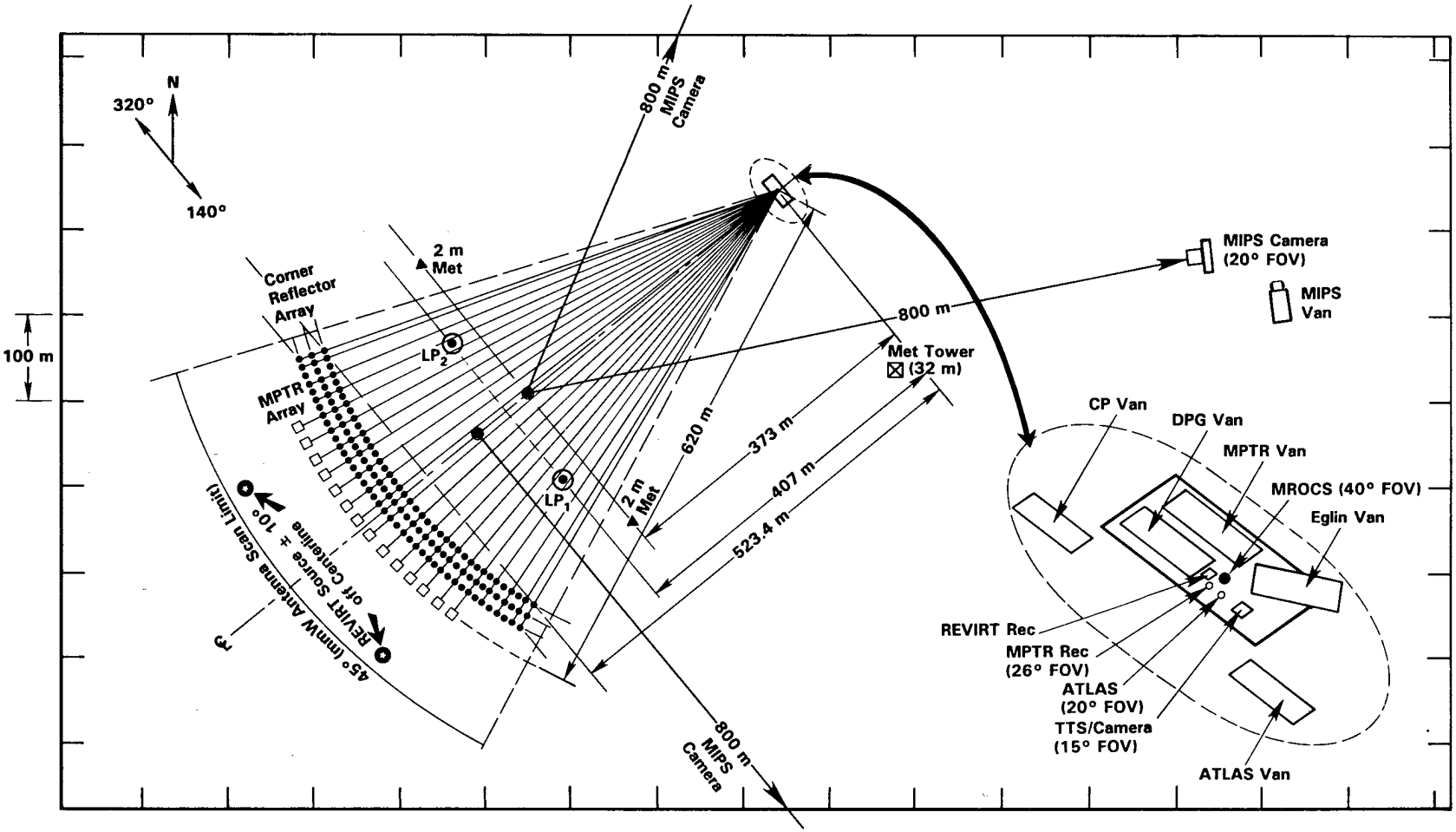


Figure 1. Test Grid Layout. Romeo Test Grid, Dugway Proving Ground, Utah.

Table 2. Listing of the cloud monitoring equipment that will be used during the field test

Equipment	Parameters Monitored	Org.	Applicable Spectrum:		
			Vis	IR	MM
Millimeter wave Radar Obscurant Characterization System (MROCS)	MM backscatter and 2-way attenuation for heights of 1, 3.5 and 6 m over a 40 degree horizontal FOV.	Eglin AFB[1]			X
Atmospheric Transmission Large-Area Analysis System (ATLAS)	FIR transmittance over a 20 degree horizontal FOV.	ASL[2]		X	
Mobile Image Processing System (MIPS)	Visible and FIR cloud growth.	DPG[3]	X	X	
Multi-Path Transmissometer/ Radiometer (MPTR)	Visible and IR 1-way attenuation at 3.5 m height over a 26 degree horizontal FOV.	ASL	X	X	
Research Visible and Infrared Transmissometer (REVIRT)	Visible, IR, and MM one-way signal attenuation at 3.5 m height.	ASL	X	X	X
Full Grid FOV Camera	Visible images of the entire grid during smoke generator operation.	DPG	X		
Tank Thermal Sight (TTS)/Visible Split Image Recording System	TTS and visible images will be combined, producing a visible/infrared split-image video of the test grid during the smoke generator trials.	DPG	X	X	

[1] = Eglin Air Force Base
[2] = Atmospheric Science Laboratory
[3] = Dugway Proving Ground

Table 3. Listing of the aerosol sampling and analysis equipment that will be used during the field test

Equipment	Parameters Monitored	Org.	Applicable Spectrum:		
			Vis	IR	MM
Cascade Impactor/Microbalance	Measures size distribution of visible-NIR obscurant particles.	Battelle	X		
Cyclone Sampler/Elzone Analysis	The Cyclone sampler captures samples of visible-FIR obscurant. Elzone analysis measures size distribution and concentration of the particles.	ERDEC[4]		X	
Guillotine/Hercules Radar Chamber	The Guillotine sampler captures MM obscurant on sticky paper. Optical and radar analysis of samples will provide number of particles per unit area and a relative measure of dissemination effectiveness, respectively.	ERDEC/ Hercules[5]			X
Electrostatic Ball/Pulse Counter	Measures size distribution and concentration of MM obscurant.	ETI[6]			X

[4] = Edgewood Research, Development, and Engineering Center
[5] = Hercules, Inc.
[6] = Engineering Technology, Inc.

Table 4. Listing of the meteorological parameters that will be monitored during the field test

Parameter	Height of Measurements (m)
Horizontal Wind Speed and Direction	2, 4, 8, 16, and 32
Vertical Wind	6
Temperature	2
Dew Point	2
Pasquill Stability Category	8
All parameters will be monitored at a 1 Hz rate, except for the vertical wind components which will be monitored at a 10 Hz rate. DPG will be responsible for monitoring meteorological conditions.	

Table 5. Listing of the obscurant consumption monitoring procedures that will be implimented during the field test

Procedure	**Purpose**	**Org.**	**Applicable Spectrum:**		
			Vis	**IR**	**MM**
Identify Trial Timing From Smoke Generator Monitoring Camera Video	Determine effective cloud formation time, delay time, generation time, dissemination duration, and feed rate	DPG	X	X	X
Weigh Auxiliary Visible-NIR Container	Determine amount of visible-NIR obscurant consumed during trial.	ERDEC	X		
Weigh Visible-FIR Obscurant Required to Reload XM56 Hopper	Determine amount of visible-FIR obscurant consumed during trial.	ERDEC		X	
Weigh MM Obscurant For Cutter	Determine amount of MM obscurant consumed during trial.	ERDEC			X
Count Number of Wafers Disseminated by WSDS	Determine amount of MM obscurant consumed during trial.	ERDEC/ Battelle			X

2. ANALYTICAL PROCEDURES

This section describes how the acquired field test data will be used to satisfy the test objectives.

2.1 Test Objective a: Establish procedures for determining effective cloud size and effective cloud duration.

Effective cloud size is defined as the horizontal extent (m) of a cloud that is ≥ a predetermined height and attenuation level. Effective cloud duration is defined as the maximum time in which there are consecutive effective cloud sizes. MROCS and MIPS data will be the primary data sources used to determine cloud size and duration in the MM and visible/IR spectral regions,

respectively. ATLAS and MPTR data will be used to approximate visible and IR signal attenuation levels associated with the MIPS data.

MROCS Data: The MROCS MM attenuation and backscatter data will be used to calculate effective MM cloud size and duration. The MROCS data will be analyzed using Battelle's "Computer Program for Analysis of Millimeter Wave (MMW) Attenuation Data", dated December, 1993. The program may require modifications if the MROCS data format has been changed. In addition, the MROCS data will be compared to the REVIRT data for validation.

MIPS Data: The MIPS visible and FIR cloud growth data will be used to calculate effective visible and FIR cloud size and duration. Cloud length, height, and duration values will be taken directly from the 3DCAV cloud dimensioning program. These data will be compared with ATLAS and MPTR data for establishing the MIPS cloud transmission level.

ATLAS Data: The ATLAS FIR transmittance contour plots will be used to calculate effective FIR cloud size and duration. Cloud length, height, and duration values will be measured directly off the contour plots. The size scaling factors used in the measurements will be calculated from the ATLAS contour plot frame radians and the distance from the cloud center to ATLAS. ATLAS transmittance contour plots will be compared with MPTR FIR transmittance data. In addition, ATLAS plots will be used to establish the FIR transmittance level of the MIPS cloud dimensioning data.

MPTR Data: The MPTR FIR transmission data will be compared with ATLAS contour plots. The MPTR visible and FIR transmission data will be used to attempt to establish the transmission level of the MIPS cloud dimensioning data.

2.2 Test Objective b: Establish procedures for determining smoke generator operation parameters (effective cloud formation time, delay time, generation time, dissemination duration, and feed rate).

Table 6. Definitions of the smoke generator operation time parameters that will be monitored during the field test

Term	Time difference between ...	
Cloud formation time	generator start	formation of an effective cloud
Delay time	generator start	initial obscurant dissemination
Generation time	generator start	generator stop
Dissemination duration	initial obscurant dissemination	final obscurant dissemination

Smoke Generator Data Sheets: Information from the Smoke Generator Data Sheets will contain trial specific parameters for every trial which will be used in correlating smoke generator operation

with particle results and cloud screening, size, and duration results. The data sheets will also contain obscurant consumption weights which are required for determining feed rates. Key information from the data logs will be imported into a summary table.

Smoke Generator Monitoring Camera Videos: Video recordings of the smoke generator during operation will be used to determine the delay time, generation time, and dissemination duration of the smoke generators for each trial. Smoke generator start and stop times will be indicated by the smoke generator operator.

Feed rate will be determined by dividing the weight of the obscurant materials consumed by the dissemination duration.

2.3 Test Objective c: Establish procedures for monitoring obscurant parameters (size distribution and condition).

Cascade Impactor Visible Obscurant Sampler Data: Visible-NIR obscurant sampling data will be used to characterize the obscurant as it exits the XM56. Average concentration and size distribution data for the hot and cold obscurant will be compared.

Elzone Analysis of Horn Samples: Elzone analysis of the Horn samples will be used to characterize the two types of visible-FIR obscurants as they exit the XM56. Particle size distribution data will be compared.

Optical and Radar Chamber Analysis of Guillotine Samples: Optical and radar chamber analysis of the Guillotine samples will be used to characterize the MM obscurant materials as they exit the Cutter and WSDS. Optical analysis will provide number of particles per unit area and percent clumping. The radar chamber analysis will provide MM attenuation data which will be compared to MM obscurant standards available at Hercules.

Electrostatic Ball MM Obscurant Sampler Data: The Electrostatic Ball detector data will be used to characterize the MM obscurant as they exit the Cutter and WSDS. Concentration and length distribution data will be reported.

2.4 Test Objective d: Evaluate cloud size as a function of generator and obscurant parameters.

Effective cloud size results from the MROCS and MIPS data will be compared with smoke generator parameters and obscurant particle results. The primary goal is to determine if there is a relationship between feed rate and effective cloud size for each type of obscurant material.

2.5 Test Objective e: Evaluating cloud duration as a function of generating time and obscurant parameters.

Effective cloud duration results from the MROCS and MIPS data will be compared with smoke generator operation timing and obscurant particle results. The primary goal is to determine if there is a relationship between generation time and effective cloud duration for each type of obscurant material.

2.6 Additional information that will be analyzed from the data.

2.6.1 Homogeneity of multispectral screening clouds.

REVIRT Data: The REVIRT visible, IR and MM signal attenuation data will be used to determine the multispectral screening effectiveness of clouds containing multiple obscurants. Attenuation levels and screening times will be compared. REVIRT data will also be used to validate the MROCS data. REVIRT LOSs will be correlated with MROCS corner reflectors and the MM attenuation data will be compared.

2.6.2 Approximate Obscurant Dissemination Velocity.

Smoke Generator Cloud Monitoring: Video images will be used to estimate the velocity of the exiting obscurant material. As the initial obscurant exits the ejector, the distance it travels per units time will be monitored. Obscurant travel distance will be approximated using images with known dimension within the FOV. Travel time will be approximate because of the limitation of the 30 frame/second video image speed.

2.6.3 Additional Support data

Full Grid FOV Monitoring Camera Videos: The Full Grid FOV video tapes will be used to qualitatively assess each trial. Selective images will be used in the final briefing package.

TTS/Visible Split Image Videos: Selective split image frames will be used in the final briefing package. The images incorporated into the briefing package will be of each of the screening clouds produced (i.e., visible, IR, MM, and combinations).

Meteorological Data: Wind speed, wind direction, temperature, dew point, and stability category data will be used to assess the effects of the meteorological conditions on the generated clouds.

3. QUICK-LOOK RESULTS

This paper was submitted for the Battlefield Atmospheric Conference just two weeks after the completion of the above described field test. As a result, the quantitative field test data was not

available for analysis. Listed below are qualitative assessments of the quick-look data that were available during the field test.

3.1 MPTR Data

Preliminary MPTR data (Valdez 1994) were reviewed to compare the screening effectiveness of the visible-NIR obscurant disseminated hot and cold. The quick-look data suggest that the hot disseminated obscurant screened visible-NIR signals more effectively and for a longer period of time.

3.2 MROCS Data

Preliminary MROCS data (Mijangos 1994) were reviewed to compare the effectiveness of the various lengths and diameters of the MM obscurant. The quick-look data suggest that the shorter lengths and shorter diameter particles screened the MM signals more effectively and for a longer period of time.

3.3 Smoke Generator Data Sheets

The Smoke Generator Data Sheets accurately documented the obscurant consumption during each trial. This information will significantly increase the ability to relate the dissemination parameters with the resulting cloud.

4. OVERVIEW

This paper illustrates repeatable procedures which can be used to monitor and analyze smoke/obscurant source parameters, aerosol characteristics, and effectiveness (size, duration, attenuation, and wavelength). These procedures will provide data that can be used to evaluate cloud size/duration as a function of generator and obscurant parameters. The point of this effort is to demonstrate that by recording generator parameters and point-of-exit aerosol data, you can adequately define generator performance in terms of anticipated cloud effectiveness.

REFEREENCE

Perry, M., Kuhlman, M., Kogan, V., Rouse, W., and Causey, M., 1994: *Study of Test Methods for Visible, Infrared, and Millimeter Smoke Clouds -- DPG: Sept. 1994.* Test Plan, Battelle and ERDEC, Contract No. DLA900-86-C-2045, Task 182.

Mijangos, Adrian, 1994: MROCS Quick-Look MM Attenuation Plots, Unpublished, Supplied to Michael Causey (ERDEC) during DPG Field Test, Eglin AFB, Florida.

Valdez, Robert, 1994: MPTR Quick-Look Visible-IR Transmittance Plots, Unpublished, Reviewed by Mark Perry (Battelle) during DPG Field Test,

ANALYSIS OF WATER MIST/FOG OIL MIXTURES

William M. Gutman and Troy D. Gammill
Physical Science Laboratory
New Mexico State University, Las Cruces, New Mexico 88003

Frank T. Kantrowitz
Army Research Laboratory Battlefield Environment Directorate
White Sands Missile Range, New Mexico 88002

ABSTRACT

The Army Research Laboratory Mobile Atmospheric Spectrometer (MAS) has been used to optically characterize obscurants at numerous tests over the past several years. These have included Smoke Weeks XIII, XIV, and XV as well as the recent Large Area Smoke Screen Experiment (LASSEX). The MAS spectrometers are usually operated as transmissometers at 4 cm^{-1} spectral resolution and this configuration provides approximately 200 measurement channels in the 8–12 μm region and 600 in the 3–5 μm region.

At LASSEX, the principal MAS line-of-sight was approximately parallel to the nephelometer line but offset by approximately by 30 m. This was sufficiently close to permit realistic time-adjusted correlation comparisons between MAS transmittance measurements and nephelometer-based mass loading data for most materials. Time adjustment was necessary to correct for the time for the material to be transported from the nephelometer line to the MAS line-of-sight or vice versa. One of the generator systems tested at LASSEX could combine water mist with fog oil smoke. Trials were conducted with that generator system with the separate materials and with the combined materials. Nephelometers normally cannot distinguish between components of a multi-component mixture. By using distinctive absorption features of separate components, however, MAS transmittance data offer a means to estimate mass loading for the separate components, although the difficulty of collecting water mist with a filter sampler introduces considerable uncertainty into the calibration of the nephelometer data. MAS transmittance spectra were used to investigate the properties of water mist/fog oil smoke mixtures, and results of that investigation are presented.

1. INTRODUCTION

For the past several years, the Army Research Laboratory Mobile Atmospheric Spectrometer has been used to characterize the infrared transmissive properties of various obscurant materials. Measurements have been made at Smoke Weeks XIII[1], XIV[2], and XV as well as at the Large Area Smoke Screen Experiment (LASSEX) which was conducted at Eglin Air Force Base, Florida during May, 1994. Over the period of time spanned by these tests, steady improvements have been made in the data acquisition repetition rate, the signal-to-noise ratio of the spectra, and the processing algorithms.

2. DATA ACQUISITION AND REDUCTION

As currently configured, the primary spectroscopic instruments in the MAS are two Fourier transform spectrometers. The original instrument is capable of 0.04 cm^{-1} spectral resolution. A second instrument that is capable of 0.5 cm^{-1} spectral resolution was added prior to LASSEX, but data collected with the original instrument are the subject of this paper. The original spectrometer is particularly well suited to the field measurement environment. The instrument uses corner

reflectors rather than flat mirrors, and it is, therefore, essentially immune to thermally-induced misalignment that can severely limit the reproducibility of flat-mirror systems. A corner reflector spectrometer achieves this immunity without the complexity of a dynamic alignment system.

2.1 Test Configuration

At LASSEX, most of the MAS data were collected in transmissometer mode. A source was set-up on the west side of the test grid at "M1" while the MAS van containing the spectrometer was set up on the east side of the grid at "S3." The source was a 1000 °C temperature-controlled blackbody collimated with a modified 60-inch searchlight. The receiver optics for the spectrometer consisted of the main 31-inch Coudé-mounted Cassegrain telescope. The Coudé telescope mount greatly facilitates spectrometer repointing when required, for example, to collect radiance spectra of munitions set on the test grid. As will be discussed below, a rotating-blade shutter was used to block the source on command from the receiver in order to obtain background and path radiance spectra. The source and spectrometer were set up so that the line-of-sight was approximately parallel to, and 30 m south of, the nephelometer line. All transmittance spectra were collected at 4-cm^{-1} spectral resolution.

2.2 Measurement Methodology

The transmittance of a sample of material at radiation frequency υ is defined as the ratio of the radiant power at frequency υ exiting the material to the radiant power at that frequency incident upon the material, i.e.

$$T(\upsilon) = \frac{I(\upsilon)}{I_0(\upsilon)}$$

Absolute atmospheric transmittance is quite difficult to measure over a path of significant length (of the order of hundreds of meters) because, except in special cases, it is impossible to collect the entire beam of radiation at the receiver. The beam spreads because of the finite size of any non-laser source, because of diffraction, and because of atmospheric turbulence. The only satisfactory broadband absolute atmospheric transmittance measurement methodology that has yet been demonstrated is to measure the transmittance at discrete frequencies using a low divergence laser whose spot size and spread and wander footprint at the receiver are small enough to allow collection of the entire beam. Even with this approach, a large collecting aperture is required for most path lengths of interest, especially during high turbulence parts of the day. The transmittance at one or more discrete frequencies, however, can be used to normalize the result of a broadband relative transmittance measurement. The broadband measurement is made by comparing a spectrum collected at the desired path length with a spectrum collected over a very short atmospheric path. This is usually called a zero-path spectrum. Dividing the long path spectrum by the zero-path spectrum corrects for the shape of the instrument response function. The resulting spectrum is the unnormalized transmittance of the part of the path that is different between the two measurements. Normalization with the laser measurement corrects for the spreading of the beam. Measurements of this type are extremely difficult.

In the case of an obscurant measurement, what is usually required is not the absolute transmittance of the entire path, but rather the transmittance of the path with the obscurant relative to the clear air path. The spreading factors and the instrument response function remain unchanged when comparing the path with the obscurant to the path without the obscurant, and so a simpler measurement methodology can be applied. In the absence of path radiance and background effects, the relative transmittance of the obscurant is the point-by-point ratio of the obscurant spectrum to the clear air spectrum. Path radiance and background radiation, i.e. scattered sunlight, and radiation emitted by the obscurant, by the optical elements in the beam

path, and by the part of the background that is not obscured by the source, may contaminate the raw signals and thus must be removed. I.e.

$$I_0(\upsilon) = S_{clear} - S_{bkg}$$

and

$$I(\upsilon) = S_{obscurant} - S_{path}$$

Therefore,

$$T(\upsilon) = \frac{S_{obscurant} - S_{path}}{S_{clear} - S_{bkg}} \qquad (1)$$

It is understood that all of the quantities on the right hand side of Eq. 1 are functions of υ..

The MAS measurement methodology is to measure these four quantities over as short a time interval as possible. It is especially important for the obscurant and path radiance data to be close together in time because of the rapidly changing nature of the typical obscurant cloud. Clear air data typically were acquired both before and after each obscurant release. Whenever possible, pre-trial clear air data were used in the analysis because they were less likely to be contaminated by residual obscurant that may not have been apparent visually. Obscurant spectra were alternated with path radiance spectra. Path radiance spectra were obtained by blocking the source with the remotely controlled rotating shutter. Two way communication with the shutter helped to ensure that it was always in its correct state. Each spectrum was the result of the addition of two interferograms. This had the effects of reducing the signal variability resulting from atmospheric turbulence and of improving the signal-to-noise ratio. The acquisition of each coadded interferogram required approximately 0.5 s, but because of the overhead associated with transfer and storage of the data, the time between spectra was approximately 1.5 s. Because of the requirement to alternate between obscurant and path radiance spectra, the overall measurement period was approximately 3 s. Transmittance spectra at LASSEX were collected at a nominal spectral resolution of 4 cm^{-1} and covered the transparent parts of the atmospheric spectrum between 800 and 3000 cm^{-1} (12.5 and 3.3 μm). Data acquisition was controlled by a computer program to ensure that opening and closing of the shutter were properly time with respect to the data acquisition. Fourier transformation of interferograms into spectra was accomplished after the conclusion of each trial. Computation of transmittance spectra from the raw spectra was controlled by a computer program. Several computational aids have been developed to facilitate analysis of the data. These include a program to display time sequence movies of spectra in a simulated three-dimensional space.

3. COMPARISON WITH NEPHELOMETER MEASUREMENTS

The proximity of the MAS line-of-sight with the nephelometer line permits realistic correlation comparisons between MAS transmittance measurements and nephelometer-based mass loading data for most materials. The correlation function expressed as a function of the time between the spectral measurement and the nephelometer measurement can be defined as

$$C(t) = \int \alpha(\tau) T(\tau - t) d\tau$$

where α is the nephelometer signal and T is the transmittance measured with the MAS. The correlation function normally has its peak value at $t = \frac{x}{v_\perp}$ where x is the displacement between

the MAS line-of-sight and the nephelometer line, and $v_{\perp}$ is the mean magnitude of the wind component perpendicular to the line-of-sight. Previous work has demonstrated good correlation with the nephelometer measurements under some meteorological conditions.

3. MULTICOMPONENT SMOKES

Obscurant performance is often enhanced by combining materials. The combination of graphite with fog oil, for example, provides good obscuration from the visible through the infrared spectral region. Measurement of the individual components of multicomponent smokes can be difficult. By using distinctive absorption features of the separate components, however, spectrally-resolved transmittance data offer a potential means to estimate the contribution from the separate components. Obviously, for this approach to be successful, at least one component of a two-component mixture must have some distinctive spectral feature.

3.1 Water Mist/Fog Oil Mixtures

One of the generator systems tested at LASSEX could combine water mist with fog oil smoke. The water component is particularly troublesome to measure. Because of its high volatility, it is not possible to use filter samplers to obtain reliable mass concentration estimates.

A number of trials were conducted at LASSEX with the water mist/fog oil system. During most of the trials, both components were generated. One trial was conducted with pure water mist, and numerous fog oil spectra have been collected with the MAS in support of other trials.

3.2 Measured Spectra

3.2.1 Fog Oil

Figure 1 is a pure fog oil spectrum. Fog oil is a poor infrared attenuator, and that fact is obvious from this figure. The strong absorption band at the high frequency end of the spectrum is characteristic of fog oil.. The band originates from the C—H single bond and is, therefore, common to most hydrocarbons. This absorption band in fog oil spectra is probably the result of gaseous material that vaporizes in the generator or that evaporates from the droplets in the fog. In general, the strength of this feature correlates with the overall attenuation level in the spectra. The depth of this feature, then can be used to estimate the contribution of fog oil to the attenuation in other parts of the spectrum, to estimate the fog oil contribution to the attenuation of a mixture, and to estimate the fog oil concentration-length product. The feature between 2000 and 2200 cm^{-1} that appears to be a weak absorption band is a weak water vapor feature that did not ratio out perfectly because of small variation in the water content between the clear air and the obscurant spectra. It is not uncommon to see this band in MAS obscurant transmittance spectra.

3.2.2 Water Mist

Figure 2 contains three spectra of water mist. These spectra were collected during LASSEX Trial 50. There are several interesting characteristics common to these spectra:

1. The overall transmittance level is fairly low, at least compared with fog oil. Water mist can be a fairly good infrared obscurant.

2. The weak water absorption band that was discernible in the fog oil spectrum is slightly more evident in the water mist spectra. It is not surprising that the water vapor content of the air might be enhanced by the presence of water droplets in the path.

3. The low frequency end of the spectrum is up-turned slightly. The origin of this effect is unknown at this time, but it seems to be common in the water mist spectra. Its strength appears to be directly related to the overall attenuation level. Although it is not

particularly strong, it offers promise as an aid in estimating the concentration-path length product of water particles.

4. The high frequency end of the spectra contain an absorption feature similar to the hydrocarbon absorption band but much weaker. This feature probably results from unburned hydrocarbons in the turbine exhaust of the generator.

The weak absorption band between 2000 and 2200 cm^{-1} holds little promise as a potential aid to analyze the separate water vapor and fog oil concentrations because it may be present in both spectra. The slightly up-turned transmittance near 850 cm^{-1}, although weak, is unique to the water spectra. The height of this feature above the baseline correlates with the overall transmittance level, and so it should be usable to aid the analysis. Because this feature is relatively weak, the uncertainty level in the resulting estimate of the transmittance and concentration-path length product would be relatively high. The presence of the weak hydrocarbon absorption in the water mist spectra does not appear to represent a serious problem because it is so weak compared with the fog oil spectra.

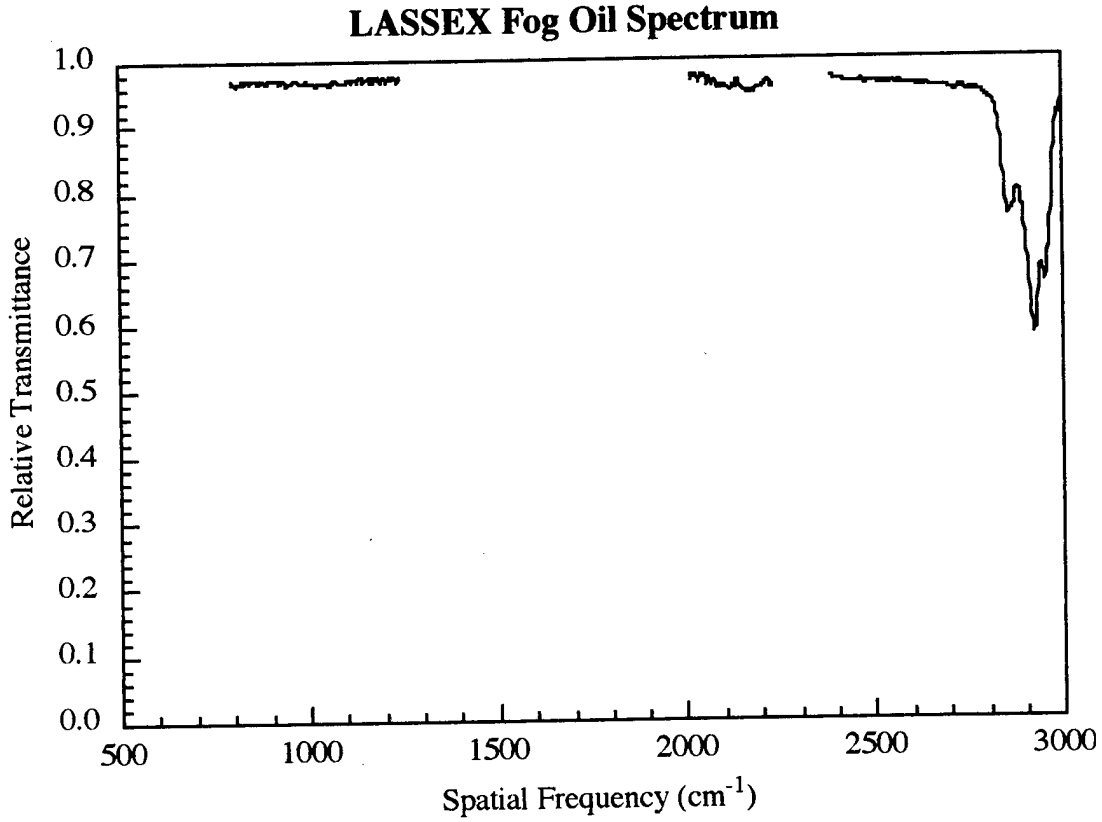


Figure 1. Typical transmittance spectrum of pure fog oil collected during LASSEX Trial 075.

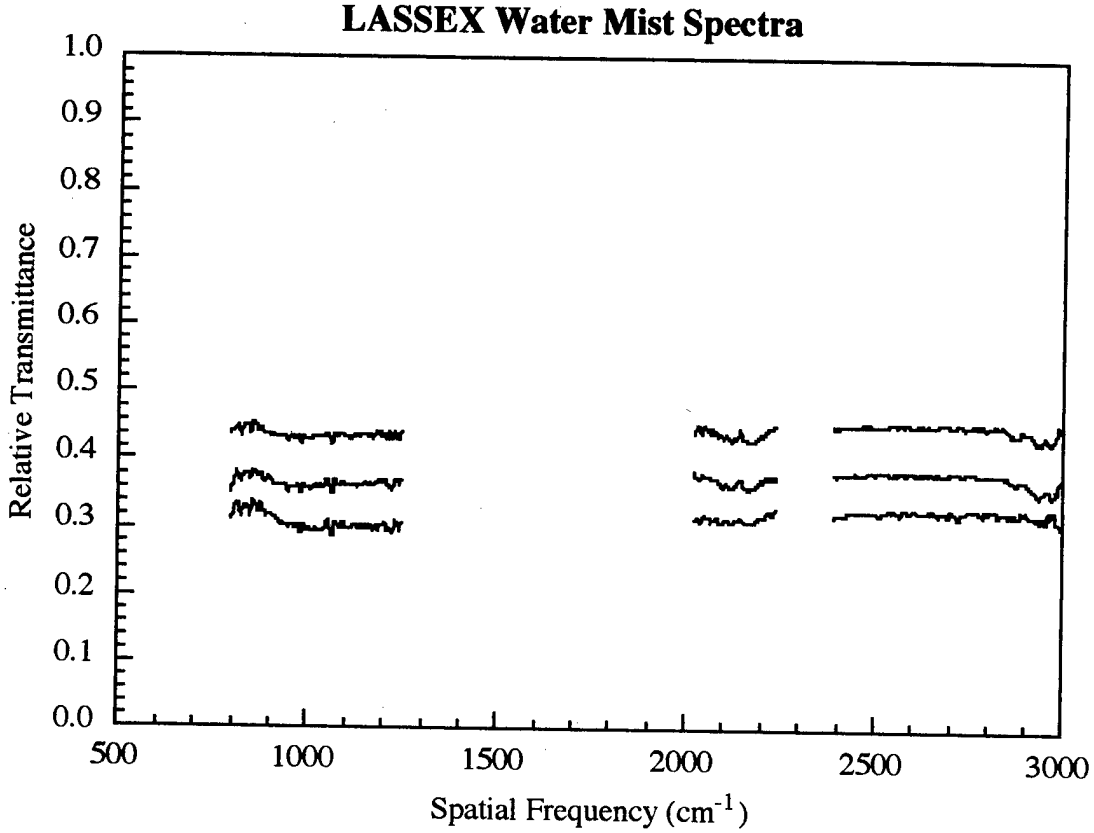


Figure 2. Three water mist transmittance spectra collected during LASSEX Trial 050. These spectra exhibit among the strongest attenuation observed for water mist.

3.2.3 Fog Oil/Water Mist Mixture

Figure 3 is a spectrum of the combined water mist and fog oil smoke. Both the strong hydrocarbon absorption band of fog oil and the up-turned baseline at 850 cm^{-1} of water mist are evident in the spectrum.

3.3 Analysis

By correlating the strength of the up-turned baseline in the pure water mist spectra with the average transmittance, and the depth of the hydrocarbon absorption with the baseline, it is straightforward to arrive at estimated values for the transmittance levels that would result from the individual components of the mixture if present at the same concentration alone. These values are approximately 0.86±0.03 for the water and 0.96±0.02 for the fog oil. The product of these numbers is 0.83±0.05, and the actual combined transmittance was measured to be approximately 0.9. Given the limited data set that has so far been examined, this appears to be reasonable agreement. No attempt was made to estimate the concentration-path length products for the separate components. This step will require detailed analysis of nephelometer data sets for both water mist and fog oil.

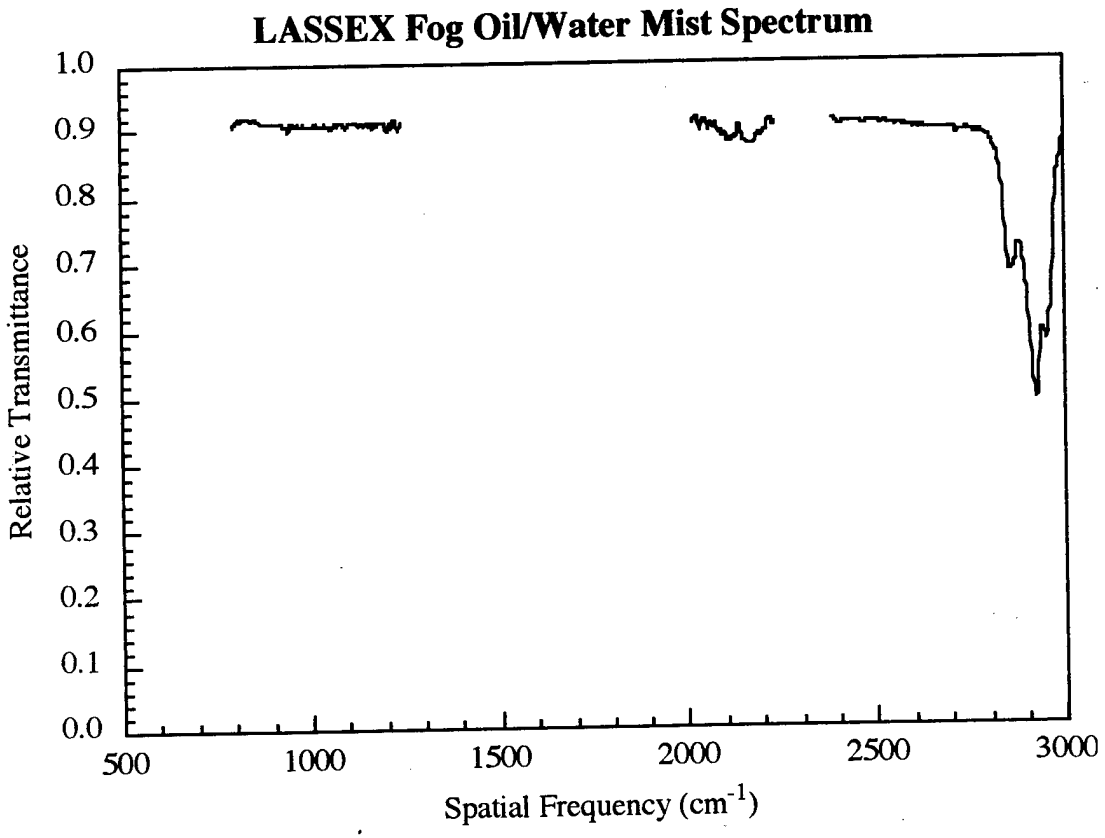


Figure 3. Typical spectrum of fog oil/water mist mixture collected during LASSEX Trial 076.

4. CONCLUSIONS AND FUTURE DIRECTIONS

Spectrally resolved transmittance measurements appear to offer an effective means to analyze the optical properties of the individual components of mixed obscurants for which no other method has been demonstrated. Future work in this area will be directed confirming and refining these results, and toward obtaining concentration-length products for the separate components.

REFERENCES

1. Peterson, W. A., D. M. Garvey, and W. M. Gutman, "Spectrally Resolved Transmittance Measurements at Smoke Week XIII," *Proceedings of the 1991 Battlefield Atmospherics Conference*, U. S. Army Atmospheric Sciences Laboratory, White Sands Missile Range, New Mexico.

2. Kantrowitz, F. T., W. M. Gutman, T. D. Gammill, and J. V. Rice, "High Resolution Spectroscopy at Smoke Week XIV," *Proceedings of the Smoke/Obscurant Symposium XVII*, Johns Hopkins University, Laurel, Maryland.

NEW MILLIMETER WAVE TRANSMISSOMETER SYSTEM

ROBERT W. SMITH
U.S.Army Test and Evaluation Command
Ft. Belvoir Meteorological Team

WILLIAM W.CARROW
EOIR Measurements,Inc
Spotsylvania,Va

ABSTRACT

The TECOM Ft Belvoir Meteorological team and the Night Vision and Electronic Sensor Directorate of CECOM contracted with EOIR Measurements,Inc to develop a new instrument which would provide atmospheric transmission data in the 35 gigahertz region. The desired instrument would have complete redundancy, long path length, compact size, stable microwave performance, easy field setup and alignment, standard data output, low development risk, and above all, low development cost. The design by EOIR consists of mostly off the shelf components with a design goal of measuring 1 percent transmission over a 5 km path in a rainfall of 64 millimeters per hour. To achieve simplicity of design and field use, and to keep the cost down, two innovations have been made. First, a new antenna design that uses optical refraction principles replaces the large and cumbersome parabolic antennas and second, an open loop frequency design, as opposed to a frequency tracking receiver,allows for the use of less expensive transmitters and receivers. In this paper we will describe the instrument, present the test procedure and look at some of the data.

2.INTRODUCTION

For many years the Army's Ft Belvoir Meteorological Team has been making measurements of atmospheric transmission in the visual and infrared regions of the spectrum. With the increasing interest in the millimeter wave region, we have been asked to extend our capability. Propagation effects are very important to millimeter wave systems. They include attenuation and scattering by precipitation,fog and dust and clear air absorption by water vapor and oxygen. Millimeter wave propagation models do exist but it remains difficult to make accurate predictions of attenuation due to differences in data bases and in the assumptions which are made during the calculations. Some of the measurements required for predictions have significant uncertainties which can effect the results. These include rainrate,drop size and distribution, water

content of fog, and the extent of precipitation or fog. Additionally, predictive models do not handle rapidly changing conditions caused by either changing weather conditions or by battlefield obscurants. Because of these considerations, we decided to obtain a system which would measure the attenuation loss directly. A brief survey of existing systems found many problems but primarily their cost exceeded the resources available.

3. DESIGN GOALS

The process of developing our system started with a set of significant features which had to be met. We required a path length of at least 5 kilometers,a compact size, stable microwave performance, easy field setup and alignment, output capable of computer processing, low development risk, high reliability and, above all, low system cost. We will expand of each of these considerations.

The system has been built with complete redundancy since we have two stand alone source units and two stand alone radiometer units. Since the computer is a standard pc, we can always back it up with another. This gives the additional flexibility of measuring two separate paths if desired.

Size and weight have been carefully controlled so that the entire source or radiometer are contained in environmental housings four feet long and eight inches in diameter. These housings which weigh about 30 pounds each will be mounted on tripods.Figure 1 provides a very simplified representation of the transmissometer system.

The performance design goal for this system is to allow the user to make path loss measurements accurately with 1% transmission over 5 km path length. This corresponds to operating in over 64 mm/hr of rainfall.

The two primary mechanisms responsible for unstable microwave operation (power and frequency drift) are changes and variations in ambient temperature and power supply. To avoid the power problem, extensive use of tightly regulated power is made. Many key components use two stages of power regulation to assure isolation from power line or generator fluctuations. Temperature stability is obtained by the use of a temperature controlled housing for the microwave head and other key components. Calculated frequency drift over a range of -20C to +40C ambient is on the order of 5 Mhz. This worst case frequency drift is easily accommodated by the 10 Mhz bandwidth of the radiometer. Worst case power drift is calculated to be on the order of 0.4% over the same range of tem-

peratures. Because of excellent power supply regulation, the temperature induced variations will dominate the performance considerations.

The system has about a 70 mr field of view (4 degrees). While this is considered narrow for radio systems, it is significantly wider than the 3 mr used on our optical transmissometers and greatly eases alignment considerations. In addition each unit is provided with an alignment system consisting of a narrow beam intense spotlight and a high quality 24 power aiming scope.

Data output from the radiometer to the user will be 0 to 10 volts analog and RS232 serial digital. These signals represent 0 to 100 % transmission. The power source provides a 0 to 10 volt power monitor signal where 10 volts represents a relative 100 % power output. We do not anticipate using lock-amp processing. Finally the source and radiometer have rear panel displays to assist in alignment.

All key components of this system are commercially available. The most critical components, the microwave transmit and receive heads, are derived from police traffic radar systems which have had over 20 years of in the field use. The entire system, consisting of two complete separate transmissometers is the result of an exhaustive survey of the U.S. microwave industry, is about 1/2 the cost of the nearest competitor and it is specifically designed for the needs of the Ft Belvoir Meteorological Team.

4. SYSTEM CONCEPT

The initial concept for this transmissometer system borrows heavily from the present Barnes Optical transmissometer system presently being used by the meteorological team. That is, a known amount of energy of the desired frequency is transmitted into space towards a companion radiometer.The radiometer is separated from the source by a known path length. After correction for free space loss over the path length, and any system loss, the amount of energy received by the radiometer is considered to represent the propagation loss of the path.

The free space loss is calculated from the formula: path loss = $1/(4 \text{ pi } R^2)$. System loss will be measured by a method of suitably attenuating a very near field signal such that path atmospheric loss can be considered zero. This calibration procedure will be more fully developed once we have field tested the unit.

Considerations unique to microwave systems require some departure from classical optical concepts. However the system presented here, for the most part, adheres to the above concepts. The source for this system uses a 34 Ghz police radar head of about 50 mw output power. The difference in signal attenuation between 34 and 35 Ghz can be assumed to be very small since these frequencies lie in an absorption minimum for water vapor and the small difference will not affect rainfall attenuation. A power monitor circuit has been included on the source which allows the user to monitor the power output of the source and to make periodic corrections to the calibration factor used to compute the per cent transmission. At a later time we may modulate the output power information onto the 34 Ghz signal to give the capability to monitor the source performance from the receiver site. Finally, the microwave section, or "front end" of the source environmental housing is temperature stabilized at about 35 degrees C (+/- 3 deg) to help obtain the required frequency and power stability. A cutaway view of the environmental housing is provided in figure 2 and a block diagram of the system is at figure 3.

At the receiver, the 34 Ghz radiometer is also temperature stabilized in the same manner and for the same reasons as at the source. The receiver signal handling method used is known as super-hetrodyne detection. This is the same method used in all modern radio and tv receivers. Super-hetrodyne detection provides superior signal to noise performance relative to unhetrodyned lockamp assisted radiometers such as used on the optical transmissometer system. The primary benefits of super-hetrodyned detection are three. First,the received signal is immediately down converted (or hetrodyned) to a more friendly frequency (34 Ghz to 30 MHz in this case) in the microwave head. The new frequency contains all of the information contained in the original frequency. The lower intermediate frequency (i.f.) of 30 MHz,however, eliminates the need for a long chain of difficult to tune microwave circuits. Second, 30 Mhz amplifiers and filters are standard electronic items, readily available at low cost. This is an important consideration for field maintenance.Third, in general i.f. amplifiers are used because they provide a stable tuned circuit with very high gain and low noise.

A second frequency conversion takes place when the 30 Mhz i.f. is electronically chopped at 1 KHz. (we will evaluate the need to put a 1 KHz reference signal in at the source after our system evaluation but it is difficult and may not be needed). This 1 KHz signal is then further filtered and amplified. Finally, a precision demodulator circuit converts the 1 khz signal to a d.c. voltage representing the received signal strength. The system uses six inch diameter dielectric lenses

to collimate and collect the transmitted energy. The efficiency of these lenses allows them to replace more costly and much more cumbersome parabolic metal dish antennas.

System performance has been calculated for a 5 kilometer path length. A free space (no attenuation) signal to noise ratio of 36 db is predicted. Assuming that a minimum signal to noise ratio of 3 db is needed to make a usable reading, we have a dynamic range of 33 db, of from 100% down to 0.05% transmission. It is likely that other factors will cause the minimum readable signal to go to the 0.1 to 1.0 per cent range, but this is a healthy performance range. Calculations indicate that it should be possible to make 5 kilometer path measurements in precipitation in excess of 64 mm/hr. Our field evaluation of the system will of course confirm these predictions.

5. DATA PROCESSING

The software for the transmissometer was developed by Chris Wolfson of EOIR Measurements,Inc who was also one of the development engineers. The voltage from the receiver output is sent to a computer by RS 232 where it is converted into transmission values. The software has a number of configuration files which are accessed by menus. The main menu offers the following selections:

OPERATION MENU - collects and processes data
CONFIGURATION MENU - sets the test parameters
CALIBRATION MENU - saves calibration and setup data
PRINTOUT MENU - controls printout of selected data

The first step after setup and alignment uses the calibration menu. In this step the calibration distance, signal strength and attenuator setting are recorded along with the specific run values for distance and attenuator setting. This menu is followed by the configuration menu is used to set run ID,sampling and recording intervals. Finally the operation menu is called. Here one has the choice of timed start/stop, user commanded start/stop, or continuous readout. When in the continuous mode, the data is only displayed, not stored. The sample interval can be varied from many times a second to a few seconds. The recording interval specifies the averaging period. The last five recording period data points are displayed.

The transmission values are calculated using the following equation:

$$T = S_m * 100 / (S_c (A_m/A_c) (D_c/D_m)^2)$$

where T is transmission in percent corrected for path loss
S is signal strength
A is attenuator setting
D is distance or path length
the subscripts c and m refer to calibration or measured

The software contains several diagnostic routines, however these are not on a menu at this time.

6. FIELD EVALUATION

The instrument was set up at the NVESD compound at FT A.P. Hill, Va on 30 August. The day was very clear and dry. The first step was calibration and checkout. We first wanted to demonstrate that the received signal intensity under good transmission conditions followed the free space loss curve. To do this we set up at 500,2000, and 5000 meters and did the necessary alignment procedures. We then took intensity data at each of the attenuation settings from each distance. The calibration distance was the 500 meter point,assuming that there we would have negligible transmission loss. We normalized the data collected at each distance and calculated the standard deviation. Figure 4 shows the results with the averaged data for each distance and the 3 sigma standard deviation. While the data did not fall exactly on the free space loss curve, the shape appears the same and the losses represent a constant percentage regardless of range. The differences can be attributed to system noise and less than perfect calibration. Also small errors in calibration distance can result in significant errors at the longer ranges. Armed with this system verification we proceeded to the collection of transmission data.

7. DATA PRESENTATION

Data will be presented for three rain events. The first event was on 26 and 27 September. This was the first day of rain after we set up the instrument. There were four measurement sites down range at 1,2,3, and 5 km. The rainrate data in firure 5 shows three periods of significant rain fall. The millimeter wave transmission data shown in figure 6 clearly was affected during these periods. However the data dropped below zero percent, which was bothersome. After investigating this data we discovered that the problem was in a linearization routine which had been turned on in the software. This routine had the effect of incorrectly distorting the received signal below about the 5% level. This routine proved to not only be erroneous but also unnecessary and was removed. Another interesting result was the reduction in transmission after the rain ended. Figure 7 shows visibility data for that

period. Most of the time it was below 5km in fog. A few days after the first event we noticed some problems with power stability and response to calibration so the instrument was returned for maintenance. After its return we again set up and calibrated. After a period of no rain, we finally had another chance on October 20. Here about 3 mm/hr of rain reduced the transmission to about 18 %. Data for this event is shown in figures 8,9, and 10. The noise in the millimeter data after 2230 hrs is caused by over ranging which we did not edit out. This was probably due to the wet ground. On October 23 we captured another rain event as shown in figure 11. Figure 12 provides the transmission data. Again the rain periods corresponded well. Figure 13 provides the visibility data.On this occasion our PMS precipitation probe was functional and some of the size distribution data is presented in figures 14 and 15. After this day, we had to pack the instrument for shipment to Alaska where it was to be used in snow conditions. However, this test was canceled, so snow data will be collected later.

CONCLUSION

We are very encouraged by the first data from the millimeter wave transmissometer but we have a lot to learn about its use.The addition of the millimeter wave transmissometer is eagerly awaited by the Ft. Belvoir Meteorological Team. It will extend their transmission measurement capability into an important region of future system development. The system has already been scheduled for two field tests. It is important to understand that this new system has been designed to fit in the overall data collection system used by the team so that no additional resources will be required for operational use. The second unit is nearly completed and incorporates changes identified during the testing of the first unit.

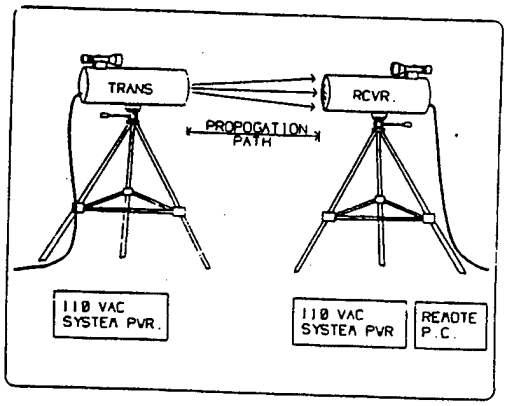


Fig 1. 34 GHZ TRANSMISSOMETER SYSTEM

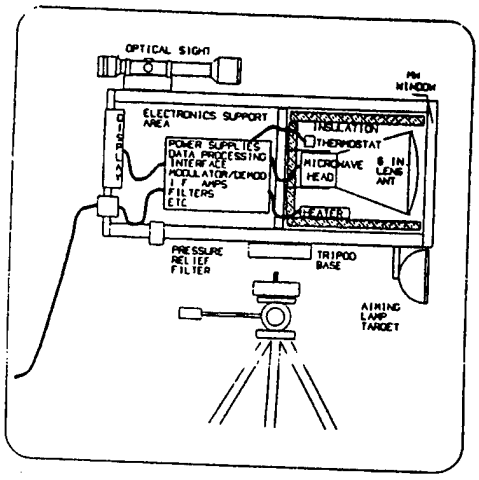


FIG 2. ENVIRONMENTAL HOUSING

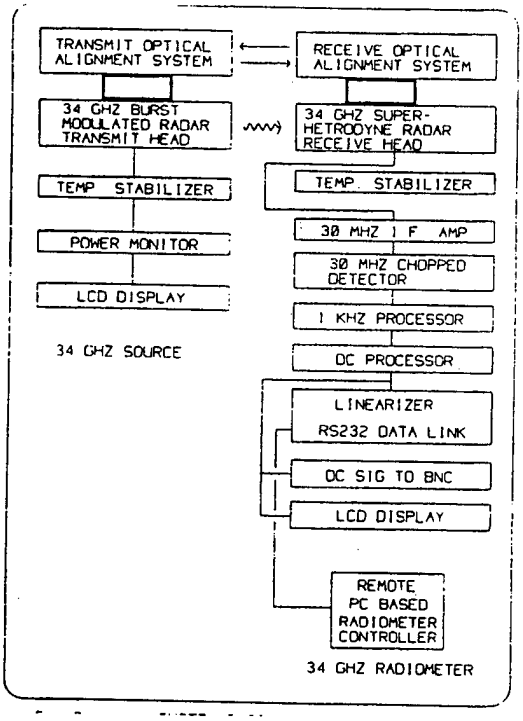


fIG 3. SYSTEM BLOCK DIAGRAM

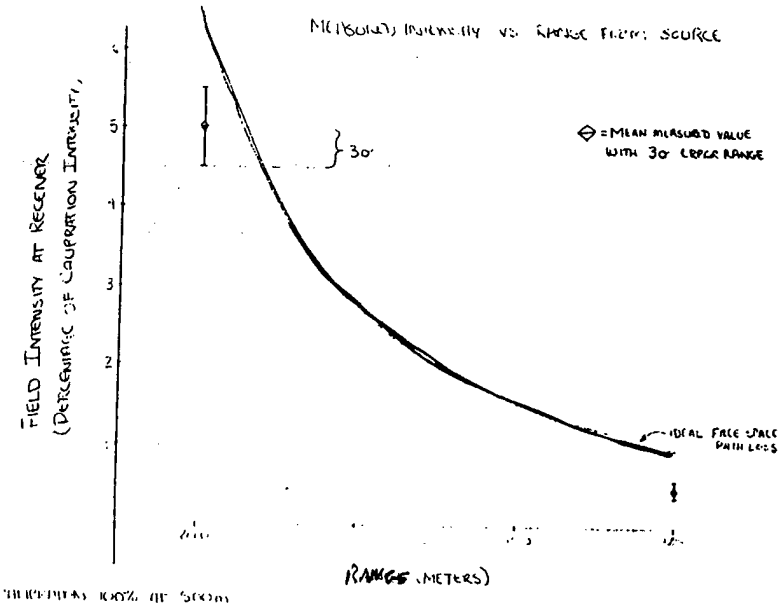


FIG 4. INITIAL FIELD PERFORMANCE TEST

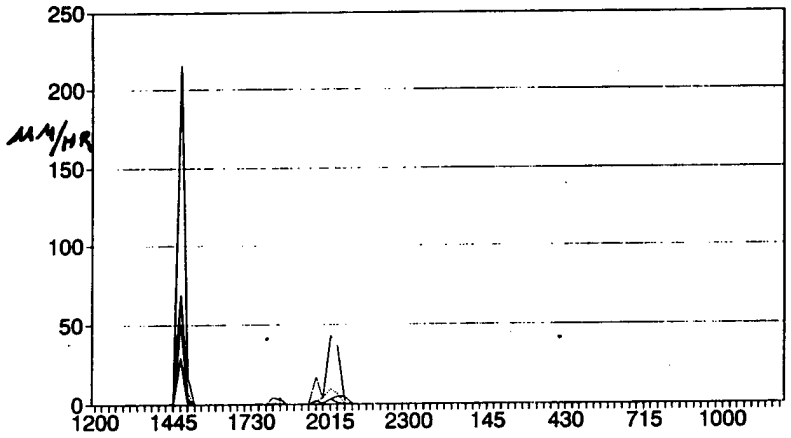


FIG 5. SEPT 26,94 RAINRATE VS TIME

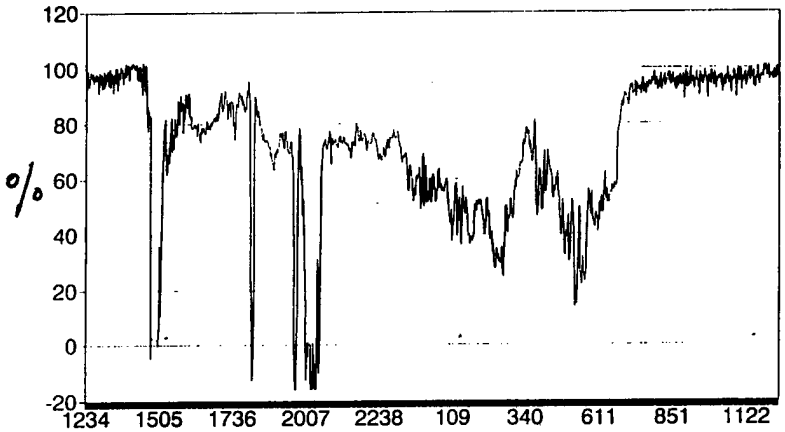


FIG 6. SEPT 26,94 MILLIMETER WAVE TRANSMISSION

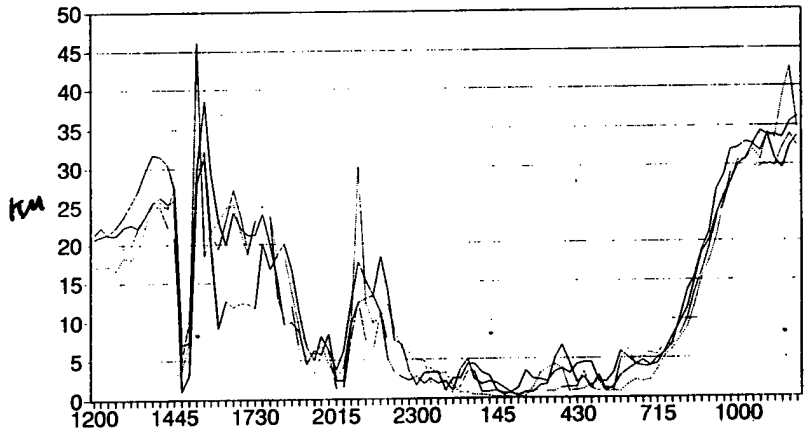


FIG 7. SEPT 26,94 VISIBILITY VS TIME

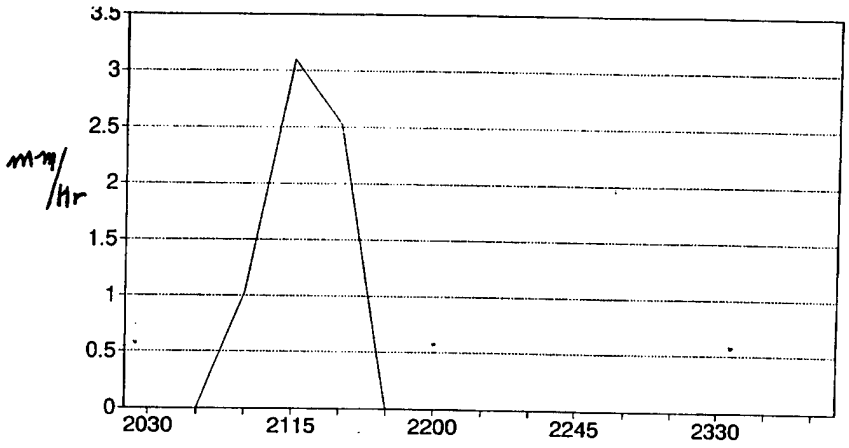


FIG 8. OCT 20,94 RAINRATE VS TIME

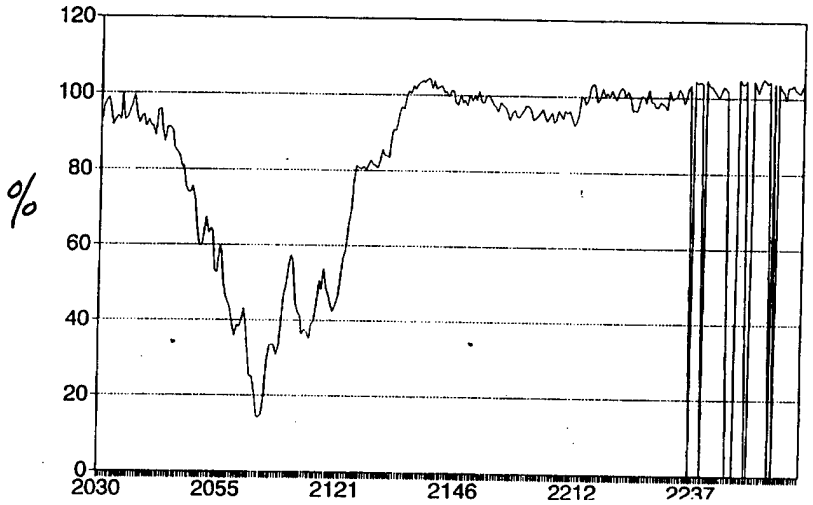


FIG 9. OCT 20,94 MILLIMETERWAVE TRANSMISSION VS TIME

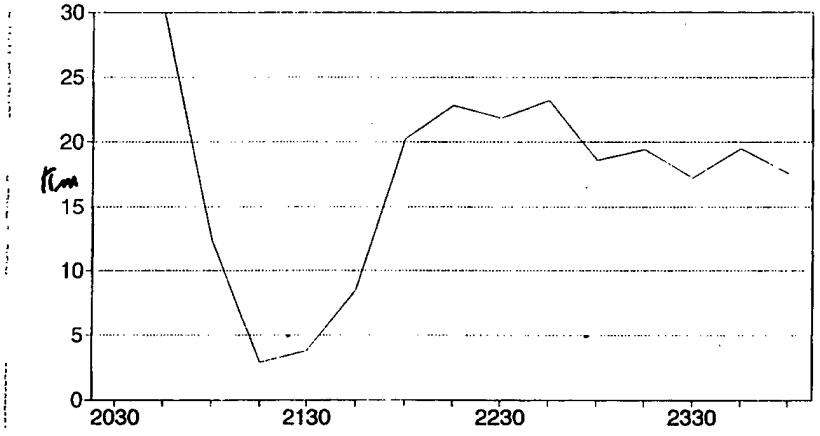


FIG 10. OCT 20,94 VISIBILITY VS TIME

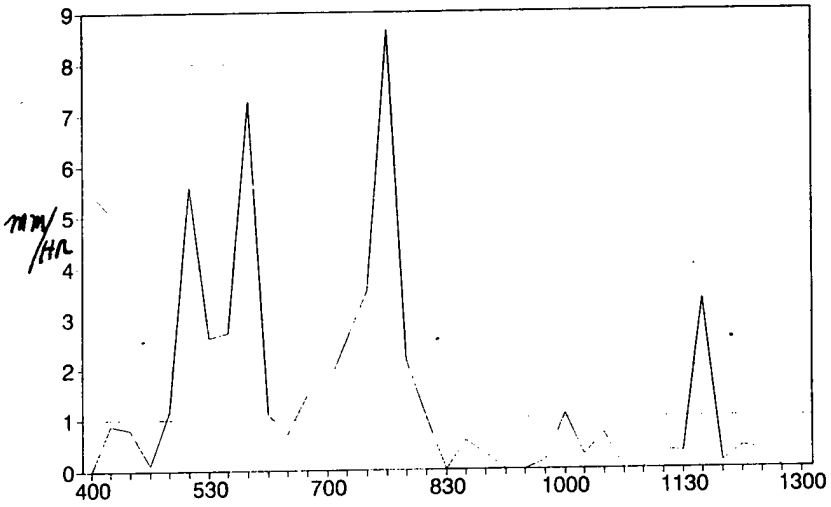


FIG 11. OCT 23,94 RAINRATE VS TIME

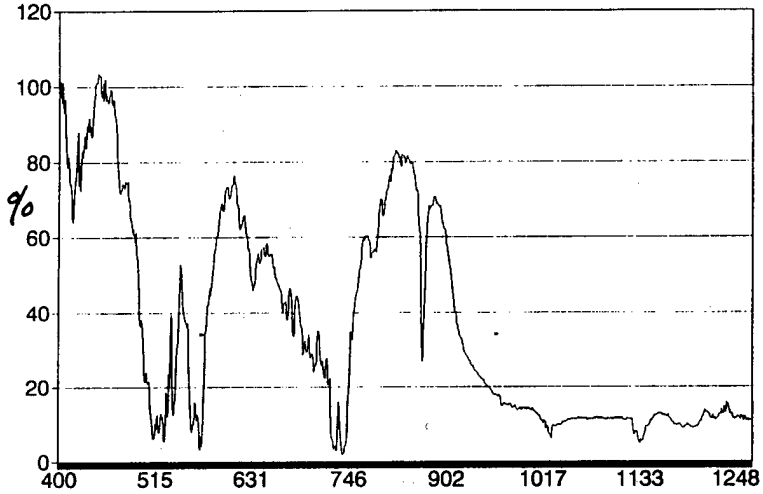


FIG 12. OCT 23,94 MILLIMETER WAVE TRANSMISSION VS TIME

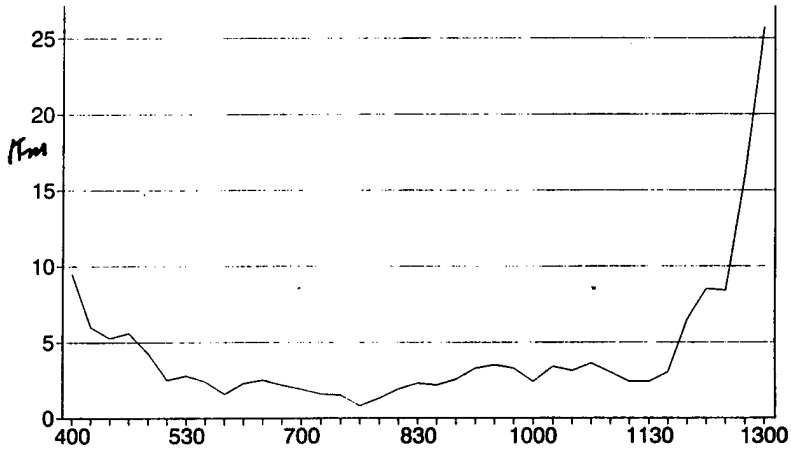


FIG 13. OCT 23,94 VISIBILITY VS TIME

Session V

ATMOSPHERIC PHYSICS

WIND FIELD MEASUREMENT WITH AN AIRBORNE CW-CO_2-DOPPLER-LIDAR (ADOLAR)

S. Rahm and Ch. Werner
German Aerospace Establishment DLR
82234 Oberpfaffenhofen, Germany

ABSTRACT

The small scale wind field in the boundary layer is an important parameter e.g. for the detection of fluxes from pollutants. For this purpose a compact cw CO2 Doppler lidar has been developed that can perform measurements from the ground as well as from an aircraft. In the airborne setup this instrument can easily be installed in the research aircraft FALCON F20 of the DLR. The instrument consists of two racks, one electronic rack (size 56 X 66 X 96 cm) and an optical rack (41 X 62 X 125 cm), which carries the transceiver, the laser and the interferometer optics all together mounted at two sides of an optical breadboard. The transceiver consists of of an 150 mm diameter off-axis-telescope and a Germanium wedge, which provides the conical scan with a cone angle of 60°. The interface to the atmosphere is a Germanium window installed in the bottom of the aircraft. One critical part is the elimination of the Doppler shift due to the platform motion. This can be done at a low flight level by the use of the ground return. At higher flight level, where the ground return is not available, the built in inertial reference system (IRS) of the aircraft will be used for this task. With this instrument was tested, that the wind field can be measured from the aircraft. For battlefield operations (ground based or airborne) the system should have an automatic operation mode. The wind measurement requirements are: wind speed 1 - 30 m/s with an accuracy of 1 m/s and 5° of the direction. The time of one measurement to get the mean wind depends for the ground based system on the atmospheric stability and surface roughness length. It will not exceed 60 s in the worst case.

1. INTRODUCTION

The knowledge of the three dimensional wind field is mandatory for the description of transport phenomena e.g. fluxes of pollutants or dust and also for small scale meteorological effects. To obtain this wind field at the condition of clear air (no rain or fog) a Doppler lidar is the appropriate instrument. For the continuous wave (cw) CO_2 lidar, the energy is focused by the telescope into the region of investigation. Some of the radiation is scattered back by small aerosol particles drifting with the wind speed through the sensing volume. The back scattered

radiation is collected by the telescope and detected by coherent technique. With the laser Doppler method one gets the radial wind component along the beam axis. To determine the magnitude and direction of the wind, some form of scanning is required. With a ground based Doppler lidar the wind of only a small region can be observed. Therefore an airborne system is a good approach to obtain the information about the wind of a larger area in a relative short time. On the other hand with an airborne system one has to deal with some additional problems as there are the influence of vibrations, the safety requirements and most important, the elimination of the platform motion by an appropriate signal processing. This presentation will deal with these problems as well as with the system design and the results of a first test flight.

2. THEORY OF THE WIND EVALUATION

One possibility to measure this wind field is the use of a conical scanning Doppler lidar. The principle of such a lidar is quite simple. Monochromatic light is transmitted into the atmosphere and scattered back by aerosols. At this process the line of sight (LOS) component of the velocity causes a Doppler shift *[eq. (1)]*.

$$\Delta\nu = \frac{2\,\upsilon_{LOS}}{\lambda} \qquad (1)$$

At a wavelength λ = 10,6 µm, 1 m/s LOS velocity corresponds to a Doppler shift $\Delta\nu$ = 189 kHz. The Doppler shift is detected by an optical heterodyning technique. If the local oscillator has the same frequency as the transmitted light, the lidar system is called homodyne, and in the other one heterodyne. If several measurements during one conical scan are evaluated, it is possible to calculate the tree dimensional wind field by applying a sinus fit for example. For this the wind field is assumed to be homogeneous in each level over the measured area. This technique is well approved for ground based systems (Schwiesow et al. 1985), (Bilbro 1980). On the other hand only a few attempts have been made to integrate a Doppler lidar into an aircraft (Bilbro 1980)(Bilbro et al. 1986)(Woodfield et al. 1983), and none of these systems were applying a conical scan. If the laser Doppler system is used on board an aircraft, the speed of the aircraft modifies of the Doppler shift *[eq. (2)]*.

$$\upsilon_{LOS} = \upsilon_{LOS}(\text{wind}) + \upsilon_{LOS}(\text{carrier}) \qquad (2)$$

where υ_{LOS}(carrier) is the carrier speed, and υ_{LOS}(wind) the wind speed both with respect to the lidar line-of-sight (LOS). Normally the wind field is the interesting parameter, therefore the platform motion has to be subtracted by the means of signal processing. This will be done at a low flight level by the use of the ground return. At higher flight level, where the ground return is not available, the built in inertial reference system (IRS) of the aircraft can be used for this task. The platform velocity contribution is the main problem together with the pointing accuracy, but like shown below the data of the IRS can fulfil these strong requirements.

3. SYSTEM SETUP

The Doppler lidar ADOLAR is a homodyne system. This means, that the magnitude of the wind field can be detected but not the sign. The principal setup of this system can be seen in figure 1.

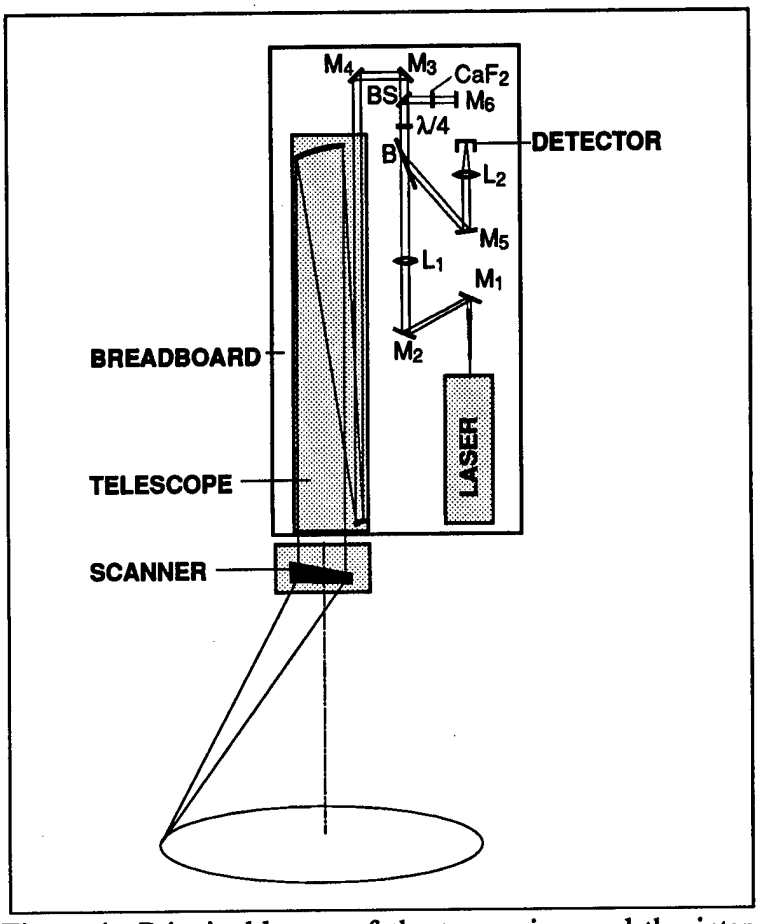


Figure 1. Principal layout of the transceiver and the interferometer optic. At the real system, the telescope is mounted at at the front side of the breadboard and the interferometer optic at the rear.

The laser is a CM1000 from Laser Ecosse with an output power of approximate 3.5 W cw. The laser is operating at single longitudinal mode (SLM), transversal at TEM_{00}, and is p-polarised. The laser beam passes the lens L_1, which is used to adopt the beam parameters of the laser to the telescope, the Brewster window B, and the quarter wave plate which converts the polarisation to a circular one. After passing the beam splitter BS (R = 10 %) the radiation is coupled into the 15 cm off-axis- telescope from Lambda/Ten Optics, which focuses the light to 180 m distance. The wedge scanner provides the conical scan with half a cone angle of 30°. At the measurements described below, one revolution of the scanner needs 20 s. The back scattered light goes the same way back, passes again the quarter wave plate, where its polarisation is converted to the s-state, so that it can be focused onto the detector via the Brewster window B, the mirror M_5, and the lens L_2. The local oscillator (lo) is realised by the beam splitter BS, the CaF_2 plate to adopt the power, and the mirror M_6. The lo-beam is also focussed on the detector and there heterodyned with the back scattered light. The mixing efficiency m (Kingston 1978) is estimated to $m \approx 0.3$ out of the calculated beam parameters (Gaussian for the lo and an Airy pattern for the received light). The detector is a LN_2 cooled MCT-diode with an active size of 200 X 200 µm, and a quantum efficiency $\eta = 0.53$ from Kolmar. The electric beat signal gets amplified with a bandwidth from 1 to 20 MHz. The low cut off frequency is necessary to eliminate EMI from the

laser power supply and the high cut off frequency to reduce the effect of aliasing of noise. The amplified signal is digitised with a sampling rate of 20 MHz and a resolution of 8 Bit. One measurement contains 8 kByte of data which represent a duration of about 0.4 ms. The repetition rate at these measurements was with 2 Hz quite low. One thing to be mentioned is, that the Nyquist frequency was with 10 MHz rather low due to a malfunction of the ADC. But the aliasing effect which occurred at some few measurements has been resolved.

To obtain a mechanical stiff and robust setup, the interferometer optic together with the laser is mounted at one side of an optical breadboard 900 X 300 mm from Newport, and the telescope is fixed at the other side. The breadboard itself is mounted in a light weight aluminium frame, which compensates the average pitch angle of 5.5° of the aircraft. The scanner is fixed below the telescope at the frame. Figure 2 shows the installation of the optical part in the Falcon F20 aircraft.

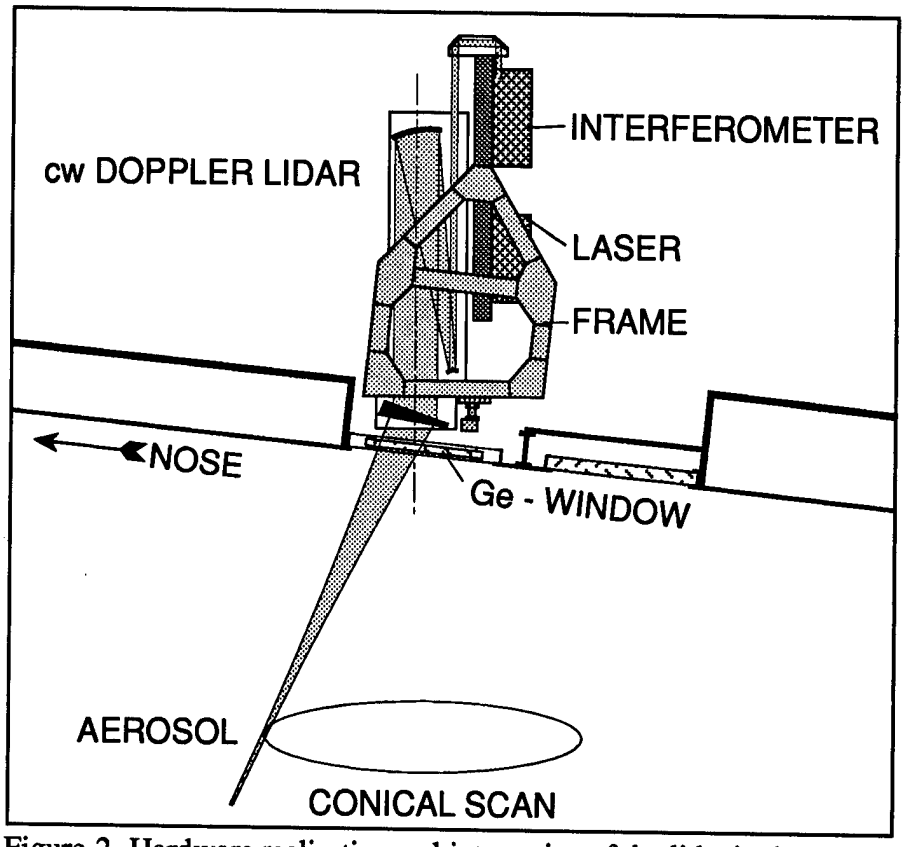


Figure 2. Hardware realisation and integration of the lidar in the Falcon F20 research aircraft.

To reduce the influence of vibration the whole instrument is connected with shock mounts to the aircraft. The electronic equipment, like the cooling unit for the laser, the A/D converter, the computer, the spectrum analyser for quick look etc. are mounted in a standard electronic rack of size 0,55 x 0,65 x 0,95 m in front of the operator.

4. MEASUREMENT OF THE WIND FIELD

In the case of an airborne Doppler lidar we had to deal with some problems. The most important one is the elimination of the platform motion in the detected Doppler signal. ADOLAR was originally designed as a test bed to gain experience concerning the points described above. However the results of the first test flight, discussed below, were so encouraging, that it is now planned to upgrade this cw-system to an operational airborne Doppler lidar for the detection of small scale wind fields. A flight test was performed on May 19, 1994. Test results of the different signatures are shown in figure 3. During this test flight measurements at several height level have been performed. The most interesting scenario, that will described here, was a part of the flight in 315 m height over the „Ammersee", a lake in Bavaria. At this day a rather strong wind was blowing, which was ideal for the test of the system, for each measurement contains information about the LOS velocity from both, the aerosols, and the ground return mostly at different frequencies, so that they can be differed from each other. The algorithm for the signal processing is quite simple. The data set of one measurement (8 kByte) is divided into 16 parts of length 512 Byte. Each of them is processed with a FFT and the resulting power spectra are averaged.

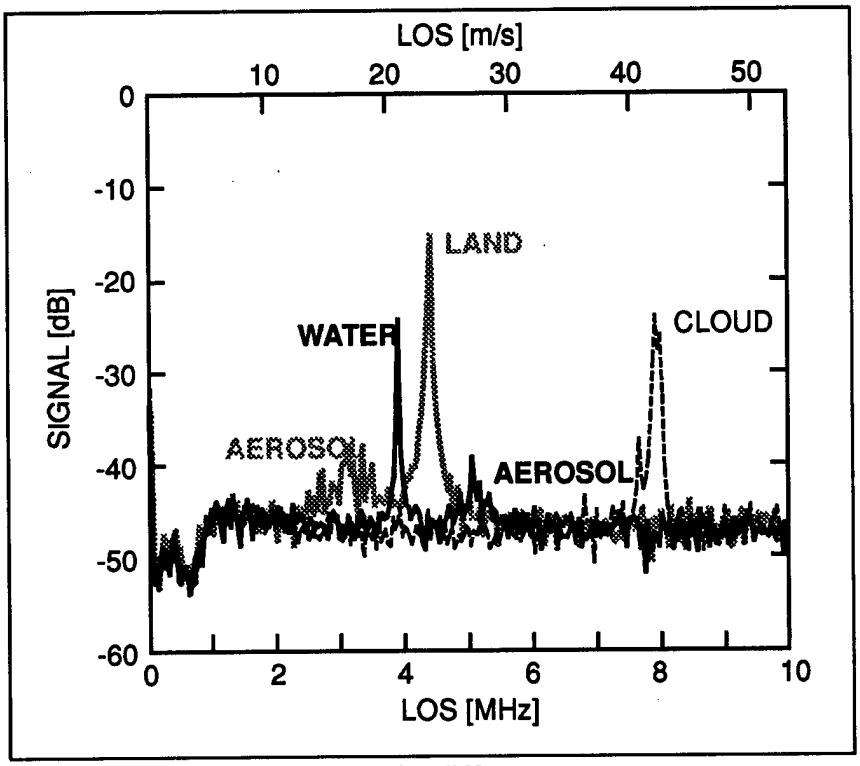


Figure 3. Doppler lidar signals for different targets

Figure 3 shows 3 single measurements at different scan direction and different time (flight altitude) for an first overview. There is a land and sea surface return each together with an aerosol (wind) signal. This is caused by the focal distance of 200 m and the stronger return of land and sea surface from outside the focal volume (*figure 2*). The wind signal is left from the land signal and right from the sea signal caused by the scanning and the aircraft velocity. The LOS difference is in the order of 8 m/s. The third signature comes from a cloud.

The strong narrow peaks in the spectra (*figure 3*) are belonging to to the ground return and the weak broad peaks to the aerosol signal. The spectral width of the peak is an indicator for the coherence time which corresponds to the turbulence. The ground return is therefore narrow, and the peak belonging to the aerosol is rather broad due to the velocity distribution in the focal regime. The intensity of the ground return in the case of water is rather low. A ground return from the land is normally about 10 - 15 dB stronger. As it can be seen (*figure 3*) are the two peaks changing their absolute position as well as their relative position to each other during the scan. This effect and the estimation of an average wind vector will now be discussed more in detail (*figure 4*).

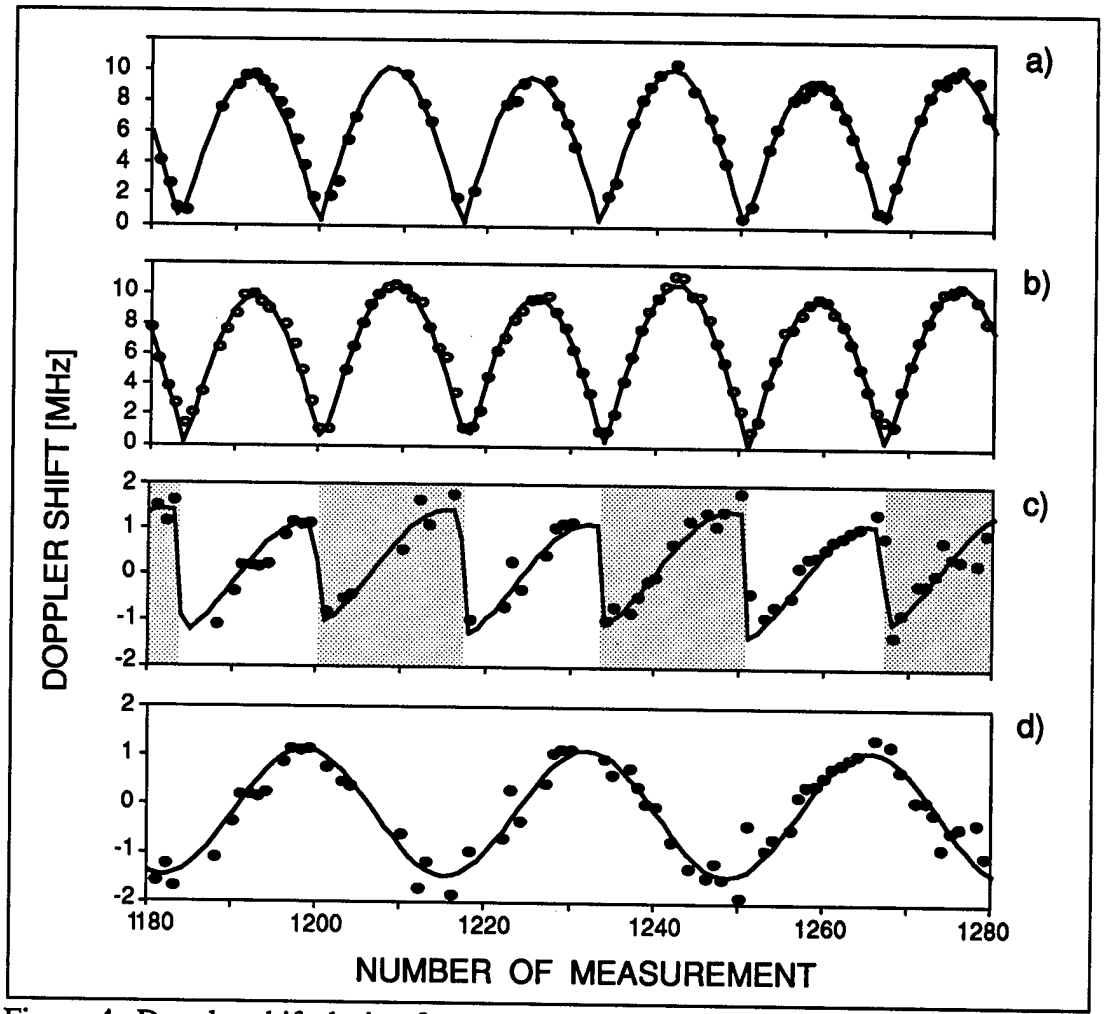


Figure 4. Doppler shift during 3 scanner revolutions. The number of measurement corresponds to the position of the scanner.
a) Doppler shift of the ground return with |sin| fit.
b) Doppler shift of the aerosol with |sin| fit.
c) Difference b)-a).
d) Corrected Doppler shift of the wind field.

The centre frequencies of both peaks (aerosol and ground return) are estimated for the measurements of 3 scanner revolutions (*figure 4a and 4b*). To each couple of points a |sin|

function has been fitted with a least square fit procedure. At a homodyne system, the influence of the platform motion cannot be eliminated by calculating the difference aerosol - ground return. This would lead to the rather confusing result shown in figure 4c. Therefore the graph (*figure 4c*) was divided into two groups of areas, where the sign of one arbitrarily chosen group was changed (*shaded in figure 4c*). This operation leads to the graph in figure 4d. There it can be seen, that mostly the measured values and the sin fit are lying quite close together, only a few points do not fit to the sinus. There are different reasons possible for this effect. First, changes of the attitude of the aircraft and small changes of it's speed are not considered at all at this discussion, and second due to the strong wind and the low level of measurement, there can be expected a lot of turbulences and variations of the wind speed during the observation time.

Out of the coefficients of the |sin| fit an average wind vector was estimated in reverence to the aircraft x-axis and the result has been compared with the data from the inertial reference system (IRS) of the aircraft. This results are shown in table 1.

Table 1. All values in m/s if not other indicated. Comparison of the measured wind field. The results in the level of 159 m over ground has been obtained by the Doppler lidar, and the results at the aircraft level by the IRS.

	Lidar	IRS
ground speed	104,5	104,1
horizontal wind speed at 315 m		19,2
horizontal wind angle at 315 m		61,7°
vertical wind speed at 315 m		0,1
horizontal wind speed at 159 m	13,5	
horizontal wind angle at 159 m	74,3 °	
vertical wind speed at 159 m	0,9	

The results of the ground speed from the lidar and the IRS fit good together. The difference in the wind parameters is due to the different levels, 159 m over ground for the lidar and 315 m for the aircraft.

These points are the most important results of this campaign. The good coincidence between the lidar and the IRS concerning the ground speed is the basis for the evaluation of a three dimensional wind field with an airborne Doppler lidar. Furthermore it has been proved that it is possible to measure a Doppler shift from aerosols with this instrument. Before the next flight the following points will be changed or improved. An acousto optic modulator will be integrated to obtain a heterodyne system so that magnitude and sign of the Doppler shift can be measured. In dependence of this the sampling rate of the ADC must be higher (≈ 100 MHz). To establish a more sophisticated signal processing the information about the attitude, the velocity of the aircraft, and the exact scanner position are required. These parameters have to be stored simultaneously together with the digitised data. With all these points improved, it should be possible to establish an operational Doppler lidar for the measurement of small scale wind phenomena.

REFERENCES

Bilbro, J. W., 1980. "Atmospheric laser Doppler velocimetry: an overview". Optical Engineering, 19: 533-542.

Bilbro, J. W., DiMarzio C., Fitzjarrald D., Johnson, S., and Jones, W., 1986. "Airborne Doppler lidar measurements". Appl. Opt., 25: 3952-3960

Kingston, R. H., 1978. *Detection of Optical and Infrared Radiation.*. Vol. 10 of Optical Sciences, Springer Verlag, New York, 24 pp.

Schwiesow, R. L., Köpp, F ., and Werner, Ch., 1985. "Comparison of cw-Lidar Measured Wind Values Obtained by Full Conical Scan, Conical Sector Scan and Two-Point-Technique". Journ. Atmospheric and Oceanic Technology, 2: 3-14

Woodfield, A. A., and Vaughan, J. M., 1983 "Airspeed and Wind Shear Measurements with an Airborne CO_2 CW Laser". International J. Aviation Safety, 1: 207-224

BEHAVIOR OF WIND FIELDS THROUGH TREE STAND EDGES

Ronald M. Cionco
Battlefield Environment Directorate
US Army Research Laboratory
White Sands Missile Range, NM, 88002-5501 USA

David R. Miller
Natural Resources Management and Engineering Department
University of Connecticut
Storrs, CT, 06269-4087, USA

ABSTRACT

Recently several investigators have indicated that the forest edge effect involves the generation of form drag forces, the appearance of a large pressure gradient, the upward (or downward) deflection of mean flow, the transport of momentum into the leading edge of the canopy, and the advection of the flow characteristics conditioned by the upstream surface across the edge. The purpose of this paper is to quantify the effects of atmospheric stability and wind regime on these edge flow processes. To analyze these effects, the huge Project WIND canopy flow and micrometeorological data base collected by the USA ASL (now the US ARL). The WIND data are tailored for this type of study. Other known data sets are notably limited for this purpose. These raw wind data sets were conditionally selected for periods when the wind was +/- 20 degrees of perpendicular to the stand edge. This procedure resulted in 132, 30 minute periods at the orchard edge and 94 periods at the forest edge. The 30 minute data runs were classified by z/L into three categories: free convection ($z/L < -1$), mixed convection ($-1 < z/L < 0$), and stable ($z/L > 0$) as similarly defined by Panofsky and Dutton. Results of this research demonstrate that the airflow properties conditioned by the upwind surface such as friction velocity, mixing length, and turbulence characteristics are advected for varying distances across and through the tree stand edge depending on the atmospheric stability.

1. INTRODUCTION

Albini (1981), Li et al (1990), Miller et al(1991) and most recently Klaassen (1992) have modeled the air flow across forest edges. They have indicated the edge effect involves the generation of form drag forces, the appearance of a large pressure gradient, the upward (or downward) deflection of mean flow, the transport of momentum into the windward edge of the canopy, and the advection across the edge of the flow characteristics conditioned by the upstream surface. Very few field measurements are available to verify these and subsequent

models. Those that are available were made for limited studies (Miller et al.,1991; Raynor,1971; Thistle, 1988; Wang, 1989; Kruijt, 1993). The data sets are therefore difficult to transfer to other sites and conditions because of instrumentation, spatial sampling, and fetch constraints. None are comprehensive enough to analyze the interactions of the forest edge and the state of the atmospheric boundary layer (stability, etc.) on the local mean wind field except for the Project WIND data base.

During Project WIND, comprehensive (spatial and temporal) micrometeorological measurements were made across the edge of an orchard and a pine forest in north central California (Cionco, 1989) conducted by the US Army Research Laboratory (formerly the USA Atmospheric Sciences Laboratory). The purpose of this paper is to use the measured wind fields at these two edges to quantify the effects of the atmospheric stability and wind regime on the mean wind flow through and over the tree stand edges. Note that although the forest setup will be mentioned, this paper will limit its scope to reporting on the results of the analysis of the Orchard Site.

2. METHODS

2.1 Field Measurements

The four phases of Project WIND were conducted in and about the Sacramento River Valley of Northern California during the period beginning June 1985 and ending October 1987 (Cionco, 1989). One site was a geometrically uniform, almond orchard on the flat terrain of the Sacramento River Valley. The other site was a more complex coniferous forest on the west slopes of the Sierra Nevada Mountains.

In each phase, data were collected over a two week time span for selected periods resulting in two full sets of daytime (1000 to 1600 hrs), nighttime (2200 to 0400 hrs), transition (sunrise and sunset) periods and two full 24 hour diurnal periods (1000 to 1000). The four phases of WIND were conducted during synoptic meteorological regimes of weak marine incursion - Jun/Jul 85, cyclonic activity - Jan/Feb 86, shallow convection - Apr/May 86, and subsidence - Sep/Oct 87.

Identical sets of eight-level micrometeorological towers were located at both orchard and forest sites at three positions during each phase as presented in Table 1. One tower (OT3) is located deep into the canopy 24 tree heights (H) from the canopy's edge. The second tower (OT2) is placed just inside (2.5H) the canopy's edge. The third tower (OT1) was on the extensive and uniformly cut open field 24 H from the canopy's edge in the clearing. Note that OT1 provides the reference profile of the surface layer ambient flow for this study. The sensor heights, variables measured, measurement frequencies and tower locations were reported in detail by Cionco (1989). Complete profiles of the wind components (u,v,w), temperature (T) and relative humidity (RH) were measured at each tower. Note that the orchard canopy was 8m tall whereas the forest canopy averaged 18m tall.

Table 1. Micrometeorological Tower Instrumentation for the Orchard

SENSOR HT	OT1	OT2	OT3
2.0TH	uvw,T/ΔT,RH	uvw,T/ΔT,RH	uvw,T/ΔT,RH
1.7	uvw,T/ΔT,	uvw,T/ΔT,RH	uvw,T/ΔT,RH
1.45	uvw,T/ΔT,	uvw,T/ΔT,RH	uvw,T/ΔT,RH,Rs
1.25	uvw,T/ΔT,	uvw,T/ΔT,RH	uvw,T/ΔT,RH
1.00TH	uvw,T/ΔT,	uvw,T/ΔT,RH	uvw,T/ΔT,RH
0.75	uvw,T/ΔT,	uvw,T/ΔT,RH	uvw,T/ΔT,RH
0.50	uvw,T/ΔT,	uvw,T/ΔT,RH	uvw,T/ΔT,RH,
0.25	uvw,T/ΔT,RH	uvw,T/ΔT,RH	uvw,T/ΔT,RH,Rs
	Rn, P		
Sfc	Hs	------	Hs

2.2 Data Reduction

The raw data sets were conditionally sampled to select all the periods, at least one hour long, when the wind direction was within + or - 20 degrees of normal to the stand edge. The data were then split into even 30 minute run periods. This procedure resulted in 132 thirty minute periods at the orchard edge (60 into the edge and 72 with the wind out of the edge) and 112 thirty minute periods at the forest edge (19 in and 93 out).

Mean fluxes of heat (θ_*) and moisture (q_*) and mixing length (l_m) and the resulting stability parameter (z/L) were calculated from the above canopy profiles by Monin-Obukhov surface layer similarity (Obukhov, 1971) where the method of Rachele and Tunick (1992) and Tunick et al.,(1994) was used in place of the diabatic influence functions of Paulson (1970) and Benoit (1977) as follows.

The 30 minute data runs were classified by z/L (measured in the open field) into three categories: free convection ($-1 < z/L$), mixed convection ($-1 <= z/L <= 0$), and stable ($z/L > 0$). These are similar to the stability classes defined by Panofsky and Dutton (1984), except we group periods when mechanical turbulence dominates and when mechanical turbulence is dampened as follows:

z/L	Panofsky and Dutton Interpretation	This Classification
Strongly negative	Heat convection dominant	Free convection
Negative,but small	Mechanical turb. dominant	Mixed convection
Zero	Solely Mechanical turbulence	Mixed convection
Slight positive	Slight damping of turbulence	Stable
Strong positive	Mech. turb. severely reduced	Stable

These groupings were used because the number of 30 minute runs with slightly positive or zero z/L were limited.

Rawindsonde measurements of the upper air profiles were available every two hours. The stability classifications determined from the surface tower data were compared to the static stability of the boundary layer determined from the rawindsonde data by the method of Stull (1993). Only runs in which both measurements of stability agreed were used. Table 2 lists the number of 30 minute runs in each stability/wind direction category.

Table 2. Numbers of 30 minute runs in each Wind Direction/Stability Category used in the Analysis.

Wind Direction	Free	Mixed	Stable
Orchard:			
Into edge	6	18	36
Out of edge	21	28	23
Forest:			
Into edge	7	10	2
Out of edge	1	5	87

3. RESULTS

The forest edge and orchard edge results were very similar. Therefore the results are presented here for the orchard only to meet space limitations.

3.1 Profile adjustments across the edge

Figure 1 presents average vertical profiles from all of the half hour periods for the three stability classes (stable, mixed convection, free convection) at each tower location with the wind blowing either into (figure 1 a,b,c) or out of (figure 1 d,e,f) the stand edge. For comparison, all the profiles, even those outside the orchard, are scaled by the wind at 8 meters which is the height of the orchard canopy.

In the open field (tower OT1, figure 1a,d) the measurements were all in the surface layer well above the short crop canopy and the scaled profiles demonstrate the effects of stability on the surface layer flow. The profiles from mixed and free convection conditions are very similar with slightly less shear during free convection conditions. The profiles in stable boundary layers diverge drastically from the profiles during convective boundary layer conditions with the overall shear much larger as expected in conditions with little vertical turbulent mixing.

Comparison of the OT1 profiles with wind into and out of the edge shows essentially no difference during convective conditions, but during stable conditions the mean profile has significantly less shear. Apparently the greater mixing capacity above the orchard is

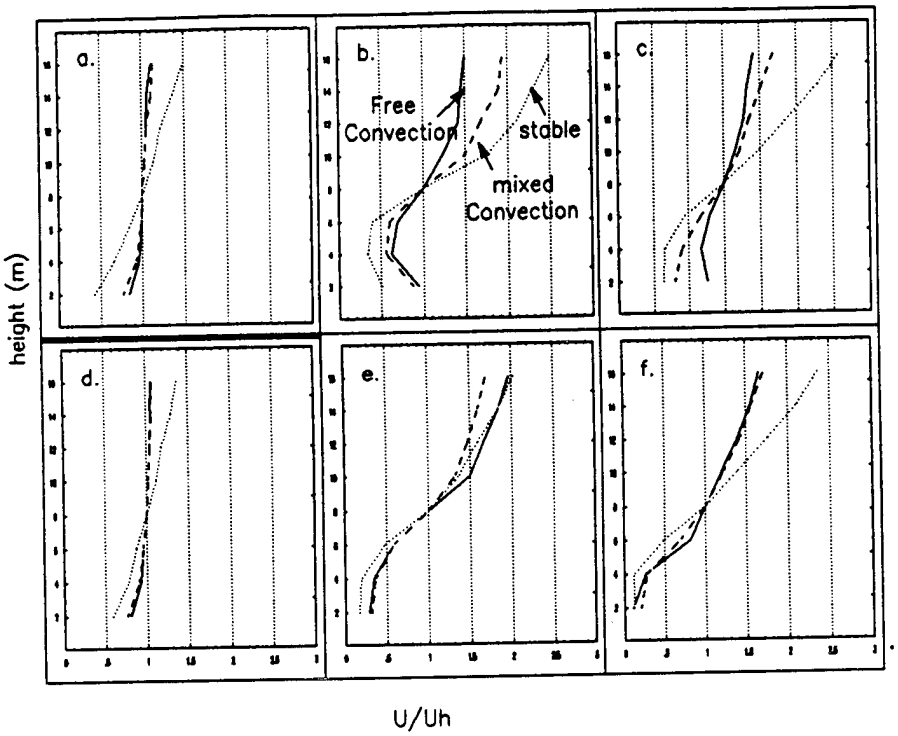


Figure 1. Mean Wind Profiles: With wind into edge: a. at OT1; b. at OT2; c. at OT3 and With wind out of the edge: d. at OT1; e. at OT2; f. at OT3.

transported further than 24 tree heights out of the edge during stable boundary layers but is transported less than 24 tree heights during convective and neutral conditions. Therefore the assumption of infinite fetch is violated at this location during stable conditions but not in a convective boundary layer.

The wind flowing into the edge at 2.5H inside the orchard edge (figure 1b), shows high shear above the canopy as the wind compresses over the top of the canopy and a relatively high wind penetrating the subcanopy trunk space as noted in previous edge studies. Stability effects the magnitude of these flows significantly. In free convection conditions, the below canopy penetration is maximized while in stable conditions the above canopy shear is maximized. Obviously the strength of vertical mixing in the upwind surface layer has a significant effect on momentum absorption and wind penetration into the edge.

At 2.5H inside the leeward orchard edge (OT2, figure 1e), the mixed convection profile is essentially the same as inside the canopy. But the stable and free convection profiles are showing the effect of the relaxation of drag 2.5H downstream from their position. The free convection profile shows greater shear above the canopy and the stable profile shows less shear above the canopy than is present inside the orchard away from the edge. Obviously the downward vertical motion at the leeward edge overshadows the effects of stability at this location.

At 24H windward inside the orchard edge (OT3, figure 1f), the relative effects of stability are similar to outside the canopy when no edge effects are present. The mixed and free convection profiles are very similar while the stable profile shows greater shear above the canopy. Below the canopy, no subcanopy maximum is present and the least penetration of momentum occurs during stable conditions, as expected. Comparison of this to figure 1c, the same position but leeward of the edge, shows the same profile during mixed convection conditions but the stable and the free convection profiles diverge significantly from figure 1f. The free convection has less shear and the stable profile has more shear above the canopy than when the edge was downwind. These characteristics were developed at the edge (figure 1b) and apparently were transported horizontally further than 24H into the edge.

3.2 Scaling Parameter Adjustment Across the Edge

Table 2 presents the mean values of the friction velocity, U*, calculated from the profile data above the canopies, for each stability and wind direction classification at the three orchard tower locations. Comparisons of OT1 and OT3 values shows that U* in the roughness sublayer above the orchard canopy, at OT3, was about two to three times that in the surface layer above the open field, reflecting the greater mechanical turbulence above the rougher surface. In all cases the greatest difference between the open and orchard friction velocities was during stable conditions and the least difference was in free convection conditions.

Table 3. Mean U*, θ* and q* Values Across The Orchard Edge In Different Stability Classes.

Wind Dir	OT1 Free	OT1 Mixed	OT1 Stb	OT2 Free	OT2 Mixed	OT2 Stb	OT3 Free	OT3 Mixed	OT3 Stb
Into Edge									
U*	.22	.39	.15	.19	.28	.24	.39	.83	.41
θ*	-.6	-.27	.005	-1	-.7	.08	-10	-1.2	.1
q*	0	0	.0007	0	-.006	-.0003	0	-.0002	.012
Out of Edge									
U*	.21	.25	.03	.22	.46	.10	.30	.62	.42
θ*	-1.1	-.8	.04	-1.1	-.17	.04	-6.5	-1.0	.11
q*	.004	.002	.004	-.002	-.0009	-.002	-.018	-.003	-.018

The OT2 edge tower data were intermediate between the open and orchard. But the edge tower generally shows U* closer to the open conditions when the wind is from the open field and closer to the orchard values when the wind was from the orchard, reflecting the horizontal advection of the upwind conditions. This is demonstrated visibly when the values in Table 2 are plotted as horizontal profiles in figure 2. The plots show concave curves when the wind is from the open field and convex curvature when the wind is from the orchard. The exception to this is during stable conditions which shows an opposite trend when the the flow is out of the edge.

Figure 3 compares the stability parameters measured simultaneously above the smooth field

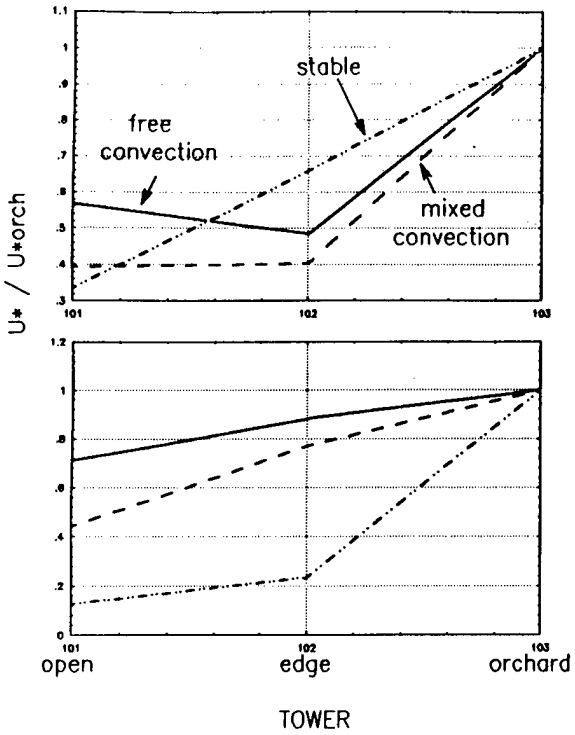


Figure 2. Horizontal profiles of scaled U* across the orchard edge.

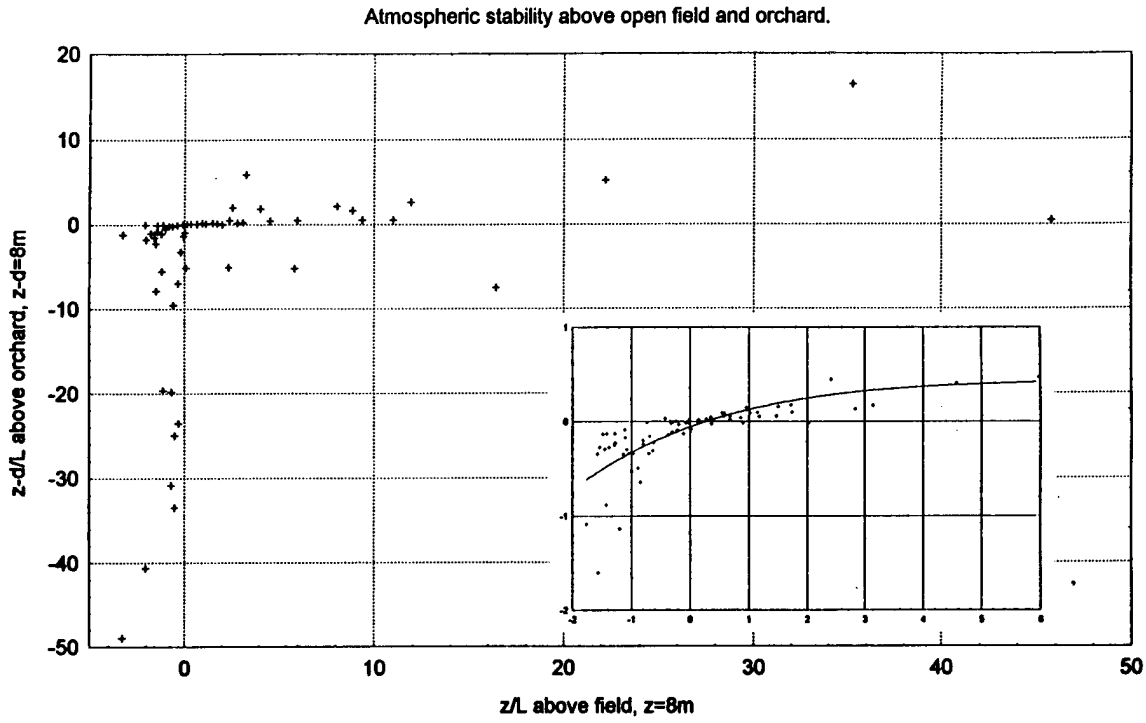


Figure 3. Comparison of stability parameters (z-d)/l and z/l for the orchard and the open field.

mechanical mixing (i.e. orchard (z-d)/L < open z/L). In a convective boundary layer the air and rough orchard. In stable conditions, the flow over the field is significantly less turbulent than that above the orchard. Thus conditions are less stable above the orchard due to higher above the orchard tended to be more unstable than that above the open field when the open z/L was less than -1. Apparently when these conditions of strong convection (high heat flux and low wind speeds) occurred, the drag of the orchard canopy slowed the wind to nearly zero and thus induced nearly free convection above the orchard. When mixed convection dominated the boundary layer ($-1 < z/L < 0$), the above relationship was reversed as shown in the inset graph in figure 3.

Vertical profiles of momentum flux inside the orchard (OT3) and just inside the edge (OT2) are shown in figure 4. The open area tower is not shown because all the measurement levels were in the surface layer and the momentum flux was essentially constant. The orchard tower (OT3) with homogeneous conditions showed profiles similar to other tree stands in the literature. With maximum momentum flux above the canopy and decreasing values below the canopy top.

Remembering that the momentum flux values at the edge tower are not vertical, but are calculated perpendicular to the stream lines, the edge tower shows a maximum at the bottom of the canopy and a minimum just above the canopy top when the wind is horizontal penetration and downward deflection of momentum below the canopy. The above canopy minimum reflects the speed up over the top of the canopy, an increase in horizontal advection and a subsequent reduction in cross streamline turbulent transport.

When the mixed convection wind is from the edge the edge profile is similar to the profile inside the canopy except that the profile is more vertical and showed lower values at all but the below canopy level. The lower vertical momentum transport is a reflection of the relaxation of the flow as it diverges and pours overs the edge.

The θ^* values show that the sensible heat flux was higher over the orchard and lowest over the open field. The very low ($\simeq 0$) q^* values reflected the lack of ET in the arid open field. The orchard was periodically irrigated during the growing season and therefore generally showed a non-zero humidity gradient.

4. DISCUSSION

4.1 Mixing Length Adjustments

Klaassen (1992) pointed out that the mixing length (l_m) adjustment across the edge was non-linear with advection of the mixing length from a different height a significant influence. He modeled the change in l_m across the edge using advection and adjustment:

$$\frac{\partial l}{\partial x} = \frac{\partial l_a}{\partial x} + \frac{\partial l_m}{\partial x} \qquad (1)$$

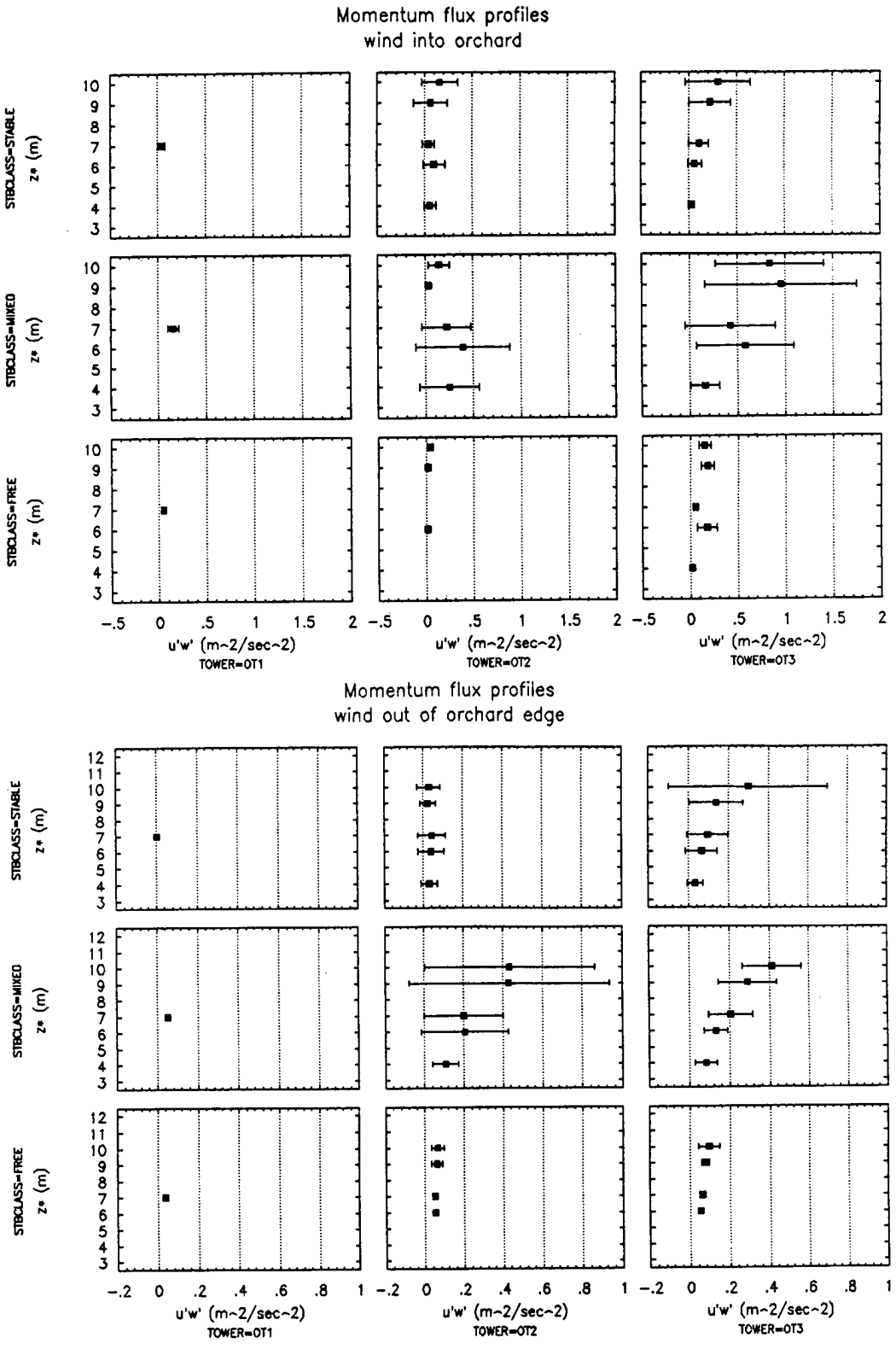


FIGURE 4. Momentum flux profiles in the orchard for flow into (at the top) and flow out of the orchard (at the bottom). Horizontal bars indicate standard deviations.

where the advection is:

$$\frac{\partial l_a}{\partial x} = \frac{w}{u}\frac{\partial l}{\partial z} \tag{2}$$

and the adjustment term is:

$$\frac{\partial l_m}{\partial x} = c_1\left(1 - \frac{l_m}{l_{ma}}\right) \tag{3}$$

where c_1 is the "rate of adjustment" constant and l_{ma} is the fully adjusted mixing length. Klaassen fit the above equation to the data of Bradley and arrived at a value of 10^{-3} for c_1. Using the profile data presented here 10^{-2} is a better fit and there is no change with stability. There is, however, a significant change in the advection term with stability because the ratio w/u changes. Mean values of w/u at the edge (2.5h inside the edge) and interior (24h inside the edge) are plotted in figure 5 for each stability class.

Outside the edge in the open the mean flow was horizontal and parallel at all levels. The slight non-zero values in these average profiles are the average leveling errors of the anemometers. In the interior canopy with no edge effects present (OT3) the mean flow above the canopy is essentially horizontal. Below the canopy there is a general downward motion reflecting the periodic penetration of gusts from above.

Near the edge with the wind blowing into the stand (OT2, figure 8b) the general upward flow over the top and the upward movement of air that penetrated the side of the stand below the canopy are apparent. The large positive below canopy values during stable flow are reflections of the relative absence of turbulent drag as air is forced into the side of the stand and then moves upward. In convective conditions, the kinetic energy of air forced into the side of the stand is dissipated more rapidly by the turbulence and the mean flow at 2.5 h inside the edge does not move upward as readily.

Near the edge with the wind blowing outward (OT2, figure 5), the above canopy flow was essentially the same as the interior flow except when the mechanical mixing was strong (mixed convection) where a slight upward motion can be seen. Below the canopy, the motion was the opposite of the interior canopy where a general upward motion can be seen during convective conditions. The exception is during stable conditions where the flow has changed from downward in the interior to horizontal near the edge. The general upward motion during turbulent conditions ahead of the drag release at the edge was accompanied by a slowdown of the wind at this position.

The streamline slope is an important indicator of how rapidly the wind field is adjusting to the height change in the new surface. Thus from figure 5, when the air is flowing out of the orchard edge, we can see that the flow reacts to the drag release at the edge well before

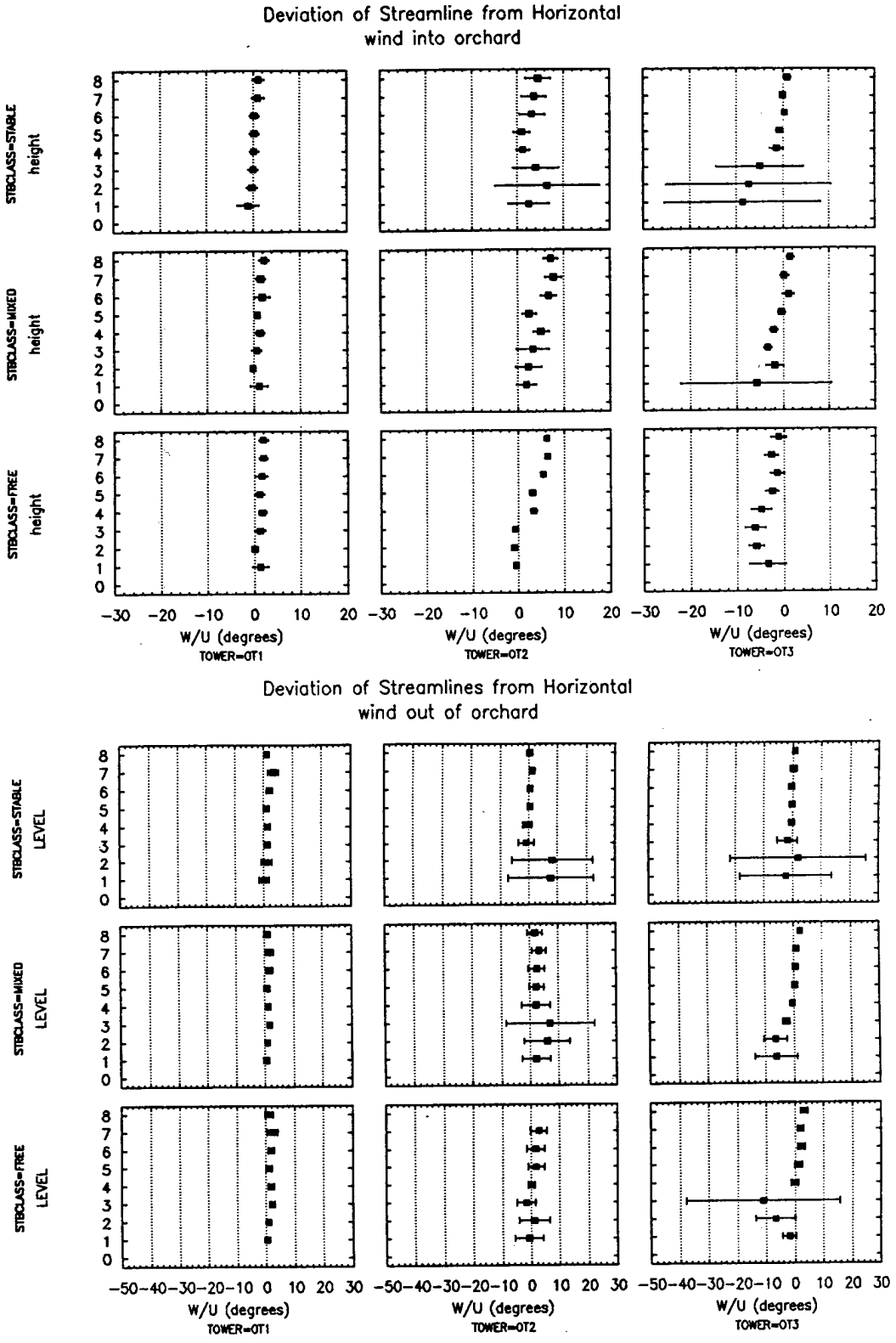


Figure 5. Profiles of the streamline angle, W/U, with wind into the stand (a) and with wind out of the stand (b). Horizontal bars indicate standard deviations.

reaching the edge. We can infer that the adjustment length of the vertical component is longest above canopy in stable conditions and shortest in free convection.

5. CONCLUSIONS

Stability has a major effect on the canopy-air interaction at tree stand edges. In a stable boundary layer, the air over the tall canopy is less stable than that over the open field due to higher turbulent mixing induced by the rougher canopy. In a convective boundary layer, the absolute wind speed interacts with the two canopies differently. At very low wind speeds, the canopy drag reduces the wind enough that free convection conditions occur above the orchard while mixed convection dominates the open field. At moderate and high wind speeds, the higher turbulence over the orchard keeps the air very close to neutral while the open field is dominated again by mixed convection.

The strength of vertical mixing in the upwind surface layer has a significant positive correlation with momentum absorption and wind penetration into the edge. Whereas at the leeward edge, the downward vertical motion overshadows the effects of stability at this location and the flow reacts to the drag release at the edge well before reaching the edge.

The greatest difference between the open and orchard scaling parameter u^* was during stable conditions and the least difference was in free convection conditions. The temperature scaling parameter, θ_*, showed that the sensible heat flux was higher over the tall canopy and lowest over the open field. q^* was zero over the non-irrigated open fields, but indicated measureable latent heat flux occurring over the tree canopies.

Upwind conditions are advected horizontally across the edges and the adjustment length depends on stability. The adjustment length of both the u and w components are longest above the orchard in stable conditions and shortest in free convection.

REFERENCES

Albini, F. 1981. A Phenomenological Model for Wind Speed and Shear Stress Profiles in Vegetation Cover Layers. *J Appl. Meteorol.* 20:1325-1335.

Benoit, R. 1977. On the Integral of the Surface Layer Profile-Gradient Functions. *J Appl. Meteorol.* Vol 16:859-860.

Cionco, R. M. 1989. Design and Execution of Project WIND. Proceedings of 19th Conference on Agr and Forest Meteorol. Charleston, SC. AMS, Boston. MA.

Klaassen, W. 1992. Average Fluxes from Heterogeneous Vegetated Regions. *Boundary Layer Meteorol.* 58:329-354.

Kruijt, B. 1994. *Turbulence Over Forest Downwind of an Edge.* PhD Dissertation, Dept. of Physical Geography, University of Groningen, The Netherlands. 156p.

Li, Z. J., J. D. Lin, and D. R. Miller. 1990. Air Flow Over and Through a Forest Edge: A Steady-state Numerical Simulation. *Boundary Layer Meteorol.* 51:179-197.

Miller, D. R., J. D. Lin, and Z. N. Lu. 1991. Air Flow Across an Alpine Forest Clearing: A Model and Field Measurements. *Agr. and Forest Meteorol.* 56:209-225.

Obukhov, A. M. 1971. Turbulence in an Atmosphere with a Nonuniform Temperature. *Boundary Layer Meteorol.* 2, 7-29.

Panofsky, H. A. and J. A. Dutton. 1984. *Atmospheric Turbulence.* John Wiley, N. Y.

Paulson, C. A. 1970. The Mathematical Representation of Wind Speed and Temperature Profiles in the Unstable Atmospheric Surface Layer. *J Appl. Meteorol.* Vol. 9:857-861.

Rachele, H. and A. Tunick. 1992. Energy Balance Model for Imagery and Electronmagnetic Propagation. Technical Report ASL-TR-0311, US Army Atmospheric Sciences Laboratory, White Sands Missile Range, NM 88002-5501.

Raynor, G. 1971. Wind and Temperature Structure in a Coniferous Forest and a Contiguous Field. *Forest Science* 17:351-363.

Stull, R. B. 1991. Static Stability-An Update. *Bul Am. Meteorol. Soc.* 72(10):1521-1529.

Thistle, H. W., Jr. 1988. Air Flow Through a Deciduous Forest Edge Using High Frequency Anemometry. Ph.D. Dissertation. Department of Natural Resources Management and Engineering, University of Connecticut, Storrs, CT 06268. 211 pp.

Tunick, A., H. Rachele, F. V. Hansen, T. A. Howell, J. L. Steiner, A. D. Schneider and S. R. Evett. 1994. Rebal '94 - A Cooperative Radiation and Energy Balance Field Study for Imagery and E. M. Propagation. Bul. American Meteorol. Soc. 73(3):421-430.

Wang, Y. 1989. Turbulence Structure, Momentum and Heat Transport in the Edge of Broad Leaf Tree Stands. Ph.D. Dissertation. Dept. of Natural Resources Management and Engineering & Civil Engineering, University of Connecticut, Storrs, CT 06268 137 pp.

Proceedings of the 1994 Battlefield Atmospherics Conference, 26 Nov - 1 Dec, 1994 White Sands Missile Range, New Mexico

TRANSILIENT TURBULENCE, RADIATIVE TRANSFER, AND OWNING THE WEATHER

R.A. Sutherland, Y.P. Yee and R.J. Szymber
U.S. Army Research Laboratory
Battlefield Environment Directorate
White Sands Missile Range, New Mexico 88002-5501

ABSTRACT

A major technical barrier encountered in modeling radiative processes in the atmospheric boundary layer involves making proper account of turbulent and radiative interactions. Exact solutions are not possible due to the problem of closure of the underlying differential equations and the complexity of both the turbulent and radiative processes. The most direct effect of the radiative interaction is to alter the energy balance at the surface and cause differential heating in the aerosol layer. These effects then alter the local vertical profiles of temperature, aerosol concentration, and other meteorological variables which have an effect on the overall stability of the layer. However most conventional micro-meteorological models either ignore radiative processes entirely or utilize sub-grid parameterization schemes which may not be applicable to the modern, aerosol-laden, "dirty battlefield" environment. On the other hand many conventional radiation models ignore the turbulent interaction by focusing only on cases where the turbulent-radiative heat flux ratio is small. In this paper we offer an approximate solution to handle both radiation and turbulence using a modified two-stream radiative transfer scheme of McDaid (1993) in combination with a relatively new "transilient" turbulence theory of Stull (1987) and others. In this paper we extend the Stull method to incorporate radiative interactions making special account for such radiative processes as absorption, extinction, thermal emission, and multiple scattering. The research is relevant to Army applications involving modeling and simulation of boundary layer processes and contributes to the scientific basis of programs in "Owning the Weather" and limited weather modification.

1. INTRODUCTION

The Army has had a longstanding interest in simulating and modeling the effects of the "dirty battlefield" on boundary layer micro-meteorological processes. The main emphasis in the recent past has been on the direct effect of aerosols on electromagnetic propagation. More recently it has been realized that these same processes can have a significant effect on critical environmental parameters (Yee, et.al. 1993a,b) and boundary layer destabilization processes (Lines and Yee, 1994; Grisogono and Keislar, 1992; Grisogono, 1990 and Telford, 1994). Other relevant work on a larger scale and not directly involving the turbulent reaction has been published for fogs by Bergstrom and Cogley (1979) and Saharan dust by Carlson and Benjamin (1980). More recently the idea of "Limited Weather Modification" through the use of aerosol obscurants and artificial fogs has been considered in the ARL "Own the Weather" program (Szymber and Cogan, 1994). Also the relevance of such a capability to the Army mission is discussed in the recent STAR 21 report published by the National Research Council (STAR 21 - Strategic Technologies for the Army of the Twenty-First Century, 1993). However one of the major technical barriers in modeling the relevant physical processes has been in the understanding of the nature of turbulent-radiative interactions and the attendant effects on the structure of the atmospheric boundary layer and it is this problem that we are addressing here.

2. PHYSICS OF THE PROBLEM

One of the questions that arose during the initial phases of this work concerned the magnitude of the radiative effect as compared to the turbulent effect. Whereas it is certainly true that for strong winds the effect of turbulence will dominate the radiative effect, it is not so clear which is more significant at the lower wind speeds. We can gain some insight into this question by examining fogs where the radiative effect has been studied. This is done in the plot of figure 1 which is based upon an expression from Oliver, et. al. (1978) which we have modified slightly to express the ratio of radiative-to-turbulent heat flux density as a function of the friction velocity, u^*.

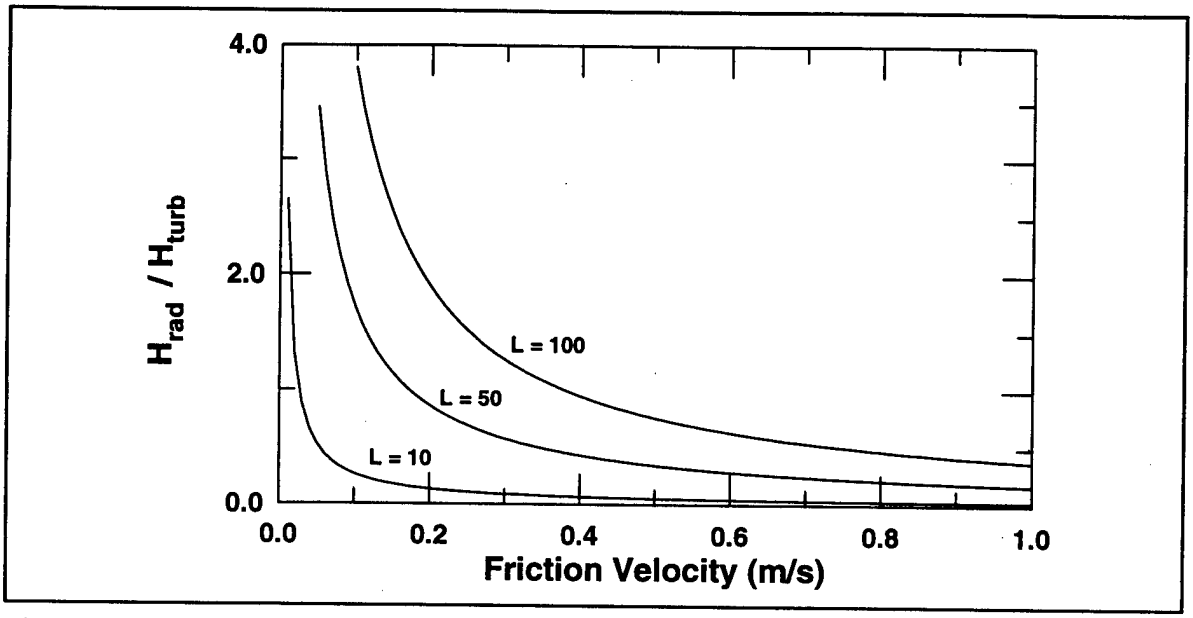


Figure 1. Plot showing the radiative-to-turbulent heat flux ratios as a function of friction velocity for fog thickness of 10, 50, and 100 meters.

As expected, the plot shows the radiative flux to dominate at low wind speeds (friction velocity) and to diminish as the wind speed increases. Note, for example, that for a layer thickness of 50 meters that the radiative flux is greater than the turbulent flux for all values of u^* less than about 0.20 m/s and is at least 10 percent of the turbulent flux out to a value of 1.0 m/s. The calculations, although approximate, do give a qualitative indication of the significance of radiative effects.

The physics of the problem is explained with the aid of the sketches in figure 2 which show a hypothetical example of the effect of radiation and turbulence on profiles of temperature, T, and aerosol concentration, C. Figure 1a sets the initial condition of a hypothetical early morning temperature inversion over an isothermal layer near the surface. It is assumed that, at some height, the inversion gives way to a lapse condition as indicated by the upper dashed line. In figure 1a we also assume a Gaussian aerosol concentration profile with a maximum in the isothermal layer.

The effect of the solar radiation is to first set up an "energy balance" at the surface that results in an increase in the sensible heat flux density, H. The second effect is to cause heating of the entire layer at a rate dependent upon the concentration and radiative properties of the underlying aerosol. Because of the presence of the higher aerosol concentration near the surface, the change in the profile due to radiative heating will be most affected near the surface. This is also where surface induced radiative and

turbulent heat fluxes are most significant. The overall effect is shown in figure 2b as an increase in the temperature of the isothermal layer and the development of an unstable lapse condition near the surface. In this step the upper level inversion remains almost unaffected by the direct heating due to the lower aerosol concentration at this level. Also during this step the aerosol concentration is not directly affected by the radiative heating.

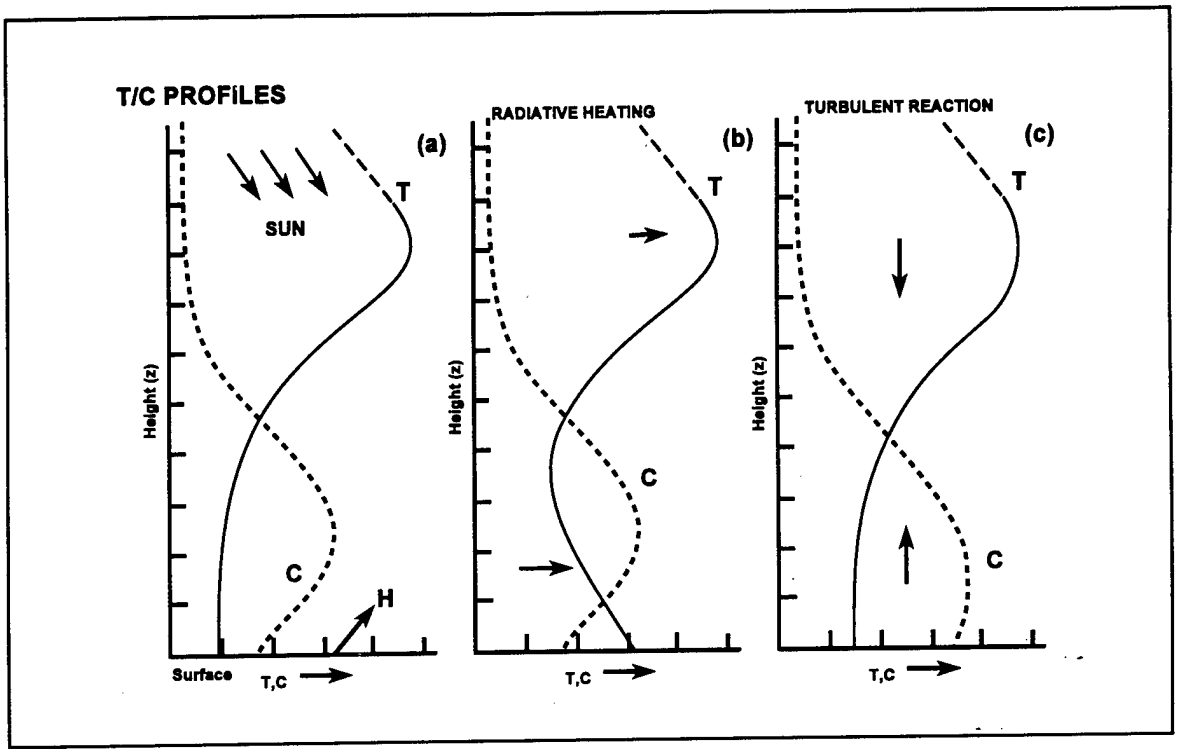


Figure 2. Sketch demonstrating the stages of the radiative-turbulent interaction and the effects on profiles of temperature, T, and aerosol concentration, C.

In figure 2c we show the combined effect of radiative cooling and the induced turbulence which tends to counteract the radiative forcing by producing an upward "mixing" of the hot air from the surface with the relatively colder air above. This step may be viewed as a (turbulent) reaction to the unstable layer created near the surface. Note from figure 2c that the overall effect results in a tendency toward neutral. Note also in figure 2c that the concentration profile has also changed due to the actual movement during the mixing process. The final step of the process that takes place simultaneously with the turbulent reaction is due to radiative cooling by thermal self emission to an extent dependent upon both the temperature profile and the concentration levels.

In this paper we present our results in modeling the processes sketched in figure 2 using a combination of radiative transfer theory and a relatively new "transilient" approach to modeling the turbulent interaction due to Stull and co-workers at the University of Wisconsin (Stull, 1984, 1986, 1993; Stull & Takehiko, 1984; Stull & Driedonks, 1987; see also Cuxart, et.al., 1994).

3. RADIATIVE MODELS

The radiative transport model consists of two parts; one to treat the effect of radiative heating of both the air column and the surface (i.e. radiative "forcing") and one to account for radiative cooling due to thermal self emission (i.e. radiative "reaction"). The radiative transport model is composed of two parts; one treating solar band (shortwave) radiation and

another treating thermal band (longwave) radiation. In both cases effects of multiple scattering and absorption are treated using a modified two-stream formulation originally due to Adamson (1975) as modified by McDaid (1993). This particular model has the advantage of relative simplicity and can be modified to treat inhomogeneities using first order corrections developed by Sutherland (1988).

Both models, and the turbulence model described later, assume a five level aerosol layer as illustrated in the sketch of figure 3. Each layer is assumed to be homogeneous and described by a single value for temperature, wind speed, humidity, and aerosol concentration.

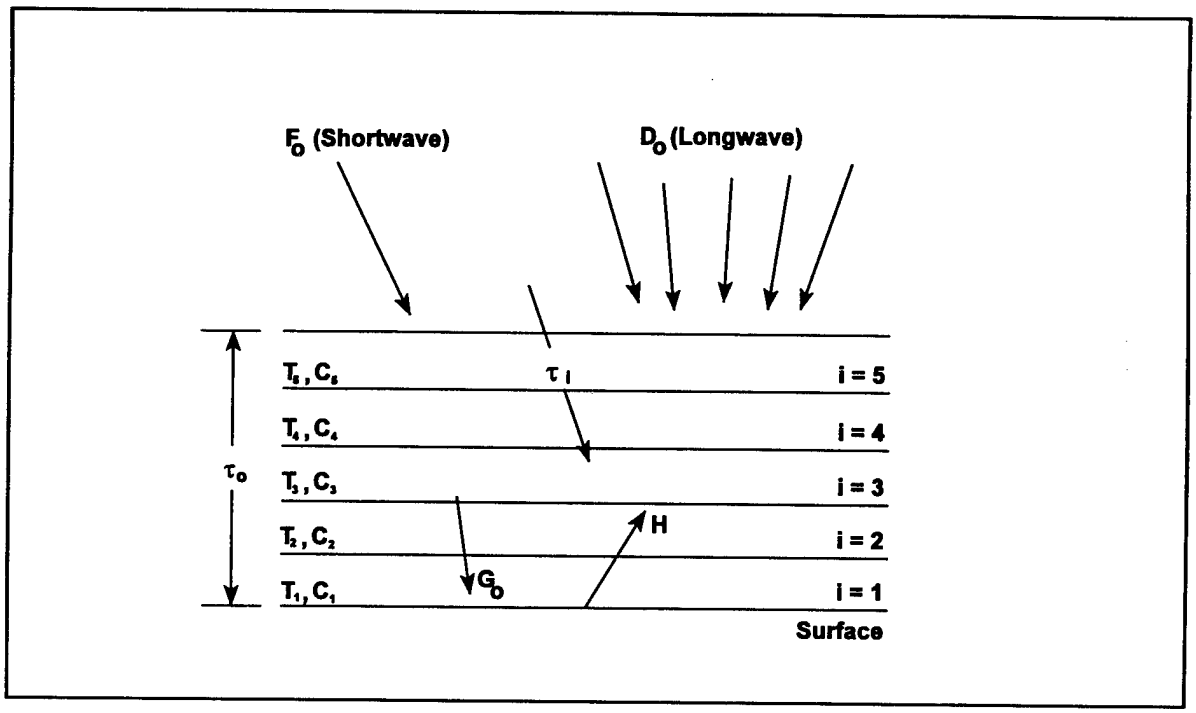


Figure 3. Sketch describing of the five layer model. Note that the optical depth, τ, is referenced positive downward.

The equations for calculating the radiative fluxes at each layer interface are written in general as follows:

Shortwave:

$$F^s(\tau) = \mu_o F_o e^{-\tau} + \mu_o F_o [T^*(\tau;\omega_o,g) - R^*(\tau;\omega_o,g)] \qquad (1)$$

$$+ A_o G_o E_3(\tau_o - \tau) + A_o G_o [T^*(\tau_o - \tau;\omega_o,g) - R^*(\tau_o - \tau;\omega_o,g)]$$

Longwave:

$$F^l(\tau) = D_o E_3(-\tau) + D_o [T^*(\tau;\omega_o,g) - R^*(\tau;\omega_o,g)] \qquad (2)$$

$$+ A_o G_o E_3(\tau_o - \tau) + A_o G_o [T^*(\tau_o - \tau;\omega_o,g) - R^*(\tau_o - \tau;\omega_o,g)]$$

where τ is the optical depth at any level inside the layer and τ_o is the

total optical depth of the layer. In eq. (1) F_o is the solar band irradiance incident at a zenith angle θ_o [$\mu_o=|Cos(\theta_o)|$] at the top of the layer and in eq. (2) D_o is the total thermal band downwelling hemispherical irradiance at the top of the layer. In both expressions A_o is the surface albedo and G_o is the downwelling surface irradiance both taken as appropriate to the particular bandpass of interest (i.e. shortwave or longwave). Other quantities are; aerosol scattering albedo, ω_o, and the optical phase function asymmetry parameter, g, both of which are a function of the aerosol type and the bandpass under consideration. In both expressions $E_3(x)$ is the well known exponential integral and the functions R^* and T^* are the diffuse transmission and reflection operators which are, strictly, complex functions of the optical depth that account for effects of multiple scattering and absorption and described in greater detail elsewhere (Sutherland 1988). For purposes here we use a less accurate but nevertheless useful approximation based upon a modified two-stream approximation due to McDaid (1993). Some typical values of the R^* and T^* functions are plotted in figure 4.

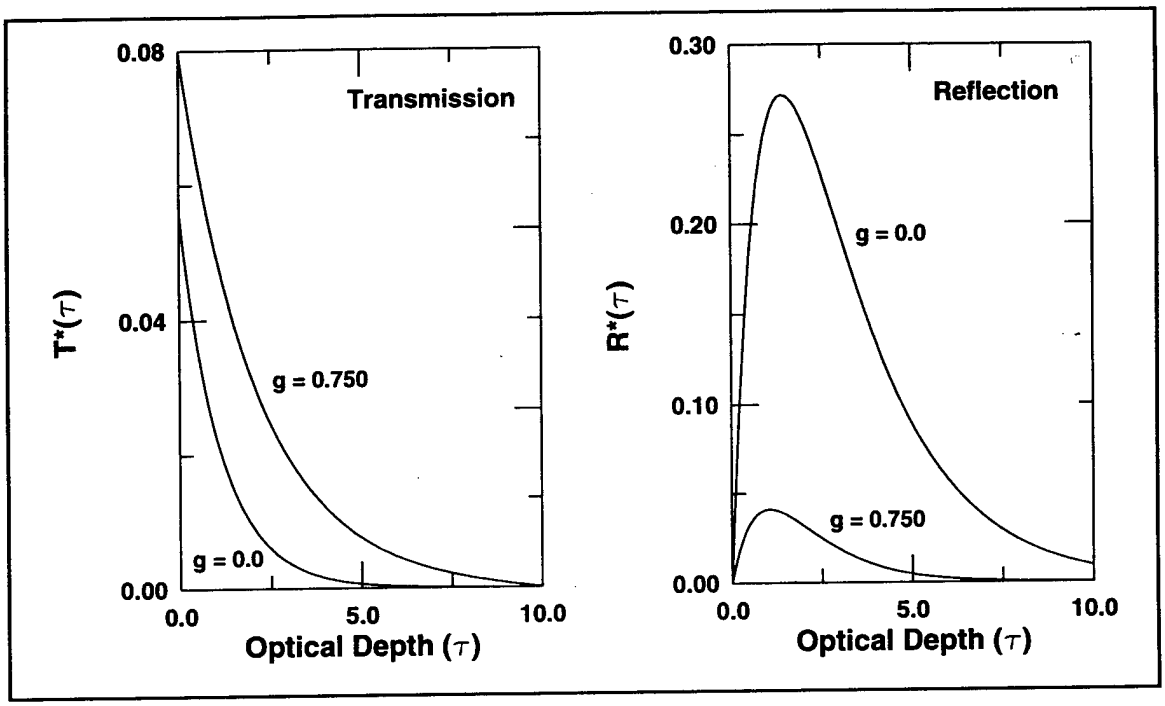


Figure 4. Representative plots of the multiple scattering functions for diffuse reflection, R^*, and transmission, T^*,.

In all of the above expressions the surface irradiance, G_o, is approximated to account for the effects of the aerosol layer as:

Shortwave:

$$G_o=\mu_o F_o[e^{-\tau_o}+T^*(\tau_o;\omega_o,g)] \quad (3)$$

Longwave:

$$G_o=D_o[E_3(\tau_o)+T^*(\tau_o;\omega_o,g)] \quad (4)$$

The net radiative flux at any level in the layer is determined by repeated application of eqs. (1) and (2), then the time rate of change of temperature due to radiative heating for each level i is given by:

$$\frac{dT_i}{dt} = \frac{1}{\rho C_p \Delta z} [\Delta F_i^s + \Delta F_i^l]; i \neq 1 \quad (5)$$

$$\frac{dT_i}{dt} = \frac{1}{\rho C_p \Delta z} [H^s + H^l]; i = 1 \quad (6)$$

where the quantity ρC_p is volumetric specific heat of air, Δz is the sub-layer thickness and ΔF_i is the net radiative flux density entering the i^{th} layer for either the shortwave (superscript s) or longwave (superscript l) spectral regime. As indicated, the second expression applies only to the layer nearest the surface and utilizes the modeled surface heat flux density, H.

In practice the above expressions are used in a matrix formulation relating temperature rate of change to height. For the radiative forcing terms this results in a diagonal matrix. For the self emission terms however there is a need to account for transfer of (thermal) radiation from one level to the next as well as the self emission. This results in a full matrix with elements approximated by:

$$R_{ij} = \epsilon_i \epsilon_j (\sigma T_i^4) E_3 |\tau_i - \tau_j|; i \neq 1 \quad \textbf{(9)}$$

$$R_{ij} = \epsilon_o \epsilon_j (\sigma T_i^4) E_3 |\tau_i - \tau_j|; i = 1 \quad \textbf{(10)}$$

where σ is the Stefan-Boltzmann constant and the layer emissivity, ϵ_i, is given simply as $\{\epsilon_i = [1 - \omega_o]\ [1 - e^{-\Delta\tau}]\}$ where $\Delta\tau$ is the layer optical thickness. As before the first layer (i = 1) is an exception and requires accounting for surface emissivity, ϵ_o.

4. TURBULENT REACTION MODEL

We now turn attention to the turbulent reaction model where we borrow strongly from the theory of "transilient turbulence" developed over the years by Stull and co-workers at the University of Wisconsin. A complete description of the theory can be found in the cited references and in the following paragraphs we give only a cursory description. The direct effect of the radiative forcing is to alter the temperature profile, and this, in turn, results in the creation of an unstable sub-layer region as explained in the discussion of figure (2). The creation of this instability then sets up (turbulent) motions in the layer which tend to oppose the cause of the forced instability. The degree to which this happens, and whether or not the reaction will be turbulent or non-turbulent, depends upon several factors including the temperature and wind speed profiles and the general environmental conditions. One quantifiable measure of the strength of the instability is the Richardson Number given by:

$$R_i = \frac{(g/T_o)\, dT/dt}{(dU/dz)^2} \quad \textbf{(11)}$$

where T is air temperature, u is wind speed, g is acceleration of gravity, and T_o is a reference temperature. The Richardson Number represents the ratio

of the thermal (static) to mechanical (turbulent) fluxes. Large values imply a stable layer and small values imply an unstable layer. Another important quantity is the turbulent kinetic energy, E_{turb}, which is a complicated function of both the thermal and mechanical forces and is given in one dimensional differential form as:

$$\frac{dE_{turb}}{dt} = -\overline{u'w'}\frac{dU}{dz} - \overline{u'w'}\frac{dV}{dz} + \frac{g}{T_o}\overline{w'\theta'} - \epsilon_{turb} \qquad (12)$$

where u', w', θ' represent turbulent fluctuations in wind and potential temperature and U,V, θ represent their time averaged counterparts. The quantity ϵ_{turb} is the turbulent energy dissipation rate.

In a classic series of papers, Stull and co-workers have worked up a theoretical scheme that utilizes the above expressions in a formulation representing the time dependent turbulent reaction effect on any scaler property. The result, when adapted to our five layer model, is expressed in matrix form as:

$$[T_k]_j = [X_{ij}]_{\Delta t}[T_k]_i \qquad (13)$$

$$[C_k]_j = [X_{ij}]_{\Delta t}[C_k]_i \qquad (14)$$

where $[T_k]$ and $[C_k]$ are five component column vectors representing the initial (subscript i) and final (subscript j) temperature and concentration profiles and $[X_{ij}]_{\Delta t}$ is the time dependent "transilient turbulence" reaction matrix.

For all of the work here we calculated the turbulent reaction matrix using the FORTRAN program described by Stull (1986) which we applied to the wind components as well as concentration and temperature.

5. RESULTS AND DISCUSSION

As a test of the full radiative-turbulent theory we used the "clear air" example described by Stull (1986) as our baseline and added an assumed aerosol concentration profile and reworked the example to include the radiative effect. The various aerosol and environmental parameters used in the study are listed in Table 1 and results are shown in table 2. For the example shown the momentum forcing fluxes were assumed to be zero and all inputs were assumed constant in time.

Short wave flux density	250 w/m^2
Long wave flux density	50 w/m^2
Surface albedo (shortwave)	0.15
Surface albedo (longwave)	0.10
Aerosol albedo (shortwave)	0.60
Aerosol albedo (longwave)	0.20
Asymmetry parameter (shortwave)	0.750
Asymmetry parameter (longwave)	0.000
Aerosol concentration	0.003 g/m^3
Extinction coefficient	1.00 km^{-1}

Table 1. Aerosol and environmental parameters used in the study.

In table 2, the case 1 example shows the effect as calculated ignoring aerosol loading (i.e. the "clear air" approximation) and case 2 shows the results as calculated using the full radiative-turbulent model without self

emission. Case 3 results include self emission and Case 4 includes self emission but omits the turbulent reaction. The final column represents Stull's original model using our calculated heat flux density for the clear air case (22.1 W/m^2).

From comparisons between case 1 and case 2 in table 2 we see that for this particular example the effect of the aerosol loading gives rise to an overall radiative contribution of about 1/2° C per hour. Comparing all cases we also see that the initial change is largest near the surface and tends to decrease with height and that the profile tends to isothermal as time proceeds. It is important to note that the results here were extrapolated over time assuming a constant solar and infrared loading. In applications there would be some variation over this time span. For simplicity we have also assumed a constant aerosol concentration.

	HEIGHT	INITIAL	CASE 1	CASE 2	CASE 3	CASE 4	STULL
	450	18.0	18.00	18.67	17.94	17.94	18.00
	350	16.0	16.00	16.58	16.07	16.19	16.00
1 HR	250	15.0	15.17	15.58	16.08	15.33	15.17
	150	15.0	15.21	15.60	16.24	15.39	15.21
	50	15.0	15.27	15.63	16.95	18.47	15.27
	450	18.0	18.00	19.34	17.41	17.88	18.00
	350	16.0	15.73	17.16	17.20	16.38	15.68
2 HR	250	15.0	15.45	16.18	17.34	15.66	15.50
	150	15.0	15.48	16.20	17.49	15.77	15.53
	50	15.0	15.64	16.23	18.18	22.07	15.58
	450	18.0	18.00	20.68	18.86	17.76	18.00
	350	16.0	15.83	18.32	19.02	16.75	15.68
4 HR	250	15.0	15.85	17.39	19.16	16.33	15.87
	150	15.0	15.88	17.40	19.30	16.54	15.90
	50	15.0	16.04	17.44	20.01	29.70	15.96
	450	18.0	18.00	22.02	20.61	17.64	18.00
	350	16.0	16.15	19.49	20.78	17.11	16.18
6 HR	250	15.0	16.17	18.59	20.92	16.98	16.20
	150	15.0	16.20	18.61	21.07	17.31	16.23
	50	15.0	16.36	18.64	21.79	37.99	16.28

Table 2. Results of the modeling exercise showing temperature profiles.

Perhaps the most marked result from the study is the effect of ignoring the turbulent reaction as evidenced by case 4 where the temperature change is in excess of 20° C for the lowest level. This unrealistic result represents the case of ignoring any exchange at all and as such represents an extreme example. It is also interesting to note from comparing case 2 and case 3 that the effect of adding the radiative reaction is to cause cooling at some levels and heating at others. This may appear unusual at first because this term generally implies cooling by self emission. This occurs because, in our model there is an added term due to multiple scattering which tends to trap the radiation, however, the most significant cause of the increase is due to increased transport in the first layer due to radiation from the surface.

5. SUMMARY AND CAVEATS

The modeling exercises reported here have demonstrated the significance of both the radiative and turbulent heating effects in boundary layer modeling, and the importance of treating both in micro-meteorological models. In particular the radiative, or "aerosol loading", component has been shown to be more significant that some have assumed for "dirty" atmospheric conditions. On the other hand there is more work to be done in developing the model for applicability over a wider set of scenarios and in comparing with measurements and in the theoretical treatment of wind profile effects.

ACKNOWLEDGEMENTS

Portions of this work were funded under the 1994 ARL Directors Research Initiative Program. We also wish to acknowledge the contribution of Dr. David Miller, University of Connecticut, for first bringing the subject of transilient turbulence to our attention.

REFERENCES

Adamson, D., 1975. *The Role of Multiple Scattering in One-Dimensional Radiative Transfer.* NASA Technical Note (NASA TN D-8084), Langley Research Center, Hampton, VA.

Bergstrom, R.W. and A.C. Cogley, 1979. "Scattering of Emitted Radiation from Inhomogeneous and Nonisothermal Layers."*J. Quantitative Spectroscopy and Radiative Transfer,* 21:279-292.

Carlson, T.N. and S.G. Benjamin, 1980. "Radiative Heating Rates for Saharan Dust."*Journal of the Atmospheric Sciences,* 37:193-213.

Cuxart, J.P. Bougeault, P. Lacarrere, and J. Noilhan, 1994. "A Comparison Between Transilient Turbulence Theory and the Exchange Coefficient Model Approaches."*Boundary Layer Meteorology, 67:251-276.*

Grisogono, B. and R.E. Keislar, 1992. "Radiative Destabilization of the Nocturnal Boundary Layer over Desert."*Boundary Layer Meteorology,* 52:221-225.

Grisogono, B., 1990. "A Mathematical Note on the Slow Diffusive Character of Long-wave Radiative Transfer in the Stable Atmospheric Boundary Layer", *Boundary Layer Meteorology,* 52:221-225.

Lines, R.T. and Y.P. Yee, 1994, "Temperature Profile of the Nocturnal Stable Boundary Layer over Homogenous Desert Using LA-TEAMS". *Proceedings of the 1994 Battlefield Atmospherics Conference,* U.S. Army Research Laboratory, White Sands Missile Range, NM 88002-5501 (in press).

McDaid, W.J., 1993. A Modified Two-Stream: Improvements over the Standard Two Stream. Master's Thesis, New Mexico State University, Las Cruces, NM 88005.

Oliver, D.A., W.S. Lewellen and G.G. Williamson, 1978. "The Interaction Between Turbulent and Radiative Transport in the Development of Fog and Low-Level Stratus."*Journal of the Atmospheric Sciences,* 35:301-316.

Stull, R.B., 1984. "Transilient Turbulence Theory. Part I: The Concept of Eddy-Mixing across Finite Distances."*Journal of the Atmospheric Sciences,* 41(23):3351-3367.

Stull, R.B. and T. Takehiko, 1984. "Transilient Turbulence Theory. Part II: Turbulent Adjustment."*Journal of the Atmospheric Sciences,* 41(23):3368-3379.

Stull, R.B. and T. Takehiko, 1984. "Transilient Turbulence Theory. Part III: Bulk Dispersion Rate and Numerical Stability."*Journal of the Atmospheric Sciences,* 41(1):50-57.

Stull, R.B. 1986. "Transilient Turbulence Algorithms to Model Mixing Across Finite Distances", *Environmental Software,* 2(1):4-12.

Stull, R.B, and A.G.M. Driedonks, 1987, "Applications of the Transilient Turbulence Parameterization to Atmospheric Boundary-Layer Simulations.", *Boundary Layer Meteorology,* 40:209-239.

Stull, R.B, 1993, "Review of Non-local Mixing in Turbulent Atmospheres: Transilient Turbulence Theory",*Boundary Layer Meteorology,* 62:21-96.

Sutherland, R.A., 1988. "Methods of Radiative Transfer for Electro-Optical Obscuration Modeling", Proceedings of the 1988 Army Science Conference, Vol. III pp 221-234.

Szymber, R.J.and J.L.Cogan, "Owning the Weather Battlefield Observations Framework" *Proceedings of the 1994 Battlefield Atmospherics Conference, U.S. Army Research Laboratory, White Sands Missile Range, NM 88002-5501 (in* press).

Telford, J.W., 1994. "Comment on Radiative Destabilization of the Nocturnal Boundary Layer over the Desert." *Boundary Layer Meteorology*, 68:327-328.

Yee, Y.P., R.A. Sutherland, R.E. Davis, S.W. Berrick, and M.M. Orgill, 1993. "The Radiative Energy Balance and Redistribution (REBAR) Program". *Proceedings of the 1993 Battlefield Atmospherics Conference*, U.S. Army Research Laboratory, White Sands Missile Range, NM, 88002-5501, pp. 181-194

Yee, Y.P., R.A. Sutherland, H. Rachele, and A. Tunick, 1993. "Effects of Aerosol-Induced Radiative Interactions on Stability and Optical Turbulence", *Proceedings of the Society of Photo-Optical Instrumentation Engineers*.

STAR 21: Strategic Technologies for the Army of the Twenty-First Century, 1993. Prepared by the Board on Army Science and Technology, National Research Council, National Academy Press, Washington, D.C.

FORECASTING/MODELING THE ATMOSPHERIC OPTICAL NEUTRAL EVENTS OVER A DESERT ENVIRONMENT

G.T. Vaucher
Science and Technology Corporation
White Sands Missile Range, New Mexico 88002, U.S.A.

R.W. Endlich
U.S. Army Research Laboratory
White Sands Missile Range, New Mexico 88002, U.S.A.

ABSTRACT

Optical turbulence can degrade seeing conditions over long paths, especially horizontal paths near a desert floor. Forecasting the onset and duration of optical turbulence minima, which we call neutral events, requires knowledge of the local energy balance through the heat flux cycles. At the High-Energy Laser Systems Test Facility (HELSTF), White Sands Missile Range, New Mexico, we collected two months of morning and evening neutral event data sets. From these, we determined first-iteration models for forecasting the timing of the morning and evening turbulence minimum. We provide a general definition for the atmospheric optical neutral event, a description of the morning and evening neutral event models over desert terrain, and an "ideal" and a "less than ideal" set of case studies for the model.

1. INTRODUCTION

For years, the degrading effects of atmospheric optical turbulence (AOT) have plagued scientists dealing with light/laser propagation. With the declassification of the adaptive optics techniques developed by Starfire Optical Range (SOR) scientists, astronomers and atmospheric optical/laser propagation researchers now have a viable alternative to these degrading atmospheric effects along a slant path (Fugate and Wild 1994). For those unable to benefit from SOR's technology, we offer this study, which integrates the properties of AOT and AOT neutral events (NE) into a forecastable phenomenon.

The AOT NE forecasting model we developed is based on a near-surface AOT data set collected along a 1-km horizontal desert path in the Tularosa Basin, White Sands Missile Range (WSMR), NM. Though the 1-km path is essentially flat, about 50 km to the east lie the Sacramento Mountains, a flat-topped range that rises about 1.5 km above the basin floor. About 25 km to the west are the San Andres Mountains, a much more jagged range also with maximum elevation around 1.5 km above the desert floor. To the north and south of the site, the terrain is relatively flat with no major obstructions.

1.1 Atmospheric Optical Turbulence Defined

Light propagates through the atmosphere in the form of a wavefront, "a surface over which an optical disturbance has a constant phase" (Hecht and Azjac 1974). Fermat's Principle describes the optical path length primarily as a function of the index of refraction. When a wavefront encounters random irregularities in the index of refraction, a well-acknowledged characteristic of the atmosphere, phase distortions occur. An accumulation of random phase differences degrades light propagation and image

system performance. Depending on the beam size and the characteristics of the index of refraction inhomogeneities, the results take the form of laser beam centroid wander, scintillation, image breakup, and blurring.

1.2 Measuring Atmospheric Optical Turbulence

Quantifying AOT requires an understanding of the AOT phenomenon, as well as of the assumptions necessary to express its effects in terms of a measurable quantity. The following sections provide a brief summary of AOT theory and a description of the main sensors used for this study.

1.2.1 Atmospheric Optical Turbulence Parameters

Atmospheric optical turbulence is a random process. Therefore, to quantify AOT characteristics, we use statistics. The primary parameter employed in our study was the index of refraction structure function, C_n^2. By definition,

$$C_n^2 = \frac{<(n_1 - n_2)^2>}{r^{2/3}} \tag{1}$$

where $<(n_1 - n_2)^2>$ is an ensemble average of the atmospheric index of refraction differences (effectively the index of refraction variance), and r is the separation between n_1 and n_2. An alternative equation, using more easily measured meteorological elements, is

$$C_n^2 = [79 \times 10^{-6} \frac{P}{T^2}]^2 C_T^2 \tag{2}$$

where P is pressure, T is temperature, and C_T^2 is the temperature structure function (Tatarski 1961). By definition,

$$C_T^2 = \frac{<(T_1 - T_2)^2>}{r^{2/3}} \tag{3}$$

where $<(T_1 - T_2)^2>$ is the ensemble average of temperature differences. When using these structure functions, we assume (1) horizontal homogeneity and isotropy within path r and (2) that the separation between sample points is within the turbulence inner and outer scales. (Tatarski 1961; Kolomogorov 1961; Clifford 1978).

1.2.2 Atmospheric Optical Turbulence and Meteorological Sensors

The AOT sensors used to collect the C_n^2 data were Lockheed Model IV scintillometers. These instruments essentially measure the log amplitude variance of a beam transmitted along a 1-km horizontal path at 8 and 32 m above ground level (AGL).

Aspirated thermistors and three-component anemometers measured temperature and wind profiles on 32-m towers at 2, 4, 8, 16, and 32 m AGL. Temperature differences between the 16- and 2-m levels (ΔT) were used to characterize the heat flux. These ΔT values were observed at the 0-, 0.5-, and 1-km positions along the scintillometer path.

1.3 Neutral Events Defined

To best understand the AOT "neutral event," one must first understand the AOT diurnal cycle. The following describes a typical sequence of AOT conditions over a desert valley floor under clear skies. The 24-hr cycle, described below, begins at 0000 hours local time. Figure 1 displays a "typical" diurnal AOT time series along with temperature and insolation for the same time period.

Under clear skies and calm winds, the desert basin atmosphere at 0000 hours (local time) is stably stratified, with the coldest temperatures at the lowest levels ($\Delta T > 0$); the heat flux is negative. The AOT is low. With the slightest wind, such as a katabatic flow, the stable layers overturn, mixing atmospheric layers with different indices of refraction. The resulting mélange of density variations increases the AOT. If winds decrease, AOT decreases.

As the sun rises under clear skies, the sun's rays begin to warm the soil. Over time, the soil radiates this warmth into the lowest layers of the atmosphere. The heat flux increases, passing through zero, and the previously stable atmosphere evolves into an adiabatic or neutral-stability atmosphere. A C_n^2 minimum is observed; this is the morning AOT NE.

As morning progresses, the sun continues to warm the ground. The ground in turn warms the atmosphere, resulting in a deeper boundary layer. The vertical temperature difference (ΔT) becomes increasingly negative, indicating an unstable atmosphere. C_n^2 increases. Atmospheric convection attempts to rebalance the unstable conditions by mixing the near-surface warm air into cooler air aloft. The heat flux is positive, and the atmosphere is unstable, with a super-adiabatic lapse rate. This persistent mixing intensifies the atmosphere's density (temperature and index of refraction) variations, increasing AOT. The peak AOT occurs around midday, or soon after.

In the late afternoon, reduced insolation decreases the magnitude of negative ΔT values. AOT also decreases. Just before sunset, the atmosphere briefly becomes adiabatic, the heat flux goes to zero, and AOT reaches a minimum. The second NE of the day occurs.

Twilight evolves into night, and the warmed soil strongly emits the solar radiation absorbed during the day. ΔT becomes positive. Though the atmosphere is stable, colder and heavier air from the surrounding mountains and hills drains into the valleys. The unequal cooling and drainage create mixing, which moderately increases AOT throughout the night.

The NE is clearly associated with sunrise and sunset. The sunrise NE occurs as the stable nighttime atmosphere makes the transition to the unstable atmosphere of the daytime (ΔT changes from a positive to a negative value). The sunset NE takes place as the daylight's unstable conditions progress into the night's stable state (ΔT changes from a negative to a positive value). The common factor in the two cases is that the atmosphere briefly becomes dry adiabatic, exhibiting the smallest index of refraction variations along horizontal and vertical paths. In terms of actual field measurements, we found that the ΔT values were slightly negative during the NE. This observation is consistent with the dry adiabatic lapse rate of 9.8 °C km^{-1}.

2. FORECASTING ATMOSPHERIC OPTICAL TURBULENCE NEUTRAL EVENTS

Figure 1 (Vaucher and Endlich 1993) is a "typical" AOT desert floor diurnal cycle. The relevant features are the two C_n^2 minima and their correlating insolation and vertical temperature time series.

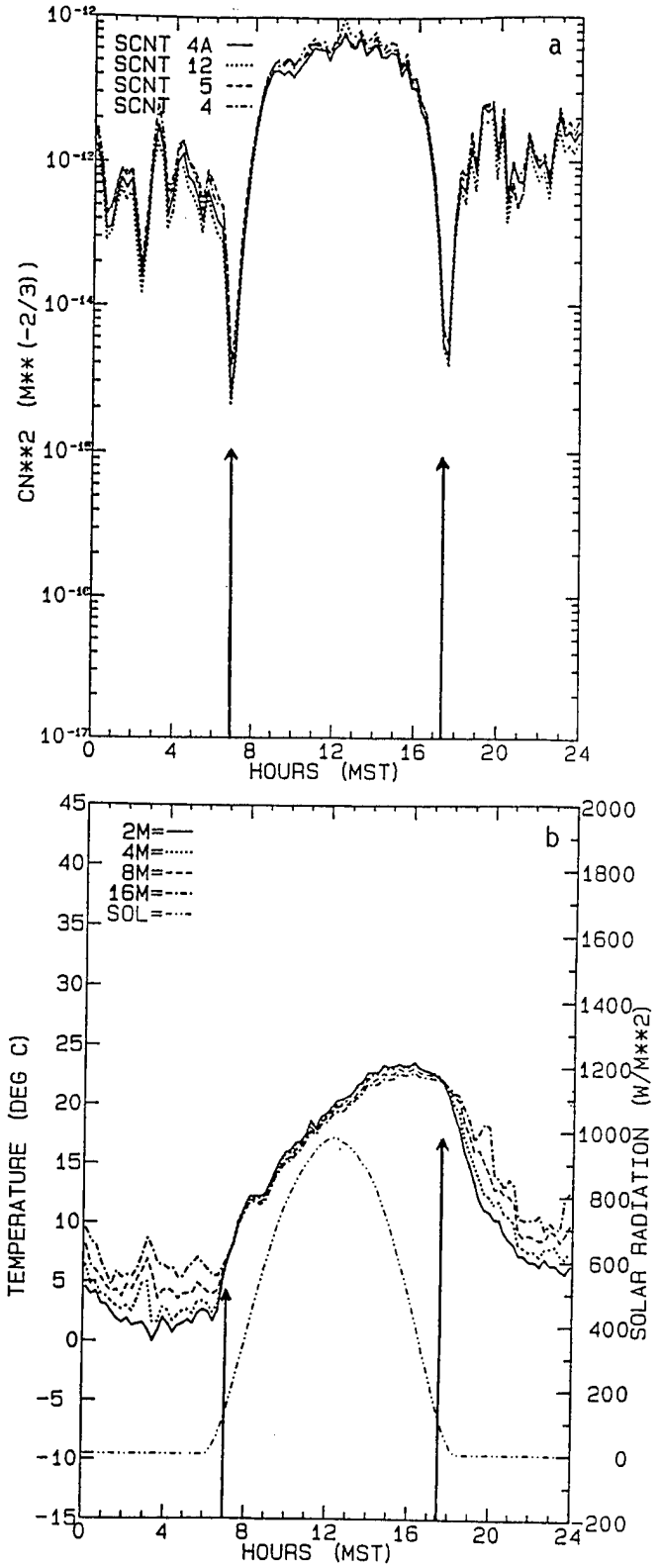


Figure 1. Optical turbulence data for 25 March 1992. (a) Index of refraction structure function, C_n^2. Sensors sampled at 1 m AGL, along a 1-km path. (b) Temperature and insolation. Temperature sensors at 2, 4, 8, 16 m, insolation sampled at 32 m.

The quasi-isothermal condition and C_n^2 minima occurred about 1 hr after sunrise (when insolation begins to increase), and again about 40 min before sunset (when insolation is approaching zero). Does this NE timing, observed near the vernal equinox, also occur when the sun's position is higher in the sky, or when clouds block the rising and setting sun? In the next few sections, we refine the "typical" March observations.

2.1 Statistical Model for Predicting the Neutral Events

AOT data were collected between April and May 1994 along a 1-km path in the desert environment of the Tularosa Basin, WSMR, NM. Based on the ΔT and 8-m C_n^2 time series, the closest minute or minutes of the NE were tabulated. A NE was considered to have occurred when the C_n^2 value reached a minimum below 10^{-15} $m^{-2/3}$ and the ΔT was near zero or slightly negative. When the minimum C_n^2 value remained constant over an extended period, the midpoint of the period was listed as the NE time. The reference point used to standardize the neutral event statistics was the astronomical sunrises and sunsets tabulated for Holloman Air Force Base, about 20 miles northeast of our site. Differences between the astronomical sunrises (sunsets) and the NE times were calculated and averaged, and a minimum and maximum NE time (with respect to tabulated sunrise or sunset) were determined.

Based strictly on the April/May 94 data set, the average occurrence of the morning NE was about 70 min after sunrise. The sunrise-NE time difference ranged between 40 and 133 min after sunrise. The evening NE occurred an average of about 60 min before sunset, with the sunset-NE time difference ranging between approximately 98 and 12 min before sunset. During the calculations and subsequent analysis, variables were identified that directly influenced the NE times. These parameters are discussed in the next section.

2.2 Field Observations

The "ideal" atmospheric conditions selected consisted of clear skies and low wind speeds. In analyzing the "less than ideal" cases, we noted the effects of cloud cover, moist soil, and mountain shadowing.

The greatest cause for variation in NE timing was cloud cover. Specifically, an isolated stratified cloud deck obscuring the sun at sunrise or sunset tended to delay the sunrise NE and cause an earlier sunset NE. The more extensive the cloud cover from the horizon to the site, the more ill-defined the NE. In fact, the C_n^2 minima for these shrouded sunrise/sunset cases were often significantly shallower than those observed under clear skies.

The muddling effects of clouds on the NE can be partially explained in that the sun goes through an estimated 25 times more atmosphere at the horizon than at the zenith. Thus, any difference from fully clear sky would result in a diffused and more irregular insolation. This weakened and erratic warming of the terrain translates into a sluggish evolution between stable and unstable atmospheric conditions.

Damp ground was another major influence on NE timing and duration. When the site experienced rain within the previous 12 hr, AOT tended to be suppressed, with the NE occurring earlier. That is, sunrise NE would occur sooner after sunrise; the sunset NE would occur longer before sunset.

Mountain shadowing was not taken into account when the table of astronomical sunrises/sunsets was calculated. The actual on-site sunrise occurred about 10 min after the calculated sunrise. For consistency, we have expressed all NE time measurements with respect to the calculated table of astronomic sunrises and sunsets.

Mountain shadowing affected the local NE times. West of the site is a very jagged mountain range, the San Andres Mountains. The extremely irregular horizon had the same effect as cloud cover. In the northern hemisphere, mid-latitude location of sunset is to the north in the summer and to the south in the winter. The exact sunset location with respect to the mountain silhouette at the local site had to be taken into account before the local NE forecast could be issued. The evenness of the mountain range on the eastern horizon minimized this effect for the sunrise NE.

We conducted a month-by-month review of the average NE timing for April through June. The sunrise NE was selected for study because of the more ideal eastern horizon. When the NE average and range were tabulated, we found that the average time separating sunrise and NE was about 50 min near the vernal equinox and around 85 min near the summer solstice. Each succeeding month displayed an increase of approximately 12 min. The fact that the NE occurred further from sunrise as the sun's position moved northward may seem inconsistent at first. The following explanation assumes clear skies and light winds.

It is true that northern hemisphere summer temperatures are warmer than winter temperatures. The AOT NE, however, is concerned with temperature differences and heat fluxes (density variations). In the winter, morning air masses are cooler than they are in summer. Therefore, the solar heat flux required to create an adiabatic environment near the surface (AOT minimum) in the winter is less than it is in summer, when the air mass over the terrain is warmer.

3. CASE STUDIES

Two case studies are presented below. The first is a sunset NE under "almost ideal" atmospheric conditions; the second is a "less than ideal" sunset NE case study.

3.1 Clear Skies Case Study

On 15 June 1994, the site had a high-pressure area to the south and a low-pressure area to the north, causing westerly winds to persist throughout the day. The skies overhead were mostly clear during the day, though scattered high clouds moved across the horizon from the northwest shortly before sunset. These clouds were well to the north of the sunset horizon. A fire on a mountain range to the southwest released large quantities of smoke visible from the site; however, westerly winds kept the smoke well to the south during the entire period. During the forecasted NE, the temperature at 2 m AGL was around 32 °C, the winds at 8 m AGL were from the west at about 5 m s^{-1}, and the dew point at 2 m AGL was around 0 °C.

The sunset horizon was free of clouds, as were the atmosphere between the sunset horizon and the site and the sky east of the site. Applying the statistical model to these "almost ideal" conditions, the NE time range forecast for 15 June 1994 was the following:

Astronomical sunset:	1914 MST
Local NE based on average:	1814 MST
Range in which the NE could occur:	1736 - 1902 MST

Figure 2 displays the C_n^2 and ΔT time series for this June case. Placing the NE C_n^2 threshold at 10^{-15} $m^{-2/3}$, the NE at both 8 and 32 m begins around 1810 MST and ends around 1848 MST. During this period, the ΔT hovers around 0 °C. The single C_n^2 minimum occurs around 1824 MST, about 10 min later than the statistical average for April/May, but well within the anticipated NE range.

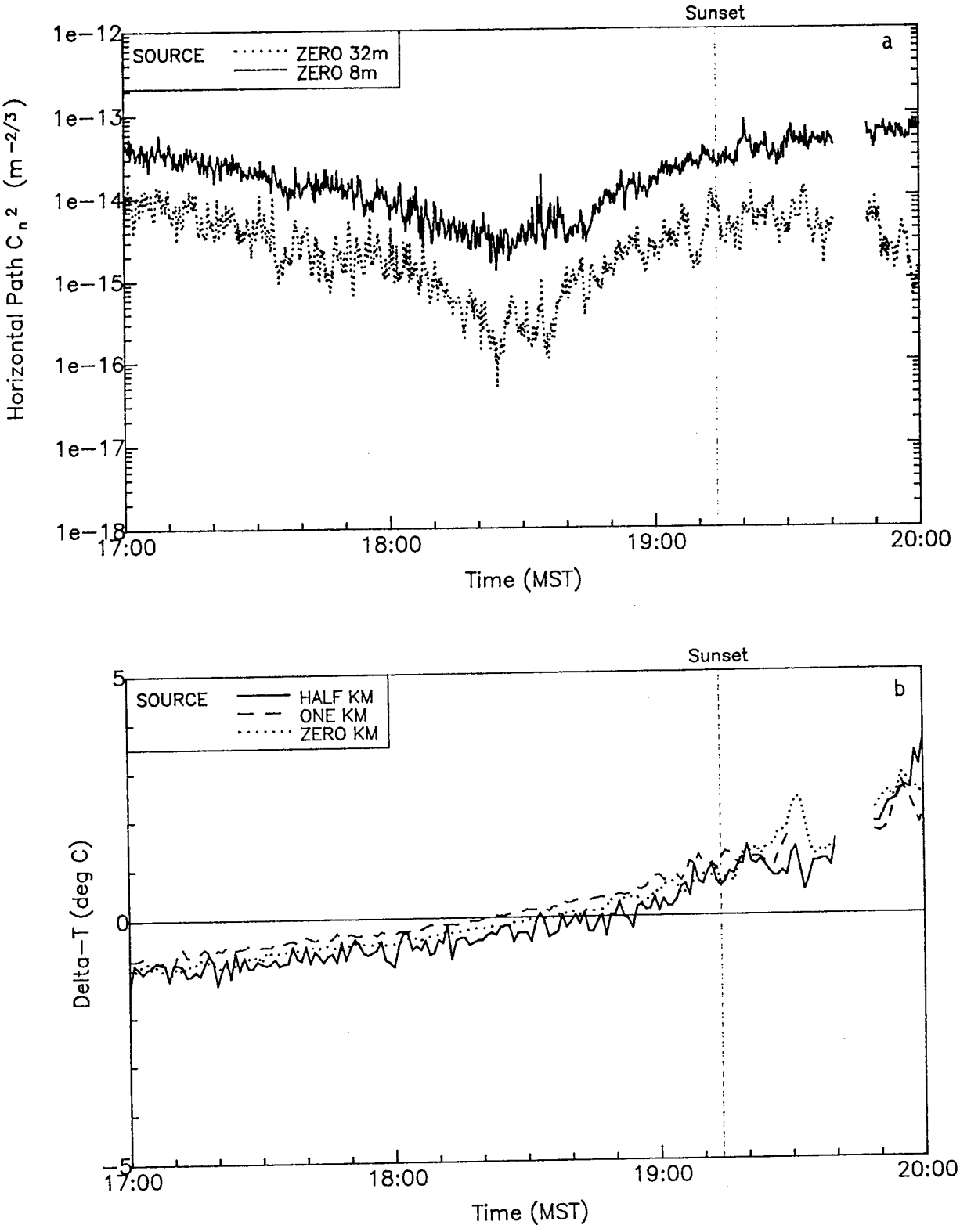


Figure 2. (a) C_n^2 and (b) ΔT time series for the "almost ideal" 15 June 1994 case study.

3.2 Effect of Overcast Skies

On 12 May 1994, a low-pressure area centered over eastern Arizona brought moist, unstable air over the site from the south. Thunderstorms, rain events, and considerable cloud cover dominated this 24-hr period. The local thunderstorm activity began soon after 0300 MDT and continued until about sunrise. Moisture and cloud cover over the site persisted throughout the day, leading to an ill-defined and extended evening NE. Winds around sunset were from the north at about 5 m s^{-1}. The statistical evening NE model forecast the NE time and range as follows:

Astronomical sunset:	1854 MST
Local NE based on average:	1754 MST
Range in which the NE could occur:	1716 - 1842 MST

Figure 3 displays the C_n^2 and ΔT time series for this ill-defined NE. In contrast to the 15 June case, the 32-m and 8-m C_n^2 magnitudes tended to coincide. They also lacked a single point minimum. In fact, there were four turbulence minima. The "best" 32-m level minimum (1708 MST) occurred *before* the "best" 8-m C_n^2 minimum (1754 MST). Note, however, that the "best" C_n^2 minimum at 8 m coincides with the forecast NE. The ΔT magnitudes hover around the 0 °C mark throughout the extended NE period.

4. SUMMARY

Atmospheric optical turbulence (AOT) was observed in order to develop a model for predicting the time of AOT neutral events (NE), which occur shortly after sunrise and shortly before sunset in a desert environment. The parameter used to quantify the AOT was the index of refraction structure function, C_n^2. The assumptions made when using C_n^2 are horizontal homogeneity and isotropy within the path and that the distance separating the two sampled points is within the turbulence inner and outer scales. Principle sensors used for this study were Lockheed Model IV scintillometers to determine C_n^2 and the aspirated thermistors to measure the ΔT (16-m − 2-m AGL temperature differences). All sampling was done along a 1-km horizontal path.

C_n^2 and ΔT data for periods near sunrise and sunset from April-May 1994 were collected. Using the astronomical sunrise and sunset for a local Air Force base, the difference between sunrise (or sunset) and the NE was calculated. An average of the time differences combined with the range in the time of occurrence allowed us to refine the forecasting model.

Based strictly on the April/May 94 data set, the average occurrence of the morning NE was about 70 min after sunrise. The difference in time between sunrise and the associated NE ranged between 40 and 133 min after sunrise. The evening NE occurred an average of about 60 min before sunset, with a sunset-NE difference ranging between approximately 98 and 12 min before sunset.

The statistical NE model was tested and a subsequent analysis identified additional factors that directly influence the NE. The greatest cause for variation in the NE timing was cloud cover. A shroud of clouds during the sunrise or sunset period tended to delay the local NE. In some cases, a shallower AOT minimum was also observed. Since the sun travels through more atmosphere at the horizon than at the zenith, one can expect a clouded horizon to affect NE timing.

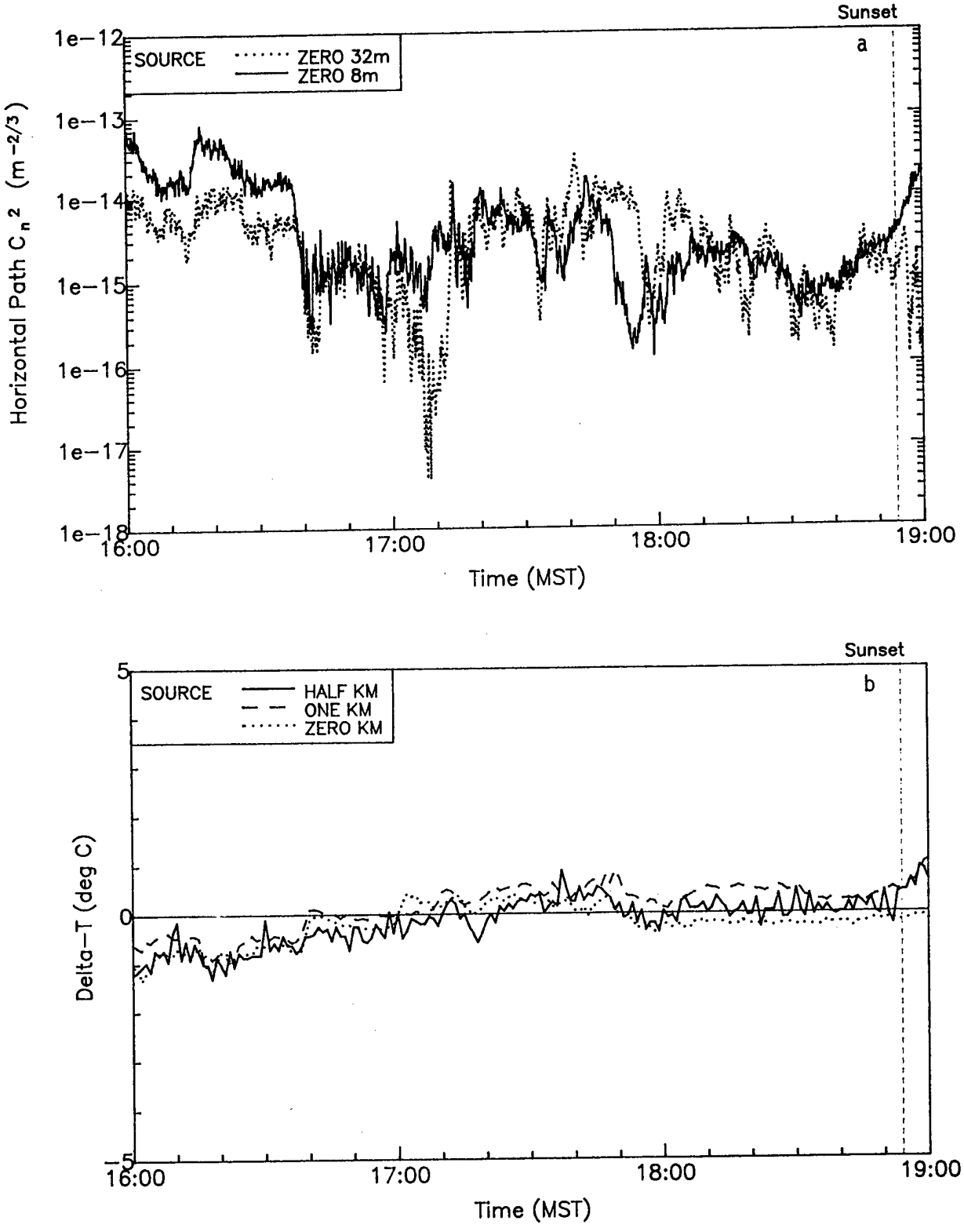


Figure 3. (a) C_n^2 and (b) ΔT time series for the "less than ideal" 12 May 1994 case study.

A second influence was soil moisture, which retarded the effects of insolation. A third influence was mountain shadowing from the surrounding horizons. The orographic profiles affected the exact timing of local sunrise or sunset, and jagged terrain occulting the sun had a similar dulling effect on the NE to that of cloud cover.

A month-by-month analysis of the sunrise NE occurrence showed the sunrise-to-NE time differential to increase by about 12 min per month during the spring. The greater heat flux required in the summer months to produce the low-level adiabatic environment associated with a C_n^2 minimum helps to explain the longer sunrise-to-NE separation. An "almost ideal" (clear skies) and "less than ideal" (cloudy) case were presented. When skies were clear, the forecasted NE generally agreed with the model. During cloudy and showery conditions, the effect of nonuniform radiation and latent heat made the simple statistical model difficult to use.

5. RECOMMENDATIONS

The above study is by no means an exhaustive investigation of AOT NE forecasting/modeling. Collecting and analyzing a full annual cycle of AOT NE data and quantitatively linking cloud cover, heat flux, and ground moisture with the AOT NE would greatly enhance the AOT NE forecast model.

ACKNOWLEDGEMENTS

A special thanks to T. Jameson for daytime observations of 12 May 94; to A. Rishel and J. Niehans for data management and assistance with the figures; and to C. Vaucher for text critique.

REFERENCES

Clifford, S.R., 1978. "The Classical Theory of Wave Propagation in a Turbulent Medium." *Topics in Applied Physics—Laser Beam Propagation in the Atmosphere*, v. 25, Springer-Verlag, Berlin, Germany, 325 pp.

Fugate, R.Q., and W.J. Wild, 1994. "Untwinkling the Stars -- Part I." *Sky and Telescope*, May 1994, 24-31.

Hecht, E., and A. Azjac, 1974. *Optics*, Addison-Wesley Publishing Co., Reading, MA, 565 pp.

Kolomogorov, A., 1961. *Turbulence, Classic Papers on Statistical Theory*. ed. by S. Friedlander and L. Topper, Interscience, New York. NY, 151 pp.

Tatarski, V.I., 1961. *Wave Propagation in a Turbulent Medium*. Dover Publications, Inc., New York, NY, 285 pp.

Vaucher, G. Tirrell, and R.W. Endlich, 1993. "Intercomparison of Simultaneous Scintillometer Measurements over Four Unique Desert Terrain Paths." *Eighth Symposium on Meteorological Observations and Instrumentation*, American Meteorological Society, Boston, MA.

Session I Posters

SIMULATION AND ANALYSIS

COMBINED OBSCURATION MODEL FOR BATTLEFIELD INDUCED CONTAMINANTS - POLARIMETRIC MILLIMETER WAVE VERSION (COMBIC-PMW)

S. D. Ayres, J. B. Millard, and R. A. Sutherland
Battlefield Environment Directorate
U.S. Army Research Laboratory
White Sands Missile Range, New Mexico 88002-5501

ABSTRACT

The COMBIC model was originally developed for Electro-Optical Systems of Atmospheric Effects Library (EOSAEL) to model aerosols for which spherical symmetry can be assumed to describe both the physical and optical properties of the aerosols. This is a reasonable assumption when considering older, conventional obscurants such as fog oil and white phosphorus; this approximation breaks down for newer developmental obscurants designed to be effective at longer wavelengths. Many of the new millimeter wave and radar obscurants are highly nonspherical. New techniques are required to model nonspherical obscurants. COMBIC-PMW is a merger between COMBIC and the techniques that account for the optical and mechanical behavior of these nonspherical battlefield aerosols. These new techniques determine electromagnetic properties such as the ensemble orientation averaged extinction, absorption, and scattering as well mechanical properties such as fall velocity and angular orientation of the obscurant particles when released into the turbulent atmospheric boundary layer. This paper describes COMBIC-PMW, its function, and how to use it. The paper also describes the range of conditions under which the model is applicable.

1. INTRODUCTION

1.1 Model Purpose

Millimeter wave (MMW) radars were developed to provide greater accuracy than conventional microwave (centimeter wave) radars even though MMW radars do not have the same all-weather capability. Although MMW radars have superior penetrability through smoke, fog, and rain over their electro-optical (EO) counterparts, they do not have the high resolution of EO systems (Sundaram 1979). MMW systems represent a compromise in which most of the advantageous characteristics of the microwave and EO regions are available and the disadvantageous effects are minimized. MMW radar systems are also much smaller because component size is related to wavelength. MMW systems are of considerable interest for applications in which size and

weight restrictions are important, as in aircraft and smart munitions. With the development of the MMW systems, the Army turned to countermeasures that can defeat these radars. The prevalent thought in the Army is that conventional battlefield obscurants hardly affect MMW (Knox 1979). The Army is developing obscurants that can defeat the MMW systems. These obscurants are different from the obscurants that can defeat conventional EO systems. Their primary dimension is approximately the same as the wavelength of the system (i.e., on the order of millimeters). Furthermore, the obscurants are not spherical, like the more conventional obscurants. The combination of these effects create situations not present with the traditional smokes. Atmospheric turbulence can affect the orientation of nonspherical particles. The orientation and scattering from nonspherical particles leads to different scattering intensities at different angles. New models are required to simulate these obscurants.

1.2 COMBIC

One of the original purposes for developing COMBIC-PMW was to assist in modeling the effectiveness of smoke screens used in wargame simulations. The COMBIC computer simulation predicts spatial and temporal variation in transmission produced by various smoke and dust sources. It models the effects of reduction in electromagnetic (EM) energy by combining the munition characteristics with meteorological information of an idealized real world. COMBIC produces transmission histories at any of seven wavelength bands for a potentially unlimited number of sources and lines of sight. It also computes concentration length, which is the integration of the concentration over the path length. Previous smoke models, like COMBIC, adequately model older conventional smokes such as fog oil and white phosphorous; this is not true of the newer developmental obscurants. Since the original development of COMBIC, which treats only spherical obscurants, new obscurants have been developed for effectiveness in the MMW regime. These obscurants are severely nonspherical in shape; therefore, new algorithms are required. The traditional simplifying assumption of spherical symmetry to describe the optical and mechanical properties of the obscurants is no longer valid for the newer obscurants. The new obscurants are actually nonspherical and require different methodologies to compute their effect on the battlefield and the effect of atmospheric turbulence on the obscurants.

1.3 MMW Obscurants

A wide variety of MMW obscurants, such as graphite, have been developed in recent years. The most efficient are the fibers modeled as finite cylinders. Very few MMW obscurants have made it to the inventory list. The fibers can be either prepackaged, precut and packed in parallel arrays having packing densities as high as .8, or precut fibers loosely packed in powder form. The Army favors the first method (Farmer, Kennedy 1991). MMW obscurants can exist in a multitude of complex shapes including helix, coils, disks, flakes, cubes, antennas, and their aggregates.

1.4 Dissemination Methods

In a dissemination system, such as a grenade or rocket, the fibers are packed coaxially in disks. Disk thickness corresponds to fiber length. The aspect ratio of diameter to fiber length is typically 1 to 1000. The disks are stacked on a center-core burster-unit that is used to break the packaging binder and spread the fibers. For artillery-shell packaging, the disks must be reinforced with a steel or aluminum superstructure. This design approach assumes that when the disks burst, the disks separate into single fibers of the same length and diameter as the original fibers used to make the disk. Electrostatic charge and other factors can cause clustering of fibers to stick together along the long axis or to agglomerate into randomly oriented sets of particles resembling bird nests. The large clusters tend to fall out of the obscurant cloud at a much greater rate than single fibers. The large clusters decrease cloud obscuration efficiency. The decrease in obscuration efficiency results from a reduction in extinction efficiency for the individual clusters relative to single particles and from a reduction of the numbers of individual fibers available for effective obscuration. COMBIC-PMW does not model this directly except through an empirically derived munition efficiency factor.

In a fiber cutter MMW smoke generator system, the obscurant material comes from the factory in multiple strand ropes, called tows, wound on spools. The material is often graphite, although other materials have been employed. The number of fibers per tow can vary from 1000 to 48,000, and there are 10 to 30 tows per belt. In a typical system, the belt material is fed to a fiber cutter consisting of two rollers in contact, in which one contacts the cutting blades at fixed spacing (typically 6.25 mm or 1/4 in). The fiber length can be varied by changing the blade spacing. The motor speed is variable allowing fiber belt speeds from 0 to 12 ft/s. Proper selection of belt speed and belt size can produce throughputs of 0 to 10 lb/min. A coanda flow ejector consists of a short cylindrical shell with a high-speed sheath (generated by air pressure expelled axially at the inside edge of the cylindrical shell). Momentum is then transferred to the air within the cylindrical shell. This device can be used to produce air flow without mechanical interference and within which shear flow can be carefully controlled. The coanda flow ejector separates and disseminates the fibers by accelerating them to very high speeds resulting in a nearly uniform nonbuoyant cloud.

A wafer storage and dispensing smoke generator disseminates fibrous material from wafers containing fibers. Wafer storage and dispensing consists of a cartridge magazine, four wafer cartridges, and a pneumatic indexing mechanism. The wafer cartridges are inserted into four bores in the cartridge magazine. In a prototype system tested at the Dugway Proving Ground (Perry et al. 1994), the wafer cartridge can contain up to 54, 6.25-mm- (1/4 in) thick wafers. Each wafer is approximately 20 g (.044 lb). Pistons in the wafer cartridges discharge the wafers into slots in the wafer turret motor that includes two rows of wafer slots. The wafer turret motor rotates until the wafer lines up with the exit from the turret housing. There a spring strikes the wafer's rear surface, ejecting the compact fibers into the turret housing. Ambient air enters at a high velocity and mixes with the aerosol and forms the exiting cloud.

2. DEFINITION OF PROBLEM

2.1 Scattering

The propagation of EM radiation in any medium containing particles is governed by the combination of absorption, emission, and scattering. Particles are a subject of great importance in determining effects of obscurants on EM radiation. Scattering and absorption depend upon the particle size, shape, refractive index, and concentration. Mathematically determining the radiation field scattered by particles of arbitrary shape at any point in space can be quite difficult. Exact analytical solutions are only available for the sphere and infinite cylinder. The scattering properties of simple geometries have been well studied (Bowman et al. 1987). Numerical techniques and approximate analytical methods are used to analyze these properties, usually over a limited range of conditions. In this first attempt to more effectively model MMW obscurants, one is limited to modeling finite cylinders. A recently held workshop entitled *Second Workshop on the Electromagnetics of Combat Induced Atmospheric Obscurants* examined all aspects of the scattering problem to determine status of existing models, measurement capabilities, field-model comparison, and where research needs to be focused.

Long-wavelength theory predicts that parallel rays encountering a cylinder are scattered axially symmetric. Short-wavelength theory predicts that parallel rays encountering a cylinder are scattered into a conical shell with a half angle equal to the angle between the incident rays and the cylinder axis. For cylinders nearly parallel to the incident radiation, the scattered radiation is contained in a small cone near the forward direction. The cone half angle increases as the angle increases between the incoming radiation and the cylinder. For an extreme case with the cylinder at right angles with the incoming radiation, the conical wave becomes a cylindrical wave propagating in a direction perpendicular to the particle axis. (Note, in this case, that backscatter can only occur when the particle is aligned perpendicular to the viewing angle.)

2.2 Polarization

2.2.1 What Is Polarization

Light waves are transverse in the far-field approximation. The displacements of the electric and magnetic vectors are not along the line of travel, like sound waves, but are perpendicular to it. For example, if the direction of travel of a given light beam is east, the electric vibrations may be up and down, or north and south, or along some other line perpendicular to the east-west axis. The transverse electrical (TE) and transverse magnetic (TM) fields are mutually perpendicular at any point in space. Polarized light is light in which the transverse components vibrate in a preferred manner. Unpolarized light is light that exhibits no long-term preference as to vibration pattern. Partially-polarized light falls somewhere in between.

2.2.2 Effects of Polarization

Laboratory obscuration effectiveness in the MMW regime is strongly dependent upon the system polarization mode. Note that in figure 1 this particular obscurant is much more effective against horizontally-polarized systems. Figure 1 shows mass extinction coefficients versus concentration for horizontal- and vertical-polarized radiation. The mass extinction coefficient average is 0.2 m^2/g for vertically-polarized radiation and 0.8 m^2/g for horizontally polarized radiation. Even unpolarized light can become polarized after encounters with scatterers, although the opposite usually occurs. Figure 2 shows plots of the (relative) magnitude of the scattered intensity as a function of the cone azimuth angle for various values of the incident angle for the TE and TM polarization modes (Sutherland, Millard 1994). When θ_{inc} is perpendicular to the cylinder, scattered TM radiation reaches a minimum at 180° (backscatter). This is not true for TE radiation which reaches a minimum at 79° and shows a significant amount of backscatter. Potential counter-countermeasures that can take advantage of scattered radiation polarization characteristics can be identified through studies of a phase-function plot for both vertical and horizontal polarization.

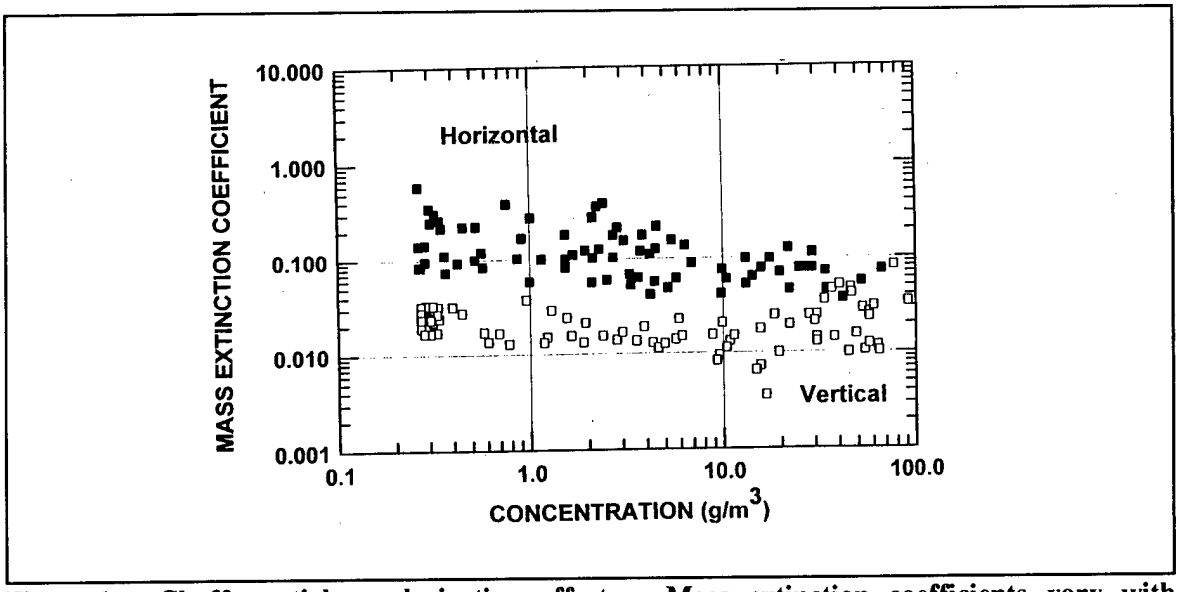


Figure 1. Chaff particles polarization effects. Mass extinction coefficients vary with polarization mode being higher for horizontal polarized incident radiation.

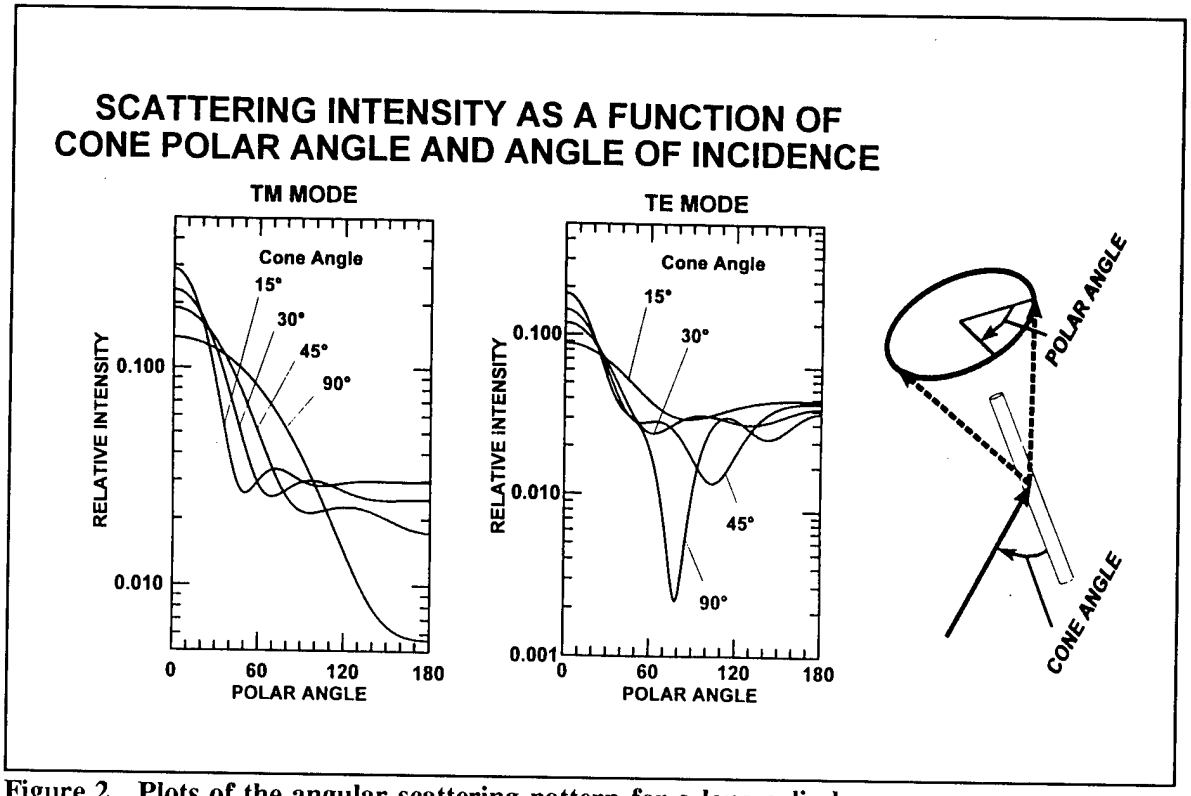


Figure 2. Plots of the angular scattering pattern for a long cylinder.

2.3 Particle Orientation

2.3.1 What Causes Particles to Orient

Under certain conditions, nonspherical particles tend to adopt a preferred orientation when falling through the atmosphere. For long cylindrical-shaped particles used to approximate MMW obscurants the stable mode occurs when the particle is oriented with long axis horizontal. Figure 3 shows the laboratory measured orientation distribution of chaff particles 2 and 10 s after release. At first the particle orientation is nearly uniform; however, after 10 s the aerodynamic and gravitation forces tend to shift the distribution to the more stable model. The degree to which the particle orients will also affect the polarimetric extinction properties of the ensemble. The fall velocity of a nonspherical particle is significantly lower than for an equivalent spherical particle of the same mass (Sutherland, Klett 1992).

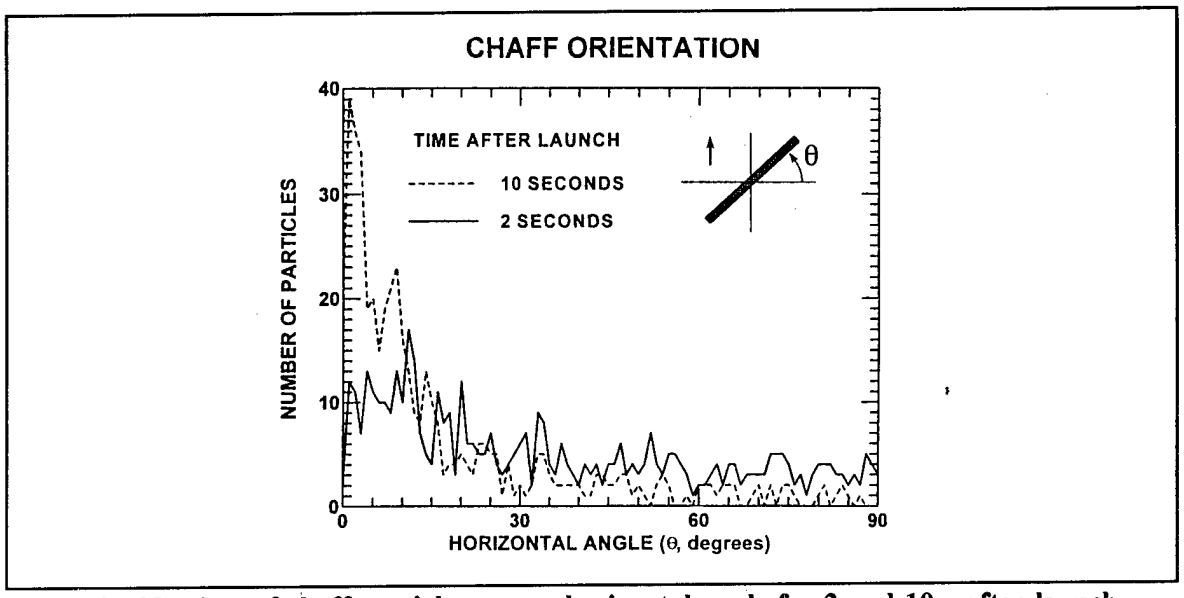


Figure 3. Number of chaff particles versus horizontal angle for 2 and 10 s after launch.

2.3.2 Role of Turbulence

Nonspherical particles tend to adopt a preferred orientation when falling through the atmosphere under quiescent conditions. Atmospheric turbulence can cause a perturbation to the stable-fall mode that can result in random tumbling for extremely turbulent conditions. The degree of perturbations depend upon the level of turbulence and cylinder length as well as the aspect ratio (ratio of particle diameter to length). Figure 4 shows results of the computation of stable-fall mode for Reynolds number versus cylinder length for different aspect ratios. Note that the small Reynolds number for stable-fall mode means the dominance of viscous forces over inertial forces for MMW obscurants. The current Army belief is that stable-fall modes are the exception rather than the rule in the turbulent atmospheric boundary layer. This belief is increasingly being challenged.

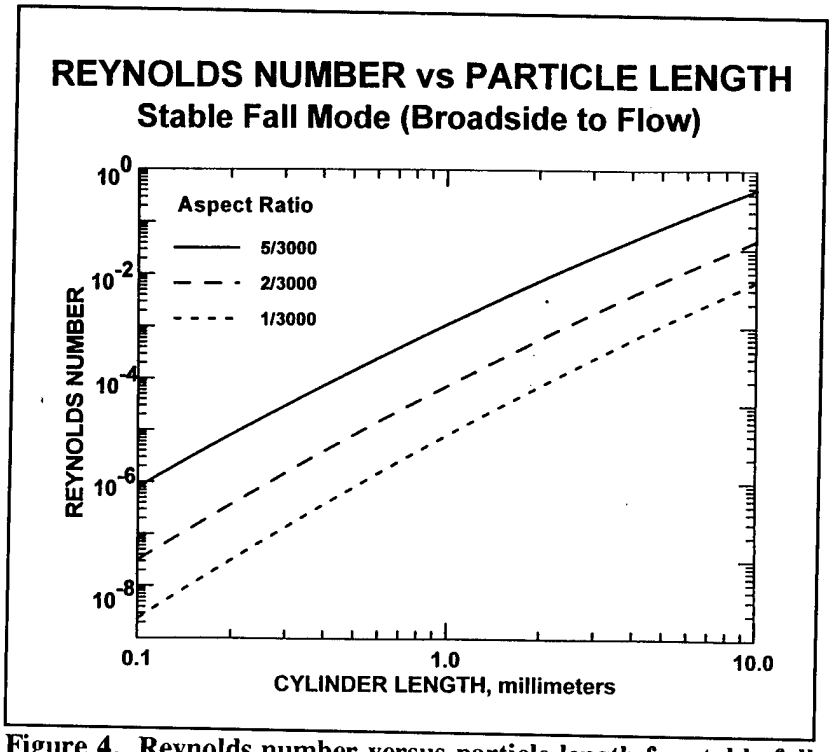


Figure 4. Reynolds number versus particle length for stable-fall mode for three different aspect ratios.

2.3.3 Effect of Particle Orientation

MMW particles will rarely all have the same orientation. The expected orientation distribution of particles in a cloud will probably fall somewhere between completely oriented to completely random for a turbulent atmosphere. The problem is not to compute obscuration efficiency for a particle at angle θ but to determine obscuration efficiency for a cloud of particles oriented at all different angles but possibly having a preferred orientation. Sutherland and Klett (1992) created a model that estimates the degree of orientation of various sized particles falling though the turbulent atmosphere. The problem is difficult and, like most problems involving the real atmosphere, is not exactly solved. Sutherland and Klett (1992) assumed that the mean square tilt angle of a large ensemble of particles is proportional to the magnitude of turbulent pressure fluctuations. Results for cylindrically-shaped particles are described elsewhere (Sutherland, Millard 1943). The theory is valid only in the inertial subrange of turbulence where the behavior of the various microscale parameters are fairly well known. Some results of Sutherland and Klett's model are shown in figures 5a and 5b. Figure 5a gives estimates of the root mean square tilt as a function of particle length for various levels of the turbulent dissipation rate ϵ. The vertical scale represents the calculated mean square tilt varying from a value of 0° (full horizontal orientation) to 90° (near total uniform random orientation). It is evident from figure 5a that larger particles tend toward the stable orientation mode ($\delta\theta = 0$) is intuitively expected. Note that as the turbulence level increases in figure 5b, the width of the function increases to the point where the distribution becomes nearly uniform (flat) at the highest turbulence levels.

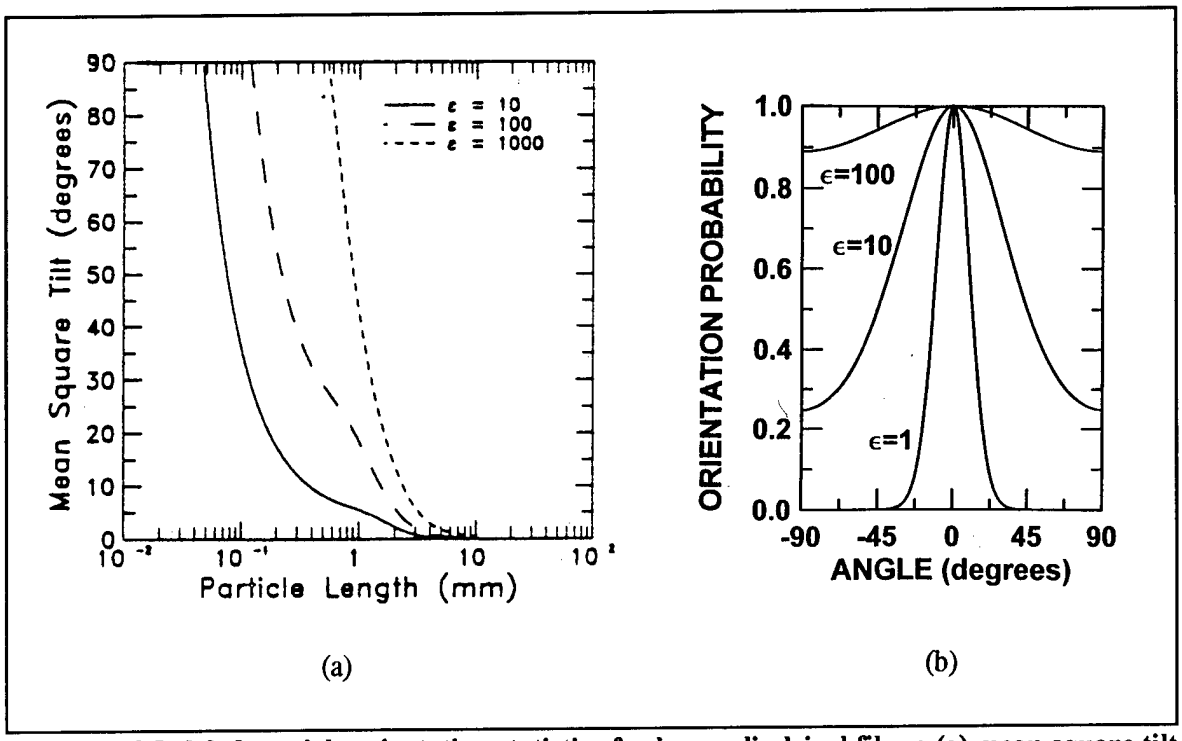


Figure 5. Modeled particle orientation statistics for long cylindrical fibers (a) mean square tilt as a function of particle length and (b) particle orientation distribution.

3. PMW RESULTS

Unlike their spherical counterparts, the extinction efficiency of nonspherical obscurants depends upon the viewing angle and the level of atmospheric turbulence. It becomes necessary to model these factors. The PMW model uses the Wentzel-Kramers-Brillouin (WKB) method to calculate the values of the ensemble averaged efficiencies and the differential scattering cross section for fibers with lengths much less than the wavelength (i.e., the Rayleigh regime). The WKB method and the quasistatic model (used to calculate the absorption efficiency), as used by PMW, are described in papers by Klett and Sutherland (1992); Evans (1991); Pederson, Pederson, and Waterman (1985); and Pederson, Pederson, and Waterman (1984). The subroutine WKB requires the following inputs: M, the complex index of refraction; R, the cylinder radius (microns); L, the cylinder length (millimeters); W, the wavelength (microns); P_0, the incident polarization angle; B, the tilt distribution parameter (as shown in figure 5); D, the maximum tilt angle (as measured from the X-Y plane); and the zenith angle (degrees). The outputs of WKB are the absorption, extinction, and scattering ensemble averaged efficiencies and the differential scattering cross section for $\phi = \pi$ and $\phi = 0$ with the vector polarizations. The polarization angle is the angle measured from the vertical, clockwise, in a plane perpendicular to the incident direction. The vector polarizations are the in the same XYZ coordinate system as the incident angle and the maximum tilt angle.

4. COMBIC-PMW

4.1 Description

COMBIC-PMW is made up of two models: one that treats transport and diffusion (the original COMBIC) and another that models the mechanical and optical properties of MMW obscurants (PMW). COMBIC calls PMW as a subroutine and passes the parameters that define the MMW obscurant such as length, diameter, and complex index of refraction as well as the polarization information described in section 3. The output is the extinction efficiency, absorption efficiency, scattering efficiency, phase function, and vector polarization for both backscatter and angle of interest. Only the extinction efficiency is used by COMBIC. Future research will make use of other parameters.

4.2 Inputs

All input data for COMBIC-PMW are entered in standard EOSAEL format, A4,6X,7E10.4. Input data are entered through 80-character, order-independent, "card" images. Tables 1, 2, and 3 describe the new input cards used in addition to the original COMBIC input cards.

Table 1. The PMWO card describes the properties of MMW obscurant. The first line shows the parameters of the record. The second line gives a typical example. Explanation of the parameters follows.

PMWO		FLENG	FDIAM	FINDEX	FDNSTY
PMWO		3.4	1.0	.5	1.8

NAME	UNITS	
FLENG	mm	Length of fiber
FDIAM	μm	Diameter of fiber
FINDEX		Complex index of refraction
FDNSTY		Density of the fiber

Table 2. The TURB card describes the turbulence and lists frequencies of interest. The first line shows the parameters of the record. The second line gives a typical example. Explanation of the parameters follows.

TURB		EPS	GHz(1)	GHz(2)	GHz(3)	GHz(4)
TURB		10.0	220	140	94	70

NAME	UNITS	
EPS		Turbulence parameter (10 = low turbulence, 100 = medium turbulence, 1000 = high turbulence)
GHz(1-4)	GHz	COMBIC-PMW computes the transmission at 6 default MMW frequencies (220, 140, 94, 70, 35, and 24 GHz). The user can change the first four.

Table 3. The TLOC describes target location and specifies if the sensor is a MMW sensor. The first line shows the parameters of the record. The second line gives a typical example. Explanation of the parameters follows.

TLOC		OBSN	XTAR	YTAR	ZTAR	TARN	PMW	PANG
TLOC		1	70	2000	3	1	1	45

NAME	UNITS	
OBSN		User assigned number matching an observer
XTAR	m	Target X location
YTAR	m	Target Y location
ZTAR	m	Target Z location
TARN		User assigned target number. One observer can have many targets.
PMW		If greater than zero, then the sensor works in MMW frequencies.
PANG	°	Incident polarization angle

4.3 COMBIC-PMW Results

Figures 6 through 9 are for identical clouds. The first two plots are crosswind views of three generators producing graphite. The second two plots are top-down views of the same three generators. In the first three examples, the atmospheric turbulence is high ($\epsilon = 1000$), and in the fourth example, the atmospheric turbulence is light ($\epsilon = 10$). The first, third, and fourth examples are for an incident polarization angle (PANG) of 0° and the second example is for an incident polarization angle of 90°. The incident angle is the only difference between the first two examples. The only difference between the third and fourth example is the turbulence parameter. Notice how the effectiveness of the exact same clouds changes with incident polarization angle and also with atmospheric turbulence.

5. CONCLUSIONS

Past models that assume spherical symmetry are not capable of treating effects of either viewing angle or atmospheric turbulence, which are highly significant according to the model of Sutherland and Millard. In general, the angular scattering pattern produced by nonspherical obscurants is much more complex than the spherical counterparts.

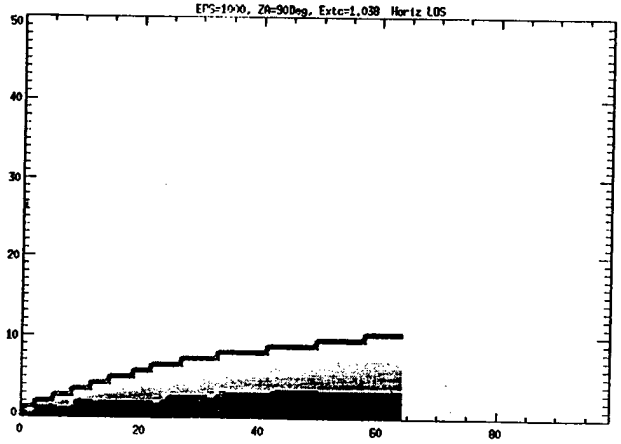


Figure 6. Contours of optical depth for three generators producing graphite fiber clouds, horizontal view (i.e., zenith angle = 90°). Fiber length is 3 mm. Frequency is 94 GHz. Atmosphere is turbulent. Horizontal polarization.

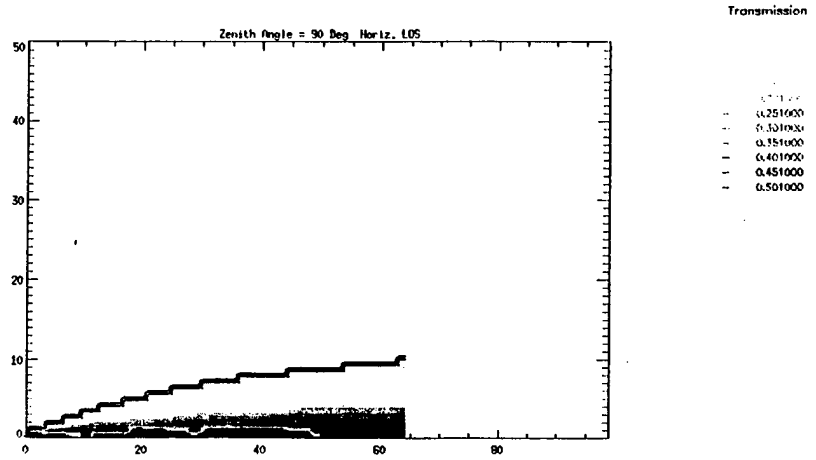


Figure 7. Contours of optical depth for three generators producing graphite fiber clouds, horizontal view (i.e., zenith angle = 90°). Fiber length is 3 mm. Frequency is 94 GHz. The atmosphere is turbulent. Vertical polarization.

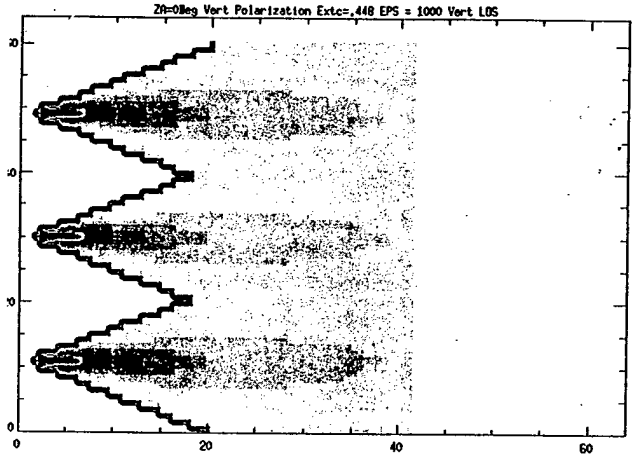


Figure 8. Contours of optical depth for three generators producing graphite clouds, top-down view (i.e., zenith angle is 0°). Fiber length is 3 mm. Frequency is 94 GHz. Atmosphere is moderate to highly turbulent. Incident angle is vertically polarized.

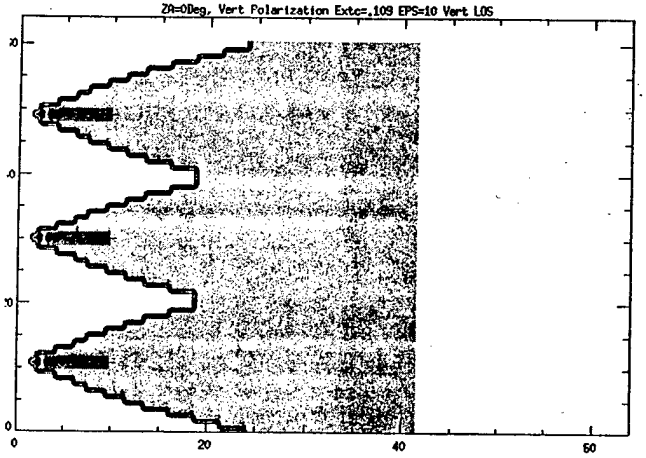


Figure 9. Contours of optical depth for three generators producing graphite clouds, top-down view (i.e., zenith angle is 0°). Fiber length is 3 mm. Frequency is 94 GHz. The atmosphere has light turbulence. Incident radiation is vertically polarized.

REFERENCES

Ayres, S. D., and S. DeSutter, 1993. *Combined Obscuration Model for Battlefield Induced Contaminants (COMBIC) User's Guide*. In Press, Department of the Army, U.S. Army Research Laboratory, Battlefield Environment Directorate, White Sands Missile Range, NM.

Bowman, J. J., T. B. A. Senior, and P. L. E. Uslenghi, 1987. *Electromagnetic and Acoustic Scattering by Simple Shapes*. Hemisphere Publishing Corporation.

Evans, B. T. N., 1991. *Laboratory Technical Report MLR-R-11231*. Commonwealth of Australia Department of Defence Materials Research, Ascot Vale, Victoria 3032, Australia.

Farmer, W. M., and B. Kennedy, 1991. *Electro-Magnetic Properties of RADAR/MMW Obscurants*. Contract Report DAAL03-86-D-0001, Bionetics Corporation, Hampton, VA. Sponsoring agency: U.S. Army Research Office, Research Triangle Park, NC.

Fournier, G. R., and B. T. N. Evans, 1991. "Approximation to Extinction Efficiency for Randomly Oriented Spheroids." *Applied Optics, 30*(15):2042-2048.

Klett, J. D., and R. A. Sutherland, 1992. "Approximate Methods for Modeling the Scattering Properties of Non-spherical Particles: Evaluation of the Wentzel-Kramers-Brillouin Method." *Applied Optics, 21*(3):373-386.

Knox, J. E., 1979. "Millimetre Wave Propagation in Smoke." In *IEEE EASCON-79 Conference Record*, Vol.2, pp 357-361.

Pederson, N. E., J. C. Pederson, and P. C. Waterman, 1984. *Recent Results in the Scattering and Absorption by Elongated Conductive Fibers*. Panametrics, Inc., 221 Crescent Street, Waltham, MA 02254.

Pederson, N. E., J. C. Pederson, and P. C. Waterman, 1985. *Absorption and Scattering by Conductive Fibers: Basic Theory and Comparison with Asymptotic Results*. Panametrics, Inc., 221 Crescent Street, Waltham, MA 02254.

Perry, M. R., M. R. Kulman, V. Kogan, W. Rouse, and M. Causey, 1994. *Test Plan - Study of Test Methods for Visible, Infrared, and Millimeter Smoke Clouds*. ERDEC-CR-115, Edgewood Research Development and Engineering Center, Aberdeen Proving Ground, MD.

Sundaram, G. S., 1979. "Millimetre Waves - The Much Awaited Technological Breakthrough?" *International Defense Review, 11*(2):271-277.

Sutherland, R. A., and J. D. Klett, 1992. "Modeling the Optical and Mechanical Properties of Advanced Battlefield Obscurants." In *Proceedings of the 1992 Battlefield Atmospherics Conference*.

Sutherland, R. A., and J. B. Millard, 1994. "Modeling the Optical and Mechanical Properties of Advanced Battlefield Obscurants: Alternatives to Spherical Approximations." In *Proceedings of the 19th Army Science Conference*.

Sutherland, R. A., and W. M. Farmer, 1994. *Second Workshop on the Electromagnetics of Combat Induced Atmospheric Obscurants*. In Press, U.S. Army Research Laboratory, Battlefield Environment Directorate, White Sands Missile Range, NM 88002-5501.

A MULTISTREAM SIMULATION OF MULTIPLE SCATTERING OF POLARIZED RADIATION BY ENSEMBLES OF NON-SPHERICAL PARTICLES

Sean G. O'Brien
Physical Science Laboratory
New Mexico State University
Las Cruces, New Mexico 88003-0002

ABSTRACT

The Battlefield Emission and Multiple Scattering (BEAMS) model has been modified to allow for simulation of the multiple scattering of polarized incident radiation by both spherically symmetric and non-spherical scatterers. The modified Stokes vector representation is used to characterize the incident and scattered radiation streams. The new model uses multiple scattering Mueller phase matrices to describe the interaction between the incident radiation and the spatial volume containing scattering particles. The theory behind necessary modifications to the BEAMS model is described, along with comparison examples of the modified model with the previous scalar version for spherical (Mie) particles. Comparisons of total scattered power between the new and scalar BEAMS versions show good agreement, indicating that the coding and normalization of the new version are fundamentally sound. BEAMS simulation examples for preferentially-oriented ensembles of non-spherical particles are also provided. Interesting features and applications of these results are discussed.

1. INTRODUCTION

The practical simulation of interactions of electromagnetic radiation sources with the environment has been an enduring topic of interest to military systems analysts and climatological modelers. One more difficult aspect of such simulations is the accurate depiction of radiative transfer through realistic atmospheres composed of scatterers of varying size, shape, and number density. By necessity, computer models developed to consider this class of problems represent compromises in both execution speed and accuracy. Scene visualization for infrared (IR) and millimeter wave (MMW) sensors in battlefield environments populated by dense inhomogeneous clouds of aerosol obscurants is a particularly demanding enterprise. Any model used in this application must have reasonably high spatial and angular resolution, and be efficient enough to allow time-stepped (but not necessarily real-time) calculations simulating relative motions of the clouds, sensors, and targets.

The BEAMS series of models (Hoock, 1987, 1991; Hoock et al., 1993; O'Brien 1993) represents an evolving effort to provide practical and efficient means for performing radiative transfer calculations used in scene visualizations. The early versions of the BEAMS models simulated the multiple scattering of monochromatic scalar (unpolarized) radiation from infinite beam (e.g., solar) and finite beam sources. This scalar scattering treatment provided a foundation for one of the major goals of the BEAMS development project, which is to model the multiple scattering of arbitrarily polarized radiation by finite, inhomogeneous aerosol clouds. The latest version of the BEAMS model (version 4.0) realizes this objective by describing the incident and propagated radiation in terms of modified Stokes 4-vector streams. These 4-vector streams replace the single scalar intensity streams of the scalar model. In place of the phase matrix used

in the scalar model, the revised model employs a 4 x 4 Mueller phase matrix to describe the scattering of the incident vector stream into scattered vector streams.

Most of this paper will be concerned with how the scalar model was modified to implement the Mueller matrix formalism. It is assumed that the reader is already familiar with the BEAMS 2.2 scalar model (O'Brien, 1993). The review of the workings of BEAMS 2.2 will thus be brief.

2. THEORY AND IMPLEMENTATION

2.1 Review of the BEAMS 2.2 Scalar Multistream Approach

As explained in an earlier paper (O'Brien, 1993), the BEAMS numerical solution of the radiative transfer problem is performed for a three-dimensional array of cubical volume elements or "cells". Each element is optically homogeneous within its own volume and may optically differ from its neighbors. Radiative transfer interactions between adjacent cells are accomplished in a center-to-center regime. The cell center receives and scatters radiation within 26 solid angle cones or "streams". Radiation scattered from one cell is transferred to its 26 immediate neighbors using the scattering cell's stream output powers as inputs to its neighbors' oppositely-directed streams. Transfer of the radiant power from the cell boundary to the center and from the center back to the boundary is effected by a simple single scattering approximation. Thus, the optical depth of the cell must be small enough to allow the single scattering approximation to be valid or the phase matrix used to describe the scattering event at the cell center must account for changes to the angular shape of that matrix due to multiple scattering.

In practice, the later versions of the scalar BEAMS model used a "multiple scattering phase matrix" built up by running a specialized version of BEAMS for homogeneous, optically thick cubical volumes composed of optically thin cubical cells. The resulting phase matrix was stored for a fixed set of optical depths along the principal axes of the optically thick cubical volume. Subsequent runs with the full BEAMS model logarithmically interpolated the phase matrix over optical depth to get the multiple scattering phase matrix for an arbitrary optical depth of a given cell.

2.2 The Mueller Matrix for Single Scattering

Central to the polarized scattering treatment in BEAMS 4.0 is the Mueller matrix used to scatter an incident modified Stokes vector. Because the Stokes vector is an intensity representation derived from the transverse electric vector (or amplitude) representation, the discussion of the scattering process begins with a description of the elliptically polarized plane wave. Figure 1 shows the ellipse swept out by the total electric vector E for a propagation vector k that is perpendicular to the plane of the paper. The plane of scattering is defined by the incident and scattered propagation vectors. If the electric vector components parallel and perpendicular to the scattering plane are designated by E_l and E_r respectively, the temporal behavior for the field at a point in space may be represented by the relations

$$E_l = E_{l0} \sin(\omega t - \epsilon_l)$$
$$E_r = E_{r0} \sin(\omega t - \epsilon_r) \qquad (1)$$

where the corresponding intensities are given by $I_l = E_{lo}^2$ and $I_r = E_{ro}^2$ and the total intensity is given by $E_o^2 = I = I_l + I_r$. It is convenient to define the

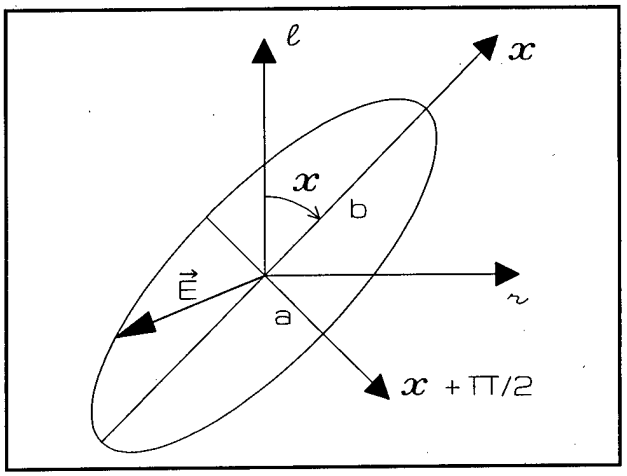


Figure 1. Polarization ellipse for elliptically polarized plane wave.

ratio of the minor axis to major axis as the tangent of a parameter β: tan β = a/b. The total E vector may be decomposed into components along the major (E_χ) and minor ($E_{\chi + \pi/2}$) axes of the polarization ellipse:

$$E_\chi = E_o \sin \omega t \cos \beta$$
$$E_{\chi+\pi/2} = E_o \cos \omega t \sin \beta \qquad (2)$$

Projecting the components E_χ and $E_{\chi + \pi/2}$ onto the parallel and perpendicular scattering planes, and expanding the Eq. 1 relations, it is seen that

$$\begin{aligned} E_l &= E_o (\sin \omega t \cos \beta \cos \chi - \cos \omega t \sin \beta \sin \chi) \\ &= E_{lo} (\sin \omega t \cos \epsilon_l - \cos \omega t \sin \epsilon_l) \\ E_r &= E_o (\sin \omega t \cos \beta \sin \chi + \cos \omega t \sin \beta \cos \chi) \\ &= E_{ro} (\sin \omega t \cos \epsilon_r - \cos \omega t \sin \epsilon_r) \end{aligned} \qquad (3)$$

Equating the coefficients of the sin ωt and cos ωt terms in Eq. 3, and using simple trigonometric identities, the amplitudes and phases in Eq. 3 are seen to obey the relations

$$\begin{aligned} E_{lo} &= E_o (\cos^2 \beta \cos^2 \chi + \sin^2 \beta \sin^2 \chi)^{1/2} \\ E_{ro} &= E_o (\cos^2 \beta \sin^2 \chi + \sin^2 \beta \cos^2 \chi)^{1/2} \\ \tan \epsilon_l &= \tan \beta \tan \chi \\ \tan \epsilon_r &= -\tan \beta \cot \chi \end{aligned} \qquad (4)$$

The components of the modified Stokes vector F = {I_l, I_r, U, V} can then be defined in terms of either their fundamental forms, involving amplitudes and phases, or one composed of intensities and the geometry of the polarization ellipse:

$$\begin{aligned} I_l &= E_{lo}^2 = I (\cos^2 \beta \cos^2 \chi + \sin^2 \beta \sin^2 \chi) \\ I_r &= E_{ro}^2 = I (\cos^2 \beta \sin^2 \chi + \sin^2 \beta \cos^2 \chi) \\ U &= 2 E_{lo} E_{ro} \cos (\epsilon_l - \epsilon_r) = I \cos 2\beta \sin 2\chi \\ V &= 2 E_{lo} E_{ro} \sin (\epsilon_l - \epsilon_r) = I \sin 2\beta \end{aligned} \qquad (5)$$

The intensity form of the Stokes vector is convenient for use by a flux transport model like BEAMS, because each of its components may be treated as an independently-propagating stream. The 4x4 transformation matrix **R** that defines the scattering process converts an incoming Stokes vector F into an outgoing vector F′ = {I_l′, I_r′, U′, V′}: **F′ = R F**.

Most single scattering models calculate the polarized scattering properties of an aerosol particle or collection of particles in the form of 2x2 amplitude scattering matrices **S**. Matrix **S** relates the complex amplitudes of the incoming and outgoing waves:

$$\begin{pmatrix} E_l' \\ E_r' \end{pmatrix} = \begin{pmatrix} S_2 & S_3 \\ S_4 & S_1 \end{pmatrix} \begin{pmatrix} E_l \\ E_r \end{pmatrix} \quad . \tag{6}$$

These amplitude (Jones) matrices may be transformed to the intensity (Mueller) form through the amplitude definitions for the Stokes vector components. The resulting mapping of a given **S** into a corresponding **R** is given by (van de Hulst, 1981)

$$R = \begin{pmatrix} M_2 & M_3 & Q_{23} & -D_{23} \\ M_4 & M_1 & Q_{41} & -D_{41} \\ 2Q_{24} & 2Q_{31} & Q_{21}+Q_{34} & -D_{21}+D_{34} \\ 2D_{24} & 2D_{31} & D_{21}+D_{34} & Q_{21}-Q_{34} \end{pmatrix} , \tag{7}$$

where

$$\begin{aligned} M_k &= S_k \, S_k^* \\ Q_{kj} &= Q_{jk} = (S_j \, S_k^* + S_k \, S_j^*)/2 \\ -D_{kj} &= D_{jk} = i \, (S_j \, S_k^* - S_k \, S_j^*)/2 \end{aligned} \quad . \tag{8}$$

The asterisk superscript in Eq. 8 denotes complex conjugation of the **S** matrix elements, which are in general complex-valued. The elements of the Mueller matrix **R** in Eq. 7 are real-valued.

2.3 Change of Coordinates between Planes of Incidence and Scattering

The Stokes vector scattering representation given by Eqs. 5-8 is directly usable if only the plane of scattering is studied. If a fixed scenario coordinate system is employed (as is the case for BEAMS), the incoming and outgoing propagation directions of the Stokes vector are essentially arbitrary. In that event, rotation matrices must be employed to rotate the Stokes vector defined in scenario coordinates into the scattering plane before the scattering event and out of that plane after scattering. The procedure for constructing such transformation matrices is straightforward (Chandrasekhar, 1960). Looking in the direction of propagation, a clockwise rotation of the reference axes about an angle α will manifest itself as an offset in the angle χ for the polarization ellipse. The defining relations in Eq. 5 then become

$$\begin{aligned} I_l' &= I \, (\cos^2 \beta \, \cos^2 (\chi-\alpha) + \sin^2 \beta \, \sin^2 (\chi-\alpha)) \\ I_r' &= I \, (\cos^2 \beta \, \sin^2 (\chi-\alpha) + \sin^2 \beta \, \cos^2 (\chi-\alpha)) \\ U' &= I \cos 2\beta \, \sin 2(\chi-\alpha) \\ V' &= I \sin 2\beta \end{aligned} \tag{9}$$

After expanding these expressions, grouping terms, and making appropriate identifications from Eq. 5, Eq. 9 defines a rotation matrix **L** that expresses the Stokes vector **F'** in the rotated coordinate system in terms of the vector **F** in the initial coordinate system (i.e., **F'** = **L F**):

$$L(\alpha) = \begin{pmatrix} \cos^2\alpha & \sin^2\alpha & \frac{1}{2}\sin 2\alpha & 0 \\ \sin^2\alpha & \cos^2\alpha & -\frac{1}{2}\sin 2\alpha & 0 \\ -\sin 2\alpha & \sin 2\alpha & \cos 2\alpha & 0 \\ 0 & 0 & 0 & 1 \end{pmatrix} \tag{10}$$

The geometry for a scattering event in the BEAMS model is shown in Figure 2. The nomenclature for angles used here follows that given by Chandrasekhar. Referring to Fig. 2, the component of the E field parallel to the meridian plane containing the Z axis (Z assumed vertical) is labeled V; the perpendicular component (which is parallel to the XY plane) is labeled H. The spherical angle between meridian plane 1 (which contains the vertical Z axis and the line of incidence through the origin) and the scattering plane (which contains the lines of incidence and scattering through the origin) is denoted by i_1. The spherical angle i_2 is formed by meridian plane 2 (containing the line of scattering through the origin and the Z axis) and the scattering plane. The scattering angle between the incoming and outgoing directions is Θ, and (θ_1, ϕ_1), (θ_2, ϕ_2) are the respective polar and azimuth angles for the incoming and outgoing directions. The transformation angles i_1 and i_2 may then be obtained from the cosine law for a spherical triangle (Smart, 1977):

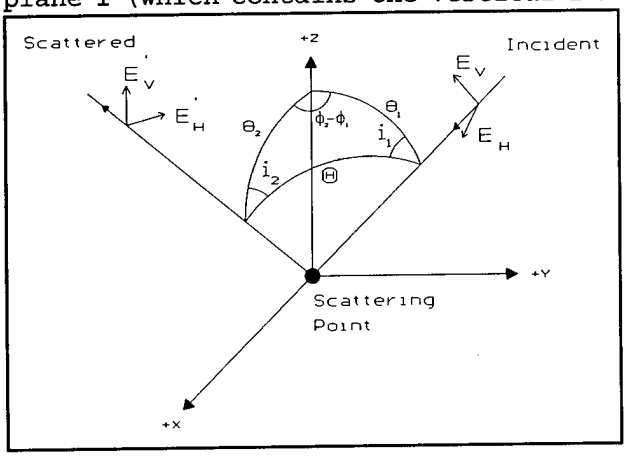


Figure 2. Geometry for Stokes vector scattering in BEAMS 4.0.

$$\cos i_1 = \frac{\cos\theta_2 - \cos\theta_1 \cos\Theta}{\sin\theta_1 \sin\Theta}$$
$$\cos i_2 = \frac{\cos\theta_1 - \cos\theta_2 \cos\Theta}{\sin\theta_2 \sin\Theta} \tag{11}$$

A Stokes vector scattering from meridian 1 to meridian 2 in Fig. 2 must be transformed by the linear transformation $\mathbf{L}(-\mathbf{i_1})$ (Eq. 10) prior to the scattering event. After scattering, another rotation $\mathbf{L}(\pi-\mathbf{i_2})$ is performed in order to express the scattered Stokes vector in terms of the orthogonal (V, H) components in meridian 2. The Mueller phase matrix $\mathbf{P_{12}}$ for scattering from meridional plane 1 to meridional plane 2 may then be stated as

$$P_{12}(\theta_1,\phi_1;\ \theta_2,\phi_2) = L(\pi - i_2)\ R(\cos\Theta)\ L(-i_1) \tag{12}$$

Eq. 12 is the fundamental result that allows the transition from the scalar scattering model of BEAMS 2.2 to the polarized scattering treatment of version 4.0. The user now must input new parameters that specify the fraction of incident flux that is polarized, the polarization angle χ, and the axial ratio parameter β of the polarized component. These quantities are used in conjunction

with Eq. 5 to construct the Stokes vector for both the polarized and unpolarized ($I_l = I_r = I/2$, $U = V = 0$) portions of the incident radiation. After propagation through the rectangular array of cubical scattering cells, the resulting Stokes vectors may be analyzed to yield degree of polarization, polarization angle, and ellipticity of polarization information for radiances at the boundary of any individual scattering cell or for any group of such cells.

2.4 The Multiple Scattering Mueller Matrix

The Stokes vector formalism allows for the construction of a Mueller phase matrix that reflects multiple scattering effects. The method used in the BEAMS 4.0 package is essentially identical to that employed by the scalar BEAMS 2.2. A single scattering model is first used to generate the scattering amplitude matrix **S**. The scattering plane Mueller matrix **R** is next generated by averaging over the BEAMS input streams and applying Eqs. 7 and 8. The single scattering Mueller phase matrix **P** is then generated for stream-to-stream scattering geometries with the relations of Eqs. 10-12. This result is stored in a file (named POLOUT.MAT) with a format that is directly usable by the BEAMS 4.0 program.

As in the scalar version of BEAMS, a dedicated version of BEAMS (named MSPPHMX) was created to generate the multiple scattering phase matrix. This version does not have the normal BEAMS output routines and takes its input from files containing the single scattering Mueller matrix **P** (POLOUT.MAT) and a uniform aerosol concentration parameter fixed at a value of unity. The code computes the stream output Stokes vector radiances for a uniform cubical 5x5x5 array of cells. The axial optical depth τ of the identical component cells is varied to give results for different total axial optical depths 5τ of the cubical array. The output radiances, when renormalized under energy conservation, provide the multiple scattering Mueller matrix for the 5τ cubical array. This matrix result can be used for an individual cell in a nonuniform rectangular scenario array in a BEAMS 4.0 production run.

The demand that creation and storage of the BEAMS 4.0 multiple scattering Mueller matrix places upon computer resources is considerable. MSPPHMX loops over 15 optical depths, creating a result for each depth. At each optical depth, the BEAMS code is executed once for each input stream direction (for a total of 26 separate runs). If the aerosol scatterers under study are spherical, display some degree of shape symmetry, or are randomly-oriented, then clearly the number of such runs could be reduced by application of symmetry. Such reductions are inconvenient because they must be applied on a case-by-case basis and require care to avoid errors caused by inappropriate symmetry assumptions. For this reason, the MSPPHMX software only considers the general case where no symmetry is assumed.

A Mueller phase matrix is computed by MSPPHMX at each of 15 optical depths, is stored in a file named MSPPHMX.MAT, and contains 26x26x4x4 = 10,816 elements. In a binary file format, a file of 15 such phase matrices slightly exceeds half of a megabyte in size. Thus, on any capable modern computer system, file size is seldom a problem. However, because BEAMS logarithmically interpolates phase matrix elements over optical depth, the entire phase matrix data set must reside in memory during a BEAMS 4.0 run. The required Mueller multiple scattering phase matrix storage, combined with that required for the scenario array of cubical aerosol scattering elements, makes the BEAMS 4.0 model impractical to use on personal computer platforms for scenario arrays with over a few thousand cells.

3.0 APPLICATIONS

3.1 Mie Scattering - Comparison of BEAMS 2.2 and BEAMS 4.0

A Mie scattering aerosol was chosen to compare the far field scattered power predicted by the scalar BEAMS 2.2 code with the total (I_l + I_r) scattered power yielded by version 4.0 of BEAMS. The 2x2 scattering amplitude matrix for the Deirmendjian Cloud C.1 aerosol (at a wavelength of 0.45 μm) (Deirmendjian, 1969) was employed for this purpose. A uniform cubical cloud with an edge length of 5 m was constructed for this case, with an axial optical depth of 5. The top (+Z face) of the cube was illuminated by an unpolarized plane-parallel infinite beam with a flux value of 1 W/m^2. Figure 3 shows how the scalar and polarized scattering versions of the BEAMS model compared. The quantity compared is the total scattered power exiting from the boundary surface of the cube into a solid angle equal to $4\pi/26$ steradians. It is apparent that the total scattered power predicted by the two versions of BEAMS compare reasonably well for this case. The BEAMS 4.0 results indicate that the scattered power in the forward hemisphere (scattering angles less than 90 degrees) is not strongly polarized. The backward hemisphere shows a marked enhancement in the horizontal polarization component, which is consistent with the polarization properties of Mie scatterers.

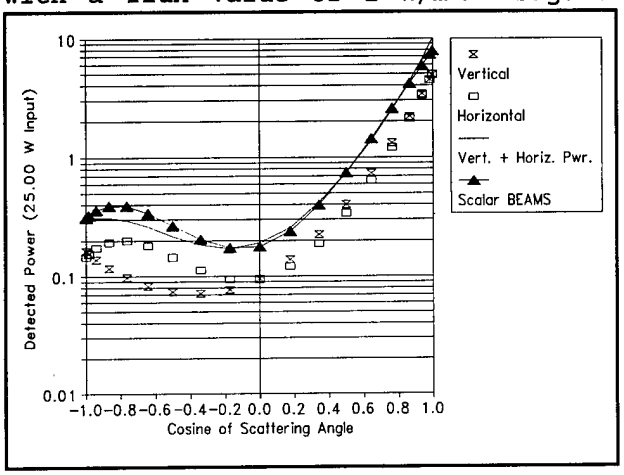


Figure 3. Comparison of detected power in the XZ plane for BEAMS 2.2 (scalar) and BEAMS 4.0 (polarized) multiple scattering phase matrices for Deirmendjian C.1 aerosol.

3.2 Ice Crystals

The BEAMS 4.0 model can be used to predict the scattered power from an ensemble of preferentially-oriented or randomly-oriented non-spherical aerosol particles. For the example shown here, a solid cylindrical ice rod with a 20:1 (length-to-diameter) aspect ratio was chosen. In order to simulate results for a randomly-oriented particle, the Digitized Green Function (DGF) model (Goedecke and O'Brien, 1988) was used to generate an averaged scattering amplitude matrix for a set of orientations of this particle. The ice rod length was set at 0.98 mm, the illuminating wavelength was fixed at 3 mm, and a complex refractive index of 1.78 + 0.00387 i was used. Figures 4 and 5 show the BEAMS 4.0 radiances for a 32 m x 8 m x 8 m uniform cloud of such crystals. The optical depths along the X, Y, Z axes of the cloud were 6.4, 1.6, and 1.6, respectively. The horizontally-polarized (H) collimated illuminating source had a uniformly-illuminated aperture of 0.5 m diameter pointing in the +X direction. Beam power was set at 10 W, and the entry point of the beam was at X = -16 m, Y = +0.5 m, and Z = +0.5 m. The emergent radiances shown here are actually the total scattered power emitted from the cloud into a solid angle of $4\pi26$ steradian.

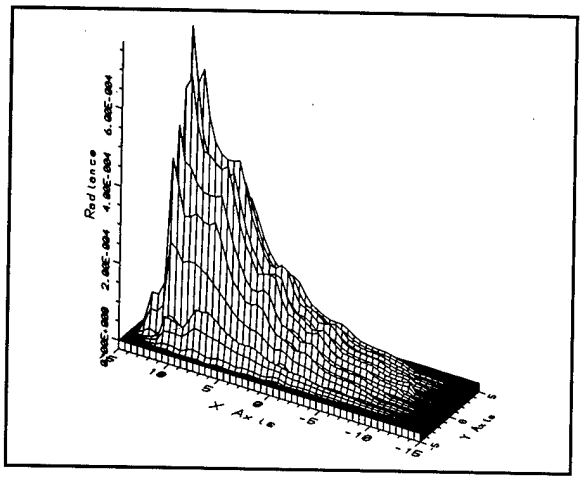


Figure 4. Orthographic perspective view of emergent radiances from ice crystal cloud: V polarization.

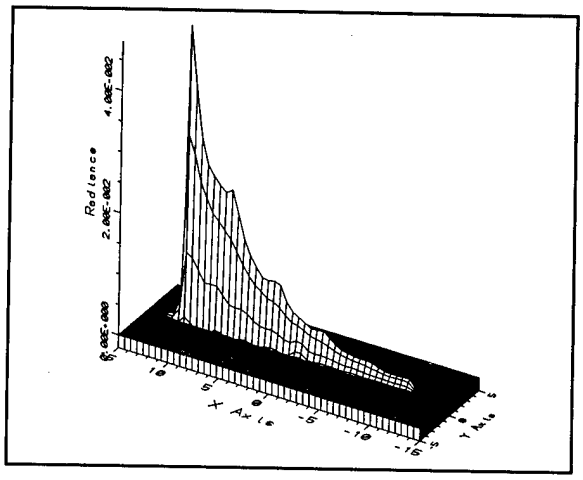


Figure 5. Orthographic perspective view of radiances from ice crystal cloud: H (incident) polarization.

The viewing direction chosen for the emergent radiance is looking down (at a zenith angle of 135 degrees) at an azimuth of 0 degrees (in the +X direction). The radiance shown here is thus due to oblique scattering in the backward hemisphere. It can be seen that the backscattered radiance from the cross-polarized (V) component (Fig. 4) is rather weak and diffuse compared to the H (incident) component (Fig. 5). Also, note the growing strength and spread of the radiance as the beam penetrates into the cloud. The relatively thin transverse optical depth of the cloud appears to be the cause of this trend.

3.3 Graphite and Metal Fibers

Preferentially-oriented graphite and copper fibers with very large aspect ratios may be used to illustrate possible applications of the BEAMS 4.0 model. The scattering amplitude matrices for such fibers (Klett, 1994; Sutherland and Klett, 1994) may be created for average particle orientations at different mechanical turbulence levels. Under low turbulence conditions, an aerosol fiber will frequently fall with its long axis wobbling in a small envelope about the horizontal (Sutherland and Klett, 1992). Both fibers were 3 mm long, with the graphite and copper having respective diameters of 7 μm and 10 μm. Both fibers were also assigned bulk material densities of 2.5 g/cm^3. The graphite fiber diameter was such that it fell with a larger amplitude of wobble than that of the copper wire fiber. The same size and optical depth were used for the aerosol cloud as in the previous (ice crystal) example, as were the source location, orientation, aperture size, power, and polarization. Figures 6 and 7 show the emergent radiance results for the graphite, and Figures 8 and 9 show the copper wire results. The direction of the emergent radiance is the same as in the previous (ice crystal) case. It can be seen that the cross-polarized radiance is considerably stronger for both the graphite and copper fibers than it is for the ice crystals, although the more preferentially-oriented copper wire scatterers show an appreciable enhancement of the H polarization radiance over that of the V component.

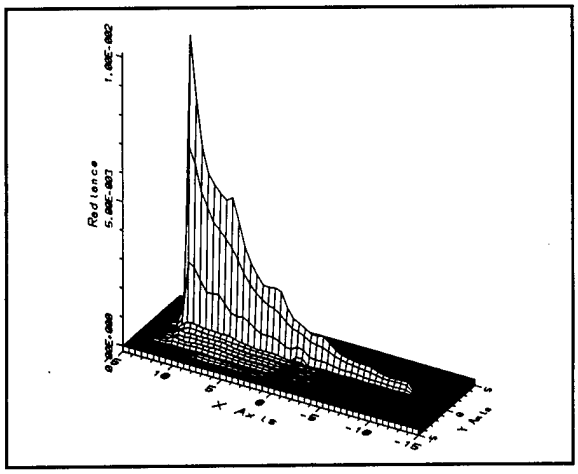


Figure 6. Emergent radiances for graphite cloud (V polarization).

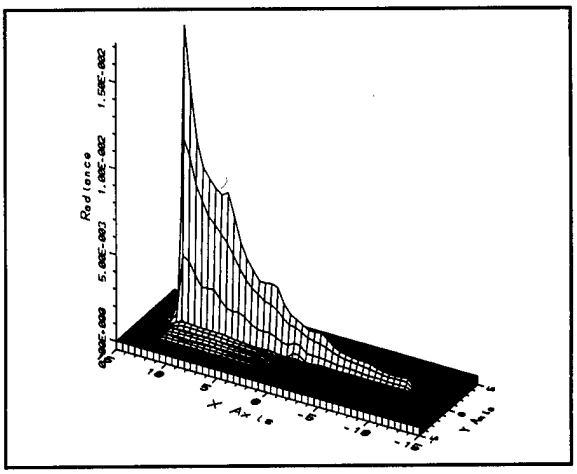


Figure 7. Emergent radiances for graphite cloud (H polarization).

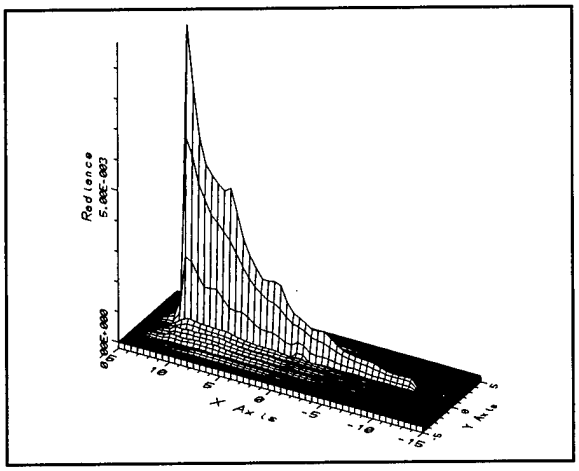


Figure 8. Emergent radiances for cloud of copper wire scatterers (V polarization).

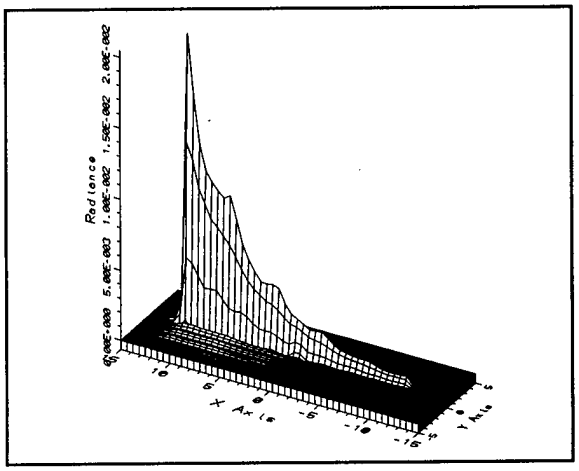


Figure 9. Emergent radiances for cloud of copper wire scatterers (H polarization).

4. CONCLUSIONS

Modifications for treating Stokes vector scattering to BEAMS 2.2 have produced a model (BEAMS 4.0) that compares well with its predecessor for Mie scattering. Preliminary BEAMS 4.0 results for scattering from randomly and preferentially oriented particles are consistent with expectations. However, more testing will be made to confirm the validity and consistency of the new model. One difficulty with the BEAMS 4.0 code is that it places considerable demands upon system resources, even in production mode. For rectangular scenario arrays (e.g., 64x32x32) with large numbers of elements, a BEAMS 4.0 execution may take several hours on a fairly capable machine (i.e., a Silicon Graphics Onyx). This does not represent a problem for the intended applications of the BEAMS model, where multiple scattering radiance statistics are examined. Nevertheless, in cases where polarization effects are not significant, it is still preferable to use one of the faster, scalar versions of BEAMS.

REFERENCES

Chandrasekhar, S., 1960. *Radiative Transfer*, Dover Publications, New York, NY, 416 pp.

Deirmendjian, D., 1969. *Electromagnetic Scattering on Spherical Polydispersions*, Elsevier, New York, NY.

Goedecke, G.H. and S.G. O'Brien, 1988. "Scattering by irregular inhomogeneous particles via the digitized Green's function algorithm", *Appl. Opt.*, 27:2431.

Hoock, D.W., 1987. "A Modeling Approach to Radiative Transfer through Inhomogeneous Dust and Smoke Clouds", *Proceedings of the 7th Annual EOSAEL/TWI Conference*, Las Cruces, NM, pp. 575-596.

Hoock, D.W., 1991. "Theoretical and Measured Fractal Dimensions for Battlefield Aerosol Cloud Visualization and Transmission", *Proceedings of the 1991 Battlefield Atmospherics Conference*, Ft. Bliss, TX, pp. 46-55.

Hoock, D.W., J.C. Giever, and S.G. O'Brien, 1993. "Battlefield Emission and Multiple Scattering (BEAMS), a 3-D Inhomogeneous Radiative Transfer Model", *Proceedings of the SPIE Vol. 1967, Characterization, Propagation, and Simulation Conference*, Orlando, FL, pp. 268-277.

Klett, J.D., 1994. *Scattering of Polarized Light by High Conductivity Fiber Aerosol in Turbulent Air*, Final Report, Contract No. DAAD07-91-C-0139, PAR Associates, 4507 Mockingbird St., Las Cruces, NM, 88001.

O'Brien, S.G., 1993. "Comparison of the BEAMS 2.2 Radiative Transfer Algorithm with other Radiative Transfer Methods", *Proceedings of the 1993 Battlefield Atmospherics Conference*, Las Cruces, NM, pp. 421-435.

Smart, W.M., 1977. *Textbook on Spherical Astronomy*, Cambridge University Press, Cambridge, UK, 431 pp.

Sutherland, R.A., and J.D. Klett, 1992. "Modeling the Optical and Mechanical Properties of Exotic Battlefield Obscurants", *Proceedings of the 1992 Battlefield Atmospherics Conference*, Ft. Bliss, TX, pp. 237-246.

Sutherland, R.A., and J.D. Klett, 1994. Private communications.

van de Hulst, H.C., 1981. *Light Scattering by Small Particles*. Dover Publications, New York, NY, 470 pp.

COMBINED OBSCURATION MODEL FOR BATTLEFIELD INDUCED CONTAMINANTS-RADIATIVE TRANSFER VERSION (COMBIC-RT)

Scarlett D. Ayres, Doug Sheets and Robert Sutherland
Battlefield Environment Directorate
U.S. Army Research Laboratory
White Sands Missile Range, New Mexico 88002-5501

ABSTRACT

The COMBIC model was originally developed for the Electro-Optical Systems Atmospheric Effects Library (EOSAEL 84) to model effects of direct transmission (i.e. Beer Law) only and ignored the more complicated effect of contrast transmission. COMBIC-RT represents an improvement in the radiative transfer algorithm to account for single and multiple scattering, and hence contrast transmission. COMBIC-RT is a merger between COMBIC and the Large Area Smoke Screen (LASS) model developed in 1985. COMBIC-RT reverts to normal COMBIC if the RT option is not exercised. If the RT option is exercised then the outputs of the model are symbolic maps displaying the direct and diffuse components of scene transmission as affected by a large-area smoke screen or a contrast transmission history. The model can be exercised with various optional inputs to determine the effects of solar angle, solar flux density, sky radiance, surface albedo, etc. The COMBIC part of the model applies the Gaussian diffusion approximation to compute obscurant concentration path length (CL product), and the LASS part applies the plane-parallel approximation to compute target-background contrast and contrast transmission. The radiative-transfer algorithms are unique to LASS and COMBIC-RT in the use of the extensive radiative-transfer tables originally published by Van De Hulst that are used together with novel scaling algorithms to account for effects of single and multiple scattering along arbitrary slant path and horizontal lines of sight (LOS). The model does not treat thermal emission and is thus restricted to visible and near-infrared regions. The obscurant phase function is taken to be of the Henyey-Greenstein form and can account for various degrees of anisotropic scattering as well as isotropic scattering. The model accounts for scattering of the direct solar beam, uniform diffuse skylight, and diffuse reflection from the underlying (earth) surface.

1. INTRODUCTION

One of the original purposes for developing COMBIC-RT model was to assist in modeling the effectiveness of smoke screens used in wargame simulations. Large area self-screening smokes are feasible at large fixed and semifixed military installations such as air bases, air fields, and ammunition supply points where attack by nap of the earth aircraft is a possibility. The commander of these military installations need to know to what degree a LASS deployment will protect his station from enemy aircraft as well as know how the LASS will effect friendly aircraft. The wargame simulations will ultimately impact the doctrine the commander will use. In these type of scenarios, contrast reduction caused by scattering of light is the major acquisition defeat mechanism. This scattering of light into the path in real world scenarios can often be of overriding significance in affecting perception. A natural example is the apparent disappearance of stars in daytime. Another common example is the backscatter from headlights when driving through fog with the brights on. The degree to which scattering can be important is indicated by the optical properties of the medium; the mass extinction coefficient α which combines absorption and scattering out of the path of propagation into one term; the single scattering albedo ($\tilde{\omega}_0$) which indicates the fractional amount of scattering, and ($1-\tilde{\omega}_0$) which indicates the fractional amount of absorption. Conventional visible band obscurants such as fog oil has $\tilde{\omega}_o \rightarrow 1$ indicating a predominance of scattering.

COMBIC-RT is made up of two sub-models: one that treats transport and diffusion (the original COMBIC) and another that treats radiative transfer (the radiative transfer algorithms of LASS). COMBIC uses a Gaussian formalism to calculate, for potential unlimited number of smoke clouds, the obscurant path-integrated concentration (CL) for either parallel LOSs over the extent of the entire screen or for just individual LOSs. The radiative transfer segment performs extensive radiative transfer calculations by using the plane parallel approximation that essentially transforms a CL map into a radiative transfer map of contrast transmission. Since the output of COMBIC-RT includes path radiance and downward-directed hemispherical surface irradiance, digital maps of these quantities may also be generated with minor code modifications. The model is primarily applicable to situations in which the observer (for example, an aircraft) is located above the screen and the target is located on the surface. The LASS computer model provides a tool for the study of large area screening systems applications and effects.

2. BACKGROUND

Models like CASTFOREM directly relate transmission to Electro-Optical (EO) system performance and smoke effectiveness by considering only the directly transmitted signal:

$$S(\vec{r}) = S(\vec{r}_o)\, T \tag{1}$$

where $S(\vec{r})$ is the optical signal received by an observer at $(\vec{r})$ from a target at $(\vec{r}_o)$. The transmission (T) includes effects of both scattering out of the path plus absorption along the path. However, EO systems respond not only to directly transmitted radiation but also to contrast. Equation (1) is thus modified to include a term representing path radiance as:

$$S(\vec{r}) = S(\vec{r}_o)\, T + S_p(\vec{r}) \tag{2}$$

where the contribution due to path radiance (S_p) may be due either to scattering of ambient radiation (sun, sky) into the path of propagation or emission along the path, or both. Path radiance has a directional nature causing asymmetries to exist between target and observer. One or the other has an optical advantage not present when one models only the direct transmission component. The LASS model was developed to model these effects. The radiative transfer algorithms were then integrated with COMBIC-RT to enable COMBIC to compute path radiance.

Most target acquisition models work by determining the number of resolvable cycles across the target. This directly relates to the target contrast X at the sensor's aperture for non-thermal sensors, and for a slant-path LOS:

$$T_C(\pm u, \phi) = \frac{1}{1 + \frac{D^*(\pm u, \phi)}{A_b \exp(-\tau)}} \tag{3}$$

where $+\mu$ is the direction cosine directed upward, $-\mu$ is the directional cosine directed downward, ϕ is the azimuth, τ is the optical depth, A_b refer to the target and background albedos. $D^*(\pm\mu,\phi)$ is called the Duntley factor, after the pioneering work of S.Q. Duntley, (Duntley, 1948) and reduces to "sky-to-ground" for a horizontal LOS.

The probability of acquisition may be calculated using the integral:
where $n_{\cdot}$ is the number of resolvable cycles across the target for an acquisition probability of 50 percent, and σ is the standard deviation of the number of resolvable cycles across the target. Using COMBIC-RT and a target acquisition

$$P_a = \frac{1}{\sqrt{2\pi}} \int_{-\infty}^{\frac{(n-n')}{\sigma}} \exp(-x^2/2)\, dx \qquad (4)$$

model like the one in CASTFOREM, it is possible to determine the probability of acquisition of a given target through a LASS cloud at any given point in space and time. This provides a direct measure of the effectiveness of smoke. Figure 1 shows the effect of sun angle on detection probabilities for different optical depths (τ). The probability of detection for τ of 1 varies from 34% in the case of the sun to the front of the observer to 63% for the sun behind the observer. This is as expected. Most of the time, it is easier to "see" with the sun to the back.

Figure 2 shows the effect that the observer azimuth angle (defined wrt North) can have on contrast transmission. Contrast transmission is shown for five CL values. The scenario is for early morning and the zenith angle of the observer is 10 degrees. Notice that low contrast transmission occurs when the observer is looking into the sun (0°) and high contrast transmission occurs with the sun to the back (180°) of the observer. Further, note that the curve flattens out as the CL increases.

3. DEFINITION OF THE PROBLEM

In a typical obscuration scenario, the problem is to compute the total radiance, both direct and diffuse, reaching an observer and emanating from the direction of the target (or background). The direct radiance includes light either emitted or reflected by the target (or background) then transmitted (with some loss due to extinction) along the LOS to the observer. The diffuse radiance is the path radiance emitted and scattered by suspended material (obscurants) at all points along the LOS then transmitted (again with some loss due to extinction) a remaining distance to the observer. The scenario, including the large-area screen, is assumed to be irradiated from above by diffuse sky radiation and from below by diffuse surface radiation (see Figure 3). For daytime scenarios, the direct solar beam is included in the sky component. For nighttime, the direct source may be the Moon, and starlight may be included in the diffuse component.

The radiance incident at the observer propagating from the direction of the target is the combination of the direct and diffuse component or more formally:

$$I(r;\mu,\phi) = I(r_o;\mu,\phi)\, e^{-\tau} + \int_0^{\tau} J(r';\mu,\phi)\, e^{-(\tau-\tau')}\, d\tau' \qquad (5)$$

where $\mu = |\cos\theta|$ is the zenith angle of the observer with respect to the target. The geometry is shown in Figure 4. The first term on the right-hand side is the familiar Beers law and represent radiance transmitted directly from the target to the observer (the direct component). The second term on the right hand side represent the diffuse component. It represents contributions due to scattering of ambient radiation into the path of propagation at all points along the path. This equation has been extensively studied but the major difficulty is the optical-source function, $J(r';\mu,\phi)$, which is itself a function of incoming radiance from all directions so that the formal solution is really quite complex.

The LASS model makes several simplifying assumptions that allow rigorous solutions of Equation 5, including all orders of multiple scattering. A major simplification is the plane-parallel approximation where the optical depths for a slant path at angle θ is equal to the vertical optical depth divided by the cosine of the angle.

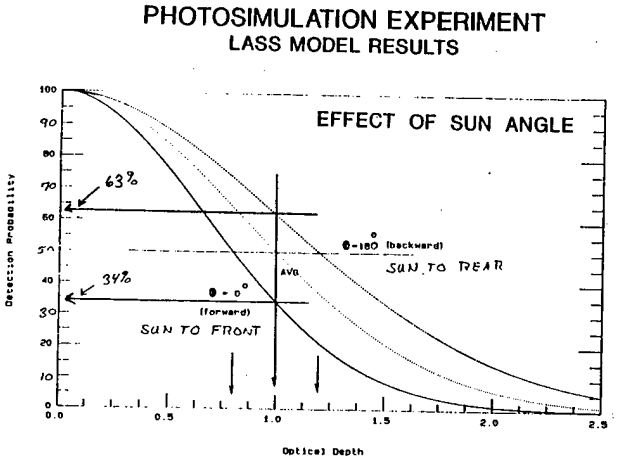


Figure 1 Plot of detection probability as a function of optical depth for various solar azimuth angles.

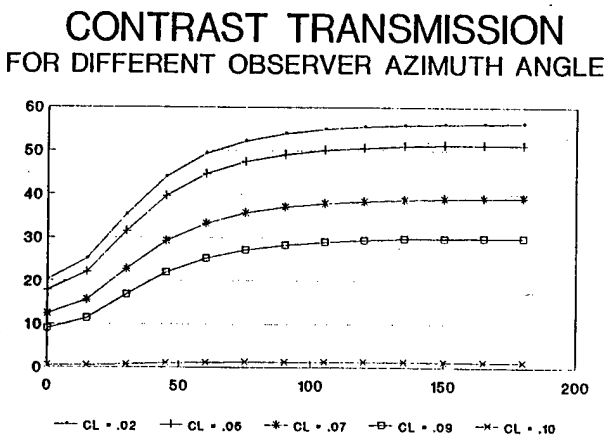


Figure 2 Plot contrast transmission vs. observer azimuth angles.

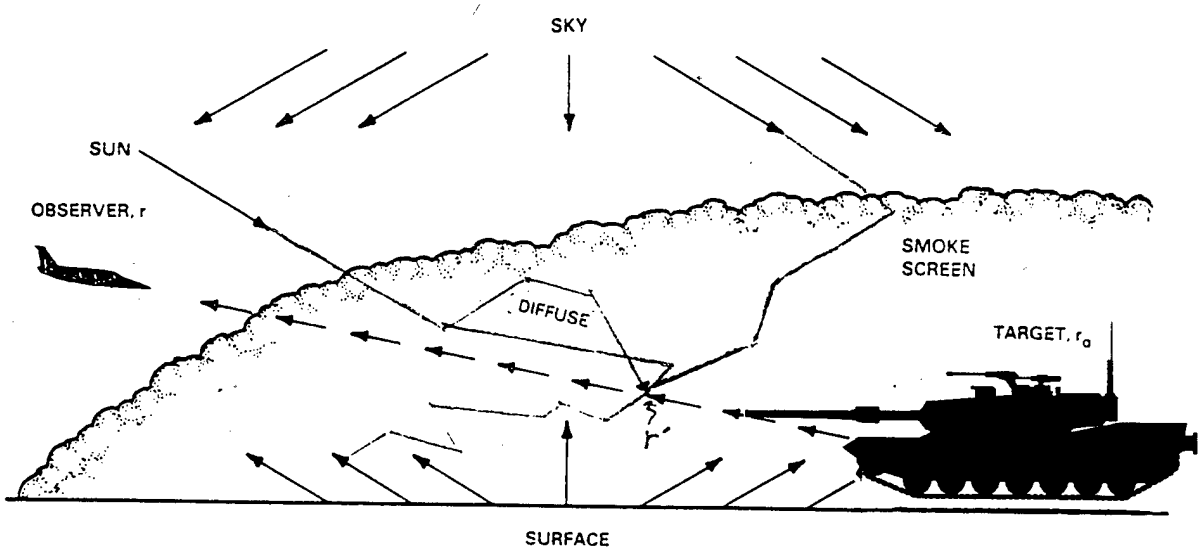


Figure 3 Typical LASS scenario.

The optical source function is dependent upon the phase function $P(\mu,\phi;\mu',\phi')$ which mathematically describes the angular-scattering properties of the obscurant. For inventory smokes, the phase function is best approximated with the Henyey-Greenstein form.

$$P(\mu,\phi;\mu'\phi') = \frac{(1-g^2)}{[1+g^2-2g\cos\psi]^{3/2}} \qquad (6)$$

where ψ is the scattering angle and g is the asymmetry parameter that determines the overall shape of the scattering phase function and can vary from -1 for strong backscatter, to zero for isotropic scattering, an on to near +1 for strong forward scattering. The use of the Henyey-Greenstein form presumes a spherical aerosol, which is reasonable for many obscurant types, especially fog oil. Plots of the Henyey-Greenstein phase function for various values of the asymmetry parameter are shown in Figure 5.

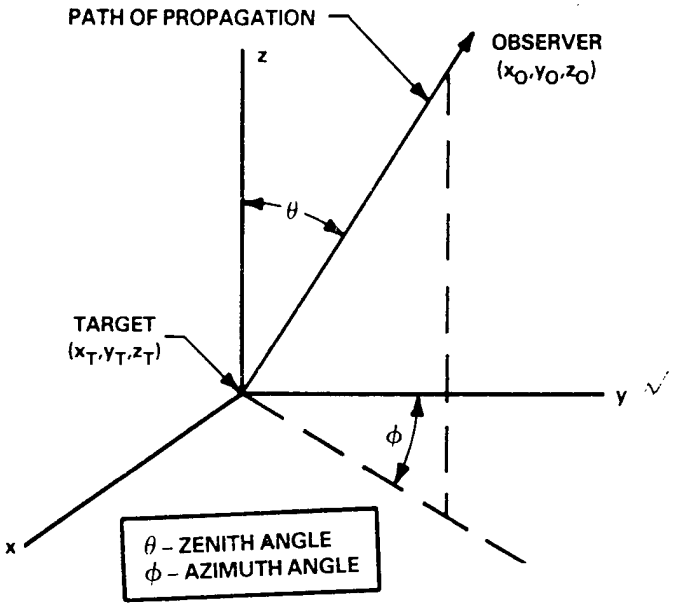


Figure 4 Geometry of the path of propagation.

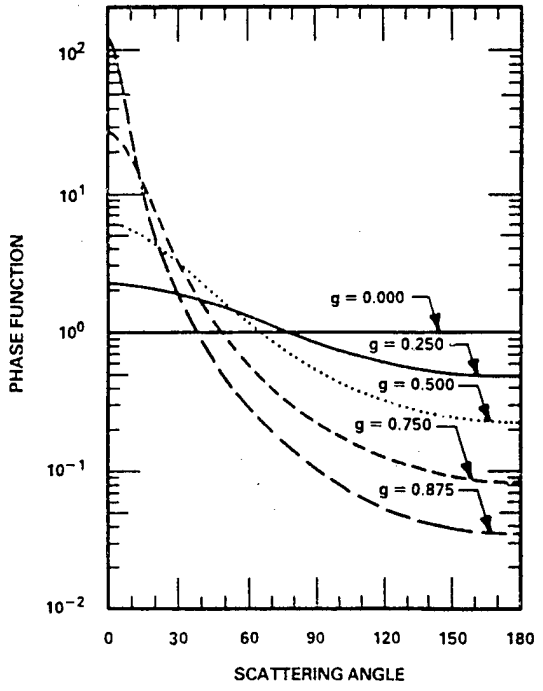


Figure 5 Plot of the Henyey-Greenstein phase function for various asymmetry.

4. REFLECTION AND TRANSMISSION FUNCTIONS

The major computational problem in modeling contrast transmission is the determination of the diffuse transmission and reflection functions. These functions account for effects of multiple scattering within the obscurant cloud which gives rise to the DIFFUSE component of the radiation field and should not be confused with the more familiar DIRECT component which is treated with the simple Beer's Law. In general the diffuse component is difficult to calculate, even under the simplifying assumption of a plane parallel atmosphere. In COMBIC-RT we use a combination of precomputed look up tables based upon rigorous solutions (Sutherland & Fowler, 1986) and special scaling algorithms to approximate the full angular dependent transmission reflection functions accounting for both absorption and scattering (Sutherland, 1988).

In Figure 6 we give an example for a Henyey-Greenstein asymmetry parameter of 0.750 which is typical of conventional visible band obscurants such as fog oil. The reflection operator, denoted in general as $R(\tau,\mu,\phi,\mu_0,\phi_0)$, represents that fraction of an incident plane parallel beam that is diffusely "reflected" into the direction denoted by polar angles θ ($\mu=|\cos\theta|$) and ϕ, where the incident beam is from the direction denoted by μ_0 ($\mu_0=|\cos\theta_0|$) and ϕ_0. The transmission operator, $T(\tau,\mu,\phi,\mu_0,\phi_0)$, is the same except that it accounts for diffuse "transmission".

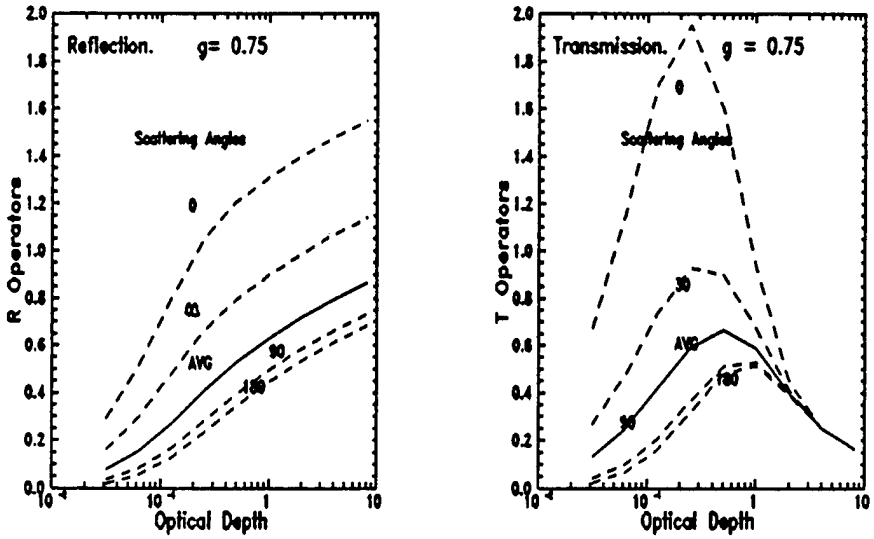


Figure 6 Plots of diffuse reflection and transmission as a function of optical depth for several azimuth angles. Solar beam zenith direction is uo=0.50 and viewing angle is u=0.10.

For example, the plots on the left in Fig. 6 show the value of the reflection operator as a function of optical depth assuming a solar incident beam direction μ_0=0.50 (θ_0=60°) and ϕ_0=0°. This example corresponds to the case of an airborne observer looking downward and solar radiation "reflected" upward from the obscurant cloud. Note that, in general, the reflected radiation increases with optical depth and eventually tends to level off at the higher values. Note also that the reflection curves are highest at ϕ=0° (forward scattering) and diminish with angle out to ϕ=180° (backscatter). This general behavior is typical of visible band obscurants and can also be qualitatively verified from casual observation of the "brightening" of water clouds as viewed from above.

The behavior of the diffuse transmission operator are shown to the right in Fig. 6. This example corresponds to the case of an observer on the ground looking upward and solar radiation being "transmitted" downward through the obscurant cloud. Note from inspection that diffuse transmission is both qualitatively and quantitatively different than that of diffuse reflection. The most apparent difference between the two sets of curves is the peak in transmission that occurs at an optical depth between 0.10 and 1.0 depending upon the particular azimuth curve. This is markedly different than the reflection function that monotonically approaches a plateau with no well defined maximum. Note that the behavior of the diffuse transmission is radically different than that of the direct transmission which monotonically decreases in accordance with Beer's Law. This effect can be observed in real world smoke clouds by observing the directional brightness relative to the sun.

5. INTEGRATING RADIATIVE TRANSFER ALGORITHMS INTO COMBIC

5.1 General

Creating COMBIC-RT is partially a matter of integrating LASS into COMBIC. The radiative transfer subroutines from LASS require as input a digital map of CL or CL from individual LOSs; the obscurant optical scattering and extinction properties; the ambient radiation levels for the sun and sky; and the

reflectivities or albedos of the target, background and earth surface. The CL digital map produced by COMBIC is a line printer digital plot. Data points are represented by a grey-scale of alphanumeric characters using the numbers 0 through 9 to depict gray-level bins. Though LASS does have the ability to generate its own CL values, any transport and diffusion (T&D) model could be used. It was decided to use COMBIC as the T&D model for several reasons. First, it is in the wargames already. Second, COMBIC plays all the smokes the wargames required and LASS plays only fog oil. Third, all that is needed for radiative transfer (RT) calculations for COMBIC produced large area screens are the extinction and scattering information for the other obscurants. Fourth, COMBIC has been updated and improved continuously over the years. COMBIC still determines CL the same way, except it now has the ability to compute contrast transmission for individual LOS and for the digital map. The model is primarily applicable to situations in which the observer (for example, an aircraft) is located above the screen and the target is located on the surface.

5.2 Inputs

All input data for COMBIC-RT are entered in standard EOSAEL format, A4,6X,7E10.4, that is, input data are entered through 80-character, order-independent, "card" images. Tables 1-4 describe the new input cards that are to be used in addition to the original COMBIC input cards. Shown are examples of the cards plus explanation and units of the various inputs. Figure 7 can be used to estimate sun and sky irradiance values for different sun angles.

Table 1: The OBSC Card.

```
        1       2       3       4       5       6       7       8
12345678901234567890123456789012345678901234567890123456789012345678901234567890
OBSC            EXTCO   GHG
```

NAME	UNITS	Obscurant optical properties
EXTCO	m^2/g	Mass extinction coefficient
GHG		Henyey-Greenstein asymmetry parameter code
		Code / Parameter, g
		0.0 / 0.0
		1.0 / 0.25
		2.0 / 0.50
		3.0 / 0.75 (fog oil)
		4.0 / 0.875

Table 2: The SOLR Card.

```
        1       2       3       4       5       6       7       8
12345678901234567890123456789012345678901234567890123456789012345678901234567890
SOLR            FSOL    ISOLMU  SOLPHI  ALBDO   SKY
```

NAME	UNITS	Solar and sky data
FSOL	W/m^2	Solar beam irradiance
ISOLMU		Solar zenith angle code
		CODE / Zenith(Angle) / COS(Zenith Angle)
		0 / 90.0 / 0.0
		1 / 84.3 / 0.1
		2 / 72.5 / 0.3
		3 / 60.0 / 0.5
		4 / 45.6 / 0.7
		5 / 25.8 / 0.9
		6 / Vert (0.0) / 1.0
SOLPHI	degrees	Solar Azimuth Angle Measured from North
ALBDO		Surface Albedo (0.0--1.0)
SKY	W/m^2	Sky diffuse irradiance

Table 3: The ALBO Card.

```
        1       2       3       4       5       6       7       8
12345678901234567890123456789012345678901234567890123456789012345678901234567890
ALBO            TGTALB  BCKALB
```

NAME	UNITS	Target and Background Albedos
TGTALB		Target albedo (0.0-1.0)
		(TGTALB) not used in this release
BCKALB		Background albedo (0.0-1.0)
		Vegetation 0.12 - 0.26
		Sand 0.11 - 0.35
		Clay 0.10 - 0.15
		loam 0.09 - 0.16
		Snow 0.80
		Water 0.01 - 0.04
		Asphalt 0.03 - 0.15
		Concrete 0.37

Table 4: The RTAZ Card. This card inputs the option to include azimuth independence

```
        1       2       3       4       5       6       7       8
12345678901234567890123456789012345678901234567890123456789012345678901234567890
RTAZ            AZDEP
```

NAME	UNITS	Option to scale R and T functions to include azimuth dependence
AZDEP		=0.0 for azimuth-dependent calculations
		=1.0 for azimuth-averaged calculations

5.3 Caveats

The model treats only scattering in the path radiance term and is thus restricted to wavelengths where thermal emission is nominally insignificant, that is, to the visible and near-infrared wavelengths. For the RT calculations to be meaningful, the phase function of any obscurant studied should be well described by an Henyey-Greenstein form with an asymmetry parameter of 0.0, 0.25, 0.5, 0.75, or 0.875. As currently programmed, the model explicitly treats only conventional M3A3 fog oil generators but can treat any semicontinuous source provided that the appropriate source characteristics are supplied as input by

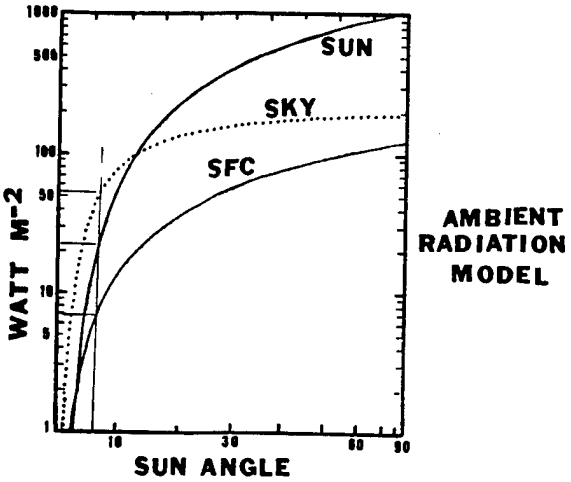


Figure 7 Ambient sun, surface and sky irradiance for different Sun Angles.

the user. The plane-parallel approximation is not strictly applicable for a finite Gaussian screen. Since the clouds are gaussian, the vertical optical thickness is not strictly constant over the horizontal extent of the screen. An equivalent vertical optical thickness is used based upon the optical depth determined by COMBIC. This will introduce errors near the edge of the screen that are, however, negligible within the screen interior. The user should also be aware that the path radiance calculations are for an *established* LASS. COMBIC can model the LASS from time = 0 seconds but the RT algorithms should not be used until the LASS is established.

6.0 EXAMPLE OUTPUT

6.1 Example 1

In the examples that follow, the obscurant is fog oil dispersed by 17 M3A3 generators. Resolution is 40 m. Wind is blowing from 40°. The time is 200 s after the generators started to produce fog oil. The cloud is mapped by using LOSs parallel to the observer-target LOS. A minimum CL defines the edge of the cloud. The CL map is shown in Figure 8.

In example 1, the scenario establishes an observer directly over the target at an altitude of 1000 m. In this example, it is decided to compare the effects of observing early morning with observing at noon time. Figure 9 shows the contrast transmission map for the early morning scenario with the sun due east (azimuth = 90°) and just above the horizon (zenith = 84°). The solar flux density is set to $10W/m^2$, and the diffuse sky irradiance is defined to be $40W/m^2$. The background, surface, and target albedos are set to 0.2. Note that the observer position in this scenario is directly over the large area smoke screen. Therefore, the observer-target (scattered radiation) LOS is nearly perpendicular to the solar-target (incident radiation) LOS. That is, the scattering angle is approximately 90°.

Figure 10 shows the contrast transmission map for the noon scenario. The same CL computations used in the morning scenario is used in this scenario. The sun is located nearly overhead (azimuth = 180°, zenith = 26°). The solar flux is set to $950W/m^2$, and the diffuse sky irradiance is $180W/m^2$. All other input parameters remain identical to those established in the morning scenario.

Recalling that the observer and solar positions set for this example establish a backscatter situation (the scattering angle is 164°), a comparison of the two

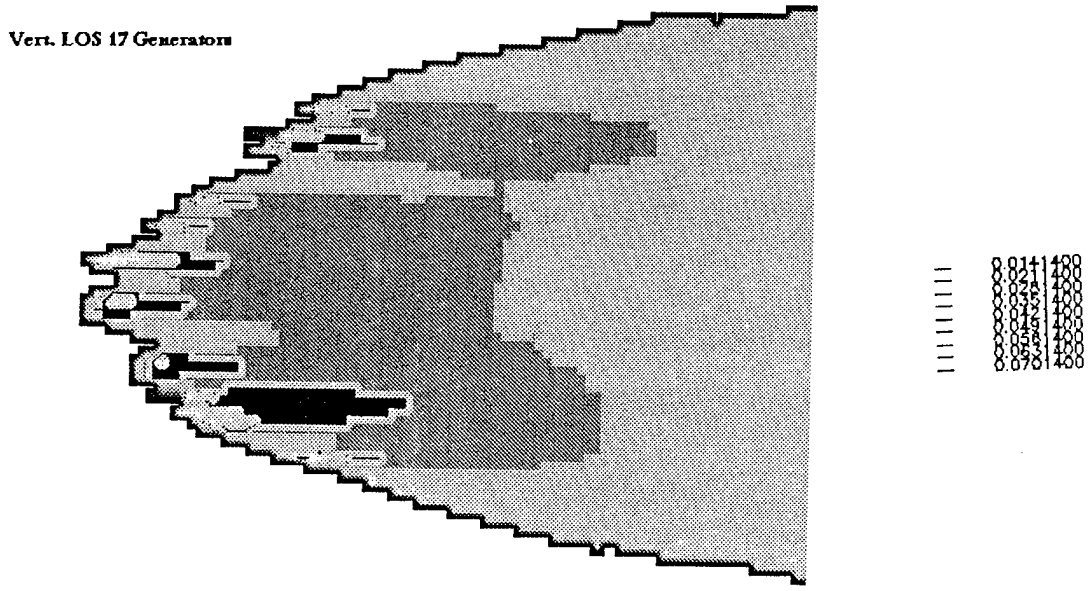


Figure 8 CL map produced for an overhead observer.

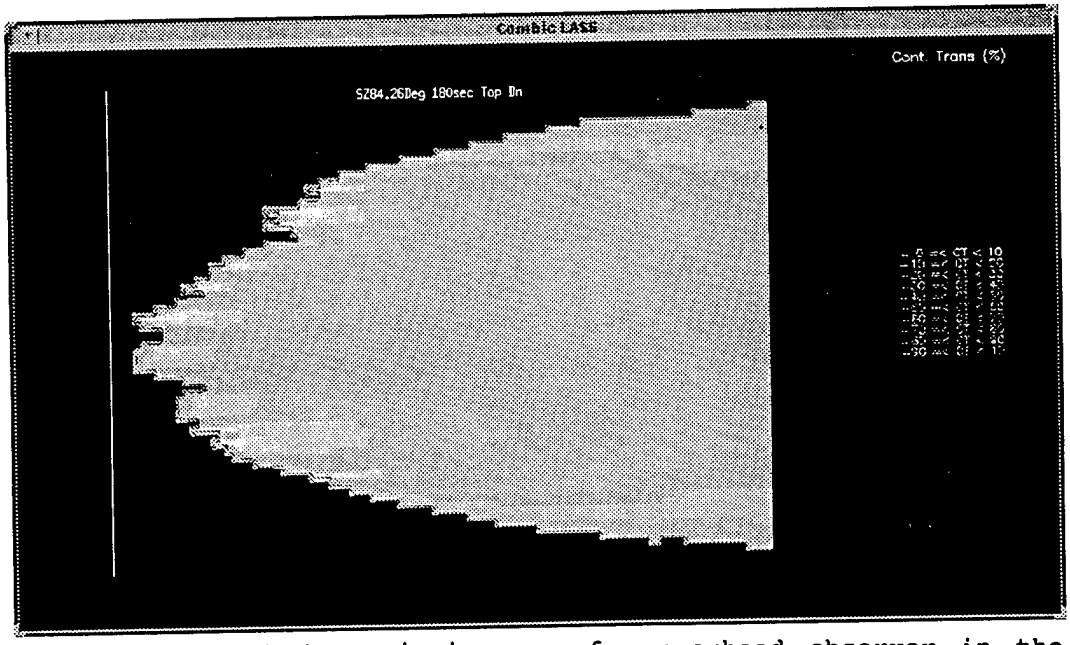


Figure 9 Contrast transmission map for overhead observer in the early morning.

contrast transmission maps illustrates the importance of sun-target-observer angles to obscurant effectiveness. This comparison reveals that the same smoke screen viewed by an overhead observer is more effective in obscuring targets in the early morning than it is at midday.

This example demonstrates the utility of COMBIC/LASS in using a single CL map to study various RT scenarios, that is, changes in solar flux, solar position, diffuse sky irradiance, and background albedo.

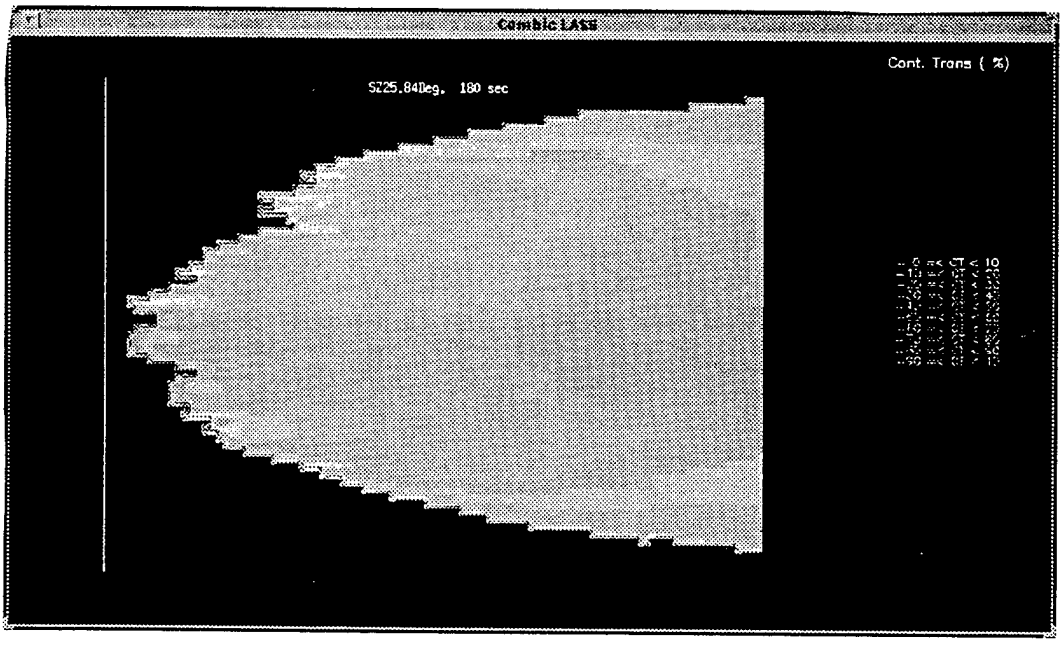


Figure 10 Contrast Transmission map for overhead LOS for a midday scenario.

6.2 Example 2

Example 2 illustrates a horizontal scenario. However, instead of using the printer-plot option, the usual transmission history file is produced. In this example, the observer's zenith is 90° and the azimuth is 270°.

TIME	OBS	TARG	CL	TRANSMISSION							CONTRAST	HORZ PATH	DIRECT
											TRANSMISSION	IRRADIANCE	IRRADIANCE
(SEC)	NO.	NO.	(G/M**2)	.4-.7	.7-1.2	1.06	3.-5.	8.-12.	10.6	94GHZ	EXTC=7.20	(W/M**2)	(W/M**2)
40.0	1	1	.004	.972	.981	.986	.999	1.000	1.000	1.000	.945	.140	2.402
60.0	1	1	.055	.684	.775	.824	.987	.999	.999	1.000	.534	1.350	1.545
80.0	1	1	.075	.597	.708	.768	.982	.998	.999	1.000	.438	1.714	1.338
100.0	1	1	.099	.509	.636	.708	.976	.998	.998	1.000	.352	2.084	1.130
120.0	1	1	.125	.424	.562	.645	.970	.997	.998	1.000	.277	2.436	0.933
140.0	1	1	.134	.399	.540	.626	.968	.997	.998	1.000	.257	2.535	0.877
160.0	1	1	.134	.399	.541	.626	.968	.997	.998	1.000	.257	2.535	0.877
180.0	1	1	.134	.400	.541	.626	.968	.997	.998	1.000	.258	2.533	0.878

REFERENCES

Ayres, S.D., and S. DeSutter, 1993: "Combined Obscuration Model for Battlefield Induced Contaminants (COMBIC) Users Guide," In Press, Department of the Army, U.S. Army Research Laboratory, Battlefield Environment Directorate, White Sands Missile Range.

Duntley, S.Q., 1948: "The Reduction of Apparent Contrast by the Atmosphere". In J Opt Soc AM, Chapter 38, pages 179-191.

Sutherland, R.A. and B.W. Fowler, 1986: "Standards for Large Area Screening Systems Modeling," US JTCG/ME Special Publication 61-JTCG/ME-85-4.

Sutherland, R.A., 1988, "Methods of Radiative Transfer for Electro-Optical Obscuration Modeling", Proceedings of the 1988 Army Science Conference.

EMISSIVE SMOKE MODELING FOR IMAGING-INFRARED SEEKER/TRACKER SIMULATION

Joseph L. Manning, Charles S. Hall, and Sheri M. Siniard
Computer Sciences Corporation
Huntsville Alabama

ABSTRACT

A computer model has been developed to generate three-dimensional time sequences of fractally textured smoke clouds for insertion into infrared scene simulations. The model includes source models for LUST bucket, L8A3 and M76 grenades, and other munitions, transport and diffusion using Gaussian methodology, thermal radiative transfer, and fractal texturing to simulate the effects of atmospheric turbulence. Modified versions of Battlefield Environment Directorate codes COMBIC, FITTE, and STATBIC are used as subroutines or procedures. A unique capability of the emissive smoke model is the ability to predict thermal emission from phosphorus wedges dispersed by munitions such as LUST buckets, and smoke plumes generated by the wedges as they burn on the ground. The model produces extinction and radiance information on a fine three-dimensional grid that may be placed anywhere in a simulated infrared image. The model has been used at MICOM to generate countermeasure smoke and battlefield fire images for use with an imaging-infrared seeker/tracker missile simulation code. Simulated imagery of engagements that include WP and fires will be shown.

1. INTRODUCTION

The Emissive Smoke Code was developed in response to the need to include realistic renderings of countermeasure smokes and obscurants, as well as incidental battlefield fires, in missile flight simulation codes for systems using imaging seeker/trackers. By using the code in conjunction with a flight simulation code it is possible to assess the performance of a missile system in the presence of obscurant countermeasures. Because Emissive_Smoke is a physical model that treats the obscurant sources and the transport and diffusion of the smoke, the assessment may include parametric variation of such physical parameters as source fill weight, wind speed, and Pasquill stability category. The code is referred to as the Emissive Smoke Code, or Emissive_Smoke, because of its ability to model the thermal clutter caused by hot smokes such as WP, but the code is applicable as well to ambient-temperature obscurants such as fog oil, brass, carbon fibers, carbon smoke from explosions, and artillery dust.

A unique feature of Emissive_Smoke is a model for obscurant munitions that disperse fragments of phosphorus over a large area. These phosphorus fragments may burn for several minutes, producing a large, uneven curtain of phosphorus smoke. The Limited Use Smoke

Test Device is a static munition that is used in field tests to simulate artillery-delivered phosphorus munitions; commonly called a LUST bucket, it consists of WP wedges in a 1-gal paint can or a 5-gal steel pail. The Emissive Smoke Code includes models for both 1-gal and 5-gal LUST bucket munitions.

Emissive_Smoke creates a file containing concentration and temperature data for a three-dimensional grid, for each time step. It is generally used with spatial resolution of 0.2 m and temporal resolution of 0.1 sec. These files are then read by the image simulation code and are added to the simulated infrared scene, which already includes a detailed target, terrain background, treeline, and sky.

Emissive_Smoke uses a subroutine version of COMBIC (Hoock, Sutherland, and Clayton, 1987) to model transport and diffusion of the smoke clouds. The fractal texturing algorithm is an adaptation of STATBIC, a code developed by Dr. Don Hoock of the Army Research Laboratory Battlefield Environment Directorate to demonstrate fractal techniques under development at BED (Hoock, undated). Fires and fire plumes are generated using a specially modified version of FITTE (Bruce, 1987). This is a separate code at present, but it follows the same formats, and is logically, if not literally, a part of Emissive_Smoke. COMBIC and FITTE are both in the EOSAEL library of computer codes that is maintained and distributed by ARL/BED.

The original emissive smoke code, called ESI, was developed by the Physical Science Laboratory at New Mexico State University (Physical Sciences Laboratory, 1993). The present code is built around the framework of ESI but includes substantial upgrading and expansion, including improved physical modeling, porting to UNIX systems, interfacing with scene rendering and missile flight simulation software, and addition of fractal texturing.

2. THE VOXEL FILE AND ITS PLACEMENT IN THE SCENE

Emissive_Smoke produces smoke data in a three-dimensional rectangular array. The volume elements of this array are referred to as voxels. At each time step, the Emissive_Smoke code writes a file that contains a measure of the transmittance and temperature for each voxel.

A voxel file contains data on smoke from one munition. That munition may produce a single plume or puff of smoke, or it may throw fragments of phosphorus, each of which produces its own smoke plume. A LUST bucket munition, for example, will generate a large puff of smoke from the initial blast plus up to 384 plumes from phosphorus wedges; all of these are included in a single voxel file.

The voxel array may be placed anywhere in the scene, and may be rotated horizontally to any orientation. Several voxel files may be included in the same scene to represent different types of smoke, or the same voxel file may be placed at several different locations in the scene to represent multiple occurrences of the same type of smoke source. When the same voxel file is used more than once in a scene, different start times may be specified for each so that the smoke clouds from the various placements do not look identical.

3. DESCRIPTION OF EMISSIVE_SMOKE CODE COMPONENTS

3.1 Smoke Source Selection

Emissive_Smoke includes a menu selection of several sources of emissive obscurants, including one-gallon and five-gallon LUST buckets, L8A3, M76, and user-defined sources that can be used for other obscurants such as bispectral obscurant or artillery dust. For each choice there are either two or three input files that are read from disk:

- a general input file, containing inputs such as the time step, voxel size, start and stop times, and the number of phosphorus wedges;
- a COMBIC input file for the main blast; and
- a COMBIC input file for the wedge plume, if the munition includes wedges.

3.2 Transport and Diffusion Using COMBIC

COMBIC is called as a subroutine. The entire COMBIC run, from time zero to the run stop time, is performed before Emissive_Smoke begins its own time sequencing. The smoke source may generate a puff and a plume; for example, the main blast of a LUST bucket produces a puff of smoke that rises and grows, and a stem of smoke (a narrow plume) connecting it back to the location of the blast. The time histories of the locations, sizes, concentrations, and temperatures of the puff and plume are returned to Emissive_Smoke.

If the munition includes wedges, COMBIC is called again to calculate the smoke plume for wedges. A single plume is calculated, and is used for each wedge. Variation in the appearance of the wedge plumes results from the fact that each wedge has its own plume start time, when the wedge lands. Further appearance variation results from the texturing calculation, if performed. The single COMBIC wedge plume therefore is used to produce simulated imagery of many distinctive-looking plumes.

3.3 Smoke Density and Radiative Transfer

At each time step, Emissive_Smoke calculates the smoke concentration and effective temperature in each voxel. The smoke concentration is the sum of the concentrations of all of the active plumes and puffs at that location. Each wedge plume starts when the wedge lands. Smoke from airborne wedges is not included in the model.

The temperature of a Gaussian plume or puff is assumed to fall off from its peak to the ambient air temperature in the same manner that concentration decreases with distance away from the center. The parameter actually saved in the voxel file is not the temperature, but the bandpass radiance R_{eff} (the Planck function integrated over the seeker bandpass) for that temperature. For a voxel affected by more than one smoke cloud, R_{eff} is the average weighted by the local concentration of each cloud. For most voxels, the smoke from the nearest cloud will dominate, and R_{eff} is approximately equal to the bandpass radiance associated with the temperature of the smoke from that cloud. Note that R_{eff} is not

necessarily the radiance emitted by smoke in the voxel -- it is simply a measure of the temperature. (It *is* the radiance emitted by the voxel if the smoke is optically thick.)

An individual voxel is considered small enough that it can be treated as if the smoke within it is distributed homogeneously. The radiance leaving the voxel in any direction is

$$L = L_0\tau + R_{eff}(1-\tau)$$

where τ is the transmittance through the voxel and L_0 is the radiance entering the voxel. The quantity R_{eff} $(1-\tau)$ is the path radiance introduced by the smoke and air in the voxel. The values saved in the voxel file are R_{eff} and the quantity $A=(1-\tau)$. The above equation can be written

$$L = L_0(1-A) + R_{eff}A$$

and repeated applications of this equation are used by the scene rendering code in the missile simulation to calculate the radiance map of the smoke clouds as seen by the seeker. The missile simulation code renders the scene using a graphics hardware blend function to perform this calculation very efficiently.

3.4 Wedges

If phosphorus wedges are part of the smoke munition, wedges are thrown along ballistic trajectories. The radiance from the hot wedges is included as part of the voxel radiance while the wedges are airborne and after they land. Wedges in the air will show up as hot spots in the simulated imagery, although they emit no smoke in the model until they land.

A wedge is much smaller than the resolution of the sensor at all but very close ranges. The temperature seen by a single sensor IFOV is determined by the fraction of the IFOV area that the wedge fills. This should depend on range, but Emissive_Smoke is run as a preprocessor to the flight simulation so no range information is available; a standard intermediate range is used instead. This weighted temperature is assigned to the entire voxel. Since the entire voxel radiates like a wedge, only one wedge per voxel is used in the algorithm.

A voxel may contain smoke and a wedge. The radiative transfer equation, modified to include wedge emission, should look like

$$L = L_0(1-A) + R_{eff}A + R_{wedge}$$

Wedge radiance is unrelated to smoke transmittance and should not be multiplied by A. There is no available hardware graphics function in this form, so the hardware blend function is used to calculate

$$L = L_0(1-A) + R'A$$

where

$$R' = R_{eff} + \frac{R_{wedge}}{A} .$$

When a wedge is in a voxel, the parameters saved in the voxel file for that location are A and R'.

3.5 Fractal Texturing

Smoke cloud structure is caused by atmospheric turbulence. Turbulent eddies of different sizes carry smoke with them as they move, break down into smaller eddies, and dissipate. A Gaussian smoke model represents an envelope that the cloud fills if a time average or ensemble average of this turbulent motion is performed. At any instant in time the cloud is an uneven distribution of smoke somewhere within the Gaussian envelope.

Turbulent motion is chaotic in nature and cannot be modeled deterministically but can be described statistically. Emissive_Smoke models the effect of turbulence on smoke clouds by generating a two-dimensional multiplicative screen that is used to modulate the optical depth of the simulated image. The mean value of all points in the screen is one, and all points are greater than or equal to zero. A region of values near zero will produce a hole in the cloud. A region of values greater than one will increase the optical depth in that region, making the cloud look denser, and usually warmer.

The turbulence texturing map is generated using an adaptation of STATBIC, a model developed by Don Hoock and his associates at ARL/BED (Hoock, undated). The spatial distributions of the regions in the screen are representative of distributions from imagery of smoke clouds in turbulence. A new screen is generated at each time step, and the time correlations are also representative of values from actual imagery. Regions of high and low multipliers drift with the wind and rise, fall, and dissipate realistically.

This model produces realistic simulated smoke imagery that includes hot regions and holes, and eliminates straight lines found in the nontextured Gaussian cloud simulations. Elimination of these straight lines is important for systems utilizing imaging seeker/trackers because the tracker may mistake these artifacts for target features.

This model is two-dimensional. The multiplier screen is applied to a horizontal, crosswind view of the smoke array. The result is an image that is put into a "billboard," a voxel array that is only one voxel deep. This "billboard" can be placed anywhere in the scene and can be viewed from any angle, although it begins to lose realism if the viewing angle varies beyond twenty or thirty degrees from crosswind.

3.6 Fire Plume Model FITTE

FITTE (Bruce, 1987) is the Fire-Induced Transmission and Turbulence Effects module of the Army's EOSAEL library of codes. It models smoke plumes from battlefield fires. FITTE models three types of fire: a burning jeep, a tank, and a fuel depot. A fourth type of fire, a fire barrel, was added for this application, since fire barrels (fires burning in 55-gal drums) are

often used in field tests. The user may also configure the inputs for smaller fires, such as small grass fires. The code predicts density, temperature, and thermal emission from smoke particles, water vapor, and carbon dioxide, based on a fire fueled by materials that typically burn in a vehicle fire, primarily diesel fuel. FITTE includes its own fractal texturing scheme. It does not include a specific model for flames, but the temperature near the source is typical of flames and with fractal texturing the appearance near the source is quite realistic. FITTE was modified to produce voxel output files using the same parameters and the same formats as discussed above.

4. MODEL DEMONSTRATION

Emissive_Smoke and the missile flight simulation code were used to reconstruct simulations of infrared scenes from missile flight tests. In these reconstructions, the smoke placement (including placement of phosphorus wedges) and other smoke parameters as well as scene parameters, such as terrain temperature, were selected to provide the best possible agreement between the real and simulated scenes. The modeled scenes, including the vehicles and the terrain, are entirely simulated.

The real imagery for each test consisted of up to two or three minutes of data at 60 frames per second, and in some cases included telemetry from the missile during its flight. The simulations consisted of five to eight seconds calculated at 10 frames per second. The goal was to produce a close match of the real and simulated images over the entire calculation interval, and to show that the missile behavior predicted by the simulation is similar to actual

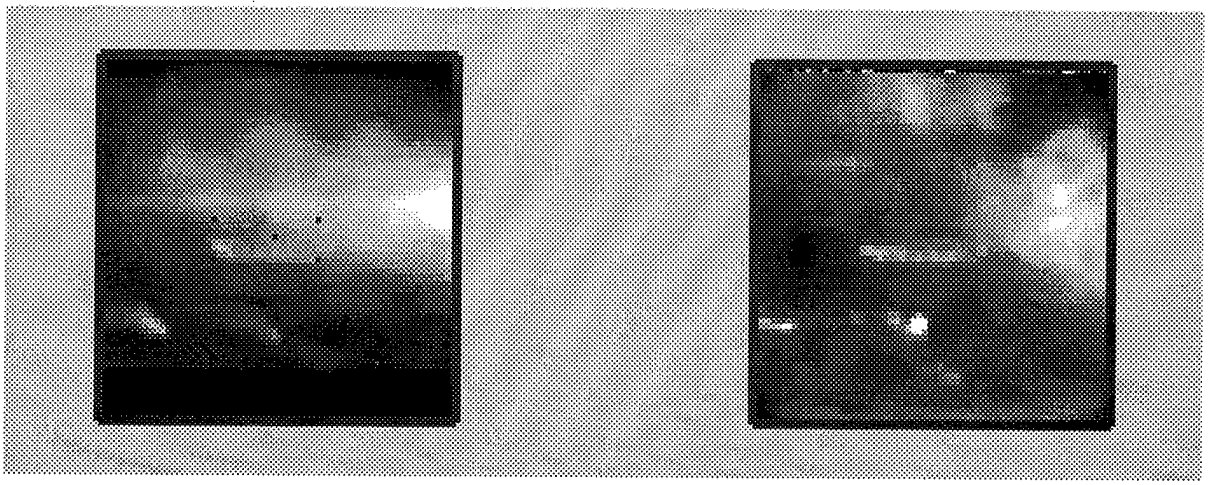


Figure 1. Simulated infrared scene (left) and real imagery (right) for a test involving WP obscurant.

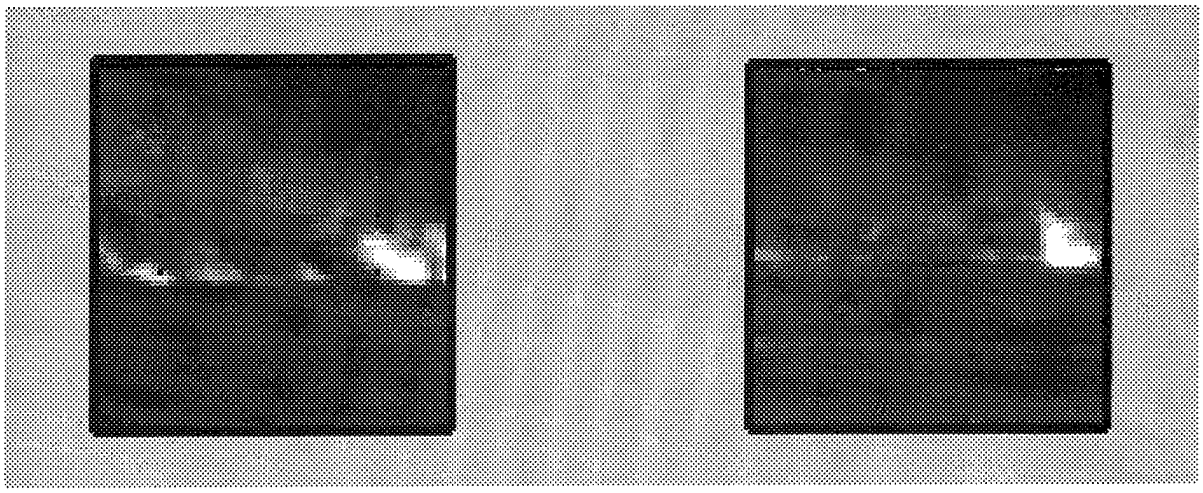


Figure 2. Simulated infrared scene (left) and real imagery involving grass fires started by phosphorus obscurant.

missile performance in the presence of similar countermeasures. The examples below show individual frames from some of these reconstructions and the corresponding frame from the real imagery.

Figure 1 compares a simulated scene and real infrared imagery for a flight test involving WP obscurant. A highly structured plume of smoke is drifting past in the foreground from right to left and is slowly rising, and three burning wedges are visible between the observer and the target.

Figure 2 compares a simulated scene and real infrared imagery for a test that was designed to include phosphorus grenades. The phosphorus started small grass fires near the target, and the resulting smoke caused strong attenuation. For this particular frame, the simulation shows somewhat more flame than the real imagery in front of the target, but the degree of attenuation near the target is about the same. The target is a tank facing to the left and turned slightly toward the viewer; a warm fender is visible just to the left of the center of the image.

Figure 3 shows simulated and real imagery for a frame shortly after detonation of a phosphorus artillery round. The target, an APC, is moving from right to left in the figure, and the foreground smoke that resulted from the initial burst is drifting to the right. All of the phosphorus fragments have landed, and are screened (both in the real imagery and in the simulation) by a small rise in front of the viewer. A substantial amount of smoke is rising

from the phosphorus, attenuating the target. After the missile was launched, the phosphorus on the ground became visible, both in the imagery and in the simulation. In the figure, the foreground temperature in the simulation appears to be too cool; this is because the terrain temperature in the simulation was chosen to give good agreement with the imagery in the region near the target in later frames.

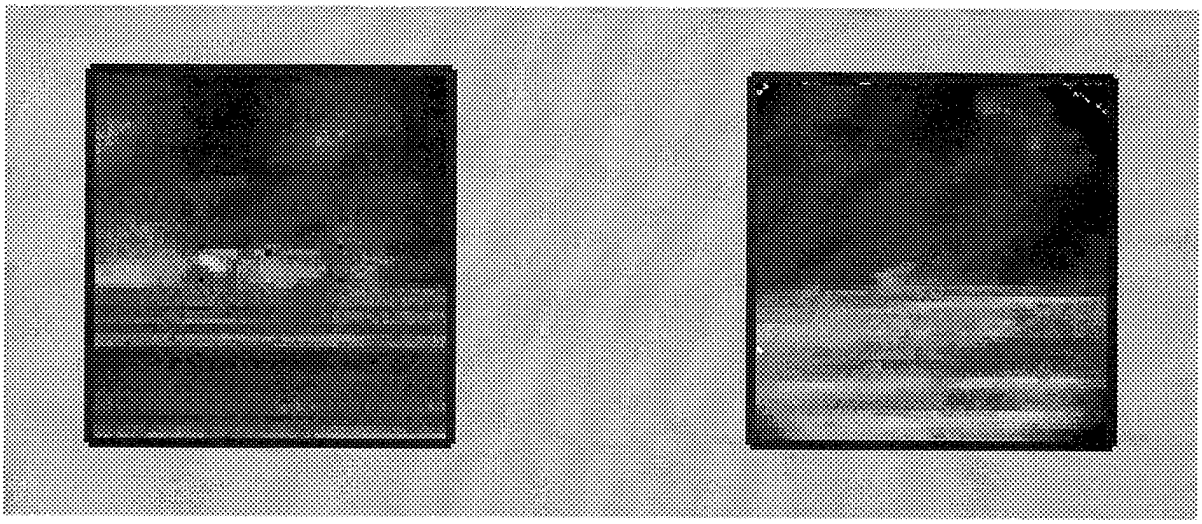


Figure 3. Simulated infrared scene (left) and real imagery (right) from a test involving phosphorus obscurant. Burning phosphorus on the ground is screened by foreground terrain.

5. CONCLUSIONS

The Emissive Smoke Code produces realistic images of smokes and fires for battlefield scenes. The imagery is based on established source models and transport and diffusion models, and the appearance of the smoke therefore depends in a realistic manner on physical parameters such as wind speed, Pasquill stability category, munition fill weight, and many other variables. The code features a model for phosphorus munitions that disperse a large number of phosphorus wedges, each of which produces smoke on the ground for up to several minutes. The Emissive Smoke Code models the infrared appearance of smokes such as phosphorus that are warmer than ambient air and produce thermal clutter as well as attenuation, but it may be used as well for ambient-temperature smokes and obscurants. Fractal texturing is used to produce holes, hot spots, and uneven edges, giving the clouds realistic appearance both to the eye and to imaging seeker/tracker systems. The Emissive

Smoke Code was developed to generate countermeasure smoke and obscurant images to be inserted into imaging infrared missile flight simulations. It makes use of several models that were developed and are maintained by ARL/BED.

REFERENCES

Bruce, D., 1987. *Fire-Induced Transmission and Turbulence Effects Module FITTE,* EOSAEL 87 Volume 15, TR-0221-11, US Army Laboratory Command, Atmospheric Sciences Laboratory.

Hoock, D.W., R.A. Sutherland, and D. Clayton, 1987. *Combined Obscuration Model for Battlefield-Induced Contaminants COMBIC,* EOSAEL 87 Volume 11, TR-0221-11, US Army Laboratory Command, Atmospheric Sciences Laboratory.

Hoock, D.W., undated. *Statistical Texturing Applied to Battlefield-Induced Clouds (STATBIC) - A Methodology for Applying Plume Fluctuations Statistics to Mean Smoke and Dust Plume Models in 2-D and 3-D, Algorithm Overview,* US Army Research Laboratory, Battlefield Environment Directorate, White Sands Missile Range, New Mexico.

Physical Science Laboratory, 1993. *Emissive Source Imaging Model Technical Report,* PSL-93/22, Physical Science Laboratory, New Mexico State University.

Session II Posters

OPERATIONAL WEATHER

PERFORMANCE OF THE U.S. ARMY BATTLESCALE FORECAST MODEL DURING OPERATION DESERT CAPTURE II

R. E. Dumais, Jr.
U.S. Army Research Laboratory
White Sands Missile Range, NM 88002-5501, USA

ABSTRACT

During April 1994, the U.S. Army Research Laboratory (ARL) participated in Operation Desert Capture II at the National Training Center (NTC), Ft. Irwin, CA. The exercise was largely a test of the possible interoperability between various systems designed to assist commanders on the battlefield and the timely dissemination of information in an understandable format to the commanders in the field. A large part of the ARL participation focused on the Battlescale Forecast Model that was run twice a day to provide 12-h forecasts of winds, temperature, and relative humidity for mission planning. During the exercise, meteorological data was compiled from 12 surface sensor locations around the NTC, providing 15-min averages of temperature, relative humidity, wind speed, and wind direction. This paper subjectively presents model results and discusses a technique that is used to statistically compare the model results with the sensor data.

1. INTRODUCTION

The U.S. Army Battlescale Forecast Model (BFM) recently participated in Operation Desert Capture II during April 1994 at the National Training Center, Ft. Irwin, CA. Scientists from the U.S. Army Research Laboratory (ARL) ran the model twice a day to provide 12-h forecasts of surface temperature, wind flow, and relative humidity to the commanders of friendly forces in the field. The forecasts were presented as TIF files that showed the contour and/or streamline fields of the forecast meteorological parameters. The contour and streamline fields were overlayed on the National Training Center (NTC) terrain, allowing a viewer the capability to assess the effect of local topography on the surface meteorological fields, which was important because it allowed the rather voluminous and complex output of the BFM to be tailored into a format that could be quickly and easily interpreted by the battlefield staff weather officer for use in briefings to his commander.

A network of 12 surface automated meteorological sensor sites (SAMS) located within the NTC domain collected meteorological data during the exercise. Temperature, wind speed, wind direction, and relative humidity were sampled every 15 min by averaging over 1-s intervals. The data are being compiled at ARL so they can be used to statistically compare the BFM results to those observed at the SAMS.

The model runs at two different horizontal resolutions, allowing for an interesting series of BFM simulations. The statistical analysis initiated at the time this paper was written endeavors to determine the meteorological forecast value added by the BFM, as opposed to only using the large-scale Global Spectral Model (GSM) guidance to predict the mesoscale. Additionally, it investigates whether very high resolution grids (less than 5 km) add enough additional forecast value to compensate for the increased computational burden they generate.

2. THE BATTLESCALE FORECAST MODEL

The U.S. Army BFM is known as the Higher Order Turbulence Model for Atmospheric Circulations (HOTMAC), developed by Dr. Tetsuji Yamada at Los Alamos National Labs. It is essentially a hydrostatic, quasi-Boussinesq, terrain following coordinate model with a 2.0 order turbulence closure. Excellent documentation of HOTMAC can be found in Yamada and Bunker (1989), Yamada (1981), and Yamada (1982).

Interactions between condensation and solar radiation are included in the model. However, ARL scientists have modified the data assimilation modules of the original HOTMAC to better serve Army operations, and it is the modified HOTMAC that is referred to as the BFM.

Initial and boundary conditions for the BFM were supplied by the U.S. Air Force GSM, which is documented in Air Force Global Weather Central Technical Note 92/001, *Computer Models*. The 12-h gridded forecast fields (valid at time t_0) provided from the GSM were interpolated to the BFM grid to supply the initial conditions. The GSM 24-h gridded forecast fields provided the boundary conditions applied to the three points nearest to the grid edge. The technique used to handle the boundary conditions is a Newtonian nudging method similar to that discussed in Yamada and Bunker (1989). Information about changes in the large-scale flow are advected in through the lateral boundaries.

To improve initial conditions, particularly those in the lower boundary layer, the model is commenced 6-h back from the initial time, during which time the fields are nudged strongly to the analysis. The nudging helps damp out small amplitude waves introduced by errors in the analysis and allows the model to gradually spin-up to the large-scale GSM momentum field. Initially, a very weak flow of uniform direction was assumed, with speed profiles determined by applying the principle of mass consistency. This procedure is referred to in Yamada and Bunker (1989) and allows the model to gradually develop terrain and radiationally forced boundary layer momentum and mass fields that are largely nonexistent in the coarse resolution GSM forecasts. Geostrophic winds above 200-m above ground level (AGL) are assumed to be the same as the GSM forecast winds, while geostrophic wind components below 200-m AGL are determined using the formula described in Yamada and Bunker (1989), based on the thermal wind.

3. MODEL DESIGN

The grid area is centered on Bicycle Lake, at latitude 35.275° N and longitude 116.648° W. Two grids of 5- and 2.5-km terrain resolution are used to run the model (figures 1 and 2). The grid system is planar Universe Transverse Mercator 130 by 130 km in size. The 5- and 2.5-km-grid dimensions are 27x27x16 and 51x51x16, respectively. Vertical levels are staggered to improve the vertical resolution in the boundary layer with a rigid top boundary of 7000-m AGL.

Because of their low resolution and to create a better analysis field, the GSM data were interpolated onto a 1000 by 1000 km grid at 5-km resolution for the coarser BFM grid and 500 by 500 km at 2.5-km resolution for the finer BFM grid. The analysis grids were also centered at Bicycle Lake and allowed more GSM points to be utilized in the Barnes analysis scheme (Barnes, 1964). For example, in the 1000- by 1000-km region eight GSM grid points were utilized for the analysis.

4. SIMULATIONS

Twenty BFM simulations were run, and the results for April 1994 (during Operation Desert Capture II) were archived. Ten simulations (five daytime and five nocturnal) were run at each resolution (5 and 2.5 km). It was felt that this partition of the simulations would allow for a good test of how the BFM could handle both upslope and downslope flows induced by radiational heating and cooling of sloped surfaces, along with its handling of the diurnal surface temperature wave (both in phase and amplitude) that drives the flows. The simulations also allow an investigation of how well large-scale boundary conditions are assimilated into the BFM grid domain.

The days and nights of the study were selected based on the availability of GSM and SAMS data; however, the degree of complexity of the large-scale forcing was also considered. Early in the exercise, strong, large-scale flow patterns existed, which might be expected to present a good challenge for the BFM.

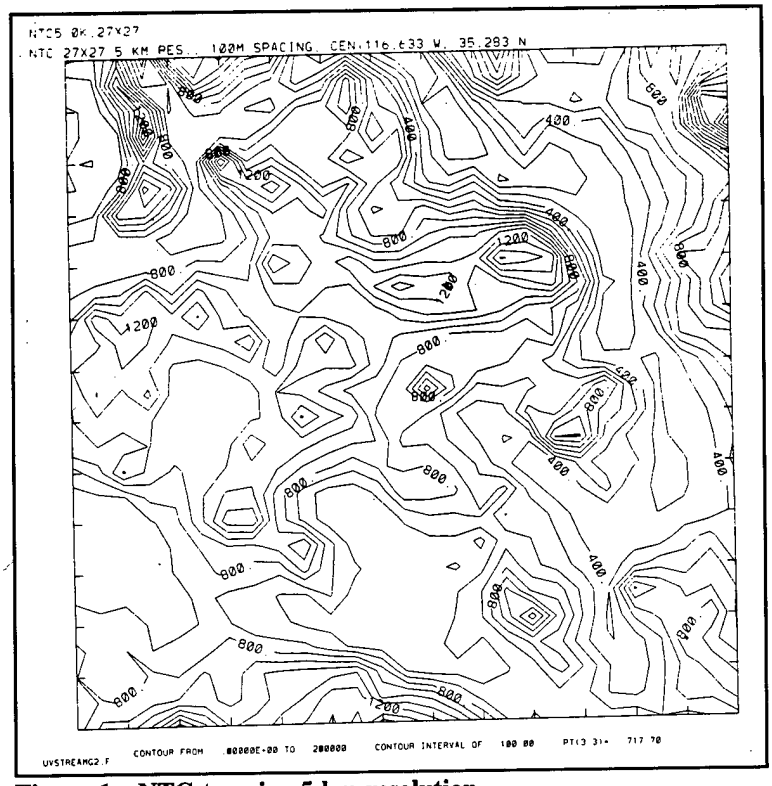


Figure 1. NTC terrain, 5-km resolution.

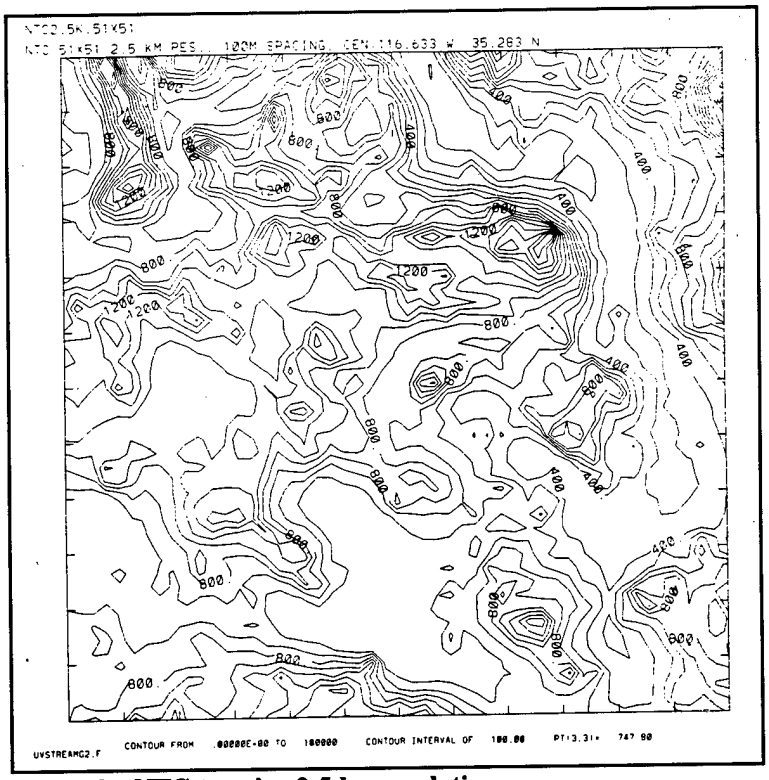


Figure 2. NTC terrain, 2.5-km resolution.

Table 1 lists the dates of the simulations, with nocturnal BFM runs initiating at 00 UTC (16 LST) and extending 12 h to 12 UTC (04 LST) and daylight BFM runs initiating at 12 UTC (04 LST) and extending 12 h to 00 UTC (16 LST).

Table 1. BFM initialization dates and times selected to generate 12-h forecasts

Night Simulations	Day Simulations
00 UTC, 11 Apr 94	12 UTC, 07 Apr 94
00 UTC, 14 Apr 94	12 UTC, 12 Apr 94
00 UTC, 17 Apr 94	12 UTC, 14 Apr 94
00 UTC, 19 Apr 94	12 UTC, 18 Apr 94
00 UTC, 21 Apr 94	12 UTC, 20 Apr 94

Figures 3 and 4 show the initial and 12-h BFM forecast surface (10-m AGL) wind fields valid at 00 and 12 UTC on 19 April, respectively. Figures 5 and 6 compare the GSM forecast fields at the same level and times. Notice the GSM surface wind field is essentially uniform out of the north at 10 kn in figure 6 while the corresponding BFM field in figure 4 is much more heterogeneous and topographically/radiationally driven. Downslope flow into the Death and Silurian Valleys on the east side of figure 4 have been generated by the surface forcing in the BFM.

Figures 7 and 8 show the initial and 12-h BFM forecast surface winds valid at 12 UTC on 18 April and 00 UTC on 19 April, respectively. Figure 8 shows the upslope winds generated around some of the steeper slopes by the BFM during the simulation. Figures 9 and 10 show more uniform initial and 12-h GSM forecast surface winds for the same period. Figures 3 through 10 are examples of the 2.5-km resolution simulations.

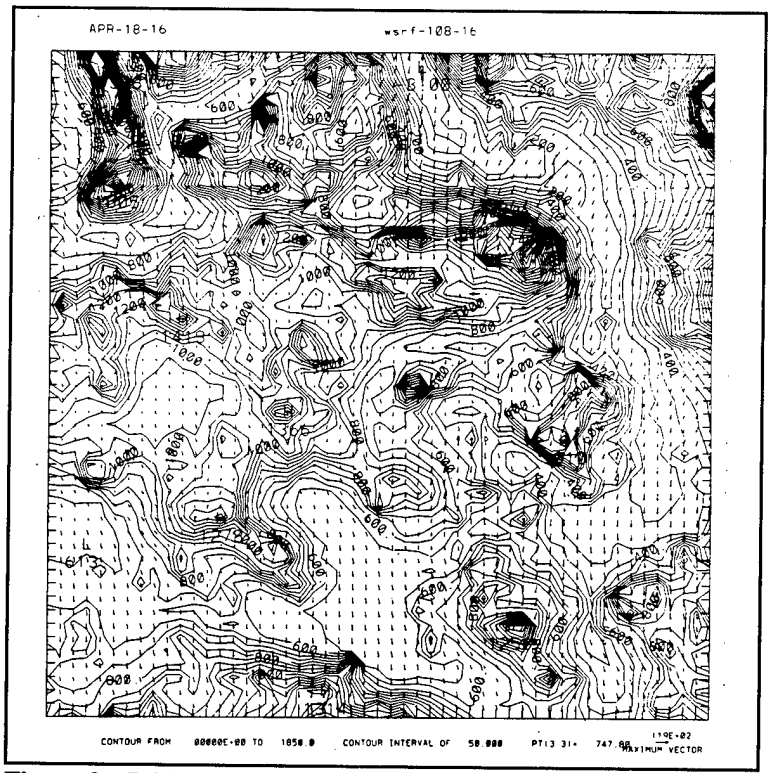


Figure 3. Initial BFM surface winds, valid 16 LST, 18 Apr 94.

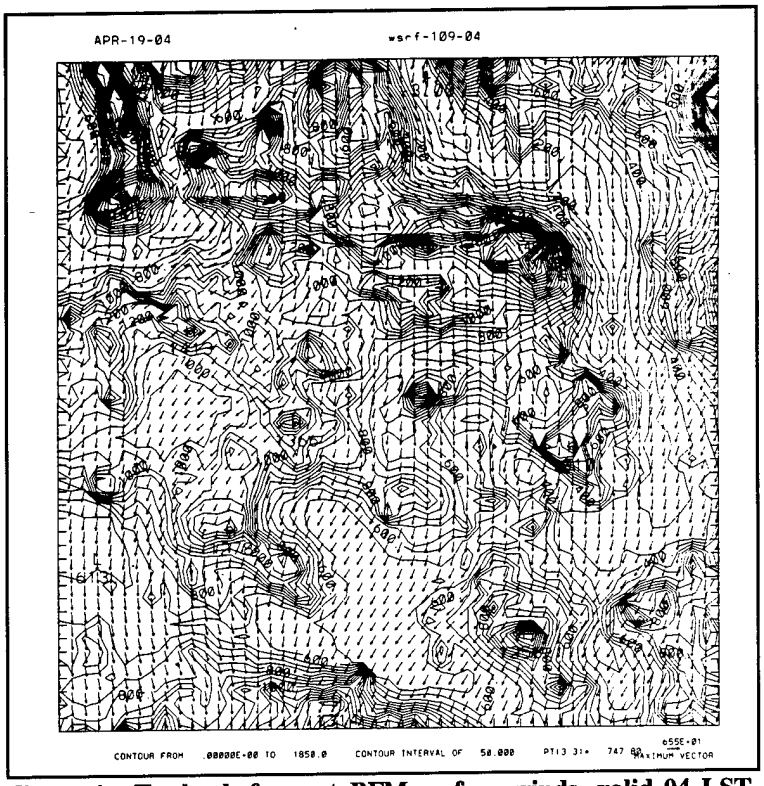


Figure 4. Twelve-h forecast BFM surface winds, valid 04 LST, 19 Apr 94.

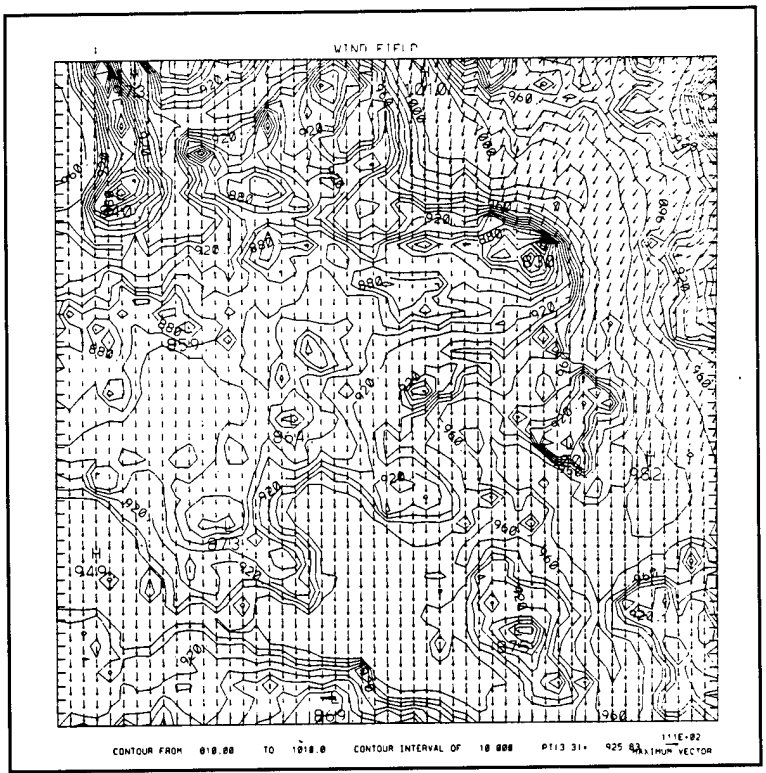


Figure 5. Initial GSM surface winds, valid 16 LST, 18 Apr 94.

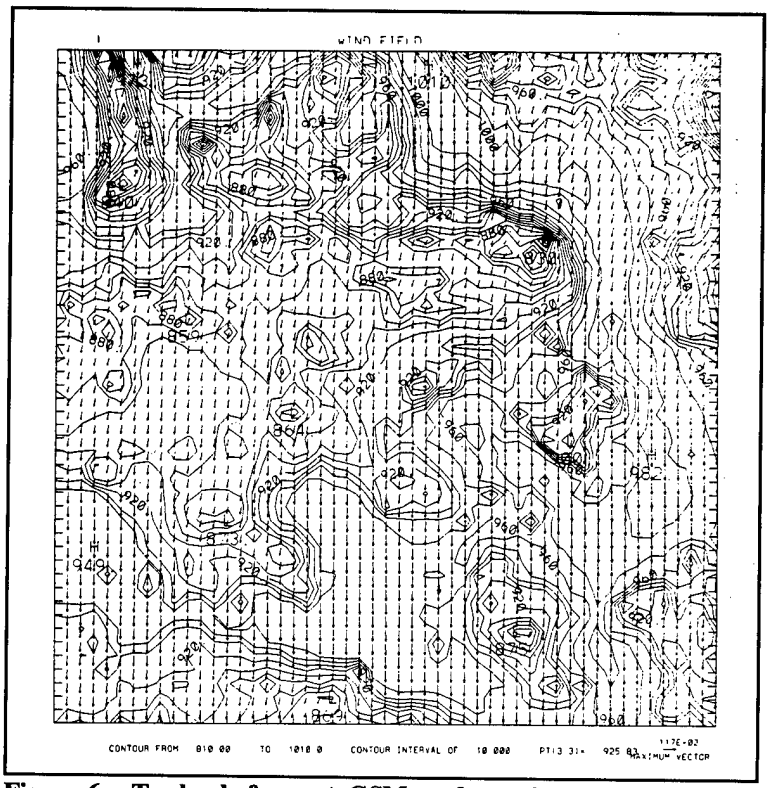


Figure 6. Twelve-h forecast GSM surface winds, valid 04 LST, 19 Apr 94.

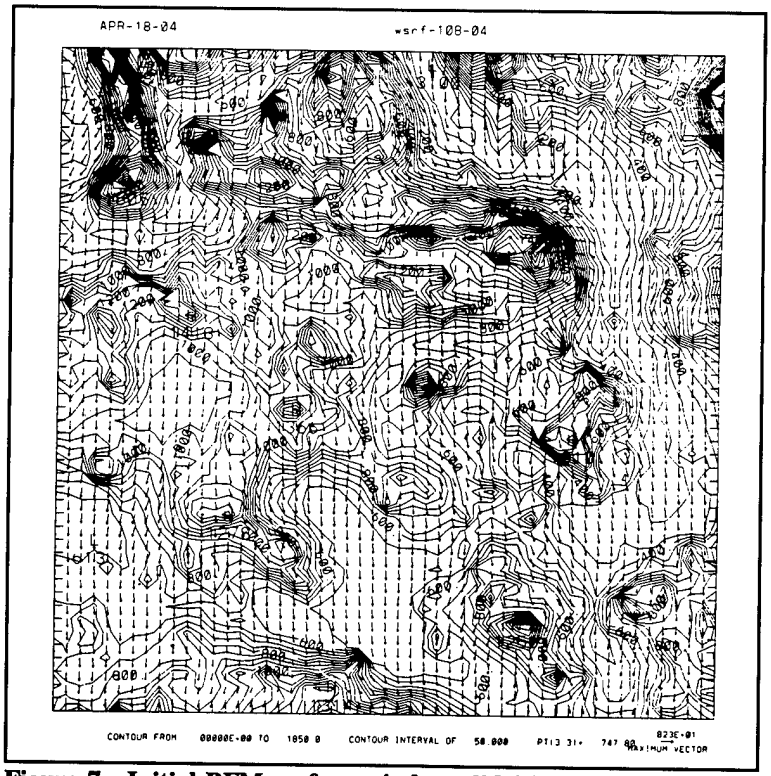


Figure 7. Initial BFM surface winds, valid 04 LST, 18 Apr 94.

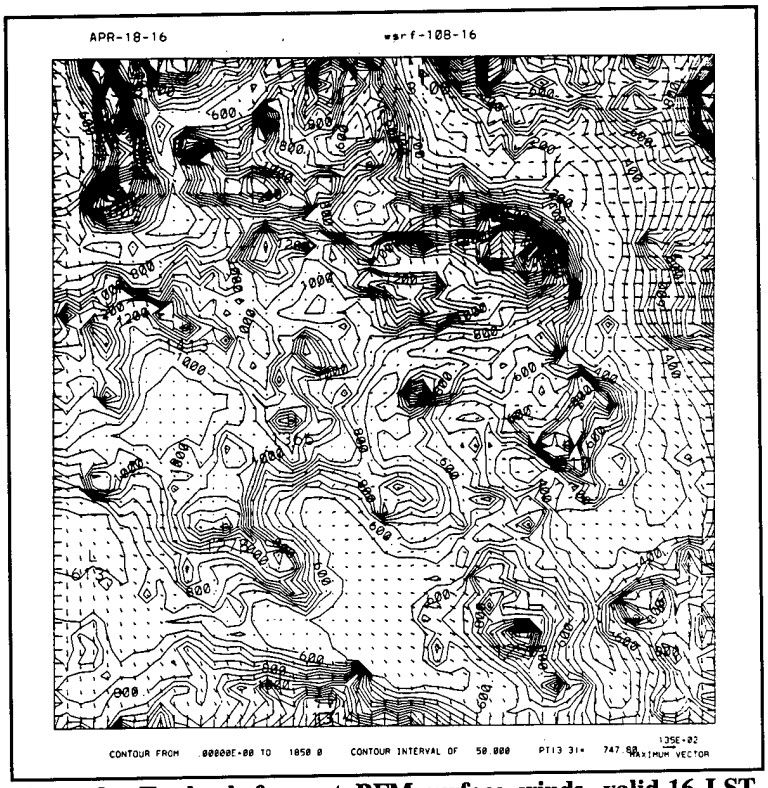


Figure 8. Twelve-h forecast BFM surface winds, valid 16 LST, 18 Apr 94.

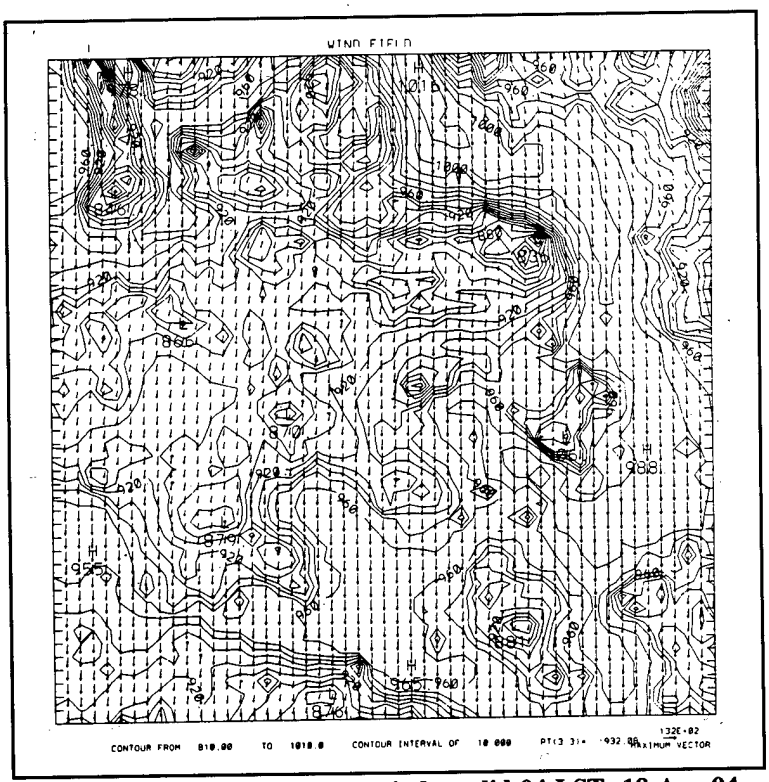


Figure 9. Initial GSM surface winds, valid 04 LST, 18 Apr 94.

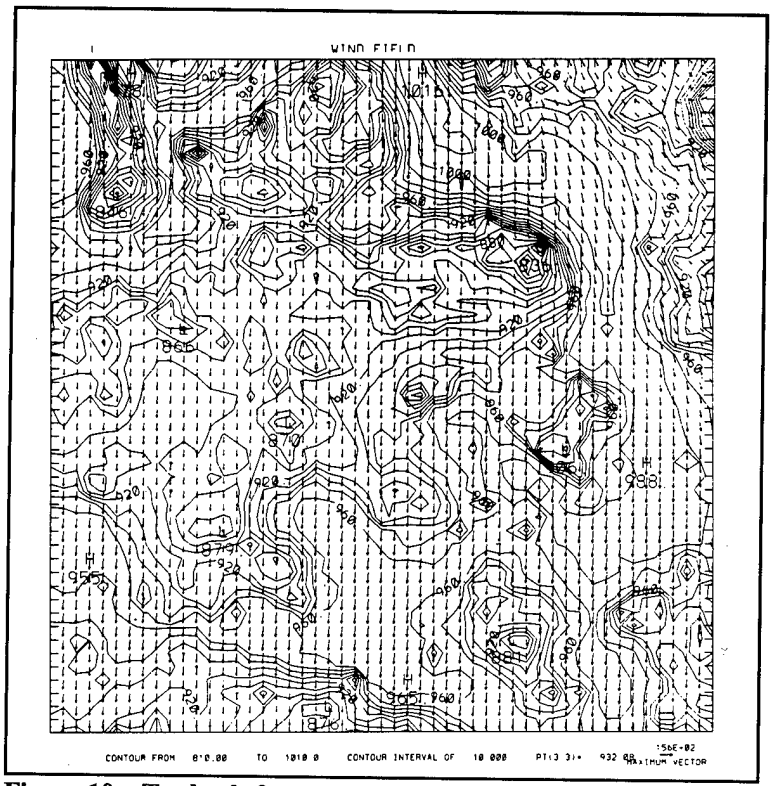


Figure 10. Twelve-h forecast GSM surface winds, valid 16 LST, 18 Apr 94.

In general, a first look at the results indicates that the BFM significantly improved the GSM forecasts for wind and temperature over the short range within the NTC domain. The BFM daily maximum and minimum temperature forecasts are much more in line with the SAMS observations, producing more realistic radiational forcing near the surface. Most likely, this combined with the fact that the BFM uses a terrain following vertical coordinate allowed BFM forecasts to simulate more realistically the kinds of upslope and drainage wind patterns often observed in complex terrain regions within weak synoptic flow regimes. Additionally, the forecast upper level BFM mass and wind fields appear to be consistent with those forecast by the GSM.

A typical 12-h simulation using the 5-km-resolution grid took approximately 14 min of user time on a 9000 series, 755 HP workstation. For the same simulation and hardware, the 2.5-km-resolution grid took nearly 1 h and 40 min of user time. In general, the resolution decreases with the time step in the model.

5. FUTURE OBJECTIVE STUDY

To objectively quantify the performance of the BFM during the exercise, a set of statistical measures were devised to compare the forecast BFM surface fields to those observed at the SAMS locations. The set of statistics used to carry out this comparison are identical to those discussed in Pielke (1984) for point to point correspondences. Equations (1) through (4) show the statistical measures.

$$E=\{\sum_{i=1}^{N}\frac{(\phi_i-\phi_{iobs})^2}{N}\}^{\frac{1}{2}} \qquad (1)$$

$$E_{UB}=\{\sum_{i=1}^{N}\frac{[(\phi_i-\phi_0)-(\phi_{iobs}-\phi_{0obs})]^2}{N}\}^{\frac{1}{2}} \quad (2)$$

$$\sigma_{obs}=\{\sum_{i=1}^{N}\frac{(\phi_{iobs}-\phi_{0obs})^2}{N}\}^{\frac{1}{2}} \quad (3)$$

$$\sigma=\{\sum_{i=1}^{N}\frac{(\phi_i-\phi_0)^2}{N}\}^{\frac{1}{2}} \quad (4)$$

where

ϕ_i	=	individual predictions at the nearest grid point
ϕ_{iobs}	=	individual observations at the nearest grid point
ϕ_0	=	average value of ϕ_i at a level
ϕ_{0obs}	=	average value of ϕ_{iobs} at a level
N	=	the total number of observations
E	=	the root mean square error
E_{UB}	=	the root mean square error after a constant bias is removed
σ	=	the standard deviation of the predictions
σ_{obs}	=	the standard deviation of the observations

From these parameters, skill is demonstrated when

(1) σ = σ_{obs},
(2) E < σ_{obs}, and
(3) E_{UB} < σ_{obs}.

The SAMS data are being compiled at ARL so the parameters can be computed for the 20 BFM simulations discussed in this paper. The parameters will be computed for the corresponding GSM forecasts, so a comparison can be made with the BFM.

Hourly data will be analyzed during each simulation. Because the SAMS data are averaged over 15-min intervals, averages of observations will be made using the five observation periods plus or minus 30 min from the hour desired to compute the statistical parameters at hourly intervals.

6. CONCLUSIONS

A brief synopsis was made of the effectiveness of the BFM during its operation at Operation Desert Capture II. An initial subjective analysis of the data looks promising, it appears that the model (in weak synoptic flow) is capable of generating terrain induced, radiationally driven surface flows, in addition to correctly assimilating the upper atmospheric (levels above the planetary boundary layer) mass and momentum fields forecast by a larger-scale numerical model (GSM). The BFM also appears to enhance the surface mass and momentum forecasts of the GSM, although this has yet to be shown quantitatively. ARL is currently processing data from the April 1994 simulations so a statistical study of the BFM and GSM can be made, and the results can be

compared. The statistical measures were outlined in this paper, and the results will be presented in a future paper.

In the future, it is desirable to supply the lateral boundary conditions to BFM from a regional-scale model rather than a global-scale model, in addition to the BFM running in a two-way interactive nesting configuration. Research will continue in this direction. In this paper, the BFM appears to show that, even without real observations to initialize and with only the forecast fields of a global scale model to apply as lateral boundary conditions, it is capable of producing 12-h forecast fields that are more physically realistic (over complex terrain) than currently available on the battlefield. The simulations were numerically stable and there appeared to be no gross propagation of high amplitude waves through the lateral boundaries.

ACKNOWLEDGMENTS

The author would like to thank Mr. John L. Ligon of Computer Sciences Corporation for compiling the SAMS data during Operation Desert Capture II and Dr. Teizi Henmi and Jeff Passner of ARL and Major Dave Knapp of OL-N, USAF for their assistance.

REFERENCES

Barnes, S. L., 1964. "A Technique for Maximizing Details in Numerical Weather Map Analysis." *J. Appl. Meteor.*, *3*:396-409.

Pielke, R. A., 1984. *Mesoscale Meteorological Modeling*, Academic Press Inc., pp 448-452.

Yamada, T., 1981. "A Numerical Simulation of Nocturnal Drainage Flow." *J. Meteor. Soc. Japan*, *59*:108-122.

Yamada, T., 1982. "A Numerical Model Study of Turbulent Airflow in and Above a Forest Canopy." *J. Meteor. Soc. Japan*, *60*:439-454.

Yamada, T., and S. Bunker, 1989. "A Numerical Model Study of Nocturnal Drainage Flows with Strong Wind and Temperature Gradients." *J. Appl. Meteor.*, *28*:545-554.

A WEATHER HAZARDS PROGRAM USED FOR ARMY OPERATIONS ON IMETS

Jeffrey E. Passner
Battlefield Environment Directorate
U.S. Army Research Laboratory
White Sands Missile Range, New Mexico 88002-5501 USA

ABSTRACT

In an effort to assist the Air Force staff weather officer, ARL has designed a number of weather products on the TEWTB that will help the forecaster make more accurate and detailed weather decisions during military operations. The data from a single sounding, as input for an automated "weather hazards" program, provides an overview of potential adverse weather conditions for operations in the battlefield. The program displays layers of the atmosphere where moisture, icing, turbulence, wind shear, clouds and inversions exist, based on the sounding data. Many of the routines are based on empirical rules developed by Air Force meteorologists and modified using upgraded data sources and meteorological information. In addition, a forecast of these weather "hazards" and the predicted upper-air observation at a location is possible employing output from a battlescale mesoscale model developed by ARL. This mesoscale data is utilized as input to run the weather hazards program and assist the Air Force weather forecasters of any possible weather hazards in the battlefield during the next 12-hr period.

1. INTRODUCTION

The Integrated Meteorological System (IMETS) will be a mobile operational automated weather data receiving, processing, and disseminating system utilized by Air Force weather forecasters in support of Army operations. To facilitate the development of IMETS, the Battlefield Environment Directorate (BED), U.S. Army Research Lab (ARL) has assembled the Technology Exploitation Weather Testbed (TEWTB) -- a prototype of IMETS. The purpose of the TEWTB is to serve as a platform for ARL to generate, evaluate, and demonstrate software products before they are actually transitioned to IMETS; Passner (1993).

In an effort to support the Air Force staff weather officer (SWO), ARL has devised a number of weather products that will assist the forecaster make more meticulous and detailed weather decisions. Of most concern to military planners is the influence of weather hazards on military operations. These hazards frequently include icing, turbulence, wind shear, moisture, inversion layers, visibility, and precipitation. The program developed by ARL

incorporates all these weather hazards to provide an expedient examination of what type of adverse weather may occur.

2. DATA SOURCES

Much of the data used to formulate the tactical decision aids (TDAs) and forecaster decision aids (FDAs) consist of large-scale and intermittent synoptic data reports. Data in use by the TEWTB presently incorporates Air Force Automated Weather Distribution System (AWDS) data and information furnished by the Automated Weather Network Data. This large-scale database merges both surface and upper-air data and is used to develop the TDAs and FDAs.

While satellite imagery, radar data, surface and upper-air observations, and contour routines provide essential information for the SWO, at certain times these advanced techniques will not be accessible because of communication problems in the battlefield. Thus, a sounding analysis program can provide sophisticated synoptic information to the forecaster.

3. THE WEATHER HAZARDS PROGRAM

In addition to the traditional stability indices and convective forecasts, the skew T - log P program can display areas of the sounding where conditions might be favorable for weather hazards. The ARL weather hazards program presents areas of a sounding where icing, turbulence, moisture, clouds, and inversions are found. In addition, automated routines have been developed to show the current surface visibility and precipitation type.

3.1 Icing

The ARL sounding analysis program has a rule-based system that assists in nowcasting and forecasting icing based on the sounding. The rules for the icing program are derived from a decision tree based on AWS/TR-80/001, an Air Force chart designed to give guidelines about icing type and severity. This chart has been decoded and placed into an expert system format to be used in the program. A small data set of 24 samples was used to verify the routine over the southeastern United States from February to April 1993. Results are displayed in Table 1. Statistics displayed are probability of detection (POD), false alarm ratio (FAR), critical success index (CSI), total skill score (TSS), and Bias:

TABLE 1. Results for icing chart method of nowcasting/forecasting icing based on 24 samples 0000 universal time coordinates (UTC) sounding from 18 February to 15 April 1993 over southeastern United States.

Icing Routine	Value
(POD)	0.67
(FAR)	0.08
(CSI)	0.63
(TSS)	0.50
Bias	0.72

Icing intensities were correct in 60 percent of the cases; however, the icing types were accurate in only 33 percent of the data samples.

3.2 Turbulence

Turbulence is generally a state of fluid in which there are irregular velocities and apparently random fluctuations; Glossary of Meteorology (1959). These oscillations in the atmosphere (the fluid) can adversely affect flight paths and endanger Army aircraft operations. Turbulence is present in and near thunderstorms, as can be expected, based on the dramatic updraft and downdraft speeds; Passner (1994).

Forecasting clear air turbulence (CAT) is a much more difficult problem. Both theoretical studies and empirical evidence have associated CAT with Kelvin-Helmholtz (K-H) instabilities. Miles and Howard (1964) indicate that the development of K-H instabilities require the existence of a critical Ri <=.25. The Ri can be expressed as a ratio of the buoyancy resistance to the energy available from the vertical shear; Keller (1990).

Since the only data source in this study is a single-sounding, the method used here was to apply wind speed, vertical wind shear and the gradient Richardson number.

Statistics for the turbulence nowcasts/forecasts were not encouraging. They are displayed in Table 2.

TABLE 2. Results for Richardson number method of nowcasting turbulence based on 62 sample 0000 UTC sounding from 18 February to 15 April 1993 over southeastern United States.

Turbulence Routine	Value
POD	0.13
FAR	0.00
CSI	0.13
TSS	0.16
Bias	0.13

3.3 Clouds and Fog

A routine to nowcast and forecast clouds has been developed using the single-station sounding. This routine is once again based upon a set of rules that is used to make a prediction of clouds. The output displays what levels these clouds are located at and whether the clouds are scattered, broken, or overcast in that layer. The program uses the relative humidity of each layer and a set of empirical rules based on the height of the layer, time of day, and season. There are also rules that determine if any fog is present based on the data of the sounding.

Verification of the cloud forecasts show that there was little difference in skill noted between 1200 UTC and 0000 UTC soundings as 53 and 59 percent of the cloud nowcasts/forecasts were accurate. However, there were some differences noted between the winter soundings and summer soundings. The summer cloud nowcasts were correct 59% of the time, but the cloud routine only correctly forecasted the cloud heights and cloud amounts 44% of the time. Table 3 shows more detailed verification statistics.

TABLE 3. Verification statistics for cloud routine using data from both summer and winter soundings at 1200 and 0000 UTC.

Forecast	Samples	% Correct	% Marginal	% Wrong
1200 UTC	188	54 %	15 %	31 %
0000 UTC	78	59 %	15 %	26 %
Summer	207	59 %	13 %	28 %
Winter	59	44 %	22 %	34 %

The fog forecasts were made based on the relative humidity of the boundary layer and layers just above the surface layer. The rule base also checked for the level of the Lifted Condensation Level to see how much moisture was available in the lowest levels of the sounding. The statistics for the fog routine using 174 samples showed that in 20 percent of the cases, fog was observed (35 samples). The POD = 0.79, FAR = 0.46, CSI = 0.48, TSS = 0.68, and Bias = 1.46 for a "yes/no" forecast of fog.

3.4 Inversion Layers

The program will display regions of the sounding where temperature inversions are noted. These inversions can play a role in many Army Operations including those involving smoke and other airborne material. The routine simply searches for layers where the temperature increases with height and displays them in the graphical output.

3.5 Visibility

Several surface variables were selected from 137 surface observations at 79 stations using both winter and summer data in an effort to develop a routine to forecast surface visibility. Multivariate discriminant analysis (using stepwise procedures) was used to determine the most significant surface visibility predictors. Employing these most significant predictors, multivariate linear regression was utilized to derive a visibility forecast equation. The variables determined to be the most significant were the surface elevation, temperature, dewpoint temperature, and surface wind speed. The regression equation is listed below:

$$Y\ (\text{miles}) = 0.01*(\text{elevation}) + 0.504*(\text{sfc temperature}) - 0.452*(\text{sfc dewpoint}) - 0.228*(\text{sfc wind speed}) + 3.301 \quad (1)$$

TABLE 4. Verification statistics for surface visibility using soundings from summer and winter at 1200 UTC and 0000 UTC.

Visibility	Samples	% Correct	% Wrong
1200 UTC	60	70 %	30 %
0000 UTC	89	70 %	30 %
Summer	116	69 %	31 %
Winter	33	73 %	27 %

3.6 Precipitation Type

The sounding values of pressure, temperature, dewpoint, and wet-

bulb temperature were used to determine the type (solid, liquid, mixed, or freezing) at the surface. Based on the similar work by Ramer (1993), it was assumed that a wet-bulb temperature at the surface greater than 2 degrees C represented cases where all the precipitation would fall as rain. In cases where the entire sounding was below 0 degrees C, the program would predict that all precipitation would fall as snow. Based on surface wet-bulb temperatures along with the wet-bulb temperatures of the sounding in the lowest 10,000 ft above ground level and the dew-point depression of the layer, a nowcast/forecast of precipitation type was developed.

4. THE PROGRAM AS A FORECASTING TOOL

Recently an effort has been made to use the output data from the battlescale forecast model (BFM) to use the weather hazards program as a forecast tool for the SWO. The BFM uses the hydrostatic approximation, however it is a relatively fast and numerically stable model that takes into account local effects on the large scale weather patterns. The BFM incorporates knowledge of the local terrain, initial conditions, and boundary conditions close to the area of operation to produce forecasted gridded fields. For more information on the BFM see Lee et al. (1995).

In this test, the BFM was initialed using 1200 UTC sounding data and the 12-hr Global Spectral Model data, which is regularly transmitted by the U.S. Air Force Global Weather Central via the AWDS. The main focus of this study was to compare the output of the BFM at 12 hours and compare it to observed soundings at several locations in the central United States. Then a 12-hr forecast for all weather hazards would be made based on the forecasted sounding data. Results were generally favorable although a few trends were noted that degraded the forecast using this small data set of nine soundings on 14 September 1994. In comparison to the observed sounding the BFM output indicated that low levels winds were veered, while mid and upper-level winds were backed. The temperature error was minimal and decreased above the boundary layer. The wind speeds were in error in the vicinity of the low level jet, however in most areas the wind speed were relatively close to the observed wind speeds. The moisture field was of the most concern, as might be expected, and there was a trend to overforecast the dew point at 850 mb, especially in regions that displayed "tropical"-like moisture sources. This led to higher than expected values of many of the stability indices and a trend to overforecast thunderstorms and precipitation amounts in the region.

5. SUMMARY AND CONCLUSIONS

Several methods of forecasting weather hazards were developed by ARL to assist the SWO in the prediction of weather phenomena on the battlefield. These meteorological events (derived from a single

sounding) included icing, turbulence, moisture, clouds, inversions, visibility, and precipitation. While most of the applications here showed forecasting skill, the results indicate that the methods tested here were not very useful in making predictions where turbulence was occurring. In addition, the nowcasts for turbulence were strongly biased toward the nonevent, which resulted in low FAR rates and high prediction rates of the nonevent.

In addition, a test was completed using the output from a 12-hr forecast from the BFM. This test indicates that the BFM forecasts can provide useful short-term information for the SWO by running the weather hazards program.

Note that the sample size for this study is relatively small. Further studies will investigate the use of the sounding as a forecasting tool derived from ARL's battlescale forecast model. Forecasts for all the weather hazards will be available using output from the mesoscale model. These forecasts can be applied for a single sounding or for a variety of soundings over a larger region.

ACKNOWLEDGMENTS

Thanks to MAJ Dave Knapp for his beneficial advice on how to verify turbulence reports, as well as his efforts to produce correlation factors on the turbulence forecasts and visibility forecasts. Special thanks to Robert E. Dumais Jr. for running the BFM and providing output for the 14 September 1994 case study over the central United States.

REFERENCES

Air Weather Service, 1984: Clear Air Turbulence Forecasting Techniques. AFGWC/TN-79/001 (Rev).

Glossary of Meteorology. Ed. Ralph E. Huschke, American Meteorological Society, Boston, MA.

Keller, L., 1990: Clear Air Turbulence as a Response to Meso- and Synoptic-Scale Dynamic Processes. Monthly Weather Review, 118, 2228-2242.

Knapp, D.I., R. Dumais, and T.J. Smith, 1993: Evaluation of Low-Level Turbulence Indices on a Mesoscale Grid. In Proceedings of the 1992 Battlefield Atmospherics Conference, U.S. Army Atmospheric Laboratory, White Sands Missile Range, New Mexico.

Miles, J. W., and L. N. Howard, 1964: Note on a Heterogeneous Shear Flow. J. Fluid Mech., 20, 331-336.

Lee, M.E., et al, 1995: U.S. Army Battlescale Forecast Model Concept of Operations. In Proceedings of the 1994 Battlefield Atmospherics Conference, U.S. Army Atmospheric Laboratory, White Sands Missile Range, New Mexico (Unpublished).

Passner, J. E., 1993: Expert Systems and Empirical Rules Used for Army Operations on IMETS. Preprint of 13th Conference on Weather Analysis and Forecasting, August 1993, Vienna, Virginia, American Meteorological Society, Boston, Massachusetts.

Passner, J. E., 1994: Forecasting Clear Air Turbulence Using a Single Sounding. In Proceedings of the 1993 Battlefield Atmospherics Conference, U.S. Army Atmospheric Laboratory, White Sands Missile Range, New Mexico.

Ramer, J., 1993: An Empirical Technique for Diagnosing Precipitation Type from Model Output. Preprint of the Fifth International Conference on Aviation Weather Systems, Vienna, VA, American Meteorological Society, Boston, MA.

Session III Posters

BATTLE WEATHER

Comparison of Radiometer and Radiosonde Derived Temperature Profiles Measured at Wallops Island, VA.

Edward M. Measure
U. S. Army Research Laboratory, WSMR, NM

Dick R. Larson
Physical Science Laboratory, New Mexico State University
Las Cruces, NM

Francis Schmidlin, Sean McCarthy
NASA Goddard Space Flight Center Facility at Wallops Island, VA

ABSTRACT

The Army Research Laboratory is developing a Mobile Profiler System (MPS) as a dual-use general purpose and Tactical Profiler demonstration system for measuring vertical profiles of atmospheric parameters. The primary requirement for the Tactical Profiler system is to supply improved meteorology for artillery aiming. A key component of the MPS is the radiometric temperature profiler. As part of a program to test equipment performance, and retrieval algorithms, a program of simultaneous measurements with microwave radiometers and radiosondes has been carried out in a wide variety of climates. The most recent were made during March of 1994 at the Wallops Island, Virginia, NASA experimental facility, and feature radar tracked balloons for precise measurement of sonde altitude.

1. INTRODUCTION

The United States Army Research Laboratory is engaged in developing a Mobile Profiler System (MPS) to measure vertical profiles of atmospheric wind, temperature, density, and moisture. Figure 1 is a graphic view indicating the MPS sensors and height coverages. Temperatures will be derived from ground and satellite based microwave radiance in addition to low level (less than 1 km) RASS

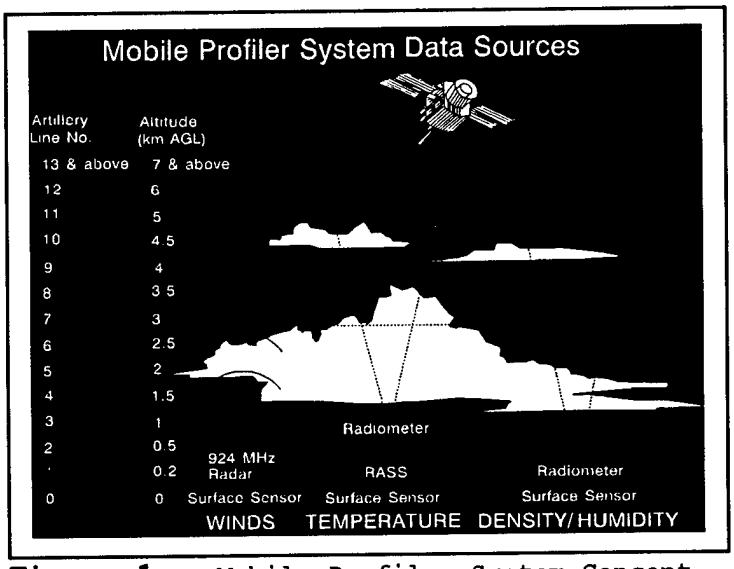


Figure 1. Mobile Profiler System Concept.

profiles. Satellite and surface based radiometric sensors are in some respects complementary for the measurement of atmospheric temperature profiles. Satellite temperatures are better in the upper atmosphere, and worst near the surface, while surface based radiometers do best near the surface but have little sensitivity above 6 kilometers.

2. THEORY OF RADIOMETRIC TEMPERATURE PROFILING

Atmospheric vertical temperature structure can be inferred from measurements of microwave brightness temperatures. For surface based measurements, in the 20 to 60 GHz region, the measured brightness temperatures approximately satisfy the following equation:

$$T_{b\nu}=\int_0^{\infty} T(s)\,\alpha_\nu(s)\exp\left[-\int_a^{s}\alpha_\nu(s')\,ds'\right]ds+T_{b\nu}^{\infty}\exp\left[-\int_0^{\infty}\alpha_\nu(s)\,ds\right] \qquad (1)$$

where

$T_{b\nu}$ = the downwelling microwave brightness temperature at frequency ν

$T(s)$ = temperature at height s

$\alpha_\nu(s)$ = the absorption coefficient

$T_{b\nu}^{\infty}$ = the downwelling cosmic microwave background brightness temperature above the atmosphere.

For downward looking microwave measurements, the equation is similar:

$$T_{b\nu}=\int_a^{g} T(s)\,\alpha_\nu(s)\exp\left[-\int_a^{s}\alpha_\nu(s')\,ds'\right]ds+T_{b\nu}^{g}\exp\left[-\int_a^{g}\alpha_\nu(s)\,ds\right]$$

where

a = altitude of the downlooking instrument

g = ground level

and $T_{b\nu}^{g}$ is the brightness temperature of the ground.

Inferring atmospheric temperature structure from microwave brightness temperature measurements thus becomes the problem of solving equations (1) and/or (2) to find T(s). Problems of this type are often referred to as inverse problems since

it is relatively simple to compute T_{bv} from a knowledge of T(s) but more difficult to obtain T(s) from T_{bv}. Although many techniques are used for attacking such problems (Westwater and Sweezy, 1983), each technique has its limitations.

3. EXPERIMENTAL PLAN

Since ARL wished to test both the temperature and pressure height measurement capabilities of the radiometer, we needed independent determinations of the radiosonde height at the time of the pressure and temperature measurements. One of the best ways to make such a height measurement to track the radiosonde with precision radar. The National Aeronautics and Space Administration (NASA) has an excellent capability for such measurements at their Goddard Space Flight Center at Wallops Island, Virginia. Since NASA regularly conducts such tracked radiosonde flights (see, e.g., Schmidlin, Olivero, and Nestler, 1983; Schmidlin, 1991), and the two NASA authors (Schmidlin and McCarthy) have extensive experience with such measurements a collaboration was arranged.

3.1 Apparatus

Experimental apparatus included two radiometers, balloon borne radiosondes and the associated launch facility, surface meteorological stations, and the NASA balloon tracking radars.

One radiometer was an oxygen radiometer operating at 4 separate frequencies in the oxygen absorption band: 51, 54, 55, and 57 GHz. For these experiments, the radiometer was fixed in azimuth but scanned in elevation, allowing the radiometer to sample at 5 separate angles to the horizontal: 9, 14, 25, 40, and 90 degrees. The second radiometer, a water vapor radiometer passively measured radiation at 2 separate frequencies at 21.6 GHz., on a water vapor absorption line, and at 31.6 GHz., which is most sensitive to liquid water. It was also scanned in elevation: 30, 42, and 90 degrees to the horizontal.

The Wallops Island balloon launch facility features a large bay, 30 or 40 feet tall, so that even large balloons can be inflated inside, out of the wind and rain. Tall garage style doors open on either of two sides of the building so that the balloon can be taken out into the wind in the most advantageous direction for a successful launch. We wanted the balloons to sample up to 20 millibars in pressure, typically 30 to 35 Kilometers above the surface.

In addition to the balloons launched at the Bldg. X-85 facility, there were balloons being launched at the NWS facility on Wallops Is., main base. The NWS facility is about 6 miles both from the Bldg. X-85 site and the ocean. This data was not used in the current study.

Also deployed was a surface met station comprised of a tripod supporting the wind vane, temperature, pressure, and humidity sensors. A suitcase-sized box, positioned next to the tripod, contained a Campbell data logger which sampled the

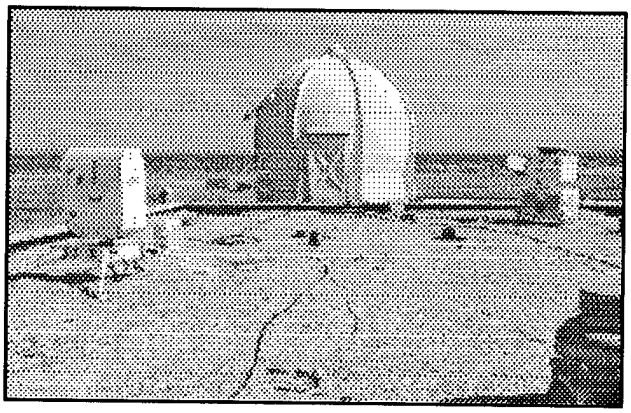
instruments and sent the sampled values to a PC via a long serial cable. We did not utilize the wind information in our profiling process, only the surface temperature, pressure, and relative humidity.

Other surface met station included one permanently attached to the balloon launch facility measured the surface values for the radiosonde data. In addition to that, data was also recorded by a third met station at X-85. Data from these stations was not used in the present study, however we do note that discrepancies of up to three degrees C were noted among the three instruments.

The balloons were tracked by NASA radar to precisely measure the height at which a profile sample was taken. Generally, Radar 6 picked up the balloon upon launch, then very quickly, turned over the tracking to Radar 18. Radar 6 was involved because the launch site was not directly visible to Radar 18.
There was a direct data feed from the radars to Bldg. X-85, so that after a balloon mission, all the necessary data was available to process a raob.

3.2 Experimental Site

The NASA Wallops Island Test Facility is located on the US East Coast. The experiment was conducted at Bldg. X-85, a balloon launch facility. X-85 is within a city block of the ocean. It is located on Wallops Island proper, not on NASA's main base facility. The two radiometers were positioned on the first-story roof of X-85. Azimuths and scanning elevations were programmed so that buildings and structures would not obstruct the path of incoming radiation. The figure shows the radiometers on the roof, and looks out across the roof, beyond the dome of nearby Bldg X-86, to the ocean.



A surface met station was positioned on the ground to the SouthEast of X-85. It was positioned too closely to X-85 and X-86 to accurately measure wind, but this is not a problem as our technique utilizes only the temperature, pressure, and relative humidity measurements.

3.3 Measurements

Measurements were intended to last for roughly one month, but failure of both radiometers, apparently due to damage by a storm, caused premature termination. We have comparison data from 16 March '94 to 31 March.

Data was collected from the Radiometers and the surface met station more or less continuously. There were typically 2 to 3 RAOB flights from Bldg. X-85 per 8 hour shift. Tried to fly a balloon during each UARS overflight. Flight was prearranged through Wallops Control with the personnel at X-85 and the two Radar groups. Data collecting computers for the balloons were readied, Sondes prepared, attached to the balloons, radar reflector attached, surface conditions noted, the two radar groups notified, and the balloons launched. The computers at X-85 began getting information from the sonde immediately. The first of the radars tracked the balloon for the first minute or so. Thereafter, the second radar picked up track and followed the balloon to burst, or until sonde signal failure.

4. RESULTS

Figures 3-7 are sample comparisons of the radiosonde observations (RAOBs), indicated by the solid black lines marked with black squares, and the radiometric retrievals, indicated by the white dotted lines. The temperature profiles shown here are virtual temperatures. The radiometric virtual temperatures are retrieved directly (Measure and Larson), while the radiosonde virtual temperatures have been derived using standard procedures (Range Commanders Council, IRIG standards), using the following equations:

$$T_V = \frac{T}{1.0 - 0.379 e/p} \qquad (3)$$

where T=temperature in Kelvins, e=vapor pressure (mbars), and p is pressure. And vapor pressure is computed from:

$$e = 0.0611 \cdot RH \cdot 10^{7.5 \cdot T/237.3 + T} \qquad (4)$$

where RH = relative humidity (%), T = temperature (°C)

These figures illustrate the virtues and vices of radiometric temperature retrieval, to wit, generally good tracking of the temperature profile but a tendency to smooth or even ignore elevated structure.

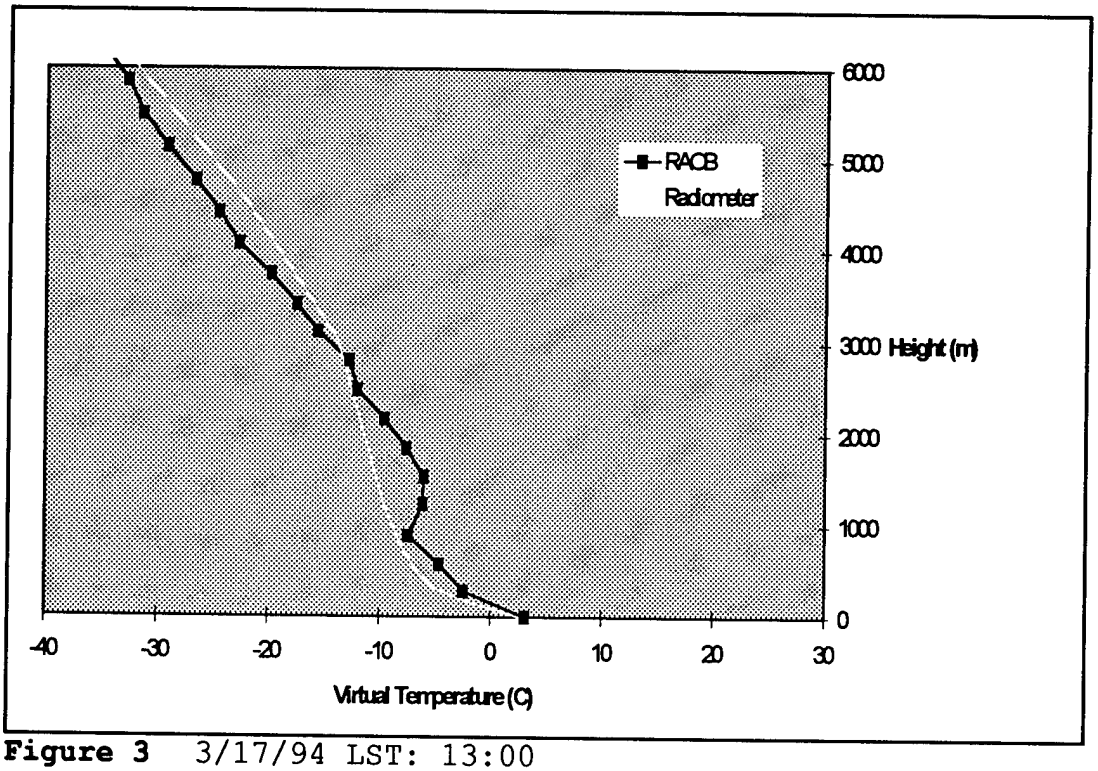


Figure 3 3/17/94 LST: 13:00

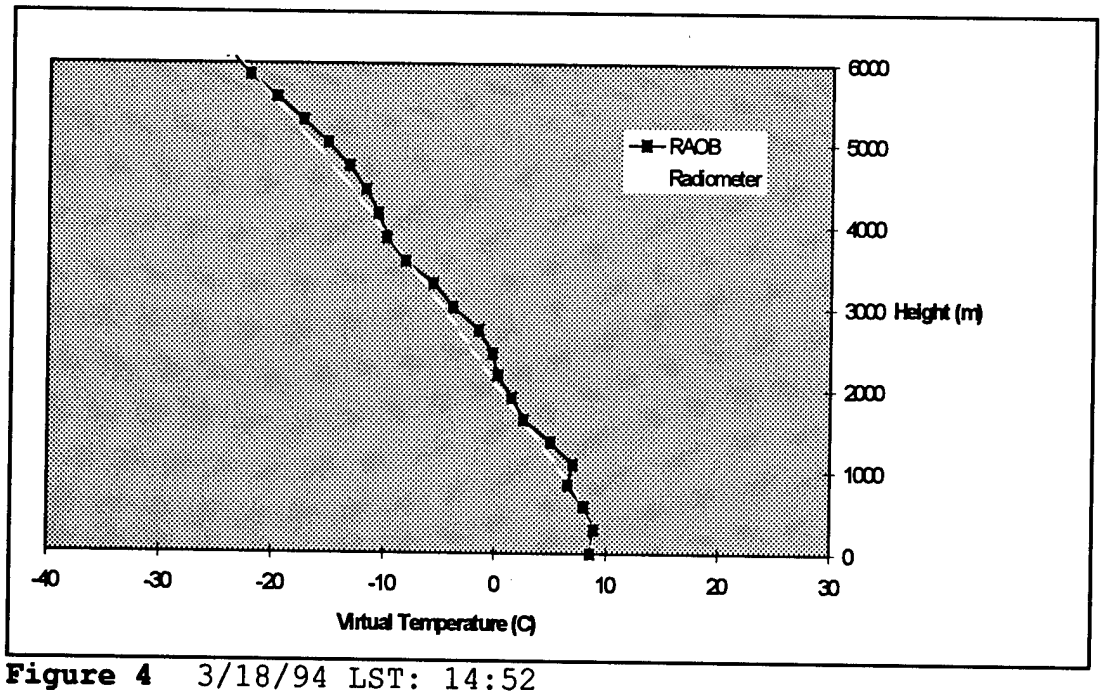


Figure 4 3/18/94 LST: 14:52

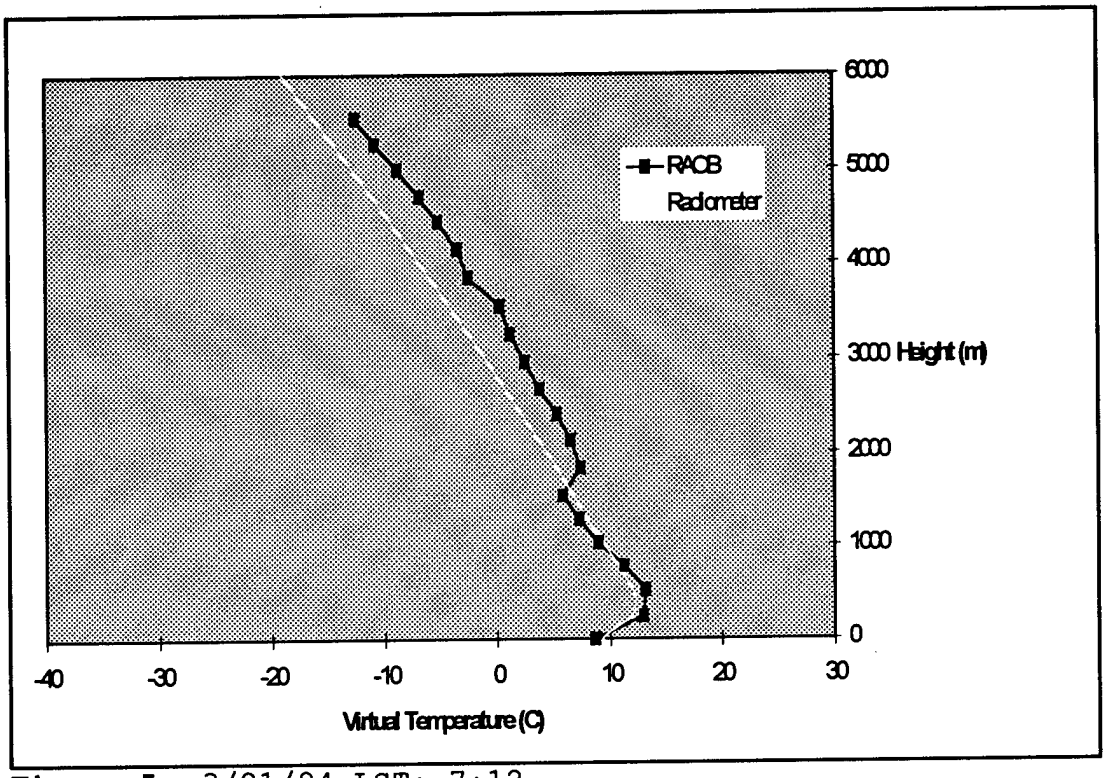


Figure 5 3/21/94 LST: 7:12

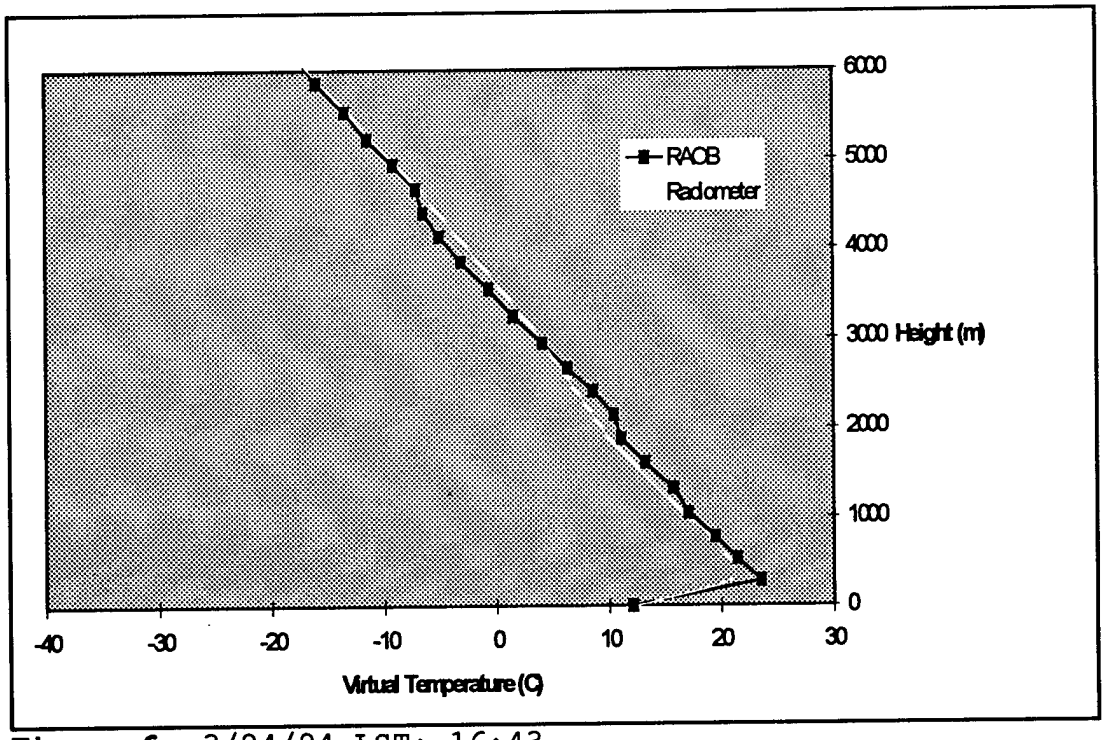


Figure 6 3/24/94 LST: 16:43

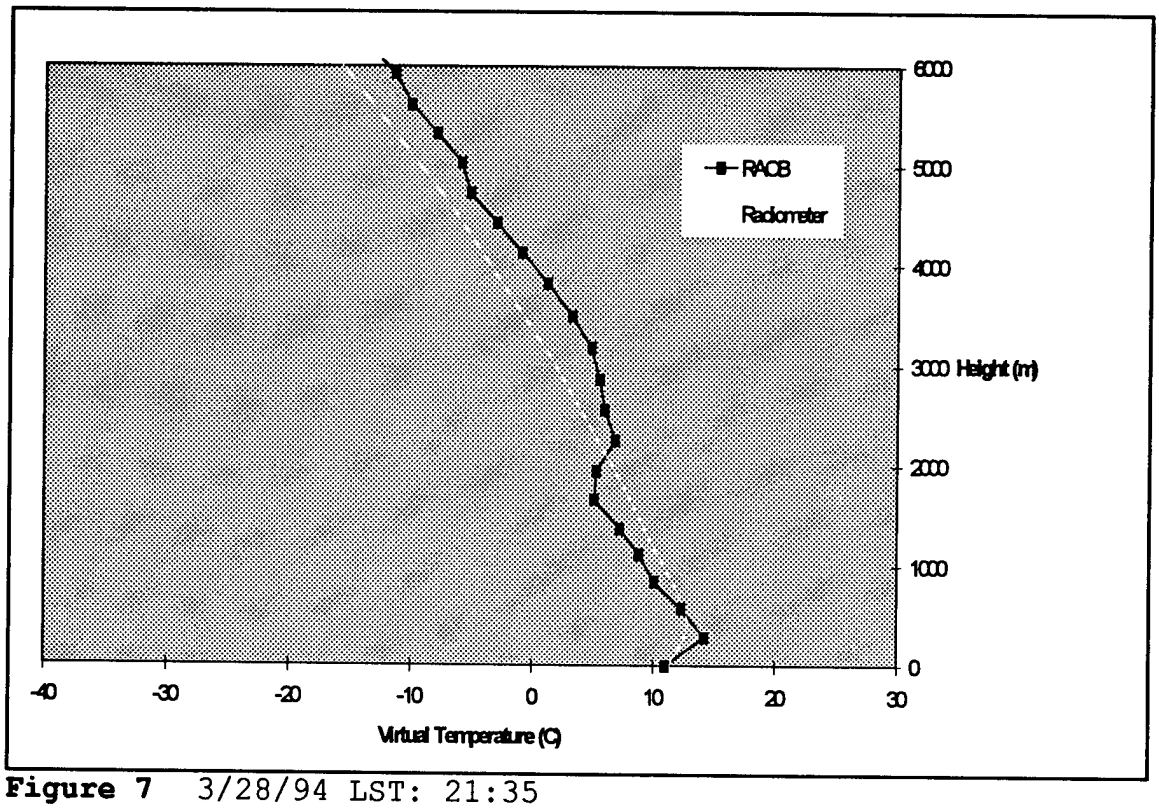


Figure 7 3/28/94 LST: 21:35

In particular, Figure 3 provides an example of how elevated structure is smoothed over by the radiometric retrieval process. In the relatively smooth profile of Figure 4, the elevated structure of the radiosonde temperature profile is of small scale, so deviations from it by the smooth radiometric profile are small. In Figure 5, the surface based inversion is tracked well, but here again the upper level structure is ignored. Even a dramatic surface based inversion like that in Figure 6 is tracked well by the radiometer, but Figure 7 again reveals the weakness of the method for upper level structure.

In figure 8 we show rms virtual temperature differences over the whole set of 34 temperature profiles for retrievals from both the radiometer data and a radiometer simulation. The radiometer simulation was constructed by using a radiative transfer code to compute what brightness temperature should be observed based on the atmosperic temperature profile measured by the radiosonde. Unsurprisingly, the simulator is better near the surface. The simulator presumeably is better because it is not affected by any errors in the measurement of either the radiosonde or the radiometer, and because the radiative transfer code used in computing its brightness temperatures is thee same as that used in computing the radiometric retrieval coefficients, it should also not be sensitive to any inadequacies of that code. Hence it represents a sort of optimal performance limit for this type of retrieval (as applied to this data set).

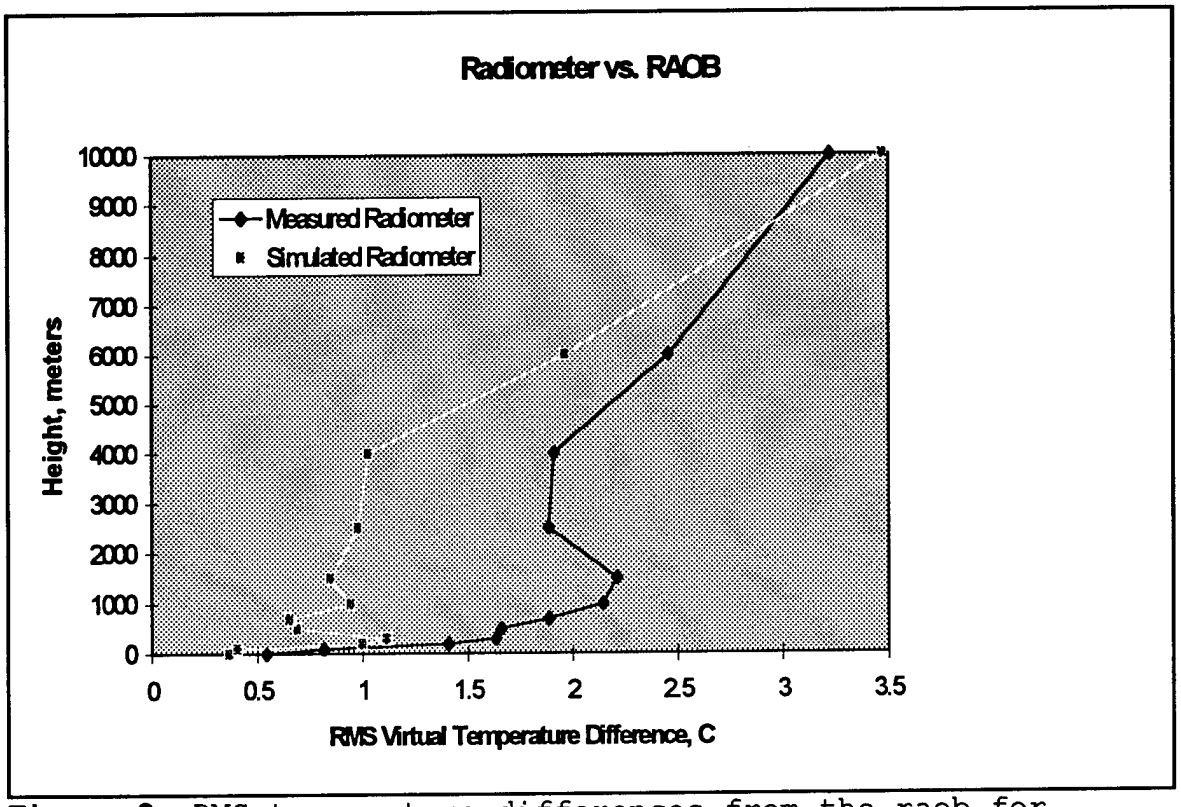


Figure 8 RMS temperature differences from the raob for both a radiometric measurements and a simulated radiometer.

REFERENCES

Gary, B.L., S.J. Keihm, and M.A. Janssen, *Optimum strategies and performance for the remote sensing of path-delay using ground-based microwave radiometers*, IEEE Trans. Geosci. Remote Sens., GE-23(4), 479-484, 1985.

Measure, Edward M., and Larson, Dick R., *Radiometric Retrieval of Virtual Temperatures*, in preparation.

Schmidlin, Francis J., Olivero, John J., and Mark S. Nestler. "Can the Standard Radiosonde System meet Special Atmospheric Research Needs." *Geophysical Research Letters*, **9**,9,1109-1112, 1982.

Schmidlin, Francis J. "Derivation and Application of Temperature Corrections for the United States Radiosonde.",

Range Commanders Council Secretariat, *IRIG Standards for Range Meteorological Data Reduction, Part 1 - Rawinsonde,* IRIG Standard 352-87, pg. 6 & 8, White Sands Missile Range, New Mexico 88001.

Westwater, E.R., and W.B. Sweezy, *"Profile retrieval algorithms used in thermal sounding of the atmosphere",* Proceedings of SPIE Conference on Inverse Optics, Arlington, VA, 1983.

THE INTEGRATED WEATHER EFFECTS DECISION AID

THREAT MODULE

D. P. Sauter
Battlefield Environment Directorate
White Sands Missile Range, NM 88002, USA

C. H. Chesley and A. R. Spillane
Science and Technology Corporation
Hampton, VA 23666, USA

ABSTRACT

This paper will present the results of recent efforts associated with the design and development of a threat module for the Integrated Weather Effects Decision Aid (IWEDA). IWEDA as demonstrated at the 1992 and 1993 Battlefield Atmospherics Conferences (BAC) contained only information for U.S. weapon systems. Issues addressed will include the acquisition of threat system environmental effects data, the display of threat system impacts, and the validity concerns regarding the comparison of friendly and threat weather impacts. An update will be provided on the status of IWEDA (e.g., enhancements to the software since the 1993 BAC and the porting of the code to the Unix/XWindows environment).

1. INTRODUCTION

Integrated Weather Effects Decision Aid (IWEDA) was demonstrated at the 1992 and 1993 Battlefield Atmospheric Conferences (for additional information on the purpose of IWEDA see the proceedings of either of these conferences). The 1992 demonstration was primarily a proof-of-concept display of prototype software. By the 1993 conference, the initial working version of the software had been developed and critiqued by both Battlefield Environment Directorate (BED) personnel and military personnel from the III Corps and 1st Cavalry Division at Ft. Hood, TX. Since then, additional systems have been added to IWEDA to bring the total number to 55. The total number of rules relating to weather or terrain impacts on systems in IWEDA is now 480. Several new features have also been added to IWEDA to make the software more powerful. Briefly, these are:

• Observation Support - This feature allows the user to enter weather data that has been observed, as opposed to forecast. Previously, both a different start and end time had to be entered before the weather and terrain data could be entered.

• Green Sensitivity - This feature allows the user to determine how close he is to approaching a yellow or marginal condition. For example, a particular weapon system becomes marginal to use at a wind speed of 20 kn and the current wind speed is 18 kn. By clicking on a green

or favorable matrix box, text is displayed indicating the system or operation is 2 kn away from becoming marginal.

• Inverse What-If - This feature allows the user to determine which systems can be substituted for an unfavorably or marginally impacted weapon system. For example, IWEDA may determine that the Cobra helicopter is unfavorable for use with the observed or forecast weather conditions. By performing a key stroke sequence, weapon systems that could potentially be substituted for the Cobra that are not adversely impacted would be displayed (e.g., the Apache). In many instances, there may not be any systems that can be substituted and the software will display a text message to this effect.

• Dynamic Rule Editor - This feature allows personnel at BED to add or modify the existing IWEDA rule base. New weapon systems can be added or existing systems can be modified. An example would be to change a critical weather impact rule on the Cobra from a 50-kn-wind gust to a 40-kn-wind gust. Because this is a very powerful tool, access to this module is currently limited to BED personnel.

The primary focus of this paper is on the design, development, and status of the IWEDA Threat Module; therefore, the rest of the paper will discuss this module.

2. THREAT MODULE DESIGN

In June 1994, all three coauthors of this paper travelled to Ft. Hood, TX to meet with Staff Weather Officer and Intelligence Officer personnel from the III Corps units. The purpose of this meeting was to propose two different options for the design of the Threat Module and receive feedback from attendees on which option to design. Before discussing the results of this meeting, the design options will be presented and discussed.

2.1 Friendly/Threat Delta

The Friendly/Threat Delta option displays graphically the difference or delta between comparable friendly and threat systems. The user would select one or more friendly and threat systems to be compared and run the threat module. IWEDA would then compute the weather effects on each system individually and assign a numeric value of 0, 1, or 2 to each system, its subsystems, and its components. Zero corresponds to an unfavorable impact, 1 to a marginal impact, and 2 to favorable or no impact. The delta is then computed by subtracting the threat numeric value from the friendly numeric value (for the comparable system, subsystem, or component). If the resultant value is greater than zero, the friendly system, subsystem, or component has an advantage over the comparable threat system, subsystem, or component. If the value is zero, neither side has an advantage and if the value is negative, the threat has the advantage. Different ways of displaying this information included textual and graphical (both spatially and temporally). While the concept is straightforward, there are some obvious difficulties in implementing this approach. For example, how are comparable friendly and threat systems defined?

2.2 Stand Alone Threat Module

The Stand Alone Threat Module has a separate threat button. When the threat button is invoked, the user can choose threat systems from an existing list. Weather impacts are then

determined and displayed by IWEDA completely separate from any friendly systems (i.e., separate and distinct output screens). Weather impact information is displayed in the same format as the existing friendly systems. There is a single screen depicting what, when, and why a threat system is being affected (figure 1). A second screen displays not only what system is being affected, but where the weather effects are for the particular system(s) (figure 2). The rectangular area on the left portion of the screen represents a geographic area. Discrete areas with different weather parameter values can be entered as shown in figure 2. There may be different weather effects regions indicated. When the software is rehosted on a Unix workstation (tentatively in the summer of 1995), a digital map background will be displayed and IWEDA weather effects regions can be overlaid. The option of displaying threat weather effects has the advantage of being exactly the same as the friendly display and would be the simplest to implement.

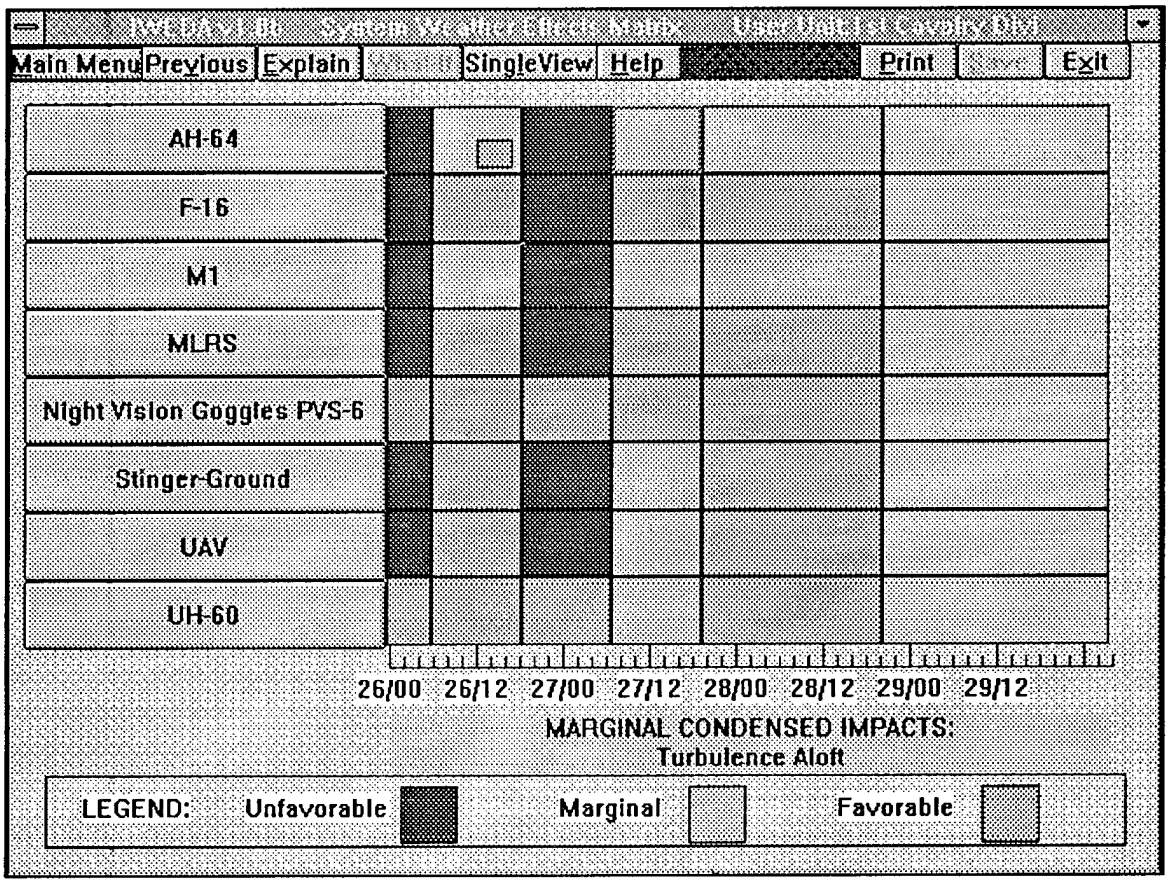


Figure 1. IWEDA System Weather Effects Matrix.

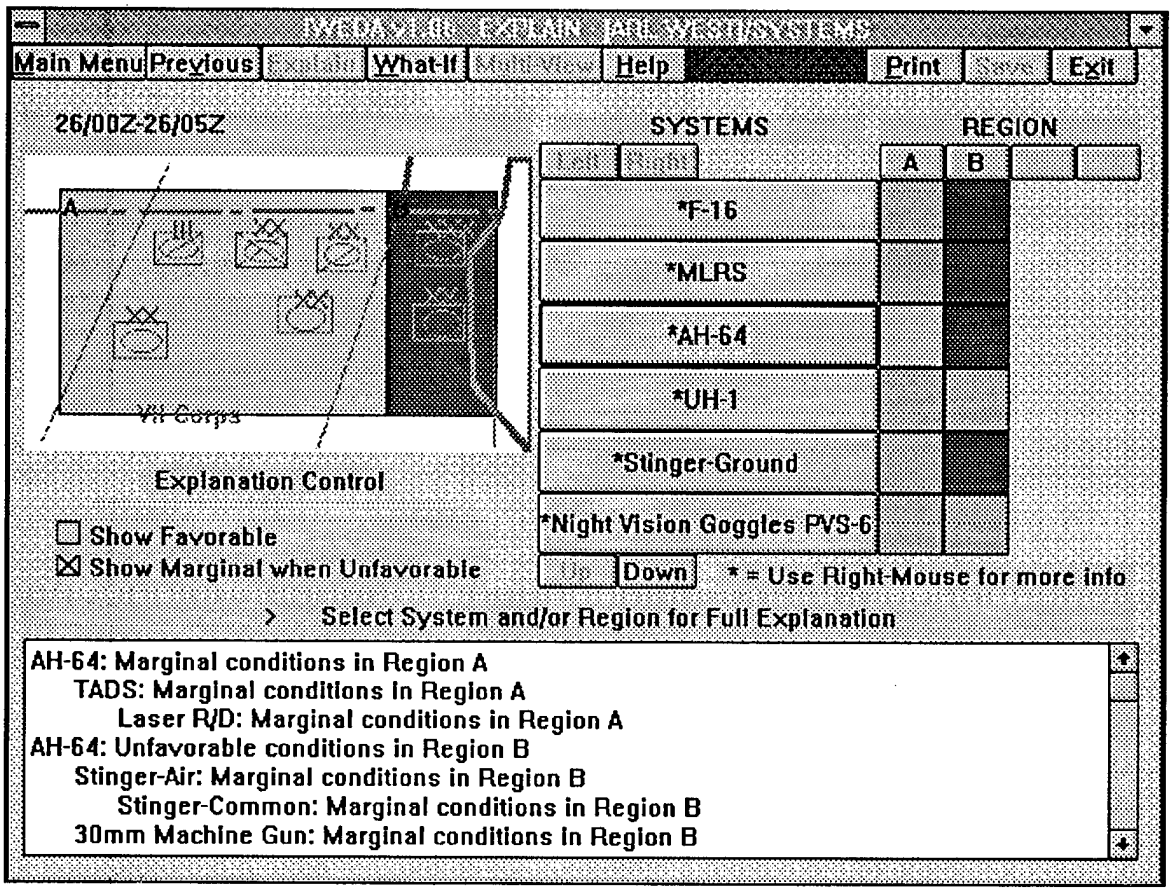


Figure 2. IWEDA System Weather Effects Matrix with map overlay.

2.2 Results of the Ft. Hood Threat Meeting

Ft. Hood intelligence officers in attendance preferred the display of threat system weather impacts separate from friendly systems. Primarily, they were wary about having the IWEDA software make a comparison between friendly and threat systems without human intervention. The officers preferred that the weather effects impacts be computed separately and that the staff weather officers or intelligence officers make any comparisons themselves. There was also a concern about defining comparable friendly and threat systems for the delta design. Initial design of the Threat Module will thus focus on the separate display of threat systems. Demonstration and distribution of this software will allow for a larger group of users to comment on the threat design.

2.3 Threat Data Collection

A trip to the III Corps library at Ft. Hood was made the week that submission of this paper was due. The purpose was to collect weather effects data on threat systems. The trip was made based on information from one of the intelligence officers from Ft. Hood who attended the Threat Module meeting in June. A data request has also been submitted to the National

Ground Intelligence Center (formerly the Foreign Science and Technology Center) for weather impacts or weather related impacts on threat systems. Hopefully, enough threat data is available between the two sources to enter at least several threat systems into a future version of IWEDA that includes the Threat Module. Unfortunately, inclusion of the threat data will result in the threat version of the code becoming classified. This classification will result in special treatment of the software. Only properly accredited hardware will be allowed to run the classified threat version.

3. RELATED EFFORTS

In addition to the new features of IWEDA mentioned in the Introduction and the work on the Threat Module mentioned above, work is underway to rehost the software to the Unix/XWindows environment. This will allow for automated ingest of several of the weather parameters that IWEDA requires as well as the display of digital map backgrounds. IWEDA could then be implemented on a server platform and be run across several client machines. The server platform could receive real time weather and have IWEDA compute the weather effects, and distribute the information to the clients. A design such as this is being considered for the Battle Command Battle Lab in Ft. Leavenworth for the Prairie Warrior demonstration in May 1995.

4. CONCLUSIONS

Incorporation of a threat module within IWEDA will allow for more complete analyses of weather effects on weapon systems by the staff weather officers and intelligence officers. Recent participation in exercises both within the U.S. and overseas have proven the utility and value of IWEDA. Rehosting to the Unix/XWindows platform will bring IWEDA one step closer to Army fielding.

OWNING THE WEATHER
BATTLEFIELD OBSERVATIONS FRAMEWORK

Richard J. Szymber and James L. Cogan
U.S. Army Research Laboratory
White Sands Missile Range, NM 88002

ABSTRACT

The concept of Owning the Weather involves the exploitation of advance knowledge of the environment and its effects to gain a decisive advantage over opponents. This requires high quality, real-time measurements of atmospheric variables combined with appropriate models to obtain as complete and accurate a picture as possible of the environment over the battle space. Surface, upper air, unmanned aerial vehicle and satellite observations are needed over the entire battlefield including target areas within enemy held territory. Several sensing systems are planned to provide this capability. By combining the strong points of a variety of battlefield sensors with proper application of models, the Army can achieve the major improvement in observing the battlefield environment necessary for Owning the Weather.

1. INTRODUCTION

The commander who can best measure and take advantage of weather conditions has a decided advantage over his opponent (HQ DA, 1993). Owning the Weather (OTW) embodies the use of advance knowledge of the environment and its effects on both friendly and threat soldiers, systems, operations and tactics to gain a decisive edge over enemy forces. The OTW operational warfighting strategy for battlefield weather exploitation involves three main steps. First, the actual weather and environmental conditions for the theater, including critical data-denied target areas, must be observed and collected in real time by a variety of battlefield sensing systems. Then, this timely weather/environmental information must be processed, analyzed, and disseminated rapidly to the user; essential is the input of the observational data into models to predict future weather conditions and their effects. The final step concerns the combat application of the observations, forecasts and effects, and their transformation into digitized weather intelligence and decisions aids/displays for mission planning, situational awareness, and advanced decision and execution support.

2. BATTLEFIELD SENSING SYSTEMS AND OBSERVATIONS

Weather elements must first be observed before they can be forecast and ultimately converted into weather intelligence. All the diverse observations required cannot be supplied by any one single sensing system. Rather, a variety of complementary and synergistic space-based, airborne and ground-based sensing systems are necessary to provide all the observations needed at the required

accuracies, resolutions and coverage. The data collected from all available sources is validated and assimilated to build a complete horizontal and vertical depiction of the atmosphere and weather over the full extent of the battlefield.

Weather observations must be taken at key locations and monitored often because weather conditions can change frequently over short periods. Hourly observations of weather conditions are required from the forward area of operations, including crucial target areas, and need to be updated hourly, or more often during rapidly changing weather conditions (USAIC&FH, 1994). The mission, terrain, threat, and time for which the forecast is required will determine the density of observations required in specific areas. Observations will be taken by a network of automated and manual means with mutually supportive capabilities selectively deployed throughout the depth of the battlefield.

Table 1. Characteristics of direct-readout WEFAX and APT imagery.

SENSING SYSTEM	DATA PARAMETER	TEMPORAL RESOLUTION	HORIZONTAL RESOLUTION
WEFAX			
GOES	visible imagery	3.0 h	8.0 km
	thermal imagery	3.0 h	8.0 km
	water vapor imagery	3.0 h	14.0 km
METEOSAT	visible imagery	0.5 h (Europe sector)	5.0 km
		1.5 h / 3.0 h (other sectors)	
	thermal imagery	0.5 h (Europe sector)	5.0 km
		3.0 h (other sectors)	
	water vapor imagery	6.0 h (all sectors)	5.0 km
GMS	visible imagery	3.0 h	8.0 km
	thermal imagery	3.0 h	8.0 km
APT			
NOAA	visible imagery	5.0 h (0 lat)	4.0 km
	thermal imagery	4.0 h (40 lat)	4.0 km
		2.5 h (60 lat)	
METEOR-2	visible imagery	same as NOAA	2.0 km
	thermal imagery		8.0 km
METEOR-3	visible imagery	same as NOAA	2.0 km
	thermal imagery		3.0 km
FENG YUN	visible imagery	7.0 h (0 lat)	4.0 km
	thermal imagery	6.0 h (40 lat)	4.0 km
		4.0 h (60 lat)	

2.1 Space Observations: Environmental Satellites

Meteorological satellites (METSATs) provide continuous, covert, reliable, global, wide area observations of many weather and

environmental parameters of critical interest to the Army. METSATs see the complete battlefield atmosphere and environment from their unique vantage point and provide the only routinely available weather observations in most data-denied areas. All available METSAT observations from a constellation of geostationary and polar orbiting operational environmental satellites will be received and utilized by the Army in near real-time.

Geostationary METSATs provide near-continuous, high temporal resolution observations of visible, infrared, and water vapor (moisture) imagery and temperature and humidity profiles over the theater of interest from approximately 60 N to 60 S latitude. The U.S. civil Geostationary Operational Environmental Satellite (GOES), GOES-Next series (GOES I-M) provides coverage of the CONUS, Latin America, South America, Caribbean, and E. Pacific and W. Atlantic oceans. The Japanese Geostationary Meteorological Satellite (GMS) provides coverage of E. and SE. Asia and the E. Indian and W. Pacific oceans. The European Meteorological Satellite (METEOSAT) provides coverage of W. and E. Europe, Africa, SW. Asia, and the W. Indian and E. Atlantic oceans. Army ground receiving equipment (i.e., the WRAASE and Small Tactical Terminal (STT)) directly receive low spatial resolution Weather Facsimile (WEFAX) imagery and weather charts from these satellites which are important for monitoring weather patterns and systems. WEFAX data characteristics are outlined in Table 1 (Rao et. al., 1990).

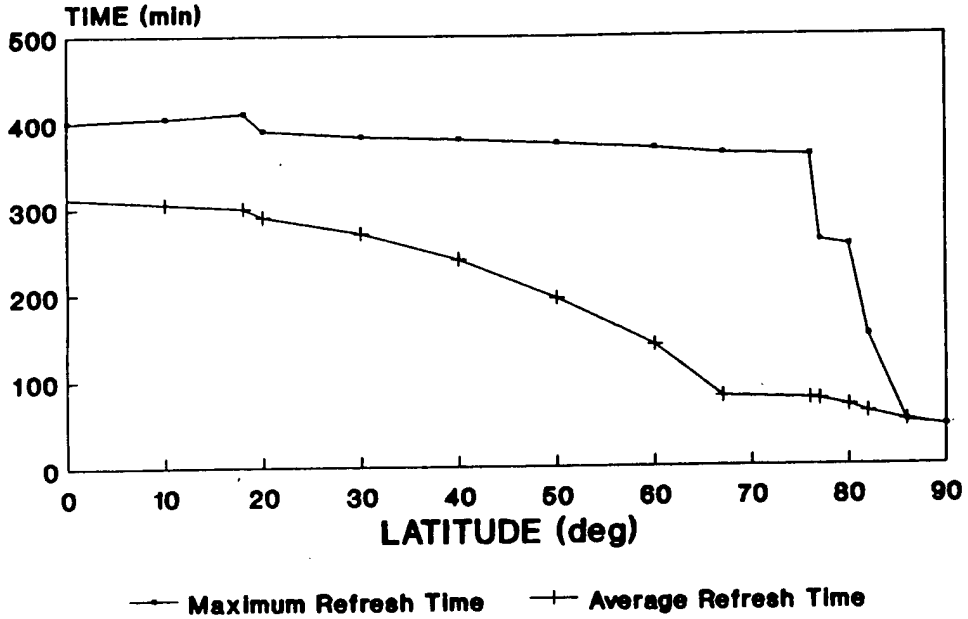


Figure 1. Polar orbiting satellite imagery temporal resolution as a function of latitude for a two satellite constellation.

Polar orbiting low altitude METSATs are capable of providing global coverage of multispectral imagery and atmospheric soundings. The Army receives low resolution Automatic Picture Transmission (APT) imagery via the WRAASE and STT from various U.S. and foreign polar

orbiting METSATs (see Table 1). High resolution METSAT data (imagery and soundings) are directly received via the Integrated Meteorological System (IMETS) and enhanced STT from the Defense Meteorological Satellite Program (DMSP) Block 5D-2 and newer Block 5D-3 satellites and National Oceanic and Atmospheric Administration (NOAA) TIROS satellites. Temporal resolution, or data refresh time, for polar orbiting METSATs varies primarily according to the latitude of the direct-readout station, the swath width (or scan angle) of the satellite sensor, and the number of satellites in orbit. Figure 1 shows how the maximum and average temporal resolution varies as a function of latitude of readout site for a two DMSP satellite constellation optimized for the Operational Linescan System (OLS) imager and for an elevation angle of 20 degrees. Average temporal resolution for a combined DMSP/NOAA four satellite operational constellation for three sample latitudes based on data type is given in Table 2.

Table 2. Polar orbiting satellite data temporal resolution for representative latitudes.

DATA TYPE	TEMPORAL RESOLUTION
IMAGERY	3.5 h (0 lat)
(visible-infrared)	2.5 h (40 lat)
	1.0 h (60 lat)
IMAGERY	7.0 h (0 lat)
(microwave)	6.0 h (40 lat)
	4.0 h (60 lat)
SOUNDINGS	4.0 h (0 lat)
(microwave/infrared)	3.0 h (40 lat)
	1.5 h (60 lat)

The DMSP Real Time Data (RTD) and Realtime Data Smooth (RDS) data transmissions are encrypted, whereas the NOAA TIROS High Resolution Picture Transmission (HRPT) broadcasts are not secure. DMSP visible, infrared, and microwave imagery possess nearly constant resolution across the entire scan swath. The DMSP OLS imager mapping accuracy is 4-7 km and swath width is 2963 km. The DMSP Special Sensor Microwave Imager Sounder (SSMIS) mapping accuracy is 7-13 km and swath width is 1707 km. Data characteristics of the DMSP Block 5D-3 SSMIS and OLS are presented in Table 3 (Heacock, 1985). The 6 channel NOAA Advanced Very High Resolution Radiometer (AVHRR) imager mapping accuracy is about 4 km and swath width is 2700 km. The NOAA Advanced TIROS Operational Vertical Sounder (ATOVS), consisting of the Advanced Microwave Sounding Unit (AMSU)-A (temperature) and -B (humidity) and High-resolution Infrared Sounder (HIRS), has a mapping accuracy of around 7 km and swath width of 2300 km. Data characteristics of the NOAA K-N series ATOVS and AVHRR/3 are found in Table 4 (Heacock, 1985). The

profile accuracies given in Table 3 and 4 are not valid in the vicinity of the tropopause.

Table 3. Characteristics of DMSP Block 5D-3 RTD data.

SENSING SYSTEM	DATA PARAMETER	ACCURACY (RMS) +/-	HORIZONTAL RESOLUTION
DMSP BLK 5D-3			
SSMIS	temperature profile	5.0 C (surface)	40.0 km
		3.0 C (1 km)	
		2.0 C (2-30 km)	
	humidity profile	25% or 2.5 g/kg	40.0 km
	geostrophic wind profile	10 m/s; 15 deg	40.0 km
	pressure profile	10.0 mb (surface)	40.0 km
		6.0 mb (1 km)	
		4.0 mb (2-30 km)	
	precipitation rate	5.0 mm/h (0-25 mm/h)	25.0 km
		10.0 mm/h (25-60 mm/h)	
	precipitation flag	7-10 km (location)	12.5 km
	soil moisture	20% (0-60%)	25.0 km
	land surface temperature	3-5 C	25.0 km
	cloud coverage	2/10 or 20%	25.0 km
	snow cover	12.5 km (edge location)	25.0 km
		3.0 cm (snow water content)	
	surface type	9 types	25.0 km
OLS	cloud and land surface	digitization= 6 bit (visible)	0.6 km
	imagery (visible/thermal)	digitization= 8 bit (thermal)	2.8 km (night VIS)
	= 3 channels	albedo = 5% (day)	
		temperature = 3-5 C	

2.2 Airborne Observations: Unmanned Aerial Vehicles (UAV)

There are two classes of UAV: tactical and endurance. The joint tactical UAV program baseline for Army applications consists of the Hunter UAV (formerly the Short Range UAV) and the Maneuver Variant UAV (formerly the Close Range). The Hunter UAV is designed to meet Army division, corps and EAC requirements with a mission endurance of 8-12 hours, maximum radius of action of 200 km, and maximum altitude of 4.5 km (15,000 feet). Each of the 32 Hunter UAV systems to be fielded include eight air vehicles and two ground control stations. The Maneuver Variant UAV flies high threat, close-in missions and is designed to provide direct support to maneuver battalions and brigades with a mission endurance of 3-4 hours, maximum radius of action of 50 km, and maximum altitude of 3.0 km (10,000 feet). Each of the 100 Maneuver Variant UAV systems

to be fielded include four air vehicles and two downsized ground control stations. The Maneuver Variant UAV is capable of rapid deployment with early entry forces and meets the deployability, mobility and flexibility requirements of maneuver combat units.

Table 4. Characteristics of NOAA K-N HRPT data.

SENSING SYSTEM	DATA PARAMETER	ACCURACY (RMS) +/-	HORIZONTAL RESOLUTION
NOAA K-N			
ATOVS	temperature profile	3.0 C (surface)	45.0 km (nadir)
(AMSU-A/B,		2.5 C (1 km)	100.0 km (end of scan)
HIRS/3)		2.0 C (2-30 km)	
	humidity profile	20% or 2.0 g/kg	same as temperature
	geostrophic wind profile	10 m/s; 15 deg	same as temperature
	pressure profile	6.0 mb (surface)	same as temperature
		5.0 mb (1 km)	
		4.0 mb (2-30 km)	
	cloud coverage	2/10 or 20%	20.0 km (nadir)
	precipitation rate	TBD	15.0 km (nadir)
	snow cover & thickness	TBD	15.0 km (nadir)
AVHRR/3	cloud and land surface	digitization = 11 bit	1.1 km (nadir)
	imagery (visible-thermal)	albedo = 5% (day)	4.0 km (end of scan)
	= 6 channels	temperature = 2-4 C	

The current plan for UAV contains meteorological sensing as one of the required missions (DOD, 1994). The UAV meteorological sensor is a miniature, lightweight weather sensor that will be carried on all UAVs. It will directly measure temperature (+/- 1.0 C), pressure (+/- 1.0 mb) and humidity (+/- 5 %) along the UAV flight path, while information from the UAV flight control navigation system is used to derive wind speed (+/- 1.0 m/s) and direction (+/- 5 deg). Accuracy of the wind data depends directly on the capability of the navigation system, with a Global Positioning System (GPS) based system providing the highest accuracy (as assumed here). The sensor can produce data continuously on a routine basis, sampled at intervals as short as a second, or data may be transmitted on demand. The load on the communications datalink will be minimal due to a data rate of only a few hundred bps. The data will be relayed from the UAV through the UAV ground control station to appropriate fire support (Artillery Meteorology sections) and intelligence (IMETS) networks.

The dropsonde for UAVs is undergoing development and preliminary requirements documents are being drafted. Future UAVs could

optionally be equipped with expendable dropsondes for high value target areas. They measure vertical profiles of temperature, wind speed and direction, humidity and pressure as the sonde falls from flight level to the ground (with measurement accuracy similar to radiosondes). The dropsonde currently under development will use GPS to obtain even better wind values in a smaller package. Overall the sonde will be a miniature and more accurate version of existing dropsondes carried on large manned aircraft. They may be carried in a removable pod capable of holding 6-10 sondes plus ejection and data receiving and processing equipment. The data rate for the dropsonde will resemble that of a radiosonde, with the data transmitted from the sonde through the UAV to the ground control station and then to appropriate users. Both the UAV meteorological sensor and dropsonde will be especially useful in acquiring target area weather data to support artillery and aviation deep operations.

2.3 Upper Air Observations: Artillery Meteorology Sections

Artillery Meteorology (ARTYMET) sections are responsible for measuring surface and upper air meteorological data and providing atmospheric data for field artillery units and to the IMETS via Mobile Subscriber Equipment. Balloon borne radiosondes measure vertical profiles of atmospheric temperature (+/- 1.0 C), pressure (+/- 1.0 mb), humidity (+/- 5 %), and wind speed (+/- 1.0 m/s) and direction (+/- 5 deg) up to 30 km AGL. Vertical resolution of the wind profiles is 250 m, and 100 m for the other variables. The equipment used is mobile and designed to move with the supported artillery units. Meteorological data are provided in various message formats to support Army needs. These data are vital for accurate artillery fires and play an important part in developing tactical weather forecasts. The Meteorological Measuring Set (MMS), AN/TMQ-38, and the HMMWV version MMS, the AN/TMQ-41, is being fielded to replace the Meteorological Data System (AN/TMQ-31). The MMS will downsize the system to a smaller team and shelter on a HMMWV, and increase mobility. During combat operations, observations are taken every two hours according to doctrine (Depts. of Army & Air Force, 1994).

Future ARTYMET sections may employ a tactical atmospheric profiler which will use advanced active and passive remote sensing technology and a miniaturized antenna system, in conjunction with satellite sensors, to derive the standard profiles of upper air elements from the surface to 30 km. It will be mounted on a HMMWV and will greatly reduce the need for a balloon-borne radiosonde. The greatest advantage of the profiler is it will provide timely atmospheric soundings as often as required, or as often as every three to five minutes, as opposed to every two hours. This will eliminate the time staleness problems of current techniques. The Mobile Profiler System (MPS) under development combines the strong points of a ground based profiling system with those of a METSAT. The MPS consists of a radar profiler for measuring wind speed and direction profiles, a radio acoustic sounding system and microwave radiometer for virtual temperature profiles, and a METSAT receiver

for satellite temperature, humidity, and derived wind (speed and direction) soundings. Pressure profiles are computed, and will be eventually measured by the radiometer. Data characteristics of the MPS can be found in Cogan (1994) and Cogan and Izaguirre (1993).

2.4 Surface Observations

The Army plans to field the Automatic Meteorological Sensor System (AMSS) in order to obtain accurate and timely surface observations forward of the division command post for support to fire and maneuver units and for combat support operations such as terrain analysis, Intelligence Preparation of the Battlefield, and chemical hazards warning and smoke employment planning. Unattended, AMSS will routinely measure surface weather and environmental elements, record them in standard format, provide local readout, and transmit them to the nearest IMETS. The modular sensors will directly measure wind speed and gust (+/- 1.0 m/s), wind direction (+/- 5 deg), air temperature (+/- 1.0 C), humidity (+/- 5 %), barometric pressure (+/- 1.0 mb), rainfall rate (+/- 2.5 mm/h) and amount (+/- 2.5 mm), soil temperature (+/- 1.0 C) and moisture (+/- 5 %), and night illumination (+/- 10 %) (based on the approved AMSS ORD, 1993). Time and location will be determined by GPS or alternate means. IMETS at division and separate brigade will automatically receive encrypted AMSS observations by area communications. The AMSS will be lightweight, man portable, and either vehicle mounted or hand emplaced. Future improvements to the AMSS may include sensor modules to measure cloud base height and visibility, and may employ direct relay of data by satellite communications.

2.5 Other Battlefield Observations

There are other potential sources of timely battlefield weather and environmental observations that can be collected and incorporated into the observational data base when available. These include: US Air Force Weather Team upper air and surface observations from deployed fixed-site airfield teams and mobile observing teams; Air Force and Army aviation pilot reports (including Target Weather Indicator (TARWI) reports); manual surface observations from Army Long Range Surveillance Units and Special Operations Forces; and any host nation indigenous observations.

3. DATA COLLECTION CONCEPT OF OPERATIONS

Optimal sensor density on the battlefield is defined as that distribution of sensors which permits an analysis such that additional sensors would not alter the results in any militarily significant way. Specifying the location/placement of sensors is another vital consideration, especially when making observations in complex terrain (Veazey and Tabor, 1986). The variety of army operations and tactics require many surface and upper air observations to account for weather variations due to complex terrain and physical geography (Depts. of Army & Air Force, 1994). Observed data is extremely perishable and must be rapidly and continuously updated and made available to end users. To

accomplish this collection and ensure data is available in the density necessary to support operations, a sensing strategy must be developed which supports the needs of the mission. The Staff Weather Officer is a key agent in developing the weather and environmental sensing strategy which must be integrated into the overall theater sensing strategy and plan. Generally, the further forward the specific area of interest, the greater the reliance upon unattended and remote sensors. A generalized view of the OTW battlefield data collection concept is presented in Figure 2.

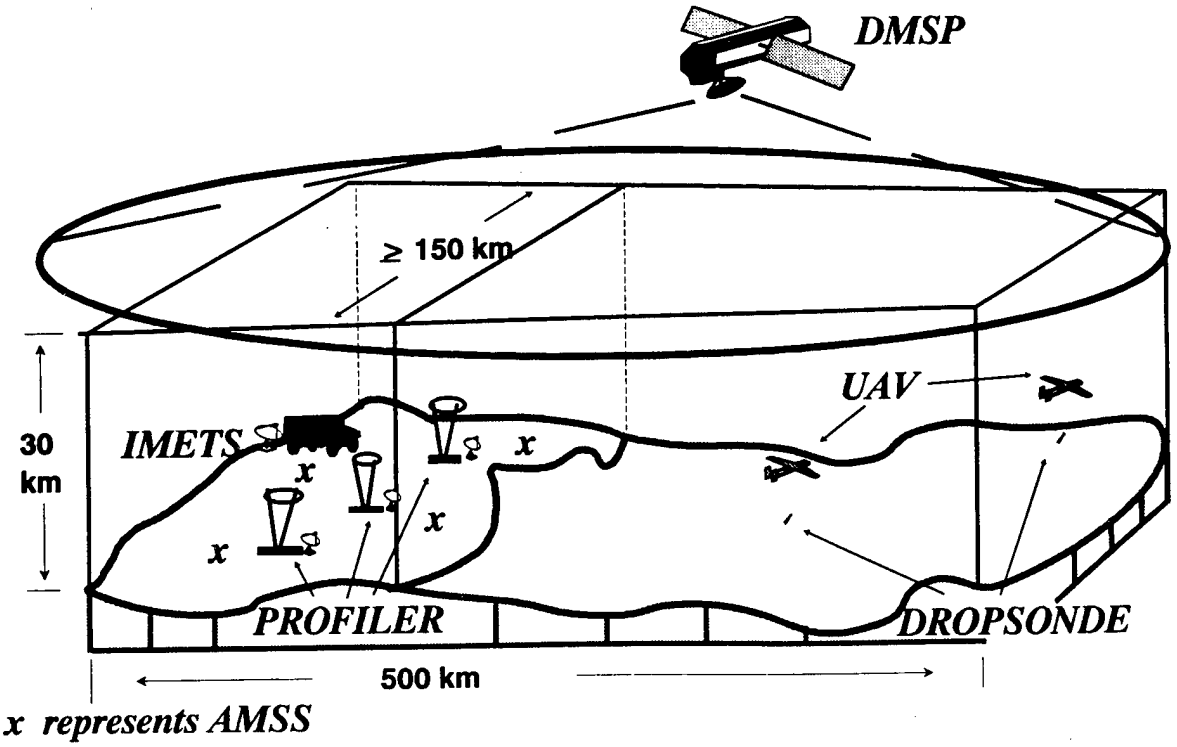


Figure 2. Conceptual three dimensional view of OTW battlefield sensing systems for collection of data over the battle space.

3.1 Satellite and UAV Observations

METSATs provide a truly unparalleled "big picture" view of the earth's surface and global atmosphere. They are the only sensing system considered here capable of wide area coverage of observations, autonomously and routinely, anywhere in the world. Direct readout high resolution imagery and sounding data from geostationary METSATs are available about every 30 minutes, and WEFAX imagery are available as scheduled with temporal resolutions given in Table 1. The temporal resolution of direct readout high resolution data from polar orbiting satellites varies and can be approximated by the values given in Table 2, which are representative of typical four-satellite DMSP/NOAA operational constellations. Fortunately, in friendly territory a relatively

ample amount of surface and upper air observations will be available to complement the METSAT data over the area. But, in forward-area data silent regions controlled by the enemy, and/or inaccessible remote regions, little of no data will exist to supplement the METSAT observations.

UAVs will be the only direct source of detailed measurements of environmental parameters over target areas in the foreseeable future. The other source of data for denied areas, METSATs, can remotely sense qualitative information and broader scale quantitative data. For example, the UAV meteorological sensor will be able to provide data at shorter than one second intervals, representing averages along the flight path of 50 to 100 m at common UAV speeds, while METSAT sounders provide atmospheric temperatures for areas 40 km in diameter. Thus the satellite provides a general picture of atmospheric conditions over the battlefield while the UAV can fill in the details for specific target areas. Target area weather information provided by both the UAV meteorological sensor and dropsonde can also be used to modify the METSAT atmospheric soundings and improve the weather information throughout the satellite swath by adjusting the satellite data to the more accurate and detailed UAV data, yielding better quantitative information over the entire battle space.

Normally a UAV could be expected to fly at an altitude high enough to avoid ground fire from small arms. The air vehicle would climb to a cruise altitude and change altitude in accordance with the mission. It is unlikely that a UAV would fly below 200 or 300 m above the ground, while the maximum altitude would depend on the variant and the mission. Under operations that do not include a specific weather mission, the meteorological sensor data will be available on a routine basis for use as needed. Special flight paths may be flown when weather has a high priority, such as for deep fire support, where the UAV would eject one or more dropsondes over or near high priority targets. Flight duration and altitude would depend on the mission or set of missions for a given vehicle. A crude profile of atmospheric parameters could be obtained from the on-board meteorological sensor as the air vehicle gained or lost altitude during a weather or non-weather mission. Ejection of a dropsonde at low altitudes would decrease the duration of the sonde's fall, but reduce altitude coverage of the profiles. For applications requiring a detailed profile from the surface to higher altitudes, the air vehicle should fly closer to its maximum flight level when releasing the sonde.

3.2 Surface and Upper Air Observations

Most mesoscale-size system features (e.g., squall lines) of Army interest can be detected and monitored with an optimal surface station separation of no more than about 30 to 35 km (House, 1964). Surface sensor system placement and density to acquire sufficiently accurate data for a division-sized area of operations in complex terrain can be accomplished by deploying up to 20 surface stations, with the exception of precipitation data (Veazey and Tabor, 1986).

To obtain high resolution measurements of precipitation rates and amounts a combination of doppler weather radar and meteorological satellites would be required. If critical parameters are required in certain areas based on the military situation then measurements must be made at that particular location. However, the battlefield may contain various avoidance areas that include mountain tops, water areas (i.e., lakes, swamps and marshes), deep snow fields, mine fields and tank crossings where weather sensors can not be placed.

The AMSS is expected to be deployed both mounted on battalion and brigade S2 vehicles and separately set up by hand on tripods. In certain situations AMSSs will be placed at key locations and left unattended. They will report automatically by secure wide area and long range communications to the nearest IMETS. The automated observation rate is expected to be as often as every 30 minutes to provide the necessary density of observations required for Army weather forecasts (HQ AWS, 1992). Additionally, three Air Force mobile observing teams may be part of the division weather team. Each team is capable of 24-hour operations and has an Army vehicle for deployment to key locations when directed by the Staff Weather Officer to take and relay surface observations back to the division Tactical Operations Center. The primary mission of these teams is to provide detailed weather observations (e.g., cloud type, height and amount, visibility (and restrictions), present weather, winds, temperature, pressure, and humidity) from locations which are critical to operations, such as along avenues of approach and air corridors.

Heavy divisions have two ARTYMET sections while light divisions and separate brigades have only one. The Artillery commander deploys his ARTYMET section where it can best support his mission. Some considerations in selecting a position include prevailing winds, location of artillery firing units, and sufficient clearance for balloon releases. The ARTYMET section is best located where balloon borne sensors will pass through or near the same portion of the atmosphere as the artillery projectiles (Depts. of Army & Air Force, 1994). In the case of the atmospheric profiler, it would be best positioned as close as possible to the firing units. The frequency of soundings to update data will vary depending on the operation, maximum height required, stability of the weather conditions, and for balloon systems the available resupply of radiosondes. For planning purposes, soundings are usually taken every two hours.

4. CONCLUSION

Adequate collection of weather and environmental observations is a prerequisite to successful battlefield meteorological support. The concept of OTW requires high quality, real-time measurements of meteorological variables combined with models to obtain a complete and detailed description of the atmosphere over the battle space. Surface, upper air, satellite and UAV observations are needed over the entire battlefield including data-denied, enemy controlled

territory. The OTW observations framework described is essential for effective target area meteorology and precision strike and deep attack operations, and greatly enhances all Army tactical operations that are affected by the environment.

REFERENCES

Cogan, J. C., 1994. A Technical Demonstration Mobile Profiler System. ARL-TR-523, U. S. Army Research Laboratory, White Sands Missile Range, NM 88002.

Cogan, J. C., and A. Iraguirre, 1993. A Preliminary Method for Atmospheric Soundings in Real Time Using Satellite and Ground-Based Remotely Sensed Data. ARL-TR-240, U. S. Army Research Laboratory, White Sands Missile Range, NM 88002.

Department of Defense, 1994. Unmanned Aerial Vehicles 1994 Master Plan.

Departments of the Army and Air Force, 1994 Draft. FM 34-81/AFM 105-4, Weather Support to Army Operations. Washington, DC.

Heacock, E. L. (ed.), 1985. ENVIROSAT-2000 Report: Comparison of the Defense Meteorological Satellite Program (DMSP) and the NOAA Polar-Orbiting Operational Environmental Satellite (POES) Program. Washington, DC, 426 pp.

House, D. C., 1964. "The problem of detecting mesoscale motion systems." Monthly Weather Review, 92:589-592.

Headquarters Air Weather Service, 1992. Concept Paper for Air Force Weather Support to Army Theater Operations 1995-2005. Scott Air Force Base, IL, 31 pp.

Headquarters Department of the Army, 1993. FM 100-5, Operations. Washington, DC.

Rao, P. K., et. al., 1990. Weather Satellites: Systems, Data, and Environmental Applications. American Meteorological Society, Boston, MA, 503 pp.

U. S. Army Intelligence Center & Fort Huachuca, 1994 Draft. US Army Intelligence, Electronic Warfare, Target Acquisition Master Plan, Vol. IV Supporting Concepts, Ch. 1 Weather Supporting Concept. Fort Huachuca, AZ.

Veazey, D. R. and P. A. Tabor, 1986. "Meteorological Sensor Density on the Battlefield." In Proceedings of the Sixth Annual EOSAEL/TWI Conference, U. S. Army Atmospheric Sciences Laboratory, White Sands Missile Range, NM 88002, pp 549-562.

ELECTRO-OPTICAL CLIMATOLOGY MICROCOMPUTER VERSION 2.2 DEMONSTRATION (EOCLIMO)

Matthew R. Williams
USAF Environmental Technical Applications Center
Scott AFB, Illinois 62225-5116

ABSTRACT

Electro-Optical Climatology Microcomputer Version 2.2 is a PC based 8-12 micron transmittance climatology display program. Transmittance was calculated using DATSAV2 surface data in the LOWTRAN7 radiative transfer model. Transmittance was calculated for a fixed geometry of a 125 m height with a 4 km slant path to the surface. Calculations were done for every three hour point for up to a 20 year period of record. Climatologies were developed using Statistical Analysis System (SAS) for more than 5,800 stations throughout the world. Among the output which can be displayed using the program are: mean transmittance by month; percent frequency of selected transmittance values (e.g. 5%, 10%, 15%, etc) by month and hour; ceiling versus transmittance by month and hour; ceiling frequency by month and hour, as well as precipitation and fog frequency by month and hour.

1. INTRODUCTION

As the use of precision guided munitions increases, the effects of weather in the planning and execution phases of employment are critical. EOCLIMO was developed to provide planners with a worldwide climatic database of 8-12 micron transmittance. In addition, conventional weather data, such as absolute humidity, visibility, and precipitation was included in the database. This allows users to determine what meteorological conditions are responsible for the transmittance at a given month and hour. Previously published reports by USAFETAC (Edson et al, 1987; Condray and Edson, 1988; Condray and Edson, 1989a; Edson and Condray, 1989; Condray and Edson, 1989b) laid the foundation for the microcomputer version of EOCLIMO. Unlike the published reports, however, EOCLIMO allows military planners rapid access to an interactive climatological transmittance database for sites throughout the world.

2. DATA AND METHODS

2.1 DATSAV2 Surface Data

Surface data from USAFETAC's DATSAV2 climatic database, described in detail in Climatic Database Users Handbook No. 4, DATSAV2 Surface (USAFETAC/UH-86/004, 1986) was used in the LOWTRAN7 radiative transfer model (Kneizys et al, 1988). All three hourly

observations available from 1973 to 1992 were loaded into DB2 relational database tables. All stations in an area of interest with a sufficient number of observations (~10,000) were used. Stations from the following areas were analyzed:

Region	# of Stations
Pacific	561
Southwest Asia/Northwest Africa	219
Central America	336
Southwest Africa	275
Northwest Africa	231
Europe	1,677
Russia (former Soviet Union)	1,849
China/Mongolia	607
Test Ranges	60
Total	5,815

2.2 Method

The surface data was input into the LOWTRAN7 model and transmittance was calculated for each observation. A fixed geometry from the surface to 125 m AGL with a slant path of 4 km was used. Each station was analyzed to determine if any maritime or desert aerosol influence was possible and the associated wind sector was flagged. The aerosol models in LOWTRAN7 (desert, maritime, fog, etc) were turned on or off based on the current weather observation. The transmittance values calculated assumed a cloud-free line-of-sight (no LOWTRAN7 cloud models were used). After LOWTRAN7 had been run against all observations, SAS was used to calculate the month-hour statistics.

3. OUTPUT

3.1 EOCLIMO 2.2

An interactive PC-based data visualization program, Electro-Optical Climatology Microcomputer Version 2.2 was developed by USAFETAC/SYS (Microcomputer Branch). This DOS-based program allows the display of the data generated by LOWTRAN7 and SAS. The program and documentation are available, in compressed form, on 131 3.5" diskettes. Uncompressed, there are 627 megabytes of data. (There is currently an effort to put the data on compact disk.) The data is graphed and displayed in four "windows" on the screen (figure 1) or on half the screen when tabular data is displayed. Maps of a region of interest can also be displayed.

3.2 PC Program Output Details

EOCLIMO output can be divided into two types: conventional weather (precipitation, visibility, ceiling, etc.) and transmittance data. The conventional weather data allows the user to determine what meteorological variables are impacting transmittance.

3.2.1 Conventional Weather Data

There are five different displays of conventional weather data. Percent frequency of occurrence of ceilings for 13 different ceiling categories can be displayed for a particular month-hour combination. Percent frequency of occurrence of precipitation, separated into light, moderate/heavy rain and light, moderate/heavy snow are given as well as the cumulative percent. Percent frequency of occurrence of fog is divided into fog with visibility 1 km or less and visibility greater than 1 km. The cumulative percent of fog is also provided. The ceiling

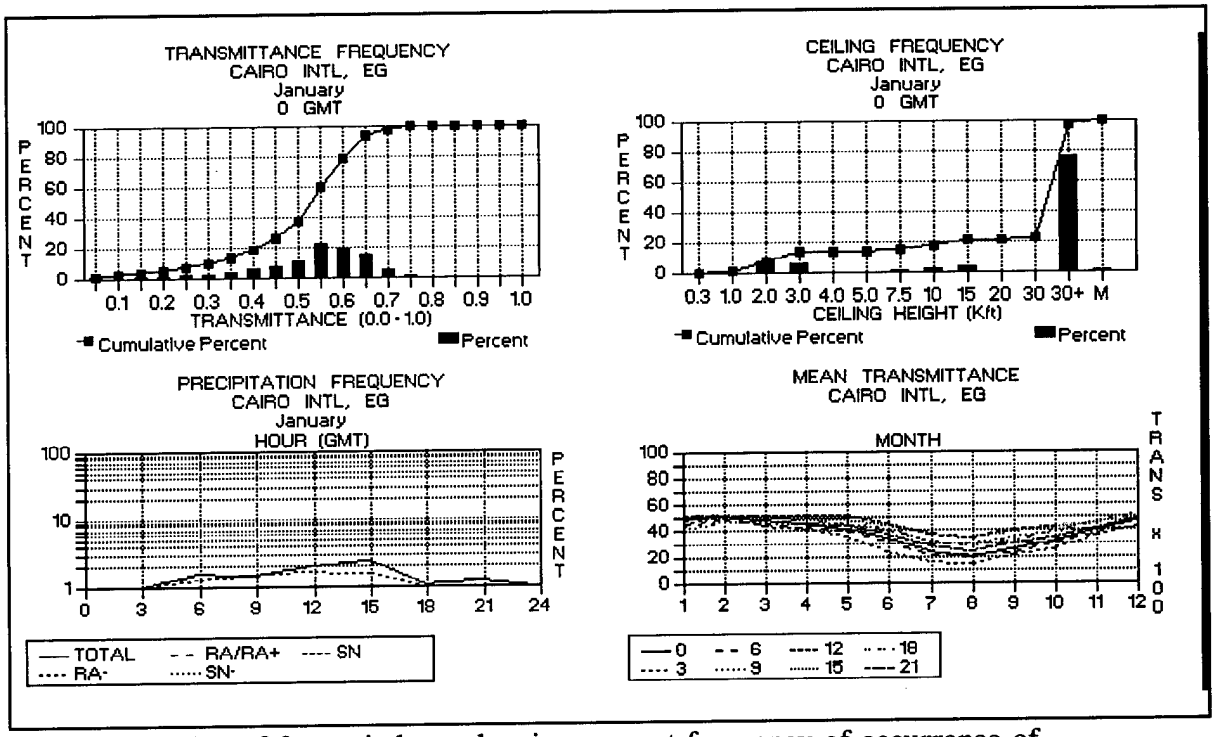


Figure 1 Display of four windows showing percent frequency of occurrence of transmittance (upper left), ceiling frequency (upper right), precipitation frequency (lower left), and mean transmittance.

criteria option of the program allows a user to display the percent frequency of a ceiling height by hour and month. Mean absolute humidity can also be displayed for month-hour combination.

3.2.2 Transmittance Data

Transmittance data can be displayed in a variety of ways. Mean transmittance for each month can be shown. A separate line is drawn for each three hourly value of mean transmittance. Transmittance can be displayed as percent frequency of occurrence in .05 increments of transmittance for a particular month-hour. There two tables which can be displayed. The first is a weather category table, which shows mean transmittance, temperature, dew point, relative humidity, absolute humidity, visibility and wind speed for occurrences of weather (i.e., rain, snow, etc) for a given month-hour. The other table provides transmittance versus ceiling height

for ten transmittance values (0.0 - 1.0) and 13 ceiling categories. A feature called EOCRIT allows the user to select transmittance and ceiling thresholds and then select two percent frequency of occurrence thresholds. A map then displays station circles in red, yellow or green depending on the thresholds. Maps can also be displayed showing stations available centered around the chosen station.

4.0 CONCLUSION

EOCLIMO 2.2 provides worldwide climatological transmittance data with high temporal resolution. The software allows quick and easy viewing of climatological transmittance data and associated climatological weather parameters. Additionally, multiple station data can be viewed simultaneously to easily compare transmittance characteristics between sites. Future plans include placing the worldwide data on a compact disk .

REFERENCES

Climatic Database Users Handbook No. 4, DATSAV2 Surface, USAFETAC UH-86/004, USAF Environmental Technical Applications Center, Scott AFB, IL 62225, Dec 1986.

Condray, P. M., and R. T. Edson, 1988; Persian Gulf Transmittance Study in the 8-12 Micron Band, USAFETAC TN-88/003, USAF Environmental Technical Applications Center, Scott AFB, IL 62225, 31pp.

Condray, P. M., and R. T. Edson, 1989a; The Caribbean Basin, An Electro-Optical Climatology for the 8-12 Micron Band, Volume I--Central America, USAFETAC TN-89/004, USAF Environmental Technical Applications Center, Scott AFB, IL 62225, 149 pp.

Condray, P. M., and R. T. Edson, 1989b; The Caribbean Basin, An Electro-Optical Climatology for the 8-12 Micron Band, Volume III--Northern South America, USAFETAC TN-89/006, USAF Environmental Technical Applications Center, Scott AFB, IL 62225, 238 pp.

Edson, R. T., and P. M. Condray, 1989; Global Transmissivity Study for Electro-Optical Weapon Systems in the 8-12 and 3-5 Micron Bands, Volume II--The West Indies, TN-89/005, USAF Environmental Technical Applications Center, Scott AFB, IL 62225, 130 pp.

Edson, R. T., R. H. Grumm and J. G. Miller, 1987; Global Transmissivity Study for Electro-Optical Weapon Systems in the 8-12 and 3-5 Micron Bands, USAFETAC PR87/002, USAF Environmental Technical Applications Center, Scott AFB, IL 62225, 170 pp.

Kneizys, F. X., E. P. Shettle, L. W. Abreu, J. H. Chetwynd, G. P. Anderson, W. O. Gattery, J. E. A. Selby, and S. A. Clough, 1988; User's Guide to LOWTRAN7, AFGL-TR-88-0177, Air Force Geophysics Laboratory, Hanscom AFB, MA 01731, 137 pp.

Session IV Posters

BOUNDARY LAYER

Technical Exchange with Australia

Patti Gillespie
James Gillespie
U.S. Army Research Laboratory
Battlefield Environment Directorate
White Sands Missile Range, NM 88002, USA

ABSTRACT

This paper will detail the technical exchange between the U.S. Army Research Laboratory (ARL) and the Australian Defence Science and Technical Organisation (DSTO) during 1994. Both authors were participants in the ARL Professional Exchange Program (APEX) and spent almost three months (July through October 1994) at DSTO in South Australia. The APEX Program is in its second year with programs existing in several European countries, and the authors initiating the program this year in Australia. Methods of formal exchange of technical information and the actual information exchanged will be discussed in this paper. An overview of the research program at DSTO will also be given. This is a reciprocal agreement program, and scientists from Australia will have an opportunity to visit Army Research Laboratory on a similar basis in the future. Continuation of the collaborative work initiated under this program will be possible through visits by Australian scientists to ARL.

1. INTRODUCTION

The International Office of the U.S. Army Research Laboratory sponsors a relatively new program called the ARL Professional Exchange Program (APEX). Under this program ARL professionals write a proposal for a short term project to be conducted in conjunction with personnel at a laboratory in another country. A group at ARL reviews these proposals and decides which proposals are to be supported. The original idea of this short term exchange was to conduct it during the summer months for a period of two to four months. Most of the exchanges thus far have fit into this structure. 1993 was the first year of existence of this Apex

program, and the Battlefield Environment (BE) Directorate sent a scientist (David Sauter) to England to work at Fort Halsted. This year Drs. James and Patti Gillespie of BE submitted proposals to work at the Defence Science and Technology Organisation (DSTO) conducting projects that included workshops on EOSAEL, simulation, and Ultra-violet (UV) research.

DSTO is located at three sites, Salisbury, South Australia; Melbourne, Victoria; and Canberra, ACT. Patti Gillespie had visited DSTO-Salisbury previously under the auspices of the Special Working Party / Modeling of Target Acquisition SWP/MOTA and had contacts with some of the scientists doing simulation. James Gillespie is a member of the TTCP panel which has members from Australia, New Zealand, Canada, United States, and UK. The specialty of the TTCP group currently is UV.

2. AUSTRALIAN DEFENCE RESEARCH STRUCTURE

The Australian defense plan is based on a number of factors among which are (1) the position of Australia in the Asia-Pacific region, (2) the role that the United States will play in the next decade as the world's only super-power and the part the United States will play in the stability of the Asia-Pacific region, (3) the extent to which the United Nations will play a part in promoting peace and stability and resolving international security issues, (4) how China, Japan, and India develop their strategic policies and power, (5) the possibilities for proliferation of weapons on mass destruction and ballistic missiles, (6) the future impact of economic inter-dependence and changing trade alignments, (7) the growing dynamism of Asia countries - which on balance - increases the stability of the region near Australia, but also if sustained over the long term - will bring change in the Australian relative national strength, (8) continued economic and social problems in the South Pacific, and (9) continued instability in the Middle East, a major world supplier of energy. As a result of all of these concepts that have been recognized by Australian national planners, Australia is attempting to forge new alliances with nations in the Asia-Pacific region. this does not mean that Australia will change its stance and support of United States and European alliances. Historically, these have always been important and will continue to be. Australia has also always been a leader in participation in the international community in peacekeeping. This role may expand in the future. The role of the civilian industry in defense is also expected to expand. The main defense threat to Australia itself is termed the threat from the north, that is, small-scale invasion by one of the Asian countries directly to the north of Australia. For this reason, most defense capabilities are designed, built, and tested with a tropical climate in mind. The United States also has an interest in developing and testing systems to work in tropical

environments, but mainly because of defense commitments to other countries. Historically, the United States has provided defense to the South Pacific since World War II, and there were significant business interests that were guarded previous to that. The United States and Australia participated side-by-side in the Vietnam conflict. Both countries have significant economic interests throughout the Pacific Rim area. Australia and New Zealand have very aligned security interests and they have pledged to help each maintain a defense against an invasion of each other. The United States-New Zealand relationship and any problems that occur are the only negative areas in the Australian-United States cooperation agreements. (New Zealand has a policy against nuclear vessels being received in their ports.)

Taking into account all of the concepts mentioned in the previous paragraph, Australia is eager to participate in a scientist exchange program with a country such as the United States. Typical Australian scientists often spend more than a year of their careers abroad, learning what is being done in the rest of the world in their field. Exchanges are most likely to occur within the Commonwealth (UK) countries, but exchanges with other countries are very welcome also. To our knowledge, three scientists participated in exchanges between Australia (DSTO) and the United States (ARL) during 1994. An Australian scientist was involved in a long term exchange with a directorate of ARL in Maryland, and Drs. James and Patti Gillespie participated in the Short Term Exchange Program in South Australia. DSTO has already had the cut-backs in personnel that ARL is currently experiencing, and the technical exchange program is considered to be part of the rebuilding process. Another consideration is that a short-term exchange is more economically feasible than a long term assignment.

After looking at the Australian posture on defense researcy in general, one should examine the actual structure of the research organization itself. DSTO is a tri-service research and development organization, whereas ARL services the Army specifically. DSTOs mission is "To enhance the security of Australia through the application of science and technology." The research priorities for DSTO are (1) command, control, and communications, (2) intelligence collection and evaluation, (3) mobile land-force operations in the North and North-West, (4) broad area surveillence, and (5) military infrastructure, in particular major naval and airforce platforms. DSTO has three major sites in the following places: (1)Salisbury, South Australia; (2)Melbourne, Victoria; and in (3)Canberra, ACT. We worked in the Land, Space, and Opto-electronics Division (LSOD) within DSTO in Salisbury, South Australia during our time in Australia. The mission for LSOD is "DSTOs LSOD in South Australia is responsible for conducting research and exploratory development in the fields of

optoelectronic surveillence and passive counter-surveillence , involving transmission, reception and countering of optical radiation in the UV to submillimeter region of the EM spectrum." LSOD was created specifically by DSTO to increase DSTO's interaction with the Australian Army. The primary interactions for Optoelectronics until recently had been with the Royal Australian Navy.

3. TECHNICAL EXCHANGE

Before we detail the various aspects of the techincal exchange, we would like to note that in any trip abroad there are many formal details that must be attended to. Australia was not one of the countries on the first years list of countries to participate in the APEX program. The ARL International Office made inquiries to the Australian Embassy in Washington, DC and were met with an enthusiastic response. Officials in the Australian Embassy smoothed the legal obstacles to such an exchange and were a real asset. From the start, Australia was an enthusiastic partner in APEX. Once the program was set up, the DSTO personnel in Salisbury helped to make the arrangements for United States citizens to come and live in their community for three months. Once again, the Australians provided excellant service in helping us to find a place to live, a place for our children to go to school, and provided basic guidance in how to do the everyday things in Australia. Generous and friendly are the two words that best describe Australians.

The Electro-Optics Systems Atmospheric Effects Library (EOSAEL) had already been given to DSTO as part of both the SWP/MOTA panel and TTCP. EOSAEL consists of more than 20 computer models that are maintained on a UNIX mainframe computer system. Without a specific directive and knowledge of how to use these models, none had been successfully installed and used on DSTO computers. The computer identified to host the EOSAEL models was a MicroVax computer system running under VMS. The most time-consuming portion of the this technical exchange consisted of the loading and installing of the EOSAEL models. These models were transported to DSTO on 3.5 inch floppy diskettes using DOS backup, instead of the usual tar backup tape for EOSAEL. Because of the very different computer environment for the EOSAEL, the Gillespies experience some problems in installing and getting all of the models working. All of these problems were overcome, and readme files were developed for the VMS systems to assist future users of EOSAEL models at DSTO.

Once all of the models were successfully installed on the VMS computer system at DSTO, the Gillespies offered a series of Workshops on technical background of the various models and how to use them. These workshops were met with enthusiasm and several of the EOSAEL models were already in use before the end of the

Gillespies's technical exchange. Once Australian scientists were interested in some of the EOSAEL models, some of the scientists uploaded these models to their PCs for use. Informal workshops on the use of some of the EOSAEL models on PCs were conducted.

As part of the technical exchange, James Gillespie offered a seminar on UV technology and its use in a variety of defense and civilian areas. UV technology has wide interest within a variety of divisions within DSTO. Scientists from outside of LSOD attended this seminar and followed up their interests with meetings with James. Patti Gillespie is involved in simulation research at ARL and offered a seminar on simulation research at the Battlefield Environment Directorate.

One of the products that DSTO is most proud of is a target acquisition model called ILLOWRA. ILLOWRA is the Aboriginal word for sea eagle, and this model was first developed for system performance modeling of the Sea Hawk system. This model is similar to the EOSAEL model TARGAC in some ways, but has much more emphasis on the optical systems and sensor performance than TARGAC. ILLOWRA uses the British Aerospace proprietary model ORACLE, instead of the Night Vision Sensor Performance model, FLIR92/ACQUIRE. Acquisition range calculations using the Johnson model are determined in this model through an algorithm developed by DSTO from Night Vision Sensor Handbook information. Most of the ILLOWRA model is written in FORTRAN, although the model control shell is written in C. The architecture of ILLOWRA is modular, consisting of five main sections: target, background, atmosphere, FLIR, and observer. The atmosphere is determined by LOWTRAN7 calculations that can be done as either a part of the ILLOWRA or as stand-alone calculations. Synthetic targets and synthetic and real backgrounds are used in ILLOWRA. A wide variety of FLIR technologies are modeled in ILLOWRA for the sensor part of the calculations. Finally, both ORACLE and Johnson predictions are used in the observer part of the model. Particular attention has been paid to sea surface radiance calculations for backgrounds, as well as ships as targets. Both Gillespies spent time learning to use the ILLOWRA model. This model will be part of the exchange to the United States, including the proprietary ORACLE model.

ILLOWRA has been used by the Australians in several ways. Some of these are identification of the best "off-the-shelf" solution, system upgrade studies, provision of data for operational analysis studies, and investigation of novel IR techniques. One application of ILLOWRA that has illuded the Australians is in mission planning. They are particularly interested in our application of target acquisition models in tactical decision aids (TDAs).

Images from the ILLOWRA model showing the effects of the optics and

atmosphere are shown here in Figure 1. In this figure a ship image is shown with effects from four different source displayed in each quadrant. In the upper left quadrant the ship image is shown prior to the effects of dynamics and optics at 8 km and D* noise added. In the image in the upper right of Figure 1, the ship image now includes the effects of the optics, but no detector effects are shown yet. The lower left quadrant of the Figure 1 shows now how the Seidel defocus effect, or general blurring impacts the image. These three images are all at 8 km. The final image, in the lower right hand quadrant, shows the ship image at 10 km, with detector effects, lower signal, and greater noise. Other effects that can be modeled are vignetting and less signal. All of these effects can be varied to study the possibilities of a variety of systems.

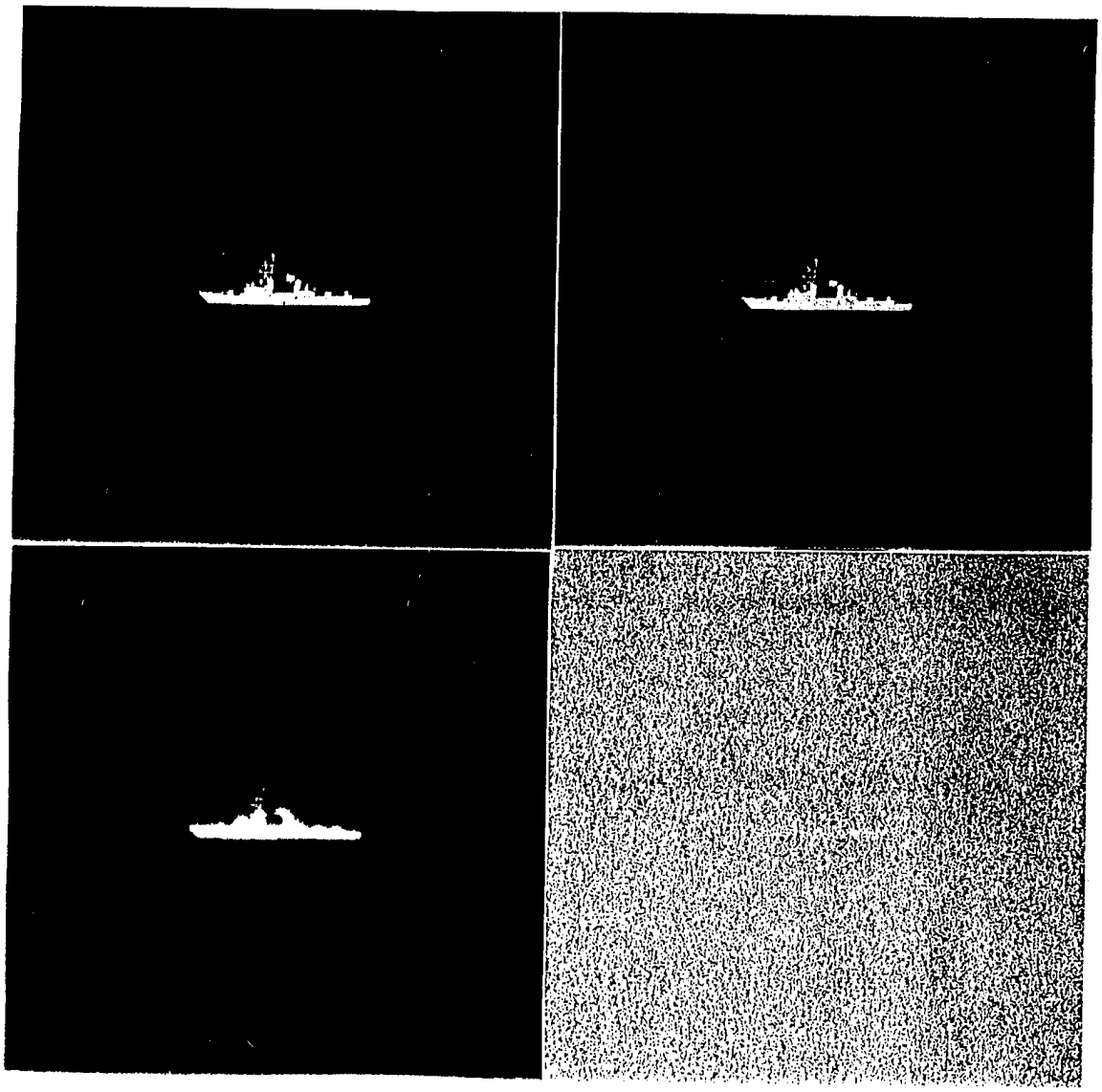


Figure 1. Images of a DDG ship as degraded by UL:8 km and D* noise,

UR:8 km and noise added, LL:8 km, noise added, and defocussed, LR:10 km, noise, and detector effects.

Another use of ILLOWRA is to use real or actual background images and insert modeled targets. Figure 2 is a TICM raster file background with a truck target inserted into it. This is a thermal image obtained in the Adelaide Hills area by the DSTO personnel.



Figure 2. TICM raster file of Adelaide Hills background with Rover truck (modeled) inserted.

A series of discussions were held with the authors concerning the types of measurements that are necessary to characterize the atmosphere for a variety of instances. Specific areas that were discussed were lidar measurements, aerosol measurements, and target acquisition in a tropical environment with obscured view.

4. SUMMARY

Dr. Tony Bedford, LSOD Division Chief, visited ARL headquarters in the early summer of 1994, before the Gillespies went to Australia. He learned some of the details about the Short Term Exchange Program from Dr. Lyons, ARL Director. Dr. Bedford has a keen interest in furthering this program based on what he has learned from Dr. Lyons and the fruitful visit by the Gillespies during 1994. Dr. Bedford has asked for volunteers from his LSOD group to go to the United States next year. A scientist has been identified that is interested in pursuing this exchange and a tentative project has also been identified. Dr. Michael Wegener of DSTO is interested in coming to ARL-BE and working on Dr. Patti Gillespie's Electro-Optics Teams on the stereo-vision project being conducted by Mr. Wendell Watkins. It is hoped that this exchange can be affected by fall of 1995.

Improvements to Modeling of Polarimetric Scattering

Michael DeAntonio
National Research Council
ARL-BED, WSMR, NM 88002

ABSTRACT

Improvements are being proposed for modeling of polarimetric scattering for obscurant clouds. These improvements will be implemented in a new code called POEMS which is expected to be completed in May 1995. Scattering from obscurant clouds is computed by taking the results from single particle scattering and building the cloud using the order of scattering method. In doing this we will include several improvements over the previous Monte Carlo methods. (1) We will propagate the scattering amplitude matrix instead of the phase function which will allow for calculation of phase and polarization properties of the entire cloud; and (2) since we are using a more exact formulation of the scattering from single particles, we expect the scattering results from the entire cloud to be more exact, as well.

These improvements will enable us to accurately describe cases which are beyond the bounds of the current models. Namely, we can treat cases where coherence becomes important, such as clouds with low particle density and clouds where the particles tend to align in their orientation. Also, since the model will reach a wider range than any currently used, it will serve well as a benchmark for all past and future approximations.

1. INTRODUCTION

The model POEMS (Polarimetric Obscurant Ensemble Mueller Scattering) calculates the scattering of light from ensembles of identical particles of arbitrary shape. Since the model propagates the phase of the light, it can obtain the correct Mueller matrix for a cloud even when the scattering is coherent. This cannot be accomplished with the Monte Carlo models currently available. Coherent scattering usually occurs when the ensemble density is small or when the particles are physically aligned. Both cases are handled well by this model.

2. OTHER METHODS

There are several methods for determining multiple scattering from the properties of single particles. The radiative transfer method is commonly used(Tsay et al. 1987), and we will compare it to the scattering amplitude matrix propagation (SAMP) method used in POEMS. The main difference between the two models is that while radiative transfer uses the scattering phase function of a particle, SAMP uses the scattering amplitude matrix. Because the scattering amplitude matrix is complex, we can keep track of the phase of the wave as it propagates. The phase function (contrary to what the name implies) has no phase associated with it(Bohren, Huffman 1983).

3. SCATTERING FROM INDIVIDUAL PARTICLES

Let us consider light scattering from nonspherical particles (e.g. cylinders). There are many ways to solve for the scattering amplitude matrix of these particles. Some of these are the discrete dipole approximation (DDA)(Draine, Flatau 1994), the digitized Green function (DGF) approximation(Goedecke, O'Brien 1988), and the Wentzel-Kramers-Brillouin (WKB) approximation(Klett, Sutherland 1992). At this time POEMS only accepts the results of DDA, but plans are being made to implement both DGF and WKB.

3.1 Discrete Dipole Approximation

The discrete dipole approximation model which is a subroutine of POEMS was created by Draine and Flatau(Draine, Flatau 1994). It treats the target as a set of electromagnetic dipoles with the polarizability

$$\alpha \approx \frac{\alpha^{\mathrm{CM}}}{1+\frac{\alpha^{\mathrm{CM}}}{d^3}\left[\left(b_1+m^2b_2+m^2b_3S\right)(kd)^2-i\frac{2}{3}(kd)^3\right]} \tag{1}$$

where

$$\alpha_j^{\mathrm{CM}} = \frac{3d^3}{4\pi}\frac{\epsilon_j-1}{\epsilon_j+2}, \tag{2}$$

$$S \equiv \sum_{j=1}^{3}\left(\hat{\alpha}_j\hat{e}_j\right)^2 \tag{3}$$

and

m = refractive index
d = side length of cubical region of constant electric field
b_1 = -1.891531
b_2 = 0.1648469
b_3 = -1.7700004
ϵ_j = dielectric function of the target material at location r_j
$\widehat{\alpha}_j$ = unit vector defining the incident direction
$\widehat{e}_j$ = unit vector describing polarization state.

The radiation from this collection of dipoles is then used to calculate the scattering amplitude matrix

$$S(\theta,\phi) = \begin{pmatrix} S_2(\theta,\phi) & S_4(\theta,\phi) \\ S_3(\theta,\phi) & S_1(\theta,\phi) \end{pmatrix} \tag{4}$$

for a single particle. Here we define the scattering amplitude matrix by

$$\begin{pmatrix} E_{\parallel \text{scat}} \\ E_{\perp \text{scat}} \end{pmatrix} = \frac{e^{ikr}}{-ikr} \begin{pmatrix} S_2 & S_4 \\ S_3 & S_1 \end{pmatrix} \begin{pmatrix} E_{\parallel \text{in}} \\ E_{\perp \text{in}} \end{pmatrix} \tag{5}$$

where

k = wavenumber of the incident light
r = distance from the scatterer to the point of observation

and the electric fields are split into components which are parallel, $E_{\parallel}$, and perpendicular, $E_{\perp}$, to the scattering plane.

3.2 Target Coordinates

The target coordinate system is defined such that the incoming wave approaches the particle along the x-axis. The y-axis and z-axis are arbitrary. The target is then oriented as shown in figure 1, where

θ_{target} = angle between the z-axis and a_1
ϕ_{target} = angle of rotation about the z-axis
β_{target} = angle of rotation about a_1.

The axes a_1, a_2, and a_3 are orthogonal axes which are determined by the target shape. The orientation (target) angles are chosen randomly by the code with a weighting input by the user. The scattering (scatter) angles are also chosen randomly in a uniform fashion and are defined by the usual polar coordinates in the target frame.

4. Global Coordinates

POEMS uses a set of Cartesian coordinates called global coordinates, which are defined by the user and identify the positions of the source, detector and cloud. Before propagation between individual targets, POEMS rotates from target coordinates to global coordinates,where

$$x_{\text{global}} = \cos\theta x_{\text{target}} - \sin\theta y_{\text{target}} \tag{6}$$

$$y_{\text{global}} = \sin\theta\cos\phi x_{\text{target}} + \cos\theta\cos\phi y_{\text{target}} - \sin\phi z_{\text{target}} \tag{7}$$

$$z_{\text{global}} = \sin\theta\sin\phi x_{\text{target}} + \cos\theta\sin\phi y_{\text{target}} + \cos\phi z_{\text{target}} \tag{8}$$

After propagation, the coordinates are rotated into a new target coordinate system defined by the direction of propagation and polarization. To do these we use the inverse transform

$$x_{\text{target}} = \cos\theta x_{\text{global}} + \sin\theta\cos\phi y_{\text{global}} + \sin\theta\sin\phi z_{\text{global}} \tag{9}$$

$$y_{\text{target}} = -\sin\theta x_{\text{global}} + \cos\theta\cos\phi y_{\text{global}} + \cos\theta\sin\phi z_{\text{global}} \tag{10}$$

$$z_{\text{target}} = -\sin\phi y_{\text{global}} + \cos\phi z_{\text{global}} \tag{11}$$

5. MULTIPLE SCATTERING

Scattering from single targets can be combined to produce total scattering from the ensemble. There are several ways to do this; however, we will look at radiative transfer which is only one of the more common methods. We will also look at the SAMP method used by POEMS.

5.1 RADIATIVE TRANSFER

Typically radiative transfer looks at the scattering phase function and calculates the probability that a photon will go in a particular direction. To do this it uses a Monte Carlo calculation with the random field weighted by the value of the scattering intensity in that direction. A similar calculation is used to account for loss of intensity due to propagation, where here the random field is weighted using Beer's law. Normally, the photons are then propagated directly to the detector using a process known as backward recursion. The total number of photons reaching the detector are then counted.

5.2 SCATTERING AMPLITUDE MATRIX PROPAGATION

SAMP chooses a direction randomly with uniform probability. It then changes the properties of a beam of photons (intensity, phase and polarization) according to the scattering characteristics given by the scattering amplitude matrix. Multiple scattering is obtained by combining a series of single scattering events, propagating to the next scattering event using Monte Carlo calculations from Beer's law. Since the phase is propagated in this method, we can now treat coherent scattering.

6. INPUTS

The position of the source and detector; as well as the cone angles and orientation of each, are defined graphically by the user. The cloud is also graphically defined as a set of ellipsoids. Other inputs (which depend on the single target scattering code that is used) are entered via a user friendly code. For DDA, the inputs include target shape and size, wavelength and polarization of the incoming light, and the extinction coefficient of the cloud.

7. PROPAGATION

Beams of photons are released from the source. As each of these beams hits a particle, they scatter to a new target. Figure 2 shows us that a portion of the beam is sent toward the detector at each scattering event. Sometimes it hits the detector, other times it does not.

This portion of the beam may not hit the detector for two reasons: (1) the propagation distance, given by Beer's law, may not be enough to take it out of the cloud before it hits another scatterer, (2) it may be outside the field of view of the detector. See figure 3.

A photon beam continues to scatter until (1) the scattering intensity falls below a given tolerance, (2) the beam hits a designated number of scatterers or (3) the beam propagates outside the cloud. See figure 4. After a beam is terminated, the process repeats with a new beam being released from the source.

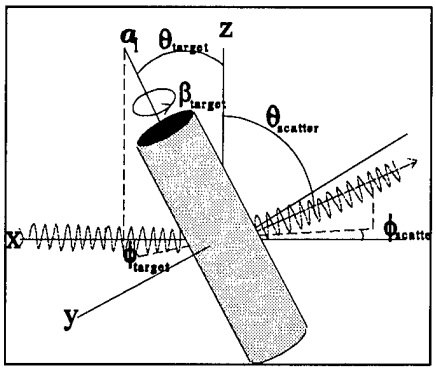


Figure 1: The orientation (target) and scattering (scatter) angles as defined by the discrete dipole approximation.

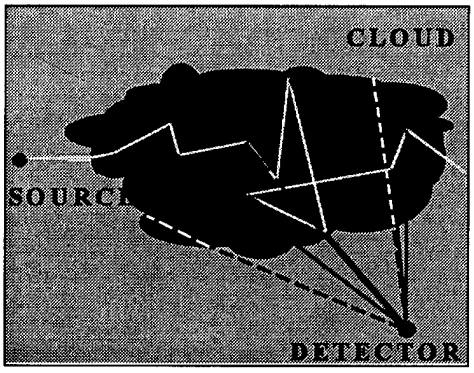


Figure 2: Beams of photons are released from the source. As each of these beams hits a particle, they scatter to a new target. A portion of the beam is sent toward the detector at each scattering event. Sometimes it hits the detector, other times it does not.

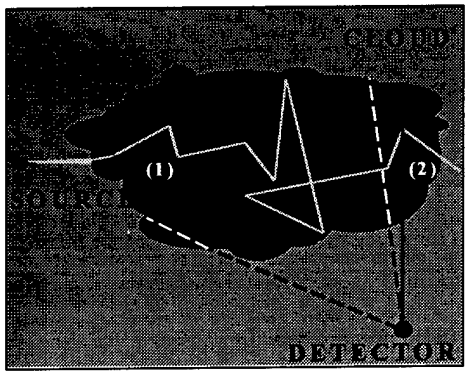


Figure 3: The portion of a beam which is sent toward a detector may not reach the detector for two reasons: (1) the propagation distance, given by Beer's law, may not be enough to take it out of the cloud before it hits another scatterer, (2) it may be outside the field of view of the detector.

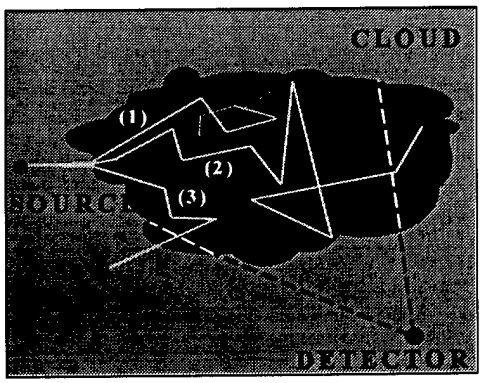


Figure 4: Photon beams continue to scatter until (1) the scattering intensity falls below a given tolerance, (2) the beam hits a designated number of scatterers or (3) the beam propagates outside the cloud.

8. RESULTS

8.1 Incoherent scattering with cylinders

In figure 5 we show the Mueller matrix elements generated using the closed-form solutions of Shi and McClain(Shi, McClain 1993) for a random ensemble of long thin cylinders, and the results generated by POEMS for the same ensemble. The M_{ab} are the elements of the Mueller matrix for the ensemble. In this case we have turned off the effects of propagation in POEMS. This roughly approximates the orientation averaging in Shi and Mclain. These graphs are for cylinders of length $L = 951.6\,\text{nm}$, radius $a = 31.72\,\text{nm}$, and for light of wavelength $\lambda = 475.8\,\text{nm}$. The number of scatterers in the cloud is $n = 30 \times 10^6$. The results are close enough to validate the POEMS code.

Figure 6 shows the same solutions as in the previous figure, except the propagation effects are added in POEMS.We see that the curve for $\frac{M_{11}}{M_{11}(0)}$ is quite different. This is due to the extremely high density of the cloud. The cloud was modeled as a sphere of radius $r = 300\,\text{m}$ and contained 30×10^6 scatterers. The high density keeps the photon beams from propagating to the end of the cloud in the forward direction.

8.2 Coherent scattering with cylinders

In figure 7 we show the Mueller matrix scattering elements generated by POEMS from an ensemble identical to that used in figure 6, with the exception that $n = 30$ which gives us a lower density.We see from $\frac{M_{11}}{M_{11}(0)}$ that the forward direction is now dominant which is significantly different than for the high density cloud of figure 6. We also see small changes in $\frac{M_{12}}{M_{11}}$ and $\frac{M_{33}}{M_{11}}$ as well as significant changes in $\frac{M_{34}}{M_{11}}$. We believe these changes are due to the coherence of the scattering. Figure 8 shows the results with $n = 30 \times 10^6$, but where all of the cylinders are aligned along the z-axis in the global coordinate system.Again these curve show changes which we believe are due to coherence.

9. SUMMARY

We were able to develop a propagation scheme for polarimetric, coherent scattering of ensembles of arbitrarily shaped particles inside a cloud. This scheme allows us to calculate the true Mueller

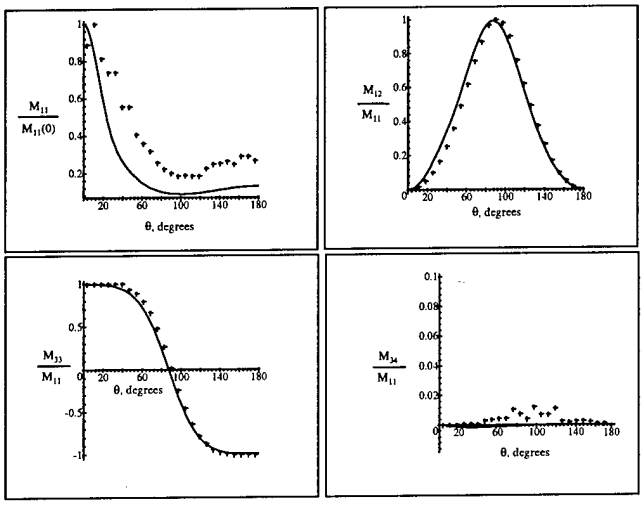


Figure 5: A comparison of POEMS without propagation and the orientationally averaged analytical solution of Shi and McClain. The analytical curves are shown as solid lines. The points represent the calculations of POEMS.

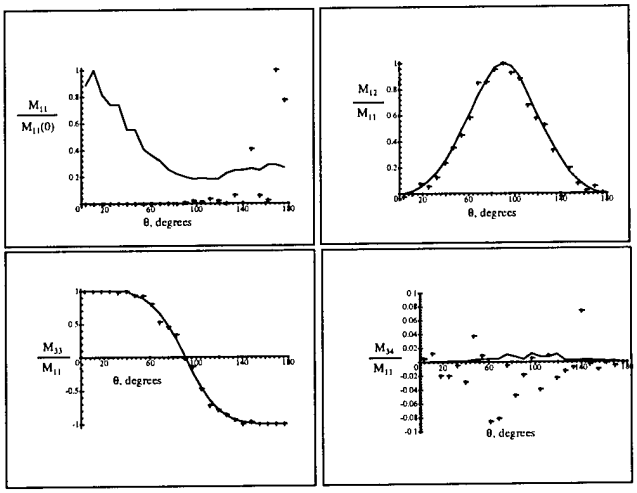


Figure 6: A comparison of POEMS with and without propagation. The curves without propagation are shown as solid lines. The points represent the calculations of POEMS with propagation.

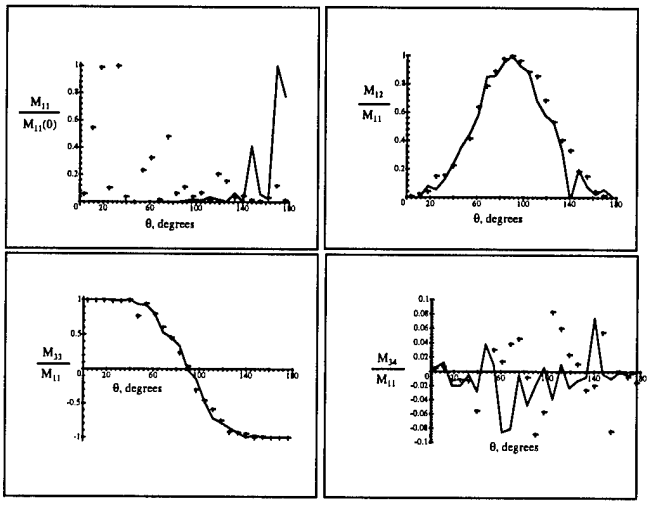


Figure 7: A comparison of POEMS for high and low density clouds. The curves for high density are shown as solid lines. The points represent the calculations of POEMS with a low particle density.

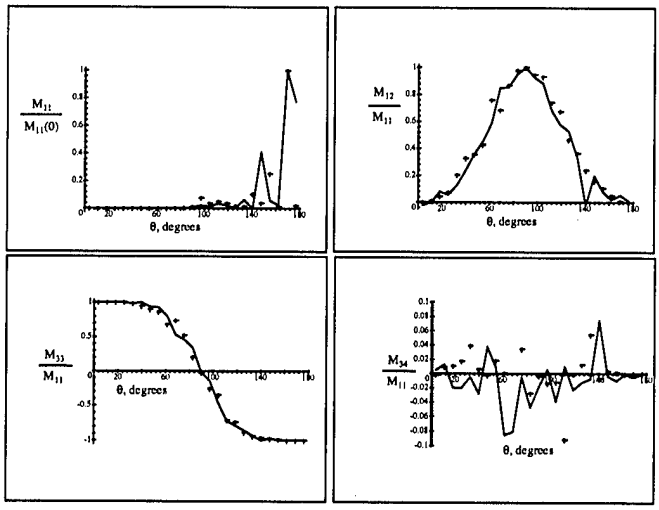


Figure 8: A comparison of POEMS with random and fixed particle orientation. The curves for random orientation are shown as solid lines. The points represent the calculations of POEMS with the orientation of the particles fixed along the global z-axis.

matrix elements of the cloud even when it is low density or all of the particles are aligned. In the future we will examine the sensitivity of the code to both density and alignment. We will also examine changes in the scattering with time in order to model temporal fluctuations in the scattering.

REFERENCES

Bohren, C. F. and D. R. Huffman, 1983. *Absorption and Scattering of Light by Small Particles.* John Wiley and Sons, NY.

Draine, B. J. and P. J. Flatau, 1994. "The Discrete Dipole Approximation for Scattering Calculations." *J. Opt. Soc. Am.,* . in press at this time.

Goedecke, G. H. and S. G. O'Brien, 1988. "Scattering by Irregular Inhomogeneous particles Via the Digitized Geen's Function Algorithm." *Appl. Opt., 27*:2431.

Klett, J. D. and R. A. Sutherland, 1992. "Approximate Methods for Modeling the Scattering Properties of Nonspherical Particles: Evaluation of the Wentzel-Kramers-Brillouin Method." *Appl. Opt., 31*:373.

Shi, Y. and W. M. McClain, 1993. "Closed-Form Mueller Scattering Matrix for a Random Ensemble of Long, Thin Cylinders." *J. Chem. Phys., 98*:1695.

Tsay, S. C., J. M. Davis, G. L. Stephens, S. K. Cox, and T. B. McKee, 1987. *Backward Monte Carlo Computations of Radiation Propagating in Horizontally Inhomogeneous Media. Part I: Description of Codes.* Technical report, National Oceanic and Atmospheric Administration.

ATMOSPHERIC CHARACTERIZATION

IN SUPPORT OF

BAT-VEHICLE FIELD TESTING

John Fox
U.S. Army Research Laboratory
White Sands Missile Range, New Mexico 88002

Prasan Chintawongvanich
Physical Science Laboratory
New Mexico State University
Las Cruces, New Mexico 88003

ABSTRACT

The brilliant anti-armor submunition (BAT) is an acoustic/infrared-guided munition which is currently under test at WSMR. The Army TACMS-BAT project office is providing specialized meteorological measurements in support of field testing. Acoustic waves propagating through the turbulent atmosphere undergo amplitude and phase distortions, which result in pointing errors of the BAT vehicle. A knowledge of these amplitude and phase fluctuations is essential to determine their effects on the BAT acoustic sensor performance and airframe stability. A technique has been developed using both in situ and remote meteorological measurements to obtain the turbulence parameters that are critical to the analysis of BAT-vehicle performance.

1. INTRODUCTION

In the study of propagation of sound waves through turbulent atmosphere, information about small-scale fluctuations in the atmospheric temperature and wind velocity is essential for comparing experimental works with theoretical predictions. The irregularities in the temperature and wind fields are directly related to the scatter of sound waves in the atmosphere. Assuming a Kolmogorov spectrum of turbulence, the scattering cross section $\sigma(\theta)$ of an acoustic beam may be expressed in terms of turbulent parameters, acoustic wave number κ, and scattering angle θ.

$$\sigma(\theta) = 0.03\kappa^{1/3}\cos^2\theta\left[0.13\frac{C_T^2}{T^2} + \frac{C_v^2}{c^2}\cos^2\frac{\theta}{2}\right]\left(\sin\frac{\theta}{2}\right)^{-11/3} \quad (1)$$

where the temperature and velocity structure parameters, C_T^2 and C_v^2, are the measures of small-scale temperature and velocity fluctuations, and c is the speed of sound at a mean temperature T (Little 1969)

In addition to scattering, acoustic waves propagating in a turbulence field suffer amplitude and phase distortions. Tatarski (1971) studied the effects of a plane sound wave propagating in a locally isotropic turbulent flow and concluded that the amplitude and phase fluctuations of acoustic waves are described by the same theory as the corresponding fluctuations of electromagnetic waves. Furthermore, the expressions of amplitude and phase fluctuations developed for electromagnetic waves are applicable to acoustic waves as well, if the acoustic refractive index structure parameter C_n^2 is taken to be

$$C_n^2 = \frac{1}{4}\frac{C_T^2}{T^2} + \frac{C_v^2}{c^2} \quad (2)$$

2. TURBULENCE STRUCTURE PARAMETERS

Knowledge of the strength of the turbulence field is very important in atmospheric acoustics. The strength of turbulence is usually measured in terms of the turbulence structure parameters C_T^2 and C_v^2. Near the ground, these parameters are often obtained directly from in situ measurements of fluctuating temperature and wind using fast response sensor such as a sonic anemometer. At heights above the ground, the structure parameters can be obtained remotely from back scattered measurements of a sodar.

At separation $\vec{r}$ of the order of inertial subrange scales, the structure parameter C_θ^2 in a locally isotropic field is defined according to Tatarski (1971) by

$$C_\theta^2 = \frac{<\left[\theta(\vec{r}_1) - \theta(\vec{r}_2)\right]^2>}{\vec{r}^{\,2/3}} \quad (3)$$

where $\theta(r_i)$ represents temperature or longitudinal wind at two points with a spatial separation $\vec{r} = |\vec{r}_1 - \vec{r}_2|$, and the angle brackets indicate ensemble average.

Under the conditions where the turbulent field is considered frozen, turbulence measurements in spatial coordinates can be transformed into corresponding measurements in time domain using Taylor's hypothesis (Stull 1988). Therefore, Eq. (3) may be rewritten as

$$C_\theta^2 = \frac{\overline{\left[\theta(t_1) - \theta(t_2)\right]^2}}{(U\Delta t)^{2/3}} \quad (4)$$

where $\theta(t_i)$ is the fluctuating temperature or longitudinal wind sampled at two instances with a temporal separation $\Delta t = t_1 - t_2$, the overbar indicates a time average, and U is a mean wind speed during the measurements. Equation (4) provides a mean to compute C_T^2 and C_v^2 directly using temperature and wind data from sonic anemometer.

For remote sensing of the turbulence, C_T^2 and C_v^2 are determined from echo intensity measurements of a sodar. Chintawongvanich and Olsen (1991) had successfully demonstrated the use of a commercially available sodar for C_T^2 measurements. They scaled values of echo intensity to inferred values of C_T^2 at the sodar minimum height range (~ 50 m). The inferred values of C_T^2 were derived using similarity theory and reference C_T^2 measurements from an in situ sensor near the ground. Gaynor (1977) applied the so-called Doppler method to obtain C_v^2 measurements utilizing Doppler wind data from a sodar. The method computes C_v^2 according to Eq. (3) using vertical wind velocities from two ranges separated by a distance that is of an order of inertial subrange scales. His measurements compared well with the corresponding C_v^2 from an in situ sensor mounted on a tower. In practice, vertical wind data from two height ranges separated by 20 to 30 m are used, and the midpoint between the two height ranges is taken to be C_v^2 height.

3. HEIGHT RELATION OF C_T^2 AND C_v^2 IN THE SURFACE LAYER

A number of studies had been made in the context of the similarity theory to determine the height relation of C_T^2 and C_v^2 in the surface layer. The similarity theory predicts that statistics of the mean turbulent flow field, when properly nondimensionized, are universal functions of only a stability parameter. On the basis of this notion, a relation for the dimensionless C_T^2 and C_v^2 as functions of the stability parameter z/L may be written

$$C_T^2 z^{2/3} / T_*^2 = F_T(z/L) \tag{5}$$

$$C_v^2 z^{2/3} / u_*^2 = F_v(z/L) \tag{6}$$

where the temperature scale T_* is equal to $-Q/u_*$, Q is the surface potential temperature flux ($Q = \overline{wT'}$), u_* symbolized friction velocity and $-u_*^2$ is equal to the streamwise surface shearing stress $\overline{uw}$, z is height above the ground, and L is the Monin-Obukhov length defined by

$$L = -u_*^3 T / kg\, Q \tag{7}$$

Here the von Karman's constant k is equal to 0.35 (Gaynor 1977), and g and T are the gravitational acceleration and mean temperature, respectively.

Results from the recent experimental study of temperature structure parameter in the surface layer (Chintawongvanich, Olsen 1991) shows the dimensionless C_T^2 in the form of Eq. (5) as a function of the dimensionless height z/L.

$$F_T(z/L) = 7.7[1 - 17\,(z/L)]^{-2/3}, \qquad z/L \le 0$$
$$F_T(z/L) = 7.7\left[\frac{1 + 36\,(z/L)}{1 + 20(z/L)}\right], \qquad z/L \ge 0 \tag{8}$$

Kaimal (1988) reexamined and refined results from the Kansas experiment through comparison with other observations. He expressed the dimensionless C_v^2 in the form of Eq. (6) as a function of the dimensionless height z/L.

$$F_v(z/L) = 4\left[1 + 0.5\,|z/L|^{2/3}\right], \qquad z/L \le 0$$
$$F_v(z/L) = 4[1 + 5(z/L)]^{2/3}, \qquad z/L \ge 0 \tag{9}$$

Combining Eqs. (5) and (8), and imposing the limiting cases for: unstable ($-17(z/L) >> 1$), neutral ($z/L = 0$), and stable ($20(z/L) >> 1$), one obtains

$$C_T^2 \approx 7/6\,(T/gk)^{2/3}\,Q^{4/3}\,z^{-4/3}, \text{ unstable} \tag{10}$$

$$C_T^2 = 7.7\,(Q/u_*)^2\,z^{-2/3}, \text{ neutral} \tag{11}$$

$$C_T^2 \approx 13.9\,(Q/u_*)^2\,z^{-2/3}, \text{ stable} \tag{12}$$

Equations (10)-(12) above show the relation of height dependence of C_T^2 under various atmospheric conditions: in an unstable atmosphere, C_T^2 is proportional to $z^{-4/3}$, and in a stable-neutral atmosphere, C_T^2 is proportional to $z^{-2/3}$.

Similarly, combining Eqs. (6) and (9), and imposing the limiting cases, one obtains

$$C_v^2 \approx 4u_*^2\,z^{-2/3}, \text{ unstable and } z << |L|$$
$$C_v^2 \approx 2u_*^2\,L^{-2/3}, \text{ unstable and } z >> |L| \tag{13}$$

$$C_v^2 \approx 4\left[z^{-1} + 5/L\right]^{2/3}, \text{ stable-neutral} \tag{14}$$

Equation (13) suggests that, under a convectively unstable condition, the height relation of C_v^2 ranges from a - 2/3 power law near the surface ($z << |L|$) to a height independence at far above the surface ($z >> |L|$). For a stable-neutral atmosphere ($L >> 5$) where the turbulence is mechanical in origin, C_v^2 is approximately proportional to $z^{-2/3}$ as depicted in Eq. (14).

One other important quantity relating the transfer of energy from the energy containing range, through the inertial subrange to the dissipation range, is the dissipation rate ε of turbulent kinetic energy. C_v^2 is related to ε (Kaimal 1988) by

$$C_v^2 = 2\varepsilon^{2/3} \tag{15}$$

In an effort to correlate the energy dissipation rate ε to height, Munson (1993) compiled data from numerous literature searches resulting in 121 data points of ε at various heights ranging from about 4 m to 10 km. Plot of $\varepsilon^{2/3}$ as a function of height for $z < 2$ km is reproduced in figure 1. A regression analysis of the data for $z < 2$ km show that ε is related to height by

$$\varepsilon^{2/3} = 0.184\, z^{-0.64} \approx 0.184\, z^{-2/3} \tag{16}$$

Using the relation of Eq. (15), it can be seen that C_v^2 is proportional to $z^{-2/3}$.

4. MEASUREMENTS OF ATMOSPHERIC TURBULENCE FOR BAT-VEHICLE

It had been determined (Chapkis 1991) that atmospheric turbulence is the primary cause of BAT-vehicle self noise. Therefore, the knowledge of the strengths of turbulence during in-flight test is essential to analyze and interpreted the flight-test measurements. Neiswander and Chapkis (1993) characterize the levels of turbulence in terms of the energy dissipation rate ε, rather than the velocity structure parameter C_v^2. Values of ε are determined utilizing Komogorov inertial subrange spectrum of fluctuating angle-of-attack as follows:

$$\phi_\alpha(f) = \frac{4}{3}\,\frac{0.5}{U^2}\left(\frac{U}{2\pi}\right)^{2/3} \varepsilon^{2/3} f^{-5/3} \tag{17}$$

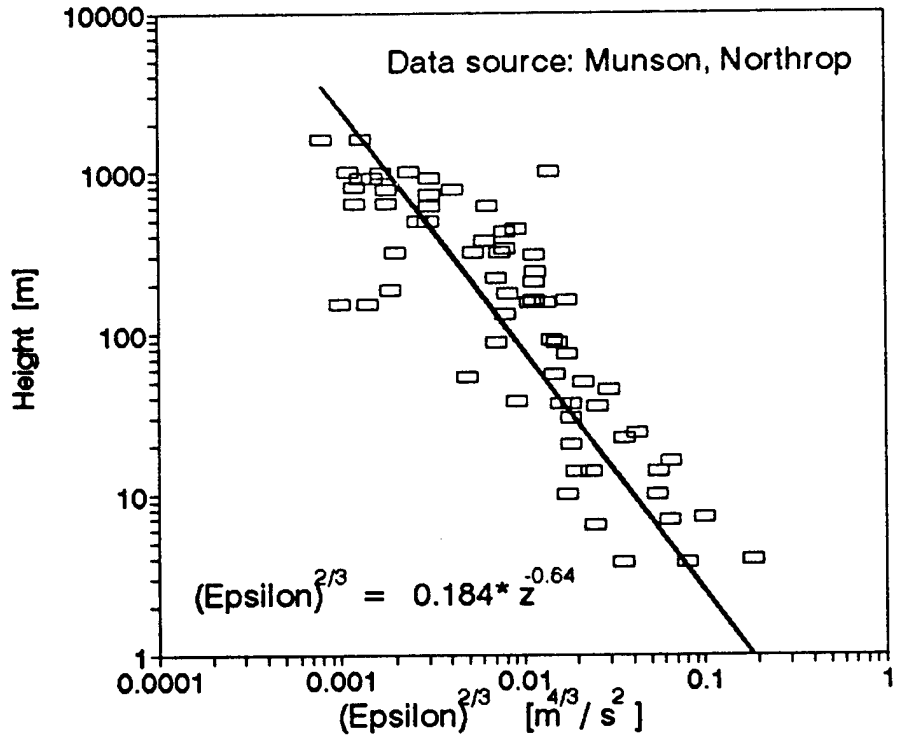


Figure 1. Energy dissipation rate as a function of height.

where $\phi_\alpha(f)$ is the inertial subrange spectrum of the fluctuating angle-of-attack α, and f is the cyclic frequency. Thus, $\varepsilon^{2/3}$ can be obtained from the above equation by measuring the variance of α, R_α^2, over a frequency range f_1 to f_2 within the inertial subrange:

$$R_\alpha^2 = \int_{f_1}^{f_2} \phi_\alpha(f)\, d_f \tag{18}$$

Solving Eq. (18) for $\varepsilon^{2/3}$ gives

$$\varepsilon^{2/3} = U^2\left(\frac{2\pi}{U}\right)^{2/3}\left(f_1^{2/3} - f_2^{2/3}\right)^{-1} R_\alpha^2 . \tag{19}$$

The attraction of Eq. (19) is its simplicity. However, it also has some shortcomings. First, it relies heavily upon filtering to avoid contamination from frequency ranges outside the inertial subrange. Second, the validity of ε depends only upon the -5/3 law; i.e., for a valid spectrum, a log-log plot of $\phi_\alpha(f)$ versus f must yield a -5/3 slope in the inertial subrange region. This implies that, for quality assurance, reconstruction of the spectra is required.

Alternatively, ε can be determined from two procedures which are developed in the following paragraphs. One direct approach is to use the time-domain method (as it will be termed) to determine ε from time-domain measurements of the angle-of-attack. The angle-of-attack perturbation $\alpha(t)$ resulting from a transverse velocity fluctuation $w(t)$ is

$$\alpha(t) \approx \tan[\alpha(t)] = \frac{w(t)}{U} \tag{20}$$

Using the definition of Eq. (4), the angle-of-attack structure parameter C_α^2 in a locally isotropic field is

$$C_\alpha^2 = \frac{\overline{[\alpha(t_1) - \alpha(t_2)]^2}}{(U\Delta t)^{2/3}} \tag{21}$$

Substituting Eq. (20) into Eq. (21)

$$C_\alpha^2 = \frac{\overline{[w(t_1) - w(t_2)]^2}}{U^2\,(U\Delta t)^{2/3}} \tag{22}$$

Equation (22) relates C_α^2 to C_w^2 by

$$C_\alpha^2 = C_w^2/U^2 \tag{23}$$

The transverse vertical velocity structure parameter C_w^2 is related to the longitudinal velocity structure parameter C_v^2 by (Kaimal, et al. 1972)

$$C_w^2 = 4/3\, C_v^2 \tag{24}$$

Finally, the energy dissipation rate is obtained by substituting Eqs. (23) and (24) into Eq. (15)

$$\varepsilon^{2/3} = \frac{3}{8} U^2 C_\alpha^2 . \tag{25}$$

The second method is to follow Chintawongvanich and Olsen (1993). They obtained the longitudinal velocity structure parameter C_v^2 from the one-dimensional spectrum of fluctuating streamwise velocity v which has the inertial subrange form

$$\phi_v(\kappa) = aC_v^2 \kappa^{-5/3} \tag{26}$$

where the constant $a = 0.25$ (Wyngaard, Izumi, Collins 1971) κ is the streamwise component of wave number, and the spectral density $\phi_v(\kappa)$ has the property

$$\int_0^\infty \phi_v(\kappa) d\kappa = \langle (v - \bar{v})^2 \rangle \tag{27}$$

By invoking the assumption of the frozen field and applying Taylor's hypothesis, spatial fluctuations of wave number can be measured as temporal fluctuations of cyclic frequency $f = \kappa U/2\pi$. After performing the proper transformation and rearranging Eq. (26), the following relation is obtained:

$$C_v^2 = \left(\frac{4\pi}{aU} \right)^{2/3} (f\phi_v(f)) f^{2/3} \tag{28}$$

Equation (28) provides a means to compute the structure parameter C_v^2 from the v-spectrum and the mean wind speed measurements. The value $f(\phi_v(f))$ is determined from the two-third slope region of a plot of $f(\phi_v(f))$ versus f. The dissipation rate ε can then be determined by following Eqs. (23)-(25).

The time-domain method offers the attraction of simplicity and ease of computation. No exotic pretreatment of the data is required other than spike-noise removal. This can be easily accomplished by a simple routine that discriminates against the fluctuating quantities on a predetermined criteria. The frequency-domain method is more rigorous, since it requires a reconstruction of the spectra. However, it holds an advantage of providing spectral characteristics of the turbulence. This feature greatly facilitates an onset identification of the data that contain spike noise. Thus, corrections may be made to adjust the derived parameters accordingly.

5. SUMMARY

The rates of energy dissipation ε can be obtained from C_v^2 measurements using the relation of Eq. (15). Near the surface, values of C_v^2 are computed directly from fluctuating wind data measured from sonic anemometer mounted on a tower. For remote measurements of C_v^2, the Doppler method described in Section 2 is used for C_v^2 measurements. In the current practice, the sodar deployed can provide reliable fluctuating wind data up to a height of 200 m. Thus, C_v^2 and, hence, ε measurements are limited to that height. However, as discussed in detail in

Section 3, the relation of height dependence of C_v^2 can be used to infer measurements of C_v^2 and ε to some greater heights.

REFERENCES

Chapkis, R. L., 1991: *Measuring Atmospheric Turbulence from Airplane*, Northrop Memorandum, K410-91-018/RLC :msr.

Chintawongvanich, P. and R. Olsen, 1991: "Experimental Study of Temperature Structure Parameter in the Surface Layer," preprint volume of the 7th Symposium on Meteorological Observations & Instrumentation (Laser Atmospheric Studies), 413-418.

Chintawongvanich, P. and R. Olsen, 1993: "Measurements of Temperature and Velocity Structure Parameters from Sonic Anemometers," *SPIE Proc.*, Vol. 1968, Atmospheric Propagation and Remote Sensing II.

Gaynor, J. E., 1977: "Acoustic Doppler Measurements of Atmospheric Boundary Layer Velocity Structure Functions and Energy Dissipation Rates," *J. Applied Meteorology.*, 16, 148-155.

Kaimal, J. C., 1988: "The Atmospheric Boundary Layer - Its Structure and Measurement," *Lecture Notes*, NOAA, Wave Propagation Laboratory, Boulder, Co.

Kaimal, J. C., J. C. Wyngaard, Y. Izumi, and O. R. Cote, 1972: "Spectral Characteristics of Surface-Layer Turbulence," *Quart. J. R. Met. Soc.*, 98, 563-589.

Little, C. G., 1969: "Acoustic Methods for the Remote Probing of the Lower Atmosphere," *Proc. IEEE*, 57, 571-578.

Munson, A. G., 1993: *Properties of Atmospheric Turbulence*, Northrop Memorandum, LM31-93-013/AGM:msr.

Neiswander, P. R. and R. L. Chapkis, 1993: *Measuring Atmospheric Turbulence*, Northrop Memorandum, K410-92-094.

Stull, R. B., 1988: *An Introduction to Boundary Layer Meteorology* , Kluwer, Boston, MA, 666 pp.

Tatarski, V. I., 1971: *The Effects of Turbulent Atmosphere on Wave Propagation*, U.S. Dept. Commerce, Nat. Tech. Inform. Serv., Springfield, VA, 472 pp.

Wyngaard, J. C., J. Izumi, and S. A. Collins, Jr., 1971: "Behavior of Refractive-Index Structure Parameter near the Ground," *J. Opt. Soc. Am.*, 61, 1646-1650.

ARL REMOTE SENSING ROVER AS A GROUND TRUTH MONITOR AT THE XM-21 CHALLENGE SYSTEM FIELD TEST

Frank T. Kantrowitz, Dale U. Foreman
Battlefield Environment Directorate
U.S. Army Research Laboratory
White Sands Missile Range, New Mexico 88002-5501, USA

William M. Gutman
Physical Science Laboratory
New Mexico State University
Las Cruces, New Mexico 88003, USA

ABSTRACT

The U.S. Army Research Laboratory (ARL) Battlefield Environment Directorate (BED) Mobile Atmospheric Spectrometer (MAS) Testbed team acted as ground truth monitors at the XM-21 chemical agent challenge system field test during the spring of 1994. The small, 4-wheel drive, off-road Remote Sensing Rover (RSR) provided great mobility for remote sensing of chemical agent simulant releases at distances as great as 3.0 km.

The key component of the RSR is a portable Fourier spectrometer that is capable of operation from 600 to 6000 cm^{-1} at 0.5 cm^{-1} resolution. The portable spectrometer with 0.26-m optics may monitor in passive or active (double-ended) modes. All electronics are powered by 2 banks of 12 volt marine batteries.

During the test, the RSR rendezvoused with FOX Nuclear, Biological, Chemical (NBC) vehicles at ranges of 0.4, 1.2, 2.5 and 3.0 km. from a chemical agent simulant release point and passively monitored sulfur hexafluoride (SF_6). Results of the studies are presented.

1. BACKGROUND

During February, March and April of 1994, an XM-21 challenge system field test occurred at Ft. Bliss, TX. A number of systems supported this mission. 8 to 12 μm broadband imagers monitored the agent simulant (sulfur hexafluoride-SF_6) cloud transmittance and near-site transport and diffusion. Point sensors obtained cloud concentration information. The primary goal of the U.S. Army Research Laboratory

(ARL) Battlefield Environment Directorate (BED) Remote Sensing Rover (RSR) team was to act as ground truth monitor by obtaining spectroscopic measurements of the simulant when co-located with FOX reconnaissance vehicles. The RSR team monitored releases at distances of 0.4, 1.2, 2.5, and 3.0 km from the release point. A secondary goal of the RSR team was to acquire cloud transmittance and concentration-length data. These data will aid in the calibration of the broadband measurements made with the IR imagers.

It is the goal of the authors to marry high resolution spectroscopic techniques with broadband IR imaging methods. While the traditional IR imager can produce 2 dimensional scenes, they cannot differentiate gases. A conventual spectrometer with a focal plane array detector and support electronics in place of the standard single element detector will be able to both image and differentiate gases. This imaging spectrometer will be highly useful in chemical agent detection, obscurant and munition characterization, rocket plume characterization and dual-use environmental technologies such as characterization of emissions from industrial stacks.

2. THE MAS TESTBED TODAY

The key components of the **MAS** are a Fourier transform spectrometer (FTS) and a 0.8-m Coudé telescope. The **MAS** FTS consists of a scanning Michelson interferometer with associated optics, control electronics, and a dedicated computer system. Depending upon the detector, beamsplitter, and source in use, the spectrometer can cover a segment of the spectral region from about 700 to 20,000 cm^{-1} (0.5 to 14 μm). The instrument is capable of spectral resolution as high as 0.04 cm^{-1}. The **MAS** Coudé-mounted telescope is a classical Cassegrain telescope consisting of a 0.8-m parabolic primary and a 0.15-m-diameter hyperbolic secondary mirror. A spin-off of the MAS was the development of the Remote Sensing Rover (RSR).

The smaller, 4-wheel drive, off-road RSR provides greater mobility for fenceline and general spectroscopic monitoring. The RSR is presented in Fig. 1. The small meteorological tower attached to the RSR now contains instrumentation for the determination of temperature, pressure, relative humidity, dew point, visibility, wind speed and direction. These data may be input to the on-board, MODTRAN based, Real-Time Transmittance Modeler (RTTM). The key component of the RSR is a portable Fourier spectrometer that is capable of operation from 600 to 6000 cm^{-1} at 0.5 cm^{-1} resolution. All electronics are powered by 2 banks of 12 volt marine batteries. The portable spectrometer with 0.26-m optics may monitor in passive or active (double-ended) modes. While this portable system enhances the defense-related mission of the **MAS**, the spectral libraries permit identification of approximately 10,000 gases, and an algorithm under development (PCGAS-PLUS) permits the determination of the concentrations of over 150 gases.

For a wide range of problems, spectrally resolved measurements provide significant advantages over broadband measurements. For example, obscurant transmittance measurements are often used to predict the performance of EO systems under real-world conditions. The predictions can be misleading, however, unless the bandwidth of the measurement device precisely matches the bandwidth of the EO system. This is a particular problem when broadband measurements are used to model the performance of laser-based systems. A typical broadband transmissometer provides a single value for the transmittance in the 8 - 12 μm spectral region. The RSR spectrometer divides this region into approximately 800 separate channels, and the channel in which the laser frequency falls is an excellent approximation to the single frequency value.

In the case of the XM-21 challenge test, the radiance of the agent simulant may contribute less than one percent to the in-band radiance detected by a 8 to 12 μm imager even under high concentration-length conditions. The simulant spectral features cover approximately 14 (of 800) channels, and baseline-corrected radiance value integrated over these 14 channels has been observed to increase by a factor as high as 2.88. This translates into a significantly better detection threshold. Of course, the RSR spectrometer processes only a single pixel.



Figure 1. The Remote Sensing Rover.

3.TRADITIONAL METHOD FOR THE DETERMINATION OF CONCENTRATION LENGTH

Cloud concentration-length (CL) and transmittance measurements are related according to Beer's law:

$$T(t) = e^{(-\alpha CL)}$$

where:

T = transmittance

t = time

α = cloud extinction coefficient in meters^2/gram

CL = Concentration-Length in grams/meter^2

The concentration length is described as follows:

$$CL(t) = \int C(r,t)\,dr$$

where:

C(r,t) = Obscurant concentration at distance r at time t

dr = change in position

L = cloud diameter

The cloud concentration-length is described as follows:

$$CL = \frac{-\ln (T(t))}{\alpha}$$

4. RSR METHODOLOGY

The passive (single-ended) method of determining cloud transmittance will be utilized at this test. In this technique, the sky acts as the source in lieu of a high temperature infrared blackbody. Fig. 2 represents a time series of the cold infrared sky before and during the release of SF_6. Five atmospheric water vapor peaks are noted. As the SF_6 is released, its feature dominates the data. This emission feature is due to approximately 11,500 individual lines that are too fine to be resolved with this instrument. Instead they appear as a broad, single feature. The method for

determining cloud radiance or transmittance is shown in the following equation:

$$L(R) = L(0)\,T + (1-T)\,L(C)$$

where:

T = transmittance
L(0) = background radiance (sky or terrain)
L(C) = inherent cloud radiance
L(R) = propagated radiance from the cloud and background

The pre-release spectra will be scaled to a FASCODE path radiance simulation. Once a scaling constant is determined, it will be applied to the release spectra. The path radiance will be stripped from the spectra containing both the path and simulant information and the residual spectra will be compared to FASCODE simulations of SF_6 for various concentration lengths. Through interpolation, the correct concentration length will be determined. Determination of cloud transmittance and concentration-length will aid in the calibration of broadband measurements made with the IR imagers.

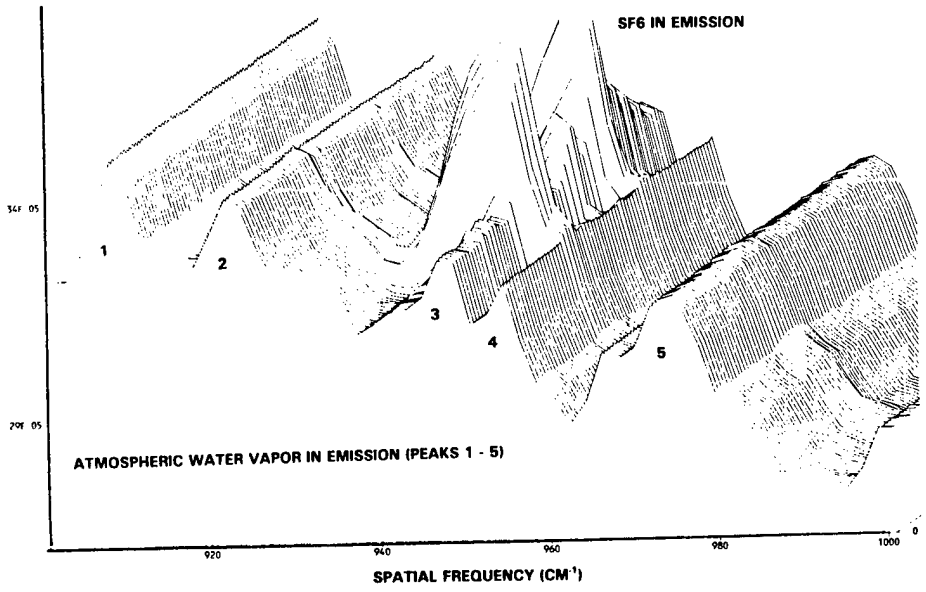


Figure 2. SF_6 in emission against a sky background.

5. STATUS

Although the RSR was totally successful in the remote detection and identification of agent simulants, determination of absolute cloud transmittance and concentration length has not been performed at this time. A computer movie of selected spectra will be shown at the Battlefield Atmospherics Conference (29 Nov. - 01 Dec. 1994) at White Sands Missile Range, NM.

LIDAR OBSERVATIONS DURING SMOKE WEEK XIV

M.P. Bleiweiss and R.A. Howerton
U.S. Army Research Laboratory
White Sands Missile Range, New Mexico 88002, U.S.A

ABSTRACT

The U.S. Army Research Laboratory, Battlefield Environment Directorate (ARL/BED) LIDAR -- ABACUS (Aerosol Backscatter And Concentration Understanding System) -- was fielded at Smoke Week XIV (SWXIV) for the purpose of testing its ability to act as a remote sensor of aerosol concentration in smoke/obscurant clouds. At that time, the LIDAR was (and still is) under development and experiencing considerable change. However, observations were made for the first two weeks of the test period and data were acquired for about 150 trials. The course of analysis has been to investigate relationships between the LIDAR measurements and other more accepted characterization tools: nephelometers and transmissometers. The results of that comparison are presented and the relationship to past Smoke Week LIDAR measurements discussed. Preliminary results show excellent agreement between LIDAR measured transmittance and REVIRT measured transmittance for a variety of obscurant types.

1. INTRODUCTION

In spite of the wide availability of LIDAR systems and the promise that they offer (e.g., Herman, Reagan and Schotland 1978) for complete characterization of smoke/obscurant clouds, their use has been limited. The promise has been to determine the three-dimensional extinction field (and thence the concentration field), from a remote sensing station. Further, it is promised that this will be accomplished with sufficient temporal resolution to "freeze" the cloud. Unfortunately, the ability to probe the cloud rapidly with high spatial resolution will have to wait until higher pulse rate laser transmitters and larger memory high speed digitizers are available. Meanwhile, it is required that more verification efforts be expended so as to ensure a stand alone capability, or at least, a capability which requires a minimal number of collateral measurements required for operation -- the focus of the present work. As part of the ARL/BED development of the Visioceilometer, an obscurant mapping LIDAR was also being investigated. That effort led to the system used in the effort described here -- Aerosol Backscatter And Concentration Understanding System (ABACUS). As an element of the ARL/BED effort to determine cloud growth dynamics, the addition of ABACUS to the MIDAS (Multispectral Image Data Acquisition System) and ATLAS (Atmospheric Transmission, Large-area Analysis System) capability should allow easier manipulation of the LIDAR equation. These latter two systems provide estimates of cloud "boundaries" and transmission through the cloud -- necessary information for solution of the LIDAR equation. What has not been satisfactorily demonstrated is that the inferred

LIDAR concentration field matches the "measured" concentration field in a smoke/obscurant cloud. An attempt to accomplish this is described in this paper.

Examples of past efforts to utilize LIDAR technology in smoke/obscurant field tests are described by Uthe and Livingston (1986), Evans and Roy (1989), Rubio, Measure and Knauss (1983), and Loveland et al. (1993). One of the more extensive efforts to verify the operation of a LIDAR system was the fielding of the Canadian Defence Research Establishment Valcartier (DREV) LIDAR system, the Laser Cloud Mapper (LCM) at SWIX. The analysis of the data acquired during that exercise is reported by Farmer, Soto, and Locke (1988) and by Evans and Roy (1989). Unfortunately, the test setup was not ideal and "one-to-one" comparisons could not be accomplished -- extensive data reduction and statistical arguments were necessary for "agreement" between the nephelometers and the LCM.

The initial results obtained with ABACUS are presented in the following discussion. First, the experimental setup at SWXIV and the ABACUS system parameters will be given and then the analysis procedures will be described. After this, the results are discussed followed by a summary and suggestions for further work.

2. EXPERIMENTAL SETUP

The ABACUS LIDAR was constructed from components remaining from the AOL which was developed as part of the Visioceilometer Project, with two exceptions: the laser transmitter and the detector/amplifier. The AOL was meant to operate at the eyesafe 1.54 μm wavelength; however, the failure of the laser equipment to function created a need for a new transmitter. The choice was an off-the-shelf 1.06 μm NdYAG system. With the addition of a new transmitter, the old detector was neither fast enough nor sensitive to the proper wavelength so a new detector/amplifier, also off-the-shelf was acquired. The resulting configuration has become the ABACUS. The specifications for this system are given in Table 1. Even though the transmitter is capable of pulsing at 20 Hz, the digitizing system, due to downloading time, was only able to capture about 1 pulse every 1-4 sec.

The setup on the test grid is shown in figures 1 and 2 where the relative locations of the ABACUS and REVIRT LOSs and the Nephelometer positions are plotted. ABACUS was operated during the first two weeks, only, of SWXIV; however, during that time, sufficient trials were observed under a variety of meteorological conditions and for a variety of dissemination techniques. The test setup desired was to place the ABACUS LOS as close to the nephelometer sampling line as was possible -- an access road on one side of the sampling line and the large number of other equipment on the other side only allowed ABACUS to be 30 m upwind from the sampling line. The vertical separation of the LOSs was minimal. The sampling resolution along the ABACUS LOS was approximately 0.3 m -- much closer than the nephelometer spacing -- and the sampling volume determined by the laser pulse length was a truncated cone about 9 m in length along the LOS with a diameter of less than one half meter. The nephelometer sampling volume is about 1 cm in diameter and the length, due to the transport by the wind is of the order of 5 m for a 1 s sampling time.

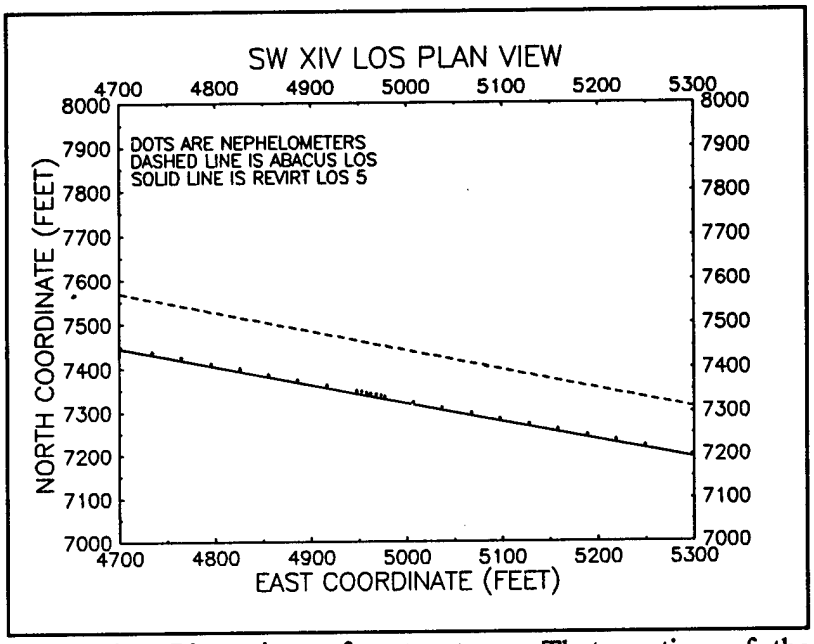


Figure 1. Plan view of test setup. That portion of the SWXIV test grid which contained the ABACUS LOS, the nephelometers, and the REVIRT LOS is shown in plan view.

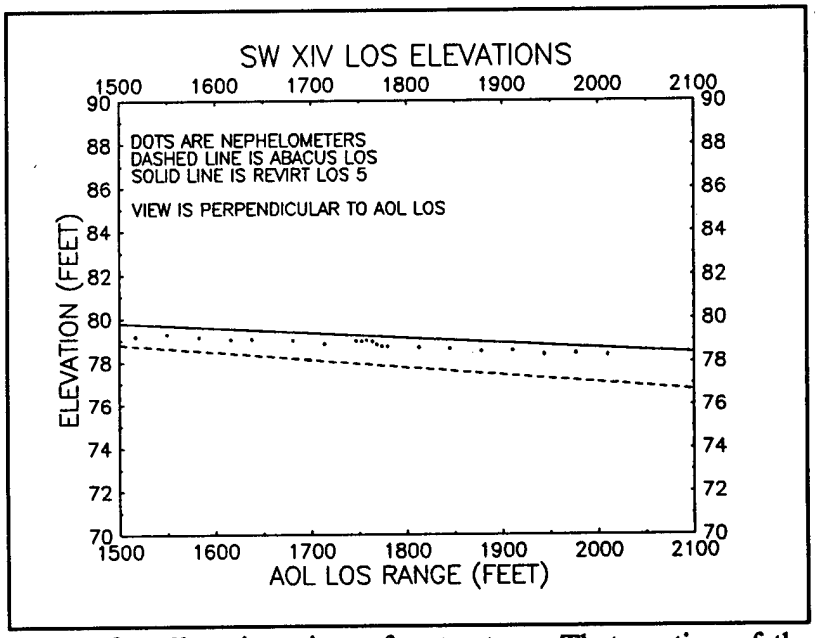


Figure 2. Elevation view of test setup. That portion of the SWXIV test grid which contained the ABACUS LOS, the nephelometers, and the REVIRT LOS (5) is shown in elevation.

Table 1. ABACUS system specifications.

SYSTEM	PARAMETER	SPECIFICATION
Transmitter	pulse energy	300 Mj
	pulse rate	20 pps, maximum
	pulse duration	6 ns (FWHM)
	divergence	0.6 mrad (FWHM)
	beam diameter	5 mm
Receiver	aperture	65 mm
	focal length	135 mm
	detector diameter	100 micrometer
	receiver divergence	0.74 mrad (FWHM)
	detector type	InGaAs
	detector bandwidth (temporal)	1 Ghz
	detector amplifier dynamic range	60 Db, linear
Digitizer	sampling rate	1 GHZ
	dynamic range	8 bits
	channels	2 (1-low gain, 1-high gain)

3. ANALYSIS

The analysis has proceeded according to several steps which begin with the determination of those trials appropriate for consideration. Of the approximately 150 trials for which data were obtained, only one representative trial for each of the several different obscurants was chosen for complete analysis at this time. Table 2 is a list of those trials by obscurant name along with some additional information which is required by the analysis. This additional information includes complex index of refraction, particle size, shape, and distribution -- this information is required for the determination of the scattering phase function and its derivative parameters. The phase function is obtained from the program IPHASE (Evans 1990). Once these parameters are determined, two other programs are run to determine the expected LIDAR signal given the concentration as determined by the nephelometers -- at this point in our endeavors, we have decided on this approach as opposed to other past efforts which attempt to compare concentration profiles which have been retrieved from the "solution" of the LIDAR equation. These programs are NBSCAT (an EOSAEL component) and a "home-grown" package which only considers single scattering (at this point). These steps are specified, in approximate order, below:

1. determine if the backscatter is within the dynamic range of the digitizer
2. determine if aerosol consists of only one component and is "static" in its properties
3. determine if nephelometer data exist for the trial
4. determine if the cloud in contained within the nephelometer array
5. determine if transmissometer (REVIRT LOS 5) data exist for the trial
6. compare transmissometer output to nephelometer results
7. obtain optical and physical properties of aerosol
8. obtain particle size distribution measurements and fit to known distribution
9. run IPHASE to determine phase function, etc. for input to NBSCAT
10. run NBSCAT
11. compare NBSCAT output with nephelometer measurements

Because of the slight offset in horizontal direction between the ABACUS and REVIRT LOSs, it was necessary to compare ABACUS transmittance (measured two-way against a backstop at approximately 800 m) with REVIRT transmittance. If there were a bad comparison, then it is not expected that the ABACUS measurements should compare with the nephelometer because the REVIRT LOS and nephelometer array were as closely co-located as were physically possible. If there were good comparison between the two transmission measurements, then it remained to compare the nephelometer measurements to the REVIRT transmission measurements -- again, if the agreement were bad, there would be no hope of arriving at agreement between ABACUS and the nephelometers. Even then, the wide variation possible in the remaining parameters which are necessary for use in NBSCAT, still leaves much opportunity for disagreement.

It is realized that this methodology is much different from what has been presented in past efforts. There, attempts were made to infer the concentration profile by inversion of the LIDAR equation. Unfortunately, the concentration data available were never good enough to confirm a successful inversion. The acquisition of better LIDAR data (at least with better range resolution) and the improved operation of the nephelometers over previous efforts has led to this approach.

Table 2. Obscurant types and their characteristics.

AEROSOL	SHAPE	SIZE/THICK (μm)	PSD	n,k	alpha (m^2/gm)
Brass	flake	5/1	Rosin-Rammler	0.6, 6.8	1 - 2
Graphite	flake	5/1	multi-modal	2.0, 1.3	1.4
Silica	grain (?)	--	--	--	--
Kaolin	grain (?)	--	--	--	1.2
Diesel	sphere	<1 (radius)	--	--	--
Fog Oil	sphere	<1 (radius)	--	1.5, 0.001	3.0

4. RESULTS

The comparison of the two transmission measurements (ABACUS and REVIRT) is shown by example in figure 3 which is for the brass trial under consideration. The plot of nephelometer data versus transmission (REVIRT) is shown in figure 4. The particle number density distribution which subjectively best fits the observed number density distribution, for this trial, is shown in figure 5. (The program IPHASE allows several different possibilities -- it was determined through trial and error, which combinations, within reason, best fit the observations.) At the time of submission, the analysis described above was not completed -- it is anticipated that it will be finished for presentation at the conference. In any case, figure 6 is a plot of the observed backscatter with range for a particular time during the brass trial being analyzed. Overlaid on this plot is the predicted NBSCAT backscatter with range. Further comments are not available until the plot is finished.

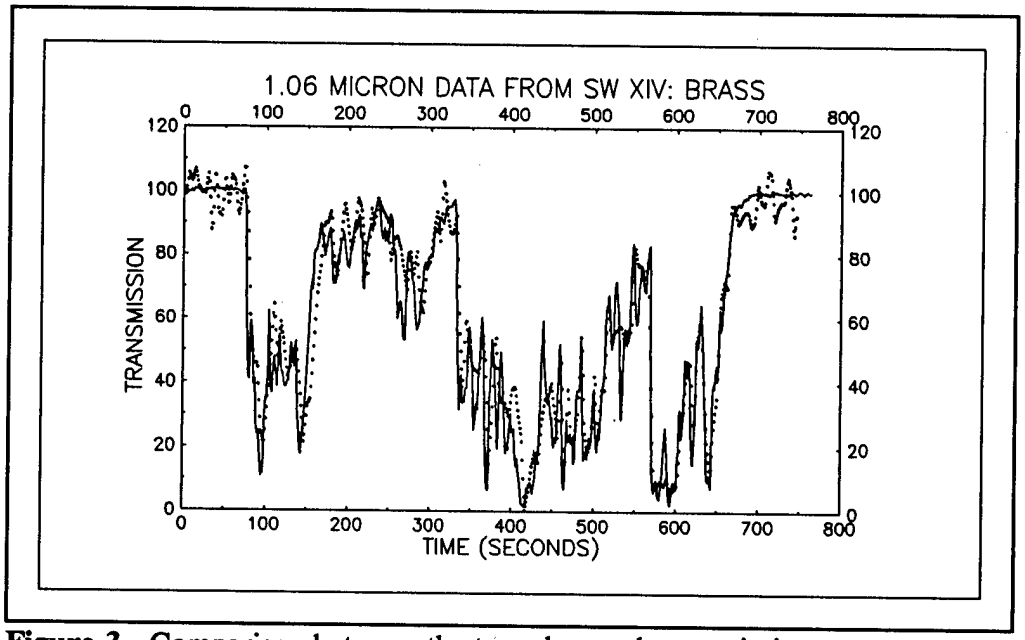


Figure 3. Comparison between the two observed transmission measurements. The ABACUS measurements have been offset in time by 11 s to account for the 30 m separation in the two LOSs and the transport of the smoke material by the wind.

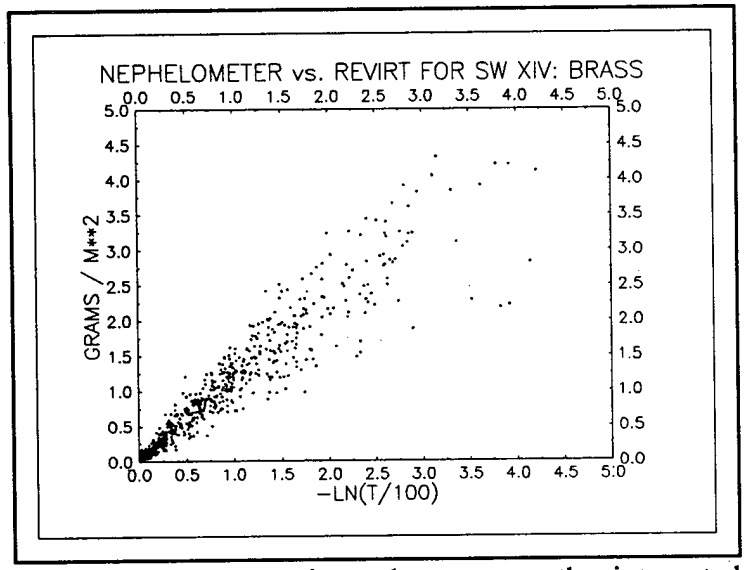


Figure 4. Comparison between path integrated concentration (nephelometer) and optical depth (REVIRT). The slope of the best fit line is the mass extinction coefficient.

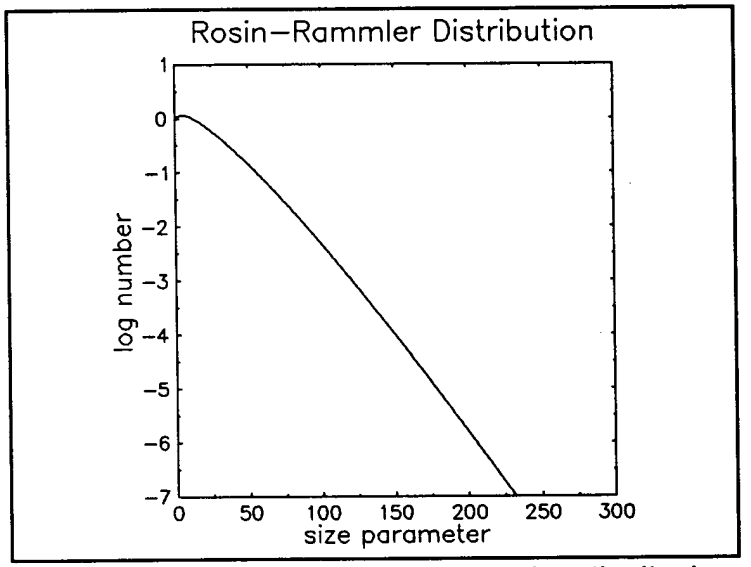


Figure 5. An example of a particle size distribution. This particular case is for a brass trial and is the result of a subjective fit between observed distribution and this type of distribution.

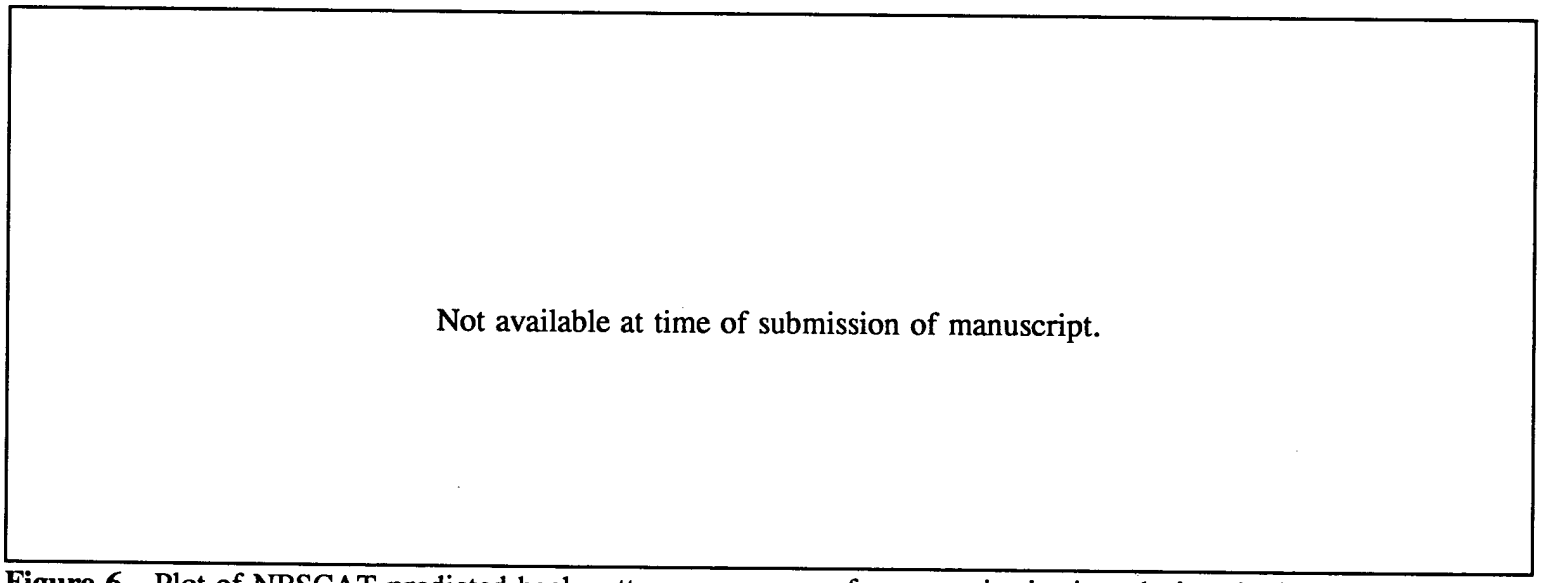


Figure 6. Plot of NBSCAT predicted backscatter versus range for one point in time during the brass trial.

5. SUMMARY AND FUTURE EFFORTS

A methodology has been demonstrated for the analysis of LIDAR measurements made during smoke and obscurant trials. The "excellent" agreement between the LIDAR measured and REVIRT measured transmittances (even with the 30 m separation of the LOSs) is encouraging as is the agreement between the transmissometer and nephelometer data. A more complete summary will have to wait for the completion of the analysis.

Future efforts will continue the analysis described above to include more trials and to develop a complete system for the three-dimensional characterization of the smoke/obscurant cloud by the integration of MIDAS and ATLAS. It is intended that this instrument also be used also for acquisition of data to support transport and diffusion modelling efforts at ARL/BED.

Hardware improvements are underway or anticipated in three areas. The first is the acquisition of a scanner/steering device which is capable of pointing ABACUS +/- 20 deg in azimuth and -15 to +105 degrees in elevation with an accuracy of 2.0 μrad and at rates compatible with "imaging" the cloud were sufficient transmitter pulse rates available. This was delivered during October 1994 (not yet received as of the writing of this paper). The second effort (in progress) is development of a digitizer capable of 1 Ghz sampling, multiple channels, and data storage/downloading capable of meeting the 20 pps rate of the current transmitter. And, the last effort which is only being considered at this point is the modification to allow eyesafe operation -- the current system is eye hazardous to 14 km.

ACKNOWLEDGMENT

Several people have assisted in the effort described above: Mr. Rafael Trujillo (ARL/BED) for his efforts with the development of the ABACUS. Mr. Dave Gose of NMSU's Physical Science Laboratory (PSL) who had worked on developing the original AOL and subsequently ABACUS, as well as participating in the SWXIV field test, Mr. Ken Payne, also of PSL for assistance in data reduction, Mr. Bill Bruce (ARL/BED) and the Obscurant Concentration Measuring System (OCMS) team from PSL (Mssrs. Tony Spence, Richard Stevens, Steve Fairchild , Billy Gammill, and James Pratt), for the nephelometer effort, Mr. Ed Butterfield (ARL/BED) and his team (Mssrs. Jerry Fields, Roberto Valdez, Bradley Poore -- all from ARL/BED and Ms. Karen Hutchison and Mssrs. David Telles and Dale Huggett from PSL) for the REVIRT data. Many useful discussions with Dr. Blair Evans and Mr. Gilles Roy of DREV are also gratefully acknowledged. Assistance was also provided by Mr. Tony Van de Wal, Mr. Walter Klimek and Mr. Robert Laughman, all currently with ARL/SLAD. Mr. Dick Farmer of the White Sands Missile Range Technical Library assisted with the literature search.

REFERENCES

Evans, B.T.N., and G. Roy, 1989. "Comparison of the Laser Cloud Mapper and Nephelometer Aerosol Concentration Data Taken at Smoke Week IX." In *Proceedings of the Smoke/Obscurants Symposium XIII*, Project Manager Smoke/Obscurants, AMCPM-SMK-CT, Aberdeen Proving Ground, MD, 21005, pp 433-447.

Evans, B.T.N, 1990. *An Interactive Program for Estimating Extinction and Scattering Properties of Most Particulate Clouds*, MRL report MRL-R-1123, Materials Research Laboratory, P.O. Box 50, Ascot Vale, Victoria 3032, Australia.

Farmer, W.M., R. Soto, and B. Locke, 1988. "Comparison of Mass Concentration Measurements Obtained with a LIDAR System and an Array of Nephelometers." In *Proceedings of the Smoke/Obscurants Symposium XII*, Program Manager Smoke/Obscurants, AMCPEO-CNS-CT, Aberdeen Proving Ground, MD, 21005, pp 433-447.

Herman, B.M., J.A. Reagan, and R.M. Schotland, 1978. *A Feasibility Study on the Use of LIDAR in the Determination of Optical Properties Under Battlefield Conditions*. ASL Report ASL-CR--78-0100-1, Atmospheric Sciences Laboratory, White Sands Missile Range, NM 88002.

Loveland, R.B., J.C. Thompson, R. Gonzalez, and A. Acosta, 1993. "Remote Measurements of the Density of Battlefield Visual Obscurants", In *Proceedings of the 1993 Battlefield Atmospherics Conference*, U.S. Army Research Laboratory, Battlefield Environment Directorate, White Sands Missile Range, NM 88002, pp 79-90.

Rubio, R., E.M. Measure, and D.C. Knauss, 1983. "LIDAR Determination of Smoke Concentrations and Linear Extinction Coefficient." In *Proceedings of the Smoke/Obscurants Symposium VII*, Project Manager Smoke/Obscurants, DRCPM-SMK-T, Aberdeen Proving Ground, MD 21005.

Uthe, E.E., and J.M. Livingston, 1986. "Lidar extinction methods applied to observations of obscurant events." *Applied Optics, 25:*678-684.

Enhanced Photon Absorption in Multi-Component Aerosol Clouds

Young P. Yee
Robert A. Sutherland

U.S. Army Research Laboratory
Battlefield Environment Directorate
White Sands Missile Range, New Mexico 88002-5501

ABSTRACT

Large area battlefield obscurants can significantly affect military operations by their effects on target signatures and electromagnetic propagation over spectral regions of interest. An important process that has been overlooked in the past is enhanced photon absorption in multi-component aerosol clouds. Research is being conducted to determine the synergistic effects of these multi-component obscurants on boundary layer processes. Under certain circumstances, highly scattering aerosols mixed with absorbing aerosols may enhance radiative absorption through the cloud by way of increasing the number of scattering/absorption events within the cloud. These aerosol interactions will change the local heating rates and temperature profiles. Computer simulations using existing models such as the Monte Carlo Radiative Transfer model are used to demonstrate relative radiative absorption changes within a smoke cloud and on the ground surface due to different aerosol cloud mixtures.

1. Introduction

In the "dirty" battlefield, it is not unusual for large-area aerosol clouds to be mixed with other natural or manmade obscurants. An important process that has been overlooked is enhanced photon absorption due to multi-component aerosols. This paper addresses the synergistic effects of these multi-component obscurants on radiative boundary layer processes. Under certain circumstances, highly scattering aerosols mixed with absorbing aerosols may enhance radiative absorption through the cloud by way of increasing the number of scattering/absorption events within the cloud. These aerosol interactions will change the local heating rates and temperature profiles.

Analytical radiative transfer models are sufficient for studying single component aerosol clouds but are not suited for aerosol clouds that contain a mixture of aerosols with different optical properties. Computer simulations with mixed aerosols using a Monte Carlo Radiative Transfer model are used to demonstrate relative

radiative absorption changes within smoke clouds with varying optical depths. Radiative changes on the ground surface due to different aerosol cloud mixtures are also investigated.

A large area Monte Carlo radiative transfer (LA-MCRT) model (Davis, et al 1993) has been developed to study the effects of multicomponent aerosol clouds on radiative fluxes. Ultimately, radiative heating within the cloud and on the ground surface will be analyzed. LA-MCRT is written in FORTRAN and the code can be run in either interactive mode or batch mode. The model was written to address a broader spectrum of problems in atmospheric radiative transfer.

2. Background

The investigation of the radiative processes that occur within a multicomponent aerosol cloud is an integral part of the Radiative Energy Balance And Redistribution (REBAR) program (Yee, et al, 1993). REBAR is a composite of specialized models that addresses the effects of large areal dispersed aerosols on the local meteorology. Since most analytical radiative transfer models do not adequately deal with multicomponent aerosols, Monte Carlo techniques were employed and tailored to fit specific realistic "dirty" battlefield scenarios.

The theoretical basis of the Monte Carlo method has been known as early as the 19th century. Since the development of high speed computers, there has been widespread applications of this technique. Application to radiative transfer problems is conceptually simple. A photon is launched into a medium along an initially defined trajectory to an interaction point, where the photon is either absorbed or scattered. If it is scattered, a new trajectory is defined and the photon is launched toward its next interaction point. Finally, if the photon is absorbed or lost (escapes the medium), a tabulation is made and a new photon is launched into the medium. Necessary calculations include the distance a photon travels between interactions and changes in photon direction.

3. Physical Concept for Radiative Fluxes

Radiation at the top of the atmosphere is currently assumed to be direct solar. Photons are injected randomly at the top surface of the atmosphere with a direction specified by the solar zenith angle. Calculation of the photon travel distance along the initial injection angle is based on a probability distribution. This defines the location of the photon at an intersection point where the photon is either absorbed or scattered depending on the single-scattering albedo. If the photon is absorbed, path computations for that photon stop, an absorption event is logged, and a new photon is injected. If the photon is scattered, another scattering angle is determined by the phase function and a new photon travel

distance is calculated. The following photon trajectory is checked to see if the photon has escaped the medium or has made contact with the lower boundary. If neither condition has occurred, the procedure is repeated.

Any time the photon encounters a boundary, either the top or sides of the medium or the ground surface, the event is logged and a new photon is injected. If the photon contacts the surface and is not absorbed, its direction is changed upward via Lambertian reflection. The new trajectory is selected by random number and the travel distance to the next destination is computed in the usual manner.

Much care is expended to locate the photon is space and to relate its trajectory to a well-defined coordinate system. At each scattering point, a scattering angle must be simulated and the coordinates of the next interaction point calculated.

Figure 1 is a depiction of the enhanced photon interactions in a multicomponent aerosol layer. A photon of incoming solar radiation is incident at the top of an aerosol cloud layer with a zenith angle of θ. One of the aerosol components in the layer is highly scattering and the other is more absorbing. In the diagram, there are more aerosol high scatterers than absorbers but the scatterers increase the number of photon interactions within the cloud which in turn increases the probability of photon absorption.

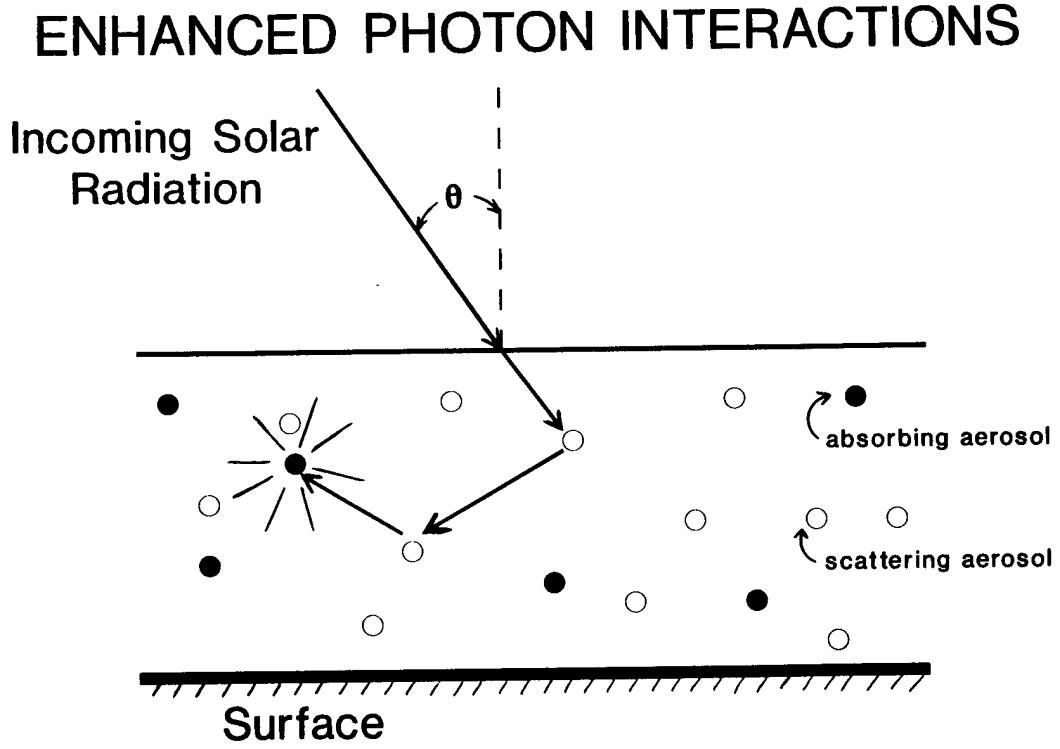


Figure 1. Schematic of enhanced photon absorptive interactions due to increased number of scattering aerosols.

4. Features of LA-MCRT

Although there are other existing Monte Carlo computer codes available (Lux and Koblinger, 1991), they often have highly specialized applications. LA-MCRT was developed to address a broad spectrum of atmospheric radiative transfer problems. The following summarizes the salient features of LA-MCRT.

- *Designed to study radiation propagation in horizontal layers*
- *A surface terrain can be defined where up to 100 surface albedos can be specified*
- *Embedded aerosol clouds (ellipsoids and cube composites) can be inserted within the area of interest*
- *Allows up to two different aerosols within an atmospheric layer*
- *Amenable to parallel processing techniques*
- *Can be run in an interactive mode and the user input responses saved*
- *Can be run in batch mode, ideal for multiple simulations*
- *Optional probability distribution functions (PDF) for Rayleigh and for Henyey-Greenstein scattering with asymmetry parameters 0 (isotropic), .5, .75, and .875*
- *User inputs are treated as character strings and then parsed into tokens which are converted into the proper data types. Error checking of user inputs.*

The Monte Carlo approach provides a physical representation of the radiative interactions within an aerosol cloud. This allows the user to construct complex atmospheric media as well as multiple aerosol clouds for computer simulation studies. The biggest tradeoff is that these techniques require intensive computations to obtain statistically meaningful results. In addition, photon interactions along the cloud boundaries need to be well defined.

5. Aerosol Mixtures in a Cloud Layer

LA-MCRT allows up to 11 layers with up to two different aerosols within each layer. For our simulation study, the layer is assumed to be homogeneously mixed with a thickness of 100 meters. A two component layer was defined with varying optical depths. The two aerosol components were dust and fog oil and their optical properties in the visible spectrum are listed in table 1. Fog oil is a highly scattering aerosol at the visible wavelengths and its mass extinction coefficient is almost 7 times greater than dust.

Table 1. Aerosol Optical Properties

	DUST	FOG OIL
Single Scattering Albedo	0.867	0.999
Mass Extinction Coefficient (m^2/g)	1.10	7.50

To obtain reasonable statistical results, simulations of 100,000 injected photons were run with a ground surface albedo of .2 for different solar zenith angles. Figure 2 shows the fraction of photons absorbed within the defined aerosol layer for a dust aerosol only case, a fog oil aerosol only case, and varying dust/fog oil cases. For all these simulations, the total medium optical depth was 2. In figure 2, the fraction of photons absorbed on the ground surface is depicted for the corresponding cases in figure 1. The absorption of photons on the surface relate to the surface heating rates which will affect the surface energy balance budget and in turn will change the local meteorology.

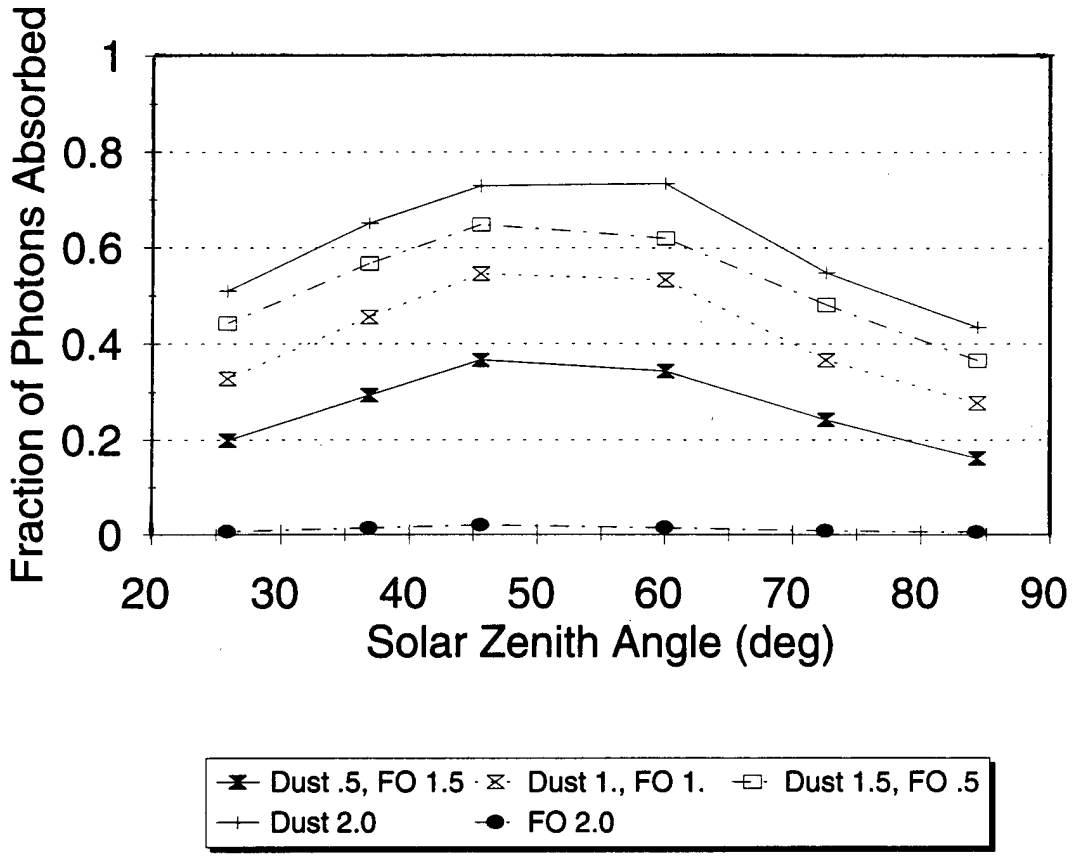


Figure 2. Fraction photons absorbed within the aerosol layer for five simulations. The total optical depth for each of the dust/fog oil mixtures is 2.0.

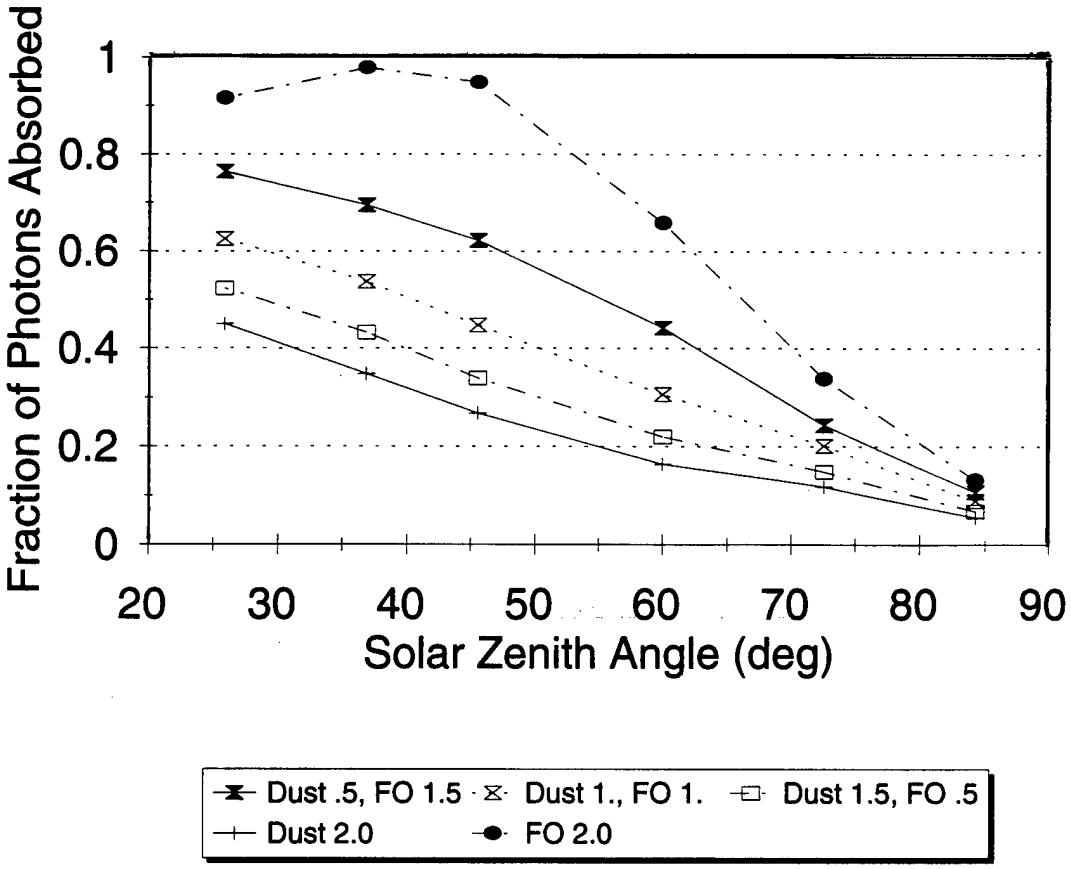


Figure 3. Fraction photons absorbed on the ground surface for five simulations. The total optical depth for each of the dust/fog oil mixtures is 2.0.

Figure 4 shows three simulations of absorption within a defined layer as a function of solar zenith angles. The dust aerosol density remains the same in all cases but the fog oil aerosol optical depth density increases from zero to .5 to 1.5. At a zenith angle of approximately 73 degrees, there is a crossover in which the fractional photons absorbed within the layer decreases even though the total optical depth of the aerosol layer increases.

6. Conclusions

The Monte Carlo technique provides the flexibility to address a boarder spectrum of radiative transfer problems such as simulating the effects of multiple aerosol mixtures on radiative interactions. Results have shown that photon absorption within an aerosol cloud layer is a complex function of the solar zenith angle and the vertical optical depth of each aerosol component. After extensive testing and development, the Monte Carlo module will eventually be integrated into the Radiative Energy Balance And Redistribution (REBAR) program.

Although the Monte Carlo approach offers a physical representation of photon absorption/scattering interactions, it requires algorithms for tracking hundreds of thousands of photons to obtain statistically sensible results. The use of computer parallel processing algorithms can alleviate a large part of these computational requirements.

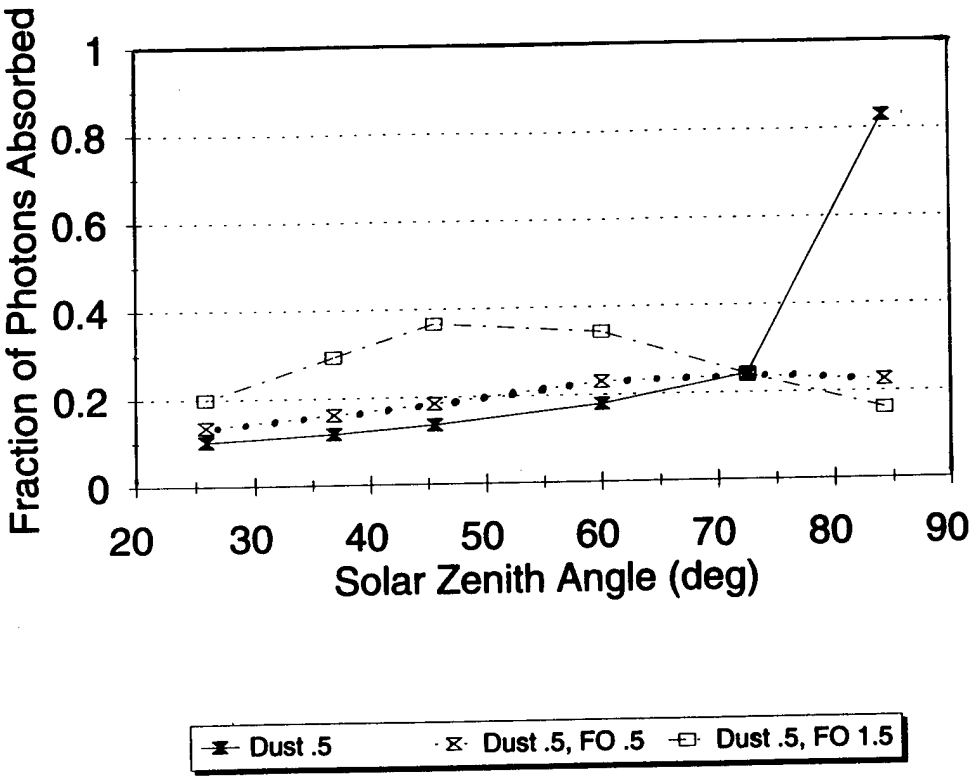


Figure 4. Fractional photon absorption within an aerosol layer as a function of solar zenith angle. The optical depth of dust aerosols is .5 for all three cases and the optical depth of fog oil varies from 0 to .5 to 1.5.

Ongoing research will involve the following topics.

- Analyze the effects of optically thick multicomponent aerosol cloud on the local atmospheric stability categories and the turbulence fields
- Determine the optimal aerosol mixtures and solar zenith angles for radiative absorption within a cloud can be used to optimize camouflage and concealment military operations
- Develop useful empirical relationships from Monte Carlo simulations

- Address thermal emissions either through direct modification of the code or indirect assimilation from the Large Area Thermal Emissions And Multiple Scattering (LA-TEAMS) model (Lines and Yee, 1993)

7. References

Davis, R.E., A. Miller, and S. Berrick, "Radiative Effects Modeling", STC Technical Report 6241, Mar 1993, Science and Technology Corporation, Las Cruces, NM.

Lines, R.T. and Y.P. Yee, 1993, "Temperature Profile of the Nocturnal Stable Boundary Layer over Homogeneous Desert using LA-TEAMS," 1994 Battlefield Atmospherics Conference, White Sands Missile Range, NM, Nov 29-Dec 1, 1994.

Lux, I. and L. Koblinger, 1991: Monte Carlo Particle Transport Methods: Neutron and Photon Calculations, CRC Press, Boca Raton, Florida.

Yee, Y.P., R.A. Sutherland, R. Davis, S.W. Berrick, and M. Orgill, 1993, "The Radiative Energy Balance And Redistribution (REBAR) Program," Proceedings of the 1993 Battlefield Atmospherics Conference, Las Cruces, NM, Nov 30-Dec 2, 1993.

VISUALIZATION OF THE MADONA DATA BASE AND USE OF SELECTED SEQUENCES IN A WIND FLOW AND DIFFUSION SIMULATION SYSTEM

Harald Weber and Welfhart aufm Kampe
German Military Geophysical Office
56841 Traben-Trarbach, Federal Republic of Germany

Ronald M. Cionco
U.S. Army Research Laboratory
White Sands Missile Range, NM 88002-5501 USA

ABSTRACT

During MADONA (**M**eteorology **A**nd **D**iffusion **O**ver **N**on-uniform **A**reas), Porton Down United Kingdom 1992 a high resolution data base was collected, composed of meteorological data and data from diffusion experiments with smoke and SF_6 as tracers. A visualization program was developed, which allows to browse through the data continuously or step by step. The data is presented on the background of the trial area map at its respective location or as separate graphs. The composition of meteorological data to be viewed from the total data base can be chosen interactively. In addition the measured SF_6 profiles and the LIDAR crosswind profiles of the smoke plumes or puffs may be displayed. Selected scenarios can be extracted for use in the HEARTS system (**H**azard **E**stimation for **A**ccidental **R**elease of **T**oxic **S**ubstances). The corresponding measured data can then be used to verify the model output. The MADONA visualization program and the HEARTS system are presented on a 486 PC.

1 .THE MADONA VISUALIZATION TOOL

The visualization tool is specially designed to present the extensive MADONA data as an overview. Data is provided in time steps of 5 min intervals. The steps may be shown continuously (movie) or as single frames running time forward or backward. The wind and concentration data is presented on the background of the trial area map at the positions of the 15 towers and the sonic sites. Separate graphs show temperature data, vertical wind profiles, and turbulence data from the sonic anemometers, as well as simple preliminary evaluations of the concentration data. The composition of meteorological data to be viewed from the total data base can be selected interactively. All plots may be rearranged and resized by the user, or removed from the display.

Selected scenarios may be stored and subsequently used as input for the HEARTS program. This allows simulation of the wind fields and concentration profiles and a comparison with the measured data for verification and demonstration purposes.

1 The Layout

The standard layout of the screen is shown in Figure. 1. The box at the lower left displays the date and time of each frame. The background shows the road network on the Porton Down Range along with arrows representing the winds measured at each of the towers currently in the view window. This window may be changed (relocation of center and zooming) to suite the user. Additionally the experimental setup for a concurrent run is shown in form of a row of circles representing the continuous plume and labels and parallel lines representing the positions and aiming direction of the lidars respectively. Perpendicular to these lines the measured concentration profiles are plotted in an arbitrary scale. The profile plotted perpendicular to the road depicts the measured SF_6 concentration profile taken within that 5 minute period.

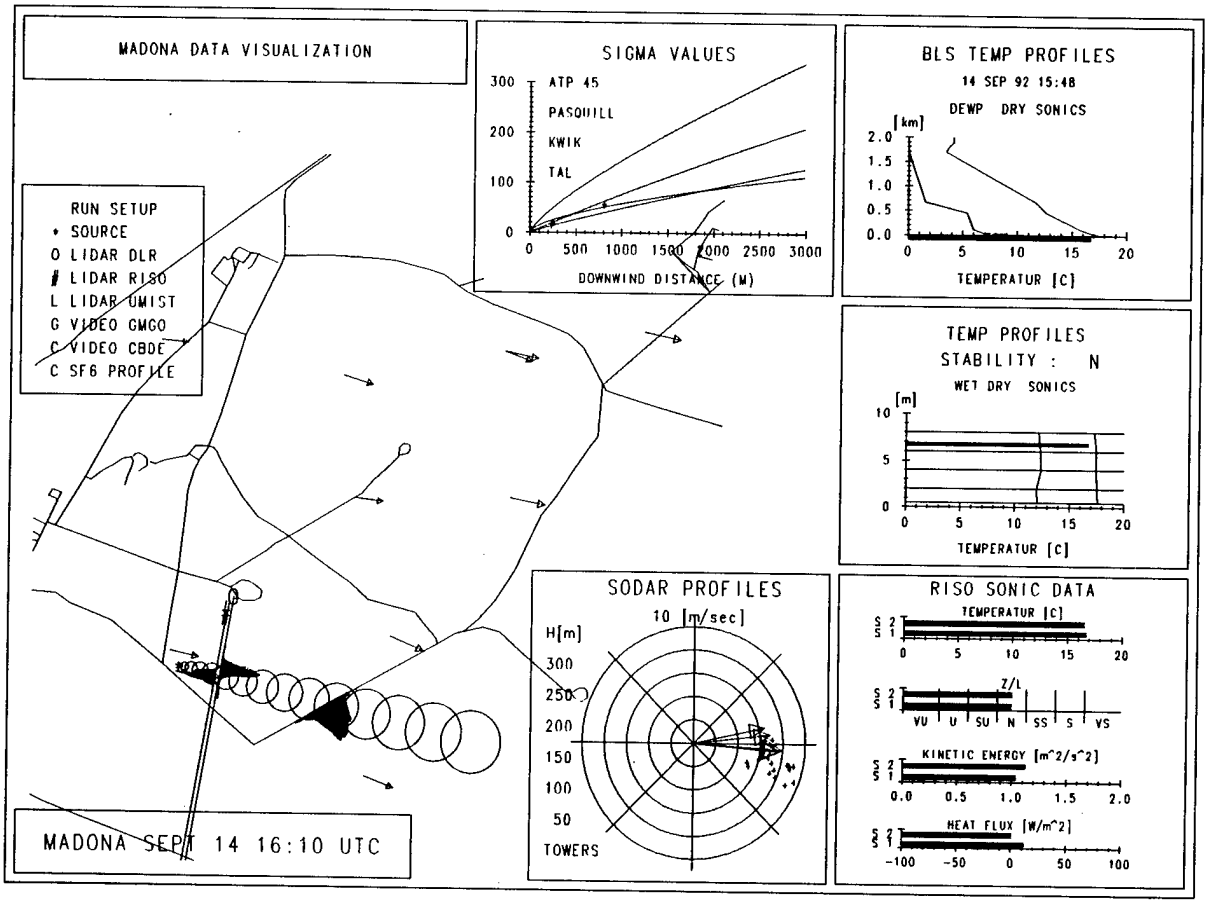


Figure 1. Standard layout of the MADONA data visualization screen.

A box on the upper left contains the legend for the experiments. Beginning at the bottom and moving counter clockwise we find displays of:

- the sodar wind profile along with a scatter diagram of all 17 wind measurements in the field (15 towers + 2 sonics).
- the sonic data
- the wet and dry temperature profiles of the 10m mast
- the boundary layer sonde profiles
- the sigma values

Each of these displays will be described in more detail in the following.

1.2. The Sodar Wind Profile Plot

Figures. 2a and 2b show the vertical wind profile measured with a sodar near the position of the source in figure 1. The arrows are color coded on the screen to represent the elevations listed in the left hand column of the plot. The points are a scatter diagram of the wind vectors at the 15 towers and the sonic sites.

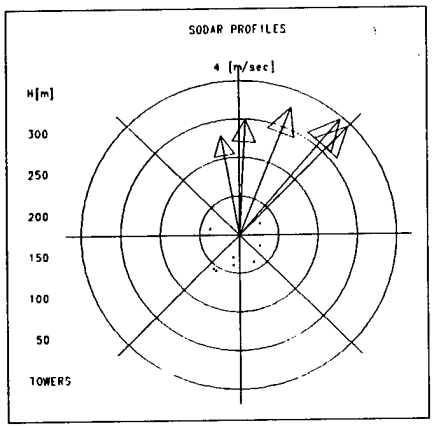


Figure 2a. Sodar profile in a low wind speed case

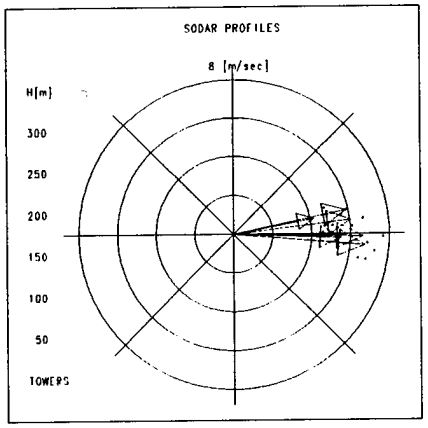


Figure 2b. Sodar profile in a high wind speed case

Figure 2a shows a situation with very low surface wind speeds and variable directions as indicated by the cluster of points within the 1 m/s circle. The sodar arrows show a well developed Ekman spiral in the layers above. Figure 2b shows a period with higher wind speeds. The surface wind directions are westerly at 7-8 m/s, and there is no significant structure in the vertical profile.

1.3. The Sonic Data Plot

Figure 3 gives an overview of the parameters provided by the sonic anemometers which were located at 7.5m above ground and spaced about 100m apart at the source in figure 1. Each sonic is represented by a separate bar. The sonics measured time series with a frequency of 20 Hz. The parameters: temperature, z/L, kinetic energy, and heat flux are averaged for the 5 minute frame and presented in the plot. The z/L scale is graded into 7 stability categories based on the classification given in table 1.

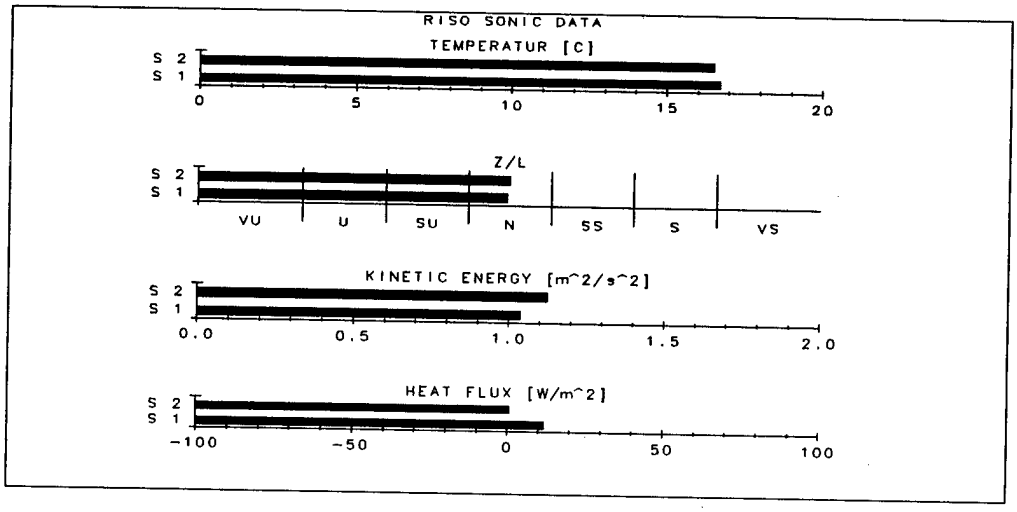


Figure 3 The 5 minute average sonic data

Table 1. Stability Classification for z/L.

Very Unstable	Unstable	Slightly Unstable	Neutral	Slightly Stable	Stable	Very Stable
< -1.	-1.0 to -0.6	-0.6 to .0.2	-0.2 to 0.2	0.2 to 0.6	0.6 to 1.0	>1.0

1.4. The Wet and Dry Temperature Profiles of the 10m Mast

Figures 4a and 4b show the wet and dry bulb temperatures at the levels 0.5m, 2m, 4m, 6m, and 8m above ground on a mast located in the valley near the center of the window in figure 1. The sensors used here were pt100 resistors. The discrete measurements were taken in a 7 minute cycle beginning at the lower level and ending at the top, going from dry to wet bulb at each level. The values for each 5 minute time step were interpolated using a time weighted mean of the two closest measurements.

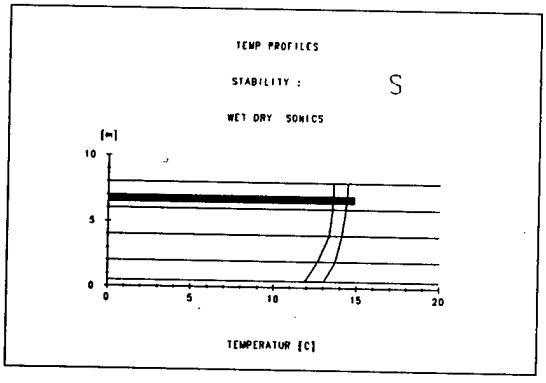


Figure 4a. Temperature profile for a stable situation

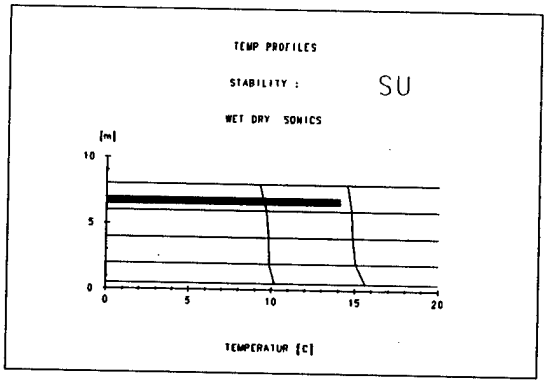


Figure 4b. Temperature profile for a slightly unstable situation

Figure 4a shows a stable situation in relatively moist air while figure 4b shows a slightly unstable situation on a drier day. The sonic temperature bar is included at the 7.5m level for reference and shows good agreement. The stability (s) is determined from the profile using the relationship:

$$s = 4 + (T_4 - T_{0.5}) / 2. \qquad (1)$$

T_4 - Temperature in 4 meters
$T_{0.5}$ - Temperature in 0.5 meters
as specified in explosive ordnance demolition field manuals.

1.5. The Boundary Layer Sonde Profiles

The boundary layer sonde was flown from the range at irregular intervals to fit into the experimental process. It was a slow rising radiosonde which produced air and dew point temperatures. The date and time of the ascent closest to the date and time of the current frame is presented in this plot along with the temperature curves up to 2km. Again a bar representing the temperature measured by the sonics an 7.5m is shown at the bottom for comparison.

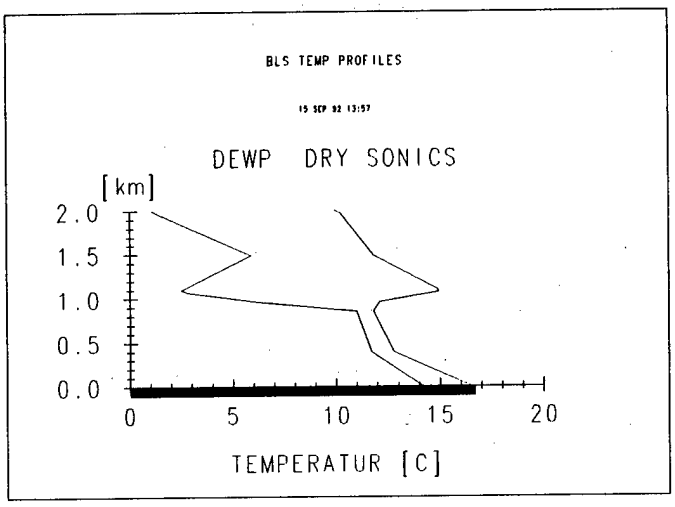


Figure 5 Boundary layer sonde profile

1.6 The Sigma Values Plot

The standard deviation of a Gaussian cross wind concentration profile (commonly referred to as sigma-y) is a value which may easily be determined from crosswind concentration measurements even if they are not absolute. Figure 6 is a zoom into the view window presented in figure 1 and shows a SF_6-profile and two lidar profiles as. The SF_6 profiles are absolute measurements and were produced by a vehicle mounted real time IR-analyser which was driven along the roads at very low speeds. A single profile was produced in about 3 - 5 minutes. The lidar concentration profiles of the smoke plumes are relative measurements taken at 3s intervals and averaged over the 5 minute period The sigma values plot (figure 7) shows 4 sigma-y curves from literature. The ones shown here are those given in the NATO STANAG 2103/ ATP 45 (used for NBC defence purposes), specified in the KWIK algorithm (for ammunition expenditure for smoke screens), determined by Pasquill for open country (from measurements at just this site), and the parameters used by the German Environmental Protection Agency for the siting of industrial plants (labelled TAL).

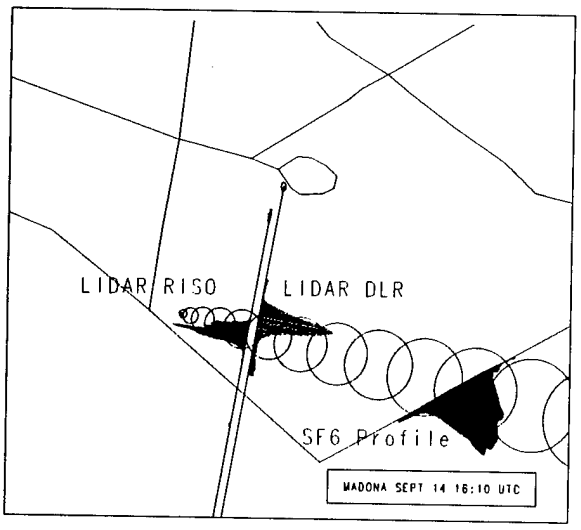


Figure 6. SF_6 - and lidar profiles

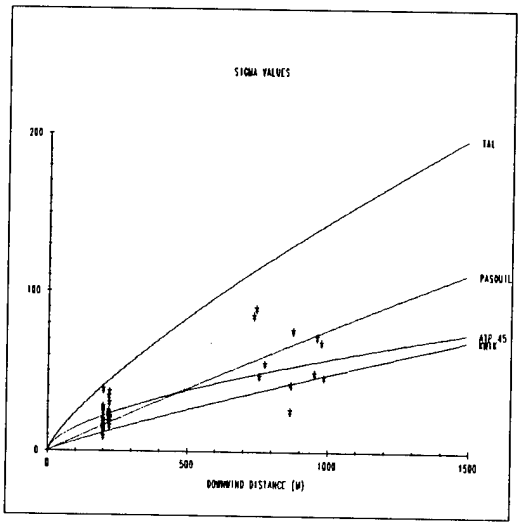


Figure 7. Sigma-y curves from literature and points derived from measurements

The latter is valid for averaging times of 1 to 2 hours the first three parameters are derived from data with an averaging time of up to 10 minutes. The points shown in the graph are the sigma-y values which were determined from the measured profiles using a simple least squares fit procedure. The relatively small sample already indicates a good agreement of the measurements with the theoretical values for shorter averaging times. But no agreement with the TAL sigma curve. Figure 7 contains more than the three values derived from the situation presented in figure 6. The visualization program superimposes all measurements onto the sigma plot for the total time period in which the stability and consequently the sigma curves do not change. This is not meant to be a rigid evaluation of the diffusion experiments but rather to give a quick look at whether the measured profiles are in general agreement with theory or not and thus to point out interesting situations for further investigation.

1.7. The Store Option

After viewing the data, it is possible to select a situation which is of interest for further investigation with the HEARTS system. A menu driven store option allows to choose the starting time, averaging time, and the number of time steps for which the weather information is to be stored in a file. All towers, selected towers, or the mean value for the entire area may be used for the wind data. The stability can be taken from the sonic data (see Table 1), from the temperature profile using (1), or entered manually by the user. If the averaging time is greater than 5 minutes the program determines the time average wind and stability for the specified time frame. The source position and the terrain elevation data of the chosen view window are stored on separate files. These three files can then in turn be used by the HEARTS system.

2. THE HEARTS SYSTEM

2.1. Short Model Description

HEARTS was developed at the German Military Geophysical Office as a program system for the estimation of hazards resulting from the accidental release of toxic or noxious substances (Weber, aufm Kampe 1992). The system includes a simple Gaussian model as well as a Gaussian puff model. The latter is a modified version of the RIMPUFF model (Thykier-Nielsen, Mikkelsen 1993) including the puff splitting technique. Both diffusion models allow the use of different parameter sets to cover different scenarios with different averaging times, including instantaneous and continuous releases. The system retrieves the terrain data for the region specified by the user and displays it as a background map, used for input and output. The LINCOM Model (Santabarbara et al. 1993) and the BALL and JOHNSON Model (1978) are integrated into the system and may be used if the problem calls for consideration of terrain effects. The source position and release information is taken from the corresponding MADONA visualization output file. The effective source strength and the physical and chemical properties of SF_6 as the substance released are input as default values.

2.2. Evaluation Example

To demonstrate the possibilities of the system a scenario from September 14, 1992 was selected. The meteorological conditions are a mean wind speed of 2 m/s and neutral stability. Figures 8a and 8b show 4 different concentration contours, which were calculated by the model as well as a measured SF_6 profile. The shading in the profile is related to the concentration level. While the inner contour line which corresponds to the highest concentration level in the measured profile encloses the profile in figure 8a it is distinctly too short in figure 8b. While the ATP 45 parameters were used in the first case, the TAL parameters were used in the latter.

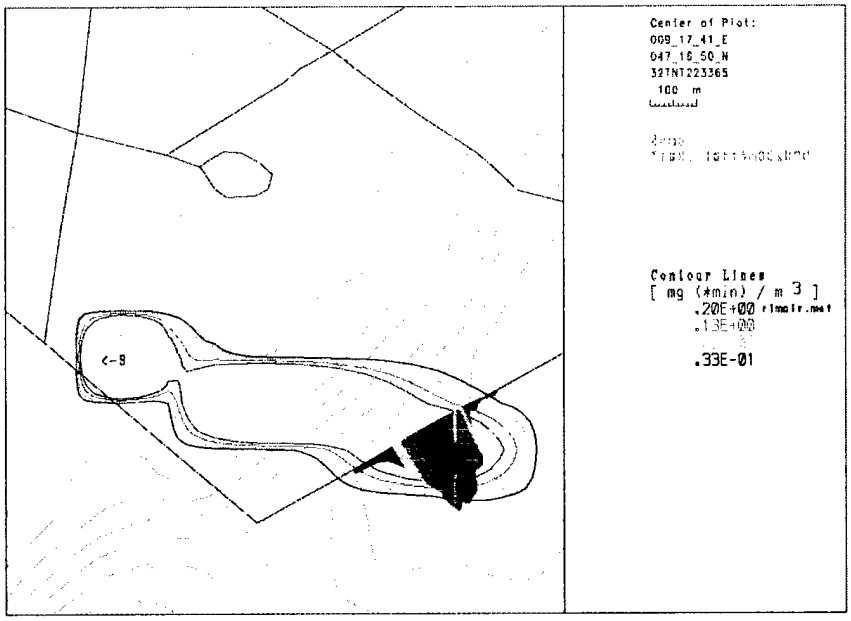


Figure 8a. Concentration contour lines calculated by HEARTS using the ATP45 parameters and showing a measured SF_6 profile

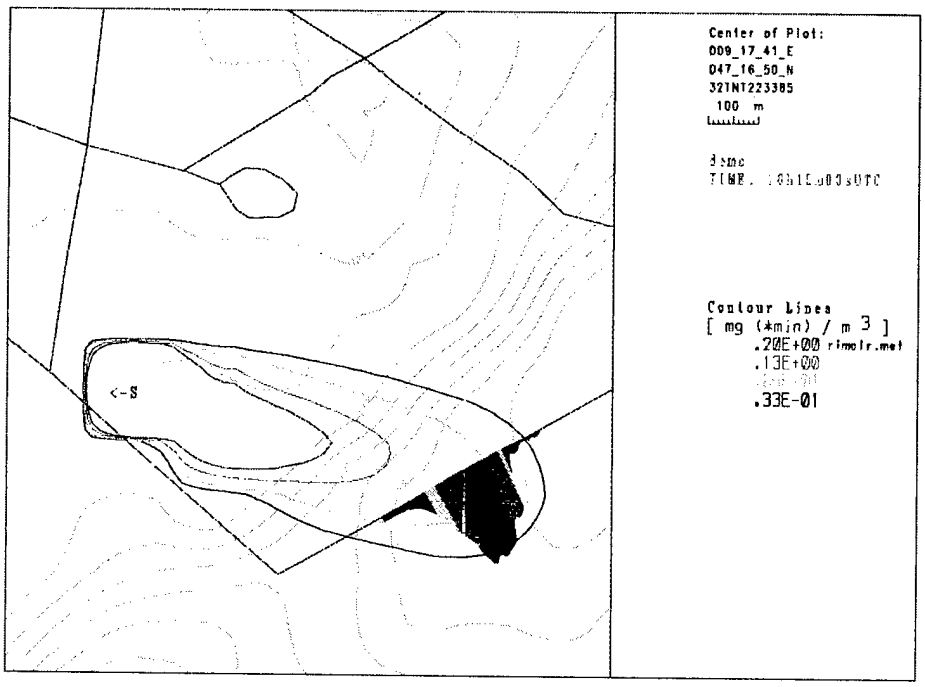


Figure 8b. Concentration contour lines calculated by HEARTS using the TAL parameters and showing a measured SF_6 profile

From this example it can easily be seen that the use of the parameter set appropriate for the problem at hand is essential. Using parameters designed for siting of industrial plants and based on long term averaging would lead to severe underestimation of the hazard in case of an accident.

REFERENCES

Ball, J., and S. Johnson, 1978: "Physically-based High-Resolution Surface Wind and Temperature Analysis for EPAMS", Report ASL-CR-78-0048-1, USA Atmospheric Sciences Laboratory (contact R. Cionco), WSMR, NM, USA.

Santabarbara, J. S., T. Mikkelsen, R. Kamada, G. Lai, and A. Sempreviva, 1993: "LINCOM Wind Flow Model", Risø-R-Report (EN), Meteorology and Wind Energy Department, Risø National Laboratory, Roskilde, Denmark.

Thykier-Nielsen, S., and T. Mikkelsen, 1993: "RIMPUFF User Guide, Version 33 (PC)", Meteorology and Wind Energy Department, Risø National Laboratory, Roskilde, Denmark.

Weber, H. and W. aufm Kampe, 1992: "Das Programmsystem "HEARTS" (Hazard Estimation after Accidental Release of Toxic Substances)",Annalen der Meteorologie 27, Deutsche Meteorologen-Tagung 1992, Selbstverlag des Deutschen Wetterdientes, ISSN 0072-4122, Offenbach am Main, Germany.

Session V Posters

ATMOSPHERIC PHYSICS

TEMPERATURE PROFILE OF THE NOCTURNAL STABLE BOUNDARY LAYER OVER HOMOGENEOUS DESERT USING LA-TEAMS

R. Todd Lines
New Mexico State University
Las Cruces, NM 88003

Young P. Yee
U.S. Army Research Laboratory
Battlefield Environment Directorate
White Sands Missile Range, NM 88002-5501

ABSTRACT

The temperature profile of the nocturnal stable boundary layer over homogeneous desert is predicted as a function of time using the Large Area Thermal Emission and Multiple Scattering (LA-TEAMS) doubling technique including thermal emission and aerosols. The LA-TEAMS model is described. A uniform, stable boundary layer is assumed. The resultant temperature profile is obtained and compared to the observed profile. The LA-TEAMS doubling technique including thermal emission is shown to describe the temperature profile under the given conditions.

1. INTRODUCTION

An idealized nocturnal stable boundary layer (NSBL) can be envisioned for uniform desert terrain (Grisogono, Keislar 1992). In such an idealized NSBL, wind speeds are low, thus heat transfer is dominated by long-wave radiative processes. Actual conditions approach this idealized NSBL late at night under calm conditions (Garratt, Brost 1982).

Formation of the idealized NSBL is governed by radiative surface cooling during the first part of the night. A temperature inversion develops and grows in strength while the surface cooling rate diminishes due to the low heat capacity of desert soil. Late at night the surface cooling rate becomes quite small. At this point the NSBL heat transfer is almost completely dominated by long-wave radiative processes.

The mature temperature inversion in the NSBL has been studied under clear sky conditions over flat terrain with negligible advection and baroclinicity (André, Mahrt 1982). The Large Area Thermal Emission and Multiple Scattering model developed by ARL is well suited to study the NSBL under these conditions.

LA-TEAMS is designed to be a component of the Radiative Energy Balance and Redistribution (REBAR) program (Yee et al. 1993), to study the effects of aerosols on the battlefield environment. LA-TEAMS can also be used as a stand-alone model, as was done here.

2. DESCRIPTION OF LA-TEAMS

LA-TEAMS is based on the standard doubling technique (Hansen 1969). This technique assumes a plane parallel stratified atmosphere consisting of semi-infinite, slab-like cloud layers. The essence of this technique is that if the reflection and transmission properties of the layers are known, then these properties can be found for a combination of layers. The algorithm begins with two optically thin identical layers and combines them. Successive combination of the results builds optically thick homogenous cloud layers. Such an optically thick cloud layer may then be combined with other layers of different properties to form complex stratified clouds. Thermal emission is added to the standard doubling technique following the work by Miller et al. (1978).

The initial layer used has a very small optical depth, $\delta\tau$, of about 2×10^{-20} due to aerosol extinction and the water vapor continuum absorption (Roberts, Selby, Biberman 1976). Clearly single scattering dominates at this optical depth. Then the well-known expressions for the scattering and reflection operators may be used (Chandrasekhar 1960)

$$S\left(\delta\tau;\mu,\phi;\mu_o,\phi_o\right) \simeq \left(\frac{1}{\mu}+\frac{1}{\mu_o}\right)^{-1}\left\{1-\exp\left[-\delta\tau\left(\frac{1}{\mu}+\frac{1}{\mu_o}\right)\right]\right\}P\left(\mu,\phi;-\mu_o,\phi_o\right)$$

$$T\left(\delta\tau;\mu,\phi;\mu_o,\phi_o\right) \simeq \left(\frac{1}{\mu}-\frac{1}{\mu_o}\right)^{-1}\left\{\exp\left(\frac{-\tau}{\mu_o}\right)-\exp\left(\frac{-\delta\tau}{\mu}\right)\right\}P\left(-\mu,\phi;-\mu_o,\phi_o\right) \quad (1)$$

where

τ = Optical Depth
$\delta\tau$ = initial (small) optical depth
μ_o = $\cos\theta_o$, where θ_o is the initial polar angle
ϕ_o = initial azimuthal angal
μ = $\cos\theta$, where θ is the scattered polar angle
ϕ = scattered azimuthal angal
P = phase function of the particulate

Likewise, for the initial layer the radiance due to thermal emission can be expressed as

$$I = (1-\omega_o)\left(1-\exp\left(\frac{-\delta\tau}{\mu}\right)\right)B\left(\nu,T\right) \quad (2)$$

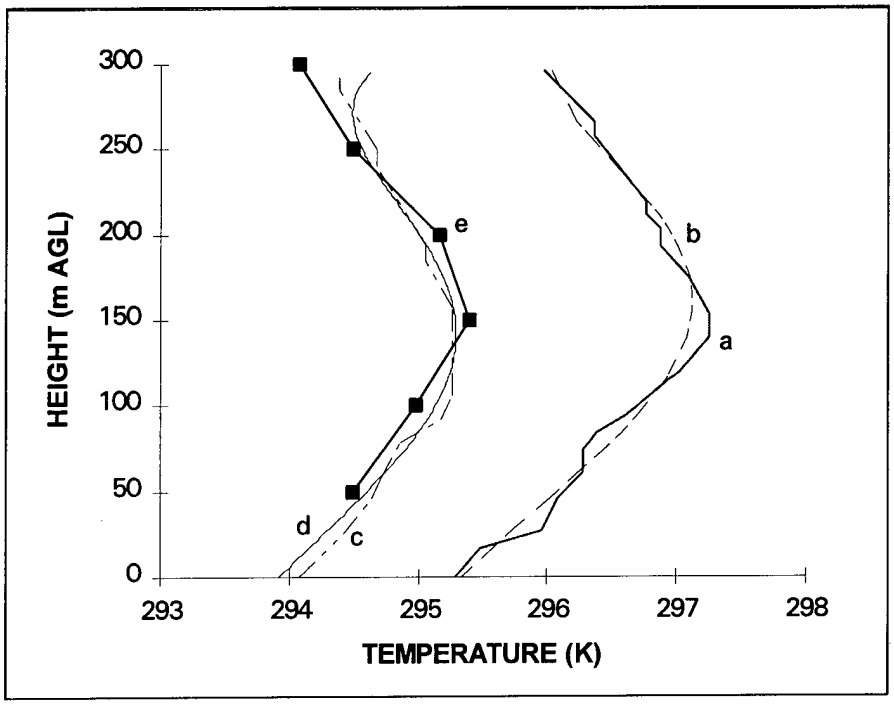


Figure 1: Comparison of LA-TEAMS simulation to observed profiles: airsonde data from 0200 LST (a), and a curve fit to this data used as a starting point for the calculations (b), airsonde data from 0400 LST (c), analytical approximation due to Grisogono and Keislar (1992) (d), and LA-TEAMS result (e).

where I is the radiance due to thermal emission, $B(\nu, T)$ is the Planck function at frequency ν and temperature T, and ω_o is the single scattering albedo. From the right hand side of *eq.* (2) a thermal emission operator can be defined analogous to the S and T operators defined in *eqs.* (1). By successive doubling, LA-TEAMS arrives at a net heat flux density for each layer and a total flux out of the top and bottom of the stratified cloud. The process is repeated for a series of wavelengths over a selectable bandwidth. The net fluxes from the individual wavelength runs are converted into change in temperature following the expression

$$\Delta T = \frac{1}{\rho C_p} Q \frac{\Delta t}{\Delta z} \tag{3}$$

where

T = Temperature
ρ = air density
C_p = specific heat
z = geometric height
t = time
Q = total net thermal flux in the cloud layer

The symbol Δ is used to indicate a change in the given quantity over time (i.e. $\Delta T = T_2 - T_1$). The value of ΔT for each layer is used to modify the temperature profile, and the whole process is repeated for an arbitrary number of time steps.

The results of this calculation are dependent on the model used for the heat loss of the surface. A simple, linear, model for the surface heat loss is currently used in LA-TEAMS.

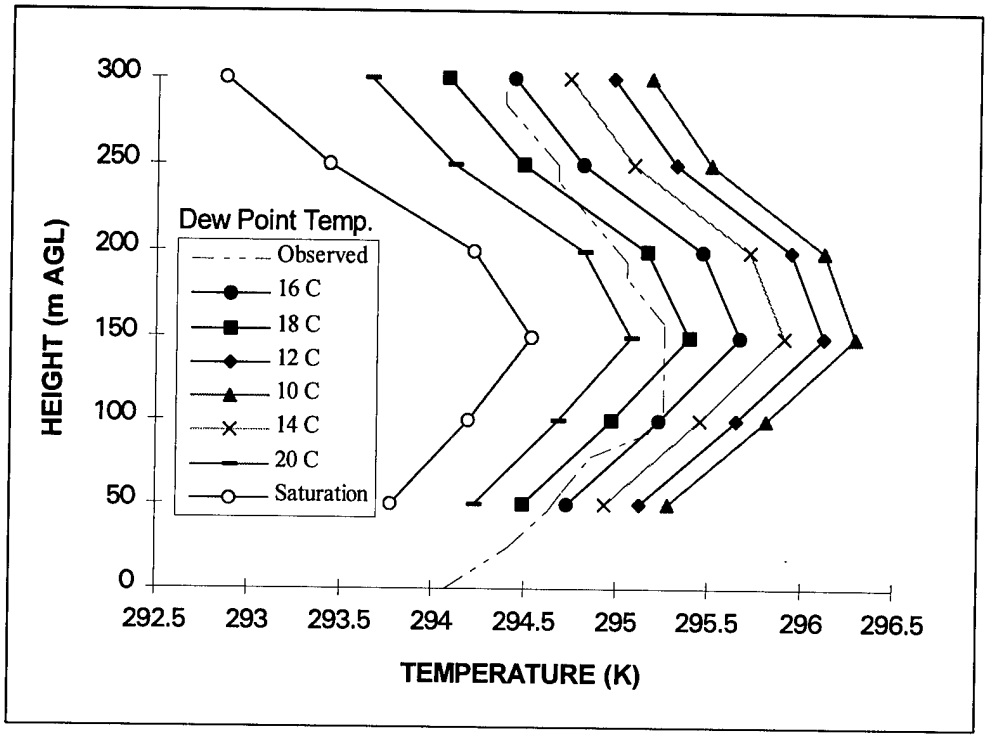


Figure 2: LA-TEAMS sensitivity to cloud dew point temperature (and therefore relative humidity). The curves range from 10 C to the saturation temperature of 23 C in 2 C increments.

3. COMPARISON TO OBSERVATION

Data from the Mohave Desert near the Cal-Nev-Ari airport (Grisogono, Keislar 1992) were compared to a LA-TEAMS simulation using 50 wavelengths over an 8 to 20 μm bandwidth, the principal absorption region for water vapor, which was responsible for nearly all absorption. The modeled atmosphere consisted of six cloud layers of 50 m each and one surface layer for a total height of 300 m (*figure* 1). The relative humidity was absent from this data set. Data from the SDC II program (Peterson et al. 1987), and inferences from the emissivity parameter given with the data, gave a probable value for the relative humidity of 65 to 75 percent. The value of 73 percent (dew point temperature about 18 C) was accepted as the most probable value and was used in the calculations. To modify the

relative humidity in the LA-TEAMS simulation, the cloud layers were created at different dew point temperatures. A sensitivity study was conducted to add confidence in the relative humidity value chosen. Predicted temperature profiles were calculated with cloud dew point temperatures ranging from 8 C to 23 C which was the saturation temperature (*figure* 2). The temperature profile was given at 0200 LST. The predicted profile at 0400 LST is given in figure 1 along with the analytical approximation given by Grisogono and Keislar (1992). The surface heat loss model was optimized for this time period.

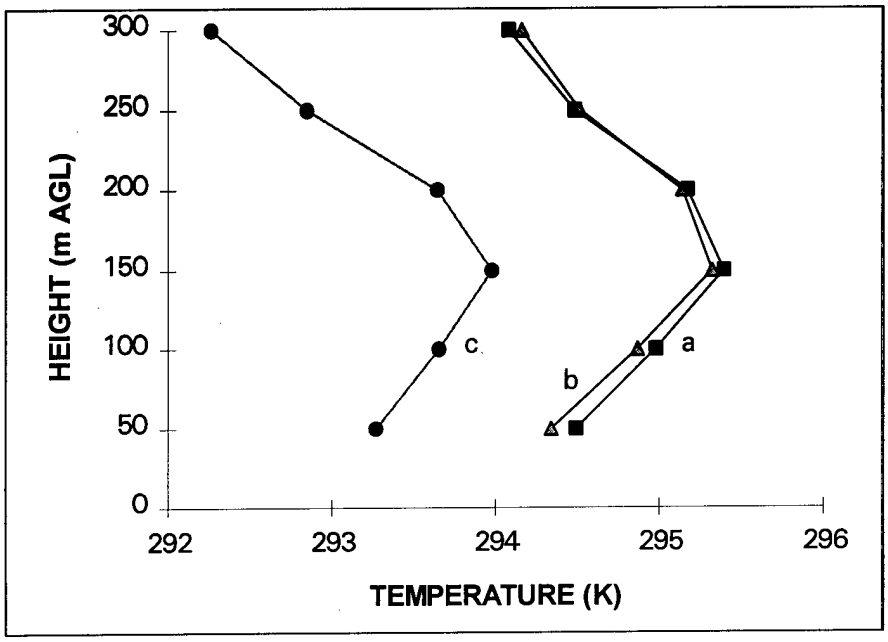


Figure 3: LA-TEAMS results without aerosol (a) and with a small dust aerosol with a concentration of $2 \times 10^{-5} g/m^3$ (b), and a water fog (at saturation) with concentration of $4 \times 10^{-4} g/m^3$ (c).

As can be seen from figure 1, the temperature profile at 0400 LST matches the actual data very well. The slight discrepancy from 200 to 300 m is due to the LA-TEAMS model having no atmospheric layers above 300 m. This results in slightly higher cooling rates than actually occur. This problem can easily be corrected by including more cloud layers in the model above 300 m, with the trade off of increased computation time. Of course less destabilization is predicted by LA-TEAMS than actually occurs because the LA-TEAMS algorithm includes only radiative effects.

The profile may be modified by adding aerosols to the atmospheric model. Figure 3 shows this modification using a dust aerosol from COMBIC (Ayres, DeSutter 1994) with a concentration of $2 \times 10^{-5} g/m^2$ (b), and a water fog under saturation conditions at a concentration of $4 \times 10^{-4} g/m^2$ (a).

4. CONCLUDING REMARKS

The LA-TEAMS model does predict the temperature profile of the NSBL with low wind speeds over homogeneous desert. Future work will include better surface heat loss models and inclusion of turbulence effects for daylight conditions.

REFERENCES

André, J. C. and L. Mahrt, 1982. "The Nocturnal Surface Inversion and Influence of Clear-Air Radiative Cooling." *J. Atmos. Sci., 39*:846–878.

Ayres, S. D. and S. DeSutter, 1994. *Combined Obscuration Model for Battlefield Induced Contaminants (COMBIC92) Model Documentation.* in press.

Chandrasekhar, S., 1960. *Radiative Transfer*. Dover, NY.

Garratt, J. R. and R. A. Brost, 1982. "Radiative Cooling Effects Within and Above the Nocturnal Boundary Layer." *J. Atmos. Sci., 38*:2730–2745.

Grisogono, B. and R. E. Keislar, 1992. "Radiative Destabilization of the Nocturnal Stable Atmospheric Boundary Layer Over the Desert." *Boundary Layer Meteorology, 61*:1–12.

Hansen, J. E., 1969. "Radiative Transfer by Doubling Very Thin Layers." *Astrophys. J., 155*:565–573.

Miller, A., R. C. Shirkey, and M. A. Seagraves, 1978. *Calculation of Thermal Emission From Aerosols Using the Doubling Technique*. ASL-TR-0020, U. S. Army Atmospheric Sciences Laboratory, White Sands Missile Range, NM 88002.

Peterson, W., F. Eaton, D. Garvey, J. Hines, K. White, and J. Kahler, 1987. *Atmospheric Characterization at White Sands Missile Range for the SDC II Program*. ASL-DR-87-0003-8, U. S. Army Atmospheric Sciences Laboratory, White Sands Missile Range, NM 88002-5501.

Roberts, R. E., J. E. A. Selby, and L. M. Biberman, 1976. "Infrared Continuum Absorption by Atmospheric Water Vapor in the 8-12-μm Window." *App. Opts., 15*:2085–2090.

Yee, Y. P., R. A. Sutherland, R. Davis, S. W. Berrick, and M. Orgill, 1993. "The Radiative Energy Balance and Redistribution (REBAR) Program." In *Proceedings of the 1993 Battlefield Atmospherics Conference*, M. E. Creegan and J. R. Elrick (Eds.), White Sands Missile Range, NM, pp. 181–194. U. S. Army Research Laboratory, Battlefield Environment Directorate.

COMPARISON OF BOUNDARY-LAYER WIND AND TEMPERATURE MEASUREMENTS WITH MODEL ESTIMATIONS

R. J. Okrasinski
Physical Science Laboratory
New Mexico State University, New Mexico 88003, USA

A. Tunick
Battlefield Environment Directorate
U.S. Army Research Laboratory
White Sands Missile Range, New Mexico 88002, USA

ABSTRACT

Five simple models that can estimate vertical profiles of wind speed or temperature in the boundary layer were evaluated by comparing their predictions with measured data. The models tested consist of three Monin-Obukhov similarity algorithms for predicting wind speed and temperature, a p-profile algorithm for estimating wind speed, and an inversion algorithm for estimating temperature. The data for the study were collected by towers, sodars, and radiosondes at Ft. Bliss in 1990 and White Sands in 1991. Using one or two levels of tower measurements, wind speed and temperature were predicted by the models at several other measurement heights and then statistically compared with the measured data. The results are presented showing the comparability of the model estimations as a function of height above the surface and time of day.

1. INTRODUCTION

A knowledge of the vertical structure of wind speed and temperature in the atmospheric boundary layer is required for many applications. This information is often obtained by merging available in situ measurements collected on a mast or tower with upper-air data collected by balloons or remote sensors. Depending on the instrumentation used, however, there may be gaps in the data. For example, there is usually a fifty to several-hundred-meter difference between the highest tower measurement and the lowest upper-air measurement. Data at some heights may, therefore, have to be estimated from measurements at other altitudes.

Five models that can be used for this purpose were evaluated in this study. Three use the similarity hypothesis of Monin and Obukhov (1954) to predict temperature and wind speed, one is a p-profile for estimating wind speed, and another is an inversion algorithm for estimating temperature. The models were evaluated using tower, sodar, and radiosonde measurements collected at three field experiments. Vertical profiles of wind speed and temperature, generated by the models using one or two levels of the tower data, were statistically compared to the other measured data to determine the relative accuracies of the model predictions as a function of altitude and time of day.

2. INSTRUMENT DESCRIPTION AND DATA COLLECTION

The data used in the analysis were collected by the U.S. Army Research Laboratory to support three acoustic propagation experiments. The first experiment was conducted June 4-25, 1990, at Ft. Bliss, New Mexico; and the other two were conducted at Dirt Site in the extreme southeast corner of White Sands Missile Range (WSMR), New Mexico, on July 11-29 and August 19-29, 1991.

WSMR is located in the south, central part of the state within a broad basin between two mountain ranges. The climate and vegetation are typical of the southwestern U.S. desert. The main Dirt Site test range, consisting of a rectangle approximately 200 m wide and 2 km long, has been plowed several times in the past 15 years to support earlier experiments, so that the area is rather flat with vegetation generally less than 1 m high. It is surrounded by mesquite-covered sand hills between 1.5 and 2.5 m high. The site elevation is about 1260 m above sea level.

The Ft. Bliss site is approximately 15 km east of the WSMR location. Vegetation and topography are similar to the unplowed portion of the WSMR site. The elevation is somewhat higher at about 1390 m above sea level.

It was very warm and dry during the Ft. Bliss experiment. The average daily maximum 2-m temperature was 36 °C, and the average dewpoint was 4 °C. It was somewhat cooler and more humid at WSMR. Mean maximum daily temperature was 31 °C, and the average dewpoint was 14 °C.

All three locations were instrumented with a 10-m tower, a radiosonde station, and a Doppler sodar in close proximity. At WSMR, there was also a 30-m tower approximately 1 km to the south of the other equipment.

The 30-m tower was instrumented at 2, 4, 8, 16, and 30 m with temperature sensors and propeller anemometers. Relative humidity was measured at 2 and 30 m. The data were averaged for 15-min periods before being recorded. During the two acoustic propagation experiments, measurements were collected only when personnel were at the site supporting the tests. Approximately 107 hours of data were collected during the July test, and about 144 hours were collected during the August experiment. Data were also recorded continuously and unattended between the two experiments from July 30 to August 13. A total

of about 610 hours of data was collected between July 11 and August 29.

The 10-m masts were instrumented at 1, 2, and 10 m. Wind speed and direction were measured by cup and vane anemometers, and temperature data were measured with thermocouples. At WSMR, 15-min averaged data were collected every day between July 9 and August 31. Except for two days, measurements were recorded 24 hours per day. Fifteen-minute data were recorded 24 hours per day on June 1-12 and June 13-25 at Ft. Bliss.

Doppler sodars were used to remotely measure wind parameters using acoustic sounding. At WSMR, 15-min averaged wind data were collected at 12 heights, 50 m apart, from 50 m to 600 m above the surface on 49 days between July 12 and August 31. More than 23 hours of data were recorded on 43 of the days. At Ft. Bliss, 15-min averaged data were collected at 15 heights, 50 m apart, from 60 m to 760 m above the surface. Approximately 279 hours of sodar data were collected during 14 days between June 4 and June 25.

Two different radiosonde systems were used. For the Ft. Bliss and July WSMR experiment, an automatic radio theodolite system was deployed which consists of a 1680 MHz sonde tracked by an automatic radio theodolite using a phase array antenna. Height, temperature, humidity, and balloon-to-ground azimuth and elevation angles were recorded for every 4-5 seconds of flight. Wind data were computed using the height and angle data for 1-min layers. For the August WSMR experiment, an Omega Navaid system was substituted to collect data at greater heights. Measurements were provided for every 10 seconds of flight, and the winds were calculated for 4-min layers. Fifty-eight radio theodolite soundings were flown at Ft. Bliss, and 33 soundings were flown at the July WSMR experiment. Each flight was tracked to about 5 km. Seven Omega sondes, tracked to 15-20 km, were released during the August 1991 WSMR experiment.

3. DESCRIPTION OF THE MODELS

3.1 Similarity Models

Three models based on the Monin-Obukhov hypothesis were evaluated. Two of them use a linear-quartic approach named the O'KEYPS representation by Yaglom (1977) from the initials of the inventors Obukhov (1946), Kanzanski and Monin (1956), Ellison (1957), Yamamoto (1959), Panofsky (1963), and Sellers (1962). In the O'KEYPS algorithms, an iterative method is used to solve for three scaling parameters which determine the change in wind speed and temperature with respect to height within the surface boundary layer. These parameters are the friction velocity u_*, the scaling temperature θ_*, and the Monin-Obukhov length L. One of the O'KEYPS models, described by Wilson (1989), uses temperature data at two heights, wind speed data at one height, and an estimate of the roughness height to compute the scaling parameters. The other one is a modification of this algorithm using two levels of wind and temperature measurements and no roughness height.

The third similarity-based technique, named the MARIAH method, was developed by Rachele et al. (1994). In this approach, the scaling parameters are calculated directly without iteration using at least two levels of wind and temperature measurements. This method is new, although based on traditional concepts of similarity. The advantages of employing the MARIAH approach are (1) the algorithm executes quickly without laborious iterative schemes imbedded into the program, (2) as many or as few levels of tower data as are available can be used to determine layer-averaged, similarity profile structure, and (3) while in use, the similarity premise of stationarity is preserved.

3.2 P-Profile

The vertical profile of wind speed with height was also estimated with p-profile curves. This concept was first postulated by Frost (1947). The wind speed S at level z is defined as

$$S = S_o \left[\frac{z}{z_o} \right]^p , \qquad (1)$$

where S_o is the wind speed at the height z_o. The exponent p is fitted to the measured wind speeds at two selected heights.

3.3 Inversion Model

This model was developed by Hopfer and Blanco (1988) to predict upper-air temperature and pressure using 24 hours of in situ tower measurements. Only the temperature predictions were considered in this study. An estimated temperature profile is created by applying a boundary layer correction to a U.S. Standard Atmosphere profile adjusted to the mean 24-hour temperature. The equation is

$$T(z,t) = T_{std}(z) + \Delta T(z,t), \qquad (2)$$

where $T_{std}(z)$ is the adjusted standard atmosphere and $\Delta T(z,t)$ is the correction. The correction is determined from the heat exchange coefficient and Fourier coefficients fitted to 24 hours of 10-m temperature measurements.

4. COMPARISON OF MODEL ESTIMATES WITH MEASURED DATA

4.1 Tower Data Comparison

The relative accuracies of the p-profile and similarity models at heights close to the surface were investigated using the 15-min averaged 30-m tower data collected at WSMR. Wind speed and temperature measured at 2 and 8 m were used to predict the same parameters at the other three tower levels at 4, 16, and 30 m. Root-mean-squares (rms) of the differences between these predictions and the measured data at the three levels were then computed for each 2-hour period of the day.

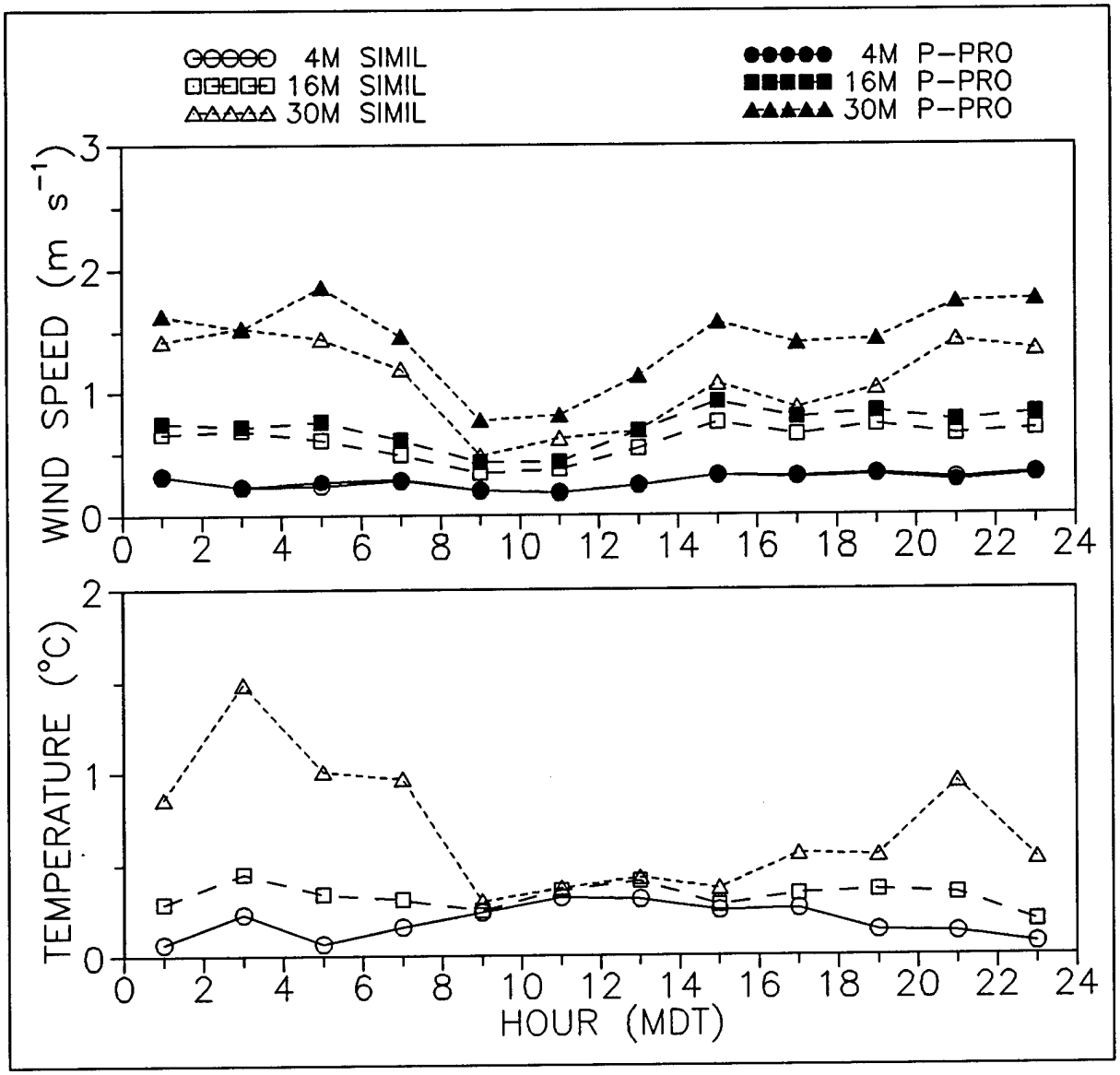


Figure 1. Root-mean-square differences between measured 4-, 16-, and 30-m wind speeds and temperatures and values estimated from 2- and 8-m measurements using Monin-Obukhov similarity and p-profile algorithms.

Statistics were first computed for the three similarity models. Only data in which all three methods converged to a solution were used in this analysis, so that the statistics for each method were computed using the same measurements. Little difference was found among the predictions of the three techniques. In particular, the MARIAH and two-level O'KEYPS method statistics were almost identical.

The same statistical comparison among the similarity, p-profile, and linear fit algorithms is shown in figure 1. The best estimates were given by the similarity model. The rms wind speed and temperature differences between the predicted and measured data were .2-.3 m s^{-1}

and .1-.3 °C, respectively, at 4 m; and .4-.7 m s^{-1} and .2-.4 °C, respectively, at 16 m. There was not much diurnal variation at these two heights. At 30 m, however, the nighttime statistics were considerably poorer than the daytime statistics. Rms wind speed differences were .5-1.0 m s^{-1} during the day and approximately 1.5 m s^{-1} at night. Temperature rms differences at 30 m were .4-.6 °C and 1.0-1.5 °C during the day and night, respectively. These results indicate that the nighttime similarity estimates are not very accurate above 16 m due to shallowness of the surface boundary layer during those times. Another problem at night is the fact that the similarity algorithm often fails to converge to a solution. In this study, a solution was obtained about 50% of the time during the early morning hours before dawn and 90-96% of the time during midday.

Agreement between the p-profile predictions and the measured data was somewhat poorer. Compared to the similarity rms differences, the p-profile rms differences were about the same at 4 m, slightly greater at 16 m, and as much as .5 m s^{-1} higher at 30 m. The statistics of both models had a similar diurnal variation.

4.2 Sodar Data Comparison

The statistical analysis described in the previous section was used to compare wind speed estimated by the similarity and p-profile models with conjunctive sodar data collected at the two test sites. Fifteen-minute averaged 2- and 10-m data collected on the 10-m mast were used by the two models to predict wind speed at the two sodar measurement heights of 50 and 200 m at WSMR and 60 and 210 m at Ft. Bliss. Statistics were computed using only data in which a solution was obtained from both models.

The results are shown in figure 2. As expected, there was better agreement between the predicted and measured data during midday when the surface layer is usually fairly deep. The rms differences between the similarity estimates and the measured data were about 2.0 m s^{-1} during those times at both measuring heights. By comparison, the rms differences between in situ wind speed measurements on a 300-m tower and conjunctive Doppler sodar measurements were found to be 1.0-1.4 m s^{-1} in a study by Chintawongvanich et al. (1989). At night, the similarity estimates were somewhat poorer at 50 and 60 m and much poorer at 200 and 210 m. The p-profile statistics were comparable with the similarity statistics at the lower height. At 200 and 210 m, the p-profile rms differences were the same or larger than the similarity differences during the day and smaller at night.

4.3 Radiosonde Data Comparison

The similarity, p-profile, and inversion models were used to estimate wind speed or temperature at several radiosonde measurement heights for statistical comparison with the radiosonde data. Fifteen-minute averaged in situ measurements collected on the 10-m mast were utilized for the model inputs. Two- and ten-meter data closest in time to the balloon release were fed into the similarity and p-profile models, and 24 hours of 10-m temperature data collected on the day of the launch were required by the inversion algorithm. The minimum radiosonde measurement heights used in the analysis were 50 m for temperature,

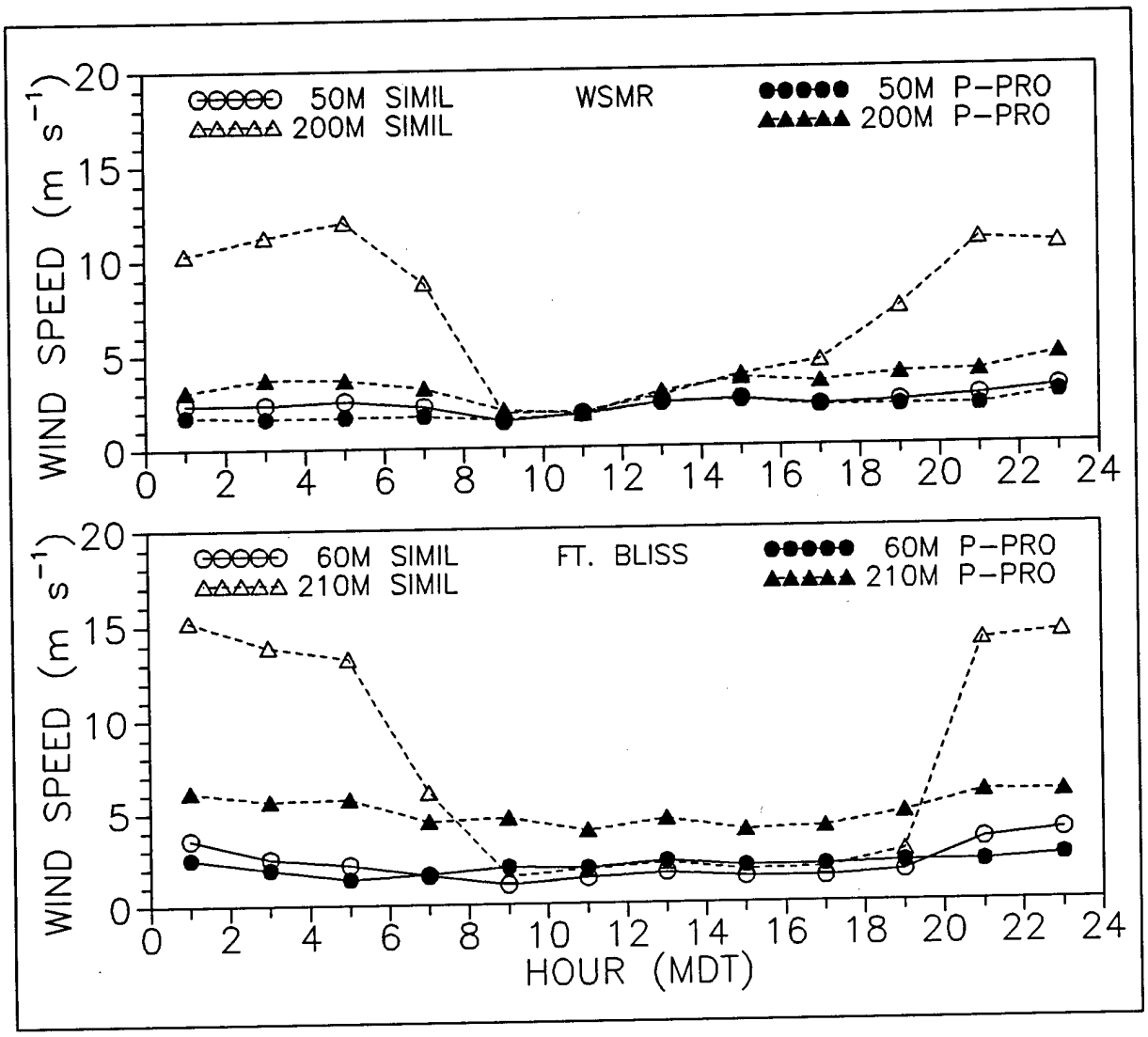


Figure 2. Root-mean-square differences between sodar wind speed measurements collected at 50 and 200 m at WSMR (top) and 60 and 210 m at Ft. Bliss (bottom) and values estimated from 2- and 10-m mast data using Monin-Obukhov similarity and a p-profile fit.

200 m for wind data collected by the radio theodolite, and 600 m for wind data collected by the Omega Navaid system. Because of the small number of radiosonde flights, statistics were computed for only two time-of-day intervals. One interval, 0900 MDT inclusive to 1900 MDT, represents the unstable daytime boundary layer; and the other, composed of the rest of the times, represents the stable nighttime atmosphere. Only data for which a solution was obtained by all three models were used in the computations.

The rms differences between the measured and predicted data are plotted in figure 3. At WSMR, the rms wind speed differences were 1.0-1.1 m s^{-1} for the similarity predictions and 1.1-1.4 m s^{-1} for the p-profile estimates up to 500 m. By comparison, the rms vector wind differences between simultaneously tracked rawinsondes were found to be 1.0-2.0 m s^{-1} in a

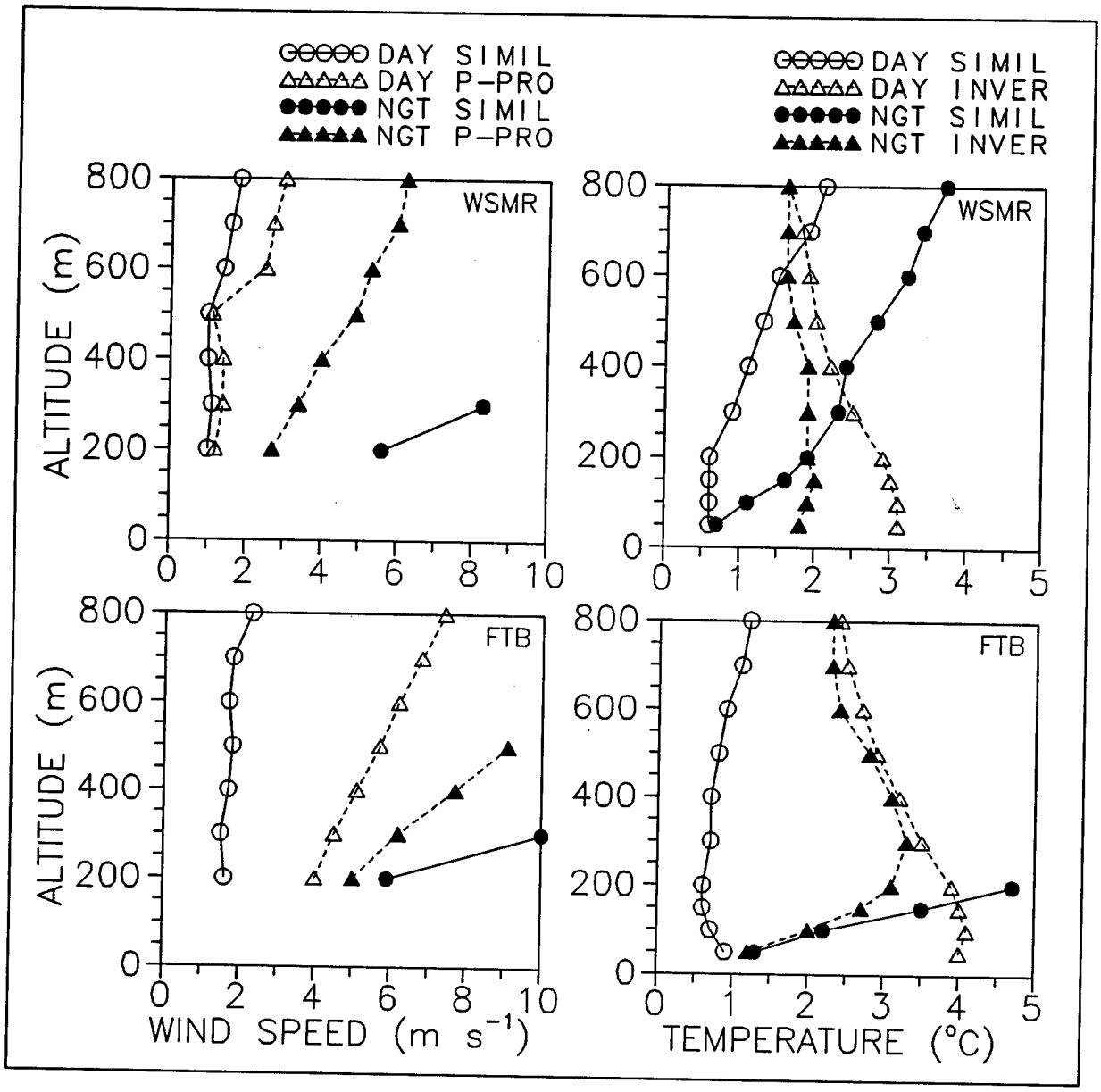


Figure 3. Root-mean-square differences between daytime and nighttime radiosonde wind speed and temperature measurements at WSMR (top) and Ft. Bliss (bottom) and data estimated from 2- and 10-m tower measurements using Monin-Obukhov similarity, p-profile fit, and inversion algorithm.

study by Olsen et al. (1991). Agreement with the measured Ft. Bliss data was somewhat poorer. For the first 500 m, similarity rms differences were 1.6-1.8 m s^{-1}. The Ft. Bliss p-profile rms differences at the same altitudes were 4.0-5.7 m s^{-1}, which is much larger than both the similarity differences and the WSMR p-profile differences. Predictions from both models were poor at night at both sites.

Rms similarity temperature differences during the day were .5-1.3 °C at WSMR and .6-.9 °C at Ft. Bliss, up to 500 m. These are not much larger than the .5 °C rms differences between

simultaneous radiosonde measurements found by Olsen et al (1991). The rms differences for the daytime inversion model predictions were much larger. At night, the comparabilities of the similarity predictions were considerably worse than the daytime predictions, except at 50 m. The nighttime inversion rms differences, which ranged between 1.2 °C and 3.3 °C, were smaller than the similarity rms differences at heights above 200 m at WSMR and above 50 m at Ft. Bliss.

5. SUMMARY

Little difference was found among the predictions of the MARIAH and two O'KEYPS similarity models. The statistics of the differences between measured wind speed and temperature estimated by the three algorithms at 4, 16, and 30 m using 2- and 8-m tower data were almost the same for each model.

There was good agreement between the similarity model predictions at 4 and 16 m and the measured data at all times of the day. In as many as half of the nighttime cases, however, no prediction was obtained, because the algorithm would not converge to a solution. Predictions at 30 m agreed well with the measured data during the day, but did not agree as well at night. This was also true at the sodar and radiosonde measurement heights. There was good agreement between the upper-air measurements and the similarity model predictions up to several hundred meters above the surface between 0900 and 1900 MDT and very poor agreement outside those times.

Compared to the similarity predictions, the agreement between the p-profile predictions and the tower data was almost the same at 4 and 16 m and somewhat poorer at 30 m. The difference in comparabilities between the two models at the latter height was generally the same at all times of day. At the sodar and radiosonde heights, the p-profile predictions were less comparable than the similarity predictions during the day and more comparable at night. The nighttime p-profile predictions were still considerably less comparable than the daytime predictions, however.

Neither the day nor night inversion algorithm estimates agreed very well with radiosonde temperature measurements within the first few hundred meters of the atmosphere, although the agreement of the nighttime inversion predictions was better than the nighttime similarity predictions at heights above 200 m at WSMR and above 50 m at Ft. Bliss.

REFERENCES

Ellison, T. H., 1957. "Turbulent Transport of Heat and Momentum from an Infinite Rough Plane." *J. Fluid Mech.*, 2:456-466.

Frost, R., 1947. "The Velocity Profile in the Lowest 400 ft." *The Meteorological Magazine*, 76:14-17.

Hopfer, A. G. and A. J. Blanco, 1988. *Boundary Layer Enhancement of a Temperature and Pressure Analytic Model.* ASL-TR-0224, Army Research Laboratory, Battlefield Environment Directorate, White Sands Missile Range, NM.

Kazanski, A. B. and A. S. Monin, 1956. *Izv. Akad. Nauk., S.S.S.R. Ser. Geofiz.*, Ser. 1, 79.

Monin, A. S. and A. M. Obukhov, 1954. "Basic Regularity in Turbulent Mixing in the Surface Layer of the Atmosphere." *Trans. Geophys. Inst. (Trudy) Acad. Sci.*, USSR, 24:163-187.

Obukhov, A. M., 1946. "Turbulence in an Atmosphere of Non-Homogeneous Temperature." *Trans. Inst. Theor. Geophy.*, USSR, 1:95-115.

Olsen, R. O., R. J. Okrasinski, and F. J. Schmidlin, 1991. "Intercomparison of Upper Air Data Derived from Various Radiosonde Systems." In *Preprints: 7th Symp. on Meteor. Observations and Instrumentation*, American Meteorological Society, Boston, MA, pp 232-236.

Panofsky, H. A., 1963. "Determination of Stress from Wind and Temperature Measurements." *Quart. J. Roy. Meteorol. Soc.*, 89:85-94.

Rachele, H., A. Tunick and F.V. Hansen, 1994. "MARIAH-A Similarity Based Method for Determining Wind, Temperature, and Humidity Profile Structure in the Atmospheric Surface Layer." To be published in *J. Appl. Meteor.* Jan/Feb 1995.

Sellers, W. D., 1962. "A Simplified Derivation of the Diabatic Wind Profile." *J. Atmos. Sci.*, 19:180-181.

Wilson, D. K., 1989. *Reconstruction of Sound Speed Profiles from Rock Springs Meteorological Data.* Unpublished report, Pennsylvania State University, PA.

Yaglom, A. M., 1977. "Comments on Wind and Temperature Flux Profile Relationships." *Bound.-Layer Meteor.*, 11:89-102.

Yamamoto, G., 1959. "Theory of Turbulent Transfer in Non-Neutral Conditions." *J. Meteor. Soc. Japan.*, 37:60-70.

OPTICAL TURBULENCE MEASUREMENTS AT APACHE POINT OBSERVATORY

Frank D. Eaton, John R. Hines, William H. Hatch
U S Army Research Laboratory
AMSRL-BE-E, WSMR, NM 88002-5501

James J. Drexler, James Northrup
Lockheed Engineering and Science Company
WSMR, NM 88002-5501

ABSTRACT

Optical turbulence measurements taken using the Atmospheric Turbulence Measurement and Observation System (ATMOS) and an acoustic sounder at the newly established Apache Point Observatory (APO) are presented for spring of 1994. The APO is located at 9200 ft. MSL about 18 miles south of Cloudcroft, NM. The ATMOS is an optical device for determining "seeing" conditions by measuring angle-of-arrival fluctuations through two subapertures of a telescope. This optical arrangement, utilizing a differential measurement technique, eliminates errors due to tracking, vibration, and wind loading.

Results shown include examples of convective activity and wave activity detected from the sodar and are displayed as time-height maps. Examples of the transverse coherence length, both day and nighttime at APO, are shown. A method to predict optical turbulence at APO is discussed.

1. INTRODUCTION

The refractive index structure parameter (C_n^2) and derived parameters such as the transverse coherence length (r_o) and the isoplanatic angle (θ_o) are of fundamental importance in understanding optical, radio, and acoustic propagation in the atmosphere and are of considerable interest to many remote sensing efforts. Optical turbulence has imposed a major problem upon optical astronomy degrading imagery observed with the large telescopes at major observatories. Ground-based optical systems, thermosondes, and remote sensors are used for sensing optical turbulence parameters (Eaton et al., 1988a). High resolution C_n^2 profiles can be obtained from radar or sodar measurements.

Brant et al.(1987) provided measured seeing values at several observatories as well as day-time seeing statistics at Sacramento Peak Observatory, New Mexico. They

cautioned comparing absolute values due to different techniques used, different local effects such as due to dome seeing, calibration of different systems, and the validity of the particular zenith angle correction used. The measured results from Sacramento Peak Observatory were taken using the solar vacuum telescope with the entrance aperture 40m above the ground (Brandt et al.,1987). Since no dome was used and this configuration avoided a large contribution of turbulence from near ground convection, the r_o values are predicted to exceed those that would be taken using a conventional near-surface dome.

The results presented here include r_o values and C_n^2 time-height displays taken at the Apache Point Observatory using a single axis sodar.

2. SITE

The Apache Point Observatory (APO) is an astronomical observatory located in the Lincoln National Forest in the Sacramento Mountains at an altitude of 2800 meters (9200 ft) MSL. It is owned and operated by the Astrophysical Research Consortium (ARC) consisting of the University of Chicago, Institute of Advanced Study, Johns Hopkins University, New Mexico State University, Princeton University, University of Washington, and Washington State University. The APO was recently established for operation (May 10, 1994) when the 3.5 meter multipurpose telescope observed a solar eclipse. This telescope is located at 32° 46′ 50.4" N, 105° 49′ 11.7" W. Three other telescopes at the APO are in various stages of completion.

One unique purpose telescope under design is the Sloan Digital Sky Survey (SDSS) telescope which will be used under appropriate seeing conditions to survey the night sky with sensitive imaging equipment. Since excellent seeing is a requirement for this effort, the enclosure for the SDSS telescope was constructed on pillars west of the mountain ridge to reduce degrading turbulent conditions. The Atmospheric Turbulence Measurement and Observation System (ATMOS) used in this study was mounted atop the pedestal that was constructed for future installation of the 2.5 meter SDSS telescope. The sodar was installed on the ridge southeast of the SDSS enclosure.

3. METHODOLOGY

Measurements were taken at the APO on May 21, 22, 23 and June 8, 9, 23, 24, 25, 1994 to examine the turbulent conditions during late spring at the SDSS site. The tests involved use of two systems at the APO, the ATMOS and a single axis sodar. The tests involved several interesting measurement considerations.

3.1 ATMOS

The classical astronomical seeing problem was put on a more quantitative basis than in the past (Fried,1966) by the formulation of the transverse coherence length (r_o) as defined as:

$$r_o = [0.423k^2 \int_o^\infty C_n^2(z)dz]^{-3/5}$$

where:

k = $2\pi/\lambda$ (λ is the wavelength of light), and
C_n^2 = refractive index structure parameter, and
z = altitude above ground for vertical viewing.

Effects of atmospheric turbulence on optical systems that are sensitive to wavefront distortions can be conveniently evaluated with knowledge of r_o. Selection and evaluation of observatory sites traditionally required an examination of astronomical seeing. Methods to appraise seeing have been used for over 50 years, including measurements of image spread and motion by photography of star trails as well as photoelectric detection of scintillation (Babcock,1963; Couder,1936; Harlen and Walker,1965; Whitford and Stebbins,1936). The Polaris seeing monitor was used for the site selection of Kitt Peak National Observatory (Meinel,1960). The literature displays a natural application of the evolution of technology to seeing monitors such as replacing film techniques with linear array CCDs and finally CCD cameras. The analysis of line spread function information obtained from stellar images using linear array CCDs to obtain r_o from the modulation function as well as the technique used in this study based on differential image motion are documented by Eaton et al.(1988). Roddier (1987) and Fried (1975) have summarized both the single and differential image motion techniques for evaluating seeing conditions.

The ATMOS uses a differential angle-of-arrival approach by collecting light from a single star with two subapertures (11-cm diameter) on a 35.5cm (14in) diameter telescope. The subapertures have optical glass wedges so that the two images can be separated and be focused onto a 2-D charged-coupled device (CCD) camera placed at the focal plane. Two nearly parallel paths of turbulence are measured at 23.5cm separation. The method eliminates common system errors caused by tracking errors, vibration, and wind loading since such effects will display identical image motion and not be included in the variance of centroid differences. The ATMOS includes a frame grabber that can vary exposure time and frame rates up to in excess of 300 fps. The CCD camera is intensified and uses an electronic shutter capable of as short as 20 μsec exposure times.

The relationship used in this study to calculate r_o with the ATMOS is:

$$r_o = \{\frac{27.5\ F^2}{k^2\ d^{1/3}\sigma_r^2}[1-\frac{25}{36}(\frac{d}{\mu})^{1/3}]\}^{3/5}$$

where:

F = the focal length of the receiving telescope
d = the diameter of each subaperture
μ = center-to-center separation of the subapertures, and

σ_r^2 = mean-square of the relative distance between the centroids of the two images.

3.2 Sodar

Sodar (sonic detection and ranging) detects the temperature structure function (C_T^2) and ultimately provides C_n^2 through calculations using simultaneous sampled ambient temperature and pressure values.

The sodar equation is:

$$C_T^2 = \frac{P_r T_o^2 e^{2\bar{\alpha}R} L_e}{E_r[P_t \cdot E_t][(\frac{c\tau}{2})(\frac{A}{R^2} \cdot G)][0.0039k^{1/3}]}$$

where:

T_o = surface temperature
α = molecular and classical adsorption
E_r = receiver efficiency
E_t = transmitter efficiency
c = speed of sound
τ = pulse length
A = antenna area
G = antenna directivity
L_e = excess attenuation coefficient

The sodar used is an Echosonde model single-axis system manufactured by Radian Corporation. Three-axis systems are used for obtaining Doppler winds. The sodar is typically operated at 1850Hz and 75 W transmitted power using a 40 ms pulse length and a 1.5m (5 ft) diameter antenna. Backscatter is averaged every 10 sec in 200 range gates to obtain C_n^2 from 30 to 1024m AGL. Some researchers obtain C_n^2 values from sodar by comparing the backscattered values to in situ values obtained from tower sensors. Calibration of the sodar used in this study was accomplished by a first principles approach.

4. RESULTS

4.1 Transverse Coherence Length (r_o) Measurements

Transverse coherence length (r_o) measurements were taken during 3 periods; 21, 22, 23 May 1994, 8, 9 June 1994, and 23, 24, 25 June 1994. All results are evaluated for 0.5 μm wavelength and corrected for zenith viewing. Figure 1 displays the results from the first data set in May. Arcturus was sensed during the first two hours at fairly high zenith angles in a direction over the Tularosa Basin, possibly contributing to the rapid increase in values. Vega was sensed from about 3:00 to 5:00 MST in a

direction over forested terrain. The next two days of data collection showed values fluctuating from a low near 1cm to a high around 15cm with the majority of the values near 8cm. The next data run, 8 to 9 June, showed somewhat higher values on the average. The values were in general low on June 23 with a slight trend of increasing r_o values to the first few hours of June 24 as shown in Figure 2. Measurements commenced during midafternoon and showed low r_o values as expected due to surface convective activity. From about 17:00 to 19:00 MST r_o increased dramatically from about 2.5cm to over 16cm. This effect is attributed to entering the evening "neutral" event and is probably enhanced due to the strong solar heating on the west-facing slope above which the measurements were taken. For the remainder of the night the r_o values fluctuated between about 10cm to 14cm.

Figure 3 shows all of the data collected during the 8 individual days plotted together vs. time. This displays the large variability that can be found even for a limited time period and conditions. The least variability shown is during the afternoon hours where surface turbulence contributes heavily to the total profile. Figure 4 displays a histogram of the total 1368 r_o measurements. Generally r_o and C_n^2 are found to show a log-normal or near log-normal distribution. The distribution (Figure 4) would appear more log-normal if there was an even distribution of measurements diurnally, with more low daytime values.

4.2 Sodar Measurements

The sodar was operated continuously during the spring campaign at APO. In general, the nighttime measurements showed some low level turbulence with the turbulence the lowest on June 8-9, 1994. This agrees with the measured r_o values. Figure 5 shows some wave activity extending to several hundred meters above the surface. This can be a source of C_n^2. Figure 6 shows the morning transition period with pronounced convective activity during the last one-third of the example. The convection was seen to generally produce turbulence during every midday.

5. SUMMARY AND RECOMMENDATIONS

From the results of this study three main points emerge regarding r_o during the 1994 spring at the APO:

1. Considerable variability in r_o values was found during nighttime, ranging from 1cm to 18cm. Data were collected under a variety of wind conditions with the surface wind predominantly coming from forested areas.
2. The onset of the evening neutral event showed a dramatic increase in r_o, presumably due to radiation balance and associated sensible heat changes on the west-facing slope immediately below the location of the ATMOS.
3. Sodar-derived time-height displays of C_n^2 data obtained at the APO show obvious large scale correlations with the patterns of r_o. These results demonstrate the contribution of local meteorological conditions on r_o.

Recommendations for future research examining r_0 effects at the APO include:

1. Measure r_0 under different conditions for an extended period to include different wind speed and wind direction conditions, jet stream effects, seasonal effects (with particular emphasis on snow cover), diurnal variation under various atmospheric stabilities, and the evolution of the morning and evening neutral periods.
2. Simultaneous sodar measurements at the APO, local meteorological measurements, and 50MHz radar measurements at the Atmospheric Profiler Research Facility should be correlated with the r_0 data to develop a "predictive seeing tool". Various parameters calculated from the data such as stability, wind shear, eddy dissipation rate, and gravity wave effects are expected to enhance the predictive capability over correlations of "raw" data.

6. REFERENCES

Babcock, H.W., 1963, Instrumental recording of astronomical seeing, Publ. Astron. Soc. Pac. 1-8

Brandt, P.N., H.A.Mauter, and R.Smartt, 1987, Day-time seeing statistics at Sacramento Peak Observatory, Astron. Astrophy. 188, pp.163-168

Couder, A., 1936, Optique atmospherique-measure photographique de l'agitation des images stellaries, C. R. Acad. Sci. Paris 205, pp 609-611

Eaton, F. D., W. A. Peterson, J. R. Hines, K. R. Peterman, R. E. Good, R. R. Beland, and J. H. Brown, 1988a, Comparisons of VHF radar, optical, and temperature fluctuation measurements of C_n^2, r_o, and θ_o, Theor. Appl. Climatol. 39, pp17-29

Eaton, F. D., W. A. Peterson, J. R. Hines, J. J. Drexler, A. H. Waldie, and D. B. Soules, 1988b, Comparison of two techniques for determining atmospheric seeing, In Proc. SPIE Vol 926, Orlando,Fl, pp319-334

Fried, D. L., 1966, Optical resolution through a randomly inhomogeneous medium for very long and very short exposures, J. Opt. Soc. Am. 567,pp1372-1379

Fried, D. L., 1975, Differential angle of arrival: theory, evaluation, and measurement feasibility, Radio Science 10, pp77-86

Harlan, E. A., M. F. Walker, 1965, A star-trail telescope for astronomical site-testing, Publ. Astron. Soc. Pac. 77, pp246-252

Meinel,A. B., 1960, Astronomical seeing and observatory site selection, Telescopes, (ed. G.P.Kuiper and B. M. Middlehurst), Univ. Chicago Press

Nastrom, G. D., and F. D. Eaton, 1983, The Coupling of Gravity Waves and Turbulence at White Sands, New Mexico, from VHF Radar Observations, Jour. of

Appl. Meteorol. Vol. 32, No 1, pp81-87

Whitford, A. E., and J. Stebbins, 1936, Photoelectric measurement of scintillation of stars, Publ. Am. Astron. 8:228

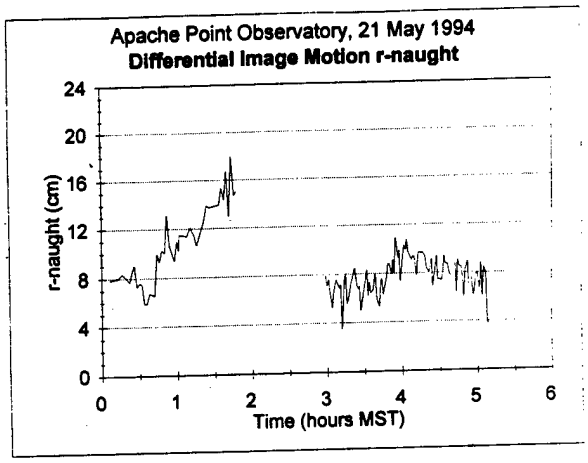


Figure 1. Measurements of r_o on 21 May 1994.

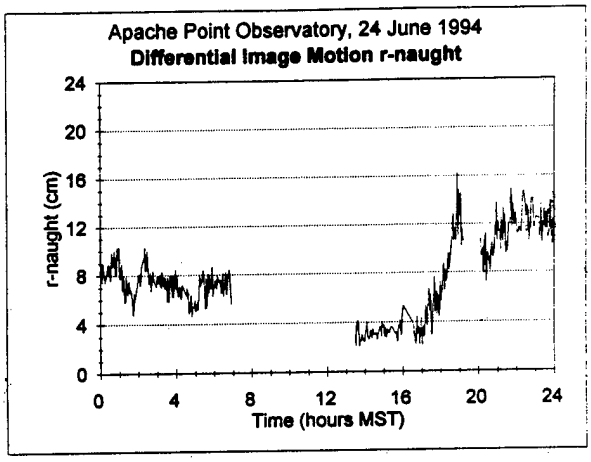


Figure 2. Measurements of r_o on 24 June 1994.

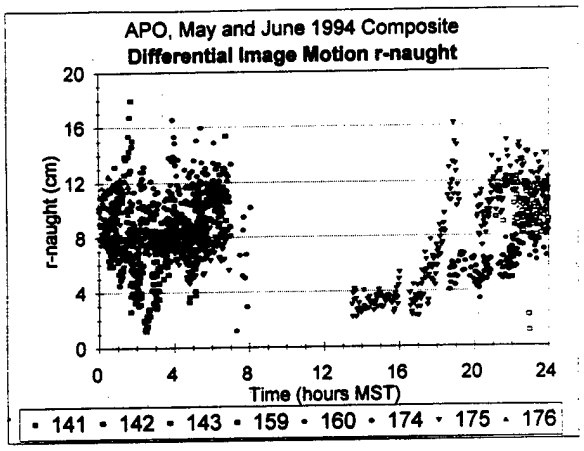


Figure 3. Composite of all r_o data measured during spring 1994 at APO.

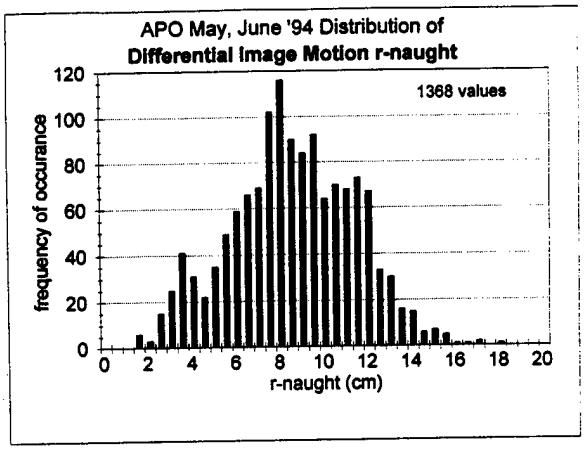


Figure 4. Histogram of all r_o measurements.

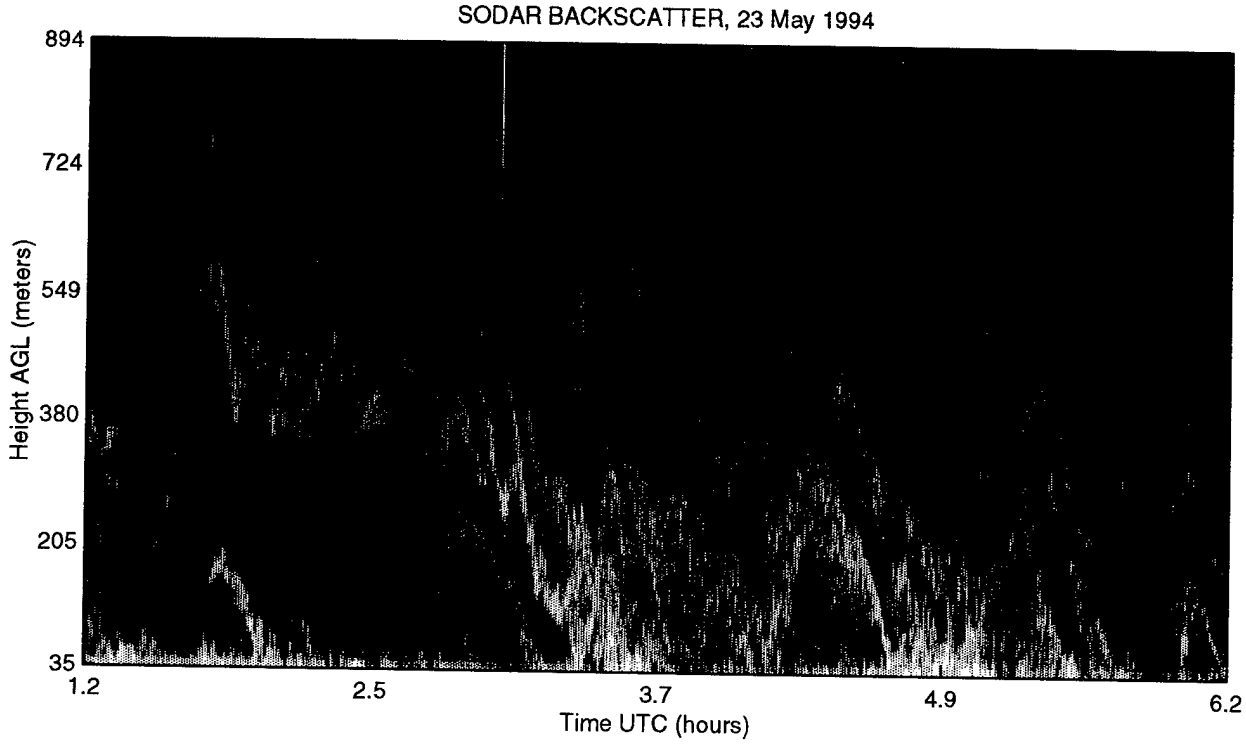


Figure 5. Wave activity sensed by the sodar.

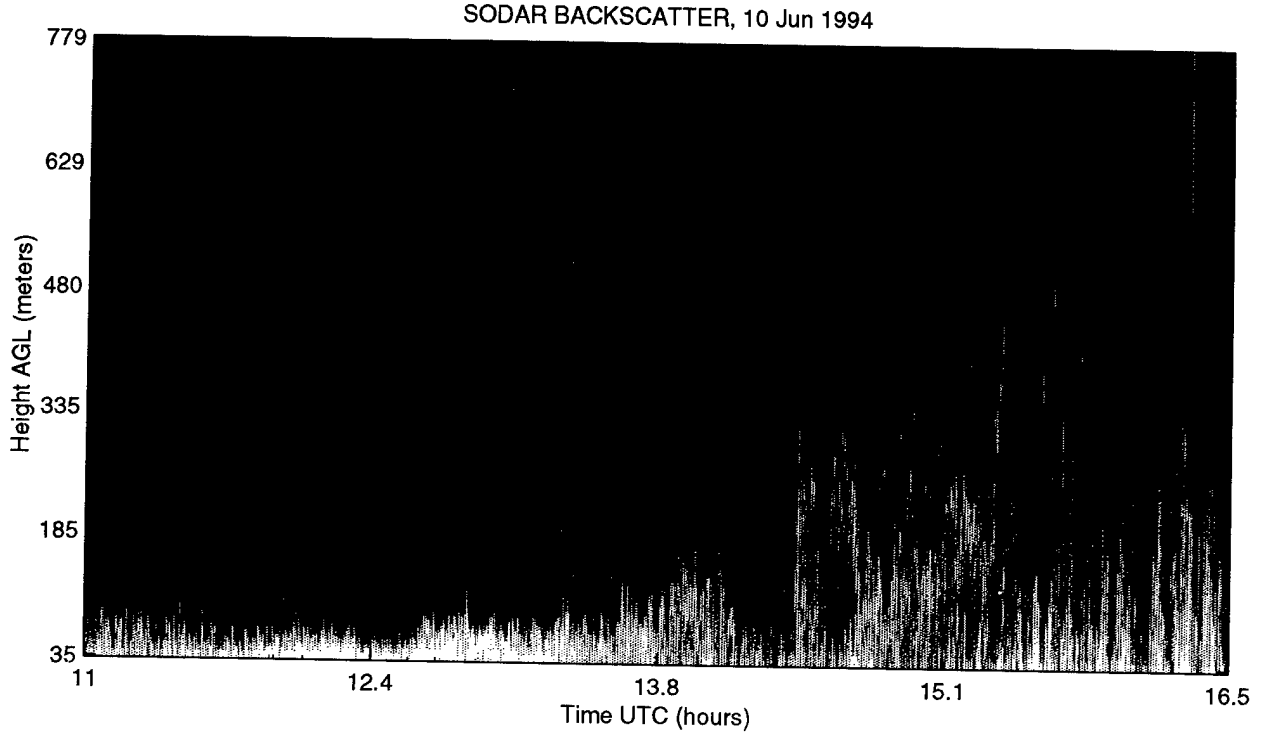


Figure 6. Morning transition period sensed by the sodar.

THE APRF SODAR: BRIDGING THE LOWER BOUNDARY LAYER

John Hines, Frank Eaton, Scott McLaughlin, William Hatch
Army Research Laboratory
AMSRL-BE-E, White Sands Missile Range, NM 88002

Glenn Hoidale, Wayne Flowers, Linda Parker-Sedillo
Science and Technology Corporation
White Sands Missile Range, NM 88002

ABSTRACT

A description, including operating parameters, of the sodar used at the Atmospheric Profiler Research Facility (APRF) is presented. Characteristics of the sodar and 924-MHz radar are given as they pertain to wind measurements. The sodar provides wind and refractive index structure parameter data from 20 m to 625 m at 25 m height resolution while the 924 MHz radar typically senses from 100 m to around 2500 m in 100 m gates. Quality control methods for both systems are discussed.

Results shown and discussed include sodar and tower-derived wind measurement comparisons as well as sodar and 924-MHz radar comparisons. Also, comparisons of the refractive index structure parameter (C_n^2) between the FM-CW radar, sodar and spatially separated temperature probe measurements on the tower are presented and discussed.

1. INTRODUCTION

The Atmospheric Profiler Research Facility (APRF) was established by the US Army (Hines, et al, 1993) at White Sands Missile Range (WSMR), NM in 1990 and became operational in March 1993. One of the goals in the development of the facility was to provide continuous, operational quality, hourly-averaged, quality-controlled vertical profiles of wind speed, wind direction, radar turbulence and virtual temperature from the surface to near 20 km Above Ground Level (AGL). The facility's hourly-averaged vertical profiling capability is of varying vertical resolution and represent a composite of data generated from anemometers located at eight levels of a 150-m tower, a sodar and 924-, 404 (low mode)-, and 50-MHz radar wind profilers.

The vertical composite profile data are available in both graphical and tabular format over **Internet** from **aprf.arl.mil (155.148.18.200)** via the file transfer protocol (ftp) or through the use of the World Wide Web **Mosaic-type** browser access to the **APRF home page (http://aprf.arl.mil/aprf.html)**. Data are available within 15 minutes of the end of a given one-hour period. Higher temporal resolution data are archived and utilized in special analysis efforts.

Specific attention is directed toward the quality control of the composite data including sodar and 924-MHz data using a continuity algorithm, system related limitations, system downtime

sources, various representative comparisons of the sodar data with the corresponding data from the 152-m tower and from the 924-MHz radar wind profiler, an example of diurnal C_n^2 as measured by the tower and the sodar, and examples of backscatter color maps obtained from the sodar and a unique FM-CW radar.

2. INSTRUMENTATION

A monostatic Radian Corporation echosonde (sodar) provides horizontal wind speed and direction at 25 m intervals from 175 to 325 m AGL to the APRF composite profile. The three-beam instrument actually samples over the range of 50 to 700 m AGL.

The sodar was originally acquired in 1982 and has subsequently undergone several modifications. Due to poor data in the 300 to 700 m AGL range, the covariance technique was replaced with the FFT (fast Fourier transform) technique. At the same time the computer was upgraded from a 286/8 type to a 486/DX50 type, thus increasing processing speed.

The antennas are pulsed sequentially every 5.83 s for 150 ms. Hence, values of U, V and W wind components are determined once every 17.49 s. This equates to just over 50 samples every 15 min. However, only 15-min average data are available for analysis. The operational parameters selected define 26 gates (wind mode) spanning the range from 50 to 700 m AGL and 200 gates (turbulence mode) spanning the range from 50 to 850 m AGL. However, as noted above only gates 6 through 12 (wind mode), corresponding to an altitude range from 175 to 325 m AGL, are utilized for the composite profile.

A single-axis sodar was temporarily located at a mountain location near the Apache Point Observatory (APO) in the nearby Sacramento Mountains. The instrument provides vertical wind speed at 25 m intervals from 50 to 700 m AGL. The antenna is pulsed sequentially every 10 s for 150 ms. Two-minute average data are available for analysis.

Both sodars also provide turbulence backscatter data over the range of 50 to 850 m AGL (APRF) and 30 to 1024 m AGL (APO). The three-beam sodar provides vertical sensed backscatter as input to the APRF developmental/calibrated index of refraction structure parameter (C_n^2) composite profile. The data represents an average of two vertical soundings (each sounding occurs approximately each 17.49 s) subsequently averaged over a 15-min average period. The single-axis sodar operates as a stand-alone instrument and reports an average of 6 vertical soundings or approximately one average report each minute.

A NOAA Wave Propagation Laboratory 924-MHz boundary layer radar provides horizontal wind speed and direction at 100 m intervals from 138 to 2038 m AGL to the APRF composite profile. The instrument actually samples over the range of 138 to 4000 m AGL.

Although only the data from certain gates from the sodar and 924-MHz radar are available over Internet in graphical and tabular format, the data from all valid gates can be made available in tabular form over Internet or other means upon special request.

A unique Radian Corporation frequency modulated - continuous wave (FM-CW) radar provides ultra-high resolution calibrated C_n^2 at 4 m intervals from 100 to 4000 m AGL in a stand-alone mode. The radar was also designed to measure winds but has never been used in that configuration due to the exceptional atmospheric turbulence reports generated. Additional

system description and relevant specifications are discussed in Eaton et al. (1995).

3. LOCATION

The APRF is nestled in the extreme southwestern corner of WSMR just 10 to 15 km east of a north-south oriented chain of mountains at 32° 24′ N and 106° 21′ E and at an altitude of 1212 m AGL. About 40 km to the east of the APRF are the densely-forested Sacramento Mountains. Individual peaks in surrounding mountains extend as high as 1500 m above the basin floor. An overhead view of the APRF site is shown in figure 1.

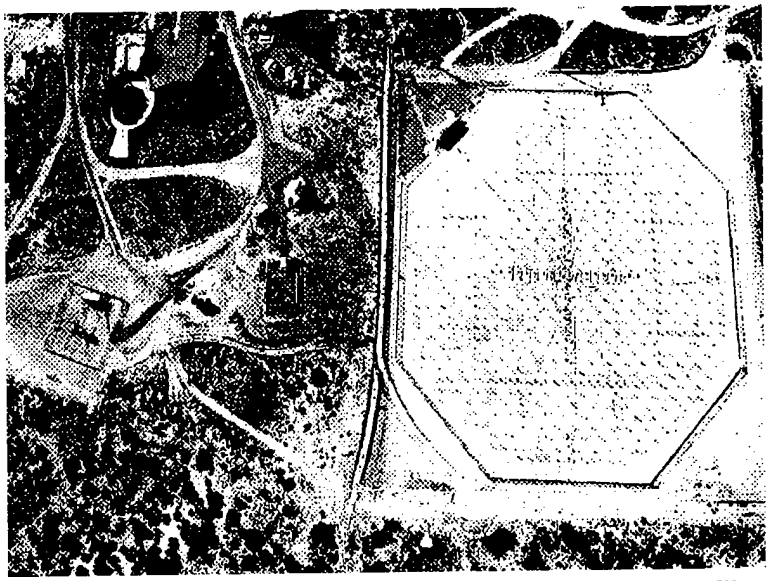


Figure 1. Aerial view of the Atmospheric Profiler Research Facility. The FM-CW radar is located at the extreme left; the 50 MHz is right-center.

Winds above the APRF are influenced by lee waves off of the mountains when the lower-level flow is from the southwest through northwest. Other atmospheric factors that are expected to contribute to small-scale vertical motion variability are convective activity, gravity waves, and precipitation.

4. COMPOSITE WIND PROFILE

Since there was no single instrument capable of providing continuous, near realtime vertical profiles of wind, radar turbulence and temperature data from the surface to near 20 km AGL, the aforementioned suite of five systems was assembled. With respect to vertical range, some data from each system overlaps the data from at least one of the other systems. To optimize the data within these regions of overlap, the system having the higher quality data and the greater availability of data was selected. The resultant composite system details are discussed in Hines et al. (1994) and Flowers et al. (1994).

For purposes of dissemination of the wind data, graphical representation of the wind profiles has been divided into two parts, one from the surface to 20 km AGL and the other from the surface to 4 km. The latter is referred to as the boundary layer profile where the boundary layer refers to the region of Army interest and not the temporally and spatially varying boundary layer familiar to meteorologists. An example of the graphical representation of the hourly-averaged boundary layer wind profiles is shown in figure 2.

5. QUALITY CONTROL

The data from each of the profilers can be contaminated with RF noise and interference, echoes from unwanted targets, and precipitation. These contaminants produce "fliers," points

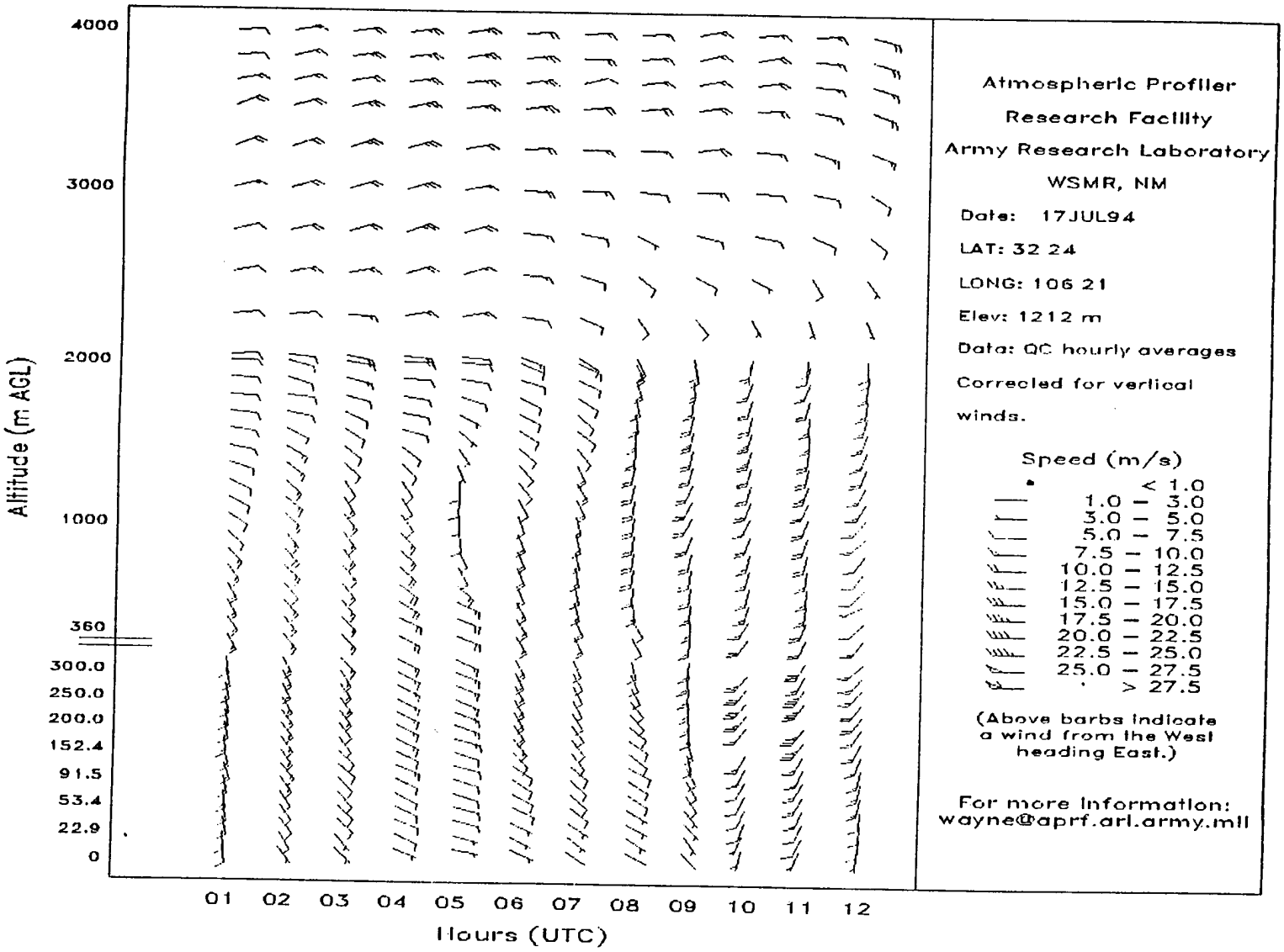


Figure 2. Example of the resultant boundary layer composite wind profile. Data source regions are: 7.5 to 152.4 m (tower), 175 to 325 m (sodar), 328 to 2028 m (924-MHz), 2000 to 3500 m (404-MHz), and 3500 to 4000 m (50-MHz).

or clusters of "bad" data.

The continuity method of Weber and Wuertz (1991) was adapted to provide quality control of the sodar and radar profiler wind data (Hines and Parker-Sedillo, 1993). Basically, the continuity method uses pattern recognition to flag discontinuous data in the 'raw' data. In this case, the 'raw' data are the 15-min (sodar), 1.5-min (924-MHz), 6-min (404-MHz), and 3-min (50-MHz) horizontal wind component data. The remaining 'good' data were then linear-averaged over the specific one-hour period.

6. LIMITATIONS

Although the APRF measurement system is operated continuously, there are periods when individual profilers are not operational. As of 1 September 1994, the percentage of hours for which quality-controlled data were available from each of the five systems during 1994 are shown in table 1.

The principle reasons for the associated downtime are power outages (primarily associated with thunderstorm activity); failure of the measurement systems, computer systems, and communication links; routine equipment maintenance; data backups; and data checks. A problem with the sodar data communication link accounts for about 90% of its downtime.

Table 1. APRF Data Availability.

System	Percent
50-MHz	70.2
404-MHz	69.3
924-MHz	86.0
Sodar	64.1
Tower	99.0

Because of the complex terrain at WSMR, the composite vertical profiles may not be representative of the entire missile range. This is particularly true in the boundary layer which can extend to as high as 5000-m AGL at WSMR during a summer afternoon.

To compare the wind data from the three radar wind profilers within their respective regions of overlap, five days during the spring of 1993 when there was a full complement of 24 hourly profiles from each system, was selected. The root mean square error (MSE) was then used to compare the wind speeds between the 50-MHz and 404-MHz systems and the 404-MHz and 924-MHz systems. The composite root MSE for the five days was 2 m s^{-1} for the 50 and 404 comparison and 2.5 m s^{-1} for the 404 and 924 comparison. The Pearson product-moment (correlation) coefficient for the U and V components was 95% in the former case and 70% in the latter case.

7. RESULTS AND DISCUSSION

Sample diurnal representations of the horizontal wind (speed and direction) as measured with the sodar and the 152-m tower are shown in figures 3 and 4. Additional examples of tower-sodar, sodar-924MHz and 924MHz-404MHz comparisons are presented in Flowers et al. (1994).

A sample diurnal variation of C_n^2 as derived from tower point measurements of C_T^2 and the sodar are shown in figure 5.

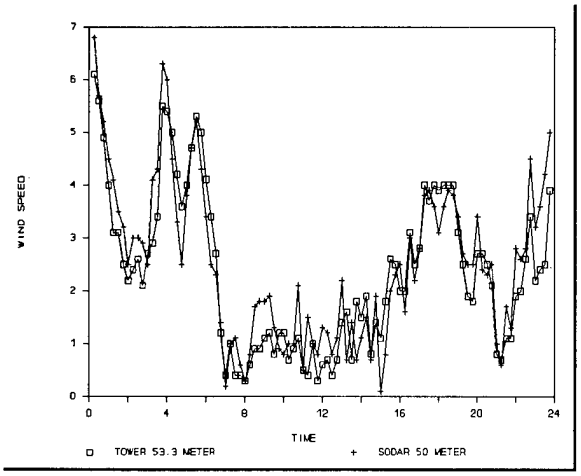


Figure 3. Diurnal variability of wind speed at a fixed height as measured by the sodar and the 152-m tower, 50 m, 2 Oct 91.

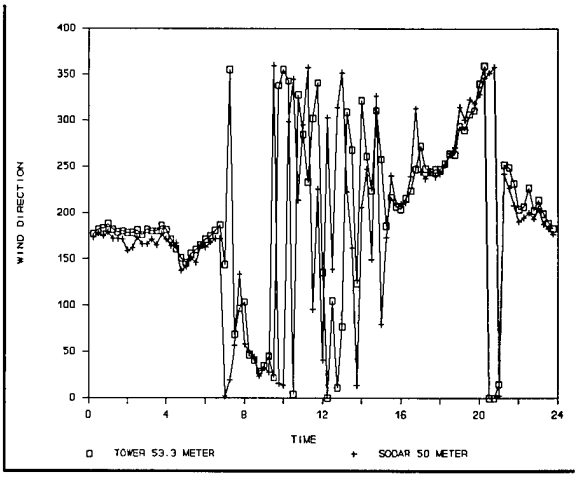


Figure 4. Diurnal variation of wind direction at a fixed height as measured by the sodar and the 152-m tower, 50 m, 2 Oct 91.

Visual comparisons of sodar backscatter and FM-CW C_n^2 maps for two separate days are shown in figures 6 thru 8. On 17 July 94 (Figures 6a and 6b) the sodar record displays the end of afternoon convection (0000-0130 UTC). This was followed by surface wave patterns, resulting in strong C_T^2 returns. The FM-CW radar record also showed some surface wave activity with a strong pattern developing near 0500 UTC. The relative stength of returns are attributed to the fact that sodar is most sensitive to temperature fluctuations while radar primarily senses humidity fluctuations. Atmospheric humidity conditions will therefore play a crucial role in the relative returns of the two sensing techniques.

Figures 7a and 7b show sodar records from measurements taken in the Tularosa Basin (APRF) and at the Apache Point Observatory (APO) on 23 May 94. As expected, the lower few hundred meters are controlled by local conditions and there is no agreement in the patterns. Very strong wave activity is seen at APO which contributes to optical turbulence.

Figures 8a and 8b display FM-CW radar data also measured on 23 May 94. There is agreement with some of the patterns sensed with the two systems, particularly from 0300 to 0600 UTC. The patterns however are intermittent. These results display the unique capabilities of sodar versus radar remote sensing techniques and exhibit the utility of simultaneous measurements.

8. REFERENCES

Eaton, F. D., S. A. McLaughlin, and J. R. Hines, 1995. A New FM-CW Radar for studying the morphology of the planetary boundary layer, In Press, *Radio Science*.

Flowers, W., L. Parker-Sedillo, G. Hoidale, J. Hines, F. Eaton, S. McLaughlin, 1994. Composite tropospheric wind profiles at White Sands Missile Range, NM, In Proc. 7th

International Symposium on Acoustic Remote Sensing and Associated Techniques of the Atmosphere and Oceans, Sec. 3, pp. 47-52.

Hines, J. and L. Parker-Sedillo, 1993. Assessment of the performance of wind profilers at White Sands Missile Range, Reprints of the 1993 Battlefield Atmospherics Conference, Las Cruces, New Mexico, 345-356.

Hines, J. R., S. A. McLaughlin, F. D. Eaton, and W. H. Hatch, 1993. The U.S. Army Atmospheric Profiler Research Facility: Introduction and capabilities, Reprints of Eighth Symposium on Meteorological Observations and Instrumentation, Anaheim, California, 237-242.

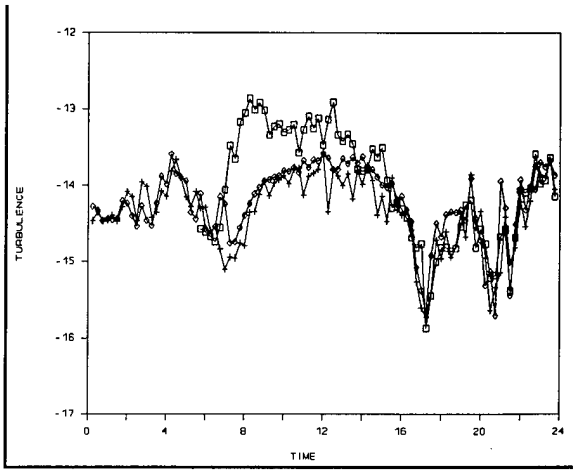


Figure 5. Diurnal variation of C_n^2 as measured by a sodar and two towers, 20 m, 2 Oct 91. (+ = sodar; □ = 152-m tower; ◇ = 20-m tower)

Hines, John, Frank Eaton, Scott McLaughlin, Glenn Hoidale, Wayne Flowers, Linda Parker-Sedillo, 1994. Composite tropospheric wind profiling at White Sands Missile Range, NM: integration, quality control and limitations, In Proc. of 3rd International Symposium on Tropospheric Profiling: Needs and Technologies, Hamburg, Germany, Supplement Proc., pp 467-469.

Weber, B. L. and D. B. Wuertz, 1991. Quality control algorithm for profiler measurements of winds and temperatures, NOAA Tech. Memo. ERL WPL-212, 32 pp.

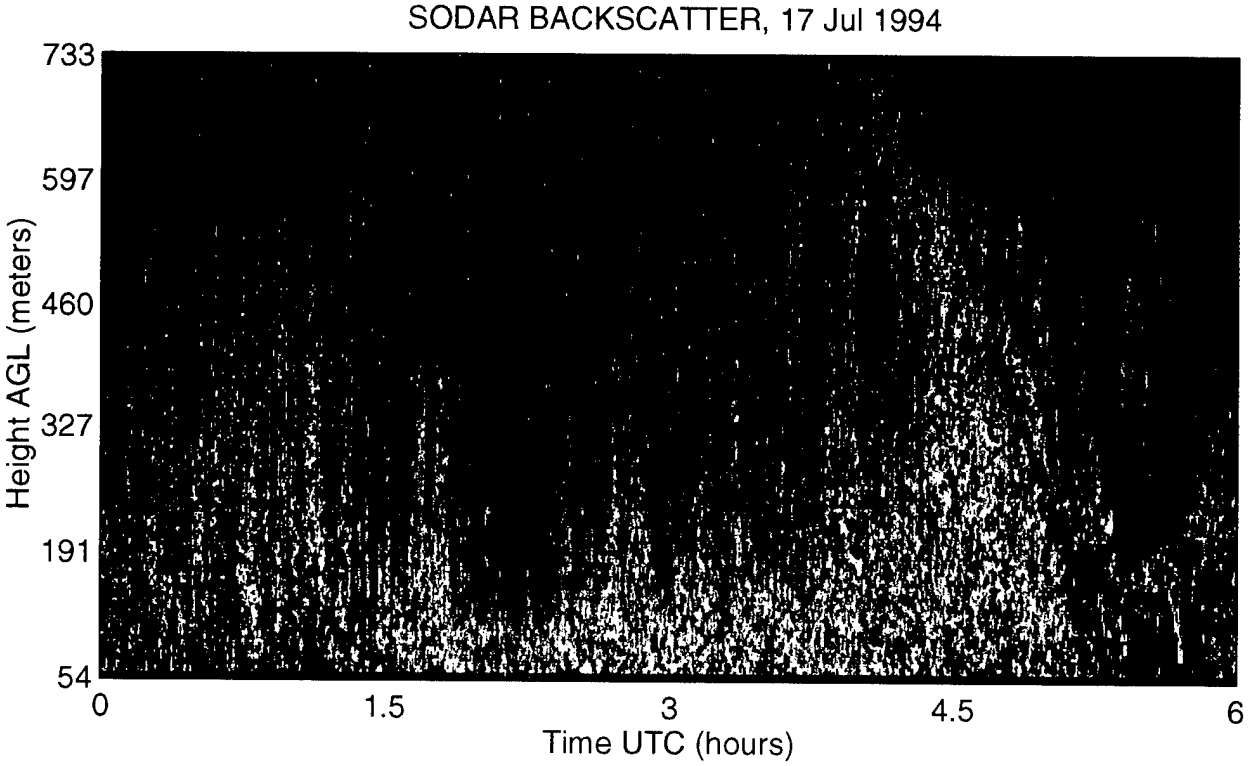


Figure 6a. Sodar backscatter report displaying late afternoon convection and evening wave activity at the APRF on 17 Jul 94.

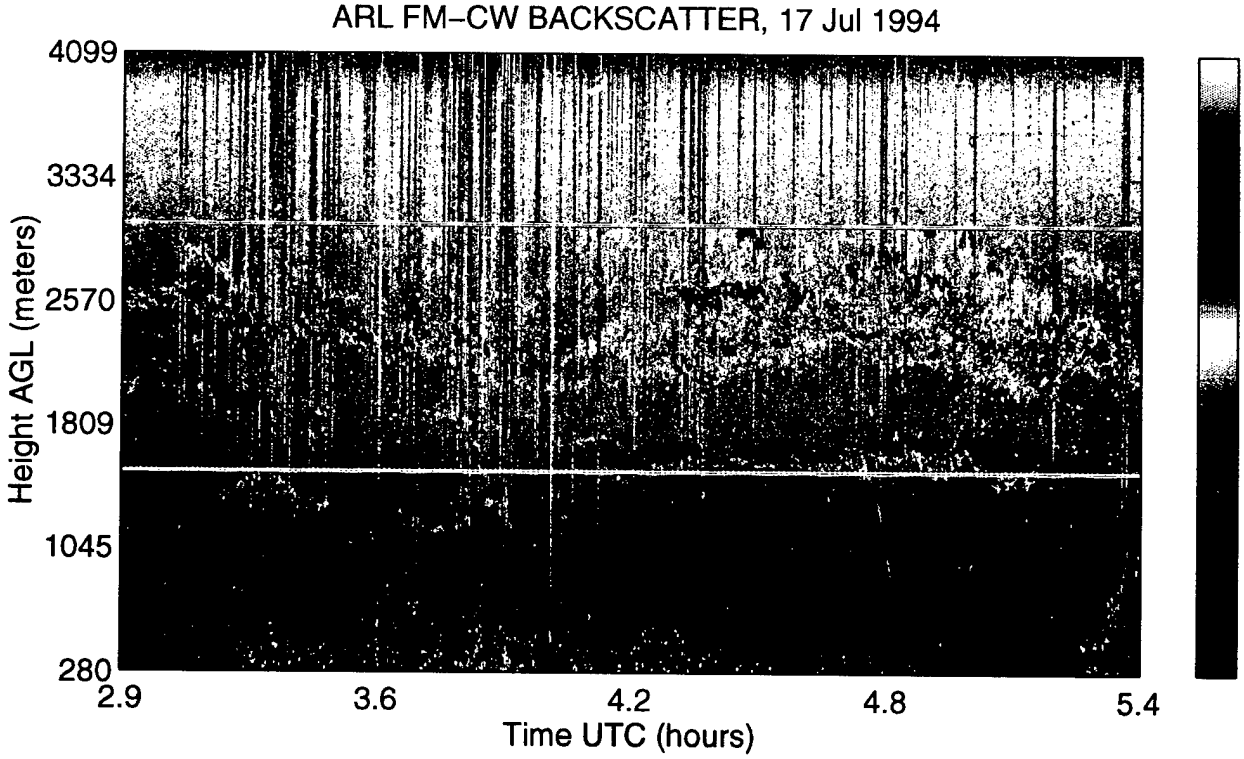


Figure 6b. FM-CW backscatter report displaying evening surface and elevated wave activity at the APRF on 17 Jul 94.

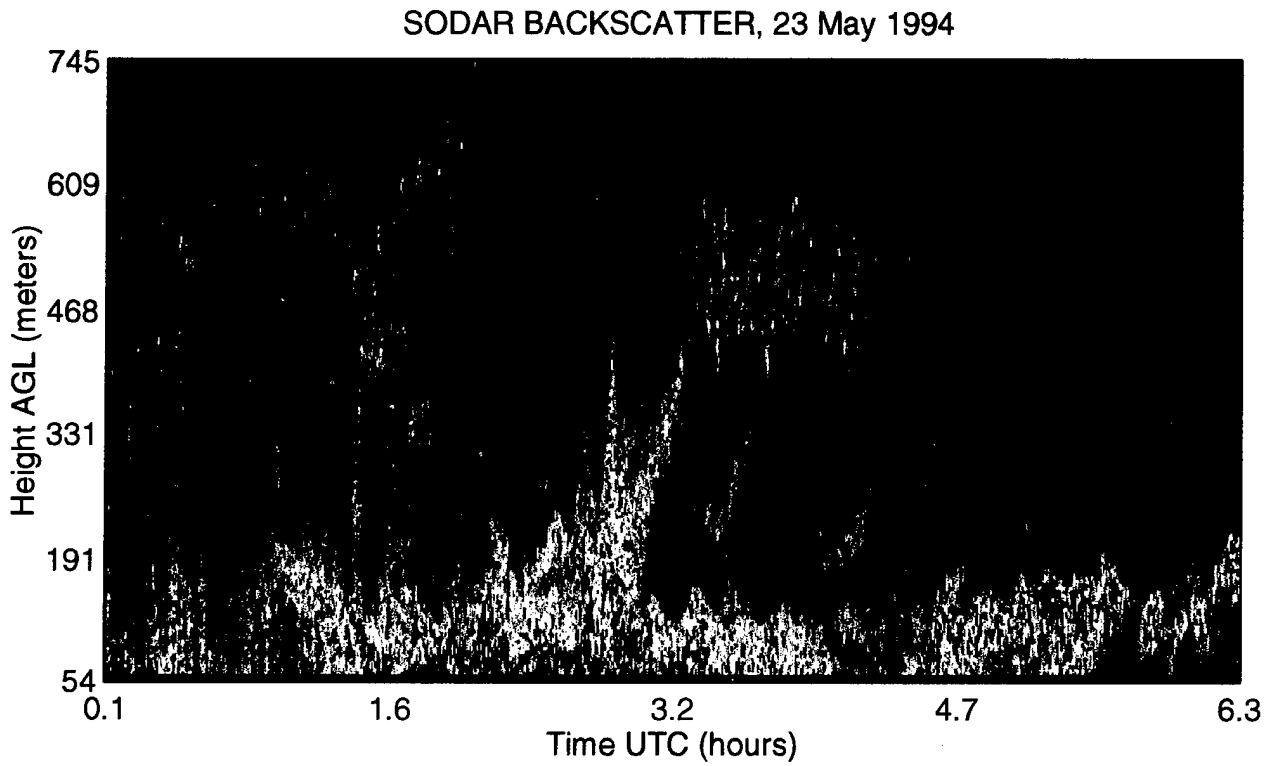


Figure 7a. Backscatter report displaying late afternoon and evening surface wave activity on 23 May 94 as sensed by the APRF sodar.

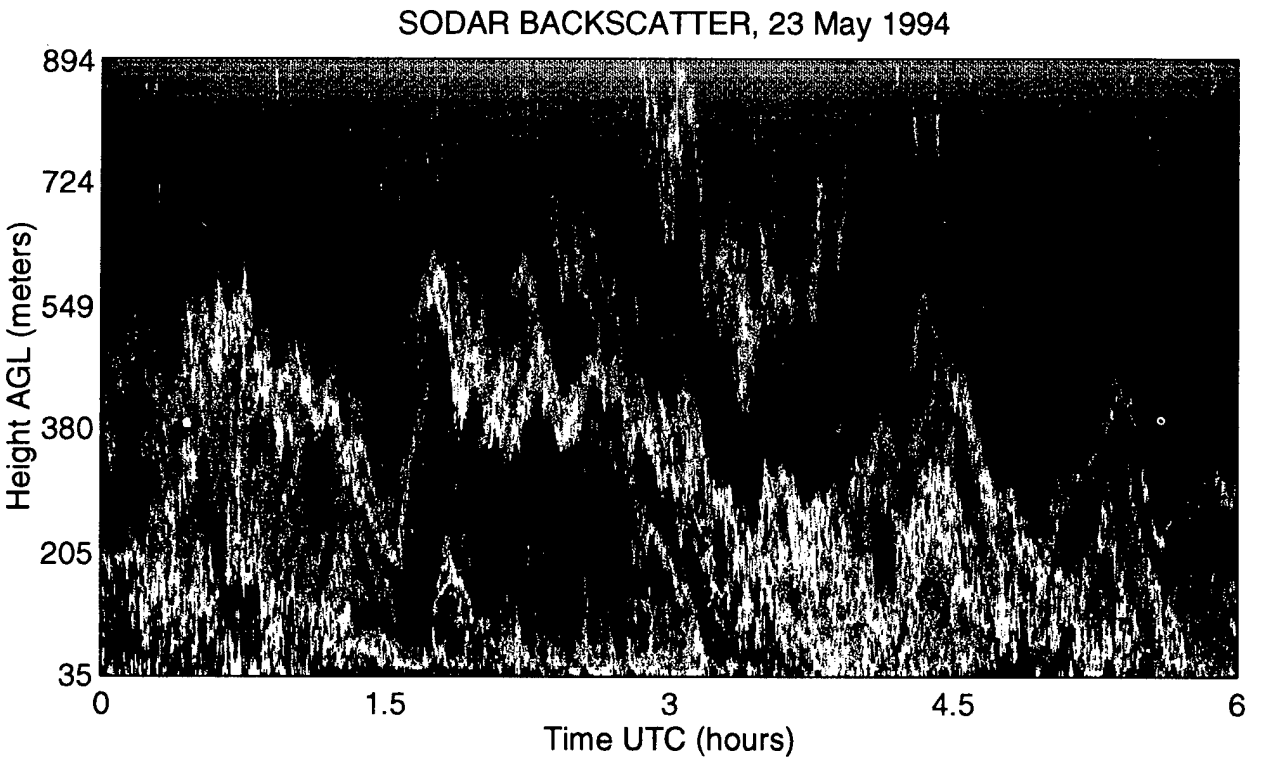


Figure 7b. Backscatter report displaying late afternoon and evening complex wave activity on 23 May 94 as sensed by the APO sodar.

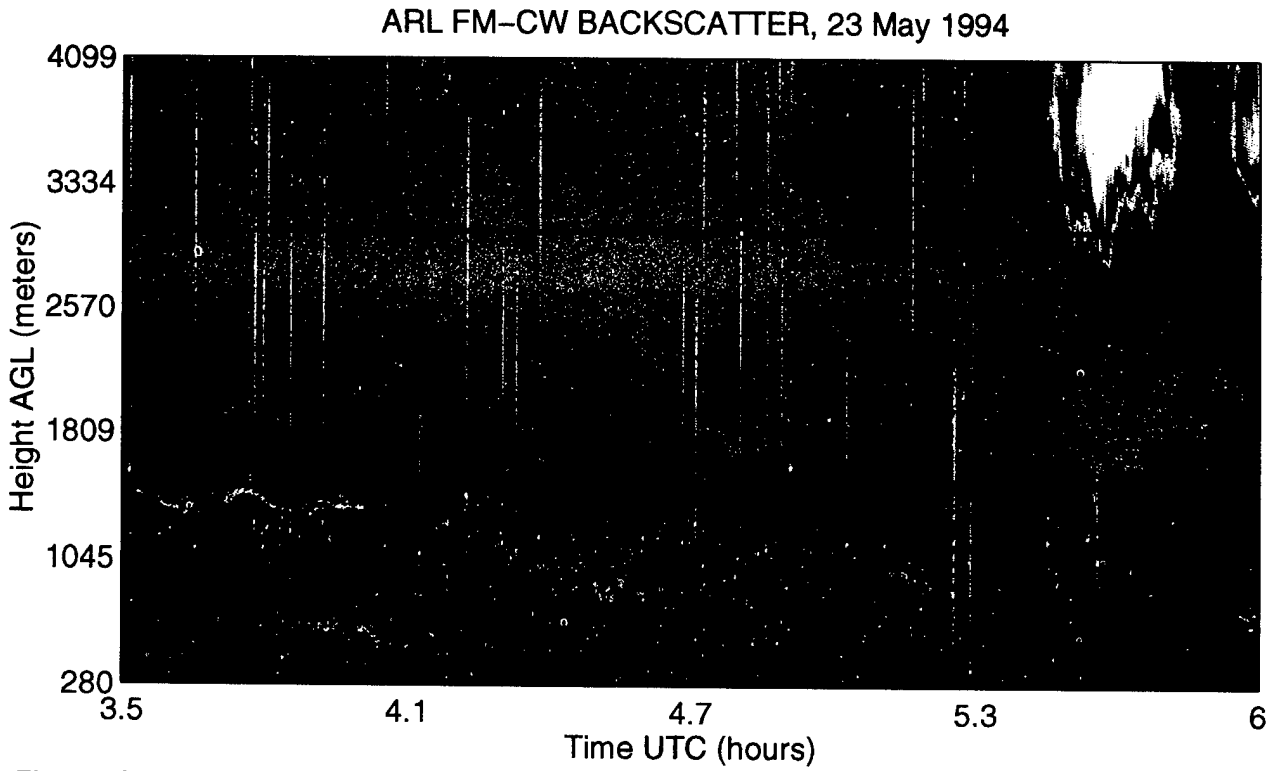


Figure 8a. FM-CW backscatter report displaying evening surface and elevated wave activity on 23 May 94 at the APRF.

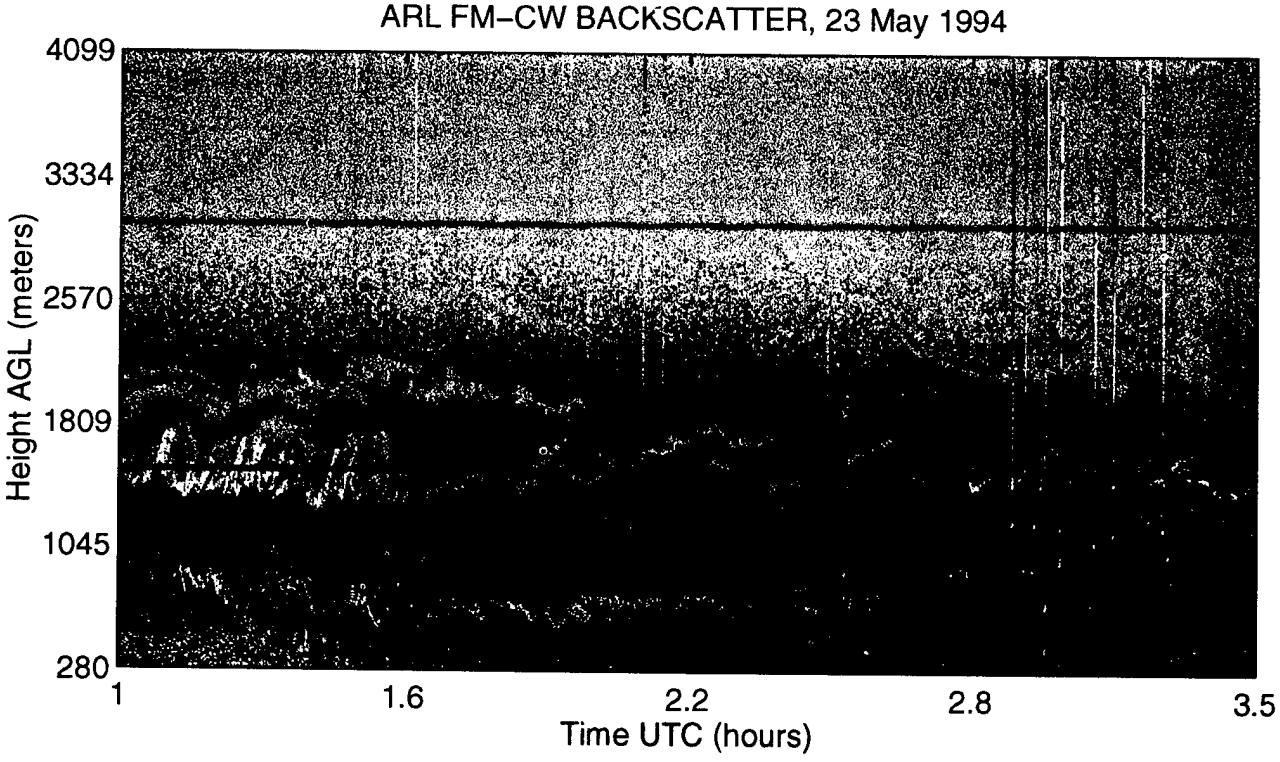


Figure 8b. FM-CW backscatter report displaying late afternoon surface and elevated wave activity on 23 May 94 at the APRF.

A LOOK AT THERMAL TURBULENCE INDUCED RADAR ECHOES IN OR NEAR RAIN CLOUDS AT THE ATMOSPHERIC PROFILER RADAR FACILITY

by Wm. H. Hatch

ARMY RESEARCH LABORATORY

White Sands Missile Range, New Mexico

ABSTRACT

There has been considerable interest in the measurement of the refractive index structure parameter (C_n^2) in or near clouds or fog. Unfortunately, normal instrumentation utilized in the measurement of this parameter are affected by the presence of the water droplets themselves, precluding any definitive conclusions as to the effect of the cloud or fog. It was decided to attempt a preliminary investigation of this optical and/or radar turbulence using the capability of the co-located 404 Mhz and 50 Mhz radar profilers at the Atmospheric Profiler Radar Facility (APRF). The 404 Mhz profiling radar has the ability to detect falling rain, while the 50 Mhz profiling radar is not affected and is calibrated for the measurement of the refractive index structure parameter. One case is presented showing that there is, indeed, an enhancement of the radar turbulence in the vicinity of a rain cloud.

INTRODUCTION

This team has been involved in the measurement of the refractive index structure parameter for several years. During this time various researchers have requested data on the behaviour of this parameter in the vicinity of clouds or fog. Until recently our sensors were limited to the measurement of the temperature structure with fast response spatial temperature probes, or the measurement of scintillation patterns. The temperature probes are fine wire resistance probes and thus subject to being affected by the water droplets. The scintillometers are double ended light gathering devices which are necessarily affected by the occlusion due to the fog.

With the advent of the Atmospheric Profiling Radar Facility another means of measuring turbulence has been added which may enhance research in this area. For this study only the 50 Mhz and the 404 Mhz radars were utilized. These two radars are co-located (within 150 meters center to center) and the other characteristics have been covered in various other presentations and publications. Of particular interest to this study are the facts that the 404 Mhz radar detects falling rain while the 50 Mhz radar, due to the longer wave length, does not, and the 50 Mhz radar signal return has been calibrated for radar turbulence.

RESULTS AND DISCUSSION

For this study a two hour period starting at 6:00 UTC on the 17th of September, 1994 was selected. The 404 Mhz radar vertical velocity profile (fig. 1) shows definite rain during this period from about 6:48 to 7:30 (the 404 Mhz radar scans are 6 minutes apart). This rain, indicated by a strong negative vertical velocity, appears to start about 4000 meters AGL. The returned signal power from the 404 Mhz (fig. 2) shows enhanced turbulence from the rain cloud up to and beyond 7000 meters AGL.

The radar turbulence profiles from the 50 Mhz radar scans are 3 minutes apart, but blanks appear during the times that the radar is performing a Radar Acoustic Sounding System (RASS) profile to measure temperature. There are also blanks for the lower 1000 meters since the 50 Mhz radar profiles do not start until 2000 meters, but the heights are selected to match the 404 Mhz radar heights.

The radar turbulence profiles from the east and north beams of the 50 Mhz radar (figs. 3 & 4) show definite enhancement up to 10000 meters AGL. These differences may be magnified by subtracting the mean turbulence over the two hour period from the profiles for each beam as shown (figs. 5 & 6). It is interesting to note that the main differences appear to be in the upper reaches of the cloud.

The difference between the radar turbulence profiles for the east and north beams (fig. 7) can also pinpoint areas of interest. As shown above in figures 5 and 6, the differences are found at higher altitudes. Of particular interest is the pattern after 7:00 UTC where the two strongly isolated layers showed marked differences.

CONCLUSIONS

The utilization of the APRF in the study of C_n^2 near clouds does show promise. A more definitive study utilizing other radars, and possibly an all-sky camera, to pinpoint the location of the clouds in relation to the radar beams could provide the some of the answers needed in the on-going research in this area.

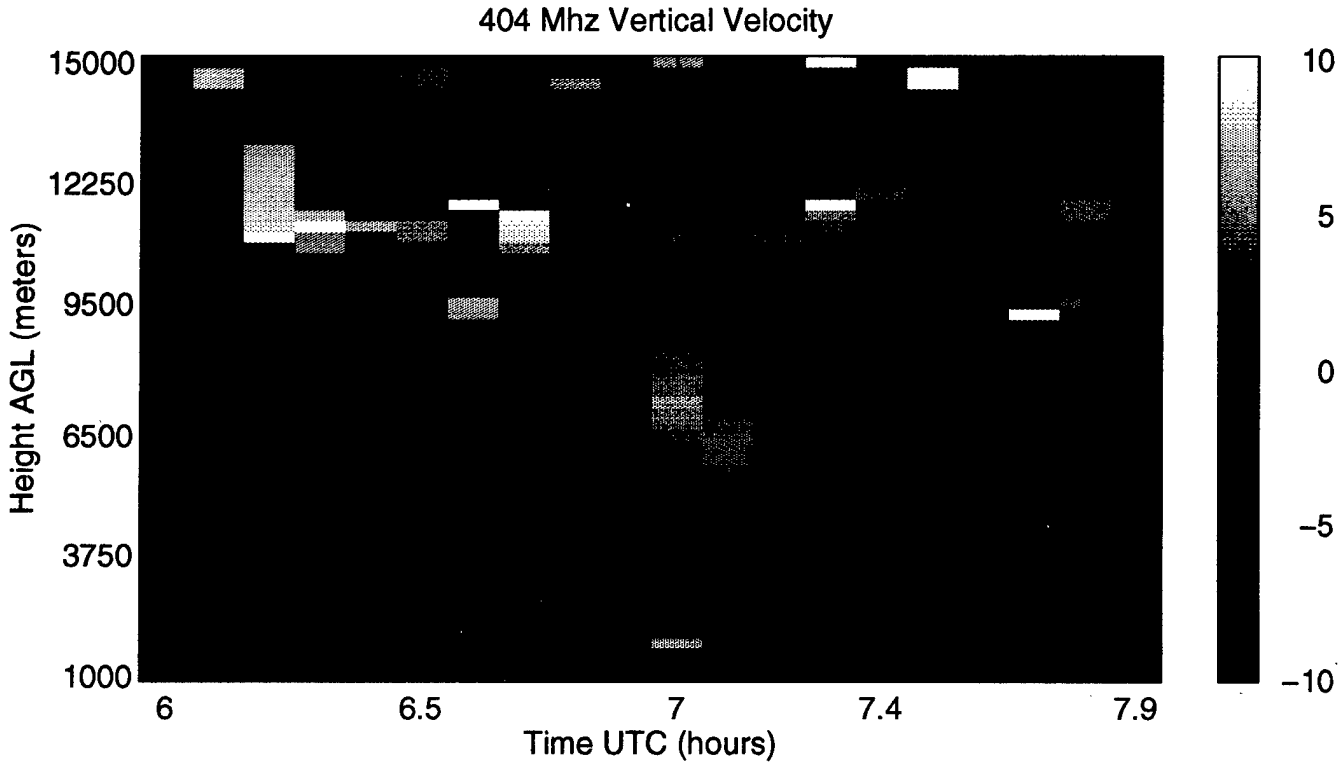


Figure 1. Vertical Velocity Profile

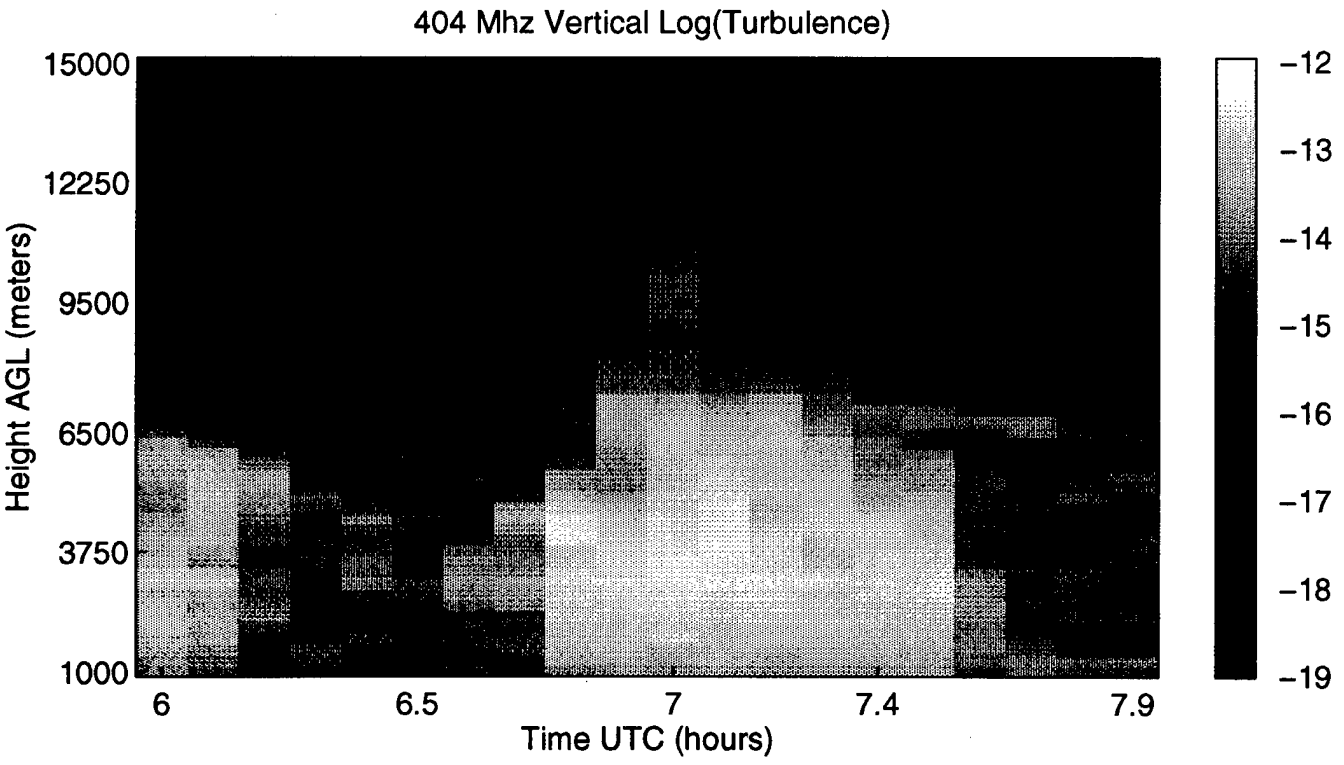


Figure 2. 404 Mhz Turbulence Profile from Vertical Beam

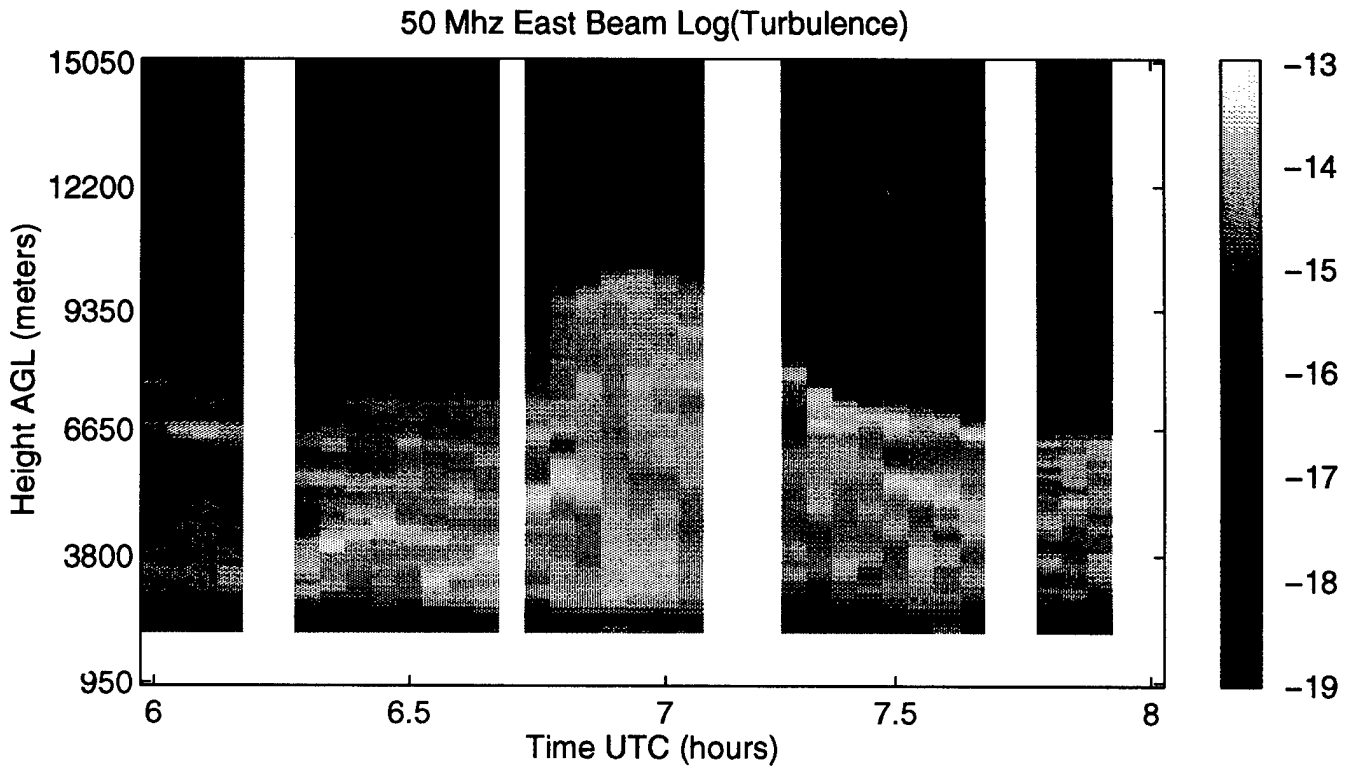


Figure 3. 50 Mhz Turbulence Profile from East Beam

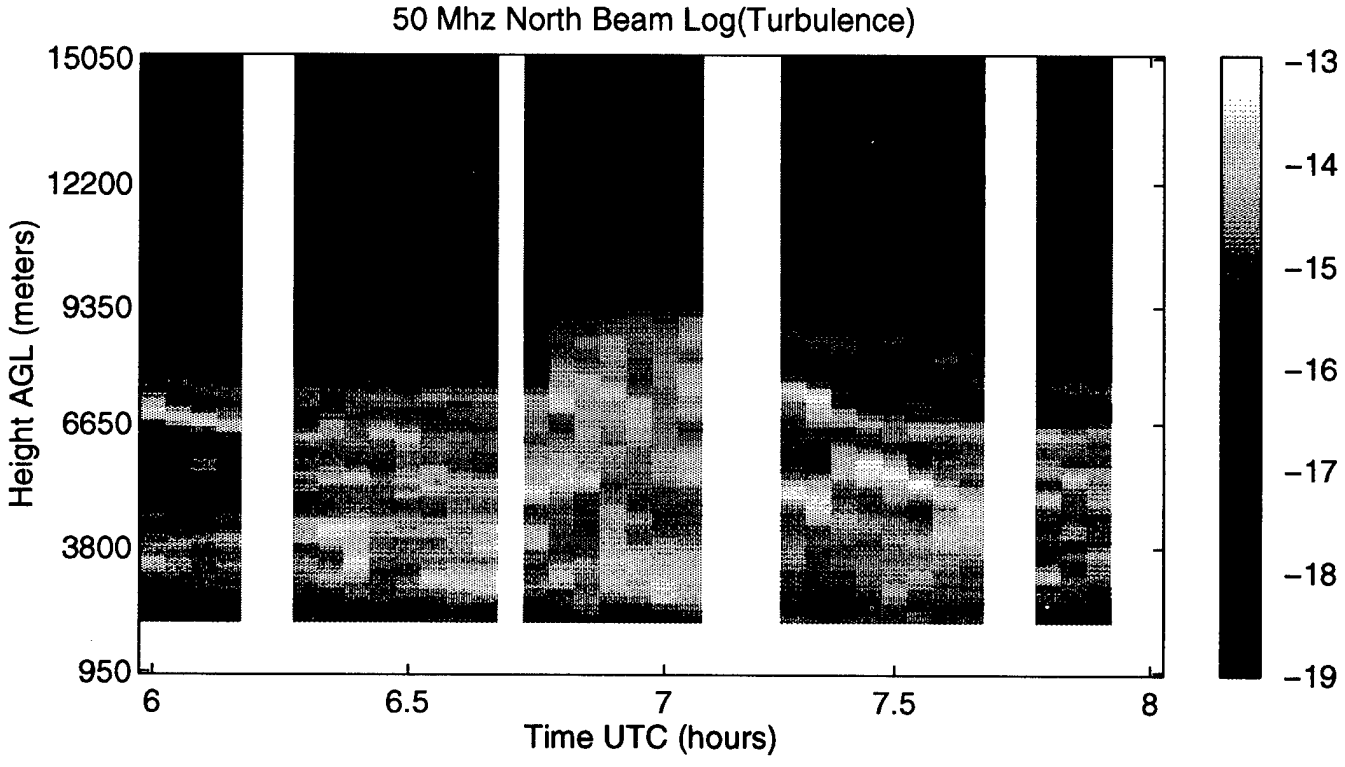


Figure 4. 50 Mhz Turbulence Profile from North Beam

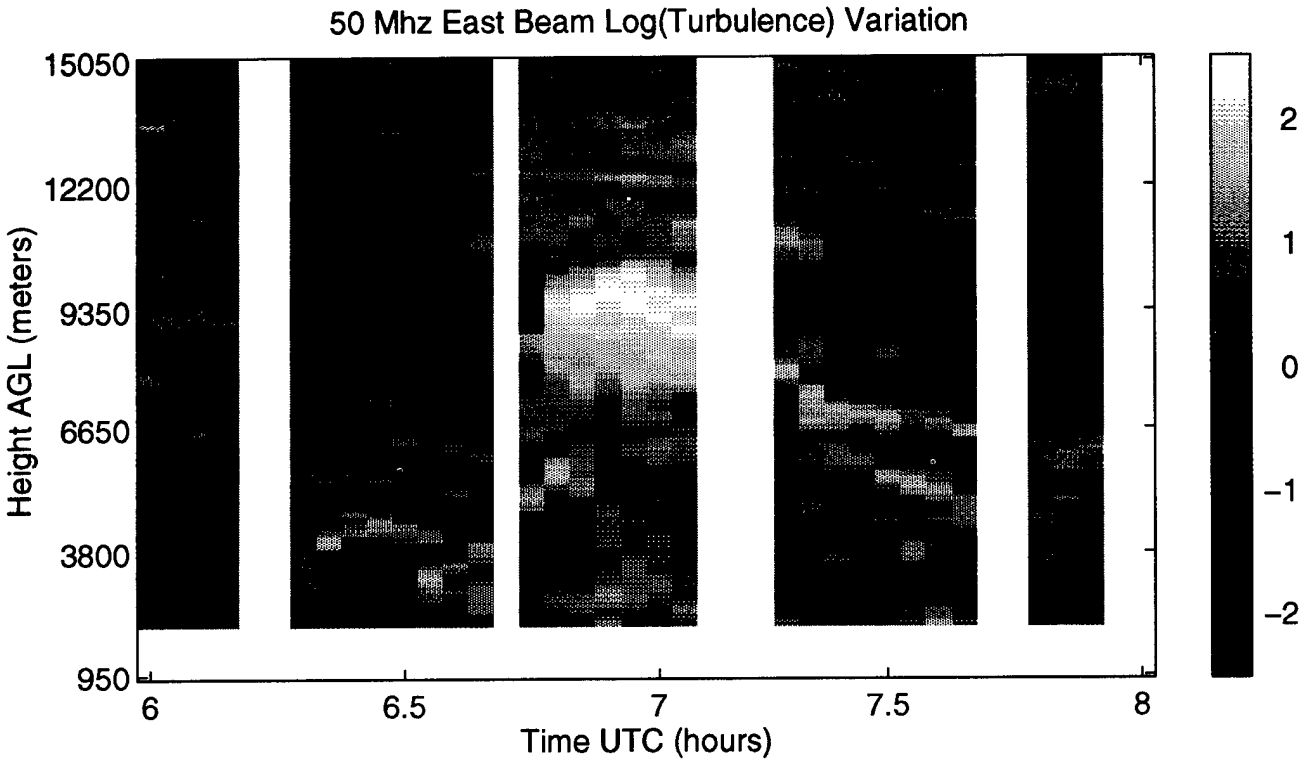


Figure 5. 50 Mhz East Beam Turbulence Variation from Average

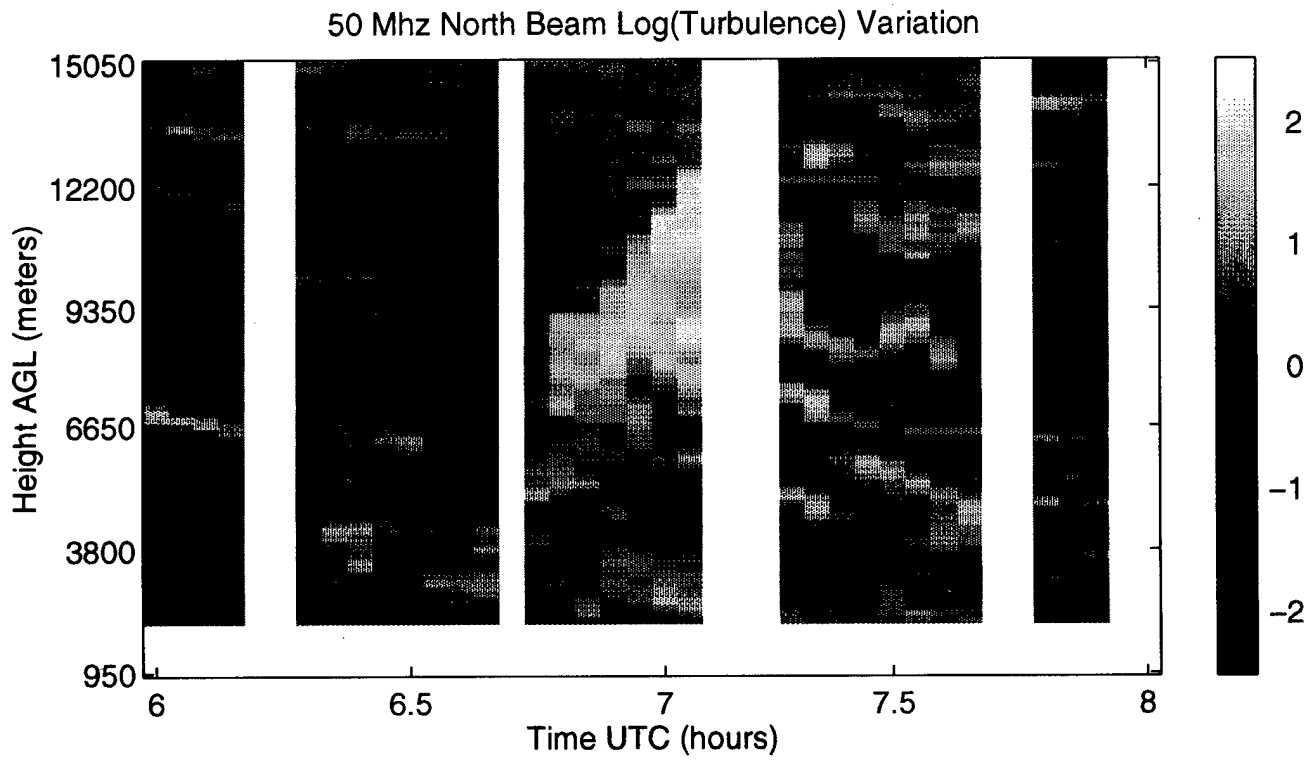


Figure 6. 50 Mhz North Beam Turbulence Variation from Average

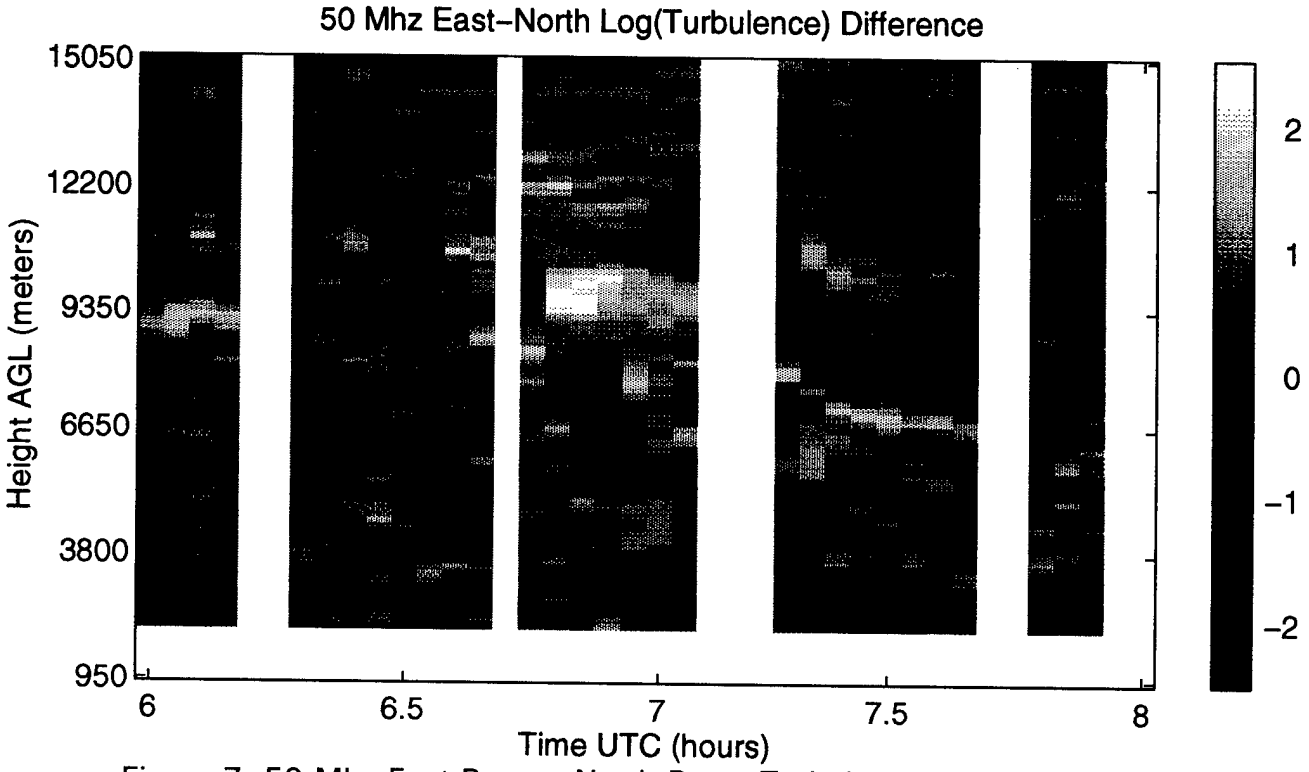


Figure 7. 50 Mhz East Beam - North Beam Turbulence Variation

BORDER AREA AIR QUALITY STUDY

B. W. Kennedy, J. M. Serna, J. R. Pridgen, D. Kessler, J. G. Moran, G. P. Steele, and R. Okrasinski; Physical Science Laboratory

J. R. Fox, R. Savage, and D. M. Garvey
U.S. Army Research Laboratory

ABSTRACT

During the period 8-11 September 1994, the Physical Science Laboratory (PSL) participated in the Border Area Air Quality Study. The program, which concentrated on an investigation of air migration patterns in southern Dona Ana County, was sponsored by the New Mexico State Highway and Transportation Department, the New Mexico Environment Department, and the National Center for Transportation and Air Quality. It brought together in a cooperative effort several government and industry groups including PSL, the Army Research Laboratory, Los Alamos National Laboratory, Santa Fe Technologies, the University of Texas at El Paso, the El Paso City County Health District, and the Texas Natural Resource Conservation Commission. Advanced technology equipment was used to make remote and in-situ measurements including UHF radar wind profilers, a SODAR wind profiler, a Laser Doppler Velocimeter wind profiler, a Mobile Atmospheric Spectrometer, an elastic backscatter LIDAR, meteorological towers, tethered and free-flight balloons, monitoring stations, carbon monoxide sensors, and infrared video and pneumatic tube traffic monitoring systems. This report presents a summary of the program and discusses some of the preliminary results of wind flow patterns and ozone levels in the Juarez/El Paso and southern Dona Ana County region during the test period.

1. INTRODUCTION

The southern area of Dona Ana County, New Mexico, will play an ever increasing and important role in the interstate and bi-national commerce between the states of New Mexico and Texas, and between the United States and Mexico. The North American Free Trade Agreement (NAFTA) which, reduces or eliminates trade barriers between the two countries, holds much promise for development of this southern New Mexico region. There already exists a relatively new port of entry at the Santa Teresa Border Crossing. A few miles north of the port of entry there exists an industrial park complex and the Dona Ana County Airport. There are plans to build an intermodal terminal in that vicinity which will handle the increased trade between the two nations. The expanding level of activity will mean an increase in volume of surface, rail, and air transportation. It is anticipated that the larger volume of traffic from all modes will cause an increase in pollution levels in an area which already suffers from non-attainment levels of ozone, carbon monoxide, and particulates.

With this future in mind, the National Center for

Transportation and Air Quality (CTAQ) proposed to the New Mexico State Highway and Transportation Department (NMSHTD) a short, intensive study of this area in order to better understand the meteorological windflow patterns during the time of year when ozone levels are high. The approved project was administered by the New Mexico Environment Department (NMED). At this time it is assumed that the high levels of pollutants migrate from the Juarez/El Paso metropolitan areas. The purpose of the study was to:

- Determine local meteorological effects on transport of pollution.

-Provide a baseline to examine the effects of the potential rise in traffic due to NAFTA.

-Complement air quality work already underway in the Juarez/El Paso areas.

- Demonstrate and promote the transfer of technology from government laboratories to the environmental arena.

The major participants is this project included the Physical Science Laboratory (PSL), New Mexico State University (NMSU); the Army Research Laboratory Battlefield Environment Directorate (ARL/BED), White Sands Missile Range (WSMR); the Los Alamos National Laboratory (LANL); and Santa Fe Technologies (SFT). Other support organizations included the University of Texas at El Paso (UTEP), the El Paso City-County Health District (EPCCH), the Texas Natural Resource Conservation Commission (TNRCC), and the New Mexico Environment Department (NMED).

2. INSTRUMENTATION

The Physical Science Laboratory and the Army Research Laboratory installed and operated the following systems in support of the air quality study:

-Four 10-meter meteorological towers, one each at Sunland Park Racetrack, NUMEX Landfill, Santa Teresa Port of Entry, and the Dona Ana County Airport. See figure 1, locations 1-4.

-A SODAR which measured winds up to approximately 600 meters height above ground level at the port of entry (figure 1, location 2).

-A UHF radar which measured winds up to about 3 kilometers at the NUMEX Landfill (figure 1, location 3).

-A Laser Doppler Velocimeter (LDV) which measured winds up to 600 meters at the Sunland Park Racetrack (figure 1, location 4).

-A tethersonde which measured meteorological parameters up to about 150 meters at the racetrack (figure 1, location 4).

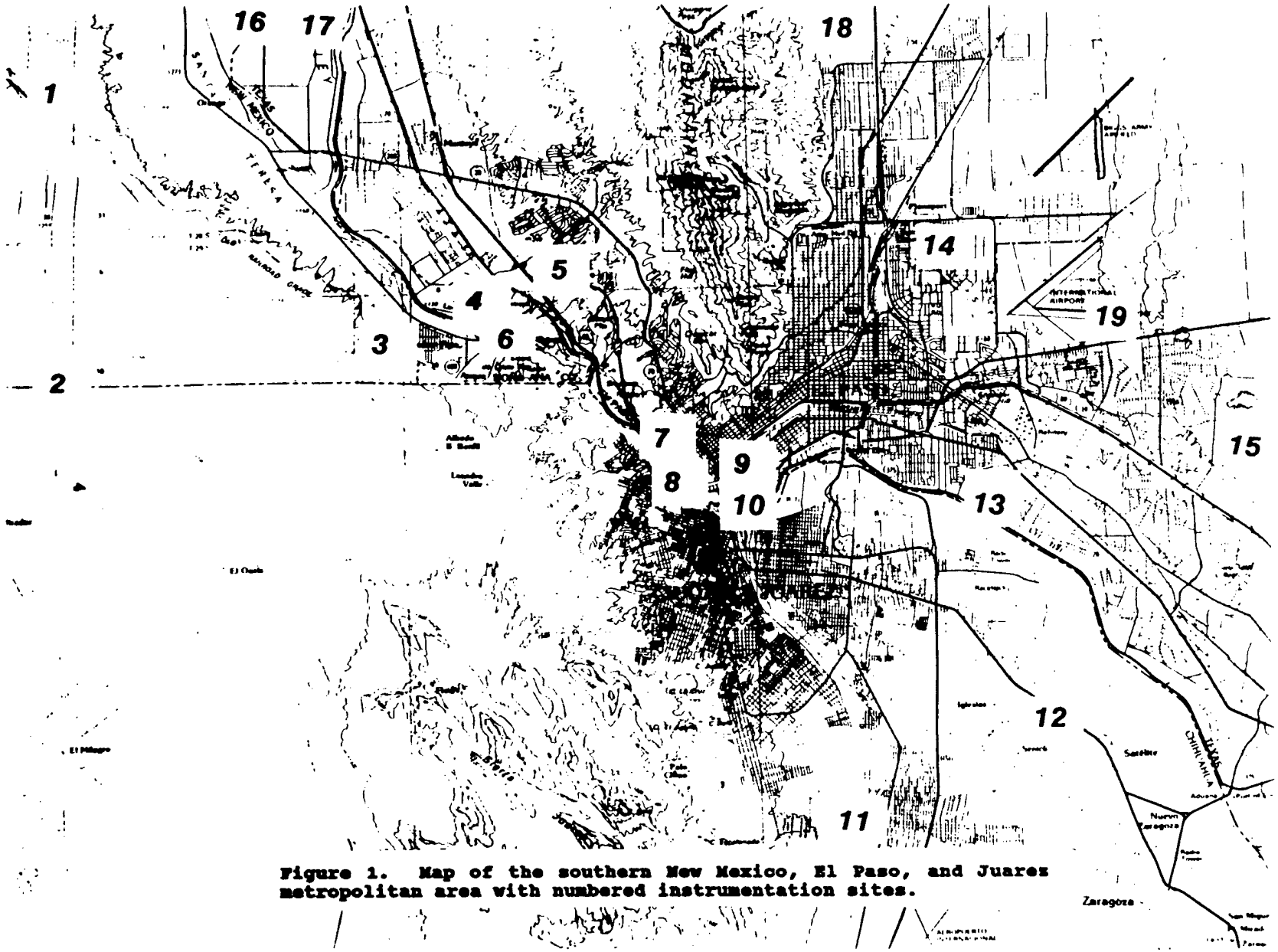


Figure 1. Map of the southern New Mexico, El Paso, and Juarez metropolitan area with numbered instrumentation sites.

-Free flight meteorological balloons released twice daily (figure 1, location 4).

-A Mobile Atmospheric Spectrometer which measured absorption spectra of atmospheric gases (carbon monoxide, ozone, etc.) over an integrated path of 250 meters at the racetrack (figure 1, location 4).

-Video imagery for counting traffic on Interstate 10 and a contrast transmissometer for measuring visibility near the Sunland Park Mall (figure 1, location 5).

Other instrumentation installed and operated specifically for this program included:

-An elastic backscatter LIDAR operated by the Los Alamos National Laboratory at the Sunland Park Mall (figure 1, location 5).

-Traffic counters and carbon monoxide sensors operated by Santa Fe Technologies in and around Interstate 10 and the Sunland Park vicinity (figure 1, locations 4 and 5).

Existing systems which provided data for the project included:

-A UHF radar operated by the Electrical Engineering Department at UTEP (figure 1, location 7).

-Air quality monitoring stations operated by NMED, EPCCH, and TNRCC in the El Paso, Juarez, and Dona Ana County areas (figure 1, locations 8-17). The NMED stations at La Union and Las Cruces are approximately 5 and 30 miles north of the map numbers.

-Synoptic weather charts and El Paso radiosonde data from the National Weather Service, El Paso International Airport (figure 1, location 19).

-Surface data from selected stations at WSMR (figure 1, location 18, approximately 40 and 80 miles north).

The LANL, video traffic count, SFT traffic counters, SFT carbon monoxide, Mobile Atmospheric Spectrometer, and visibility results will not be presented in this report.

3. ANALYSIS OF MEASUREMENTS

3.1 Synoptic weather conditions

Synoptic weather charts were obtained for 8-10 September for surface and 700 millibar height. On 8 September at 0600 MDT the southern New Mexico region was dominated by a high pressure system both on the surface and aloft. Pressure gradients were very weak. Surface winds at the El Paso airport were east-southeast at less

than three knots. Winds at the 700 millibar level (3180 meters) were from the north at 3-7 knots. September 9 continued with the same dominating high pressure system. The 0600 MDT winds at both levels are very light from the northwest. Pressure gradients were weak. September 10 was a virtual repeat of conditions on the 9th. Winds were northwesterly and very light. Charts are not available for September 11.

3.2 Radiosonde measurements

High altitude meteorological data were collected from radiosonde releases at the National Weather Service in El Paso and from balloons released by the Army Research Laboratory at the Sunland Park Racetrack. Parameters measured included temperature, pressure, relative humidity, wind speed, and wind direction. The NWS releases were at 1200Z (0600 MDT) and 0000Z (1800 MDT), while the ARL balloons were released at mid-morning and mid-afternoon to fill in the gaps.

3.3 Remote measurements of wind flow

The boundary layer was measured continuously using four systems: the SODAR at the Santa Teresa Port of Entry, a UHF radar at the NUMEX Landfill, the Laser Doppler Velocimeter (LDV) at Sunland Park Racetrack, and a UHF radar at the University of Texas at El Paso. The Laser Doppler Velocimeter (LDV) was located at the Sunland Park Racetrack and operated during daylight hours on 9-11 September. Besides taking scans for wind profiles up to 600 meters above ground level, the LDV provided calibration information for the Los Alamos LIDAR located at the Sunland Park Mall. An example of graphical analysis of the remote sensors is shown in (figure 2). The arrows indicate the approximate direction of the flow, and the numbers are the wind speed in meters per second.

3.4 Tethersonde measurements

The tethersonde system, which was located at Sunland Park Racetrack, was operated periodically during the daytime hours. Its purposes were to calibrate the LIDAR and LDV, to collect meteorological data at about 100 and 150 meters above the ground, and to carry the Santa Fe Technologies carbon monoxide sensor as needed.

3.5 Surface measurements

PSL installed towers at the Dona Ana County airport, Santa Teresa Port of Entry, NUMEX Landfill, and Sunland Park Racetrack Instruments were placed at the 2- and 10-meter levels. The 2-meter level included winds, temperature (heat shield, non-aspirated), relative humidity, total solar flux, net radiation, and barometric pressure (barometer at Sunland Park only). The 10-meter level

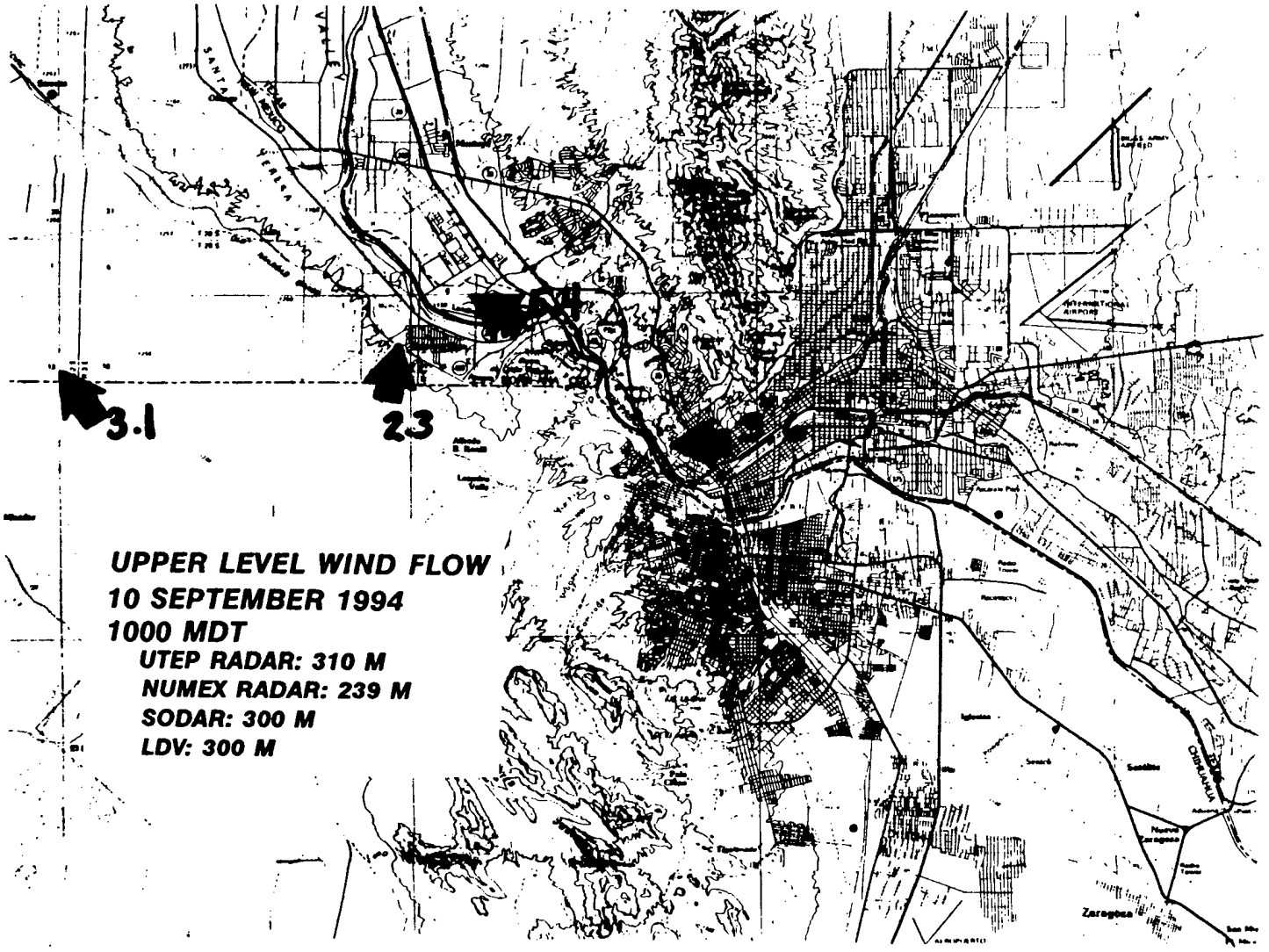


Figure 2. Upper level wind pattern for September 10, 1000.

included winds and temperature. A precipitation gauge was placed on the ground, and soil temperature was measured with a thermocouple wire positioned about 1 inch beneath the surface. All data were logged into a Campbell 21X data logger and recorded to a cassette recorder. One-minute and 15-minute averaged data were recorded 24 hours per day.

The data from existing surface monitoring stations in and around the El Paso, Juarez, Sunland Park, White Sands Missile Range, and Las Cruces area were obtained from the operating agencies. These included New Mexico Environment Department, El Paso City-County Health District, Texas Natural Resource Conservation Commission, and White Sands Missile Range.

An example of the analysis of surface level winds is shown in figure 3. On 10 September the winds were from the southeast at 1000. Ozone for this day reached its peak for the four day test period in downtown El Paso, Sunland Park, UTEP, and La Union. Figures 4 and 5 show the peak ozone levels for the four-day study. September 8 and 9 were Thursday and Friday normal work days. Friday levels were lower than Thursday. Saturday, which probably had an increase in mid-day traffic compared with the weekdays, showed significantly higher ozone peaks at four locations: downtown El Paso, UTEP, La Union, and Sunland Park. Sunland Park recorded the highest level at 105 parts per billion. Sunday, as would be expected because of reduced vehicular activity, recorded a sharp drop in ozone level. All four of these stations are in the airflow migration pattern from the southeast. In Juarez (Advanced Transformer and Technological Institute) and Ascarate Park it was highest on Thursday and lower on every day thereafter. A possible explanation is that the Juarez stations are away from the central city area and Ascarate Park is in the El Paso suburb. Las Cruces, while recording significantly lower levels of ozone than El Paso and southern Dona Ana County, also showed an increase in peak value on Saturday, September 10, as compared to the other three days of the study period.

4. SUMMARY AND CONCLUSIONS

This report represents just a cursory look at the multitude of data produced as a result of the Border Area Air Quality Study. In addition to this data set, the Los Alamos LIDAR data will add significant information about particulate transport and diffusion in the Sunland Park locale. The information presented in this report already shows wind patterns which can transport ozone and other pollutants during midday from the Juarez/El Paso area to Sunland Park and La Union, New Mexico. For the first time a coordinated effort was organized and executed which will try to explain wind patterns not only at the surface but in the atmospheric boundary layer.

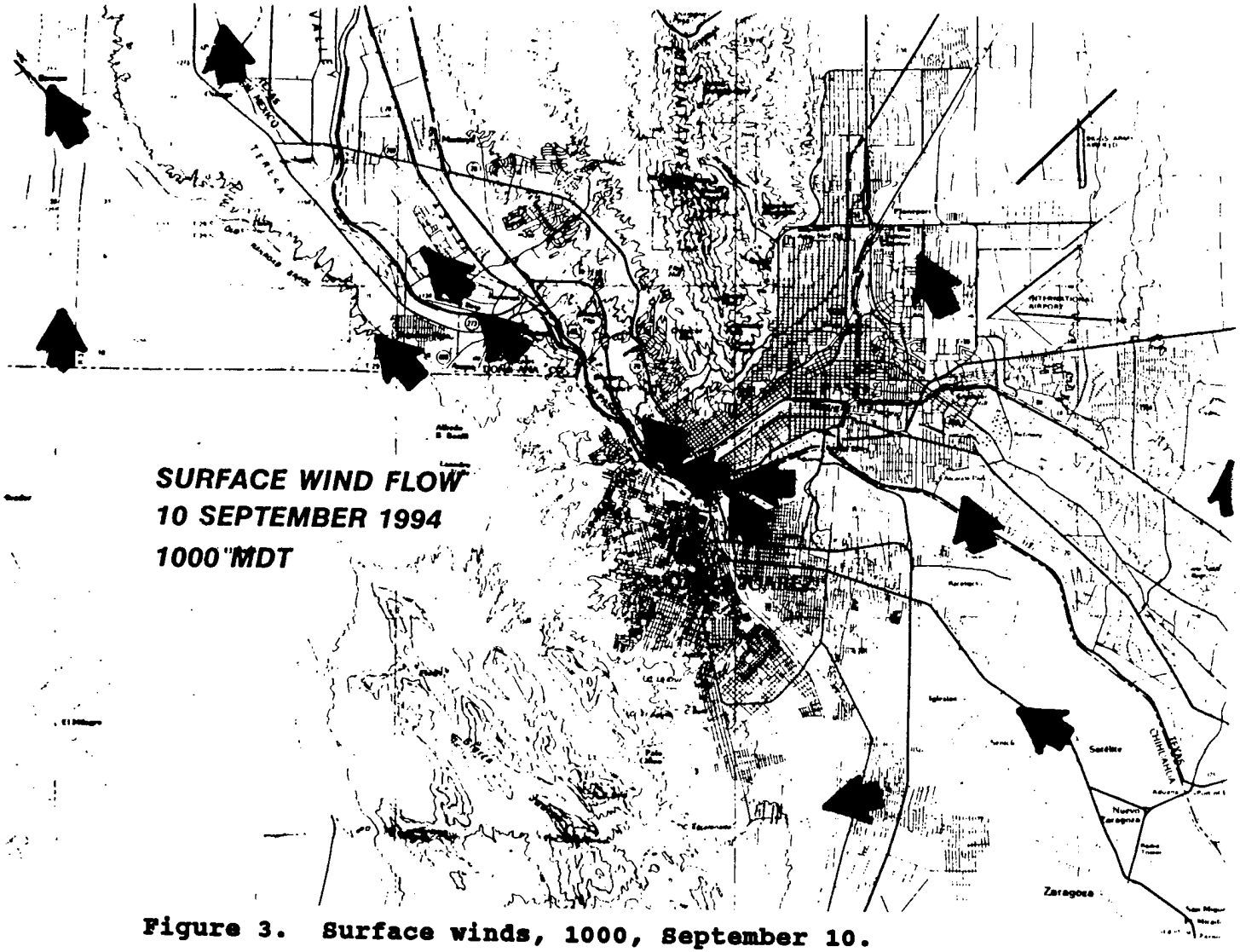


Figure 3. Surface winds, 1000, September 10.

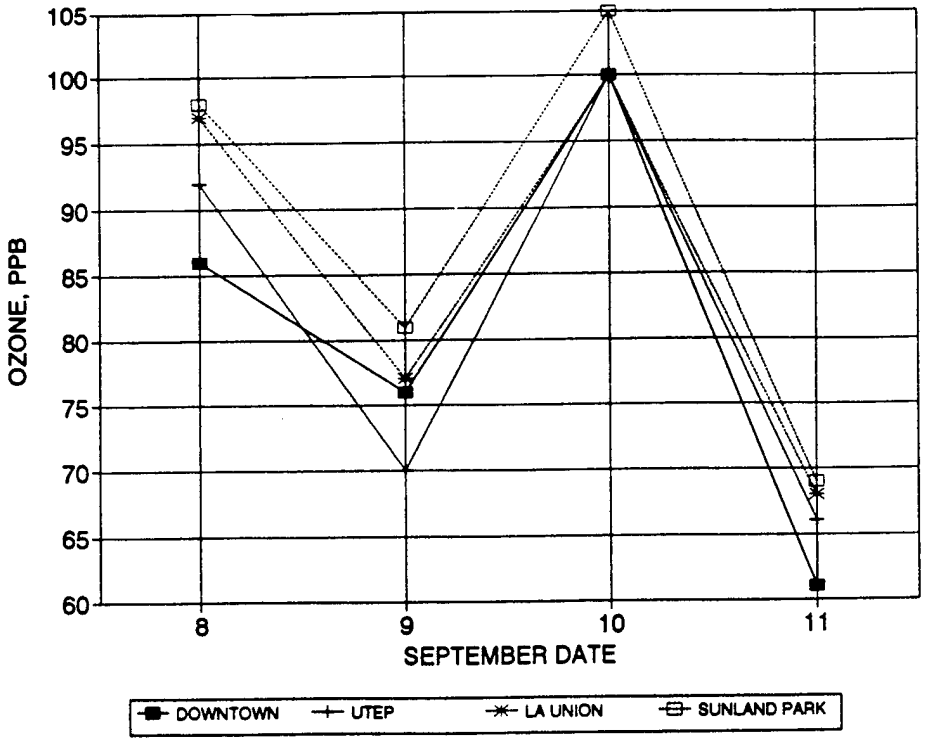


Figure 4. Ozone peaks from downtown El Paso, UTEP, La Union, and Sunland Park.

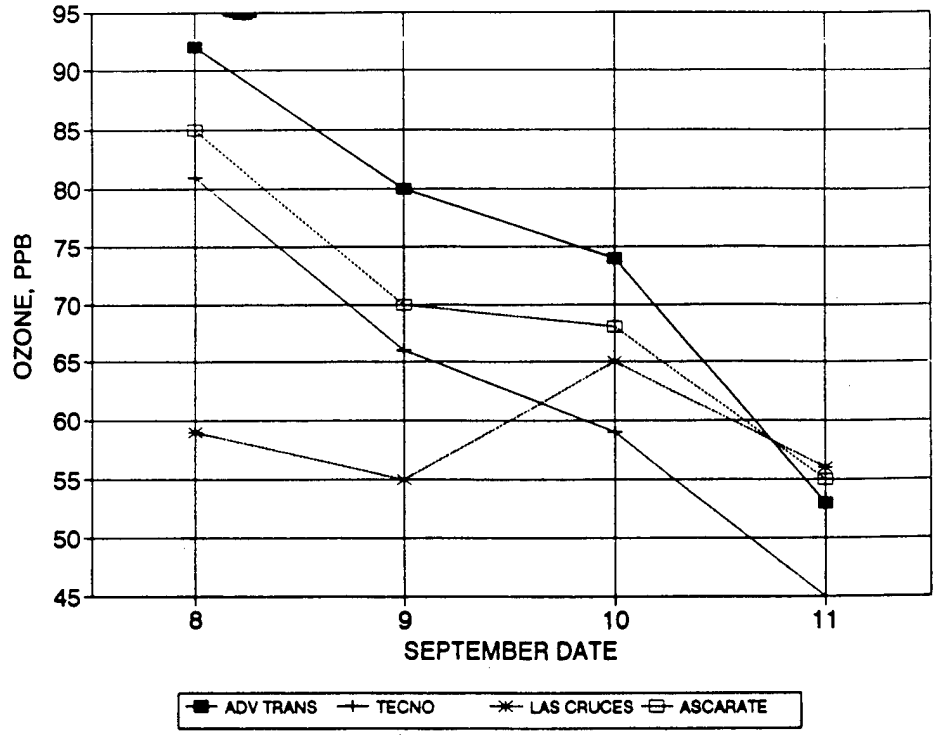


Figure 5. Ozone peaks from Advanced Transformer and Technical Institute (Juarez), Las Cruces, and Ascarate Park.

Technology demonstration was an important part of the study. Measurement devices which are commonly used by government laboratories and universities but are rarely seen in local pollution applications were used in this program. Laser technology was used in both the PSL LDV and the LANL LIDAR. The ARL MAS measured gaseous constituents over an integrated path. Video technology in both the visible and infrared wavelengths were used to demonstrate traffic counting. Radars and SODAR continuously monitored wind profiles over their respective locations. All of this equipment, which is normally used to support Department of Defense and Department of Energy research, was brought to bear on a very important problem---air pollution.

APPENDIX A

AGENDA



Tentative Agenda

Tuesday, 29 November 1994

0730 **REGISTRATION**
(Coffee & Tea)

0830 **Welcome, BG Jerry L. Laws**, Commanding General, WSMR

0840 **Administrative Announcements**
Introduction of Keynote Speaker
Don R. Veazey, Directorate Executive, BED

0900 **Keynote Address, MG Joe W. Rigby**, Army Digitization Office

1000 **BREAK** (Refreshments)

SESSION I: SIMULATION/ANALYSIS

1030 Introduction

1040 A High Resolution Numerical Model to Understand and Predict Air-Sea-Land Interactions in the Littoral Zones
Rangarao V. Madala and *Richard Hodur*, Naval Research Laboratory, *Liang Xu* and *Sethu Raman*, North Carolina State University

1100 Visualization of Obscuration and Contrast Effects Using the Beams Models
Donald W. Hoock, U.S. Army Research Laboratory; *John C. Giever* and *John W. Grace*, New Mexico State University

1120 A Portable System for Data Assimilation in a Limited Area Model
Keith D. Sashegyi and *Rangarao V. Madala*, Naval Research Laboratory; *Frank H. Ruggiero*, Phillips Laboratory; *Sethu Raman*, North Carolina State University

1140 Effect of High Resolution Atmospheric Models on Wargame Simulations
Scarlett D. Ayres, *Robert Sutherland*, and *Doug Sheets*, U.S. Army Research Laboratory; *Steve Lamotte*, Physical Science Laboratory

1200 **LUNCH** at the Community Club

1300 An Assessment of the Potential of the Meteorological Office Mesoscale Model for Predicting Artillery Ballistic Messages
J.D. Turton, Defence Services Division, Meteorological Office, United Kingdom; *Maj T.G. Wilson*, Projects Wing, Royal School of Artillery, United Kingdom.

1320 Results of the Long-Range Overwater Diffusion (LROD) Experiment
James F. Bowers; U.S. Army Dugway Proving Ground; *Roger Carter* and *Thomas B. Watson*, NOAA Air Resources Laboratory

1340 Modeled Ceiling and Visibility
Capt Robert J. Falvey, U.S. Air Force Environmental Technical Applications Center

1400 A New PCFLOS Tool
Kenneth E. Eis, Science Technology Corporation

1420 The Influence of Scattering Volume on Acoustic Scattering by Atmospheric Turbulence
Harry J. Auvermann, U.S. Army Research Laboratory; *George H. Goedecke* and *Michael D. DeAntonio*, New Mexico State University

1440 Relationship Between Aerosol Characteristics and Meteorology of the Western Mojave Desert
L.A. Mathews, Naval Air Warfare Center; **P.L. Walker**, Naval Postgraduate School

1500 Poster Introduction

1520 **BREAK** (Refreshments)

1550 Poster Session

1700 Adjournment

Wednesday, 30 November 1994

SESSION II: OPERATIONAL WEATHER

Session Chair: Col Weaving, HQ, Air Weather Service

0800 Introduction

0810 Electro-Optical Tactical Decision Aid Sensor Performance Model Evaluation
Steven B. Dreksler, *Samson Brand* and *Adreas Goroch*, Naval Research Laboratory

0830 U.S. Army Battlescale Forecast Model Concept of Operations
Martin E. Lee, **James E. Harris**, *Robert W. Endlich*, *Teizi Henmi*, and *Robert E. Dumais*, U.S. Army Research Laboratory; *Maj David I. Knapp*, Operating Location N, Headquarters Air Weather Service; *Danforth C. Weems*, Physical Science Laboratory

0850 Development and Verification of a Low-Level Aircraft Turbulence Index Derived from Battlescale Model Data
Maj David I. Knapp and *MSgt Timothy J. Smith*, Operating Location N, Headquarters Air Weather Service

0910 Current and Future Design of U.S. Navy Mesoscale Models for Operational Use
Richard M. Hodur, Naval Research Laboratory

0930 **BREAK** (Refreshments)

1000 Operational Applications of the Air Force Dial-In System
Capt Gregory T. Engel, Air Force Global Weather Central

1020 Operational Use of Gridded Data Visualizations at the Air Force Global Weather Central
Kim J. Runk, *John V. Zapotocny*, Air Force Global Weather Central

1040 Combat Weather System Concept
James L. Humphrey, **Maj George A. Whicker**, *Capt Robert E. Hardwick*, *2nd Lt Jahna L. Wollard*, Air Weather Service

1100 Small Tactical Terminal Concept and Capabilities
2nd Lt Stephen T. Barish, *George N. Coleman III*, Air Weather Service

1120 Uniform Gridded Data Fields (UGDFs) for War-Fighters
MSgt Thompson, Air Weather Service

1140 Theater Forecast Model Selection
R.M. Cox, Defense Nuclear Agency; *J.M. Lanicci*, Air Force Global Weather Central; *H.L. Massie, Jr.*, Air Weather Service

1200 **LUNCH** at the Community Club

1300 Air Weather Service: Evolving to Meet Tomorrow's Challenges
Col William S. Weaving, *Maj Dewey E. Harms*, **Capt Donald H. Berchoff**, and *Capt Timothy D. Hutchison*, Air Weather Service

1320 Air Force Weather Modernization Planning
Lt Col Alfonse J. Mazurowski, Air Weather Service

1340 Uses of Narrative Climatologies and Summarized Airfield Observations for Contingency Support
Mr. Walters, U.S. Air Force Environmental Technical Applications Center

1400 USAFTAC Dial-In Access
Capt Kevin L. Stone, U.S. Air Force Evaluation Environmental Technical Applications Center

1410 Astronomical Models Accuracy Study
Capt Chan W. Keith and *Capt Thomas J. Smith*, U.S. Air Force Environmental Technical Applications Center

1430 Atmospheric Transmissivity in the 1-12 Micron Wavelength Band for Southwest Asia
Capt Chan W. Keith, *Rich Woodford*, U.S. Air Force Environmental Technical Applications Center

1450 **BREAK** (Refreshments)

1500 Poster Session

1700 Adjournment

1800 **Banquet** at the Hilton Hotel, Las Cruces, NM
Speaker - **Gen Glenn K. Otis (Retired)**

Thursday, 1 December 1994

SESSION III: BATTLE WEATHER

0800 Introduction

0810 Owning the Weather: It Isn't just for Wartime Operations
Richard J. Szymber, *Mary Ann Seagraves*, *James L. Cogan*, and *Odell M. Johnson*, U.S. Army Research Laboratory

0830 The Real Thing: Field Tests and Demonstrations of a Technical Demonstration Mobile Profiler System
James L. Cogan, *Edward M. Measure*, *Edward D. Creegan*, *Dewitt Littell*, and *James Yarbrough*, U.S. Army Research Laboratory; *B. Weber*, *M. Simon*, *A. Simon*, *D. Wolfe*, *D. Merritt*, *D. Weurtz*, *D. Welsh*, Environmental Technology Laboratory, NOAA

0850 Characterizing the Measured Performance of CAAM
Abel J. Blanco, U.S. Army Research Laboratory

0910 Evaluation of Battlescale Forecast Model (BFM)
Teizi Henmi and *Martin E. Lee*, U.S. Army Research Laboratory; *MSGT Timothy J. Smith*, Operating Location N, Air Weather Service

0930 Verification and Validation of the Night Vision Goggle Tactical Decision Aid
John R. Elrick, U.S. Army Research Laboratory

1000 **BREAK** (Refreshments)

SESSION IV: BOUNDARY LAYER

1030 Introduction

1050 Clutter Characterization using Fourier and Wavelet Techniques
J. Michael Rollins, Science and Technology Corporation; *William Peterson*, U. S. Army Research Laboratory

1110 Validation Results for SWOE Scene Generation Process
Max P. Bleiweiss, U.S. Army Research Laboratory; **J. Michael Rollins**, Science and Technology Corporation

1140 The Vehicle Smoke Protection Model Development Program
David J. Johnston, OptiMetrics, Inc.; *William Rouse*, Edgewood Research, Development and Engineering Center

1200 **LUNCH** at the Community Club

1300 Smoke Evaluation Methods
William Rouse and *Michael Causey*, Edgewood Research, Development and Engineering Center; **Mark R. Perry** and *Michael R. Kuhlman*, Battelle

1320 Analysis of Water Mist/Fog Oil Mixtures
William M. Gutman and *Troy D. Gammill*, Physical Science Laboratory; *Frank T. Kantrowitz*, U.S. Army Research Laboratory

1340 Millimeter Wave Transmissometer System
Robert W. Smith, U.S. Army Test and Evaluation Command; *William W. Carrow*, EOIR Measurements, Inc.

SESSION V: ATMOSPHERIC PHYSICS

1400 Introduction

1410 Wind Field Measurement with an Airborne cw-CO_2-Doppler-Lidar (ADOLAR)
Stephan Rahm and *Christian Werner*, German Aerospace Establishment DLR

1430 Behavior of Wind Fields through Tree Stand Edges
Ronald M. Cionco, U.S. Army Research Laboratory; *D. R. Miller*, The University of Connecticut

1450 **BREAK** (Refreshments)

1510 Remote Wind Profiling and the White Sands Missile Range Reference Atmosphere
John Hines, Frank Eaton, Scott McLaughlin, Atmospheric Profiler Research Facility; *Wayne Flowers, Linda Parker-Sedillo* and **Glenn Hoidale**, Science and Technology Corporation

1530 Role of Transilient Turbulence Theory and Radiative Transfer in Owning the Weather
Robert A. Sutherland, *Young P. Yee* and *Richard J. Szymber*, U.S. Army Research Laboratory

1550 Turbulent Length Scales of Eddy Structures in the Surface Layer of the Convective Boundary Layer
Dennis M. Garvey, *Jill Thompson, Raul Gonzalez*, U.S. Army Research Laboratory; *David Miller*, Department of Natural Resources, University of Connecticut

1610 Forecasting/Modeling the Atmospheric Optical Neutral Events over a Desert Environment
Gail Tirrell Vaucher, Science and Technology Corporation; *Robert W. Endlich*, U.S. Army Research Laboratory

1620 Atmospheric Variability Measured by POAM-II
John Hornstein, *Richard Bevilacque* and *Eric Shettle*, Remote Sensing Division, Naval Research Laboratory, Washington, DC

1640 Closing Remarks
Presentation of Awards
Photographs

1700 Adjournment

****

Tuesday, 29 November 1994

SESSION I: SIMULATION AND ANALYSIS
POSTERS

Combined Obscuration Model for Battlefield Induced Contaminants - Polarimetric Millimeter Wave Version (COMBIC-PMW)
Scarlett D. Ayres, *Brad Millard* and *Robert Sutherland*, U.S. Army Research Laboratory

A Multistream Simulation of Multiple Scattering of Polarized Radiation by Ensembles of Non-Spherical Particles
Sean G. O'Brien, Physical Science Laboratory

Three Dimensional Rendering of Cloud Radiance Fields
David H. Tofsted, U.S. Army Research Laboratory; *Rhonda A. Reumann*, Physical Science Laboratory

Interactive Computer Programs for Analysis of Atmospheric Effects on Ultraviolet Signatures
James B. Gillespie and *David L. Rosen*, U.S. Army Research Laboratory; *David Braddi*, Physical Science Laboratory

Combined Obscuration Model for Battlefield Induced Contaminants-Radiative Transfer Version (COMBIC-RT)
Scarlett D. Ayres and *Robert Sutherland*, U.S. Army Research Laboratory

Numerical Simulation of Cloudy Convective Layer
Wen-Yih Sun, Purdue University

Wednesday, 30 November 1994

SESSION II: OPERATIONAL WEATHER POSTERS

Results of the U.S. Army Battlefield Forecast Model Performance during Operation Desert Capture
Robert E. Dumais, Jr. and *Teizi Henmi*, U.S. Army Research Laboratory

Forecasting Weather Hazards on the Battlefield
Jeffrey E. Passner, U.S. Army Research Laboratory

Thursday, 1 December 1994

SESSION III: BATTLE WEATHER POSTERS

Comparison of Radiometer and Radiosonde Derived Temperature Profiles Measured at Wallops Island, VA
Edward M. Measure, U.S. Army Research Laboratory; *Dick R. Larson*, Physical Science Laboratory; *Francis Schmidlin*, *Sean McCarthy*, NASA Goddard Space Flight Center Facility at Wallops Island, VA

The Integrated Weather Effects Decision Aid Threat Module
David P. Sauter, U.S. Army Research Laboratory; *Carl H. Chesley* and *Andrew R. Spillane*, Science and Technology Corporation

Neural Network Derived Thermal Profiles: Analysis and Comparison with Rawinsonde Data
Arthur W. Dudenhoeffer and *Donald D. Bustamante*, Physical Science Laboratory; *James L. Cogan*, U.S. Army Research Laboratory

Owning the Weather Battlefield Observations Framework
Richard J. Szymber and *James L. Cogan*, U.S. Army Research Laboratory

Development of a Rawinsonde-Trained Neural Network for Retrieving Atmospheric Thermal Profiles
Donald D. Bustamante and *Arthur W. Dudenhoeffer*, Physical Science Laboratory; *James L. Cogan*, U.S. Army Research Laboratory

Electro-Optical Climatology Microcomputer Version 2.2 Demonstration (EOCLIMO)
Capt Matthew R. Williams, U.S. Air Force Environmental Technical Applications Center

Air Weather Service's "For Your Information" Pamphlets
Capt Julie A. Hayes, Air Weather Service

SESSION IV BOUNDARY LAYER POSTERS

Technical Exchange with Australia
James Gillespie and **Patti Gillespie**, U.S. Army Research Laboratory

Improvements to Modeling of Polarimetric Scattering
Michael DeAntonio, National Research Council Post Doc, U.S. Army Research Laboratory

Atmospheric Acoustic Characterization in Support of BAT Field Testing
John R. Fox, U.S. Army Research Laboratory; *Prasan Chintawongvanich*, Physical Science Laboratory

ARL Remote Sensing Rover as a Ground Truth Monitor at the XM-21 Challenge System Field Test
Frank T. Kantrowitz and *Dale U. Foreman*, U.S. Army Research Laboratory; *William M. Gutman* and *Troy D. Gammill*, Physical Science Laboratory

Small Scale Attenuation Analysis of Fibrous Millimeter Wave Obscurant
William G. Rouse, Edgewood Research, Development and Engineering Center; *W.C. Schimpf*, Hercules Incorporated Delaware; *R.G. Boe*, Hercules Incorporated Utah

Lidar Observations During Smoke Week XIV
Max P. Bleiweiss and *Roger A. Howerton*, U.S. Army Research Laboratory

Evaluation of the Holodar Optical Scintillometer
Robert W. Smith, U.S. Army Test and Evaluation Command; *John Dove* and *Stephen Kupiec*, Dove Electronics, Incorporated

Enhanced Photon Absorption in Multi-Component Aerosol Mixes and Effects on Radiation Profiles
Young P. Yee and *Robert A. Sutherland*, U.S. Army Research Laboratory; *Roger E. Davis*, Science and Technology Corporation

SESSION V: ATMOSPHERIC PHYSICS POSTERS

Temperature Profile of the Nocturnal Stable Boundary Layer over Homogeneous Desert using LA-Teams
R. Todd Lines and **Young P. Yee**, U.S. Army Research Laboratory

Comparison of Boundary-Layer Wind and Temperature Measurements with Model Estimations
Richard Okrasinski, Physical Science Laboratory; *Arnold Tunick*, U.S. Army Research Laboratory

Clear-Air Inhomogeneous Boundary Layer Structure and Possible Effect on Radar Remote Sensing Systems
Scott McLaughlin, *Frank Eaton* and *John Hines*, U.S. Army Research Laboratory

Optical Turbulence Measurements at Apache Point Observatory
Frank D. Eaton, *John R. Hines, Scott A. McLaughlin, William H. Hatch*, U.S. Army Research Laboratory; *James J. Drexler, James Northrup*, Lockheed Engineering and Sciences Company

The APRF SODAR: Bridging the Lower Boundary Layer
John Hines, *Frank Eaton* and *Scott McLaughlin*, U.S. Army Research Laboratory; *G. Hoidale, W. Flowers, L. Parker-Sedillo*, Science and Technology Corporation

A Look at Thermal Turbulence Induced Radar Returns In or Near Rain Clouds at the Atmospheric Profiler Research Facility
William H. Hatch, U.S. Army Research Laboratory

The Large Eddy Simulation Probability Density Function for Concentration Fluctuations
Ronald E. Meyers and *Keith S. Deacon*, U.S. Army Research Laboratory

LDV Wind Profile Measurements Within and Above an Urban Domain
Ronald M. Cionco and *Brian L. Orndorff*, U.S. Army Research Laboratory

APPENDIX B

LIST OF ATTENDEES

Lt Col Richard B. Bensinger

HQ 5WS/DO (U.S. Forces Korea SWO)
Unit 15173
APO AP 96205-0108
Telephone: 011-82-2-7915-6509
DSN 725-6509
FAX: Ext 3096
Email: hq5ws@emh2.korea.army.mil

Capt Donald H. Berchoff

Hq, Air Weather Service
102 W. Losey St, Room 105
Scott AFB, IL 62225-5206
Telephone: (618) 256-4721 x430
DSN 576-4721 x430
FAX: Ext 6300
Email: berchoff@hqaws;safb.af.mil

Dr. Paul A. Birkel

The MITRE Corporation
MS Z421
7525 Colshire Drive
McLean, VA 22102-3481
Telephone: (703) 883-6399
FAX: Ext 6435

Mr. Abel J. Blanco

U.S. Army Research Laboratory
Battlefield Environment Directorate
ATTN: AMSRL-BE-W
White Sands Msl Range, NM 88002-5501
Telephone: (505) 678-3924
DSN 258-3924
FAX: Ext 3385
Email: ablanco@arl.mil

Mr. Max P. Bleiweiss

U.S. Army Research Laboratory
Battlefield Environment Directorate
ATTN: AMSRL-BE-A
White Sands Msl Range, NM 88002-5501
Telephone: (505) 678-3504
DSN 258-3504
FAX: Ext 8822
Email: mbleiwei@arl.mil

Maj John Boggs

HQ TRADOC
ATTN: ATDO-IW
Fort Monroe, VA 23651-5000
Telephone: (804) 727-2319
DSN 680-2319
Email: boggsJ@monroe-emh1.army.mil

Mr. James F. Bowers

West Desert Test Center
ATTN: STEDP-WD-M
Dugway Proving Ground, UT 84022-5000
Telephone: (801) 831-5101
DSN 789-5101
FAX: Ext 5289

Dr. Douglas R. Brown

U.S. Army Research Laboratory
Battlefield Environment Directorate
ATTN: AMSRL-BE
White Sands Msl Range, NM 88002-5501
Telephone: (505) 678-1225
DSN 258-1225
FAX: Ext 1230
Email: dbrown@arl.mil

Lt Col Raymond C. Brown

HQ USMC (ASL-44)
2 Navy Annex
Washington, DC 20380-1775
Telephone: (703) 614-1835
DSN 224-1835
FAX: Ext 7343

Mr. Robert C. Brown

U.S. Army Research Laboratory
Battlefield Environment Directorate
ATTN: AMSRL-BE-E
White Sands Msl Range, NM 88002-5501
Telephone: (505) 678-4301
DSN 258-4301
FAX: Ext 8366
Email: bbrown@arl.mil

Dr. Chuck Bruce

U.S. Army Research Laboratory
Battlefield Environment Directorate
ATTN: AMSRL-BE-E
White Sands Msl Range, NM 88002-5501
Telephone: (505) 678-1585
DSN 258-1585
Email: cbruce@arl.mil

Dr. Dorothy Bruce

U.S. Army Research Laboratory
Battlefield Environment Directorate
ATTN: AMSRL-BE-S
White Sands Msl Range, NM 88002-5501
Telephone: (505) 678-5524
DSN 258-5524
FAX: Ext 8366
Email: dbruce@arl.mil

Maj Michael J. Buell

Naval Meteorology & Oceanography Cmd
1020 Balch Blvd
Stennis Space Center, MS 39529-5005
Telephone: (601) 688-5051
DSN 485-5051
FAX: Ext 5332
Email: n331@cnmoc.navy.mil

Mr. Brian R. Bullard

Science and Technology Corporation
555 Telshor Boulevard, Suite 200
Las Cruces, NM 88011-0000
Telephone: (505) 521-4353
FAX: Ext 9062

Mr. John H. Byers

U.S. Army Research Laboratory
Battlefield Environment Directorate
ATTN: AMSRL-BE-E
White Sands Msl Range, NM 88002-5501
Telephone: (505) 678-3951
DSN 258-3951
FAX: Ext 2053
Email: jbyers@arl.mil

Mr. Ronald Catherson

Science and Technology Corporation
555 Telshor Boulevard, Suite 200
Las Cruces, NM 88011-0000
Telephone: (505) 521-4353
FAX: Ext 9062

Ms. Carolin Chatham

ILFX Sys, Inc.
2500 Fry Blvd
Sierra Vista, AZ 85635
Telephone: (602) 538-6647
DSN 879-6647
FAX: (602) 458-3013

Mr. Ronald M. Cionco

U.S. Army Research Laboratory
Battlefield Environment Directorate
ATTN: AMSRL-BE-E
White Sands Msl Range, NM 88002-5501
Telephone: (505) 678-5210
DSN 258-5210
FAX: Ext 2053
Email: rcionco@arl.mil

Ms. Pamela A. Clark

U.S. Army Research Laboratory
ATTN: AMSLC-AT
2800 Powder Mill Road
Adelphi, MD 20783-1145
Telephone: (301) 394-3594
DSN 290-3594
FAX: Ext 4697
Email: pclark@arl.mil

Dr. James L. Cogan

U.S. Army Research Laboratory
Battlefield Environment Directorate
ATTN: AMSRL-BW-W
White Sands Msl Range, NM 88002-5501
Telephone: (505) 678-2094
DSN 258-2094
FAX: Ext 3385
Email: jcogan@arl.mil

Dr. Darrell Collier

U.S. Army SSDC
PO Box 15280
Arlington, VA 22215-0280
Telephone: (703) 607-1876
DSN 327-1876
FAX: Ext 3854
Email: dcollier@ssdcw-usassdc.army.mil

Mr. Wendell L. Cook

Nichols Research Corp.
4040 S. Memorial Parkway
Huntsville, AL 35802
Telephone: (205) 890-2274
FAX: Ext 2299
Email: cookw@puzzler.nichols.com

Maj Michael F. Corbett

USAIC & FH Weather Support Team
ATTN: ATZS-CDI-W
Ft. Huachuca, AZ 85613-0000
Telephone: (602) 538-6472
DSN 879-6493
FAX: Ext 6679

Mr. Joseph J. Cox

System Sciences, Inc.
2707 Artie Street, Suite 7
Huntsville, AL 35805-0000
Telephone: (205) 551-0707
FAX: Ext 0776

Maj Robert M. Cox

Defense Nuclear Agency
SPWE
6801 Telegraph Road
Alexandria, VA 22310-3398
Telephone: (703) 325-1282
DSN 221-1282
FAX: Ext 0398

Mr. John N. Crain

Science and Technology Corporation
555 Telshor Boulevard, Suite 200
Las Cruces, NM 88011-0000
Telephone: (505) 521-4353
FAX: Ext 9062

Mr. Edward D. Creegan

U.S. Army Research Laboratory
Battlefield Environment Directorate
ATTN: AMSRL-BE-W
White Sands Msl Range, NM 88002-5501
Telephone: (505) 678-4684
DSN 258-4684
FAX: Ext 3385
Email: ecreegan@arl.mil

Lt Col Joseph Czarniecki

2nd Weather Flight
Bldg 130, Anderson Way
Ft. McPherson, GA 80330-5000
Telephone: DSN 572-2234
FAX: Ext 2744

Dr. Roger E. Davis

Science and Technology Corporation
555 Telshor Boulevard, Suite 200
Las Cruces, NM 88011-0000
Telephone: (505) 521-4353
FAX: Ext 9062

Mr. Keith Deacon

U.S. Army Research Laboratory
Battlefield Environment Directorate
ATTN: AMSRL-BE-E
White Sands Msl Range, NM 88002-5501
Telephone: (505) 678-4037
DSN 258-4037
FAX: Ext 4393
Email: kdeacon@arl.mil

Mr. Michael D. DeAntonio

National Research Council/ARL-BED
ATTN: AMRSL-BE-S
White Sands Msl Range, NM 88002-5501
Telephone: (505) 678-3258
DSN 258-3258
FAX: Ext 2053
Email: mdeanton@arl.mil

Dr. Adarsh Deepak

Science and Technology Corporation
101 Research Drive
Hampton, VA 23666-1340
Telephone: (804) 865-1894
FAX: Ext 1294

Mr. Robert E. Dekinder, Jr.

U.S. Army Research Laboratory
Battlefield Environment Directorate
ATTN: AMSRL-BE-S
White Sands Msl Range, NM 88002-5501
Telephone: (505) 678-7371
DSN 258-7371
FAX: Ext 8366
Email: dekinder@arl.mil

Dr. Nathan Dinar

Israel Institute for Biological Res
Department of Mathematics
PO Box 19
70450 Ness-Ziona
ISRAEL
Telephone: 972-8-381430
FAX: Ext 401404
Email: natan@math.wxiibr.co.il

Mr. Steven B. Dreksler

Computer Sciences Corporation
Naval Research Laboratory
7 Grace Hopper Avenue
Monterey, CA 93940-0000
Telephone: (408) 656-4784
DSN 878-4784
FAX: Ext 4769
Email: dreksler@arlmry.navy.mil

Dr. Arthur W. Dudenhoeffer

Physical Science Laboratory
Applied Analysis
P.O. Box 30002
New Mexico State University
Las Cruces, NM 88003-0002
Telephone: (505) 522-9343
FAX: Ext 9434
Email: adude@psl.nmsu.edu

Mr. Robert E. Dumais, Jr.

U.S. Army Research Laboratory
Battlefield Environment Directorate
ATTN: AMSRL-BE-W
White Sands Msl Range, NM 88002-5501
Telephone: (505) 678-4650
DSN 258-4650
FAX: Ext 3385
Email: rdumais@arl.mil

Dr. Frank D. Eaton

U.S. Army Research Laboratory
Battlefield Environment Directorate
ATTN: AMSRL-BE-E
White Sands Msl Range, NM 88002-5501
Telephone: (505) 678-3956
DSN 258-3956
FAX: Ext 7623
Email: featon@arl.mil

Mr. Kenneth E. Eis

STC-METSAT
515 S. Howes Street
Fort Collins, CO 80521-0000
Telephone: (303) 221-5420
FAX: (303) 493-3410

Mr. D. Scott Elliott

U.S. Army Research Laboratory
Battlefield Environment Directorate
ATTN: AMSRL-BE-W
White Sands Msl Range, NM 88001-5501
Telephone: (505) 678-6509
DSN 258-6509
FAX: Ext 3385
Email: selliott@arl.mil

Mr. John R. Elrick

U.S. Army Research Laboratory
Battlefield Environment Directorate
ATTN: AMSRL-BE-W
White Sands Msl Range, NM 88002-5501
Telephone: (505) 678-3691
DSN 258-3691
FAX: Ext 3385
Email: jelrick@arl.mil

Mr. Robert Endlich

U.S. Army Research Laboratory
Battlefield Environment Directorate
ATTN: AMSRL-BE-W
White Sands Msl Range, NM 88002-5501
Telephone: (505) 678-6297
DSN 258-6297
FAX: Ext 3385
Email: bendlich@arl.mil

Capt Gregory T. Engel

Air Force Global Weather Service
DOO
MBB 39
106 Peacekeeper Drive, Ste 2N3
Offutt AFB, NB 68113-4039
Telephone: (402) 294-1631
DSN 271-1631

Ms. Joanne M. Esparza

Physical Science Laboratory
New Mexico State University
P.O. Box 30002
Las Cruces, NM 88003-0002
Telephone: (505) 522-9117
FAX: Ext 9389
Email: jesparza@psl.nmsu.edu

Prof Oskar M. Essenwanger

University of Alabama in Huntsville
Atmos & Environmental Science Dept
Research Institute, Room A-11
610 Mountain Gap Drive
Huntsville, AL 35803-1630
Telephone: (205) 895-6296
FAX: (205) 922-5755

Capt Fred Fahlbusch

National Air Intelligence Center
NAIC/TATW
4115 Hebble Creek Road, Ste #31
Wright Patterson AFB, OH 45433-5635
Telephone: (513) 257-7071
DSN 787-7071
FAX: Ext 9888
Email: flfl11@naic.wpafb.af.mil

Dr. Herbert F. Fallin, Jr.

Office of the Assistant Secretary
(Research, Development and
Acquisition)
ATTN: SARD-ZD
103 Army Pentagon, Room 2E673
Washington, DC 20310-0103
Telephone: (703) 697-2653
DSN 227-2653
FAX: (703) 695-9069 DSN 225-9069

Capt Gary R. Faltinowski

Space and Naval Warfare Systems
Command
2451 Crystal Drive, PMW 175, Rm 301
Arlington, VA 22245-5200
Telephone: (703) 602-3891
DSN 332-3891
FAX: Ext 1535
Email: faltinow@spacwar.navy.mil

Capt Robert J. Falvey

USAFETAC
Simulations and Techniques Branch
859 Buchanan Street, Rm 3118
Scott AFB, IL 62225-5116
Telephone: (618) 256-5412
DSN 576-5412
FAX: Ext 3772
Email: sytrjf@etacrs1.safb.af.mil

Dr. W. Michael Farmer

OPTIMETRICS
505 S. Main, Ste #200
Las Cruces, NM 88001-0000
Telephone: (505) 527-5623
FAX: Ext 5633

Capt Robert J. Farrell, Jr.

USAF ROME LAB /WE
26 Electronic Pkwy
Griffiss AFB, NY 13441-4516
Telephone: (315) 330-3085
DSN 578-3085
FAX: Ext 3909
Email: we@admin.lonexa.rl.af.mil

Mr. Bryan Folk

HQ AFOTEC
Simulations and Techniques Branch
859 Buchanan Street, Rm 3118
Scott AFB, IL 62225-5116
Telephone: (618) 256-5412
DSN 576-5412
FAX: Ext 3772

Mr. John Fox

U.S. Army Research Laboratory
Battlefield Environment Directorate
ATTN: AMSRL-BE-S
White Sands Msl Range, NM 88002-5501
Telephone: (505) 678-2110
DSN 258-2110
FAX: Ext 8366
Email: jfox@arl.mil

Dr. K. Patrick Freeman

Science and Technology Corporation
555 Telshor Boulevard, Suite 200
Las Cruces, NM 88011-0000
Telephone: (505) 521-4353
FAX: (505) 522-9062

Dr. Dennis M. Garvey

U.S. Army Research Laboratory
Battlefield Environment Directorate
ATTN: AMSRL-BE-E
White Sands Msl Range, NM 88002-5501
Telephone: (505) 678-5677
DSN 258-5677
FAX: Ext 3042
Email: dgarvey@arl.mil

Dr. James Gillespie

U.S. Army Research Laboratory
Battlefield Environment Directorate
ATTN: AMSRL-BE-S
White Sands Msl Range, NM 88002-5501
Telephone: (505) 678-6609
DSN 258-6609
FAX: Ext 8366
Email: jgillesp@arl.mil

Dr. Patti Gillespie

U.S. Army Research Laboratory
Battlefield Environment Directorate
ATTN: AMSRL-BE-S
White Sands Msl Range, NM 88002-5501
Telephone: (505) 678-1817
DSN 258-1817
FAX: Ext 8366
Email: pgillesp@arl.mil

Raymond H. Godin

Deputy, Prog Int Div, US Naval Observ
Oceanographer of the Navy
N961B
3450 Masschusetts Ave, NW
WASH, DC 20392-5421
Telephone: (202) 653-1616
DSN 294-1616

Mrs. Shlomit Grossman

TAAS - Israel Industries Ltd.
Israel Military Industries
P.O. Box 1044/45
Ramat Hasharom 47100
ISRAEL
Telephone: 972 3 5484265
FAX: Ext 306

Mr. Kristan P. Gurton

2200 Corley Drive, Apt 6G
Las Cruces, NM 88001-0000
Telephone: (505) 678-1585
DSN 258-1585

Dr. William M. Gutman

Physical Science Laboratory
New Mexico State University
P.O. Box 30002
Las Cruces, NM 88003-0002
Telephone: (505) 521-9573
FAX: (505) 522-9434
Email: gutman@psl.nmsu.edu

Dr. Patrick E. Hagerty

UNITED DEFENSE, L.P.
4800 E. River Road
Minneapolis, MN 55421-1498
Telephone: (612) 572-4787
FAX: Ext 4991

Mr. James E. Harris

U.S. Army Research Laboratory
Battlefield Environment Directorate
ATTN: AMSRL-BE-W
White Sands Msl Range, NM 88002-5501
Telephone: (505) 678-5424
DSN 258-5424
FAX: Ext 3385
Email: jharris@arl.mil

Dr. Edward J. Harrison, Jr.

CSC/PSG
Ap 2, Suite 4000
2611 Jefferson Davis Hwy
Crystal City, VA 22202-0000
Telephone: (703) 418-8534
FAX: Ext 4972

Mr. William H. Hatch

U.S. Army Research Laboratory
Battlefield Environment Directorate
ATTN: AMSRL-BE-E
White Sands Msl Range, NM 88002-5501
Telephone: (505) 678-1561
DSN 258-1561
FAX: Ext 7623
Email: whatch@arl.mil

Capt Julie A. Hayes

Hq, Air Weather Service
HQ AWS/XOTT
102 W. Losey St., Room 105
Scott AFB, IL 62225-5206
Telephone: (618) 256-4721x234
DSN 576-4721x234
FAX: Ext 6300
Email: hayes@hqaws.safb.af.mil

Dr. Teizi Henmi

U.S. Army Research Laboratory
Battlefield Environment Directorate
ATTN: AMSRL-BE-W
White Sands Msl Range, NM 88002-5501
Telephone: (505) 678-3519
DSN 258-3519
FAX: Ext 3385
Email: thenmi@arl.mil

Ms. Joyce R. Henry

U.S. Army Tradoc Analysis Center
ATTN: ATRC-WEA
White Sands Msl Range, NM 88002-0000
Telephone: (505) 678-4789
DSN 258-4789
FAX: Ext 5104

Mr. Richard F. Himebrook

U.S. Army Research Laboratory
ATTN: AMSRL-BE-A
White Sands Msl Range, NM 88002-5501
Telephone: (505) 678-4917
DSN 258-4917
FAX: Ext 2432
Email: rhimebro@arl.army.mil

Mr. John R. Hines

U.S. Army Research Laboratory
Battlefield Environment Directorate
ATTN: AMSRL-BE-E
White Sands Msl Range, NM 88002-5501
Telephone: (505) 678-1561
DSN 258-1561
FAX: Ext 7623
Email: jhines@arl.mil

Dr. Donald B. Hodges

HUGHES STX
109 Massachusetts Avenue
Lexington, MA 02173-0000
Telephone: (617) 862-0713
FAX: (617) 863-2357

Dr. Richard M. Hodur

Naval Research Laboratory
Box 2 NRL
7 Grace Hopper Ave
Monterey, CA 93943-5502
Telephone: (408) 656-4788
DSN 878-4788
FAX: Ext 4769
Email: hodur@nrlmry.navy.mil

Capt David W. Holt

Headquarters, Air Weather Service
SYDC
102 W. Losey St, Room 105
Scott AFB, IL 62225-5206
Telephone: (618) 256-3268 x309
DSN 576-3268 x309
FAX: Ext 8359
Email: holt@hqaws.safb.af.mil

Dr. Donald W. Hoock

U.S. Army Research Laboratory
Battlefield Environment Directorate
ATTN: AMSRL-BE-S
White Sands Msl Range, NM 88002-5501
Telephone: (505) 678-5430
DSN 258-5430
FAX: Ext 8366
Email: dhoock@arl.mil

Maj George F. Howard, III

U.S. Army Intelligence Center &
Ft. Huachuca
ATTN: ATZS-CDI-W
Ft. Huachuca, AZ 85635-0000
Telephone: (602) 538-6472
DSN 879-6472
FAX: Ext 6679

Mr. Robert E. Introne, Jr.

The Analytic Sciences
Corporation(TASC)
55 Walkers Brook Drive
Reading, MA 01867-0000
Telephone: (617) 942-2000 x 2331
FAX: (617) 942-7100
Email: reintrone@tasc.com

Mr. Jeffrey O. Johnson

U.S. Army Research Laboratory
Battlefield Environment Directorate
ATTN: AMSRL-BE-E
White Sands Msl Range, NM 88002-5501
Telephone: (505) 678-3569
FAX: Ext 7623
Email: jeffj@arl.mil

Mr. Odell M. Johnson

U.S. Army Research Laboratory
Battlefield Environment Directorate
ATTN: AMSRL-BE-W
White Sands Msl Range, NM 88002-5501
Telephone: (505) 678-3608
DSN 258-3608
FAX: Ext 3385
Email: ojohnson@arl.mil

Mr. David J. Johnston

OptiMetrics, Inc.
2107 Laurel Bush Road, Suite 209
Bel Air, MD 21015-0000
Telephone: (410) 569-0293
FAX: Ext 0295
Email: johnston@omi.com

Mr. Frank T. Kantrowitz

U.S. Army Research Laboratory
Battlefield Environment Directorate
ATTN: AMSRL-BE-E
White Sands Msl Range, NM 88002-5501
Telephone: (505) 678-1526
DSN 258-1526
FAX: Ext 8366
Email: fkantrow@arl.mil

Dr. Hadassah Kaplan

Israel Institute for Biological Res
Department of Mathematics
PO Box 19
70450 Ness-Ziona
ISRAEL
Telephone: 972-8-381440
FAX: Ext 401404
Email: hadas@math.wxiibr.co.il

Mr. Dennis D. Kasparek

Science and Technology Corporation
555 Telshor Blvd, Suite 200
Las Cruces, NM 88011-0000
Telephone: (505) 521-4353
FAX: (505) 522-9062

Capt Chan W. Keith

U.S. Air Force Environmental
Technical
Applications Center
USAFETAC/SYT
859 Buchanan St., Rm 311N
Scott AFB, IL 62225-5116
Telephone: (618) 256-5211
DSN 576-5211
FAX: Ext 3772
Email: sytcwk@etacrs1.safb.af.mil

Capt Jonathan L. Keely

ESC/WE
Hanscom AFB, MA 01731-2122
Telephone: (617) 377-3238
DSN 478-3238

Dr. Neal H. Kilmer

Physical Science Laboratory
New Mexico State University
P.O. Box 30002
Las Cruces, NM 88003-0002
Telephone: (505) 522-9495
FAX: Ext 9389 or 9434
Email: nkilmer@arl.mil

Mr. Steven F. Kirby

U.S. Army Research Laboratory
Battlefield Environment Directorate
ATTN: AMSRL-BE-W
White Sands Msl Range, NM 88002-5501
Telephone: (505) 678-7474
DSN 258-7474
FAX: Ext 3385
Email: skirby@arl.mil

Dr. Moshe Kleiman

Israel Institute for Biological Res
PO Box 19
Ness-Ziona 70450
ISRAEL
Telephone: 972-8-381654
FAX: Ext 401404

Dr. Bill Klein

Science and Technology Corporation
PO Drawer 250
White Sands Msl Range, NM 88002-0250
Telephone:
(505) 679-5078
FAX: Ext 5228

Mr. Frank J. Klein

Science and Technology Corporation
PO Drawer 250
White Sands Msl Range, NM 88002-0250
Telephone: (505) 679-5078
FAX: Ext 5228

Mr. Walter G. Klimek

U.S. Army Research Laboratory
Survivability/Lethality Analysis Dir
ATTN: AMSRL-SL-CO
Aberdeen Prov Ground, MD 21010-5423
Telephone: (410) 671-2260
DSN 584-2260
FAX: Ext 3471
Email:
wgklimek@cbdcom@apgea.army.mil

Maj David I. Knapp

OL-N, HQ AWS
U.S. Army Research Laboratory
ATTN: AMSRL-BE-W
White Sands Msl Range, NM 88002-5501
Telephone: (505) 678-8148
DSN 258-8148
FAX: Ext 3385
Email: dknapp@arl.mil

Dr. William T. Kreiss

Georgia Institute of Technology
Georgia Tech Research Institute
EOEML/315 Baker Building
925 Dalney Street
Atlanta, GA 30332-0800
Telephone: (404) 894-4392
FAX: Ext 6285
Email: bill.kreiss@gtri.gatech.edu

Mr. Arthur C. Kyle

STC/U.S. Army Space Command
1925 Aerotech Drive, Suite 212
Colorado Springs, CO 80916-4219
Telephone: (719) 570-8715
FAX: (719) 574-2594

Mr. Martin E. Lee

U.S. Army Research Laboratory
Battlefield Environment Directorate
ATTN: AMSRL-BE-W
White Sands Msl Range, NM 88002-5501
Telephone: (505) 678-5593
DSN 258-5593
FAX: Ext 3385
Email: mlee@arl.mil

Mr. R. Todd Lines

ARL/BE (NMSU)
1314 McArthur Drive
Las Cruces, NM 88001-0000
Telephone: (505) 678-7668
DSN 258-7668
Email: tlines@arl.mil

Capt J. Bryan Mackey

12th Air Support Operations Squadron
Bldg 11210 Slewitzke Rd
Biggs AAF
Ft. Bliss, TX 79918-5000
Telephone: (915) 568-8702/8409
DSN 978-8702/8409
FAX: Ext 8945

Mr. Mat V. Maddix

U.S. Army Missile Command
ATTN: AMSMI-RD-SS-AA
Redstone Arsenal, AL 35898-5000
Telephone: (205) 876-2339
DSN 746-2339
FAX: Ext 6799

Mr. Joseph L. Manning

Computer Science Corporation
4815 Bradford Drive
Huntsville, AL 35805-0000
Telephone: (205) 876-8295
DSN 746-8295
FAX: (205) 837-4301

Cdr David G. Markham

Space and Naval Warfare Systems Command
COMSPAWARSYSCOM PMW-175, Room 301
2451 Crystal Drive
Arlington, VA 22245-5200
Telephone: (703) 602-7039
DSN 332-7039
FAX: Ext 1535
Email:
markhamd@smtp-gw.spawar.navy.mil

Lt Paul E. Matthews

U.S. Special Operations Command
J-2 METOC, USSOCOM SOJ2-METOC
7701 Tampa Point Blvd
McDill AFB, FL 33621-5323
Telephone: (813) 828-6041/2
DSN 968-6041

Lt Col Alfonse J. Mazurowski

HQ AWS/XOT
102 West Losey St, Room 105
Scott AFB, IL 62225-5206
Telephone: (618) 256-5631x421
DSN 576-5631x421
FAX: Ext 6306
Email: maz@hqaws.safb.af.mil

Dr. Robert A. McClatchey

Phillips Lab/Geophysics Lab
ATTN: AFGL/LY
29 Randolph Road
Hanscom AFB, MA 01731-5000
Telephone: (617) 377-2975
DSN 478-2975
FAX: Ext 8892

Mr. Steve J. McGee

Physical Science Laboratory
New Mexico State University
PO Box 30002
Las Cruces, NM 88003-0002
Telephone: (505) 522-9374
FAX: Ext 9434
Email: smcgee@psl.nmsu.edu

Mr. Charles P. McGrath

Naval Command, Control and Ocean Surveillance Center, RDT&E Division
NCCOSC RDTE DIV 543
53170 Woodward Road
San Diego, CA 92152-7385
Telephone: (619) 553-1416
DSN 553-1416
FAX: Ext 1417
Email: mcgrath@nosc.mil

Capt Stephen R. McMillan

46 OSS/OSWT
601 W. Choctawhatchee, Ste 60
Eglin AFB, FL 32542-5719
Telephone: (904) 882-5960
DSN 872-5960
FAX: Ext 3341
Email: mcmillan@eglin.af.mil

Mr. Gary McWilliams

U.S. Army Research Laboratory
Battlefield Environment Directorate
ATTN: AMSRL-BE-W
White Sands Msl Range, NM 88002-5501
Telephone: (505) 678-4388
DSN 258-4388
FAX: Ext 3385
Email: gmcwilli@arl.mil

Dr. Edward M. Measure

U.S. Army Research Laboratory
Battlefield Environment Directorate
ATTN: AMSRL-BE-W
White Sands Msl Range, NM 88002-5501
Telephone: (505) 678-3307
DSN 258-3307
FAX: Ext 3385
Email: emeasure@arl.mil

Mr. Ronald E. Meyers

U.S. Army Research Laboratory
Battlefield Environment Directorate
ATTN: AMSRL-BE-S
White Sands Msl Range, NM 88002-5501
Telephone: (505) 678-4037
DSN 258-4037
FAX: Ext 4393
Email: rmeyers@arl.mil

Mr. John M. Miller

U.S. Army Research Laboratory
ATTN: AMSRL-SS-S (Mr. John Miller)
2800 Powder Mill Road
Adelphi, MD 20783-1197
Telephone: (301) 394-5000
DSN 290-5000
FAX: Ext 5410
Email: jmiller@arl

Dr. John D. Molatoris

Lawrence Livermore National Lab
PO Box 808, L-262
Livermore, CA 94500-0808
Telephone: (510) 423-3496
FAX: (510) 422-5844
Email: molitoris1@llnl.gov

Ms. Mary Beth Morris

Naval Surface Warfare Center
Dahlgren Division
NSWC-DD Code B51
Dahlgren, VA 22448-5100
Telephone: (703) 663-8621
DSN 249-8621
FAX: Ext 4253
Email:
mbmorris@tularemia.nswc.navy.mil

Dr. Joel R. Mozer

AF Phillips Lab
Geophysics Directorate
PL/GPAA
29 Randolph Rd.
Hanscom AFB, MA 01731-3010
Telephone: (617) 377-2945
DSN 478-2945
FAX: Ext 2984
Email: mozer@plh.af.mil

Lt Col Ken Nash

Phillips Lab/GPOA
29 Randolph Road
Hanscom AFB, MA 01731-0000
Telephone: (617) 377-3667
DSN 478-3667
FAX: Ext 3661

Mr. Ronald J. Nelson

Science and Technology Corporation
12452 Towner N.E.
Albuquerque, NM 87112-0000
Telephone: (505) 275-6663
FAX: Ext 6663

Lt Brian Newton

Pillips Lab (AFMC)/Atmospheric
Sciences Division
29 Randolph Rd.
Hanscom AFB, MA 01731-3010
Telephone: (617) 377-4729
DSN 478-4729
FAX: Ext 8892

Mr. James R. Norton

Hughes STX Corporation
4400 Forbes Boulevard
Lanham, MD 20706-0000
Telephone: (301) 794-5002
FAX: Ext 7106

Dr. Sean G. O'Brien

Physical Science Laboratory
New Mexico State University
PO Box 30002
Las Cruces, NM 88003-0002
Telephone: (505) 521-9560
FAX: (505) 522-9389/9434
Email: sobrien@psl.nmsu.edu

Mr. Richard J. Okrasinski

Physical Science Laboratory
New Mexico State University
P.O. Box 30002
Las Cruces, NM 88003-0002
Telephone: (505) 522-9496
FAX: Ext 9389
Email: rokras@psl.nmsu.edu

Dr. Montie M. Orgill

Science and Technology Corporation
PO Drawer 250
White Sands Msl Range, NM 88002-0000
Telephone: (505) 521-4353
FAX: (505) 522-9062

Mr. Brian L. Orndorff

U.S. Army Research Laboratory
Battlefield Environment Directorate
ATTN: AMSRL-BE-E
White Sands Msl Range, NM 88002-5501
Telephone: (505) 678-1803
DSN 258-1803
FAX: Ext 2053
Email: borndorf@arl.mil

Mr. William M. Oseles

Technical Solutions, Inc.
PO Box 1148
Mesilla Park, NM 88047-1148
Telephone: (505) 524-2154
FAX: (505) 525-5801

Dr. Clem Z. Ota

Science and Technology Corporation
555 Telshor Boulevard, Suite 200
Las Cruces, NM 88011-0000
Telephone: (505) 521-4353
FAX: (505) 522-9062

Maj Doug Owen

HQ Air Combat Command (ACC)
Weather Division
HQ ACC/DOW
205 Dodd Blvd, Ste 101
Langley AFB, VA 23665-2789
Telephone: (804) 764-8445
DSN 574-8445
FAX: Ext 8455
Email: owend@doymail.acc.af.mill

Mr. Stan Parsons

U.S. Army Research Laboratory
Battlefield Environment Directorate
ATTN: AMSRL-BE-E
White Sands Msl Rng, NM 88002-5501
Telephone: (505) 678-1561
DSN 258-1561

Mr. Jeffrey W. Passner

U.S. Army Research Laboratory
Battlefield Environment Directorate
ATTN: AMSRL-BE-W
White Sands Msl Range, NM 88002-5501
Telephone: (505) 678-3193
DSN 258-3193
FAX: Ext 3385
Email: jpassner@arl.mil

Mr. Wayne L. Patterson

Office of Naval Research
Ocean, Atmosphere, and Space Department
Ballston Tower #1, Rm 428-14
800 North Quincy Street
Arlington, VA 22217-5660
Telephone: (703) 696-7042
DSN 226-7042
FAX: Ext 3390
Email: patterw@onrhq.onr.navy.mil

Mr. Mark R. Perry

Battelle
505 King Avenue
Columbus, OH 43201-0000
Telephone: (614) 424-3532
FAX: Ext 3776
Email: perrym@battelle.org

Dr. William A. Peterson

U.S. Army Research Laboratory
Battlefield Environment Directorate
ATTN: AMSRL-BE-A
White Sands Msl Range, NM 88002-5501
Telephone: (505) 678-1465
DSN 258-1465
Email: wpeterso@arl.mil

CMSgt Robert W. Platt

Det 1, 33STRS
Combat Weather Facility
Bldg 91027
595 Independence Road
Hurlburt Field, FL 32544-5618
Telephone: (904) 884-5493
DSN 5779-5493
FAX: Ext 5503

Dr. Stephan Rahm

German Aerospace Establishment DLR
Institut fur Optoelektronik
PO BOX 11 16
D82230
WESSLING GERMANY
Telephone: 8153-28-2564
FAX: Ext 8153-28-2243

Capt Phil Reding

Detachment 4, HQs, Air Weather Service
595 Independence Road, Bldg 91027
Hurlburt Field, FL 32544-5618
Telephone: (904) 884-5730
DSN 527-5730
FAX: Ext 5503

Maj Michael Remeika

Phillips Lab (AFMC)
Atmsopheric Sciences Division
29 Randolph Rd.
Hanscom AFB, MA 01731-3010
Telephone: (617) 337-3497
DSN 478-3497
FAX: Ext 8892
Email: remeika@plh.af.mil

Maj Peter Rice

HQ Air Weather Service
AWS/XOO
102 W. Losey St, Room 105
Scott AFB, IL 62225-5206
Telephone: (618) 256-4110/221
DSN 576-4110/221
FAX: Ext 6300

Col Gerald F. Riley

Headquarters, Air Weather Service
Asst Dir of Technology, Plans & Progs
102 W Losey St., Rm 105
Scott AFB, IL 62225-5206
Telephone: (618) 256-3363 x251
DSN 576-3363 x251
FAX: Ext 6300

Lt Col John R. Roadcap

Phillips Laboratory (PL/WE)
3550 Aberdeen Avenue, SE
Kirkland AFB, NM 87117-5776
Telephone: (505) 846-4722
DSN 246-4722
FAX: Ext 4394

Mr. Ronald L. Rodney

Wright Research and Development Center
WL/DOWA, Bldg 22, Ste 2
ATTN: WRDC/WEA
2690 C Street
Wright Patterson AFB, OH 45433-7409
Telephone: (513) 255-1978
DSN 785-1978
FAX: Ext 7552
Email: rodneyrlcaa.wl.wpafb.af.mil

Dr. J. Michael Rollins

Science and Technology Corporation
555 Telshor Blvd., Suite 200
Las Cruces, NM 88011-0000
Telephone: (505) 521-4353
FAX: (505) 522-9062

Maj Arnold Rothlein

Battlefield Environment Directorate
ATTN: AMSRL-BE-W
White Sands Msl Range, NM 88002-5501
Telephone: (505) 678-1339
DSN 258-1339
FAX: Ext 3385
Email: arothlei@arl.mil

Mr. Keith D. Sashegyi

Naval Research Laboratory
Remote Sensing Physics Branch
Code 7225
WASH, DC 20375-5351
Telephone: (202) 767-3350
FAX: Ext 9130
Email: sashegyi@atmos.nrl.navy.mil

Mrs. Barbara Sauter

U.S. Army Research Laboratory
Battlefield Environment Directorate
ATTN: AMSRL-BE
White Sands Msl Range, NM 88002-5501
Telephone: (505) 678-2840
DSN 258-2840
FAX: Ext 2432
Email: bsauter@arl.mil

Mr. David P. Sauter

U.S. Army Research Laboratory
Battlefield Environment Directorate
ATTN: AMSRL-BE-W
White Sands Msl Range, NM 88002-5501
Telephone: (505) 678-2078
DSN 258-2078
FAX: Ext 3385
Email: dsauter@arl.mil

Maj Kevin D. Scasny

2nd Weather Flight
Bldg 130, Anderson Way
Ft. McPherson, GA 30330-5000
Telephone: DSN 527-2234
FAX: Ext 2744

Mr. Warren C. Schimpf

Hercules Incorporated
Research Center
500 Hercules Road
Wilmington, DE 19808-1599
Telephone: (302) 995-3389
FAX: Ext 4612

Mr. Dennis R. Schlegel

U.S. Army Research Laboratory
Battlefield Environment Directorate
ATTN: AMSRL-BE-E
White Sands Msl Rng, NM 88002-5501
Telephone: (505) 678-1561
DSN 258-1561
FAX: Ext 7623
Email: dschlege@arl.mil

Mr. Jose M. Serna

Physical Science Laboratory
New Mexico State University
PO Box 30002
Las Cruces, NM 88003-0002
Telephone: (505) 522-9333
FAX: Ext 9434
Email: jsern@psl.nmsu.edu

Dr. Richard C. Shirkey

U.S. Army Research Laboratory
Battlefield Environment Directorate
ATTN: AMSRL-BE-S
White Sands Msl Range, NM 88002-5501
Telephone: (505) 678-5470
DSN 258-5470
FAX: Ext 8366
Email: rshirkey@arl.mil

Dr. David Smarsh

WL/DOW, Bldg 45
2130 Eighth St, STE 11
Wright Patterson AFB, OH 45433-9552
Telephone: (513) 255-5496
DSN 785-5496
FAX: Ext 7045
Email: wl/dow@wrdc.wpafr.af.mil

Capt Bradley P. Smith

ODDDRE 3
ATTN: E&LS (Rm 3D129)
3080 Defense Pentagon
WASH, DC 20301-3080
Telephone: (703) 695-9604
DSN 225-9604
FAX: (703) 693-7042
DSN 223-7042

Mr. Robert W. Smith

TECOM
Ft. Belvoir Meteorological Team
ATTN: AMSRL-RD-NV-VISP
10221 Rubeck Rd, Ste 430
Fort Belvoir, VA 22060-5506
Telephone: (703) 704-1762
DSN 654-2574
FAX: Ext 3083
Email: bsmith@nvl.army.mil

MSgt Timothy J. Smith

OL-N, HQ AWS
U.S. Army Research Laboratory
Battlefield Environment Directorate
ATTN: AMSRL-BE-W
White Sands Msl Range, NM 88002-5501
Telephone: (505) 678-8148
DSN 258-8148
FAX: Ext 3385
Email: tsmith@arl.mil

Dr. Donald E. Snider

U.S. Army Research Laboratory
ARL Dir Staff Military Oper &
Analysis ATTN: AMSRL-MO-TB
2800 Powder Mill Road
Adelphi, MD 20783-1145
Telephone: (301) 394-5166
DSN 290-4489
FAX: Ext 4889
Email: dsnider@arl.mil

Dr. Peter Soliz

Applied Sciences Laboratory, Inc.
PO Box 92858
Albuquerque, NM 87199
Telephone: (505) 823-2920
FAX: Ext 1952
Email: zilospx@rt66.com

Mr. Roberto F. Soto

Science and Technology Corporation
555 Telshor Blvd, Suite 200
Las Cruces, NM 88011-0000
Telephone: (505) 521-4353
FAX: (505) 522-9062

Mr. John Spalding

Physical Science Laboratory
New Mexico State University
PO Box 30002
Las Cruces, NM 88003
Telephone: (505) 522-9298
FAX: Ext 9389
Email: spalding@psl.nmsu.edu

Lt Col Richard St. Pierre

HQDA, DAMI-BSS
Room 2B457
1000 Army Pentagon
Washington, DC 20310-1067
Telephone: (703) 695-5509
DSN 225-5509
FAX: (703) 697-8849
DSN 227-8849

Mr. Ralph Steinhoff

U.S. Army Research Laboratory
Battlefield Environment Directorate
ATTN: AMSRL-BE-A
White Sands Msl Range, NM 88002-5501
Telephone: (505) 678-4481
DSN 258-4481
Email: rsteinho@arl.mil

Capt Kevin L. Stone

U.S. Air Force Environmental
Technical Applications Center
859 Buchanan St., Room 424
Scott AFB, IL 62225-5116
Telephone: (618) 256-3743
DSN 576-3743
FAX: Ext 3772
Email: syskls@thunder.safb.af.mil

Mr. James W. Surhigh

STRICOM
ATTN: AMCSTI-EI
12350 Research Parkway
Orlando, FL 32826-3276
Telephone: (407) 380-4351
DSN 960-4351
FAX: Ext 4258

Dr. Robert A. Sutherland

U.S. Army Research Laboratory
Battlefield Environment Directorate
ATTN: AMSRL-BE-E
White Sands Msl Range, NM 88002-5501
Telephone: (505) 678-4520
DSN 258-4520
FAX: Ext 2432
Email: rsutherl@arl.mil

Mr. Richard J. Szymber

U.S. Army Research Laboratory
Battlefield Environment Directorate
ATTN: AMSRL-BE
White Sands Msl Range, NM 88002-5501
Telephone: (505) 678-5236
DSN 258-5236
FAX: Ext 2432
Email: rszymber@arl.mil

Dr. Amos Talmi

AT Scientific Systems, Ltd.
Poria Ellit, Lower Gallil 15208
ISRAEL
Telephone: 972-6-752275
FAX: Ext 751147

Mr. Paul Tattelman

Geophysics Directorate
Phillips Laboratory
ATTN: PL/GPAA
29 Randolph Rd
Hanscom AFB, MA 01731-0000
Telephone: (617) 377-5956
DSN 478-5956
FAX: Ext 2984

Mr. Charles S. Taylor

U.S. Army Field Artillery School/DCD
ATTN: ATZF-TA
Fort Sill, OK 73503-5600
Telephone: (405) 442-2352
DSN 639-2352
FAX: Ext 4802

Mr. David D. Telles

Physical Science Laboratory
New Mexico State University
P.O. Box 30002
Las Cruces, NM 88003-0002
Telephone: (505) 522-9371
FAX: Ext 9434
Email: davidt@psl.nmsu.edu

Dr. Lennart Thaning

National Defence Research
Establishment
Department of NBC Defence
S-901 82 Umea
SWEDEN
Telephone: 4690 106650
FAX: Ext 106800
Email: thaning@ume.foa.se

Ms. Jill C. Thompson

U.S. Army Research Laboratory
Battlefield Environment Directorate
ATTN: AMSRL-BE-E
White Sands Msl Range, NM 88002-5501
Telephone: (505) 678-2434
DSN 258-2434
Email: jthompso.arl.mil

Mr. Michael Thurston

U.S. Army Research Laboratory
Battlefield Environment Directorate
ATTN: AMSRL-BE-E
White Sands Msl Range, NM 88002-5501
Telephone: (505) 678-1585
DSN 258-1585
Email: mthursto@arl.mil

Mr. Andrew R. Tooth

British Aerospace (Operations) Ltd.
Sowerby Research Centre
FPC 267, P.O. Box 5
Filton, Bristol
UNITED KINGDOM
Telephone: 44-272-36-3095
FAX: Ext 3733
Email: andy.tooth@src.bae.co.uk

Mr. Mario Torres

STC
Battlefield Environment Directorate
ATTN: AMSRL-BE-S
White Sands Msl Range, NM 88002-5501
Telephone: (505) 678-3280
DSN 258-3280
FAX: Ext 8366
Email: mtorres@arl.mil

Mr. Arnold D. Tunick

U.S. Army Research Laboratory
Battlefield Environment Directorate
ATTN: AMSRL-BE-S
White Sands Msl Range, NM 88002-5501
Telephone: (505) 678-4832
DSN 258-4832
FAX: Ext 8366
Email: atunick@arl.mil

Lt Col Chuck Tuttle

Combined Arms Command
Staff Wx Officer
USACAC
ATTN: ATZL-CAW-E
Ft. Leavenworth, KS 66027-5300
Telephone: (913) 684-4897
DSN 552-4897
FAX: Ext 3945
Email: tuttlec@leav-emh.army.mil

Mr. Johathan David Turton

Meteorological Office
(Defence Services)
Room 126, London Road
Bracknell, Berks, RG12 2SZ
UNITED KINGDOM
Telephone: (44) 344-856991
FAX: Ext 856967
Email:
acsteele@email.meto.govt.uk

Capt David Valler

HQ AWS/XOX
102 W. Losey St., Room 105
Scott AFB, IL 62225-5206
Telephone: (618) 256-5631 x442
DSN 576-5631 x442
FAX: Ext 6306
Email: valler@hqaws.safb.af.mil

Capt Glenn E. Van Knowe

USAFETAC/SYT
859 Buchanan St
Scott AFB, IL 62225-5116
Telephone: (618) 256-4107
DSN 576-4107
FAX: Ext 3772
Email: sytgvk@thunder.safb.af.mil

Ms. Gail T. Vaucher

Science and Technology Corporation
PO Box 250
White Sands Msl Rnge, NM 88002-0250
Telephone: (505) 679-5078
DSN 258-5078
FAX: Ext 5228

Mr. Don R. Veazey

Directorate Executive
U.S. Army Research Laboratory
Battlefield Environment Directorate
ATTN: AMSRL-BE
White Sands Msl Range, NM 88002-5501
Telephone: (505) 678-1225
DSN 258-1225
FAX: Ext 1230
Email: dveazey@arl.mil

SSgt Antonio C. Vieira

12th Air Support Operations Squadron
Bldg 11210 Slewitzke Rd Biggs AAF
Ft. Bliss, TX 79918-5000
Telephone: (915) 568-8702/8409
DSN 978-8702
FAX: Ext 8945

Dr. Christian Von Rusten

German Military Geophysical Office
Mont Royal
D-56841 Traben-Trarbach
GERMANY
Telephone: 6541-18-349
FAX: Ext 296

Mr. Arnold E. Wade

U.S. Army Research Laboratory
Battlefield Environment Directorate
ATTN: AMSRL-BE-W
White Sands Msl Range, NM 88002-5501
Telephone: (505) 678-1761
DSN 258-1761
FAX: Ext 3385
Email: awade@arl.mil

Mr. Richard L. Wagner

DG Met Oc
National Defence Headquarters
Vanier Building, 3rd Floor
222 Nepean Street
Ottawa, Ontario K1A 0K2
CANADA
Telephone: (613) 996-3659
DSN 846-3659
FAX: Ext 4197
Email: ad180@freenet.carleton.ca

Dr. Philip Walker

Naval Postgraduate School
Physics Department
CODE PH
833 Dyer Road, Room 105
Monterey, CA 93943-5117
Telephone: (408) 656-2674
DSN 878-2674
FAX: Ext 2834
Email: walker@physics.nps.navy.mil

Mr. Kenneth Walters, Sr.

U.S. Air Force Environmental
Technical Applications Center
(USAFETAC)
859 Buchanan Street
Scott AFB, IL 62225-5116
Telephone: (618) 256-3465
DSN 576-3465
FAX: Ext 3772

Mrs. Sandra K. Weaver

Wright Lab Staff Meteorology
WL/DOWA, Bldg 22
2690 C Street, Ste 2
Wright Patterson AFB, OH 45433-7409
Telephone: (513) 255-6697
DSN 785-6697
FAX: Ext 7552

ORR Harald Weber

German Military Geophysical Office
(GMGO)
Mont Royal
D-56841 Traben-Trarbach
GERMANY
Telephone: 6541-18-345
FAX: Ext 296

Mr. Michael E. Wells

Wells Consulting, Inc
3812 Gelnmont Drive
Fort Worth, TX 76133-0000
Telephone: (817) 292-2378
FAX: Ext 2378

Mr. Franz Westermeier

U.S. Army Engineer School
ATTN: ATSE-CDS-T
Fort Leonard Wood, MO 65473-6640
Telephone: (314) 596-0131 x7350
DSN 676-7350
FAX: (314) 563-4089
DSN 676-4089

Dr. Alan E. Wetmore

U.S. Army Research Laboratory
Battlefield Environment Directorate
ATTN: AMSRL-BE-S
White Sands Msl Range, NM 88002-5501
Telephone: (505) 678-5563
DSN 258-5563
FAX: Ext 2432
Email: awetmore@arl.mil

Capt Matthew R. Williams

U.S. Air Force Environmental
Technical Applications Center
859 Buchanan Street
Scott AFB, IL 62225-5438
Telephone: (618) 256-5944
DSN 576-5944
FAX: Ext 3772
Email: docmrw@thunder.safb.af.mil

Mr. Young P. Yee

U.S. Army Research Laboratory
Battlefield Environment Directorate
ATTN: AMSRL-BE-E
White Sands Msl Range, NM 88002-5501
Telephone: (505) 678-6468
DSN 258-6468
Email: yyee@arl.mil

Col Karl Zeller

USAF/XOW (MA)
3717 NCR 25E
Bellevue, CO 80512-0000
Telephone: (303) 498-1238
FAX: (303) 498-1010

AUTHORS INDEX

Auvermann, Harry J. 75
Ayres, Scarlett D. 25, 367, 391
aufm Kampe, Welfhart 519

Barish, Stephen T. 141
Berchoff, Donald H. 161
Blanco, Abel J. 231
Bleiweiss, Max P. 273, 501
Bowers, James F. 47
Brand, Samson 97

Carrow, William W. 309
Carter, Gary J. 133
Carter, Roger G. 47
Causey, Michael T. 291
Chesley, Carl H. 443
Chintawongvanich, Prasan 487
Cionco, Ronald M. 331
Cogan James L. 211, 221, 449
Coleman, George N. III 141
Cox, Robert M. 155
Creegan, Edward D. 221

Davis, Peter F. 37
Davis, Roger E. 511
DeAntonio, Michael D. 75, 475
Donahue, Christopher A. 181
Dreksler, Steven B. 97
Drexler, James J. 545
Dumais, Robert E. Jr. 107, 117, 413

Eaton, Frank D. 545, 553
Eis, Kenneth E. 65
Elrick, John R. 255
Endlich, Robert W. 107, 355

Falvey, Robert J. 57
Finlinson, J. 85
Flowers, Wayne 553
Foreman, Dale U. 495
Fox, John R. 487, 569

Gammill, Troy D. 301
Garvey, Dennis M. 569
Giever, John C. 3
Gillespie, James 467
Gillespie, Patti 467
Goedecke, George H. 75
Goroch, Adreas 97
Gutman, William M. 301, 495

Hall, Charles S. 401
Hansen, Patsy S. 3
Hardwick, Robert E. 133
Harms, Dewey E. 161
Harris, James E. 107
Hatch, William H. 545, 553, 563
Henmi, Teizi 107, 245, 413
Hines, John R. 545, 553
Hodur, Richard M. 125
Hoidale, Glenn 553
Hoock, Donald W. 3
Howerton, Roger A. 501
Humphrey, James L. 133
Hutchinson, Timothy D. 161

Johnson, Odell M. 211
Johnston, David J. 281

Keith, Chan W. 191, 201
Kennedy, Bruce W. 569
Kessler, Damian 569
Knapp, David I. 107, 117
Kantrowitz, Frank T. 301, 495
Kunschke, Tod M. 141

LaMotte, Steve 25
Lanicci, J. M. 155
Larson, Dick R. 433
Lee, Martin E. 107, 245
Lines, Todd R. 529
Littell, Dewitt 221

Madala, Rangarao V. 15
Manning, Joseph L. 401
Massie H. L. Jr. 155
Mathews, L. A. 85
Mazurowski, Alfonse J. 171
McCarthy, Sean 433
McLaughlin, Scott 553
Measure, Edward M. 221, 433
Merritt, D. 221
Millard, J. Brad 367
Miller, David R. 331
Moran, James G. 569

Northrup, James 545

O'Brien, Sean G. 3, 381
Okrasinski, Richard J. 535, 569

Parker-Sedillo, Linda 553
Passner, Jeffrey W. 423
Pena, Robert G. 185
Perry, Mark R. 291
Peterson, William 263
Pridgen, James R. 569

Rahm, Stephan 323
Raman, Sethu 15
Rollins, Michael J. 263, 273
Rouse William G. 281, 291
Ruggiero, Frank H. 15
Runk, Kim J. 151

Sashegyi, Keith D. 15
Sauter, David P. 443
Savage, Richard 569
Schmidlin, Francis 433
Seagraves, Mary Ann 211
Serna, Jose M. 569
Sheets, Doug 391
Simon, M. 221
Simon, A. 221
Siniard, Sheri M. 401
Smith, Thomas J. 191
Smith, Timothy J. 117, 245
Smith, Robert W. 309
Spillane, Andrew R. 443
Steele, Gary P. 569
Stone, Kevin L. 185
Sutherland, Robert 345, 367, 391, 511
Szymber, Richard J. 211, 345, 449

Tunick, Arnold 535
Turton, Jonathan D. 37

Vaucher, Gail T. 355

Walker P. L. 85
Walters, Kenneth R. Sr. 181
Watson, Thomas B. 47
Weaving, William S. 161
Weber, Harald 519
Weber, B. 221
Weems, Danforth C. 107
Welsh, D. 221
Werner, Charles 323
Weurtz, D. 221
Whicker, George A. 133
Williams, Matthew R. 462
Wilson, Tim G. 37
Wolfe, D. 221
Wollard, Jahna L. 133
Woodford, Richard A. 201

Yarbrough, James 221
Yee, Young P. 345, 511, 529

Zapotocny, John V. 151

*U.S. GOVERNMENT PRINTING OFFICE: 1995-774-543/45003